Study of the influence of americium on thermodynamic and structural properties of (U,Pu)O2±x mixed oxides

Pauline Fouquet-Métivier

THESE DE DOCTORAT

NNT : 2022UPASF034

université PARIS-SACLAY

Study of the influence of americium on thermodynamic and structural properties of $(U,Pu)O_{2\pm x}$ mixed oxides

Etude de l'influence de la présence d'américium sur les propriétés thermodynamiques et structurales des oxydes mixtes $(U,Pu)O_{2\pm x}$

Thèse de doctorat de l'université Paris-Saclay

École doctorale n° 571, Sciences Chimiques : Molécules, Matériaux, Instrumentation et Biosystèmes (2MIB)
Spécialité de doctorat : Chimie
Graduate School : Chimie. Référent : Faculté des sciences d'Orsay

Thèse préparée dans l'unité de recherche **Service de la Corrosion et du Comportement des Matériaux dans leur Environnement (Université Paris-Saclay, CEA)**, sous la direction de **Christine GUENEAU**, Directrice de recherche, et le co-encadrement de **Philippe MARTIN**, Ingénieur Chercheur

Thèse soutenue à Paris-Saclay, le 02 juin 2022, par

Pauline FOUQUET-METIVIER

Composition du Jury

Gianguido BALDINOZZI Directeur de recherche, Centrale Supélec, Université Paris-Saclay	Président
Yann LE PETITCORPS Professeur, Université de Bordeaux	Rapporteur & Examinateur
Hans SEIFERT Professeur, Karlsruhe Institute of Technology (Allemagne)	Rapporteur & Examinateur
Dario MANARA Chargé de recherche, JRC-Ispra, European Commission (Italie)	Examinateur
Christine GUENEAU Directrice de recherche, CEA, Université Paris-Saclay	Directrice de thèse

Acknowlegments

Almost four years after I was accepted to do this PhD, this great adventure has come to an end. What has been a roller coaster, with lots of ups and downs, would not have been the same without several people who supported me during each step.

First, I would like to thank Pr. Hans Seifert, Pr. Yann Le Petitcorps, Pr. Gianguido Baldinozzi and Dr. Dario Manara for accepting to review this PhD work, for the time taken to read the manuscript and for their valuable insights given during the defense.

Many thanks to you, Christine, for your support during these years. I know it has not always been easy, I went through hard phases of doubts, but you were always there to cheer me up and motivate me to keep fighting. I grew up during these years with your help, professionally and personally, and I will keep only the best in mind.

My deepest gratitude to you Philippe, for handling me almost daily during this tough period that has been this PhD. Thank you for pushing me, staying on my side and supporting me when I needed it the most. I know I was stubborn many times (if not all the time) but you remained patient and calm and never gave up during all the downs we had in this thesis. I could not have wished for a better supervisor and I will always be grateful for your help.

I would also like to thank my former colleagues of the LCC/LMAT of ATALANTE who shared part of my PhD or all of it during these years. Many thanks to my two ex-chefs de labo, Loïc Marchetti and Emmanuel Excoffier, for their continuous fights for me to be able to do this PhD in good conditions. Thank you to Romain L., Jean-Robert, Elodie, Camille, Méghan, Lise, Stéphanie, Mathilde for being the best technicians team and always being supportive. Thank you Florent for always being available to discuss and give an opinion on the results. Thank you to all the non-permanents, Mathieu, Axel, Julie, Orhun and Rafael, for making it lighter to work there and for all the moments we shared together. Good luck for the future and all the best.

Many thanks to all the people of the LM2T Saclay for welcoming me during my various stays and for their encouragements and interest during this PhD.

My stay at the JRC Karlsruhe was turbulent because of Covid but I am grateful for this big opportunity I had to work there. Thank you to Rudy Konings, Ondrej Benes, Davide Robba, Luka Vlahovic and Dragos Staicu for welcoming me, their help with the experiments and the fruitful discussions that enriched my PhD.

Life in Karlsruhe would not have been the same without them, probably because of the many beers we shared. Many thanks to Emanuele, Luana and Tommaso, Concettina, Mathieu, Luca B. and the girls of the football team. Thank you to Guilhem for immediately welcoming me in Saclay and Karlsruhe and for all the other moments shared in Bagnols during these covid times.

I had the best office partner in Marcoule, with whom I shared coffee breaks but mainly a lot of food! Many thanks Marie-Margaux, I know it has not always been easy but we stood together and we are still here. All the best for you future Dr., you deserve it.

Thank you Fanny, for the time spent together and for showing me what taking care of a teenager looks like ! Thank you for always being there when I needed it.

Seven years later, after Montpellier, an internship together in Karlsruhe, Marcoule in the same lab and a lot of moments and chats together outside of work, thank you Laetitia. I should not follow you anymore after this, I promise!

I met many new people during this PhD but I would like to thank older friends for their support, their patience and their encouragements. Thank you to my engineering school friends (the Spys, Antoine, Cec, …), my complaining group (Maureen, Mogo and Rachel) and my friends from childhood (Gautier, Charlotte, Camille, Louise, Hugo, Kévin).

Tommy, grazie di tutto, e più di tutto grazie di esserci. You know already everything I need to say, so thank you.

Et enfin, merci à ma famille d'avoir toujours été là et surtout très patients pendant ces dures années. Merci d'avoir toujours essayé de comprendre ce que je fais, au moins les grandes lignes! Merci à ma mère, ma sœur et mon frère et à notre étoile, toujours avec nous.

My apologies if I forgot anyone, the list is long and thank you again, you all contributed to the success of this PhD!

CONTENTS

Contents **5**
List of figures **9**
List of tables **17**
Glossary **19**
1. Introduction **21**
2. State of the art of the U-Pu-Am-O system **27**
2.1. Phase diagrams 27
2.1.1. Binary systems 27
2.1.2. Ternary systems 30
2.2. Structural data 33
2.2.1. Introduction to crystal structures 34
2.2.2. Lattice constants at room temperature 37
2.2.3. Thermal expansion 46
2.3. Thermodynamic properties 52
2.3.1. Enthalpy, entropy, heat capacity 52
2.3.2. Oxygen potential 59
2.3.3. Melting behaviour 66
2.4. Thermodynamic models 72
2.4.1. Binary systems 72
2.4.2. Ternary systems 74
2.5. Conclusion 76
3. Materials and methods **79**
3.1. CALPHAD method 79
3.1.1. Principles 79
3.1.2. Models for the U-Pu-Am-O system 82
3.2. Materials of interest 84
3.2.1. $Pu_{1-z}Am_zO_{2-x}$ oxides 84
3.2.2. $U_{1-y-z}Pu_yAm_zO_{2\pm x}$ oxides 85
3.3. Experimental techniques 88
3.3.1. Room temperature X-Ray Diffraction (XRD) 88
3.3.2. Scanning Electron Microscopy (SEM) 89
3.3.3. Electron Probe Microanalyser (EPMA) 89
3.3.4. X-ray Absorption Spectroscopy (XAS) 90
3.3.5. High temperature X-Ray diffraction 92
3.3.6. Laser heating technique 94
3.3.7. Drop calorimetry 97
3.3.8. ThermoGravimetric Analysis (TGA) 98
3.4. Conclusion 100
4. Experimental investigation of the Pu-Am-O system **103**
4.1. Chemical and structural investigation at room temperature 104
4.1.1. Chemical and isotopic compositions 104
4.1.2. Macro- and microstructure 104
4.1.3. Crystal structure 105
4.1.4. Cationic charge distribution 110
4.1.5. Conclusion 114
4.2. Solid state phase equilibria 115
4.2.1. Experimental determination 115
4.2.2. Results and discussion 115
4.2.3. Conclusion 125
4.3. Phase equilibria in $Pu_{0.77}Am_{0.23}O_{2-x}$ at 1673 K 126

4.3.1. Oxygen potential data ... 126
4.3.2. Phase equilibria ... 130
4.3.3. Conclusion ... 132
4.4. Solid/Liquid phase transitions in $Pu_{0.49}Am_{0.51}O_{2-x}$ ... 133
4.4.1. Experimental procedure ... 133
4.4.2. Results and discussion ... 134
4.4.3. Conclusion ... 140
4.5. Conclusion ... 140
5. Experimental investigation of the U-Pu-Am-O system ... 143
5.1. Chemical and structural investigations at room temperature ... 144
5.1.1. Chemical and isotopic compositions ... 144
5.1.2. Phases and crystal structure ... 146
5.1.3. Cationic charge distribution ... 148
5.1.4. Conclusion ... 152
5.2. Lattice thermal expansion ... 153
5.2.1. Experimental determination ... 153
5.2.2. Results ... 153
5.2.3. Discussion ... 156
5.2.4. Conclusion ... 161
5.3. Enthalpy increment and heat capacity ... 161
5.3.1. Experimental procedure ... 161
5.3.2. Results ... 162
5.3.3. Discussion ... 166
5.3.4. Conclusion ... 168
5.4. Solid/Liquid phase transitions ... 169
5.4.1. Experimental procedure ... 169
5.4.2. Results ... 169
5.4.3. Discussion ... 178
5.4.4. Conclusion ... 189
5.5. Conclusion ... 190
6. Thermodynamic modelling of the U-Pu-Am-O system ... 193
6.1. Re-assessment of the Pu-O system ... 193
6.1.1. Selected data ... 193
6.1.2. Gibbs energy of the liquid phase ... 194
6.1.3. Results ... 194
6.1.4. Conclusion ... 196
6.2. Re-assessment of the solid/liquid phase transitions in the U-Pu-O system ... 196
6.2.1. Selected data ... 196
6.2.2. Gibbs energy of the liquid phase ... 197
6.2.3. Results ... 198
6.2.4. Discussion on the solid/liquid phase transitions ... 200
6.2.5. Conclusion ... 209
6.3. Thermodynamic assessment of the Pu-Am-O system ... 210
6.3.1. Selected experimental data ... 210
6.3.2. Re-assessed parameters ... 211
6.3.3. Results ... 212
6.3.4. Comparison with the experimental data obtained in this work ... 215
6.3.5. Conclusion ... 221
6.4. Thermodynamic investigation of the U-Pu-Am-O system ... 222
6.4.1. Cationic site fractions at room temperature ... 222
6.4.2. Enthalpy and heat capacity ... 223
6.4.3. Solid/liquid phase transitions ... 226
6.4.4. Oxygen potential data ... 232
6.4.5. Conclusion ... 233

6.5. Conclusion.....234
7. General conclusion and perspectives 237
References 242
Appendixes..... 254
Résumé - Etude de l'influence de la présence d'américium sur les propriétés thermodynamiques et structurales des oxydes mixtes (U,Pu)$O_{2\pm x}$ 268

LIST OF FIGURES

Figure 1-1: Energy consumption by source in the world between 1960 and 2019 [1]. 21
Figure 1-2: Schematic representation of a Sodium Fast Reactor. 21
Figure 1-3: Fuel pellets of $U_{0.71}Pu_{0.28}Am_{0.01}O_{1.98}$ for SFR (height: 11 mm – diameter: 5.4 mm). 22
Figure 1-4: Schematic representation of the CALPHAD method [6]. 23
Figure 2-1: (a) Calculated U-O phase diagram from Guéneau *et al.* [13], (b) detailed section from 1.9 < O/M < 2.4 after Higgs *et al.* [15], compared to available experimental data. L and G stand for liquid and gas, respectively. 27
Figure 2-2 : (a) Calculated Pu-O phase diagram, (b) detailed section from 1.38 < O/M < 2.13, using the model developed by Guéneau *et al.* in 2011 [6]. The dashed lines on (b) represent the model of Guéneau *et al.* of 2008 [23]. 28
Figure 2-3 : Calculated Am-O phase diagram using the model developed by Epifano *et al.* [28]. 29
Figure 2-4 : Partial isothermal section at 298 K of the U-Pu-O phase diagram [31]. 30
Figure 2-5 : Calculated U-Pu-O phase diagram at 473 K, with a detailed section from 0.60 < x(O) < 0.70, using the model developed by Guéneau *et al.* [6]. 30
Figure 2-6 : Isothermal sections at 473, 673 and 873 K of the U-Pu-O phase diagram focusing on the UO_2-PuO_2-Pu_2O_3 domain, for an O/M ratio ranging from 1.50 to 2.0 [36]. 32
Figure 2-7 : Calculated Pu-Am-O phase diagram at 1273 K, using the model developed by Gotcu-Freis et al. [26]. 32
Figure 2-8 : Calculated isothermal section at 300 K of the U-Am-O phase diagram, with a zoom on the oxide domain (right), using the model of Epifano [28]. 33
Figure 2-9 : MO_2 fluorite structure with metals and oxygen atoms in grey and green, respectively. 34
Figure 2-10: Representation of the 2:2:2 Willis cluster. The corners of the cubes are the normal sites for oxygen atoms. The cluster contains two O' (a), two O'' (b) and two oxygen vacancies (c) [49]. 35
Figure 2-11 : A-M_2O_3 sesquioxide structure with plutonium atoms in black and oxygen atoms in grey [56]. 35
Figure 2-12 : Variations in the lattice parameter of $U_{1-y}Pu_yO_{2.00}$ mixed oxides as a function of the Pu content at room temperature, extracted from Vauchy et al. [79]. 39
Figure 2-13 : Variation in the lattice parameter of the fluorite structure of $Pu_{1-z}Am_zO_2$ as a function of the Am content at room temperature (experimental data available in Appendix B from [42], [44], [73], [78], [81], [82]). 40
Figure 2-14 : Variations in the lattice parameter of $U_{1-z}Am_zO_2$ as a function of the Am content at room temperature compared to the available experimental data ([28], [83]–[91]). 40
Figure 2-15 : Variation in the lattice parameters of the fluorite structure of $U_{1-y-z}Pu_yAm_zO_{2.00}$, as a function of the Am content, calculated data from equation **(2.2)** [78]. 41
Figure 2-16: Variation in the lattice parameter as a function of the plutonium content and O/M ratio obtained via Equation (2.5) (Duriez et al.) [76] and Equation (2.6) (Kato and Konashi) [78]. The dashed lines represent the extrapolation of the Equation (2.5) above its validity range [54]. 44
Figure 2-17 : Self-irradiation induced for (a) $U_{1-y}Pu_yO_{2\pm x}$ [107] and (b) $U_{1-z}Am_zO_{2\pm x}$ [109], [110]. 45
Figure 2-18: Heat released during the annealing process for a UO_2 sample doped with 10 wt.% of α-emitters [111]. 46
Figure 2-19 : Comparison of the variation in the lattice parameter of the fluorite structure of AmO_2 measured by Epifano *et al.* [6], Vauchy *et al.* [73] and Fahey *et al.* [118]. 48
Figure 2-20: Comparison of the variation in the lattice parameter as a function of the temperature of UO_2 [112], PuO_2 [116] and AmO_2 [6]. 48
Figure 2-21 : Variation in the lattice parameter of the fluorite structure of $U_{1-y}Pu_yO_2$ as a function of temperature and Pu content [122]. 49
Figure 2-22 : (a) Variation in the lattice parameter of the fluorite structure of $Pu_{1-z}Am_zO_{2-x}$ and (b) of the estimated O/M ratio as a function of temperature and Am content [73]. 50

Figure 2-23 : Variation in the thermal expansion of $U_{0.74}Pu_{0.22}Am_{0.035}Np_{0.005}$ as a function of temperature, compared to UO_2 [124]. 52
Figure 2-24: Heat capacity of various actinides dioxides (Konings et al. [125]) from [131]. 54
Figure 2-25 : Heat capacity of UO_2, PuO_2 and $U_{1-y}Pu_yO_2$ for different plutonium contents [113]. . 56
Figure 2-26 : Molecular Dynamics calculations for (a) enthalpy increments (Cooper et al. [132]) and (b) for heat capacity (Bathellier et al. [140]) for $U_{1-y}Pu_yO_{2\pm x}$ with y = 0, 0.25, 0.5, 0.75, compared to the recommendation of J.K. Fink [128]. 56
Figure 2-27 : Heat capacity of $Pu_{1-z}Am_zO_2$ recommended in the EUROTRANS project [141], compared to the ones of PuO_2 [128], AmO_2 [129], Pu_2O_3 [125] and Am_2O_3 [125]. 57
Figure 2-28: Enthalpy increments measured by Epifano et al. (full symbols) and Vălu et al. (empty symbols) measured for $U_{1-z}Am_zO_{2-x}$ [142], [143]. 58
Figure 2-29 : Heat capacity calculated by Epifano et al. (full symbols) and Vălu et al. (empty symbols) measured for $U_{1-z}Am_zO_{2-x}$ [142], [143]. 59
Figure 2-30 : Variation in the oxygen potential of $UO_{2\pm x}$ as a function of the O/U ratio from 800 to 2700 K, experimental (symbols) and computed values (solid lines) [7]. 60
Figure 2-31 : Variation in the oxygen potential of the plutonium-oxygen system as a function of O/Pu ratio at different temperatures, experimental (symbols, from [144]–[148]) and computed data (solid lines) [23]. 60
Figure 2-32 : Calculated oxygen potential data using the CALPHAD model from Epifano et al. [6] (solid lines) and Gotcu-Freis et al. [26] (dashed lines), compared to experimental data of (a) Chikalla and Eyring [151], (b) Casalta [149] and Otobe et al. [150]. 61
Figure 2-33: Comparison of the oxygen potentials for $UO_{2\pm x}$, PuO_{2-x} and AmO_{2-x} at 1600 K [131]. 62
Figure 2-34 : Oxygen potential of (a) $U_{0.9}Pu_{0.1}O_{2\pm x}$ (Woodley [148] and Markin and McIver [160]) and (b) $U_{0.7}Pu_{0.3}O_{2\pm x}$ (Kato et al. [159]) as a function of the O/M ratio and temperature. The full lines represent the computed values using the model of Guéneau et al. [161] and the dashed lines on (b) were calculated using the point defect model of Kato et al. [159]. 62
Figure 2-35 : Variation in the oxygen potential of $U_{1-y}Pu_yO_{2\pm x}$ at 1873 K with the plutonium and for different O/M ratios [153]. 63
Figure 2-36 : Variation in the oxygen potential of $Pu_{1-z}Am_zO_{2-x}$ as a function of the O/M ratio, the plutonium content and the temperature compared to the experimental values of Osaka et al. [43] and Otobe et al. [44] [26] and the calculated values of Gotcu-Freis et al. [26]. 64
Figure 2-37 : Oxygen potential variation for $U_{0.50}Am_{0.50}O_{2\pm x}$ measured by Bartscher and Sari [167] compared to calculations using the model of F. Lebreton for U-Am-O [46]. 65
Figure 2-38 : Variation in the oxygen potential of $U_{1-y-z}Pu_yAm_zO_{2\pm x}$ at 1273 K with the O/M ratio compared to the experimental values of [29], [37], [145], [148], [155], [167], [168]. 65
Figure 2-39: Experimental melting data available in the literature for $U_{1-y}Pu_yO_{2.00}$ [24], [174], [176], [180], [181], [184]. 69
Figure 2-40 : Solidus/liquidus temperatures of $U_{1-y}Pu_yO_{2\pm x}$ calculated using the CALPHAD model of Guéneau et al. [7], compared to the experimental values of De Bruycker et al. [24], Kato et al. [174] and Lyon and Baily [180]. 70
Figure 2-41 : Solidus temperatures as a function of Am content and atmosphere in $U_{1-z}Am_zO_{2\pm x}$ by Epifano et al. [48] and Prieur et al. [47]. 71
Figure 2-42: Calculated enthalpy increments using the CALPHAD model of E. Epifano [28] for U-Am-O, compared to experimental data obtained by Epifano et al. [143] for z = 0.10, 0.50 and 0.70. 75
Figure 3-1: Representation of the sublattice model. 81
Figure 3-2 : Graphical representation of the CALPHAD method. 81
Figure 3-3: BRUKER D8-Advance with nuclearized sample stage. 88
Figure 3-4: CAMECA SX100 device for EPMA at CEA Marcoule. 89
Figure 3-5: Example of a XAS spectrum of AmO_2 and $U_{0.90}Am_{0.10}O_2$ at the Am L_3 edge by Epifano *et al.* [55]. 91

Figure 3-6: (a) BRUKER D8-Advance diffractometer in its dedicated glovebox, (b) High Temperature MRI Chamber with direct and radiant heating elements, (c) High Temperature chamber during operation [214]. 93
Figure 3-7: Schematic representation of the laser heating setup. 95
Figure 3-8: Drop calorimeter installed in a glovebox at JRC-Karlsruhe (left box: electronics parts) [224]. 97
Figure 3-9: Schematic representation of a SETSYS Evolution [226]. 99
Figure 4-1: SEM images of PuAm 50/50 ((a) and (b)) and PuAm 20/80 ((c) and (d)). 105
Figure 4-2: XRD pattern on powder of (a) PuAm 80/20, (b) PuAm 50/50-A and (c) PuAm 20/80 (*: XRD reflections of the Mo strip). 106
Figure 4-3: Results of the fits for the PuAm 80/20 ((a) and (b)) and PuAm 20/80 ((c) and (d)) using one fluorite phase ((a) and (c)) and two fluorite phases ((b) and (d)). 107
Figure 4-4: Lattice parameters obtained in this work compared to the one at the manufacturing [197] and the Vegard's law between the pure poles PuO_2 and AmO_2. 108
Figure 4-5: XANES spectra collected at the Pu M_4 and Am M_5 edges for the PuAm 80/20, PuAm 50/50 and PuAm 20/80 samples and their references. 111
Figure 4-6: Linear Fitting Combination of PuAm 80/20 sample at (a) Pu M_4 edge and (b) Am M_5 edge. 112
Figure 4-7: Evolution of the diffraction patterns between 26 and 34° 2θ as a function of the temperature for PuAm 80/20. 116
Figure 4-8: Ratio of the intensities between the peak at 31° 2θ and the (111) reflection of the fcc phase as a function of the temperature for the PuAm 80/20 sample. The dashed line represents the average value. 116
Figure 4-9: Variation of the a (in blue) and c (in red) lattice parameters as a function of temperature for A-Pu_2O_3 (dotted lines), A-Am_2O_3 (dashed lines) and PuAm 80/20 (theoretical values, full lines). 118
Figure 4-10: Calculated phase diagram of the Ce-O system (TAF-ID V13), with the cooling path of the HT-XRD experiment in blue for He/H_2 4% with $pO_2 = 10^{-28}$ atm. 119
Figure 4-11: Evolution of the diffraction patterns between 26 and 33° 2θ as a function of the temperature for PuAm 50/50-A, where * corresponds to the peaks already present for PuAm 80/20 and * to the new peaks. 120
Figure 4-12: Zoom on the diffraction pattern acquired at 1873 K for PuAm 50/50-A and possible reflections. 120
Figure 4-13: Successive diffractions patterns obtained at 1873 K (red, blue and green respectively) and 1773 K (pink, turquoise and orange respectively), from front to back, for PuAm 20/80. The * indicates the peaks already present for PuAm 20/80 and PuAm 50/50-A, while * represents the new peaks. 121
Figure 4-14: Evolution of the diffraction patterns between 26 and 33° 2θ as a function of the temperature for PuAm 20/80, where * represents the peaks already observed for PuAm 80/20 and PuAm 50/50-A and * the additional ones for PuAm 20/80. 122
Figure 4-15: Variation of the lattice parameter of the fcc phase as a function of the temperature for PuAm 80/20 (blue), PuAm 50/50-A (green) and PuAm 20/80 (red), and lattice parameters at room temperature before thermal cycle (the uncertainties correspond to the size of the symbol). 124
Figure 4-16: Variation of the mass signal and temperature as a function of time for PuAm 80/20. The orange dashed line corresponds to the temperature signal and the black dashed lines on (b) to the change of oxygen partial pressure. 128
Figure 4-17: Oxygen potentials of PuAm 80/20 at 1673 K as a function of the O/M ratio. 129
Figure 4-18: Diffraction patterns of PuAm 80/20 at 1673 K as a function of the O/M ratio. 130
Figure 4-19: Lattice parameter of the fluorite phase as a function of the global O/M ratio for PuAm 80/20 at 1673 K. 131
Figure 4-20: PuAm 50/50-B sample (a) before shots, with pilot laser used for the alignment and (b) after one shot. 134

Figure 4-21: (a) Thermograms recorded for a PuAm 50/50-B sample for the shots 2, 3 and 4, with the corresponding laser power profile and (b) with a zoom on shot 4. 135
Figure 4-22: Solidus and liquidus temperatures measured for PuAm 50/50-B under Ar. 136
Figure 4-23: Variation of the oxygen partial pressure measured at the exit of the melting chamber throughout the five shots for PuAm 50/50-B. 137
Figure 4-24: Variation of the solidus and liquidus temperatures along the shots as a function of the O/M ratio obtained after each shot. 139
Figure 5-1: Mapping of the Pu distribution (false colours) determined by EPMA on a 1 mm² surface for (a) PHENIX29, (b) CAPRA4 and (c) TRABANT40. The grey spots correspond to porosities, obtained by differences in U and Pu maps. 145
Figure 5-2: Gaussian surface distribution of the Pu content within the PHENIX29 pellet, from [54]. 145
Figure 5-3: XRD pattern on powder of a PHENIX29 sample (*: reflections of the internal Au standard). 147
Figure 5-4: XANES spectra collected at the U M_4, Pu M_4 and Am M_5 edge for the PHENIX29, CAPRA4 and TRABANT40 samples and their references. 149
Figure 5-5: Diffraction patterns acquired at room temperature before the thermal cycle (in red), after the thermal cycle (in blue) and at 1873 K (in green) for the PHENIX29 sample (*: XRD reflections of the Mo strip). 154
Figure 5-6: Iso-intensity map of the (111) peak of the fcc structure between 1873 and 303 K for (a) PHENIX29, (b) CAPRA4 and (c) TRABANT40 samples. 154
Figure 5-7: Variation of the lattice parameters as a function of temperature for (a) PHENIX29, (b) CAPRA4, (c) TRABANT40 samples. The uncertainty on T corresponds to the symbol size. 155
Figure 5-8: Thermal expansions of the matrix for PHENIX29, CAPRA4 and TRABANT40, from 300 to 1873 K, compared to the recommendation of D.G. Martin [10] and Kato et al. [238]. The dashed lines represent the uncertainties on the recommendation of D. G. Martin. 156
Figure 5-9: Variation in the O/M ratio of the samples with temperature (He/H_2 4% + 55 ppm H_2O). 158
Figure 5-10: Thermal expansions of (a) PHENIX29, (b) CAPRA4 and (c) TRABANT40, compared to the recommendation of Kato et al. with varying O/M ratio [238]. 158
Figure 5-11: Lattice parameters of the PHENIX29 and CAPRA4 samples as a function of the temperature. 159
Figure 5-12: Fits of the thermal expansions of PHENIX29, CAPRA4 and TRABANT40 samples. 160
Figure 5-13: Enthalpy increments of a CAPRA4 sample measured in this work, (a) compared to the values of Fink for the pure poles UO_2 and PuO_2 [128], (b) compared to experimental literature values of Kandan et al. [135] and calculated data using the Neumann-Kopp's additivity rule. 164
Figure 5-14: Different fits obtained in this work compared to the experimental values and the fit of Kandan et al. [135]. 165
Figure 5-15: Heat capacity function obtained for the CAPRA4 sample, (a) compared to the values of Fink for the pure poles UO_2 and PuO_2, (b) compared to experimental literature values of Kandan et al. [135] and calculated data using the Neumann-Kopp's additivity rule. 166
Figure 5-16: PHENIX29 sample (a) before shots, (b) after 1 shot, (c) after 4 shots and (d) after 8 shots. 170
Figure 5-17: Thermogram recorded in a laser melting measurement of PHENIX29 in argon for the shot n°7, (a) with the laser power profile in black and (b) zoom on the $T_{solidus}$ range. 170
Figure 5-18: Comparison of the eight successive thermograms recorded for PHENIX29. 171
Figure 5-19: Solidus temperature of PHENIX29 recorded for each shot in Ar. 172
Figure 5-20: Variation of oxygen partial pressure measured at the exit of the melting chamber throughout the eight shots for PHENIX29. 173
Figure 5-21: Variation of the oxygen partial pressure measured at each shot for PHENIX24, CAPRA4, TRABANT40, TRABANT45, PHENIX29-OM and TRABANT40-OM samples (dashed line: residual pO_2). 174

Figure 5-22: Variation of the O/M ratio of PHENIX29 obtained after each shot. 175
Figure 5-23: Variation of the solidus temperature of PHENIX29 as a function of the O/M ratio. 176
Figure 5-24: Variation of the solidus temperature as a function of the O/M ratio for the PHENIX24, PHENIX29, CAPRA4, TRABANT40 and TRABANT45 samples. 177
Figure 5-25: Variation of the solidus temperature as a function of the O/M ratio for the PHENIX29-OM and TRABANT40-OM samples. 178
Figure 5-26: Comparison of the solidus temperatures obtained in this work with the existing literature. 179
Figure 5-27: Variation of the oxygen partial pressure recorded during four successive pre-heating tests on a fresh PHENIX29 sample. 181
Figure 5-28: Solidus temperature of a PHENIX29 sample as a function of the O/M ratio in case where (a) 100 %, (b) 6 % and (c) 2% of the sample is taking up oxygen. 183
Figure 5-29: Simulated temperature gradient among the sample for a pulse of 290 ms at 810 W by Welland et al. [245]. 184
Figure 5-30: Variation of the solidus temperature as a function of the plutonium content (Am content = 0.01 and O/M = 1.990). 185
Figure 5-31: Variation of the solidus temperature as a function of the americium content (Pu content = 0.28-0.30 and O/M = 2.00). 186
Figure 5-32: Variation of the solidus temperature as a function of the O/M ratio for (a) the PHENIX29 and PHENIX29-OM samples and (b) TRABANT40 and TRABANT40-OM samples. 188
Figure 5-33: (a) Map of the Pu content by EPMA, (b) cartography of the T_{2g} position by Raman spectroscopy and (c) cartography of the O/M ratio obtained by combination of (a) and (b), for the PHENIX29 sample [54]. The grey spots correspond to points removed due to a lack of signal. . 189
Figure 6-1: (a) Calculated phase diagram of the Pu-O system as a function of the O/Pu ratio and (b) Zoom on the 1.4 < O/Pu < 2.2 composition range. 195
Figure 6-2: Schematic representation of the model of the liquid phase for the U-Pu-O system. In green: parameters re-assessed in this version. 197
Figure 6-3: Calculated $UO_{1.98}$-$PuO_{1.96}$ phase diagram compared to (a) Guéneau et al. (dashed line) [7] and (b) the selected experimental data of Kato et al. [174] and Böhler et al. [176]. 198
Figure 6-4: Calculated isopleths sections of the U-Pu-O diagram for y = (a) 0.12, (b) 0.20 and (c) = 0.40, compared to the selected experimental data of Kato et al. [185] and Böhler et al. [176]. The experimental uncertainties (± 35 K) are not represented here for sake of clarity. 199
Figure 6-5: Calculated isothermal sections at (a) 1500 K (b) 2500 K and (c) 3000 K of the U-Pu-O system. 200
Figure 6-6: 3D map of the liquidus (in blue) and solidus (in green) temperatures in the U-Pu-O system for 0.60 < x(O) < 0.69, (a) from the $UO_{2\pm x}$ side and (b) the PuO_{2-x} side. 201
Figure 6-7: (a) Solidus temperature and (b) O/M ratio at the congruent melting as a function of the Pu content for $U_{1-y}Pu_yO_{2\pm x}$. 201
Figure 6-8: Configurational entropy of (a) Pu, (b) U, (c) O and (d) total at 3000 K as a function of the O/M ratio for y = 0.50. 203
Figure 6-9: Calculated site fractions at 3000 K as a function of the O/M ratio for y = 0.50. 204
Figure 6-10: 3D map of (a) the Gibbs energy, (b) the enthalpy, (c) the entropy of $U_{1-y}Pu_yO_{2\pm x}$ as a function of the x(O) and x(Pu) at 3000 K (dashed line: UO_2-PuO_2 composition line). 205
Figure 6-11: Calculated (a) solidus temperatures compared to the experimental data of Kato et al. [174] and Böhler et al. [176] and (b) O/M ratio at the solidus temperature as a function of Pu content, under air in red and argon in green. Calculations performed for 5 moles of gas and 3 moles of samples. 206
Figure 6-12: Solidification paths for $U_{0.75}Pu_{0.25}O_{2\pm x}$ as a function of the O/M ratio of the solid phase. Calculated for 5.10^{-4} moles of gas and 1.10^{-4} moles of sample under Air (in red) and Ar (in green) at 0.3 MPa. 208

Figure 6-13: Variation of calculated (a) liquidus temperature and (b) O/M ratio for $U_{0.75}Pu_{0.25}O_{2\pm x}$ as a function of the number of moles of gas reacting with the sample (red: air - argon: green) at 0.3 MPa. 209
Figure 6-14: Schematic representation of the model of the MO_{2-x} phase for the Pu-Am-O system. 212
Figure 6-15: (a) Ternary Pu-Am-O phase diagram at 1273 K obtained with the re-assessment performed in this work, (b) section for 1.5 < O/M < 2.1 compared to the experimental data of Miwa et al. [42]. 213
Figure 6-16: Isopleth section of $Pu_{0.91}Am_{0.09}O_{2-x}$ compared to the experiments of Miwa et al. [42]. 213
Figure 6-17: Oxygen potential data calculated using the updated model with the formed phases (domains 1, 2, 3), compared to the experimental data of (a) Osaka et al. [29] and Otobe et al. [30] and (b) Matsumoto et al. [31]. 214
Figure 6-18: Calculated phase diagram of the Pu-Am-O system at 300 K, with the experimental points determined in Chapter 4 – section 4.1. 216
Figure 6-19: Variation of the O/M ratio as a function of temperature for the PuAm 80/20 sample in equilibrium with air. The dashed line corresponds to the O/M ratio determined experimentally in Chapter 4 – section 4.1.4. 217
Figure 6-20: Site fractions calculated for $Pu_{0.77}Am_{0.23}O_{2-x}$ at (a) 300 K and (b) 2250 K, compared to the experimental values obtained by XANES for the PuAm 80/20 sample. The experimental uncertainties correspond to the size of the symbols (± 0.01). 218
Figure 6-21: Calculated oxygen potentials for $Pu_{0.77}Am_{0.23}O_{2-x}$, compared to the experimental values and the model of Gotcu-Freis et al. [26]. The uncertainties are represented by the size of the symbols. 219
Figure 6-22: Isopleth section calculated for $Pu_{0.77}Am_{0.23}O_{2-x}$, compared to the domains evidenced by HT-XRD and ATG for the PuAm 80/20 sample. 220
Figure 6-23: Calculated isopleth section for $Pu_{0.49}Am_{0.51}O_{2\pm x}$, compared to the solidus/liquidus temperatures and associated O/M ratios obtained in Chapter 4 – section 4.4.2. 221
Figure 6-24: Cationic site fractions of the CAPRA4 sample calculated at 1600 K, compared to the experimental data measured by XANES in Chapter 5 – section 5.1.3. The experimental uncertainties correspond to the size of the symbol for the site fractions. 223
Figure 6-25: Enthalpy increments of the CAPRA4 sample compared to the calculated data for $U_{0.70}Pu_{0.28}Am_{0.02}O_{2.00}$ (black full line), $U_{0.70}Pu_{0.30}O_{2.00}$ (red dashed line) and $U_{0.72}Pu_{0.28}O_{2.00}$ (green dashed line). 224
Figure 6-26: Heat capacity of the CAPRA4 sample (blue), compared to the calculated data for $U_{0.70}Pu_{0.28}Am_{0.02}O_{2.00}$ (black full line) and $U_{0.72}Pu_{0.28}O_{2.00}$ (green dashed line). 225
Figure 6-27: Isopleth sections of (a) PHENIX24, (b) PHENIX29, (c) CAPRA4, (d) TRABANT40 and (e) TRABANT45 samples. Comparison between the experimental points obtained in Chapter 5 and the calculated solidus and liquidus curves using the CALPHAD model. 226
Figure 6-28 : Solidification paths of (a) PHENIX29 and (b) PHENIX29-OM samples, compared to the final O/M ratio (dashed orange line) and initial O/M ratio (dashed purple line). Calculations performed for 1.10^{-4} mol of gas (Ar + pO_2 = $3.5x10^{-6}$ atm) and $3.98x10^{-5}$ mol of molten pool. 228
Figure 6-29: Oxygen potentials as a function of temperature for the samples studied by laser heating in Chapter 5, compared to the oxygen potential of the gas (Ar with pO_2 = 3.10^{-6} atm). The yellow rectangle represents the temperature range where the equilibrium O/M ratio would be reached during cooling. 229
Figure 6-30: Solidification path of the PHENIX24 sample, compared to the final O/M ratio determined in Chapter 5 – section 5.4.2.2. Calculations performed for 1.10^{-4} mol Ar + pO_2 = $3.5x10^{-6}$ atm and $3.98x10^{-5}$ mol of molten pool. 230
Figure 6-31: Variation of the calculated solidus and liquidus curves of $U_{1-y-z}Pu_yAm_zO_{2\pm x}$ for 1-y-z = 0.60, 0.70 and 0.80 and $0 \leq z \leq 0.05$. 231

Figure 6-32: Oxygen potentials calculated for (a) $U_{0.623}Pu_{0.350}Am_{0.027}O_{2-x}$, (b) $U_{0.665}Pu_{0.311}Am_{0.024}O_{2-x}$ and (c) $U_{0.685}Pu_{0.270}Am_{0.045}O_{2-x}$, compared to the experimental data of Hirooka et al. [170], Nakamichi et al. [169] and Osaka et al. [168], respectively. 233
Figure 0-1 : Calculated U-Pu phase diagram [29]. 255

LIST OF TABLES

Table 2-1 - Crystal structures of uranium, plutonium and/or americium oxides with O/M > 2.1. .37
Table 2-2 - Crystallographic data at room temperature for uranium, plutonium and americium oxides. .38
Table 2-3 - Ionic radii of U, Pu and Am in the oxidation states and coordination numbers [83]. .42
Table 2-4 - Coefficients b_0, b_1, b_2, b_3, b_4 and b_5 of Equation (2.15) by Kato *et al.* [122]. .50
Table 2-5 - Lattice parameter variation for $U_{1-z}Am_zO_{2\pm x}$ with temperature - Parameters of Equation (2.16) from E. Epifano [28]. .51
Table 2-6 - Standard enthalpy of formation, standard entropy and heat capacity at 298.15 K for UO_2, PuO_2 and AmO_2 [125]. .53
Table 2-7 – Enthalpy increments for UO_2, PuO_2 and AmO_2 - ai coefficients of Equation (2.17). .53
Table 2-8 – Heat capacity of UO_2, PuO_2 and AmO_2 - bi coefficients of Equation (2.18). .54
Table 2-9 – Enthalpy increment for $U_{1-y}Pu_yO_2$ - Parameters of Equation (2.19) (Kandan et al. [134], [135]) .55
Table 2-10 – Experimental solidus/liquidus data available in the literature for $U_{1-y}Pu_yO_{2\pm x}$. .68
Table 2-11 - Gaseous species in the thermodynamic models of the gas phases for the U-O, Pu-O and Am-O systems. .72
Table 2-12 – Sublattice models for the liquid phase for U-O, Pu-O and Am-O systems. .73
Table 2-13 – Sublattice models for the $MO_{2\pm x}$ phase for U-O, Pu-O and Am-O systems. .73
Table 3-1 - $Pu_{1-z}Am_zO_2$ powder characteristics [197]. .85
Table 3-2 - Sintering conditions for the four batches manufactured by metallurgy process. .86
Table 3-3 - Pellets characteristics for the five $U_{1-y}Pu_yO_{2\pm x}$ batches. .87
Table 3-4 –Manufacturing technique and initial main characteristics (dimensions and density) of the samples used in this work. .101
Table 4-1 – $Pu_{1-z}Am_zO_{2-x}$ samples and their availability at CEA Marcoule and JRC Karlsruhe. .103
Table 4-2 - Chemical and isotopic compositions of the three $Pu_{1-z}Am_zO_{2-x}$. .104
Table 4-3 - Refined lattice parameters obtained in this work for the $Pu_{1-z}Am_zO_{2-x}$ samples, compared to the ones at the manufacturing. .107
Table 4-4 - Proportions of the cations of the probed elements and corresponding O/M ratios. .112
Table 4-5 – Cationic charge distribution proposed by Osaka et al. [37] for $Pu_{1-z}Am_zO_{2-x}$. .113
Table 4-6 - Samples compositions determined in this section. .115
Table 4-7 – Formed phases and associated proportions from 1873 K to 3030 K for PuAm 80/20, PuAm 50/50-A and PuAm 20/80. .124
Table 4-8 – Oxygen potential and O/M ratios determined for PuAm 80/20 at 1673 K. .129
Table 4-9 – Conditions of the shots performed on PuAm 50/50-B. .134
Table 4-10 - Solidus and liquidus temperatures measured for PuAm 50/50-B. .135
Table 4-11 – Mass of oxygen released by the sample and difference compared to the initial O/M ratio. .138
Table 4-12 – Comparison of the solidus temperatures for various mixed oxides. .139
Table 5-1 - Samples used in this work and their availability. .143
Table 5-2 – Pu content of the $U_{1-y-z}Pu_yAm_zO_{2\pm x}$ matrix phase and proportions of U- and Pu-rich agglomerates obtained by EPMA for the PHENIX29, CAPRA4 and TRABANT40 samples. .146
Table 5-3 – Refined lattice parameters and estimated O/M ratio of $U_{1-y-z}Pu_yAm_zO_{2\pm x}$ samples. .147
Table 5-4 - Proportions of the cations of the probed elements and corresponding O/M ratios, calculated using the Pu content determined by EPMA, compared to the ones determined by XRD. .150
Table 5-5 – Comparison between the cations expected by the model of Osaka et al. [37], [237] and the ones determined experimentally. .151
Table 5-6 - Samples composition and availability. .153

Table 5-7 - Parameters of Equation (5.1) for the thermal expansion of PHENIX29, CAPRA4 and TRABANT40 samples. 160
Table 5-8 – Molar enthalpy increments (in kJ.mol^{-1}) measured for a CAPRA4 sample. 163
Table 5-9 - Parameters of Equation (5.5), compared with literature values of Kandan et al. [135]. 164
Table 5-10 – Conditions, oxygen uptaken and variation in the O/M ratio for each pre-heating test at 1700 K on a fresh PHENIX29 sample. 180
Table 6-1 – Initial O/M ratio, temperature $T_{ox/red}$ at which $\Delta GO2(gas) = \Delta GO2(sample)$ and final experimental values (obtained after the melting of the samples in Chapter 5 – section 5.4.2.2). 230

GLOSSARY

Term	Definition
bcc	body-centered cubic
BET	Brunauer-Emmett-Teller surface area analysis
CALPHAD	CALculation of PHAse Diagram
CEA	Commissariat à l'Energie Atomique et aux Energies Alternatives
CEF	Compound Energy Formalism
DSC	Differential Scanning Calorimetry
DTA	Differential Thermal Analysis
EDS	Energy Dispersive X-Ray Spectroscopy
EMF	ElectroMotive Force
EPMA	Electron Probe Micro Analysis
ESNII	European Sustainable Nuclear Industrial Initiative
EUROTRANS	EUROpean Research Programme for the TRANSmutation of High Level Nuclear Waste in an Accelerator Driven System
EXAFS	Extended X-ray Absorption Fine Structure
fcc	face-centered cubic
GoF	Goodness of Fit
HT-XRD	High Temperature – X-Ray Diffraction
JRC	Joint Research Centre
MOX	Mixed Oxides
OECD-NEA	Organisation for Economic Co-operation and Development - Nuclear Energy Agency
O/M	Oxygen/Metal ratio
SEM	Scanning Electron Microscopy
SER	Stable Element Reference state
SFR	Sodium-cooled Fast Reactor
TAF-ID	Thermodynamics of Advanced Fuels – International Database

TD	Theoretical Density
TGA	ThermoGravimetric Analysis
TIMS	Thermal Ionization Mass Spectrometry
XANES	X-ray Absorption Near Edge Structure
XAS	X-ray Absorption Spectroscopy
XRD	X-Ray Diffraction

1. INTRODUCTION

With the continuous increase of the world's population, managing the energy needs constitutes a significant challenge. To this day, more than 80 % of the energy consumed in the world is produced using fossil fuels, such as coal, oil, gas (Figure 1-1) [1].

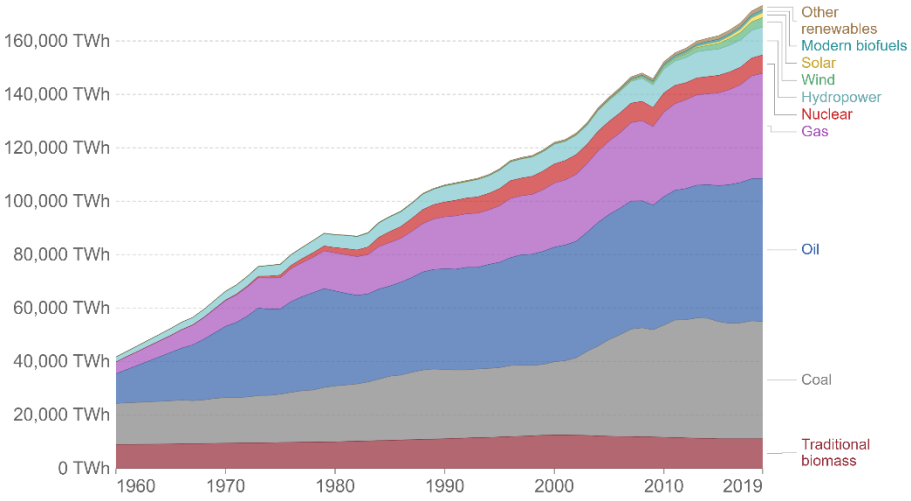

Figure 1-1: Energy consumption by source in the world between 1960 and 2019 [1].

However, these energy sources are highly contributing to global warming and the need to reduce the greenhouse gas emissions becomes more and more urgent every day. To face these requirements, nuclear energy represents a suitable surrogate. However, nuclear energy raises numerous concerns in the population, in particular regarding its safety and durability.

In order to answer the economic, environmental and social requirements of our current society, a new generation of nuclear reactors (Generation IV) is currently investigated. One of the main goals of this reactor technology is the management of the wastes and resources with the introduction of a closed fuel cycle. Among several types of reactors, France chose the development of Sodium-cooled Fast Reactors (SFR) (Figure 1-2) [2].

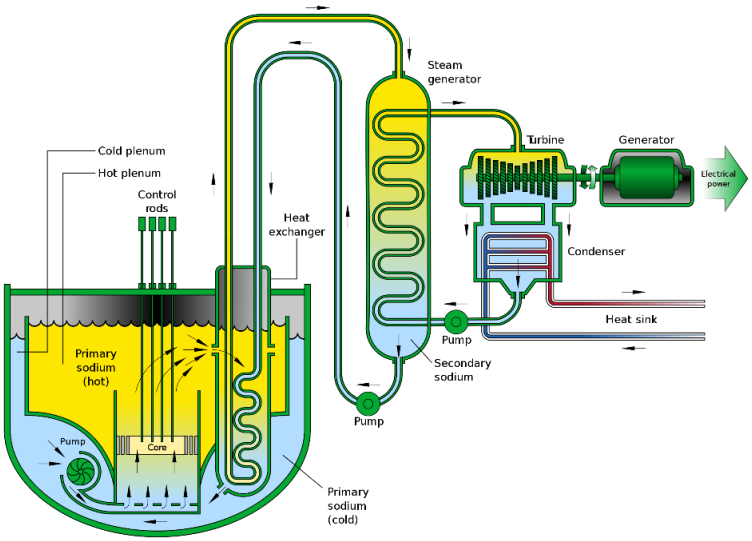

Figure 1-2: Schematic representation of a Sodium Fast Reactor.

In this technology, a multi-recycling (multi-reprocessing) of the plutonium and the minor-actinide spent-fuel components is envisaged. This would lead to a sustainable electricity production by decreasing the Pu inventory and reducing the radiotoxicity and heat load of the waste for an easier storage and disposal. Within this framework, innovative mixed oxide $U_{1-y}Pu_yO_{2-x}$ is studied. These fuels exhibit higher plutonium contents ($y > 0.19$) compared to the ones currently used in Light Water Reactors of Generation II (0.08-0.10). However, recycling Pu from irradiated MOX fuel induces drastic changes in the isotopic vector of the resulting plutonium. Thus, a decrease in the ^{239}Pu content and an increase in the proportions of ^{238}Pu and ^{241}Pu are foreseen. Furthermore, due to the half-life of ^{241}Pu ($\lambda_{1/2}$ = 14 years) and the elapsed time between fabrication and irradiation, ^{241}Am will be produced through β-decay of ^{241}Pu. Thus, due to the high Pu contents of the materials, significant amount of ^{241}Am (around 2-3 % of Am/(U+Pu+Am)) could accumulate in the fuels. An example of SFR fuel pellets is given in Figure 1-3.

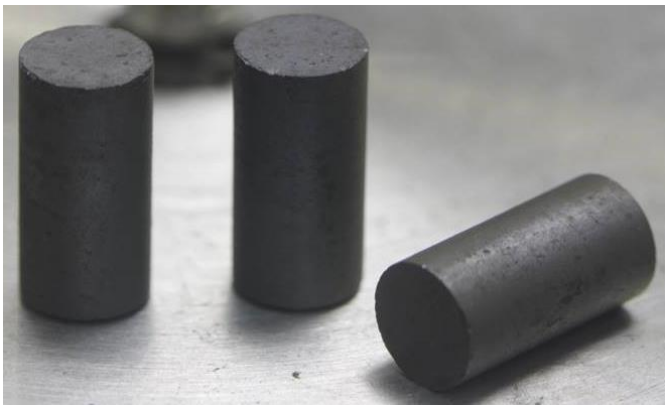

Figure 1-3: Fuel pellets of $U_{0.71}Pu_{0.28}Am_{0.01}O_{1.98}$ for SFR (height: 11 mm – diameter: 5.4 mm).

The accurate knowledge of the impact of ^{241}Am on fuels thermodynamic and structural properties is then essential to foresee its behaviour during irradiation. Indeed, the temperature can reach up to 2200 K in normal operating conditions at the centre of the fuel-pin and about 773 K at the pellet edge [3]. This results in the formation of a temperature gradient along the pellet radius, which causes a redistribution of oxygen and metal atoms within the pellet at the beginning of the irradiation. The SFR fuel specifications directly affect the plutonium and oxygen contents. Indeed, the O/M (Oxygen/Metal) ratio needs to range between 1.94 and 2.00. The lower limit is settled to prevent an insufficient thermal conductivity of the mixed oxide, which could lead to the fuel melting. The upper limit is fixed to minimize the corrosion of the stainless steel cladding. This property is also supposed to vary within the pellet, with a low O/M ratio at the centre of the fuel (associated with a higher Pu content) and an O/M ratio close to 2.00 at the limit between the cladding and the pellet (associated with a lower Pu content) [3].

The goal of this thesis is to study the influence of americium on thermodynamic and structural properties of $U_{1-y}Pu_yO_{2\pm x}$ mixed oxides. Indeed, these properties, such as the melting temperature or the formed phases under specific temperature and atmosphere, could affect the safety margins and the behaviour of the fuel in the reactor during normal or accidental conditions. In order to study the margin to fuel melting, the Conductivity Integral Margin to melting (CIM), expressed in **(1.1),** is studied.

$$CIM = \int_{T_{op}}^{T_{melt}} \lambda(T)dT \quad \textbf{(1.1)}$$

$$\text{with } \lambda(T) = \alpha(T) \times C_P(T) \times \rho(T)$$

Where T_{op} is the operational fuel temperature, T_{melt} the melting temperature, λ the thermal conductivity and T the absolute temperature. The thermal conductivity is described as a function of the thermal expansion coefficient α, the heat capacity C_P and the density ρ, with their dependence in temperature.

Several parameters can affect these properties, such as the plutonium and americium contents as well as the O/M ratio.

In order to predict the nuclear fuels behaviour as a function of both temperature and atmosphere (oxygen potential), the international TAF-ID (Thermodynamics of Advanced Fuel-International Database) project was started in 2013 from the OECD/NEA to develop a thermodynamic database for nuclear materials [4]. This PhD was performed within the framework of this project, with the aim of improving the existing database for the U-Pu-Am-O quaternary system using the CALPHAD method.

CALPHAD, acronym for CALculation of PHAse Diagram, is a semi-empirical method allowing the prediction of thermodynamic properties and phase diagrams for multicomponent systems, based on the assessment of thermodynamic functions (Gibbs energies) [5]. The linear combination of the Gibbs energy functions of all the phases present in the system results in the total Gibbs energy of the system, for a given pressure, temperature and composition. The lowest value of the latter corresponds to the equilibrium state of the system. The assessment of these functions is the aim of the CALPHAD method. The various steps of this method are described in Figure 1-4.

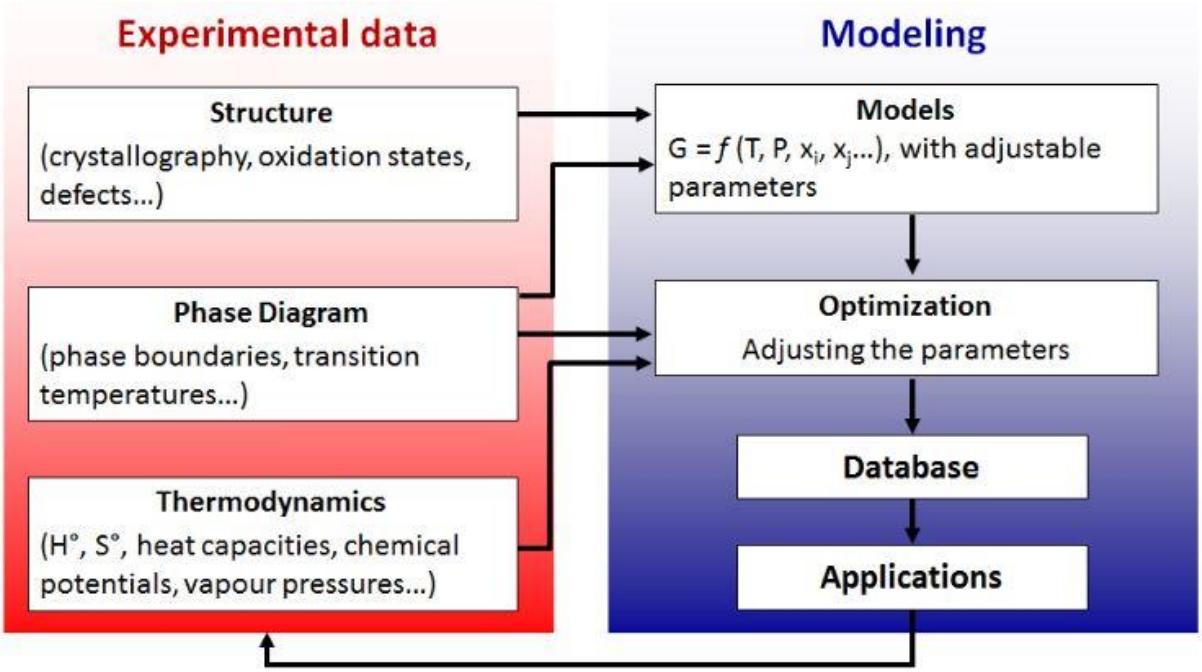

Figure 1-4: Schematic representation of the CALPHAD method [6].

In a first step, the critical review of the existing experimental data on the systems of interest is performed. If they are not sufficient, experimental campaigns need to be performed to gain new input data. Three types of data are necessary when using the CALPHAD method: structural data (crystallographic structures, oxidation states…), phase diagram data (phases in presence, phase transitions…) and thermodynamic data (melting temperature, heat capacity, oxygen potential for oxides…). Based on these data, thermodynamic models can be built, *i.e.* Gibbs energy functions are derived to describe each phase. The interactions parameters used in these functions are adjusted using a least square minimization method to reproduce as best as possible the experimental results. The assessment of high order systems can be then performed by extrapolation from lower order systems, called sub-systems. To this aim, in order to study the quaternary U-Pu-Am-O system, the binary sub-systems need to be described first, followed by the ternary sub-systems. This method has already proven to be useful to describe actinides-bearing systems [6]–[8].

This work is divided in five chapters. It was structured following the logic of the CALPHAD method previously described. Indeed, in Chapter 2, the critical review of the available phase diagram, structural and thermodynamic data on the U-Pu-Am-O system and its sub-systems is presented. The influence of the plutonium and americium contents, as well as the O/M ratio, are discussed on each property of interest. The lack of data on americium-bearing oxide systems, in particular on Pu-Am-O and U-Pu-Am-O, is highlighted. Thus, based on these findings, the conclusion is that new experimental campaigns have to be performed to gain additional knowledge on the structural, thermodynamic and phase diagram data of these systems.

In Chapter 3, the principle of the CALPHAD method and the different formalisms used for the thermodynamic models are explained first. Then, the materials of interest, $Pu_{1-z}Am_zO_{2-x}$ and $U_{1-y-z}Pu_yAm_zO_{2\pm x}$, and the different characterizations techniques used in this work are described.

The experimental investigations performed on the Pu-Am-O system are detailed in Chapter 4. Structural data (phases in presence and oxidation states), phase diagram data (solid phase equilibria) and thermodynamic data (oxygen potential by TGA and melting temperatures using a laser heating technique) obtained are described.

The quaternary U-Pu-Am-O system is then investigated experimentally, in Chapter 5. In a first part, new input data on the structural properties with the formed phases and the cationic distribution are described. The solid phase equilibria are studied in a second section, followed by the enthalpy increment and the heat capacity. The solid/liquid phase transitions are discussed in a last section, with the assessment of the O/M ratio variation occurring during the melting.

Finally, based on the sets of data newly obtained in this work, the thermodynamic modelling of the U-Pu-Am-O system is presented in Chapter 6, with the re-assessments of the Pu-O, U-Pu-O and Pu-Am-O sub-systems first. Finally, thermodynamic investigations of mixed oxides with americium contents up to 5 mol.% are performed.

This work was performed within the framework of two European projects. The thermodynamic calculations, as well the drop calorimetry and laser heating experiments, are part of the Work

Package 1 of the INSPYRE[1] project, focusing on the margin to fuel melting of GEN-IV reactors. The $U_{1-y}Pu_yO_{2\pm x}$ samples studied in this work were provided by the ESFR-SMART[2] project, aiming at ensuring the safety of GEN-IV Sodium Fast Reactors. The experiments were carried out in two facilities: in the ATALANTE (ATelier Alpha et Laboratoires pour ANalyses, Transuraniens et Etudes de retraitement) in the CEA Marcoule (France) and at the Joint Research Centre Karlsruhe (Germany).

[1] INSPYRE: Investigations Supporting MOX Fuel Licensing for ESNII Prototype Reactors European project funded under H2020-Euratom-1.2, Grant agreement ID: 754329, 2017-2022. (http://www.eera-jpnm.eu/inspyre/)

[2] ESFR-SMART: European Sodium Fast Reactor Safety Measures Assessment and Research Tools European project funded from the Euratom Research and Training Programme, Grant agreement ID: 754501, 2017-2022, (http://esfr-smart.eu/)

2. STATE OF THE ART OF THE U-PU-AM-O SYSTEM

The objective of this chapter is to discuss the structural and thermodynamic properties of interest for using the CALPHAD method and the influence of various parameters such as the plutonium and americium contents or the O/M ratio. It constitutes a non-exhaustive state of the art of the quaternary U-Pu-Am-O system and its associated binary and ternary sub-systems. Although significant knowledge was gained in the last decades on nuclear oxides, this chapter higlights the remaining uncertainties on broad regions of the various systems. A significant lack of data is reported on the structural and thermodynamic properties of americium-bearing systems, in particular on Pu-Am-O and U-Pu-Am-O. This chapter evidences the needs for additional experimental campaigns in order to obtain reliable thermodynamic models.

2. STATE OF THE ART OF THE U-PU-AM-O SYSTEM

This review gathers the data available in the literature on the quaternary U-Pu-Am-O system and its sub-systems. In section 2.1, the phase diagrams of the oxide sub-systems U-O, Pu-O, Am-O, U-Pu-O, Pu-Am-O and U-Am-O are detailed. Then, in section 2.2, crystallographic data of the associated oxides are introduced. The influence of the O/M ratio, the self-irradiation and the temperature on the cell parameters is discussed in sections 2.2.2 and 2.2.3. Thermodynamic properties of single and mixed dioxides of uranium, plutonium and americium, such as enthalpy, oxygen potential or melting behaviour, are presented in section 2.3. The influence of the actinide composition, the O/M ratio and the temperature on these properties is discussed. Finally, in section 2.4, the thermodynamic models of the various systems studied in this work are briefly described.

2.1. PHASE DIAGRAMS

In this section, the state of the art of phase equilibria in the U-O, Am-O, Pu-O, U-Pu-O, Pu-Am-O and U-Am-O sub-systems is presented. The description of the metallic systems U-Pu, Pu-Am and U-Am can be found in Appendix A.

2.1.1. Binary systems

2.1.1.1 Uranium-Oxygen

Since the fifties, a large amount of experimental and modelling investigations on the U-O system was performed. The experimental thermodynamic and phase diagram data available were critically reviewed by Labroche *et al.* [9], [10] and Baichi *et al.* [11], [12], whose reviews were used in the CALPHAD description of the U-O system proposed in 2002 by Guéneau *et al.* [13]. This CALPHAD model was modified in 2011 [7], based on the solidus and liquidus temperatures measured during container-less laser experiments performed by Manara *et al.* [14]. This model is shown in Figure 2-1.

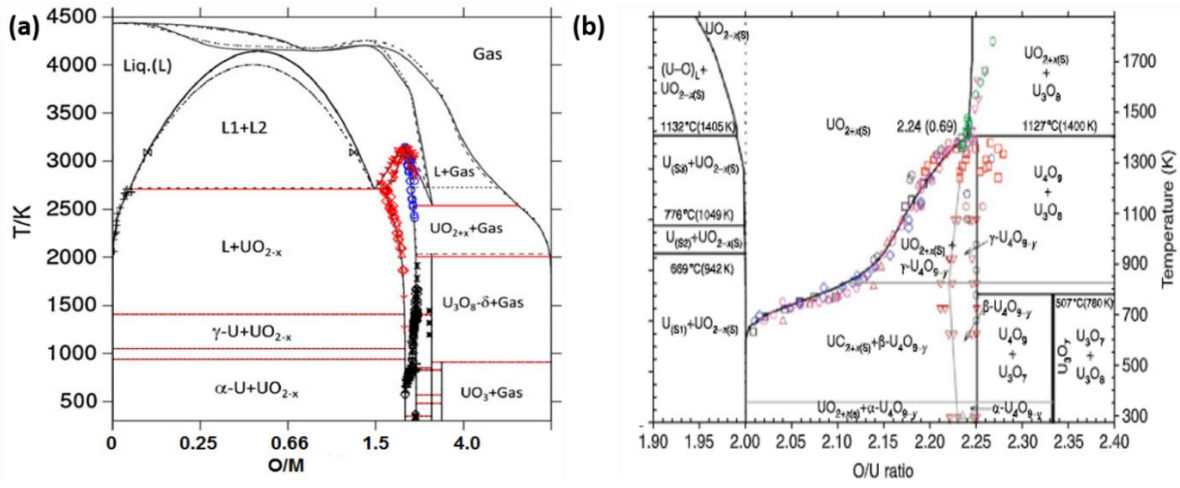

Figure 2-1: (a) Calculated U-O phase diagram from Guéneau *et al.* [13], (b) detailed section from 1.9 < O/M < 2.4 after Higgs *et al.* [15], compared to available experimental data. L and G stand for liquid and gas, respectively.

Stable uranium oxides exist over a large range of temperature and O/U ratio, with phases varying from UO_{2-x} to UO_3, corresponding to oxidation states ranging from +3 to +6. At ambient temperature and atmospheric pressure, increasing the O/U ratio leads to the following oxides: UO_2, U_4O_9, U_3O_7, U_3O_8 and UO_3. At room temperature, uranium dioxide is stoichiometric (O/U = 2.00) but can exhibit O/U variations at higher temperatures: the hyper-stoichiometric range appears above 500 K, whereas the hypo-stoichiometric range is only observed above 1200 K. The O/U ratio existence domain of the fluorite phase $UO_{2\pm x}$ ranges from 2.00 to 2.22 at 1073 K and from 1.60 to 2.30 at 2673 K. Except for UO_2, each compound presents several polymorphs (described more in details in section 2.2.1.4) : three forms for U_4O_9 and metallic U, three forms for U_3O_8 and five for UO_3 [16]. U_4O_9 and U_3O_8 exhibit a small range of hypo-stoichiometry in oxygen (U_4O_{9-x} with $0 < x < 0.02$ and U_3O_{8-x} with $0 < x < 0.10$), not modelled by Guéneau *et al.*.

2.1.1.2 Plutonium-Oxygen

Similarly to the U-O system, the Pu-O system was widely studied for decades [17]–[20]. In the solid state, plutonium accepts two oxidation states in the oxide phase (+3 and +4). Although several authors indicated the existence of the +5 oxidation state in the dioxide [21], [22], the scientific community does not commonly recognize this hyper-stoichiometric material. The Figure 2-2 represents the plutonium-oxygen system based on the model of Guéneau *et al.* from 2011 (full lines) [7], with a zoom on the O/Pu range of interest for nuclear fuels [7]. The dashed lines represent the previous assessment of the Pu-O system performed by Guéneau *et al.* in 2008 [23]. In 2011, the model was modified to better describe the miscibility gap in the dioxide and take into account the melting point of PuO_2 measured using laser heating by De Bruycker et *al.* [24].

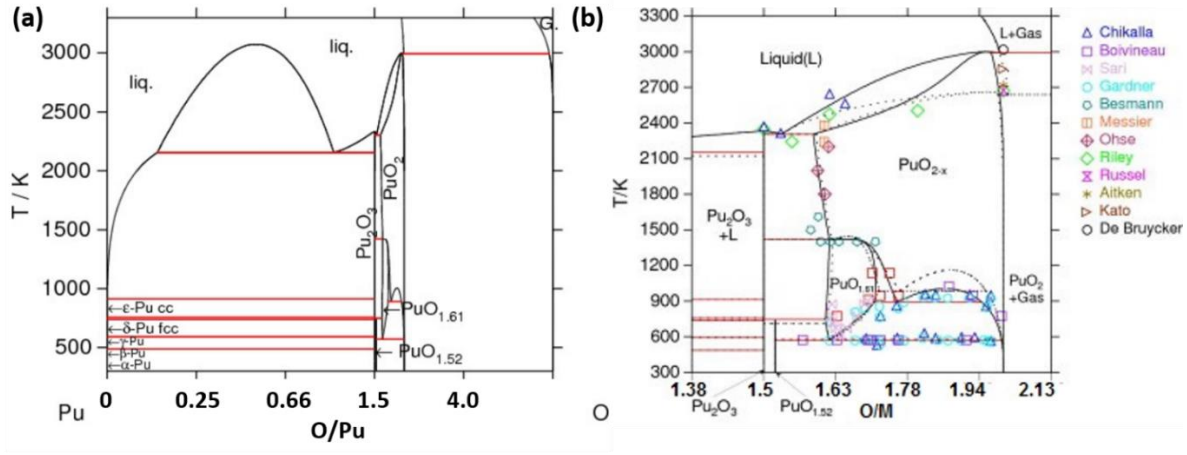

Figure 2-2 : (a) Calculated Pu-O phase diagram, (b) detailed section from 1.38 < O/M < 2.13, using the model developed by Guéneau *et al.* in 2011 [6]. The dashed lines on (b) represent the model of Guéneau *et al.* of 2008 [23].

The reference oxide is $PuO_{2.00}$, stable at room temperature in air at atmospheric pressure. The dioxide can be reduced into hypo-stoichiometric PuO_{2-x} above 600 K. A miscibility gap is reported to exist in a limited domain, for $1.78 < O/Pu < 1.94$ and $900 < T < 1000$ K [17], [20], composed of two face-centred cubic (fcc) PuO_{2-x} phases with different oxygen contents [19]. For $T \leq 873$ K, the body-centered cubic (bcc) $PuO_{1.52}$ phase appears at low temperature in equilibrium with

PuO_2 and with the sesquioxide Pu_2O_3 [23]. Another bcc phase, $PuO_{1.61}$ can also be observed above 573 K, with an extended homogeneity range from O/Pu = 1.61 to 1.69 [19].

2.1.1.3 Americium-Oxygen

Compared to U-O and Pu-O, few experiments are available in the literature concerning the thermodynamic and structural investigation of the phases in the Am-O system. Among these data, significant discrepancies between the measurements exist. The first representation of the phase diagram was proposed by Sari and Zamorani in 1970 [25]. In this representation, a miscibility gap was reported in the americium dioxide AmO_{2-x} phase, from O/Am = 1.7 to 1.94, with a critical temperature around 1300 K. A first description of the Am-O system based on a CALPHAD assessment was proposed by Gotcu-Freis *et al.* in 2011 [26], including three metallic forms of americium [27], as well as the gas phase. In 2017, a re-assessment of the Am-O phase diagram, shown in Figure 2-3, was performed by Epifano *et al.* [28], based on their experimental results obtained for O/Am ratios between 1.59 and 2.00 and temperatures from 700 to 1500 K.

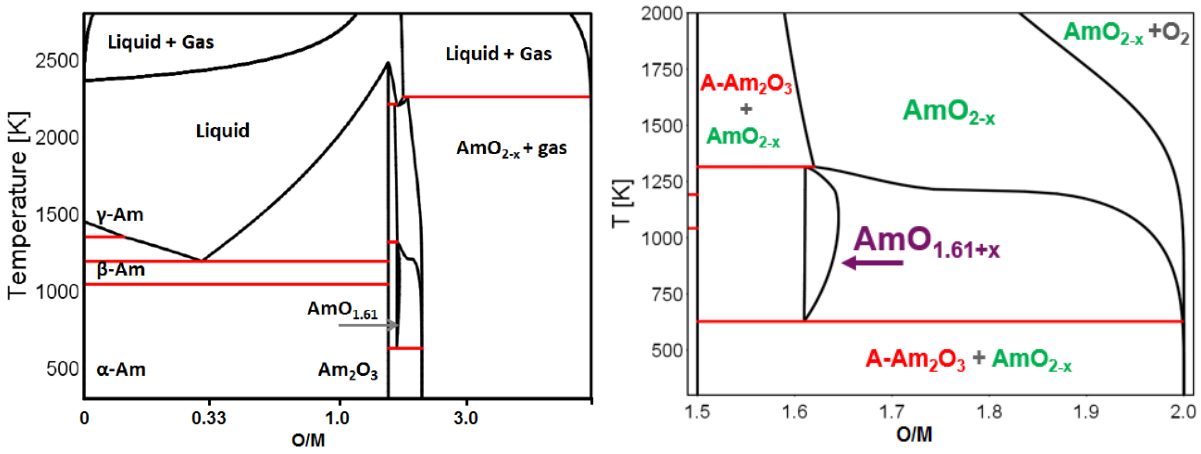

Figure 2-3 : Calculated Am-O phase diagram using the model developed by Epifano *et al.* [28].

In this updated phase diagram, contrary to the previous representations, no miscibility gap is present in the AmO_{2-x} region. In the range of composition studied experimentally, three phases are proposed: the dioxide AmO_{2-x}, the sesquioxide A-Am_2O_3 and the intermediate bcc phase $AmO_{1.61+x}$. At room temperature, the americium dioxide is stoichiometric and presents a large hypo-stoichiometric domain for T > 600 K. The intermediate bcc phase C' (named $AmO_{1.61+x}$ on the diagram) exists from 570 K T < 1315 K. Its lower O/Am ratio limit is not well defined but is established around 1.62, whereas its upper limit is calculated at 1.68 [29].

Thermodynamic data are missing for the intermediate $AmO_{1.61+x}$ phase and only few data are available in the $AmO_{1.61}$-Am_2O_3 domain. The existence of another sesquioxide from 1100 to 1300 K with bcc structure is also controversial [30].

2.1.2. Ternary systems

2.1.2.1 Uranium-Plutonium-Oxygen

2.1.2.1.1 At low temperature (T ≤ 473 K)

The first representation at room temperature of the U-Pu-O phase diagram was proposed by Markin and Street in 1967 [31]. This representation was later updated by Sari *et al.* in 1970 [32] (Figure 2-4).

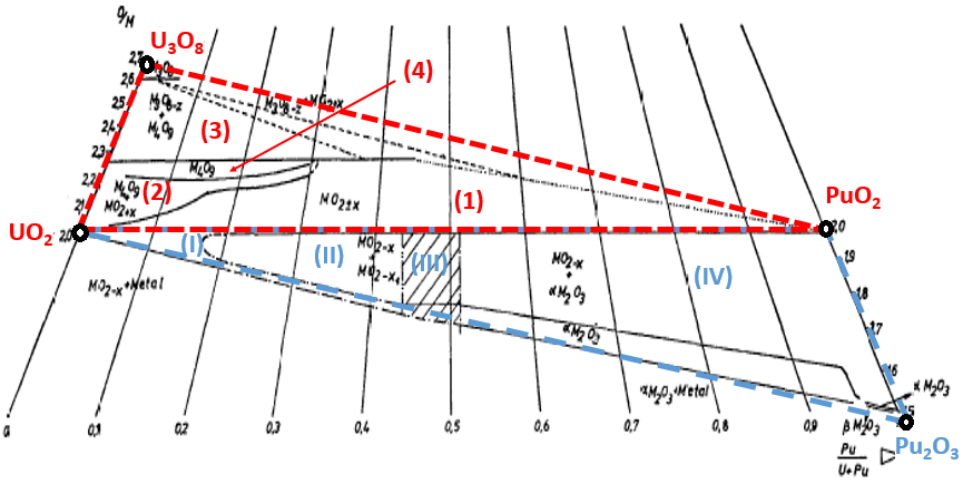

Figure 2-4 : Partial isothermal section at 298 K of the U-Pu-O phase diagram [31].

Several studies of the U-Pu-O system were carried out to determine the phase equilibria as well as the crystallographic structures of the different phases [33]–[36]. Different models, based on thermodynamic calculations, were proposed in the literature for the hyper- and hypo-stoichiometric regions [37], [38]. Based on a critical review of all experimental data available, Guéneau *et al.* [7] proposed in 2011 a model using the CALPHAD method, leading to the phase diagram of Figure 2-5. In this representation, MOX indicates the $U_{1-y}Pu_yO_{2\pm x}$ phase. In this model, the solubilities of plutonium in U_4O_9 and U_3O_8 and of uranium in Pu_2O_3 and $PuO_{1.61}$ were not considered.

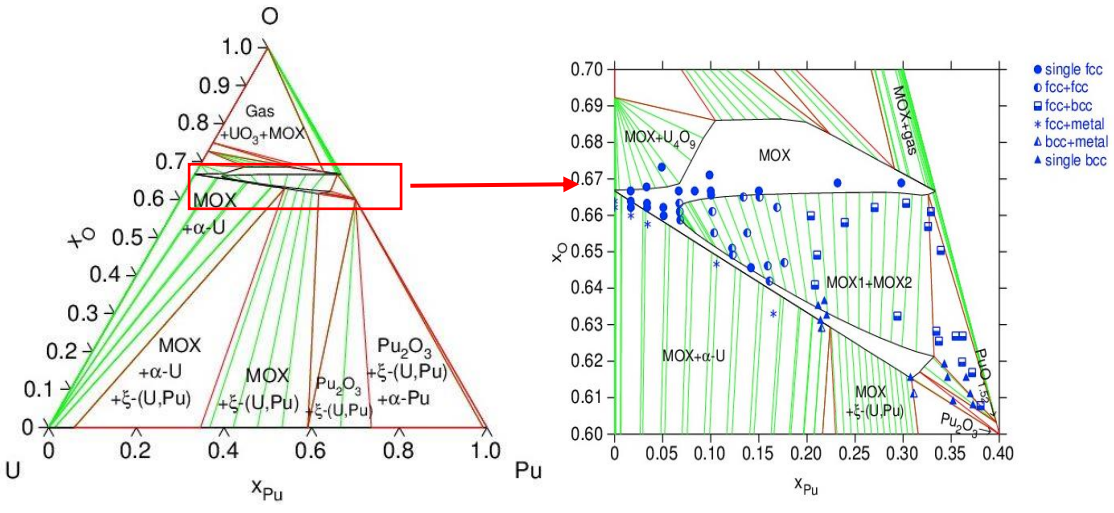

Figure 2-5 : Calculated U-Pu-O phase diagram at 473 K, with a detailed section from 0.60 < x(O) < 0.70, using the model developed by Guéneau *et al.* [6].

The domain of interest for nuclear fuels is limited to the regions of the hyper- and hypo-stoichiometric domains around the O/M ratio (with M = U + Pu) of 2.00. At room temperature, two domains can be distinguished (see Figure 2-4):

- The hyper-stoichiometric domain **UO_2-U_3O_8-PuO_2** with 2.67 ≥ O/M ratio ≥ 2.00 (red triangle on Figure 2-4). Four sub-domains can be found :
  - The first domain **(1)** represents the monophasic solid solution $U_{1-y}Pu_yO_{2+x}$ of fcc structure. The stability domain of this phase broadens when increasing the Pu content up to y = 0.31-0.32, as the material can accept a continuously higher hyper-stoichiometry. The maximum possible O/M ratio is then stable up to y = 0.45 (higher Pu contents are represented with a black dash line as the results in this region need to be confirmed).
  - The second domain **(2)** is biphasic and constituted of two fcc phases $U_{1-y}Pu_yO_{2+x}$ and M_4O_{9-z} with different plutonium contents. When increasing the plutonium content, this domain gradually shrinks and ultimately vanishes for y > 0.30, in favour of the formation of the $U_{1-y}Pu_yO_{2+x}$ monophasic domain.
  - The third domain **(3)** contains two phases: one cubic phase M_4O_{9-z} and one orthorhombic phase M_3O_{8-z}. Strach *et al.* determined a maximum solubility of plutonium into the M_3O_{8-z} phase of 8 mol.% at 1573 K [39].
  - The fourth domain **(4)** is constituted of one cubic phase M_4O_{9-z}.

- The hypo-stoichiometric domain **UO_2-PuO_2-Pu_2O_3** (blue triangle on Figure 2-4), with O/M ratio ≤ 2.00. At room temperature, four sub-domains can be found:
  - The monophasic domain **(I)** is constituted of a solid solution $U_{1-y}Pu_yO_{2-x}$ with a fcc structure.
  - The second domain **(II)**, with plutonium content y ranging from 0.15 to 0.40, is biphasic and represents a miscibility gap, originating from the Pu-O system, constituted of two fcc phases MO_{2-x1} and MO_{2-x2}. In this region, one phase is slightly hypo-stoichiometric compared to the other one with an O/M ratio close to 2.00, whereas the second phase exhibis a lower O/M ratio. Discrepancies can be found in the literature for the lowest Pu content limit of this miscibility gap but a minimum value y between 0.15 and 0.20 at room temperature is accepted by most of the authors [32], [40].
  - The third domain **(III)** is constituted of three phases, with two fcc phases MO_{2-x1} and MO_{2-x2} in equilibrium with a sesquioxide phase M_2O_3. The existence of this domain was evidenced by Truphémus *et al.* [40] for 0.45 < y < 0.65.
  - The last domain **(IV)** is constituted of two phases, a fcc phase MO_{2-x} in equilibrium with the sesquioxide phase M_2O_3, for plutonium content above 0.65.

2.1.2.1.2 At T > 473 K

Few experimental studies on the U-Pu-O system at high temperatures are available in the literature [31], [35], [40], [41]. The diagram proposed by Markin *et al.* [31] was reviewed by Truphémus *et al.* [40], who investigated the miscibility gap in the fluorite phase existing for O/M ratios < 2.00. The isotherm sections at 473, 673 and 873 K are shown in Figure 2-6.

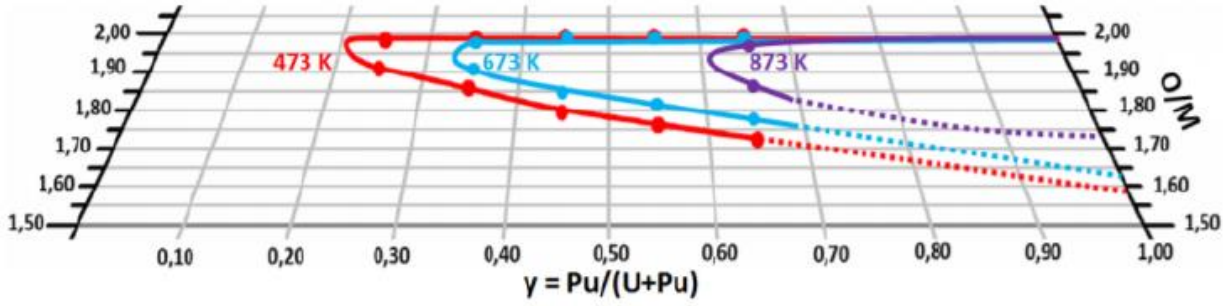

Figure 2-6 : Isothermal sections at 473, 673 and 873 K of the U-Pu-O phase diagram focusing on the UO_2-PuO_2-Pu_2O_3 domain, for an O/M ratio ranging from 1.50 to 2.0 [36].

When increasing the temperature, the extent of the miscibility gap decreases and is shifted towards compositions with higher plutonium contents, leading to a monophasic zone $MO_{2\pm x}$ appearing at low plutonium contents. Above 1073 K, no miscibility gap is observed and only a continuous mixed oxide solid solution $U_{1-y}Pu_yO_{2\pm x}$ exists.

2.1.2.2 Plutonium-Americium-Oxygen

Experimental results on the ternary Pu-Am-O system are limited, with only oxygen potential measurements and vapour pressures data on few compositions [42]–[45].The first phase diagram of the Pu-Am-O system was proposed in 2007 by Miwa *et al.* based on X-Ray Diffraction and Differential Thermal Analysis (DTA) experiments on $Pu_{0.91}Am_{0.09}O_{2-x}$ [42]. A second representation of this system was proposed in 2011 by Gotcu-Freis *et al.*, using the CALPHAD method and their vapour pressure measurements on $Pu_{0.756}Am_{0.244}O_{2-x}$ (Figure 2-7) [26].

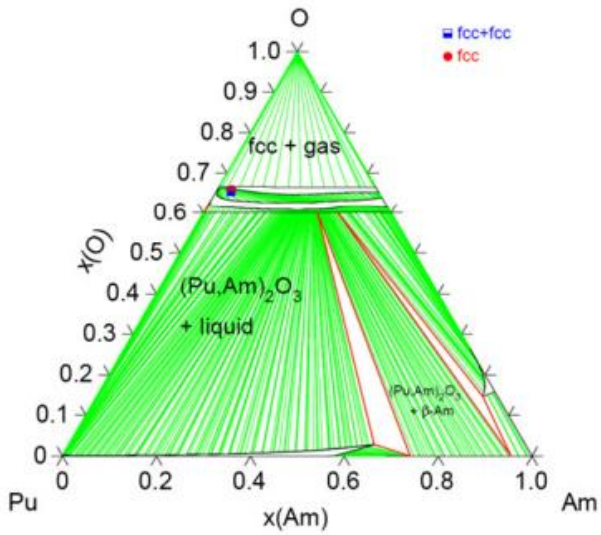

Figure 2-7 : Calculated Pu-Am-O phase diagram at 1273 K, using the model developed by Gotcu-Freis *et al.* [26].

This model predicts the presence of a miscibility gap in the $(Pu,Am)O_{2-x}$ domain, with two fcc phases, consistently with its existence in the Pu-O and Am-O sub-systems. This representation also considers a continuous solid solution $(Pu,Am)_2O_3$ between Pu_2O_3 and Am_2O_3.

2.1.2.3 Uranium-Americium-Oxygen

The first representation of the U-Am-O system was proposed in 2014 by F. Lebreton [46] based on a thermodynamic assessment using the CALPHAD method. Very few experimental results were available at that time on this ternary system. According to this model, a miscibility gap in the mixed dioxide $(U,Am)O_{2-x}$ exists in the oxygen hypo-stoichiometric region ($0 < x < 0.5$), with a critical temperature around 1200 K.

Additional experimental results on the U-Am-O system were later obtained by E. Epifano [28] (*e.g.* melting temperatures of Am-doped uranium oxide [47], structural and thermodynamic studies on uranium-americium mixed oxides [28]). From these new measurements, the CALPHAD model was updated by E. Epifano [28] (Figure 2-8), taking into account her latest assessment of the Am-O system [6] (see section 2.1.1.3). The parameters of the liquid phase were later reassessed in 2020 by Epifano *et al.*, to take into account new sets of melting points on $U_{1-z}Am_zO_2$ oxides [48].

At room temperature, for O/M < 2.00, $(U,Am)O_{2-x}$ is in equilibrium with a U-metallic phase in the U-rich corner and an Am-metallic phase in the Am rich corner. This triphasic equilibrium is due to the existence of a miscibility gap in the U-Am system (see Appendix A). In this part of the phase diagram, a miscibility gap is also predicted to exist in the fcc phase (indicated as C1 on Figure 2-8) for americium contents higher than 0.5. A small two-phase region exists between the mixed oxide C1 and the Am_2O_3 sesquioxide in the Am-rich side. In the hyper-stoichiometric domain of the diagram, two miscibility gaps are identified: one in the C1 phase for high Am contents (indicated as C1+C2) and one in the U-rich region. This is likely an artefact of the model, generated by the parameters of the C1 phase, as no investigations have evidenced their presence. However, as experimental data in the hypo-stoichiometric range are missing, uncertainties remain on this model.

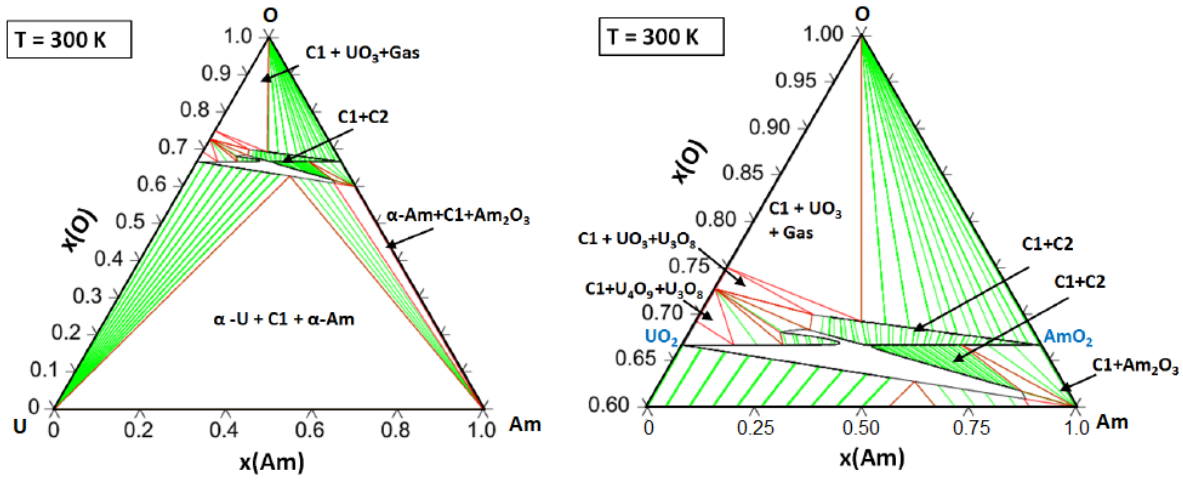

Figure 2-8 : Calculated isothermal section at 300 K of the U-Am-O phase diagram, with a zoom on the oxide domain (right), using the model of Epifano [28].

2.2. STRUCTURAL DATA

In this section, a non-exhaustive review of the crystallographic data of the oxides existing in the U-Pu-Am-O system, as well as the binary and ternary sub-systems, is performed. A description

of the crystallographic structures is provided, starting with the fluorite-type structure, common to uranium, plutonium, americium single and mixed dioxides. The other hypo- and hyper-stoichiometric forms are then described. Quantitative structural data, namely the lattice parameters, are also reported. Finally, the influence of the O/M ratio and the self-irradiation on the structural data of the oxides is discussed.

2.2.1. Introduction to crystal structures

In the following parts, the letter M refers to the metals U, Pu, Am and/or the solid solutions constituted of a combination of two and/or three of these elements. As the hyper-stoichiometric oxides (O/M > 2.1) are not of prime interest in this work, only a brief description of their crystal structures is given here.

2.2.1.1 MO_2

The dioxides UO_2, PuO_2, AmO_2, and their solid solutions exhibit a fluorite-type structure (CaF_2, often noted face-centred cubic (fcc) phase), of space group $Fm\bar{3}m$ (n°225). Stoichiometric UO_2, PuO_2 and AmO_2 consist in tetravalent cations (U^{4+}, Pu^{4+} and Am^{4+}) arranged in a fcc metal lattice with O^{2-} anions occupying the tetrahedral sites (Figure 2-9).

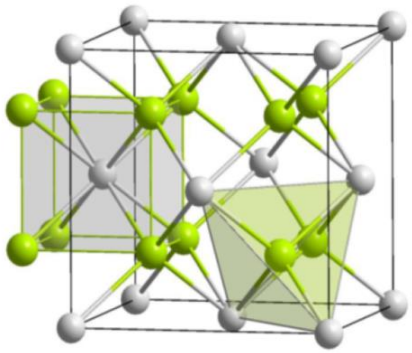

Figure 2-9 : MO_2 fluorite structure with metals and oxygen atoms in grey and green, respectively.

In this structure, the coordination numbers of uranium/americium/plutonium cations and oxygen anions are 8 and 4, respectively. Actinide materials crystallizing in a fluorite structure can accept a hypo-stoichiometry (MO_{2-x}) and hyper-stoichiometry (MO_{2+x}) (only for uranium) in oxygen. The departure from ideal stoichiometry is related to the formation of oxygen vacancies for O/M < 2 and oxygen interstitials and clusters for O/M > 2.

In the case of a positive deviation from stoichiometry (0.01 < x < 0.13), the formulation of the 2:2:2 Willis cluster (see Figure 2-10) was pointed out by neutron diffraction studies [49], [50] for UO_{2+x}. In this structure, the excess oxygen atoms occupy two interstitial positions labelled O' and O". Compared to the "ideal" interstitial position (0.5, 0.5, 0.5), O' and O" positions are shifted along the <110> and <111> directions, respectively. The formation of oxygen vacancies occurs with the formation of interstitials. Each cluster contains two O' interstitials, two O" interstitials and two oxygen vacancies. No change of the position of the cations is evidenced, only an increase of their oxidation state to maintain the electro-neutrality.

For x > 0.13, several authors proposed the formation of cuboctahedral clusters, formed by a complex rearrangement of the oxygen sublattice in 8 vacancies and 12 interstitials [51]–[53].

The latter are composed of 8 oxygen atoms, originally in their normal sites, and 4 added interstitials. These clusters lead to the formation of the U_4O_9 and U_3O_7, described briefly in section 2.2.1.4.

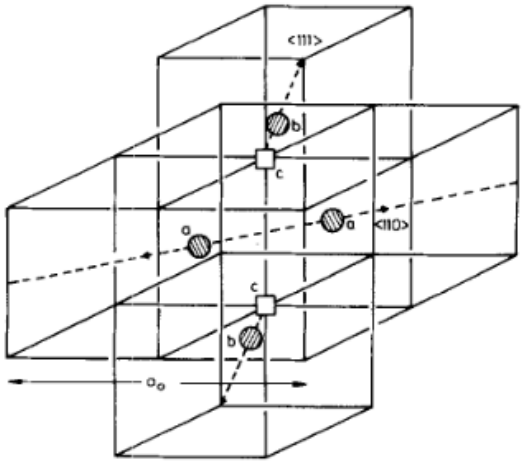

Figure 2-10: Representation of the 2:2:2 Willis cluster. The corners of the cubes are the normal sites for oxygen atoms. The cluster contains two O' (a), two O'' (b) and two oxygen vacancies (c) [49].

In the case of fcc solid solutions of mixed oxides, such as $U_{1-y}Pu_yO_{2\pm x}$ or $U_{1-z}Am_zO_{2\pm x}$, a more complex behaviour has been evidenced in terms of oxidation states, in particular by L. Medyk [54] and by Epifano *et al.* [55]. Indeed, the simultaneous presence of U^{5+} and Pu^{3+} in $U_{1-y}Pu_yO_{2\pm x}$ and of U^{5+} and Am^{3+} in $U_{1-z}Am_zO_{2\pm x}$ was determined in XANES studies, even for stoichiometric oxides (O/M = 2.00), evidencing a charge compensation mechanism.

2.2.1.2 M_2O_3

In the case of the M_2O_3 (sesquioxide) compounds, two allotropic forms exist: the A-type and the B-type. The A-type M_2O_3, stable in the Pu-O (700 < T < 2352 K) and Am-O (up to 2481 K) systems, exhibits a trigonal structure, belonging to the space group $P\bar{3}m1$ (n°164) [30], (Figure 2-11 [56]).

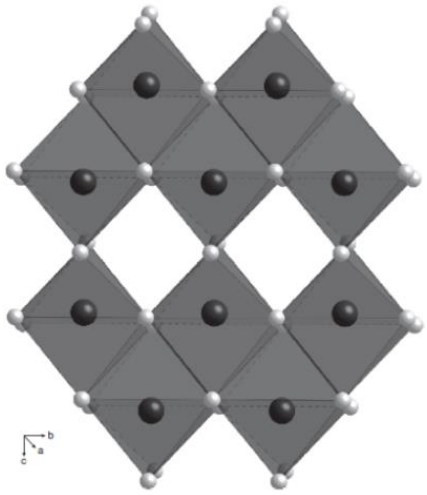

Figure 2-11 : A-M_2O_3 sesquioxide structure with plutonium atoms in black and oxygen atoms in grey [56].

The metastable B-type M_2O_3, exhibiting a monoclinic structure (space group $C2/m$, n°12), was observed in the Am-O system by XRD measurements [29], [57] but its exact existence domain in stoichiometry and temperature remains unknown. The $(Pu,Am)_2O_3$ solid solution is assumed to exist but no experimental information on its exact structure (space group) are available in the literature [26]. In the U-Pu-O system, the $(U,Pu)_2O_3$ phase is expected to exist but the solubility of U in Pu_2O_3 is unknown.

2.2.1.3 $MO_{1.5+x}$-$MO_{1.61+x}$

These compounds, also called C-type phases, are reported in the literature in the Pu-O [23] and Am-O [26] systems. The two phases $MO_{1.51+x}$ and $MO_{1.61+x}$ present a body-centered cubic (bcc) structure (space group $Ia\bar{3}$ (n°206)) and correspond to a super-structure of the fluorite-type one, in which the accumulation of oxygen vacancies leads to a reorganization of their structure. Consequently, their lattice parameters are almost twice the one of the MO_2 *fcc* structure. The $MO_{1.5+x}$ phase is observed from room temperature to 573 K in Am-O [6] and up to 623 K in Pu-O [17]. The $MO_{1.61+x}$ phase is stable only at high temperature (570 < T < 1300 K and from 1.61 to 1.68 in the Am-O system [6] and 573 < T < 1450 K from 1.61 to 1.69 in Pu-O [58]).

2.2.1.4 Hyper-stoichiometric oxides (O/M > 2.1)

As these oxides will not be studied in details in this thesis, only a brief summary of their crystal structures is given in this section and summarized in Table 2-1 where M refers to U, (U,Pu) or (U,Am).

For the M_4O_9, M_3O_7 and M_3O_8 oxides, the polymorphisms and the corresponding transitions temperatures are indicated in Table 2-1. The space group of the γ-U_3O_7 phase has not been well identified yet [59]. For the M_3O_8 phase, a maximum solubility of 8 at.% Pu [39] and 10 at.% Am, respectively, into the U_3O_8 phase [60] was measured. The transitions between the different polymorphisms of the UO_3 phase are not well defined and depend on sets of parameters such as the starting material and the oxygen partial pressure. Moreover, the space group of the ε-UO_3 is unknown.

Table 2-1 - Crystal structures of uranium, plutonium and/or americium oxides with O/M > 2.1.

Phase	M =	Polymorphisms	Structure / Space group	Existence domain
M_4O_9	U [8], [47] (U,Pu) [32], [62]	α-M_4O_9 [63]	Trigonal ($R3c$, n°161)	T < 350 K
		β-M_4O_9 [16]	Cubic ($I4\bar{3}d$, n°230)	350 < T < 893 K
		γ-M_4O_9 [16]	Cubic ($I4\bar{3}d$, n° 230)	893 < T < 1400 K
M_3O_7	U [64]	α-U_3O_7 [51]	Tetragonal ($I4/m$, n°87)	Metastable
		β-U_3O_7 [51]	Tetragonal ($I\bar{4}2d$, n°122)	
		γ-U_3O_7 [65]	Tetragonal (unknown)	
M_3O_8	U_3O_8 [66] $(U,Am)_3O_8$ [60] $(U,Pu)_3O_8$ [32], [39]	α-U_3O_8 [67]	Orthorhombic ($C2mm$, n°38)	T < 480 K
		β-U_3O_8 [66]	Orthorhombic ($Cmcm$, n°63)	483 < T < 568 K
		α'-U_3O_8 [68]	Hexagonal ($P\bar{6}2m$, n°189)	T > 480 K
MO_3	U [16]	α-UO_3 [69]	Orthorhombic ($C222$, n°21)	Formation conditions depending on the starting materials, temperature and oxygen pressure [70], [71]
		β-MO_3 [69]	Monoclinic ($P2_1$, n°4)	
		γ-MO_3 [69]	Orthorhombic ($Fddd$, n°70)	
		δ-MO_3 [69]	Cubic ($Pm\bar{3}m$, n°221)	
		ε-MO_3 [69]	Triclinic (unknown)	

2.2.2. Lattice constants at room temperature

A summary of crystallographic data at room temperature for uranium, plutonium, americium binary oxides and for ternary mixed oxides is presented in this section.

2.2.2.1 Binary oxides

As a wide range of lattice parameters values can be found in the literature for the binary oxides, the Table 2-2 presents only the commonly accepted values. As the oxides with O/M > 2.1 are not of interest in this work, they are not reported here.

Table 2-2 - Crystallographic data at room temperature for uranium, plutonium and americium oxides.

		Lattice parameters						
	Space group	**a (Å)**	**b (Å)**	**c (Å)**	**α (°)**	**β (°)**	**γ (°)**	**Ref.**
UO_2	$Fm\bar{3}m$	5.471	5.471	5.471	90	90	90	[72]
PuO_2	$Fm\bar{3}m$	5.396	5.396	5.396	90	90	90	[17]
AmO_2	$Fm\bar{3}m$	5.375	5.375	5.375	90	90	90	[73]
A-Pu_2O_3	$P\bar{3}m1$	3.841		5.958	90	90	120	[16]
C-Pu_2O_3	$Ia\bar{3}$	11.02	11.02	11.02	90	90	90	[16]
$PuO_{1.61}$	$Ia\bar{3}$	10.95-11.01	10.95-11.01	10.95-11.01	90	90	90	[17]
A-Am_2O_3	$P\bar{3}m1$	3.821	3.821	5.984	90	90	120	[57]
B-Am_2O_3	$C2/m$	14.35	3.55	8.92		100.4		[74]
C-Am_2O_3	$Ia\bar{3}$	11.01	11.01	11.01	90	90	90	[75]
$AmO_{1.61}$	$Ia\bar{3}$	10.96	10.96	10.96	90	90	90	[74]

A decrease in the lattice parameter is observed when increasing the atomic number, with a higher lattice parameter measured for UO_2 than PuO_2 than AmO_2. In the case of the A-M_2O_3, C-M_2O_3 phases and $MO_{1.61}$ phases, similar lattice parameters are obtained independently of Pu or Am, as it can be seen in Table 2-2.

2.2.2.2 Mixed oxides

In this part, only the mixed dioxides of uranium, plutonium and americium are presented, as they constitute the compounds of interest for nuclear fuel applications.

2.2.2.2.1 $U_{1-y}Pu_yO_{2.00}$

For $U_{1-y}Pu_yO_{2.00}$, numerous experimental data are available. However, comparing the lattice parameters available in the literature can be difficult as they depend on several factors. Indeed, the O/M ratio has a significant impact on the lattice parameter, as well as the impurities (*e.g.*

americium, lanthanides…) and the age of the samples (self-irradiation effect), which information are not always provided in the articles.

The variation in the lattice parameter of stoichiometric $U_{1-y}Pu_yO_{2.00}$ mixed oxides with the plutonium content is shown in Figure 2-12. It follows a Vegard's law between $UO_{2.00}$ and $PuO_{2.00}$ (Equation **(2.1)**) [76]:

$$a\left(U_{1-y}Pu_yO_{2.00}\right)[\text{Å}] = 5.470 - 0.074 \times y \qquad \textbf{(2.1)}$$

In this equation, 5.470 Å corresponds to the lattice parameter of $UO_{2.00}$ determined for Grønvold *et al.* in 1955 [77], which was taken as reference by Duriez *et al.* [76] in 2000. This value slightly differs from the one reported in Table 2-2 (5.471 Å), determined later in 2015 from Leinders *et al.* in 2015 [72].

The lattice parameter of these oxides can also be calculated using the law developed by Kato *et al.* [78], based on the ionic radii of the elements, as it will be described in section 2.2.2.2.4.

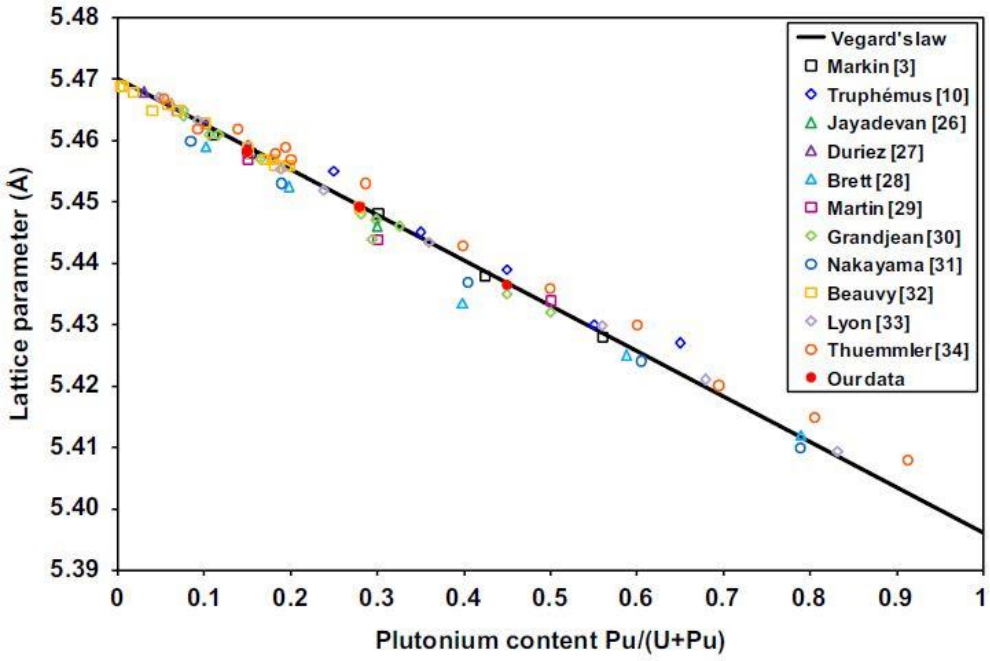

Figure 2-12 : Variations in the lattice parameter of $U_{1-y}Pu_yO_{2.00}$ mixed oxides as a function of the Pu content at room temperature, extracted from Vauchy *et al.* [79].

Deviations from the Vegard's law are observed due to a variation in the O/M ratio and/or to the α self-irradiation effects [80], as it will be explained later in this study (see 2.2.2.3 Influence of O/M ratio on the lattice parameters at room temperature).

2.2.2.2.2 $Pu_{1-z}Am_zO_{2.00}$

Structural studies of $Pu_{1-z}Am_zO_{2.00}$ are still scarce in the literature [42], [73] (Figure 2-13). Similarly to the U-Pu mixed oxides, the variation in the lattice parameter of $Pu_{1-z}Am_zO_{2.00}$ seems to follow a Vegard's law between PuO_2 and AmO_2 (represented by the dashed line on Figure 2-13) [73]. The experimental values are reported in Appendix B. However, some discrepancies can be observed, especially for low americium contents. As mentioned before, this deviation

from the Vegard's law can be explained by the self-irradiation damages or a possible reduction of the samples.

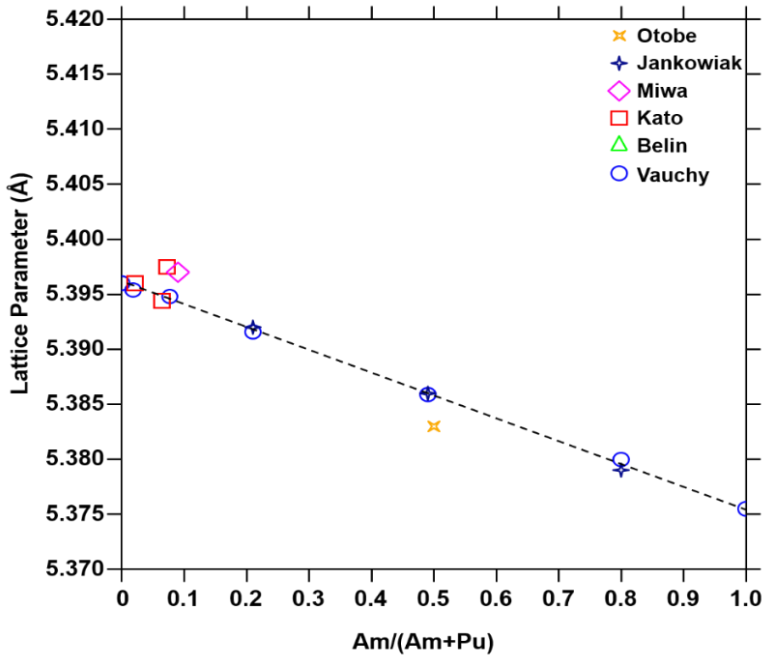

Figure 2-13 : Variation in the lattice parameter of the fluorite structure of $Pu_{1-z}Am_zO_2$ as a function of the Am content at room temperature (experimental data available in Appendix B from [42], [44], [73], [78], [81], [82]).

2.2.2.2.3 $U_{1-z}Am_zO_{2.00}$

In $U_{1-z}Am_zO_{2.00}$ mixed oxides, the lattice parameter of the fcc phase decreases with the americium content (Figure 2-14).

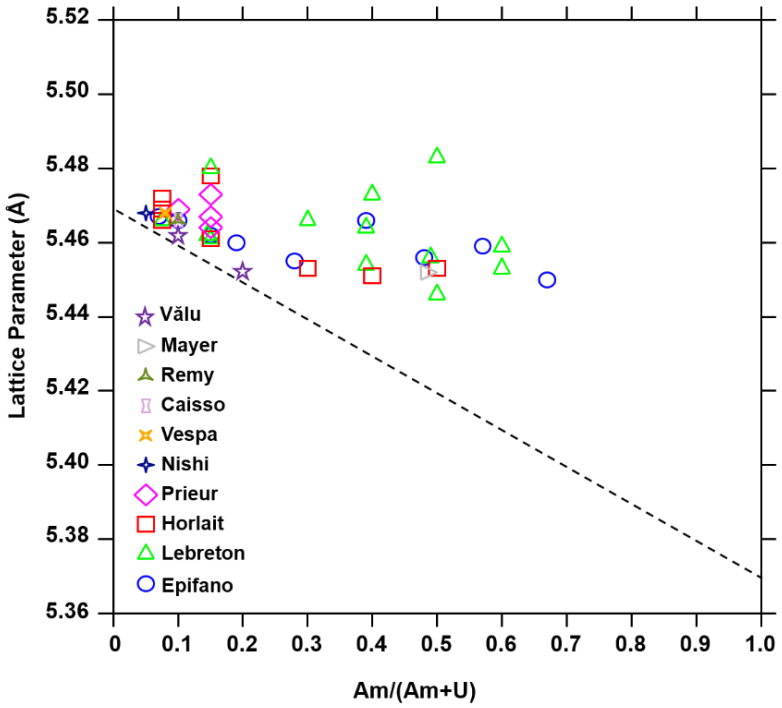

Figure 2-14 : Variations in the lattice parameter of $U_{1-z}Am_zO_2$ as a function of the Am content at room temperature compared to the available experimental data ([28], [83]–[91]).

However, various authors [46], [83], [84] reported that the magnitude of this decrease is smaller than the one expected from the Vegard's law between UO_2 and AmO_2 (represented by the dashed line in Figure 2-14). Possible explanations for this scattering were provided using X-ray Absorption Spectroscopy (XAS), probing the oxidation states of Am and U in various $U_{1-z}Am_zO_{2\pm x}$ [28], [92], [93]. It was evidenced that, regardless of the annealing atmosphere, americium was purely trivalent up to z = 0.50 and a mix of Am^{3+}/Am^{4+} was observed for higher americium contents. It was also shown that a partial oxidation of U^{4+} into U^{5+} occurred. In the Vegard's law, the pure poles are UO_2 and AmO_2, thus it is a relation between U^{4+} and Am^{4+}. However, based on the oxidation states determined by XAS, Am_2O_3 and U_4O_9 should also be considered as end members. Moreover, a systematic reduction of the samples was observed for z > 0.30, with the XAS results. This observation leads to a drift from Vegard's law. Thus, contrarily to $U_{1-y}Pu_yO_{2\pm x}$, the lattice parameter of $U_{1-z}Am_zO_{2\pm x}$ cannot be used to determine the O/M ratio of the sample knowing its americium content, and inversely.

2.2.2.2.4 $U_{1-y-z}Pu_yAm_zO_{2\pm x}$

Kato and Konashi studied some mixed $U_{1-y-z}Pu_yAm_zO_{2\pm x}$ oxides with different Am contents (Figure 2-15), as well as oxides containing both Am and Np: $U_{1-z-y-y''}Pu_yAm_zNp_{y''}O_{2.00}$. The authors proposed an expression of the lattice parameter as a function of the Pu, Am, Np contents **(2.2)**:

$$a = \frac{4}{\sqrt{3}}\left[\left(r_U(1-z-y-y') + r_{Pu}y + r_{Am}z + r_{Np}y'\right) + r_a\right] \quad \textbf{(2.2)}$$

Where a is the lattice parameter, r_U, r_{Pu}, r_{Am} and r_{Np} the ionic radii of U, Pu, Am and Np, and r_a the ionic radius of anion.

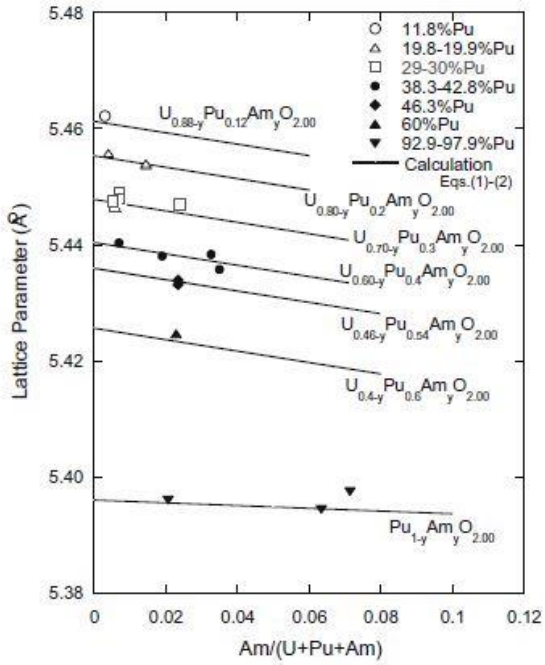

Figure 2-15 : Variation in the lattice parameters of the fluorite structure of $U_{1-y-z}Pu_yAm_zO_{2.00}$, as a function of the Am content, calculated data from equation **(2.2)** [78].

A more exhaustive list of lattice parameter data for $U_{1-y-z}Pu_yAm_zO_{2\pm x}$ mixed oxides is reported in Appendix C. As for all the mixed oxides containing americium, the lattice parameter of the phase is found to decrease when increasing the americium content. For compounds with low

americium content, the lattice parameters exhibit a slight deviation towards the Vegard's law described by Equation **(2.1)** [94].

2.2.2.3 *Influence of O/M ratio on the lattice parameters at room temperature*

Apart from the chemical composition in metal atoms, several parameters have a significant influence on the lattice parameters, namely the O/M ratio and the α self-irradiation. In this section, the observations are valid for room temperature.

In actinide oxides, the O/M ratio has a strong effect on the lattice parameters, which can be explained by the difference between the ionic radii of U, Pu and Am for the different oxidation states of the cations and the coordination numbers of interest (Table 2-3). Indeed, when the oxide is reduced, the trivalent species Pu^{3+} and/or Am^{3+} are present. As the ionic radii of these cations are bigger of 15 % for Am and 18 % for Pu than the ones of their tetravalent form, the reduction thus causes an expansion of the lattice. On the contrary, when the oxide is oxidized, pentavalent uranium is formed and because its ionic radius is 16 % smaller than U^{4+}, a contraction of the lattice occurs. The simultaneous presence of U^{5+}/Am^{3+} or Pu^{3+} evidenced by Epifano et al. and L. Medyk are not described here. Furthermore, another reason for the change in lattice parameter is the increase or decrease of the cation repulsion shielding provided by oxygen atoms when the material is reduced or oxidized, respectively.

Table 2-3 - Ionic radii of U, Pu and Am in the oxidation states and coordination numbers [83].

	U^{4+}	**U^{5+}**	**Pu^{3+}**	**Pu^{3+}**	**Pu^{4+}**	**Am^{3+}**	**Am^{3+}**	**Am^{4+}**	**O^{2-}**
Ionic radius (Å)	1.000	0.840	1.142	1.000	0.960	1.090	0.975	0.95	1.380
Coordination number	8	8	8	6	8	8	6	8	4

2.2.2.3.1 $UO_{2\pm x}$-U_4O_9

In hyper-stoichiometric uranium dioxide UO_{2+x}, with $0 \leq x \leq 0.15$, an empirical relation (Equation **(2.3)**) between the lattice parameter a and the deviation from stoichiometry x (independent from the temperature) was determined by Teske *et al.* [95], based on the experimental results of Grønvold *et al.* obtained by XRD [77].

$$a\ [\text{Å}] = 5.4705 - 0.132 \times x \qquad \textbf{(2.3)}$$

The lattice parameter of UO_{2+x} decreases hence linearly when increasing the O/U ratio, in agreement with the smaller ionic radius of U^{5+} compared to U^{4+} (see Table 2-3). However, when looking at the U-O phase diagram (Figure 2-1), for O/M > 2.03, the UO_{2+x} phase is in equilibrium with the U_4O_9 phase. The upper limit of validity (x = 0.15) is fixed by the detection limit of U_4O_9 (oxidation of UO_2 in U_4O_9), underlined by Elorrieta *et al.*, where a change of slope is observed in the decrease of the lattice parameter with the stoichiometry [96]. This equation is thus limited for lattice parameters comprised between 5.471 Å ($a(UO_2)$) and 5.444 Å ($a(U_4O_9)$).

Experimental data, obtained by N.A. Javed [97], are available on hypo-stoichiometric UO_{2-x}. No significant changes in the lattice parameters are observed when decreasing the O/U ratio.

2.2.2.3.2 $PuO_{2\pm x}$

Haschke *et al.* [22] determined a linear variation in the lattice parameter of the fluorite PuO_{2+x} phase as a function of the deviation from stoichiometry x (0 < x <0.27) (Equation **(2.4)**):

$$a\,[\text{Å}] = 5.3643 + 0.01746 \times x \qquad \textbf{(2.4)}$$

However, care should be taken while using this relation. Indeed, the substitution of Pu^{4+} by Pu^{5+} assumed by the authors should lead to a contraction of the lattice, partially compensating the expansion induced by the insertion of oxygen atoms, and not an increase in the lattice parameter as observed here. Moreover, the existence of the hyper-stoichiometric PuO_{2+x} phase is controversial. In addition, the commonly accepted value for stoichiometric $PuO_{2.00}$ is 5.396 Å, significantly higher than the value used by Haschke *et al.* in equation **(2.4)**.

Experimental data are available for hypo-stoichiometric PuO_{2-x} [17] but no correlation between the lattice parameter and the stoichiometry is proposed in the literature. Gardner *et al.* reported an increase of the lattice parameter when decreasing the O/Pu ratio [17], in agreement with the bigger ionic radius of Pu^{3+} compared to Pu^{4+}.

2.2.2.3.3 $U_{1-y}Pu_yO_{2\pm x}$

For $U_{1-y}Pu_yO_{2\pm x}$, Duriez *et al.* [76],[98] established a relation based on a review of the available experimental data. The authors derived a linear variation in the lattice parameter with the deviation stoichiometry x and the plutonium content y, based on the Vegard's law between UO_2 and PuO_2 (Equation **(2.1)**) leading to Equation **(2.5)**):

$$a\,[\text{Å}] = 5.470 - 0.075 \times y + 0.32 \times x \qquad \textbf{(2.5)}$$

In this equation, as explained in 2.2.2.2.1, 5.470 Å corresponds to the lattice parameter of $UO_{2.00}$ determined for Grønvold *et al.* in 1955 [77], available as the time of Duriez *et al.* [76] in 2000, and slightly differs from the one reported in Table 2-2 (5.471 Å), determined later in 2015 from Leinders *et al.* in 2015 [72].

This relation was initially limited by Duriez *et al.* to a monophasic hypo-stoichiometric domain with $y \leq 0.3$ and O/M > 1.925. However, it appears to be valid in the biphasic domain for $0.3 \leq y \leq 0.45$, as Vauchy *et al.* used it to calculate the lattice parameters of each phase within the miscibility gap, at y = 0.45 [99] and O/M > 1.819.

2.2.2.3.4 $U_{1-y-z}Pu_yAm_zO_{2-x}$

The expression **(2.1)** proposed by Kato and Konashi linking the lattice parameter to the ionic radii of U, Pu, Am and Np in $(U_{1-z-y-y''}Pu_yAm_zNp_{y''})O_{2-x}$ was also proposed by the same authors as a function of the oxygen hypo-stoichiometry **(2.1)**, for 0 < x < 0.03 [78]. The additional term $(1 + 0.112x)$ indicates the increase of the lattice parameter when decreasing the O/M ratio.

$$a = \frac{4}{\sqrt{3}}[(r_U(1-z-y'-y'') + r_{Pu}z + r_{Am}y' + r_{Np}y'')(1+0.112x) + r_a] \quad \textbf{(2.6)}$$

The Figure 2-16 represents the variation in the lattice parameter as a function of the plutonium content and O/M ratio according to Equation **(2.5)** from Duriez *et al.* and Equation **(2.6)** from Kato and Konashi. The decrease of the lattice parameter when increasing the Pu content and the decreasing the O/M ratio is evidenced.

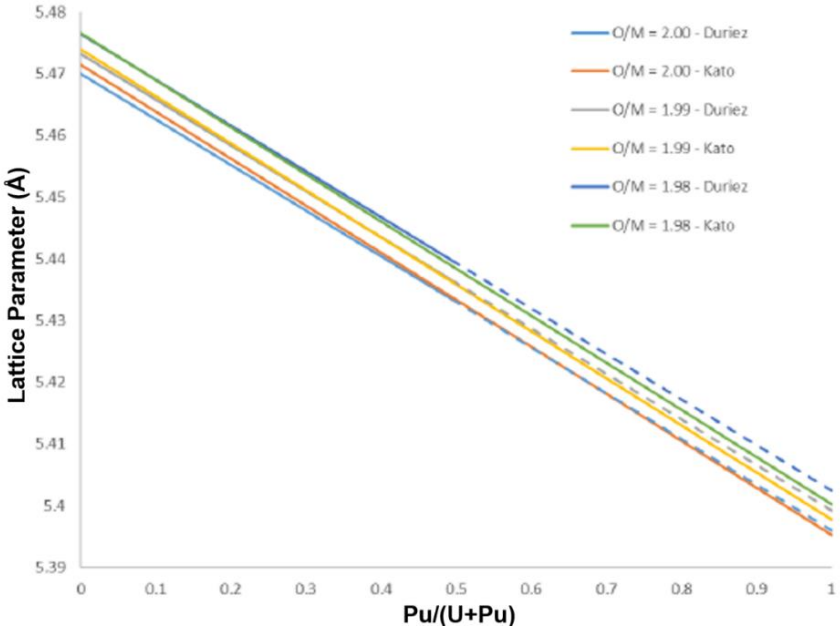

Figure 2-16: Variation in the lattice parameter as a function of the plutonium content and O/M ratio obtained via Equation (2.5) (Duriez *et al.*) [76] and Equation (2.6) (Kato and Konashi) [78]. The dashed lines represent the extrapolation of the Equation (2.5) above its validity range [54].

2.2.2.4 Influence of α self-irradiation on the lattice parameter at room temperature

The α self-irradiation effect on structural properties refers to the irradiation triggered by the α decay of a radioactive isotope ${}^{A}_{Z}M$ present in a material. Indeed, various isotopes of actinides (in particular of Pu and Am) are α-emitters according to equation **(2.7)**:

$${}^{A}_{Z}M \rightarrow {}^{A-4}_{Z-2}N + {}^{4}_{2}\alpha \quad \textbf{(2.7)}$$

During this decay, a recoil particle N as well as a α particle, corresponding to a helium nucleus, are emitted with a recoil energy of 80-100 keV and a kinetic energy of 5-6 MeV. After emission, the α particles interact with the surrounding atoms in the material structure by two distinct phenomena: electronic and ballistic collisions.

During a ballistic collision, a part of the kinetic energy of the incident particle is transmitted to the targeted atom, which is then displaced. As the displacement threshold of O and U in UO_2 are respectively 20 and 40 eV [100], the α decay can produce the movement of many atoms in the lattice. If the transmitted energy is sufficient, a new collision can occur. This succession of point defects (vacancies and interstitials) generated by α decay is called a displacement cascade. However, because of the proximity of the point defects and the local temperature increase, a near-instantaneous annihilation of many of the vacancies and interstitials occurs. The remaining point defects can be stabilized by formation of defect clusters, dislocations and cavities [101].

For the recoil particles, approximately 95% of its energy is dissipated along 20-30 nm by means of ballistic collisions, whereas this value for the energy of α particles results from electronic interactions is approximatively 20 µm.

The effects of the α self-irradiation have been studied for various actinides mixed oxides [75], [81], [102]–[105]. No amorphization of the materials is observed. Different types of microscopic damages can be observed in these materials, such as the formation of nanometric size gas cavities attributed to He bubbles [106], phase transitions [102] (mostly allotropic) and/or dislocation loops.

Another possible damage is the swelling of the crystal structure. The following equation **(2.8)** describes the volume expansion of the crystal structure as a function of the storage time and the initial isotopic composition of the self-irradiated samples:

$$\frac{\Delta a}{a_0} = \frac{a_t - a_i}{a_t} = A \times \left(1 - e^{B \times \lambda \times t}\right) \quad \textbf{(2.8)}$$

Where a_t the lattice parameter (in Å) at a generic time t (in s), a_i the initial undamaged lattice parameter (in Å), A and B two dimensionless constants and λ the half-life constant based on the isotopic composition (in s^{-1}) and t the duration of the self-irradiation (in s).

In the case of $U_{1-y}Pu_yO_{2\pm x}$, A and B are respectively equal to 2.9×10^{-3} and -12 000 [107].

In the case of fluorite-structured actinide mixed oxides, the structural swelling related to the α self-irradiation reaches a saturation value. The latter corresponds to the constant A in Equation **(2.8)**. It is important to underline that the fcc structure is maintained through the creation of these defects. For plutonium dioxide, Noe and Fuger measured the lattice parameter evolution of a $^{238}PuO_2$ sample [108]. It was observed that the lattice parameter progressively increased until reaching a maximum value of $\frac{\Delta a}{a_0} = 2.6 \times 10^{-3}$, where it stabilizes. For americium dioxide, this value is ranging from 0.29 to 0.40 % depending on the authors [29], [106].

The Figure 2-17 illustrates this saturation behaviour for (a) $U_{1-y}Pu_yO_{2\pm x}$ [107] and (b) $U_{1-z}Am_zO_{2\pm x}$ [46], [109].

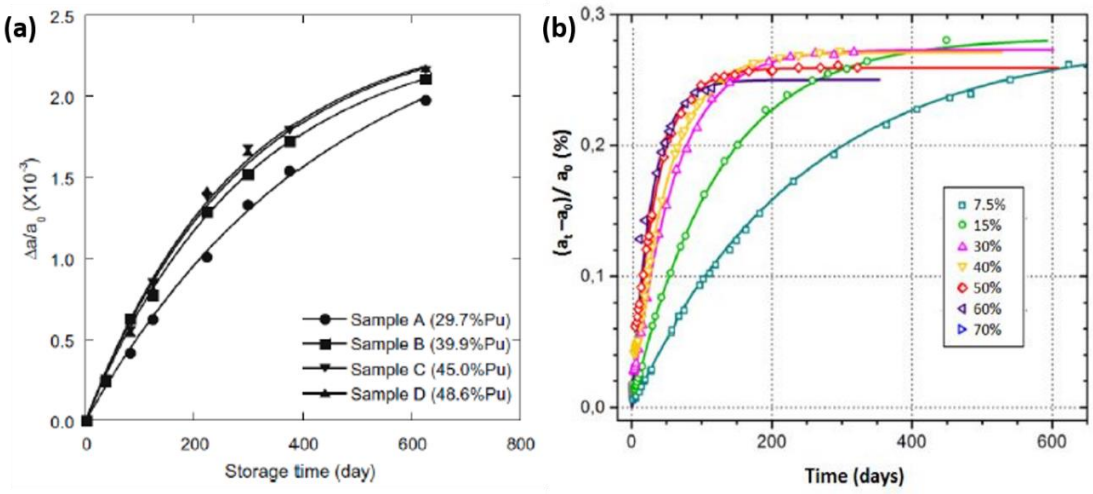

Figure 2-17 : Self-irradiation induced for (a) $U_{1-y}Pu_yO_{2\pm x}$ [107] and (b) $U_{1-z}Am_zO_{2\pm x}$ [109], [110].

It can be noticed that the swelling of the lattice increases with the plutonium content in $U_{1-y}Pu_yO_{2\pm x}$ and the saturation value is not reached in this case after two years of storage. However, the saturation value and the time needed for reach it depends on the isotopic composition of the samples. In the case of the $U_{1-z}Am_zO_{2\pm x}$ (Figure 2-17(b)), the swelling kinetics was found to increase with the americium content and thus with the sample's activity. However, the saturation values are lower for high americium contents. It was proven that the shorter the decay period of the isotope, the faster the maximum lattice parameter value is reached [107].

The defects produced by the α self-irradiation can be annealed by performing thermal treatments. A gradual restructuration of the lattice is observed from 400 to 1500 K in the case of $U_{1-y}Pu_yO_{2\pm x}$, independently of the plutonium content. A study performed by Staicu *et al.* allowed to differentiate four steps in the annealing (Figure 2-18) [111]. The first step corresponds to the recombination of the Frenkel defects in the oxygen sublattice, the second step to the recombination of the Frenkel defects in the cationic sublattice, the third step to the formation of dislocation loops and the fourth step to the release of He. These annealing temperatures are similar to the ones obtained by Weber for PuO_2 [105].

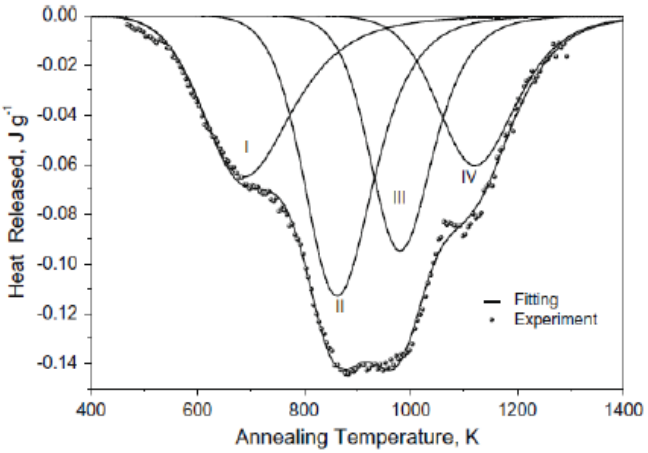

Figure 2-18: Heat released during the annealing process for a UO_2 sample doped with 10 wt.% of α-emitters [111].

2.2.3. Thermal expansion

The temperature also affects the lattice parameter of the materials. Generally, a temperature increase causes an expansion of the fluorite structure for all actinide oxides. In this section, the lattice parameter variation measured by High Temperature-X-Ray Diffraction (HT-XRD) and/or the thermal expansion data determined by dilatometry are presented for binary and ternary dioxides.

2.2.3.1 Binary dioxides

2.2.3.1.1 UO_{2+x}

Available thermal expansion data obtained by dilatometry for stoichiometric UO_2 and for UO_{2+x} with $0 < x < 0.13$ and $0.23 < x < 0.25$ were critically assessed by D.G. Martin [112]. The following equations **(2.9)** and **(2.10)** were deduced for temperatures up to 3120 K. These relations were later confirmed by Carbajo *et al.* [113] and Fink [114].

$$a(T)_{UO_2} = a_{273K}(9.9734 \times 10^{-1} + 9.802 \times 10^{-6} \times T - 2.705 \times 10^{-10} \times T^2 + 4.391 \times 10^{-13} \times T^3) \quad \text{for } 273 \leq T \leq 923 \text{ K} \quad \textbf{(2.9)}$$

$$a\,(T)_{UO_2} = a_{273K}(9.9672 \times 10^{-1} + 1.179 \times 10^{-5} \times T - 2.429 \times 10^{-9} \times T^2 + 1.219 \times 10^{-12} \times T^3) \quad \text{for } 923 \leq T \leq 3120 \text{ K} \quad \textbf{(2.10)}$$

With a the lattice parameter of the sample at T (in Å) of the fluorite phase and T the temperature (in K).

2.2.3.1.2 PuO_2

For stoichiometric plutonium dioxide, several studies were conducted by Uchida *et al.*, Yamashita *et al.* and Kato *et al.* by HT-XRD and dilatometry [115]–[117] leading to equation **(2.11)**, valid from room temperature to 1300 K:

$$a(T)_{PuO_2} = 538.1 + 4.452 \times 10^{-3} \times T + 7.184 \times 10^{-7} \times T^2 + 1.995 \times 10^{-11} \times T^3 \quad \textbf{(2.11)}$$

With a the lattice parameter (in pm) of the fluorite phase and T the temperature (in K).

However, care should be taken when using this equation. Indeed, the reference lattice parameter for $PuO_{2.00}$ at room temperature was admitted to be equal to 5.396 Å, determined by Gardner *et al.* [17], and not 5.381 Å [116], as admitted in this equation. Moreover, a reduction of stoichiometric PuO_2 into PuO_{2-x} most likely occurs at high temperature, influencing the lattice parameter.

2.2.3.1.3 AmO_{2-x}

Lattice thermal expansion of AmO_2 was measured by HT-XRD in pure oxygen up to 1230 K by Fahey *et al.* [118] and in air up to 1500 K by Minato *et al.* [119].

Recently, Vauchy *et al.* [73] proposed in Equation **(2.12)** a relation between the lattice parameter of $AmO_{2.00}$ and the temperature for T < 1100 K:

$$a\,(T)_{AmO_2} = 5.356 + 6.533 \times 10^{-5} \times T \quad \textbf{(2.12)}$$

With a the lattice parameter (in Å) of the fluorite phase and T the temperature (in K).

However, it can be noticed that the lattice parameter determined for AmO_2 using this equation at room temperature differs from the value recommended by the same authors, *e.g* 5.375 Å. Thus, care should be taken while using this equation.

This relation was found to be close to the one obtained by Epifano *et al.* [120] (see Equation **(2.13)** for x = 0).

Indeed, the variation of the lattice parameter of AmO_{2-x} as a function of both temperature and O/Am ratio was studied by Epifano *et al.* [6], who proposed the following equation **(2.13)** for 300 < T < 1900 K and 0 < x < 0.4.

$$a\,(T, O/Am) = 5.376 + 6 \times 10^{-5}\,(T - 298.15) + 0.248 \times x \qquad \textbf{(2.13)}$$

This equation was considered to be more reliable as the lattice parameter obtained for AmO_2 at room temperature follows the recommendation.

Comparison between the recommendations proposed by Epifano *et al.* [6], Vauchy *et al.* [73] and Fahey *et al.* [118] for the variation in the lattice parameter of AmO_2 as a function of the temperature is proposed in Figure 2-19. As stated, the variations measured by Epifano *et al.* and Vauchy *et al.* are similar, whereas smaller lattice parameters were observed by Fahey *et al.*. This difference can originate from slightly hypo-stoichiometric oxides in the case of the two first authors induced by a slow re-oxidation rate, which leads to higher lattice parameters.

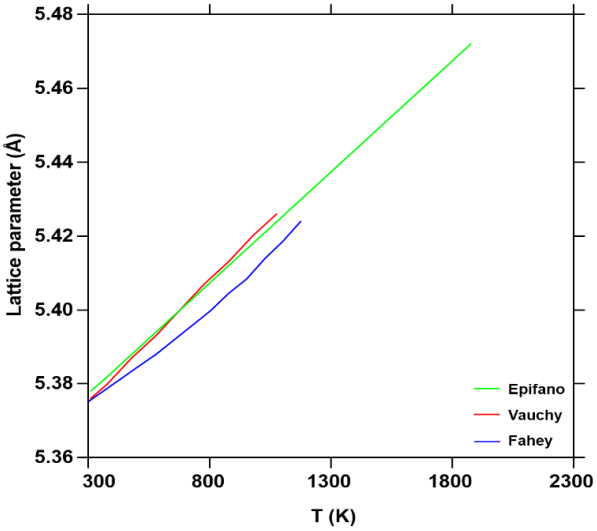

Figure 2-19 : Comparison of the variation in the lattice parameter of the fluorite structure of AmO_2 measured by Epifano *et al.* [6], Vauchy *et al.* [73] and Fahey *et al.* [118].

A comparison between the thermal expansions of the three binary oxides UO_2 (by D.G. Martin [112]), PuO_2 (by Yamashita *et al.* [116]) and AmO_2 (by Epifano *et al.* [6]) is plotted in Figure 2-20.

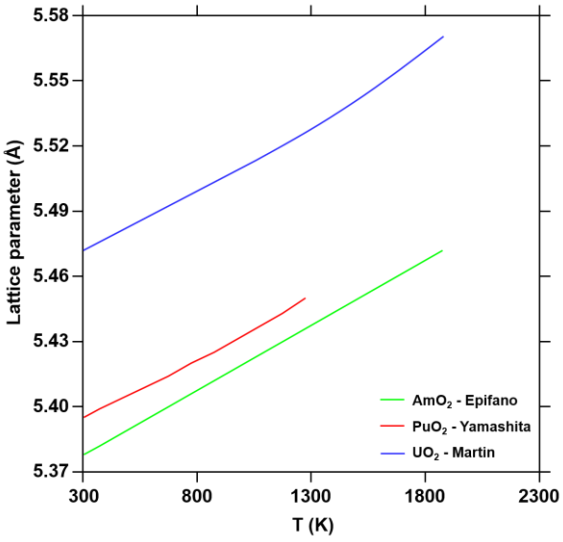

Figure 2-20: Comparison of the variation in the lattice parameter as a function of the temperature of UO_2 [112], PuO_2 [116] and AmO_2 [6].

As it can be seen, the lattice parameters of the three oxides in temperature follows the same trend than at room temperature (see section 2.2.2.1): higher values are obtained for UO_2, followed by PuO_2 and then AmO_2. However, care should be taken when comparing these results, as the deviation from stoichiometry occurring at high temperature may influence the lattice parameters obtained here. For the three oxides, further experiments are needed to take into account the influence of hypo- and hyper-stoichiometry on the thermal expansion.

2.2.3.2 Mixed dioxides

2.2.3.2.1 $U_{1-y}Pu_yO_{2\pm x}$

Several measurements of the lattice thermal expansion of $U_{1-y}Pu_yO_{2\pm x}$ are available in the literature, for example by Tsuji *et al.* [121], Vauchy *et al.* [41] or Kato *et al.* [117]. Over the whole plutonium content range, the lattice parameter of the *fcc* phase increases linearly with the temperature and the variation depends on the plutonium content (Figure 2-21).

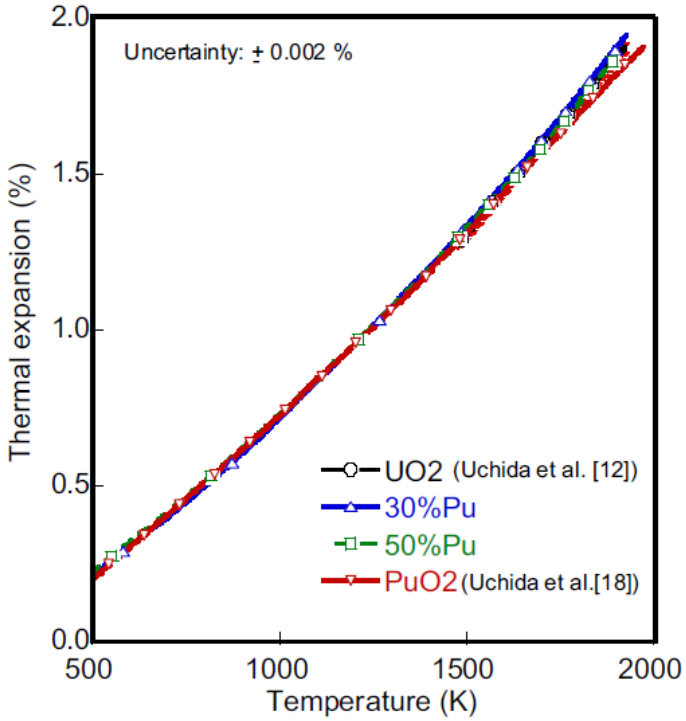

Figure 2-21 : Variation in the lattice parameter of the fluorite structure of $U_{1-y}Pu_yO_2$ as a function of temperature and Pu content [122].

In the review of D.G. Martin [112], the thermal expansions measured for $U_{1-y}Pu_yO_{2.00}$ with $y \leq 0.25$ are similar to the one of $UO_{2.00}$. Thus, the author suggested the use of the Equations **(2.9)** and **(2.10)** for stoichiometric uranium-plutonium mixed oxides for $y \leq 0.25$. A correction was proposed by the author to take into account the influence of the hypo-stoichiometry in oxygen ($0 < x < 0.06$) based on few sets of experimental data.

A more reliable study was performed by Kato *et al.* [122], who determined the influence of the O/M ratio on the variation in the lattice parameter at different temperatures using dilatometry. The thermal expansion $\frac{\Delta L}{L_0}$ as a function of the temperature T (RT to 1923 K), the molar fraction of plutonium C_{Pu} ($0 < C_{Pu} < 1$) and the deviation from stoichiometry x ($0 < x < 0.03$) was determined for $U_{1-y}Pu_yO_{2-x}$ **(2.14)**:

$$\frac{\Delta L}{L_0} = a_0 + a_1 T + a_2 T^2 + a_3 T^3 \quad \textbf{(2.14)}$$

$$a_i = b_0 + b_1 C_{Pu} + b_2 x + b_3 C_{Pu}^2 + b_4 x^2 + b_5 C_{Pu} x \quad \textbf{(2.15)}$$

The coefficients b_i are reported in Table 2-4.

Table 2-4 - Coefficients b_0, b_1, b_2, b_3, b_4 and b_5 of Equation (2.15) by Kato *et al.* [122].

	b_0	**b_1**	**b_2**	**b_3**	**b_4**	**b_5**
a_0 ($x10^{-3}$)	-2.8809	0.0301	-4.3954	0.0156	-15.1759	2.5642
a_1 ($x10^{-6}$)	9.5024	-0.1864	15.8173	-0.0229	7.6285	-7.5789
a_2 ($x10^{-10}$)	2.0894	2.9483	-19.9227	-1.0355	73.8931	11.6442
a_3 ($x10^{-13}$)	4.4096	-1.4263	23.5638	0.0251	-54.751	-14.418

This equation is assumed to be valid for all plutonium contents. However, only four plutonium contents (0, 0.30, 0.48 and 1) were studied in the work of Kato *et al.*. Thus, further experiments with other plutonium contents are needed to confirm the validity range of the equation.

2.2.3.2.2 $Pu_{1-z}Am_zO_{2-x}$

A single study on the thermal expansion of $Pu_{1-z}Am_zO_{2-x}$ is reported in the literature by Vauchy *et al.* by HT-XRD [73]. The lattice parameter variation as a function of the temperature and the americium content is represented in Figure 2-22(a).

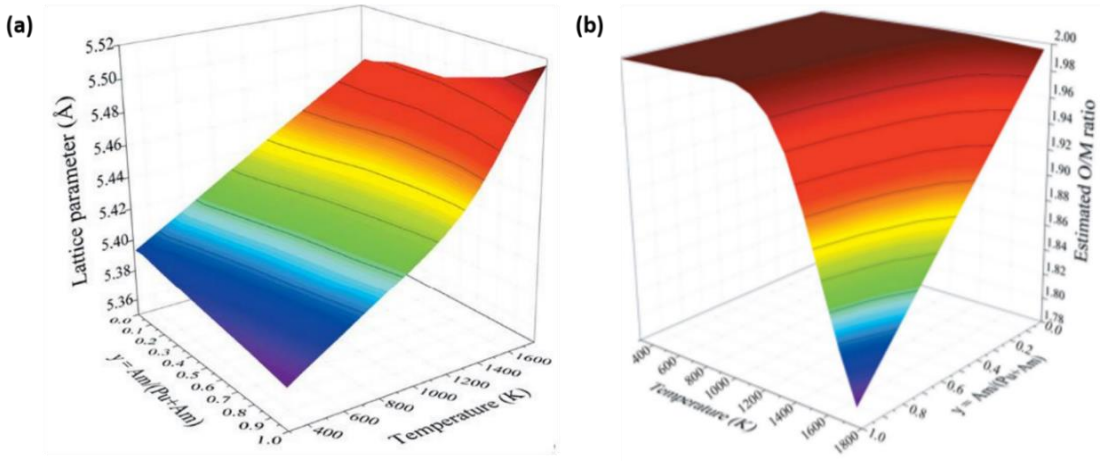

Figure 2-22 : (a) Variation in the lattice parameter of the fluorite structure of $Pu_{1-z}Am_zO_{2-x}$ and (b) of the estimated O/M ratio as a function of temperature and Am content [73].

As expected, the lattice parameter increases with the temperature and decreases with the americium content. In this study, the change of slope observed at high temperature is explained by the assumed reduction of the sample occurring at high temperature as it can be seen in Figure 2-22(b). However, only an estimation of the O/M ratio is proposed here and experimental determinations are needed to confirm.

2.2.3.2.3 $U_{1-z}Am_zO_{2\pm x}$

For $U_{1-z}Am_zO_{2\pm x}$, few high temperature data exist. Prieur *et al.* [123] studied the lattice expansion of self-irradiated samples with z = 0.20 using HT-XRD between room temperature and 1573 K. F. Lebreton [46] performed HT-XRD measurements under reducing atmosphere for z = 0.50, 0.60 and 0.70 for 298 < T < 1700 K. E. Epifano also studied some $U_{1-z}Am_zO_{2\pm x}$ oxides, for 0.10 ≤ z ≤ 0.70, by HT-XRD from room temperature to 1473 K and proposed the equation **(2.16)**) for the lattice parameter as a function of the temperature (298 < T < 1473 K):

$$a(T) = a_{298.15} + b \times (T - 298.15) \quad \textbf{(2.16)}$$

With a the lattice parameter (in Å) at T, $a_{298.15}$ the lattice parameter at 298 K (in Å) and T the temperature (in K). The $a_{298.15}$ and b coefficients [28] can be found in Table 2-5.

In the work of Epifano, as the experiments were performed under air, oxidation of some samples occurs, resulting in the formation of M_4O_9 and M_3O_8 phases. In addition, comparison between the thermal expansions obtained by the three authors is not possible as different americium contents and atmosphere were used.

Table 2-5 - Lattice parameter variation for $U_{1-z}Am_zO_{2\pm x}$ with temperature - Parameters of Equation (2.16) from E. Epifano [28].

z	$\boldsymbol{a_{298.15}}$ **[Å]**	**b** $\boldsymbol{\times 10^5}$ **[Å.** $\boldsymbol{K^{-1}}$**]**
0.10	5.430	5.6
0.15	5.434	5.9
0.30	5.432	7.3
0.50	5.440	6.9
0.70	5.431	6.5

2.2.3.2.4 $U_{1-y-z}Pu_yAm_zO_{2-x}$

Only one study on the variation in the lattice parameter of $U_{1-y-z}Pu_yAm_zO_2$ as a function of the temperature is available in the literature from Prieur *et al.* [124]. The linear thermal expansion of $U_{0.74}Pu_{0.22}Am_{0.035}Np_{0.005}O_{1.98}$ (Am-MOX) and $U_{0.74}Pu_{0.22}Am_{0.02}Np_{0.02}O_{1.99}$ (Np-MOX) was studied using HT-XRD from RT to 1970 K. The data of the Am-MOX and Np-MOX are very close to the thermal expansion of UO_2 (Figure 2-23).

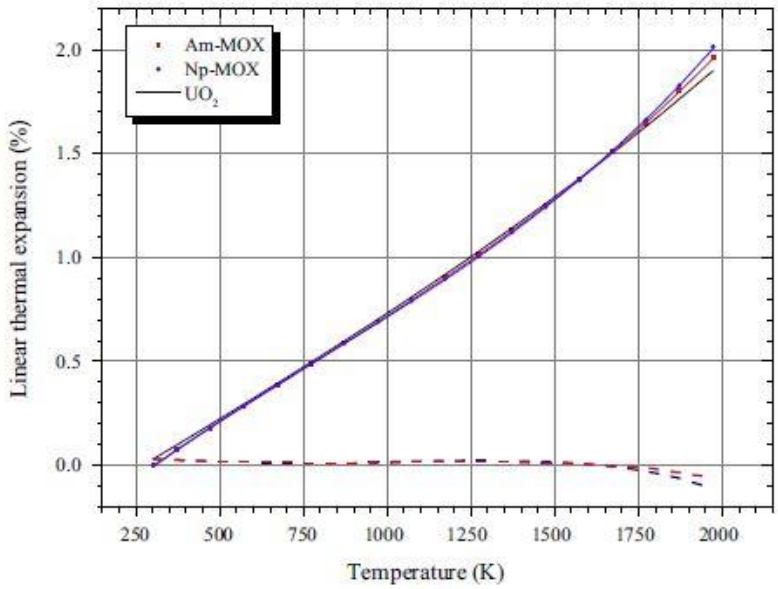

Figure 2-23 : Variation in the thermal expansion of $U_{0.74}Pu_{0.22}Am_{0.035}Np_{0.005}$ as a function of temperature, compared to UO_2 [124].

However, a deviation from the recommendation for UO_2 is noticed for T > 1750 K, which is slightly higher in the case of the Np-MOX. This difference is explained by a reduction of the samples, leading to bigger lattice parameters. Further studies on a broader range of contents are needed for this system.

2.3. THERMODYNAMIC PROPERTIES

In this section, the thermodynamic properties of uranium, plutonium and americium binary and ternary dioxides are presented. The enthalpies of formation, standard entropies and heat capacities data are described. Then, the oxygen potential variation with the composition, the temperature and the O/M ratio is also reported. Finally, the melting behaviour of these compounds is discussed. For these thermodynamic properties, numerous simulations using atomic scale methods or Molecular Dynamics are available in literature. Examples of these results are briefly discussed in this work but no exhaustive review will be performed.

2.3.1. Enthalpy, entropy, heat capacity

2.3.1.1 Binary dioxides

Enthalpy of formation and standard entropy at 298.15 K of the different actinide dioxides (uranium, plutonium and americium) reviewed by Konings *et al.* [125] are reported in Table 2-6.

Table 2-6 - Standard enthalpy of formation, standard entropy and heat capacity at 298.15 K for UO_2, PuO_2 and AmO_2 [125].

Oxide	$\Delta_f H^\circ(298.15\ K)$ **(kJ.mol^{-1})**	$S^\circ(298.15\ K)$ **(J.K^{-1}.mol^{-1})**	$C_P(298.15\ K)$ **(J.K^{-1}.mol^{-1})**
UO_2	-1085.0 ± 1.0	77.0 ± 0.2	63.6
PuO_2	-1055.8 ± 1.0	66.1 ± 0.30	66.3
AmO_2	-932.2 ± 3.0	75.5 ± 3.0	64.3

Available experimental data on enthalpy increments above room temperature for UO_2, PuO_2 and AmO_2, obtained for example by drop calorimetry [126], [127], were critically reviewed by Carbajo *et al.* [113] and Konings *et al.* [125]. For all the actinide dioxides, the following polynomial equation is used to describe the enthalpy increment in temperature **(2.17)**:

$$H(T) - H(298.15\ K) = a_0 + a_1 \times t - a_2 \times t^2 + a_3 \times t^3 + a_4 \times t^4 - a_5 \times t^5 + a_6 \times t^{-1} \quad \textbf{(2.17)}$$

Where $t = T/1000$, T the temperature in K, and $H(T) - H(298.15\ K)$ in kJ.mol^{-1}.

The a_i coefficients are reported for the three oxides in Table 2-7.

Table 2-7 – Enthalpy increments for UO_2, PuO_2 and AmO_2 - a_i coefficients of Equation (2.17).

	a_0	a_1	a_2	a_3	a_4	a_5	a_6
$UO_{2.00}$ (J.K. Fink [114])	-21.176	52.174	43.973	- 28.080	7.885	0.527	0.714
$PuO_{2.00}$ (J.K. Fink [128])	-32.034	84.495	5.319	0.204	-	-	1.901
$AmO_{2.00}$ (Nishi *et al.* [129])	-0.0378	8.824x10^{-5}	-6.575x10^{-10}	-	-	-	3.423

Heat capacities of UO_2, PuO_2 and AmO_2 were also measured using a laser pulse method [130] or derived from the enthalpy increments and reviewed by Carbajo *et al.* [113] and Konings *et al.*. Recommended functions follow the equation **(2.18)**:

$$C_p = b_0 + b_1 \times T - b_2 \times T^2 + b_3 \times T^3 - b_4 \times T^{-2} \quad \textbf{(2.18)}$$

The b_i coefficients can be found in Table 2-8.

Table 2-8 – Heat capacity of UO_2, PuO_2 and AmO_2 - b_i coefficients of Equation (2.18).

	b_0	b_1	b_2	b_3	b_4
$UO_{2.00}$ (Konings *et al.* [125])	66.744	43.139×10^{-3}	35.640×10^{-6}	11.655×10^{-9}	1.169×10^{6}
$PuO_{2.00}$ (Konings *et al.* [125])	35.295	0.152	127.255×10^{-6}	36.289×10^{-9}	3.476×10^{5}
$AmO_{2.00}$ (Konings *et al.* [125])	78.972	3.836×10^{-3}	-	-	1.406×10^{6}

The high-temperature heat capacities of various actinides oxides, recommended by Konings *et al.* [125], are plotted in Figure 2-24 [131]. Only the trend of UO_2, PuO_2 and AmO_2 will be commented here as they are the main oxides of interest.

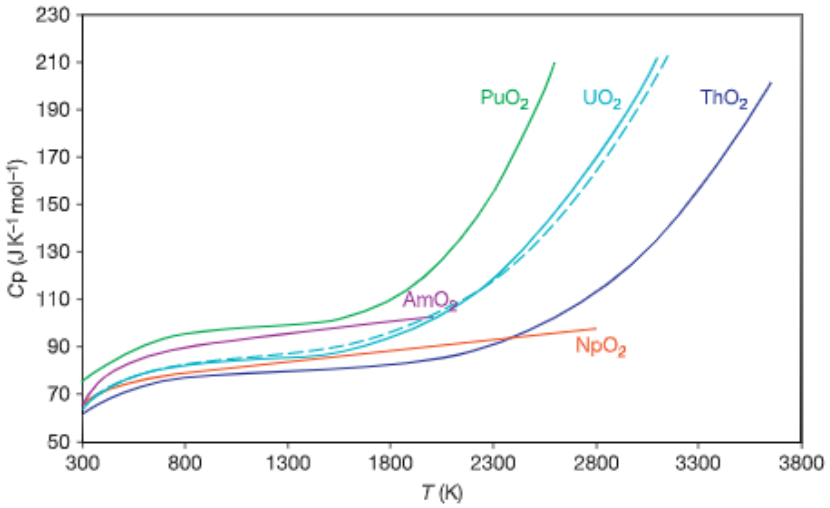

Figure 2-24: Heat capacity of various actinides dioxides (Konings et al. [125]) from [131].

For UO_2, a sharp increase in the heat capacity is noticed above 1700 K, attributed to the creation of defects such as oxygen Frenkel pairs. Recently, laser flash measurements performed by Pavlov *et al.* on UO_2 evidenced a peak at 2715 ± 100 K in the heat capacity (not represented on Figure 2-24), allowing the identification of a superionic transition, referred to as the Bredig transition. This peak is not described by the Equation **(2.18)** and was attributed by the authors to a competition between oxygen defect creation and saturation of the possible oxygen interstitial site. The heat capacity of PuO_2 follows the same trend as the one of UO_2. A superionic transition (not represented here) was also observed around 2400 K by molecular dynamics simulations performed by Cooper *et al.* [132] but disagrees with the experimental results of J. Ralph, who reported a continuous increase up to 2600 K [133]. A different trend is observed for AmO_2, where no sharp increase is observed. However, the experimental data were obtained by Nishi *et al.* only up to 1100 K [129].

2.3.1.2 Mixed dioxides

For all mixed oxides of uranium, plutonium and americium, the Neumann-Kopp rule is often used to estimate the heat capacity. In such case, the heat capacity of the mixed oxide, considered as an ideal solution, is calculated by a linear combination of the end-members.

2.3.1.2.1 $U_{1-y}Pu_yO_{2\pm x}$

A first review of the available experimental data of enthalpy increment for $U_{1-y}Pu_yO_{2\pm x}$ was performed by Carbajo *et al.* [113]. Additional measurements were performed by Kandan *et al.* [134], [135] for y = 0.21, 0.28, 0.40, 0.45, 0.55 and 0.65, and by Vălu *et al.* for 0.25, 0.50, 0.75, 0.80 and 0.90 [136]. The enthalpy increments data (in $kJ.mol^{-1}$) were fitted by a least-square method using a 4-term polynomial function in temperature (see Equation **(2.19)**). The coefficients obtained from the fits for the different mixed oxides of Kandan *et al.* are reported in Table 2-9 [134], [135].

$$H(T) - H(298.15\,K) = c_0 + c_1 \times T + c_2 \times T^2 + c_3 \times T^{-1} \quad \textbf{(2.19)}$$

Table 2-9 – Enthalpy increment for $U_{1-y}Pu_yO_2$ - Parameters of Equation (2.19) (Kandan *et al.* [134], [135]).

Plutonium content	c_0	c_1	c_2 x 10^3	c_3 x 10^{-5}	Temperature [K]
0.21	-29534	79.895	3.905	16	298-1800
0.28	-28710	77.841	5.606	14.917	298-1800
0.40	-28944	78.263	5.881	15.166	298-1800
0.45	-28803	77.983	6.121	14.9325	298-1803
0.55	-28502	77.419	6.537	14.4257	298-1782
0.65	-29691	79.757	6.051	16.0203	298-1797

Heat capacity functions of $U_{1-y}Pu_yO_2$, obtained using the Neumann-Kopp rule (equation **(2.20)**), were assessed by Carbajo *et al.* [113] and Duriez *et al.* [76] in their reviews.

$$C_p(T, U_{1-y}Pu_yO_2) = (1-y) \times C_p(T, UO_2) + y \times C_p(T, PuO_2) \quad \textbf{(2.20)}$$

The Figure 2-25 shows calculated and experimental data for UO_2, PuO_2 and $U_{1-y}Pu_yO_2$ with y = 0.05, 0.20 and 0.25 [113]. As expected, the heat capacity values for y = 0.05 are close to the ones of UO_2, contributing to 95% of the total value. It can be noticed that the calculated values agree with the experimental data of Leibowitz *et al.* [137] and Gibby *et al.* [138] for y = 0.20 and 0.25.

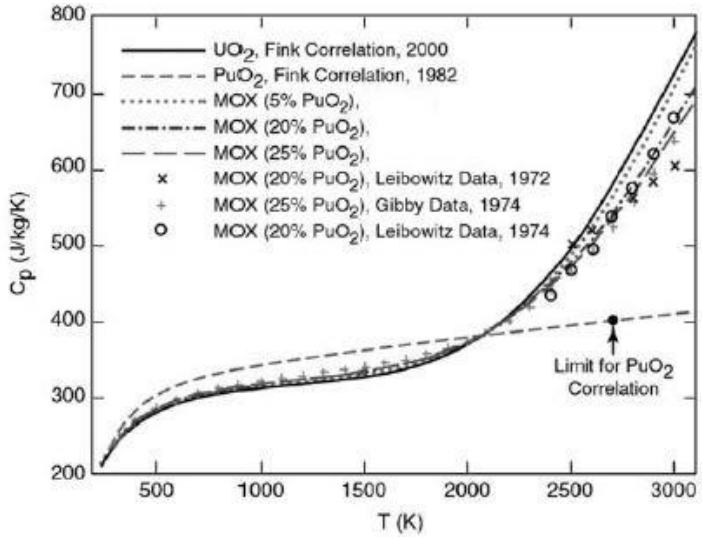

Figure 2-25 : Heat capacity of UO_2, PuO_2 and $U_{1-y}Pu_yO_2$ for different plutonium contents [113].

Another experimental campaign was performed in the frame of the ESNII+ European Project, where heat capacities of $U_{1-y}Pu_yO_{2\pm x}$ were measured, in the associated deliverable D.7.4.1 [139]. The results obtained (not shown here) were compared to the recommendation of Duriez *et al.* and were consistent with the literature data.

In addition, calculations of the enthalpy increments and heat capacities for $U_{1-y}Pu_yO_{2\pm x}$ (y = 0, 0.25, 0.75 and 1) were also performed using molecular dynamics by Cooper *et al.* [132] (Figure 2-26(a)) and Bathellier *et al.* [140] (Figure 2-26(b)).

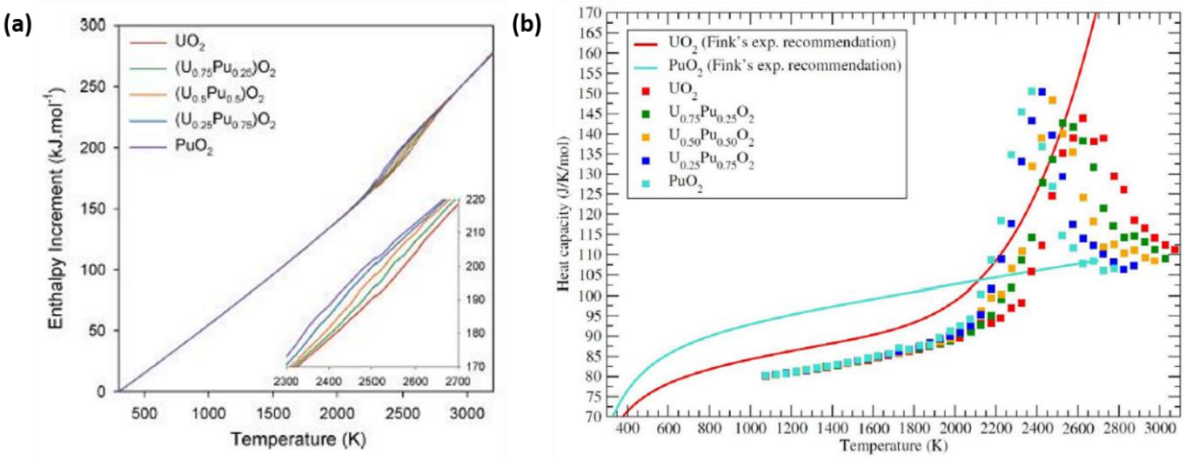

Figure 2-26 : Molecular Dynamics calculations for (a) enthalpy increments (Cooper *et al.* [132]) and (b) for heat capacity (Bathellier *et al.* [140]) for $U_{1-y}Pu_yO_{2\pm x}$ with y = 0, 0.25, 0.5, 0.75, compared to the recommendation of J.K. Fink [128].

In the calculations of Cooper *et al.*, the enthalpy increments increase approximately linearly with the temperature up to 2000 K, independently of the plutonium content. Above 2000 K, a steeper increase is observed up to 3000 K. Between 2300 and 2800 K, an influence of the plutonium content is observed, with higher enthalpy increments when increasing the Pu content. This difference in trend is also visible in the heat capacity calculations of Bathellier *et al.*. Indeed, in this temperature range, a peak, corresponding to the Bredig transition, is also evidenced for $U_{1-y}Pu_yO_2$, as it is the case for UO_2. However, one has to keep in mind that these data are only calculated and experimental works are needed to validate these results.

2.3.1.2.2 $Pu_{1-z}Am_zO_{2-x}$

For $Pu_{1-z}Am_zO_{2-x}$, no experimental or calculated values of enthalpy increments are available in the literature.

One set of experimental data is reported for heat capacities of $Pu_{1-z}Am_zO_{2-x}$ (with y = 0.20, 0.50 and 0.80), measured by Differential Scanning Calorimetry (DSC) in the frame of the EUROTRANS European project [141]. The initial O/M ratio of these oxides was not determined in the work. As shown in Figure 2-27, a small dispersion of about 10% between the curves of the three samples can be noticed. Because of the similar heat capacity values (in $J.kg^{-1}.K^{-1}$) obtained for the three different americium contents, a common correlation was recommended (Equation **(2.21)**).

$$C_p(T,(Pu,Am)O_2) = 469.3 - 3.821 \times 10^{-1} \times T + 1.949 \times 10^{-4} \times T^2 - 195.246 \times 10^5 \times T^{-2} \quad \textbf{(2.21)}$$

However, care should be taken when considering this equation. Indeed, the authors reported that the results obtained in this work are closer to the literature values of Pu_2O_3 and Am_2O_3 as to the ones of PuO_2 and AmO_2 (see Figure 2-27). Furthermore, a difference in the trend can be seen, with a slow increase from 500 to 1000 K and a sharper increase above, originating probably from the reduction of the samples. Additional experimental studies are necessary for this system.

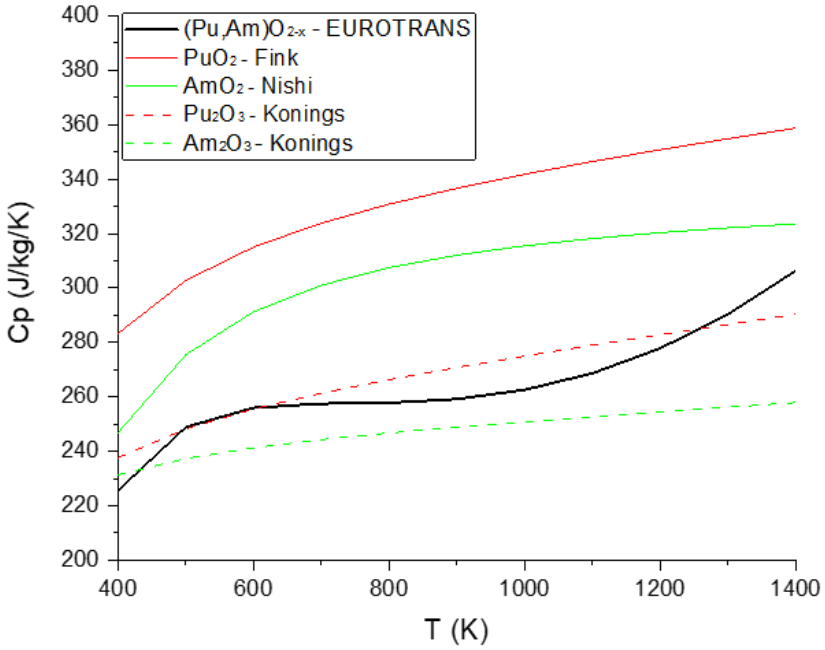

Figure 2-27 : Heat capacity of $Pu_{1-z}Am_zO_2$ recommended in the EUROTRANS project [141], compared to the ones of PuO_2 [128], AmO_2 [129], Pu_2O_3 [125] and Am_2O_3 [125].

2.3.1.2.3 $U_{1-z}Am_zO_{2\pm x}$

For $U_{1-z}Am_zO_{2\pm x}$, only two sets of experimental data are reported in the literature [142], [143]. Enthalpy measurements for z = 0.09 and 0.19 were performed by Vălu *et al.* using drop calorimetry from 425 to 1790 K [142]. Epifano *et al.* determined the enthalpy increments for z = 0.30, 0.40, 0.50, 0.60 and 0.70 by means of drop calorimetry from 470 to 1750 K [143]. The experimental results obtained by the two authors are plotted in Figure 2-28 and compared

to the one of UO_2 [114] and AmO_2 (the latter extrapolated for T > 1100 K) [129]. Similar enthalpy trends are observed for z < 0.4 but above this content, higher enthalpy increments are noticed. Epifano *et al.* associated this deviation to the reduction of the samples. The need for an additional term in the enthalpy increment function to take into account the formation of oxygen vacancy was highlighted by the author.

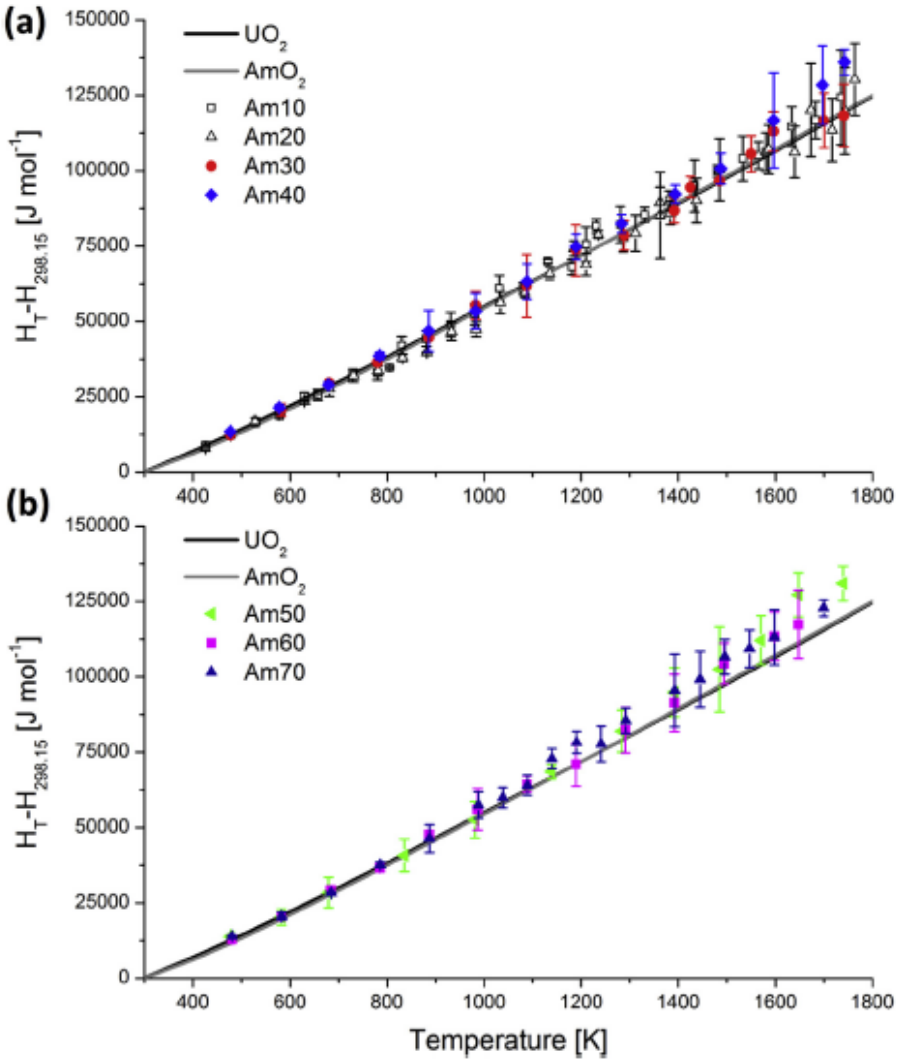

Figure 2-28: Enthalpy increments measured by Epifano *et al.* (full symbols) and Vălu *et al.* (empty symbols) measured for $U_{1-z}Am_zO_{2-x}$ [142], [143].

Heat capacity data were obtained by derivation of the enthalpy increment functions obtained by Vălu *et al.* and Epifano *et al.* (see Figure 2-29). Moreover, using a hybrid adiabatic relaxation calorimetry, Vălu *et al.* determined experimentally the low-temperature (10 to 300 K) heat capacity of $U_{1-z}Am_zO_{2-x}$ for z = 0.08 and 0.20 [91]. Except for z = 0.30, the heat capacity curves obtained are higher than those of UO_2 and AmO_2, especially for T > 800 K. This observation indicates that the results do not follow the Neumann-Kopp additivity rule, justifying the introduction of an excess term in the correlations, as explained for the enthalpy increments. The quantification of the reduction of the samples occurring at high temperature and thus the effect of the oxygen vacancies need further analyses.

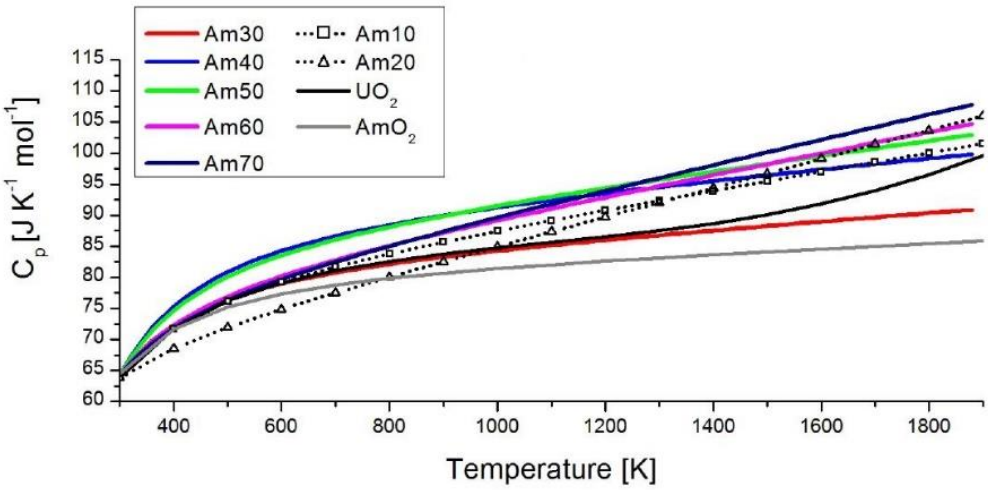

Figure 2-29 : Heat capacity calculated by Epifano *et al.* (full symbols) and Vălu *et al.* (empty symbols) measured for $U_{1-z}Am_zO_{2-x}$ [142], [143].

2.3.2. Oxygen potential

When an oxide achieves thermodynamic equilibrium state with the surrounding atmosphere, the oxygen partial pressure of the gas is equal to the oxygen activity in the solid. The following equilibria **(2.22)** and **(2.23)** take place:

$$\frac{1}{2}O_2(g) \leftrightarrow O_{(g)} \quad \textbf{(2.22)}$$

$$O_{(g)} \leftrightarrow O_{(sol)} \quad \textbf{(2.23)}$$

The partial molar free enthalpy of oxygen $\Delta\bar{G}_{O_2}$, commonly named oxygen potential, is a key property used in thermodynamic studies of non-stoichiometric oxides. It is defined by Equation **(2.24)**, deduced from the equilibria **(2.22)** and **(2.23)**, at $pO_2^0 = 1$ bar.

$$\Delta\overline{G_{O_2}} = \mu_{O_2} - \mu_{O_2}^0 = RT\ln(pO_2) \quad \textbf{(2.24)}$$

This equation implies that, if the solid oxide (sol) is in contact with a gas (g) of different oxygen potential, *i.e.* a partial pressure of O_2 not corresponding to the equilibrium, an exchange of oxygen between the solid and the gas will take place. Thus, if $\Delta\bar{G}_{O_{2(sol)}} > \Delta\bar{G}_{O_{2(g)}}$, the oxide will release oxygen towards the atmosphere and a reduction of the compound will occur, and respectively, if $\Delta\bar{G}_{O_{2(sol)}} < \Delta\bar{G}_{O_{2(g)}}$, the oxygen will be transferred from the gas to the solid. The oxygen potential then directly influences the O/M ratio of a compound and its determination is thus of prime interest.

2.3.2.1 Binary dioxides

2.3.2.1.1 $UO_{2\pm x}$

Numerous oxygen potential measurements of uranium dioxide $UO_{2\pm x}$ were performed and critically reviewed by Labroche *et al.* [9] and Baichi *et al.* [12]. Using these critical reviews, the thermodynamic model of the U-O system, derived by Guéneau *et al.* [7], gives an accurate representation of the oxygen potential of $UO_{2\pm x}$ (Figure 2-30).

A "S shape" curve is obtained for the variation in the oxygen potential as a function of the O/U ratio (at various temperatures), with a steep variation near O/U = 2.00. This shape is related to the possibility to both reduce and oxidize UO_2 upon temperature. This can be explained by the formation of oxygen vacancies in UO_{2-x} and oxygen interstitials and defect clusters in UO_{2+x}.

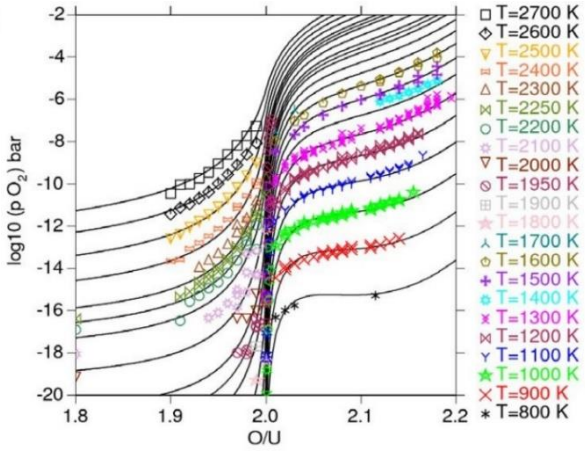

Figure 2-30 : Variation in the oxygen potential of $UO_{2\pm x}$ as a function of the O/U ratio from 800 to 2700 K, experimental (symbols) and computed values (solid lines) [7].

2.3.2.1.2 PuO_{2-x}

Numerous experimental oxygen potential data, obtained for example by Swanson using thermogravimetry [144] or by Markin *et al.* using ElectroMotive Force (EMF) [145], are available in the literature for PuO_{2-x} and were critically reviewed by Guéneau *et al.* [23]. The experimental data measured in two-phase and single PuO_{2-x} regions are compared with the calculations using the model of Guéneau *et al.* in Figure 2-31 [23]. The dashed lines represent the calculated phase boundaries of the Pu-O phase diagram.

As plutonium dioxide does not present a hyper-stoichiometric form, no S shape is obtained. The plateaus correspond to the two-phase regions. In the PuO_{2-x} region, the oxygen potential increases until O/Pu = 2.00. It can be noticed that the computational results are in agreement with the existing experimental data.

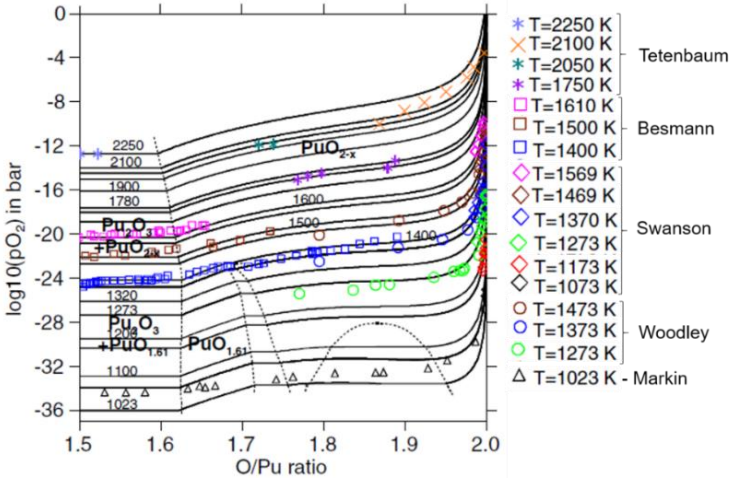

Figure 2-31 : Variation in the oxygen potential of the plutonium-oxygen system as a function of O/Pu ratio at different temperatures, experimental (symbols, from [144]–[148]) and computed data (solid lines) [23].

2.3.2.1.3 AmO_{2-x}

In the case of americium oxide, only three sets of experimental oxygen potentials (Chikalla and Eyring using thermogravimetry, Casalta [149] and Otobe *et al.* [150] using EMF) are reported in the literature. These three studies are not consistent and not easy to compare as they do not cover the same temperature and O/Am ratio ranges. A critical analysis was first performed by Gotcu-Freis *et al.* for the assessement of the Am-O CALPHAD model [26], by considering only the data of Casalta [149] and Chikalla [29].

As described in 2.1.1.3, Epifano *et al.* [6] proposed a new version of the Am-O model, modified from Gotcu-Freis *et al.* [26]. The updated calculated oxygen potentials of americium dioxide are compared with the results of Gotcu-Freis *et al.* and the available experimental data in Figure 2-32. The experimental trend for the oxygen potential from Casalta and Chikalla and Eyring is qualitatively reproduced by the CALPHAD model proposed by Epifano *et al.* [6].

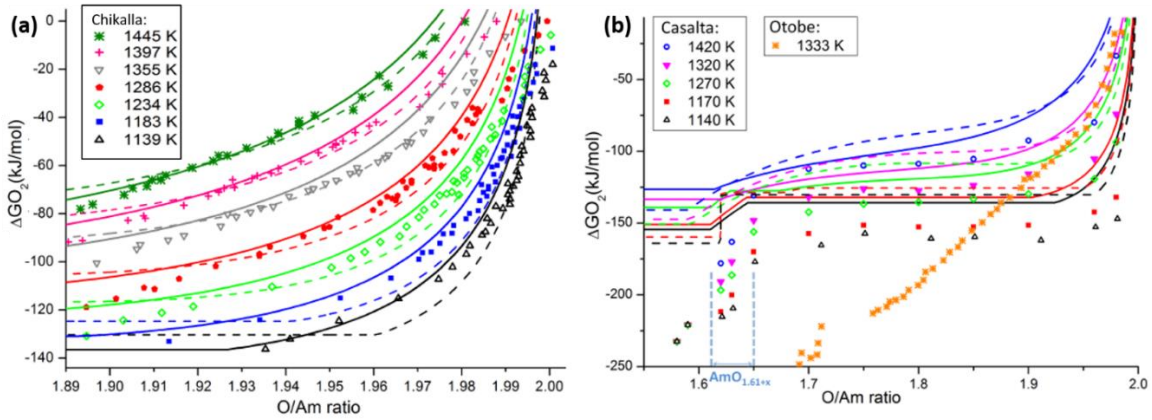

Figure 2-32 : Calculated oxygen potential data using the CALPHAD model from Epifano *et al.* [6] (solid lines) and Gotcu-Freis *et al.* [26] (dashed lines), compared to experimental data of (a) Chikalla and Eyring [151], (b) Casalta [149] and Otobe *et al.* [150].

For O/Am < 1.94, the description was improved by Epifano *et al.*. On the contrary, a better description of the near-stoichiometric region (1.99 < O/Am < 2) is obtained with the model of Gotcu-Freis *et al.* [26]. However, since the oxygen potentials vary rapidly in a narrow composition range, these data are affected by large uncertainties in this region and are therefore the least reliable. The data of Otobe *et al.* [150] are not reproduced by the two models. On the contrary, the data of Chikalla and Casalta are well reproduced by the model of Epifano *et al.*.

A comparison of the oxygen potentials obtained at 1600 K for $UO_{2\pm x}$, PuO_{2-x} and AmO_{2-x} is shown in Figure 2-33.

The data for AmO_{2-x} correspond to the model of Thiriet and Konings [152] and the ones of $UO_{2\pm x}$ and PuO_{2-x} originate from the models of Guéneau *et al.* [13], [23]. As it can be seen, the oxygen potential of AmO_{2-x} is the highest, followed by PuO_{2-x} and then $UO_{2\pm x}$. This trend corresponds to the decreasing stability of the oxides and the tendency for the oxides to be reduced or oxidized at high temperature.

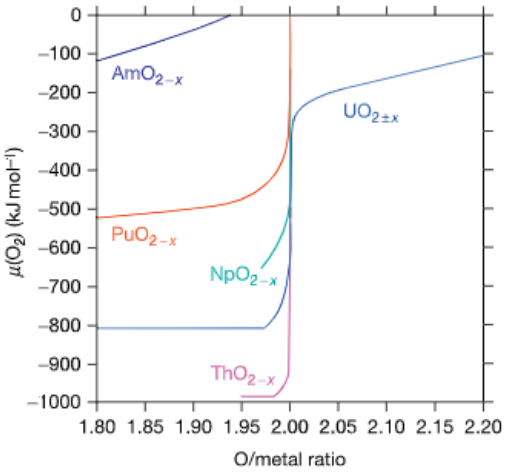

Figure 2-33: Comparison of the oxygen potentials for $UO_{2\pm x}$, PuO_{2-x} and AmO_{2-x} at 1600 K [131].

2.3.2.2 *Mixed dioxides*

2.3.2.2.1 $U_{1-y}Pu_yO_{2\pm x}$

The oxygen potentials of $U_{1-y}Pu_yO_{2\pm x}$ have been widely studied at different temperatures (757 to 1973 K), plutonium contents (from 0.10 to 0.65) and O/M ratio (1.86 to 2.08) using thermogravimetry or EMF [58], [153]–[157]. Reviews of these data were performed by Besmann and Lindemer [158], Kato *et al.* [159] and Guéneau *et al.* [131].

The Figure 2-34 illustrates the oxygen potential obtained for (a) $U_{0.90}Pu_{0.10}O_{2\pm x}$ by R.E. Woodley [148] and Markin and McIver [160] and (b) $U_{0.70}Pu_{0.30}O_{2\pm x}$, by Kato *et al.* [159], compared to the computed values using the model of Guéneau *et al.* for U-Pu-O [7].

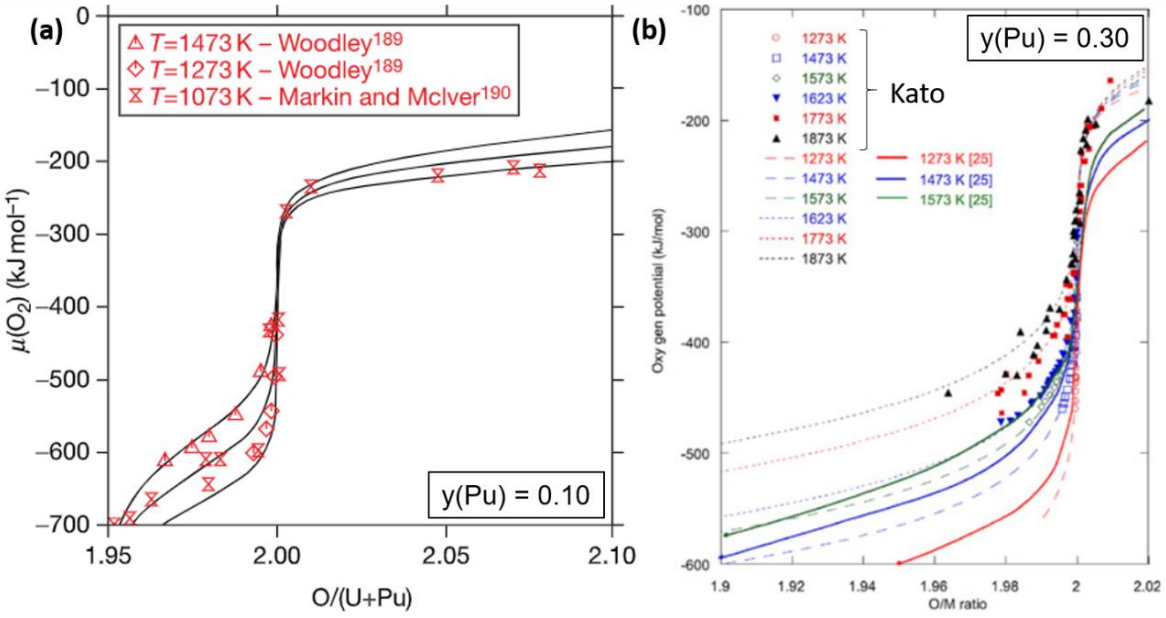

Figure 2-34 : Oxygen potential of (a) $U_{0.9}Pu_{0.1}O_{2\pm x}$ (Woodley [148] and Markin and McIver [160]) and (b) $U_{0.7}Pu_{0.3}O_{2\pm x}$ (Kato *et al.* [159]) as a function of the O/M ratio and temperature. The full lines represent the computed values using the model of Guéneau *et al.* [161] and the dashed lines on (b) were calculated using the point defect model of Kato *et al.* [159].

For $U_{1-y}Pu_yO_{2\pm x}$, a S-shape is also observed, as for $UO_{2\pm x}$. An increase in the oxygen potential is observed when increasing the temperature. Indeed, when performing a heat treatment, the temperature variation induces a modification in the chemical oxygen potential of the gas. When the temperature increases, a decrease in the magnitude of the $\Delta\bar{G}_{O_2}$ S-shape curves near O/M = 2.00 is observed (Figure 2-34). This shrinkage is due to the increase of the coexistence domain of the Pu^{4+} and U^{4+} cations, allowing a hypo-stoichiometric material to easily move to the hyper-stoichiometric form. A good agreement between the model and the experimental data is observed.

For a given temperature and a known O/M ratio, the oxygen potential is influenced by the plutonium content in $U_{1-y}Pu_yO_{2\pm x}$ [17], [162]. The Figure 2-35 illustrates the variation in the oxygen potential as a function of the plutonium content ($0.12 \leq y \leq 0.30$) and for fixed O/M ratios (from 1.95 to 2.01), plotted by Kato *et al.* [153]. First, an increase in the oxygen potential is noticed when increasing the plutonium content, in agreement with higher oxygen potential measured for PuO_{2-x} compared to $UO_{2\pm x}$ (Figure 2-33). For any additional 1% plutonium, an increment in the oxygen potential of approximatively 2-5 $kJ.mol^{-1}$ is observed [163].

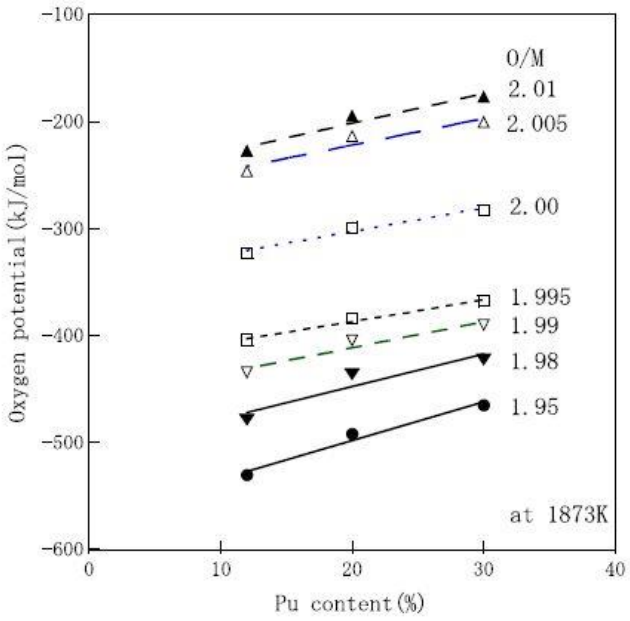

Figure 2-35 : Variation in the oxygen potential of $U_{1-y}Pu_yO_{2\pm x}$ at 1873 K with the plutonium and for different O/M ratios [153].

2.3.2.2.2 $Pu_{1-z}Am_zO_{2-x}$

Very few experimental oxygen potential data for $Pu_{1-z}Am_zO_{2-x}$ are available in the literature: Osaka *et al.* for z = 0.09 from 1123 to 1423 K by TGA [43], Otobe *et al.* for z = 0.50 from 1173 K to 1333 K by EMF [44] and Matsumoto *et al.* for z = 0.072 from 1473 to 1873 K using TGA [164]. Another set of experiments was performed in the frame of the European project EUROTRANS [165], using EMF, for americium contents between 0.061 and 0.50, from 973 to 1373 K [166]. These data are not presented here but are in agreement with the results obtained by Osaka *et al.* [43]. The experimental oxygen potential data obtained by Osaka *et al.* and Otobe *et al.* are plotted in Figure 2-36 and compared to the computed results obtained using the model of Gotcu-Freis *et al.* for the Pu-Am-O system [26]. Comparison is difficult as different americium contents were measured at different temperatures.

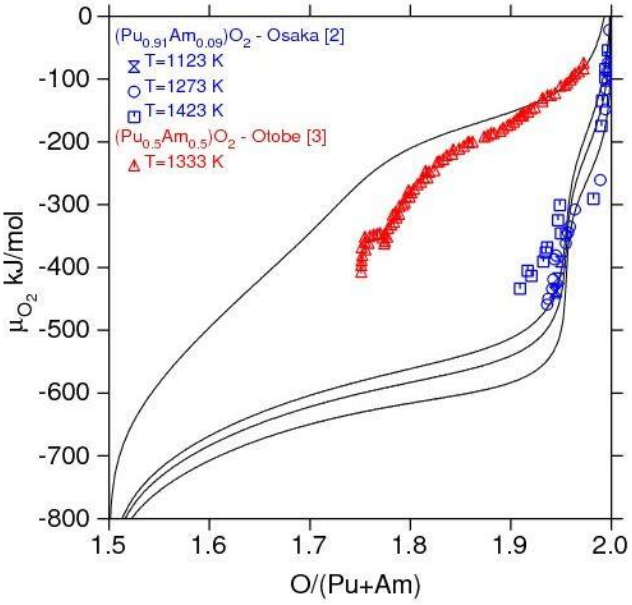

Figure 2-36 : Variation in the oxygen potential of $Pu_{1-z}Am_zO_{2-x}$ as a function of the O/M ratio, the plutonium content and the temperature compared to the experimental values of Osaka *et al.* [43] and Otobe *et al.* [44] [26] and the calculated values of Gotcu-Freis *et al.* [26].

For given O/M ratio and temperature, an increase in the oxygen potential can be noticed when increasing the americium content of the samples, in agreement with the higher potential data of AmO_{2-x} compared to PuO_{2-x} (Figure 2-33). Moreover, for a fixed americium content, the oxygen potential data increase when increasing the temperature.

The model of Gotcu-Freis *et al.* [26] cannot describe all the experimental data (Figure 2-36). Indeed, for z = 0.50 and O/M < 1.90, the calculations overestimate the oxygen potential compared to the experimental data. On the contrary, the calculated data are too low compared to the experimental data for z = 0.09. This discrepancy questions the reliability of the Pu-Am-O model. New measurements are required to improve the knowledge on this system. In addition, the oxygen potential variation with the O/M ratio needs to take into account the existence of different phase regions and the formation of other phases such as sesquioxides and intermediate oxide with O/M ≈ 1.6.

2.3.2.2.3 $U_{1-z}Am_zO_{2\pm x}$

For $U_{1-z}Am_zO_{2\pm x}$, only one set of experimental data is reported in the literature by Bartscher and Sari [167], for $U_{0.50}Am_{0.50}O_{2\pm x}$ ($1.87 \leq x \leq 2.09$) from 873 to 1573 K by TGA, as illustrated in Figure 2-37. The computed values using the model proposed by F. Lebreton for the U-Am-O system are also plotted for comparison. As for $UO_{2\pm x}$, a S shape profile can be distinguished, indicating the tendency to form both hyper- and hypo-stoichiometric oxides. An increase in the oxygen potential is also noticed when increasing the temperature. Moreover, a good agreement between the model and the experimental data is highlighted.

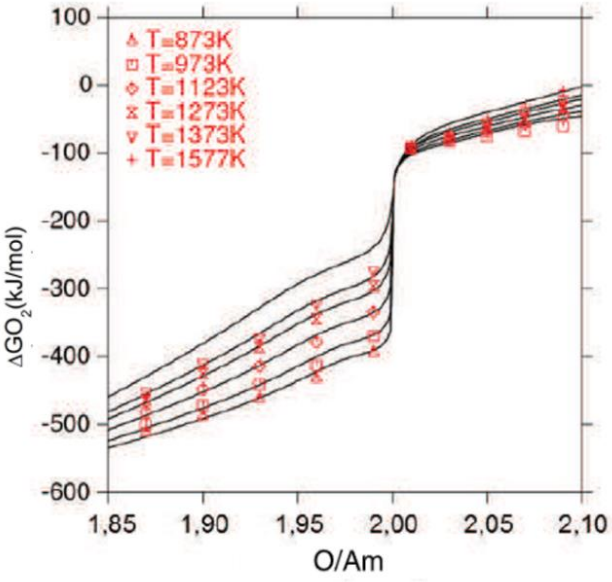

Figure 2-37 : Oxygen potential variation for $U_{0.50}Am_{0.50}O_{2\pm x}$ measured by Bartscher and Sari [167] compared to calculations using the model of F. Lebreton for U-Am-O [46].

2.3.2.2.4 $U_{1-y-z}Pu_yAm_zO_{2\pm x}$

The influence of americium on the oxygen potential of uranium-plutonium mixed dioxides was studied by Osaka *et al.* [168], Nakamichi *et al.* [169], Hirooka *et al.* [170] and Kato *et al.* [163] by TGA for $0.01 \leq z \leq 0.045$. In some cases (Nakamichi *et al.* and Kato *et* al), few mol.% of Np were also present in the samples. Comparing all these experimental data is complicated because of the different americium contents and temperatures studied. The Figure 2-38 illustrates the variation in the oxygen potential measured by Osaka *et al.* for $U_{0.685}Pu_{0.270}Am_{0.045}O_{2-x}$ with the O/M ratio at 1273 K, compared with literature data for other oxides.

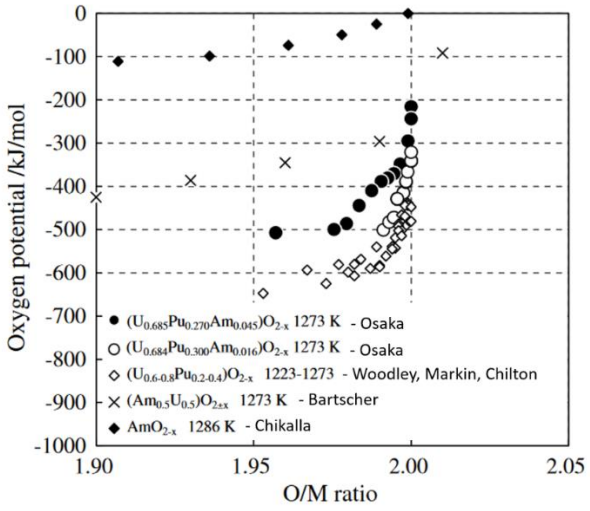

Figure 2-38 : Variation in the oxygen potential of $U_{1-y-z}Pu_yAm_zO_{2\pm x}$ at 1273 K with the O/M ratio compared to the experimental values of [29], [37], [145], [148], [155], [167], [168].

An increase of the oxygen potential is noticed with the addition of americium in $U_{1-y}Pu_yO_{2\pm x}$, as observed by all the authors. However, the oxygen potentials measured by Osaka *et al.* are lower than the one measured for $U_{0.50}Am_{0.50}O_{2-x}$ [167] and AmO_{2-x} [29].

Available experimental data on oxygen potentials are numerous in the literature for $UO_{2\pm x}$, PuO_{2-x} and $U_{1-y}Pu_yO_{2\pm x}$. However, data on americium-bearing oxides, namely AmO_{2-x}, $U_{1-z}Am_zO_{2\pm x}$, $Pu_{1-z}Am_zO_{2-x}$ and $U_{1-y-z}Pu_yAm_zO_{2\pm x}$ are limited and very scarce. Indeed, only three studies for the Am-O, one for U-Am-O, four for Pu-Am-O and four for the U-Pu-Am-O systems are available on narrow ranges of plutonium and americium contents, temperatures and O/M ratio. Further experimental studies are thus needed to overcome this lack of data and allow a better thermodynamic description of the systems.

2.3.3. Melting behaviour

In this part, the melting behaviours of uranium, plutonium and americium binary and ternary oxides are reviewed.

2.3.3.1 Single dioxides

2.3.3.1.1 $UO_{2\pm x}$

The melting behaviour of $UO_{2\pm x}$ has been widely studied over the past decades. Reviews of the solidus/liquidus temperatures were performed by Carbajo *et al.* [113], Baichi *et al.* [11] and Konings *et al.* [125]. As already discussed by Guéneau *et al.* and Kato *et al.* [7], [171], these data exhibit large discrepancies, attributed to possible experimental technique artefacts, uncertainties in the O/M ratio evaluation and/or impurities.

Manara *et al.* developed a laser heating technique, based on a self-crucible method, to determine the melting points of various materials [14]. With this setup, the melting temperature of UO_2 was measured at 3147 ± 20 K [14] and is higher than the ones obtained by thermal arrests using Re or W crucibles (3077 ± 25 K [172]). Among the reported melting temperatures of $UO_{2.00}$, Konings *et al.* [125] selected 3130 ± 20 K.

For hypostoichiometric uranium dioxides UO_{2-x} ($0 < x < 0.5$), the only existing solidus/liquidus data were determined by Latta and Fryxell [173] using thermal analysis. As these temperatures were obtained using closed Re or W crucibles, they were corrected using Raoult's cryoscopic law, as detailed by Baichi *et al.* [11]. Lower temperatures than the ones obtained for $UO_{2.00}$ were measured through the hypostoichiometric range, with a solidus temperature of approximately 2690 K for $UO_{1.69}$ and a liquidus temperature of 2790 K for $UO_{1.55}$.

In the UO_{2+x} domain ($0 < x < 0.21$), the solidus/liquidus data of Manara *et al.* [14] obtained by laser heating were selected instead of the higher values obtained by Latta and Fryxell [173], as the laser set-up was considered to be more reliable (no material-crucible interaction). A decrease in the melting point was observed when increasing the O/U ratio (for $UO_{2.21}$, solidus temperature of 2410 K and liquidus temperature of 2795 K).

2.3.3.1.2 PuO_{2-x} - Pu_2O_3

Large discrepancies on the melting temperatures of plutonium dioxide exist in the literature. In 2001, Carbajo *et al.* performed a first review of the available PuO_2 melting points (by thermal arrest technique using closed W crucibles) and recommended the value of 2701 ± 35 K [113]. In 2008, Kato *et al.* obtained a higher value of about 100 K (2822 K), using Re crucibles [171], [174]. However, an interaction between the crucible and the material was still observed. In 2012, Konings *et al.* performed a review of the literature data and recommended 3017 ± 28 K

for the melting temperature of $PuO_{2.00}$ [125], measured by De Bruycker *et al.* [175] by laser heating and self-crucible system. In 2014, Böhler *et al.* used the same setup and determined the melting point of $PuO_{2.00}$ at 3040 ± 60 K [176].

In the PuO_{2-x} domain, only one study is reported in the literature by Kato *et al.* [177]. The authors determined a melting temperature of 3031 ± 20 K for $PuO_{1.76}$ using a thermal arrest technique. The existence of a maximum of the melting temperature for this composition was assumed in this study, followed by a decrease of the temperature when increasing the O/M ratio. It can be noticed that the temperature obtained for $PuO_{1.76}$ (3031 ± 20 K) is close to the one measured by Böhler *et al.* for PuO_2 (3050 ± 59 K).

Care should be taken when considering these data, as they originate from two different experimental techniques: thermal arrest using W or Re crucibles and self-crucible laser heating technique with a self-crucible system respectively. Indeed, when using containers, interactions between the material and the crucible were noticed, resulting in an underestimated melting temperature with a larger uncertainty [175]. In the case of the laser heating technique, uncertainties remain on the exact O/M ratio of the plutonium dioxide at the solidus/liquidus, as no composition measurement was performed. Furthermore, the work of Kato *et al.* highlighted the presence of a maximum in the solidus temperature between $PuO_{1.76}$ and $PuO_{2.00}$. However, its exact O/M ratio has not been determined yet. A change in the oxygen composition of the samples could also occur due to vaporization when using thermal analysis in close crucibles if the free volume is enough in the crucibles.

For Pu_2O_3, the melting point was recommended at 2352 ± 10 K by Konings *et al.* [125], based on the consistent measurements of Chikalla *et al.* [20] and Riley [178]. Few solidus/liquidus measurements were performed between Pu_2O_3 and PuO_2 but a large scattering was observed between the values and uncertainties remain on the final sample composition [174].

2.3.3.1.3 AmO_{2-x}

Only one melting temperature of $AmO_{2.00}$ was reported in the literature at 2383 K by R.E. McHenry [179]. Care should be taken while using this value, as no details are available on the experimental procedure and the announced O/Am ratio is not ensured. In fact, at high temperature (T > 1100 K), americium dioxide is being reduced (see Figure 2-3). Thus, the determination of the melting point of $AmO_{2.00}$ is difficult and the value measured by R.E. McHenry most likely corresponds to AmO_{2-x}, where x is unknown.

2.3.3.2 Mixed dioxides

2.3.3.2.1 $U_{1-y}Pu_yO_{2\pm x}$

The melting behaviour of $U_{1-y}Pu_yO_{2\pm x}$ has been extensively studied over the past decades by Lyon and Baily [180], Aitken and Evans [181], Reavis [182], Konno and Hirosawa [183], Kato *et al.* [171], [174] by classical thermal analysis and later by De Bruycker *et al.* [24], Böhler *et al.* [176] and Strach *et al.* [184] by laser heating. Reviews of the literature data were performed by Kato *et al.* [185] and Guéneau *et al.* [7]. The composition range and the methods of the available measurements are reported in Table 2-10.

Table 2-10 – Experimental solidus/liquidus data available in the literature for $U_{1-y}Pu_yO_{2\pm x}$.

Reference	Composition	Experimental technique
Lyon and Baily (1967) [180]	$0 < y \leq 0.85$ O/M = 2.00	Thermal arrest using a sealed W crucible
Aitken and Evans (1968) [181]	$0.20 \leq y \leq 0.60$ $1.76 \leq O/M \leq 2.00$	Thermal arrest using a sealed W crucible
J.G. Reavis (1972) [182]	y = 0.25 O/M = 1.97 and 1.98	Differential Thermal Analysis using W crucible
Konno and Hirosawa (1998) [186]	y = 0.29 O/M=1.95 and 1.99	Thermal arrest technique a sealed W crucible
Kato *et al.* (2008) [174] [171] [177]	$0.117 \leq y \leq 0.60$ $1.922 \leq O/M \leq 2.00$	Thermal arrest using sealed W or Re crucible
De Bruycker *et al.* (2011) [24]	$0.75 \leq y \leq 0.90$ O/M=2.00	Laser heating under Ar and air
Böhler *et al.* (2014) [176]	$0.037 \leq y \leq 0.90$ O/M=2.00	Laser heating under Ar ($y < 0.50$) and air ($y > 0.50$)
Strach *et al.* (2016) [184]	$0.14 \leq y \leq 0.62$ O/M = 2.00	Laser heating technique under Ar and air

One difficulty in these experimental studies is that in some cases, only one thermal arrest is observed. It is then difficult to identify the phase transition as a liquidus point (temperature at which the first solid germ appears in the cooling liquid) or a solidus point (temperature at which the last drop of cooling liquid becomes solid, with the initial composition) [24], [48]. However, according to Böhler *et al.*, it corresponds to the solidus temperature as this transition is the most energetic one [176].

The available experimental solidus/liquidus data for $U_{1-y}Pu_yO_{2.00}$ are plotted in Figure 2-39, where only the data for stoichiometric dioxides are represented for sake of clarity. Large discrepancies can be noticed for both solidus/liquidus temperatures.

Lyon and Baily ($0 < y \leq 0.85$, O/M = 2.00), followed by Aitken and Evans ($0.20 \leq y \leq 0.60$), used first a thermal arrest technique with stoichiometric $U_{1-y}Pu_yO_{2.00}$ samples encapsulated in W crucibles [180], [181]. Their study depicted an ideal solution model between UO_2 and PuO_2, with a melting point of PuO_2 around 2700 K and a decrease of the solidus temperatures when increasing the PuO_2 content. In the study of Aitken and Evans, hypo-stoichiometric $U_{1-y}Pu_yO_{2-x}$ were also studied, with $1.76 \leq O/M \leq 2.00$ [181]. The influence of the O/M ratio was highlighted, with a maximum of solidus/liquidus around O/M = 1.75. The stabilization of $U_{1-y}Pu_yO_{2\pm x}$ by the interactions between Pu^{3+} and Pu^{4+} for $O/M < 2.00$ was admitted by the authors.

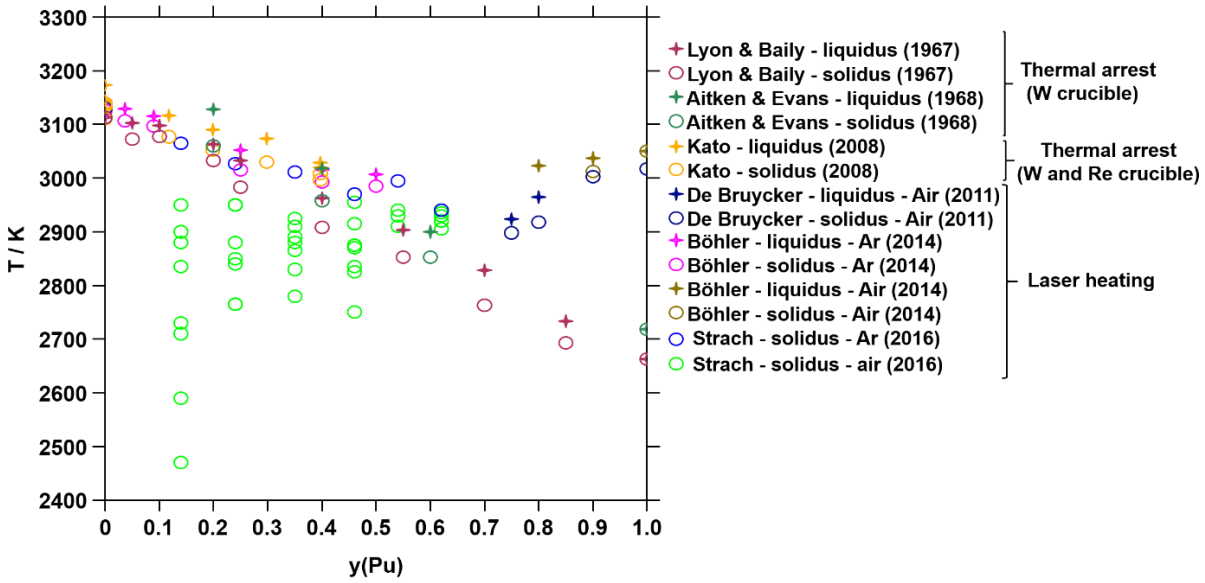

Figure 2-39: Experimental melting data available in the literature for $U_{1-y}Pu_yO_{2.00}$ [24], [174], [176], [180], [181], [184].

In 2008, Kato *et al.* performed further investigations on the solidus/liquidus temperatures of $U_{1-y}Pu_yO_{2-x}$ ($0.117 \leq y \leq 0.60$ and $1.922 \leq O/M \leq 2.00$) using also the thermal arrest method with W crucibles [171]. However, for $y > 0.20$, interactions between the samples and the W containers were observed [171] and another study was conducted by Kato *et al.* using rhenium capsules to overcome this interaction [174]. Solidus/liquidus temperatures higher of 100 K were obtained compared to the ones with W crucibles. An ideal solution model was also suggested with a PuO_2 melting point of 2843 K, as described in 2.3.2.1.2. However, interactions between the material and its capsule were also occurring with Re crucibles for $y > 0.50$ [174], [176]. For hypo-stoichiometric samples, an increase of the solidus/liquidus temperatures was evidenced when decreasing the O/M ratio. In all the studies of Kato *et al.*, small fractions of americium were present in the materials, originating from the natural decay of plutonium.

In order to eliminate possible interactions, solidus/liquidus temperatures were measured using a laser heating technique by De Bruycker *et al.* on $U_{1-y}Pu_yO_{2.00}$ ($0.75 < y < 0.90$, $O/M = 2.00$), whose results were found to be significantly higher than the ones obtained by thermal arrest [24]. This study was not consistent with the ideal solution model previously described as a minimum in the melting temperatures was found for $0.50 < y < 0.80$. Böhler *et al.* used the laser heating technique on $U_{1-y}Pu_yO_{2.00}$ over the whole plutonium content range [176] and observed the same minimum in the solidus/liquidus curve for $0.40 < y < 0.70$. The results obtained for $y < 0.50$ were found to be in agreement with the ones of Kato using thermal arrest [171]. Strach *et al.* also performed measurements of solidus/liquidus temperatures of $U_{1-y}Pu_yO_{2.00}$ ($0.14 \leq y \leq 0.62$, $O/M = 2.00$) using laser heating [184], with values in agreement with the ones of De Bruycker *et al.* and Böhler *et al.*. In the work of Strach *et al.*, the influence of the atmosphere of melting was also studied. Indeed, uranium-rich samples tend to oxidize under air, leading to a progressive decrease of the melting temperature [184]. In case of Pu-rich samples, air was used to maintain the O/M ratio at 2.00. Moreover, Strach *et al.* performed experimental campaigns on $U_{1-y}Pu_yO_{2.00}$ under argon and air, and significantly lower solidus temperatures were obtained in the case of air (2470 K) as comparted to argon (3065 K) for $U_{0.86}Pu_{0.14}O_{2.00}$ [184].

The influence of several parameters on the solid/liquid phase transitions were highlighted with these studies. First, the plutonium content plays a role in the values obtained experimentally. Indeed, contrarily to what has been stated for decades, a non-ideal solution between UO_2 and PuO_2 is observed, with a decrease of the melting temperatures up to a minimum located between y = 0.40 and 0.80, followed by an increase up to PuO_2. As stated by Aitken and Evans and Kato *et al.* [171], [181], the O/M ratio also has an influence on the melting temperatures. Moreover, the use of different techniques (thermal arrest or laser heating) can explain the discrepancies in the temperatures obtained, as the thermal arrest method tends to underestimate them due to interactions between the samples and the crucibles. Finally, the importance of the surrounding atmosphere (air or argon) was also highlighted [184]. In some studies, the O/M ratio of molten samples was determined *post mortem* at room temperature by combining XRD, XANES and/or Raman spectroscopy measurements [24], [176]. No significant oxygen losses were observed, resulting in a final O/M ratio close to the initial value of 2.00. Unfortunately, in all the experiments, no *in-situ* measurements of the O/M ratio at high temperature were available and thus, the exact O/M ratio at which the solid/liquid transition occurs remains unknown.

In the thermodynamic modelling of the U-Pu-O system from Guéneau *et al.*, the solidus/liquidus temperatures obtained by De Bruycker *et al.* and Kato *et al.* [24], [185] were selected (Figure 2-40). The data of Lyon and Baily were discarded for the modelling but are represented for comparison [180].

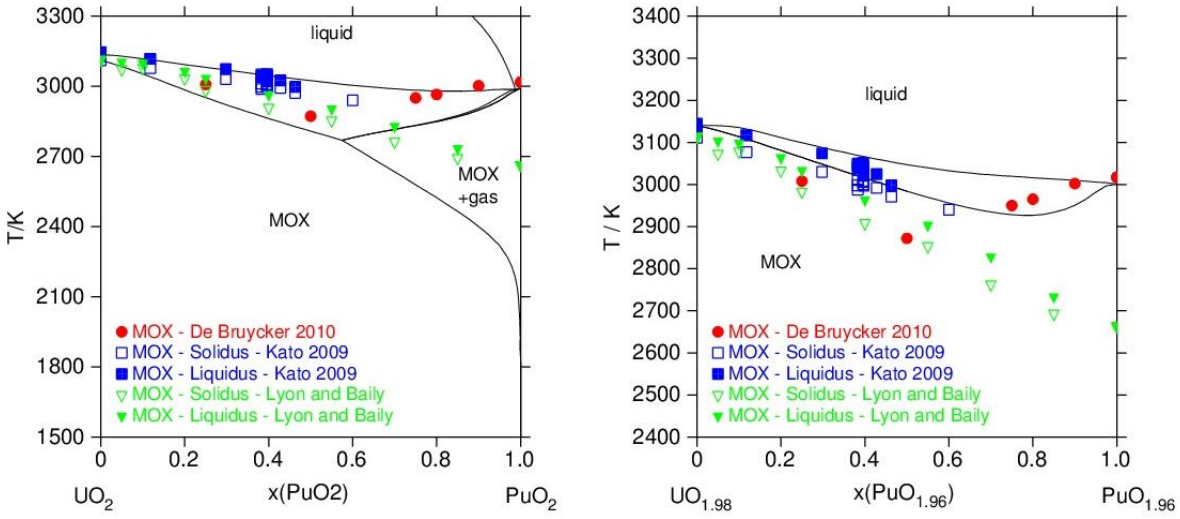

Figure 2-40 : Solidus/liquidus temperatures of $U_{1-y}Pu_yO_{2\pm x}$ calculated using the CALPHAD model of Guéneau *et al.* [7], compared to the experimental values of De Bruycker *et al.* [24], Kato *et al.* [174] and Lyon and Baily [180].

2.3.3.2.2 $Pu_{1-z}Am_zO_{2-x}$

Only one study, performed by Kato *et al.*, exists on the melting temperatures of $Pu_{1-z}Am_zO_{2-x}$ samples [174]. The authors measured the solidus and liquidus temperatures of $Pu_{0.979}Am_{0.021}O_{2.00}$ by thermal arrest using Re crucible at 2830 ± 35 K and 2937 ± 35 K, respectively. Unfortunately, they reported an interaction between the crucible and the sample and discarded the use of these results and no other experimental data exist in the literature.

2.3.3.2.3 $U_{1-z}Am_zO_{2\pm x}$

For $U_{1-z}Am_zO_{2\pm x}$, two studies were performed by Prieur *et al.* and Epifano *et al.* by laser heating [47], [48]. The Figure 2-41 presents the experimental data obtained for the two authors, under air and argon. As the initial and final O/M ratios of the samples were not exactly known, the dashed line represented in the figure between UO_2 and AmO_2 was only drawn for visual representation.

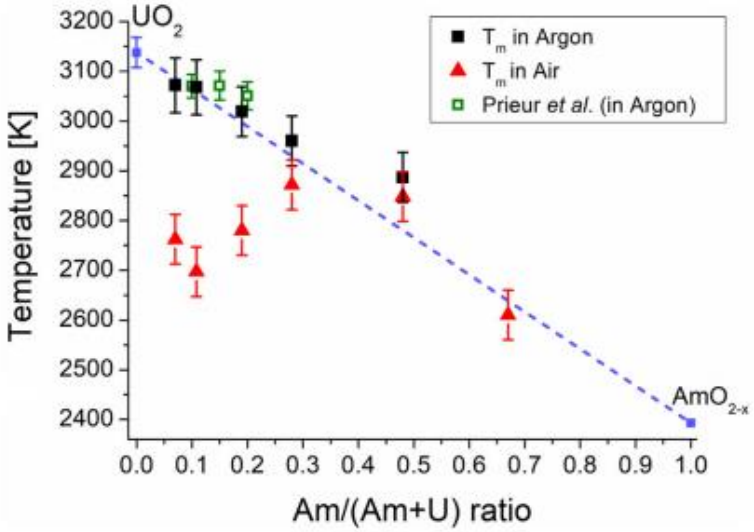

Figure 2-41 : Solidus temperatures as a function of Am content and atmosphere in $U_{1-z}Am_zO_{2\pm x}$ by Epifano *et al.* [48] and Prieur *et al.* [47].

In argon, the melting point decreases when increasing the americium content. On the contrary, a more complex behaviour is observed in air. Indeed, AmO_2 exhibits a tendency to lose oxygen above 1100 K, even under pure oxygen. Thus, the presence of oxygen in the environment enhances the oxidation of uranium in the samples, resulting in a decrease of the melting temperature (see Figure 2-41).

For $z < 0.3$, the solidus temperature measured in air increases with the Am content, while the one measured in argon decreases. For $z = 0.50$, the temperatures obtained under air and argon are similar, indicating that the O/M is closer to 2 for these samples.

Post-melting characterizations (XANES) were performed by Epifano *et al.* to determine possible changes in the uranium and americium contents, as well as in the O/M ratio of the samples after melting [48]. For the samples melted under air, higher O/M ratios were determined after melting (up to O/M = 2.28 for $z = 0.10$), evidencing the oxidation of the samples during the experiments. In the case of the samples melted under Ar, a reduction of the sample (O/M = 1.93) was observed for $z = 0.50$, while the rest remain stoichiometric. Moreover, slight changes in the americium content were evidenced for some samples (increase of 2-3%).

This study highlights the importance to perform post-melting characterizations, or even in-situ measurements, as a direct influence of the americium content and the O/M ratio is evidenced on the solidus temperature.

2.3.3.2.4 $U_{1-y-z}Pu_yAm_zO_{2\pm x}$

Only one study performed by Kato *et al.* by thermal arrest takes into account the effect of the americium content on the melting temperature of $U_{1-y-z}Pu_yAm_zO_{2\pm x}$ ($0.38 \leq y \leq 0.40$ and $0.005 \leq z \leq 0.035$) [185]. It was reported that a 1% Am addition led to a decrease of the melting temperature of about 3 K. However, the uncertainty on the melting temperature was reported to be between 15 and 25 K. Thus, care should be taken while considering the influence of Am-addition on the melting point as it lays within the uncertainty range.

2.4. THERMODYNAMIC MODELS

As the aim of the present work is the thermodynamic modelling of the U-Pu-Am-O system for the TAF-ID, only the models compatible with those used in the TAF-ID are described, and thus only the models obtained by the CALPHAD method (described with more details in Chapter 3 – section 3.1) [5].

In this section, the sublattice models used to describe the gas, liquid and solid phases are reported for the binary and ternary sub-systems of the quaternary U-Pu-Am-O are briefly described. Further details on the Gibbs energy functions used to describe the phases are provided in Chapter 3 – section 3.1.2.The metallic solid solutions are not discussed here.

2.4.1. Binary systems

As mentioned in 2.1.1, thermodynamic models using the CALPHAD method are available for the U-O, Pu-O and Am-O systems [6], [7], [13], [26]. These assessments were performed based on the various sets of phase diagram data (phase boundaries, transition temperatures) and thermodynamic data (oxygen potentials, enthalpies, heat capacity …) previously described.

The gas phases of these binaries are described as an ideal mixture of gaseous species as reported in Table 2-11 for each system.

Table 2-11 - Gaseous species in the thermodynamic models of the gas phases for the U-O, Pu-O and Am-O systems.

System	Species	Reference
U-O	U, O, O_2, O_3, UO, UO_2, UO_3	Guéneau *et al.* [13]
Pu-O	Pu, O, O_2, O_3, PuO, PuO_2	Guéneau *et al.* [7]
Am-O	Am, O, O_2, O_3, AmO, AmO_2	Epifano *et al.* [6]

The liquid phase is described using the ionic two-sublattice model, where the first sublattice contains a mixture of cations and the second a mixture of anions, charged vacancies and neutral species. The charges of the cations are chosen to correspond to the stable oxide with the lowest oxidation state for the system. The other oxides are described as neutral species in the second sublattice. The sublattice models of the three binary systems are described in Table 2-12.

Table 2-12 – Sublattice models for the liquid phase for U-O, Pu-O and Am-O systems.

System	Model of the liquid phase	Reference
U-O	$(U^{4+})_P\,(O^{2-},Va^{Q-},O)_Q$	Guéneau *et al.* [13]
Pu-O	$(Pu^{3+})_P\,(O^{2-},Va^{Q-},O,PuO_2)_Q$	Guéneau *et al.* [7]
Am-O	$(Am^{3+})_P\,(O^{2-},Va^{Q-},O)_Q$	Gotcu-Freis *et al.* [26]

In this model, P and Q are equal to the average charge of the opposite sublattice to maintain the electro-neutrality of the phase. Q is equal here to 4 for U-O and 3 in the case of Pu-O and Am-O systems. P varies with the composition via the site fractions of the different species.

The solid fluorite phase $MO_{2\pm x}$ (with M = U, Pu or Am) is described using the Compound Energy Formalism [187]. Two or three sublattices were used for the assessment, depending on the tendency of the oxide to allow hyper-stoichiometry. The models for the $MO_{2\pm x}$ phases of the three binaries are described in Table 2-13.

Table 2-13 – Sublattice models for the $MO_{2\pm x}$ phase for U-O, Pu-O and Am-O systems.

System	Model of the $MO_{2\pm x}$ phase	Reference
U-O	$(U^{3+},U^{4+},U^{5+})_1\,(O^{2-},Va)_2(O^{2-},Va)_1$	Guéneau *et al.* [7]
Pu-O	$(Pu^{3+},Pu^{4+})_1\,(O^{2-},Va)_2$	Guéneau *et al.* [7]
Am-O	$(Am^{3+},Am^{4+})_1\,(O^{2-},Va)_2$	Epifano *et al.* [6]

The first sublattice corresponds to the crystal site for cations in the fluorite structure (see Figure 2-9). The second sublattice describes the normal site for oxygen in the fluorite structure, where the addition of vacancies (denoted "Va") allows the modelling of the hypo-stoichiometric region of the dioxides. The third sublattice is the site for interstitial oxygen to represent the hyper-stoichiometric composition range. In these models, no clustering of defects is considered in order to reduce its complexity and the number of adjustable parameters.

For the U-O system, initially, U^{+6} was introduced in the first sublattice but was later replaced by U^{+5} to better describe the point defect chemistry [7], [13]. In this system, all the phases described in sections 2.2.1.1 and 2.2.1.4 are included. The pure metallic elements and the oxides U_4O_9, U_3O_8 and UO_3 were assessed as stoichiometric compounds [7]. As numerous data are available on this system, the thermodynamic model of Guéneau *et al.* is complete and in good agreement with the experimental data of the literature.

For the Pu-O system, a first version was proposed by Guéneau *et al.* in 2008 [23] and updated by the same author in 2011 [7], where all the phases are also included in the thermodynamic model. The oxides A-Pu_2O_3 and $PuO_{1.52}$ are modelled as stoichiometric phases, while the following sublattice model is used for the high temperature phase $PuO_{1.61}$ [7].

$$(Pu^{3+}, Pu^{4+})_2\ (O^{2-})_3 (O^{2-}, Va)_1 \qquad \textbf{(2.25)}$$

In the case where Pu^{4+} is in the first sublattice and O^{2-} in the third, the composition corresponds to the metastable cubic bcc PuO_2 with respect to the fluorite form. On the contrary, if Pu^{3+} is present in the first sublattice and vacancies in the third, the metastable cubic Pu_2O_3 phase with respect to the hexagonal form is assessed. This sublattice model allows describing the composition range of this phase existing only at high temperature.

The thermodynamic model of Guéneau *et al.* is in good agreement with the available experimental data [7]. However, uncertainties remain at high temperature, especially in the solidus/liquidus temperature range between Pu_2O_3 and PuO_2, where experimental data are missing.

For the Am-O system, as few data are available on the metastable B-Am_2O_3 phase, this later is not considered in the model. Moreover, as for Pu-O, the A-Am_2O_3 phase is described as a stoichiometric compound, while the $AmO_{1.61}$ phase is represented by a sublattice model similar to **(2.25)** (with Am^{3+} and Am^{4+} in the first sublattice). With the model of Epifano *et al.* [6], a better understanding of the Am-O system was obtained. However, difficulties in predicting thermodynamic properties such as oxygen potentials or phase boundaries remain, highlighting the need of new sets of experimental data.

2.4.2. Ternary systems

The same sublattice models used to describe the binary systems are used in the assessment of the ternary systems U-Pu-O, Pu-Am-O and U-Am-O. These assessments were also performed based on the various sets of phase diagram data (phase boundaries, transition temperatures) and thermodynamic data (oxygen potentials, enthalpies, heat capacity …) previously described in sections 2.1.2 and 2.3.

For all the phases, the sublattice models of the binary sub-systems were combined to describe the corresponding ternary systems. Ternary interactions parameters were added in each system to fit the available experimental data on the ternary systems.

2.4.2.1 U-Pu-O

The model of the U-Pu-O system was improved over the last decades by Guéneau *et al.* [7]. A good agreement is found with the phase diagram and thermodynamic data of the literature (see Figure 2-40 for the solidus and liquidus temperatures of U-Pu-O). However, the mixed oxides M_4O_9, M_3O_8 (with M = U+Pu) in the hyper-stoichiometric region are not described as solubility of Pu in U_4O_9 and U_3O_8 is unknown. Uncertainties still remain on the model due to the lack of experimental data, in particular in the biphasic MO_{2-x} + M_2O_3 region or at high temperature in the hypo- and hyper-stoichiometric $U_{1-y}Pu_yO_{2\pm x}$ domains for example. Further experimental investigations are needed for a complete assessment of the thermodynamic model of this system.

2.4.2.2 Pu-Am-O

A representation of the Pu-Am-O system using the CALPHAD method was proposed by Gotcu-Freis *et al.* [26], as explained in section 2.1.2.2. This model reproduces well the oxygen

potential data of Osaka *et al.* for $Pu_{0.91}Am_{0.09}O_{2-x}$ [43] but the calculated oxygen potential are overestimated compared to the results of Otobe *et al.* for $Pu_{0.50}Am_{0.50}O_{2-x}$ [44] (see Figure 2-36).

However, as few experimental data are available for this system, large uncertainties remain on several regions such as a possible continuous solid solution between $PuO_{1.61}$ and $AmO_{1.62}$ or the existence of the miscibility gap in the $Pu_{1-z}Am_zO_{2-x}$ phase. Additional experimental campaigns are thus essential for a more accurate description of the system. In addition, based on a recent assessment of the Am-O system by Epifano *et al.* [6], a re-evaluation of the thermodynamic model of the Pu-Am-O system is needed.

2.4.2.3 U-Am-O

A first tentative representation of the U-Am-O system using the CALPHAD method was proposed by F. Lebreton in his Ph.D. thesis, based on the oxygen potential data of Bartscher and Sari [167]. An updated thermodynamic model was proposed by E. Epifano based on the sets of experimental data obtained in her Ph.D. work [28].

This assessment was focused on the $U_{1-z}Am_zO_{2\pm x}$ solid solution, for which interaction parameters were assessed. A good agreement between the model and the experimental enthalpy increments and vapour pressure data is obtained for low americium contents, while discrepancies are found for high americium contents (see Figure 2-42 for the enthalpy functions).

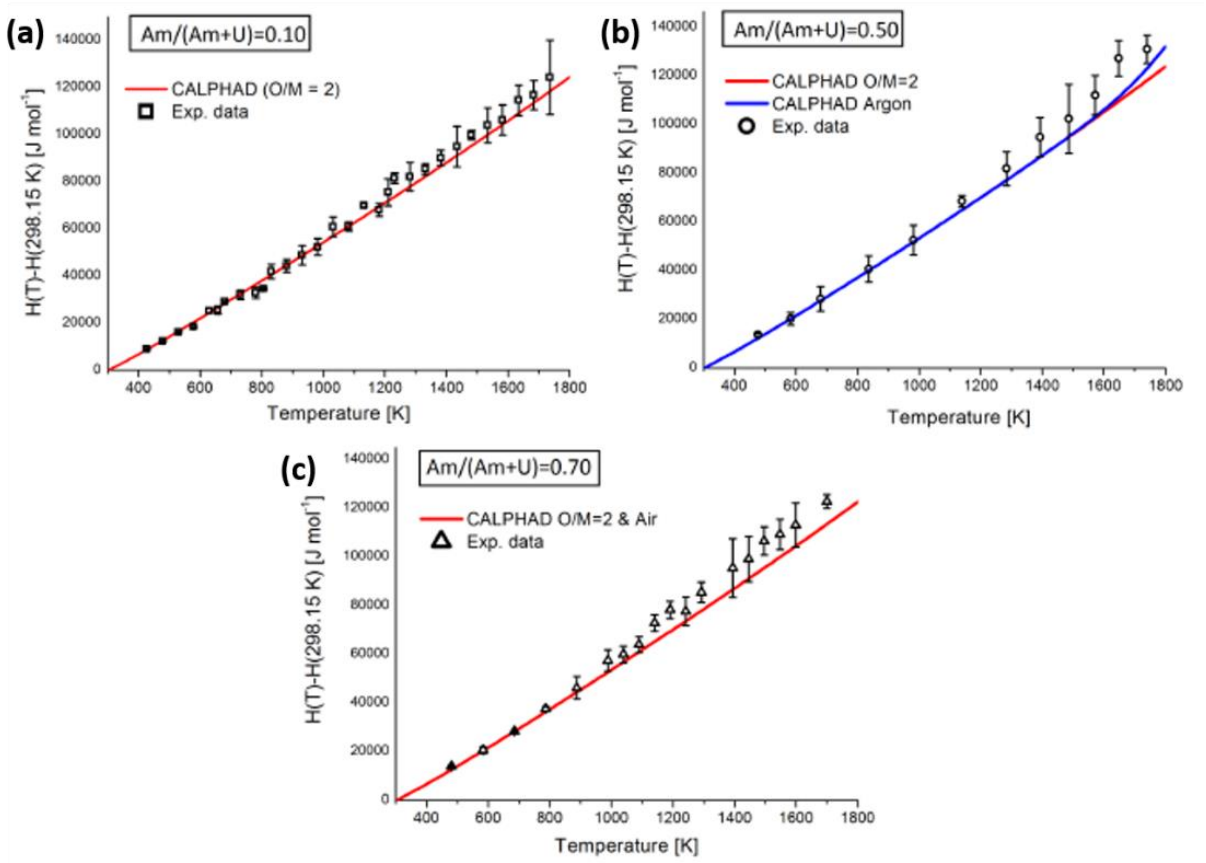

Figure 2-42: Calculated enthalpy increments using the CALPHAD model of E. Epifano [28] for U-Am-O, compared to experimental data obtained by Epifano *et al.* [143] for z = 0.10, 0.50 and 0.70.

An artefact of the model induces the existence of metastable miscibility gaps in the domain for hyperstoichiometric $U_{1-z}Am_zO_{2+x}$. Moreover, experimental investigations performed by Caisso *et al.* [60] and Epifano *et al.* [188], [189] evidenced a solubility of americium in the M_4O_9 and M_3O_8 phases, which is not included in the model. As explained by E. Epifano, because of the lack of available data, this model constitutes a preliminary assessment and further experimental investigations, in particular oxygen potential, are needed to obtain a reliable CALPHAD model.

2.5. CONCLUSION

This chapter reports the available structural and thermodynamic data, as well as the phase diagram representations of the U-Pu-Am-O quaternary system and its binary and ternary sub-systems.

For the binary U-O and Pu-O systems, numerous data are reported in the literature over the past decades, leading to reliable thermodynamic models using the CALPHAD method [13], [23]. On the contrary, due to the high radiotoxicity of Am isotopes, experimental investigations on the Am-O system are limited and the representation of the phase diagram of this system was recently improved by Epifano *et al.* [6].

Concerning the ternary systems, the U-Pu-O system is well known. Various $U_{1-y}Pu_yO_{2\pm x}$ were studied at both low and high temperature, resulting in an accurate phase diagram representation of the ternary at low Pu contents [7]. However, few experimental data are available for $y > 0.60$, especially at high temperature, justifying the need for new measurements campaigns.

As previously explained, few experimental campaigns on Am-bearing oxides were performed.

In the case of the Pu-Am-O system, a tentative representation exists in the literature from Gotcu-Freis *et al.* [26], based on the few data available on structural and thermodynamic properties, such as vapour pressures [26] and oxygen potentials [43], [44].

Thanks to recently obtained data by Epifano *et al.*, a more accurate knowledge of the U-Am-O system is now available [28]. However, uncertainties remain in some ranges of the phase diagram, for example on the possible existence of a miscibility gap for $O/M < 2$. In addition, oxygen potential data are missing to get an accurate thermodynamic model.

In the case of the U-Pu-Am-O system, few experiments take into account the influence of the americium addition on the properties of $U_{1-y}Pu_yO_{2\pm x}$. Lattice parameters at room and high temperatures, vapour pressure data, melting temperatures and oxygen potentials are available in the literature for several compositions with few mol. % of americium. It was noticed, for example, that an addition of ^{241}Am tends to decrease both the lattice parameter and melting point of mixed oxides of uranium and plutonium, while it increases the oxygen potentials of these compounds.

The most recent thermodynamic CALPHAD models of these systems, used in the TAF-ID database, were briefly reviewed, with the description of the sublattice models for the gas, liquid and solid phases.

Although some experimental data are available on the uranium-plutonium-americium mixed dioxides, it was proven that this is not sufficient to have an accurate model on the quaternary system. The need to perform new experimental campaigns on $Pu_{1-z}Am_zO_{2-x}$ and $U_{1-y-z}Pu_yAm_zO_{2\pm x}$ was thus highlighted in this chapter.

3. MATERIALS AND METHODS

The needs to perform additional experimental campaigns on the Pu-Am-O and U-Pu-Am-O systems was highlighted in the previous chapter. In this chapter, the principles of the CALPHAD method are described first, as well as the formalisms used to represent the different phases. As the samples used in this work were manufactured in the framework of various projects historically, the manufacturing techniques are described for the three $Pu_{1-z}Am_zO_{2-x}$ ($z = 0.23, 0.51, 0.80$) and the five $U_{1-y-z}Pu_yAm_zO_{2\pm x}$ ($0.235 \leq y \leq 0.39$ and $0.005 \leq z \leq 0.02$) samples studied here. Their main characteristics at the manufacturing are also summarized. The various experimental techniques used in this work to gain knowledge on the structural and thermodynamic properties of the samples of interest are also described, with the data acquisitions and the analysis procedures.

3. MATERIALS AND METHODS

The goal of this work is the study of the structural and thermodynamic properties of $U_{1-y-z}Pu_yAm_zO_{2\pm x}$ samples.

In order to develop the thermodynamic model of the corresponding U-Pu-Am-O system, the CALPHAD method is used. Its principles and the thermodynamic models and formalisms used in this work are described in section 3.1. As already stated in Chapter 1, experimental data are needed as input data to obtain a reliable model. To this aim, experimental campaigns were performed on $Pu_{1-z}Am_zO_{2-x}$ and $U_{1-y}Pu_yO_{2\pm x}$ (exhibiting few mol.% of Am by decay of ^{241}Pu) to investigate the ternary Pu-Am-O and the quaternary U-Pu-Am-O systems. The manufacturing of these samples is explained in section 3.2. Finally, the different experimental techniques used during this work to measure structural and thermodynamic properties of the samples are detailed in section 3.3.

3.1. CALPHAD METHOD

3.1.1. Principles

CALPHAD, acronym for CALculation of PHAse Diagram, is a semi-empirical method allowing the determination of thermodynamic properties and phase diagrams for multicomponent systems [5]. This approach is based on the Gibbs energy G, described by the following equation **(3.1)**:

$$G = H - TS = U + PV - TS \quad \textbf{(3.1)}$$

Where H is the enthalpy (the heat content of the system) in J.mol^{-1}, T the temperature in K, S the entropy of the system (its randomness) in J.mol^{-1}.K^{-1}, U the internal energy (the kinetic and potential energies of atoms) in J.mol^{-1}, P the pressure in Pa and V the volume in m^3.

The equilibrium state of a system, at constant pressure, temperature and number of moles of components, is the state in which the total Gibbs energy of the system is the lowest ($dG = 0$). This function is the linear combination of the Gibbs energy of the phases, G_m^{φ}, present in the system, as it can be seen in Equation **(3.2)**:

$$G = \sum_i m^{\varphi} G_m^{\varphi} \quad \textbf{(3.2)}$$

Where m^{φ} is the mole fraction of phase φ.

In the CALPHAD method, mathematical models are derived to describe the Gibbs energies of all the solid, liquid and gas phases as a function of temperature, composition and pressure (only for the gas). The thermodynamic equilibrium is then calculated by minimizing the total Gibbs energy of the system.

The Gibbs energy functions are referred to the enthalpy of the pure elements in their stable state at 298.15 K and 1 bar, H_i^{SER}, where SER means Stable Element Reference.

In case of a stoichiometric phase φ, the molar Gibbs energy is expressed by Equation **(3.3)**:

$$G_m^{\varphi} - \sum_i b_i H_i^{SER} = a_0 + a_1 T + a_2 T \ln T + a_3 T^2 + a_4 T^{-1} + \cdots \quad \textbf{(3.3)}$$

where b_i is the stoichiometric coefficient of the element i in the phase φ and T the temperature in K. This equation is applicable for pure elements, stoichiometric compounds as well as for the end-members of non-stoichiometric phases, for which each sublattice contains only one species.

In the case of a binary solution (A,B), the molar Gibbs energy can be written as the sum of following contributions:

$$G_m^{\varphi} = G_{ref}^{\varphi} + G_{id}^{\varphi} + G_{ex}^{\varphi} + G_{mag}^{\varphi} \quad \textbf{(3.4)}$$

With

$$G_{ref}^{\varphi} = x_i^{\varphi} \, {}^{\circ}G_i^{\varphi}(T) \quad \textbf{(3.5)}$$

$$G_{id}^{\varphi} = R\,T\,x_i^{\varphi} \ln(x_i^{\varphi}) \quad \textbf{(3.6)}$$

$$G_{ex}^{\varphi} = x_A^{\varphi}\, x_B^{\varphi}\, L_{A,B}^{\varphi} \quad \textbf{(3.7)}$$

Where G_{ref}^{φ} is the reference term, G_{id}^{φ} the ideal random mixing entropy term, G_{ex}^{φ} the excess Gibbs energy and G_{mag}^{φ} the magnetic contribution. ${}^{\circ}G_i^{\varphi}(T)$ corresponds to the Gibbs energy of the element i pure in the phase φ. x_i^{φ} is to the molar fraction of the element i in the phase φ. $L_{A,B}^{\varphi}$ is the interaction parameter between atoms A and B.

In most cases, the interaction parameter $L_{A,B}^{\varphi}$ depends on the composition x_A and x_B and is expressed by the Redlich-Kister polynomial function [190], according to Equation **(3.8)**:

$$L_{A,B} = \sum_{\nu=0} (x_A - x_B)^{\nu} \, {}^{\nu}L_{A,B} = {}^{0}L_{A,B} + {}^{1}L_{A,B}\,(x_A - x_B) + {}^{2}L_{A,B}\,(x_A - x_B)^2 + \cdots \quad \textbf{(3.8)}$$

For non stoichiometric phases, the Compound Energy Formalism (CEF) is used [191] [192] [187]. This model allows the connection between thermodynamics and crystallography. The sublattices correspond to equivalent crystal positions, *i.e.* sites belonging to the same Wyckoff position. A single sublattice model is used for all the phases with the same crystal structure (Figure 3-1). For example, all the phases exhibiting a fcc or bcc structure are described by the sublattice models $(A)_1(Va)_1$ and $(A)_1(Va)_3$, respectively, where "Va" denotes vacancies.

A phase is described by several sublattices in the form of $(A,B)_m\,(C,D)_n\,(E,F)_p\ldots$, exhibiting preferential occupancy by one or more constituents (atoms, charged ions or vacancies) in each sublattice, as described in Figure 3-1. The description of the sublattice can be of different orders, for which the zeroth order has one constituent in each sublattice and is referred to as an "end-member". A first order array has two constituents in one of the sublattices and one single constituent in any additional sublattice, whereas a second order one exhibits two constituents in one sublattice and two in the followings.

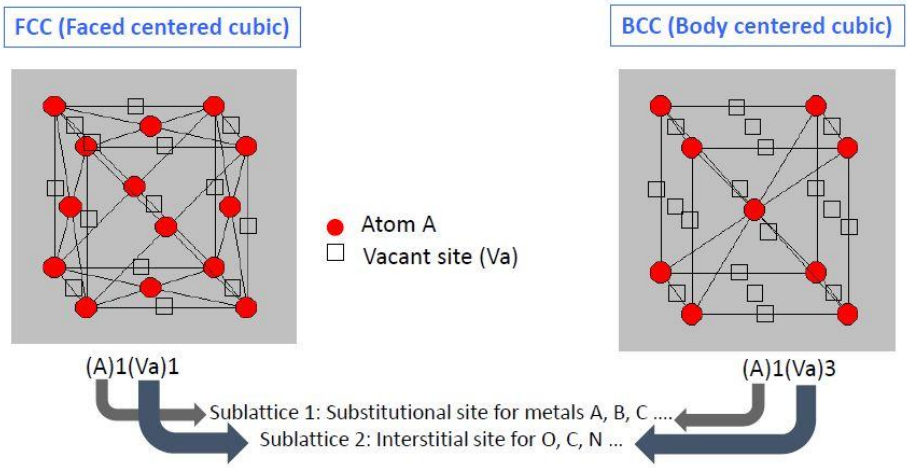

Figure 3-1: Representation of the sublattice model.

The CALPHAD method is particularly useful to describe and predict properties of a multicomponent (high order) system, based on the extrapolation of its sub-systems (lower order). Indeed, models are derived first for the binary and ternary sub-systems. The variables of Equations **(3.3)-(3.8)** are then adjusted to reproduce available crystallographic, thermodynamic and phase diagram data. A schematic representation of this approach is shown in Figure 3-2.

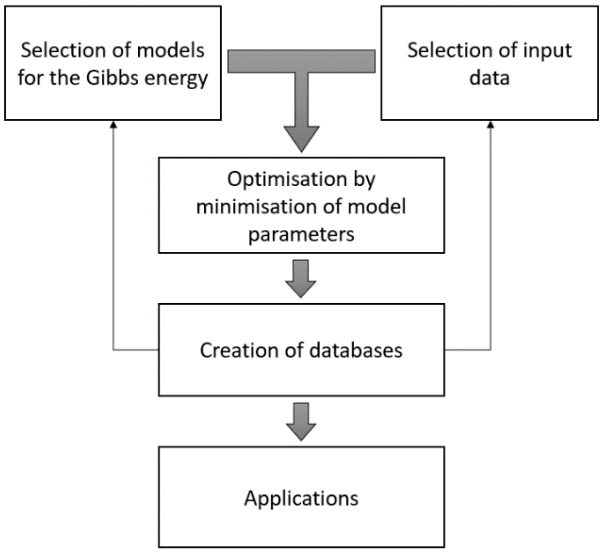

Figure 3-2 : Graphical representation of the CALPHAD method.

The first step of the thermodynamic assessment consists in the critical review of the available experimental data. The data used for the CALPHAD method can be classified in different categories: the structural data (lattice parameters, defects…), the phase diagram data (transition temperatures, phase equilibria…) and thermodynamic data (enthalpy of formation, standard entropy, heat capacity, chemical potential, activities…). If the experimental results are not sufficient or not reliable enough, new experimental campaigns need to be performed.

In the frame of this work, the Thermo-Calc software is used [193] [194]. As starting point, the models of the TAF-ID (Thermodynamic for Advanced Fuel – International Database, developed by the nine organizations of the NEA states) are chosen [195]. This database is a joint project

started in 2013, coordinated by the OECD-NEA, with a goal of supporting the development of Gen IV nuclear reactors and the lifetime extension, safety improvement and safety analysis for the Gen II and III systems. Within this project, thermodynamic calculations on different types of fuels including minor actinides, fission products and structural materials, are performed [195].

3.1.2. Models for the U-Pu-Am-O system

In this part, the CALPHAD models for the gas, liquid and solid mixed dioxide phases are described, as they constitute the phases of main interest of this work and only the Gibbs energies of these phases are modified in this work. The models and values of the assessed parameters constituting the Gibbs energy functions can be found in the literature for the various sub-systems: U-O from Guéneau *et al.* [13], Pu-O from Guéneau *et al.* [7], Am-O from Epifano *et al.* [6], U-Pu-O from Guéneau *et al.* [7], Pu-Am-O from Gotcu-Freis *et al.* [26] and U-Am-O from E. Epifano [28].

3.1.2.1 Gas

As explained in Chapter 2 – section 2.4, the gas phase is described as an ideal mixture of gaseous species. Its Gibbs energy is described as follows:

$$G^{gas} = \sum_i y_i \left[{}^0G_i^{gas} - \sum_j b_{ij} H_j^{SER} + RT \ln y_i \right] + RT \ln \left(\frac{p}{p_0} \right) \quad \textbf{(3.9)}$$

Where y_i are the constituent site fractions, b_{ij} is the number of atoms j in the species i. p_0 corresponds to the standard pressure and is equal to 10^5 Pa and G_i^{gas} is the standard Gibbs energy of the gaseous species i.

3.1.2.2 Liquid

To describe the liquid phase of a metal-oxide system, the ionic two-sublattice model is used [196] **(3.10)**:

$$(C_i)_P (A_j, Va^{Q-}, B_k)_Q \quad \textbf{(3.10)}$$

In this model, the first sublattice contains a mixture of cations (C_i), whose charges correspond to the lowest oxidation state for which a stable oxide compound is observed for each element. The second sublattice contains anions (A_j, here O^{2-}), charged vacancies Va^{Q-} and neutral species (B_k). In order to maintain the electro-neutrality of the liquid phase, the site numbers P and Q are equal to the average charges on the opposite sublattice as follows **(3.11),(3.12)**:

$$P = \sum_{A_j} \upsilon_{A_j} y_{A_j} + Q y_{Va} \quad \textbf{(3.11)}$$

$$Q = \sum_{C_i} \upsilon_{C_i} y_{C_i} \quad \textbf{(3.12)}$$

Where υ_i is the charge of species i, y_i corresponds to its site fraction, C_i stands for any cation and A_j for any anion. The sum of the constituent site fractions in each sublattice is equal to one.

The Gibbs energy **(3.13)** is divided into three terms:

$$G^{liq} = {}^{ref}G^{liq} + {}^{id}G^{liq} + {}^{exc}G^{liq} \quad \textbf{(3.13)}$$

The reference term ${}^{ref}G^{liq}$ is defined in Equation **(3.14)**.

$$ {}^{ref}G^{liq} = \sum_C \sum_A y_C y_A {}^0G^{liq}_{(C)(A)} + Q y_{Va} \sum_C y_C {}^0G^{liq}_{(C)} + Q \sum_B y_B {}^0G^{liq}_{(B)} \quad \textbf{(3.14)}$$

Where ${}^0G^{liq}_{(C)(A)}$ represents the Gibbs energy of $(v_A + v_C)$ moles of liquid Cv_AAv_C, ${}^0G^{liq}_{(C)}$ the Gibbs energy of the pure liquid C and ${}^0G^{liq}_{(B)}$ the Gibbs energy of the liquid neutral species B.

The ideal term ${}^{id}G^{liq}$ corresponds to the random configurational entropy on both sublattices **(3.15)**:

$$ {}^{id}G^{liq} = RT\left[P\sum_C y_C \ln y_C + Q\left(\sum_A y_A \ln y_A + y_{Va} \ln y_{Va} + \sum_B y_B \ln y_B\right)\right] \quad \textbf{(3.15)}$$

The excess term ${}^{exc}G^{liq}$ is defined according to the following equation **(3.16)**:

$$\begin{aligned} {}^{exc}G^{liq} = {} & \sum_{C_1}\sum_{C_2}\sum_A y_{C_1} y_{C_2} y_A L^{liq}_{(C_1,C_2)(A)} + \sum_{C_1}\sum_{C_2} y_{C_1} y_{C_2} y_{Va}^2 L^{liq}_{(C_1,C_2)(Va)} \\ & + \sum_C \sum_{A_1}\sum_{A_2} y_C y_{A_1} y_{A_2} L^{liq}_{(C)(A_1,A_2)} + \sum_C \sum_A y_C y_A y_{Va} L^{liq}_{(C)(A,Va)} \\ & + \sum_C \sum_A \sum_B y_C y_A y_B L^{liq}_{(C)(A,B)} + \sum_C \sum_B y_C y_B y_{Va} L^{liq}_{(C)(B,Va)} \\ & + \sum_{B_1}\sum_{B_2} y_{B_1} y_{B_2} L^{liq}_{(B_1,B_2)} \end{aligned} \quad \textbf{(3.16)}$$

The interactions between the different species in each sublattice are represented by the L interaction parameters. When several species are interacting in the same sublattice, a coma is used to separate them.

In the case of the U-Pu-Am-O system, the sublattice model of the liquid phase is the following:

$$(U^{4+}, Pu^{3+}, Am^{3+})_P (O^{2-}, Va^{Q-}, PuO_2, AmO_2, O)_Q \quad \textbf{(3.17)}$$

3.1.2.3 Mixed oxide $MO_{2\pm x}$

The following three-sublattice model is used to describe the mixed dioxide **(3.18)**:

$$(U^{3+}, U^{4+}, U^{5+}, Pu^{3+}, Pu^{4+}, Am^{3+}, Am^{4+})\ (O^{2-}, Va)_2 (O^{2-}, Va) \quad \textbf{(3.18)}$$

The first sublattice is the site for cations, the second sublattice is the normal site for oxygen in the fluorite structure, where the addition of vacancies allows describing the hypo-stoichiometric region of the dioxides, and the third sublattice is the site for interstitial oxygen to represent the hyper-stoichiometric composition range. At equilibrium, the phase has to remain electronically

neutral. For $U_{1-y-z}Pu_yAm_zO_{2-x}$, the presence of oxygen vacancies on the normal site for oxygen (second sublattice) is compensated by adding U^{3+}, Pu^{3+} and/or Am^{3+} in the first sublattice. For $U_{1-y-z}Pu_yAm_zO_{2+x}$, the insertion of oxygen anions in the third sublattice is compensated by the presence of U^{5+} in the first sublattice.

The Gibbs energy associated to the model is:

$$G_m^{MOX} = \sum_i \sum_j \sum_k y_i y_j y'_k \, {}^0G_{i:j:k}^{MOX} + RT\left(\sum_i y_i \ln y_i + 2\sum_j y_j \ln y_j + \sum_k y'_k \ln y'_k\right) + {}^{exc}G^{MOX} \quad \textbf{(3.19)}$$

$${}^{exc}G^{MOX} = \sum_{i_1} \sum_{i_2} \sum_j \sum_k y_{i_1} y_{i_2} y_j y_k \left[{}^0L_{i_1,i_2:j:k}^{MOX} + (y_{i_1} - y_{i_2})\,{}^1L_{i_1,i_2:j:k}^{MOX}\right] + \sum_{i_1} \sum_{i_2} \sum_{i_3} y_{i_1} y_{i_2} y_{i_3} L_{i_1,i_2,i_3:*:*}^{MOX} \quad \textbf{(3.20)}$$

Where y_i represents the fraction of the species i in the sublattice, ${}^0G_{i:j:k}^{MOX}$ the Gibbs energies of the different end-members formed by considering the species i in the first sublattice, j and k in the second and third sublattices, respectively. As O^{2-} and Va are present in both the second and third sublattices, the notation y' is used for the site fraction of the third sublattice. ${}^nL_{i_1,i_2:j:k}^{MOX}$ are the interaction parameters of the two cations in the first sublattice, when the other sublattice are fully occupied by a single species. When these interactions are considered independent of the occupations of those two last sublattices (oxygens or vacancies), the notation * is introduced. The $L_{i_1,i_2,i_3:*:*}^{MOX}$ terms correspond to ternary interactions between three cations of the first sublattice.

In order to validate the models, as described in Figure 3-2, experimental data are needed. As evidenced in Chapter 2, few data exist on the Am-bearing systems and to this aim, new experimental campaigns were performed in this work on $Pu_{1-z}Am_zO_{2-x}$ and $U_{1-y-z}Pu_yAm_zO_{2\pm x}$ samples. The materials of interest and the experimental technique used in this work are described in the following sections.

3.2. MATERIALS OF INTEREST

In order to gain knowledge on the structural and thermodynamics properties of the U-Pu-Am-O system, historic $Pu_{1-z}Am_zO_{2-x}$ and $U_{1-y-z}Pu_yAm_zO_{2\pm x}$ samples were studied in this work. Their manufacturing processes, as well as their characteristics, are described in this section.

3.2.1. $Pu_{1-z}Am_zO_{2-x}$ oxides

3.2.1.1 Manufacturing process

Three batches of $Pu_{1-z}Am_zO_2$, with z = 0.22, 0.49 and 0.80, were manufactured in 2007 in the ATALANTE facility at CEA Marcoule, France, as described in [197], [198].

The $Pu_{1-z}Am_zO_2$ starting powder was obtained by oxalate co-conversion technique. The two following steps were performed:

1) Formation of a precipitate in nitric acid medium with excess of oxalate:

$$(Am^{3+}, 3NO_3^-)_{x_1} + (Pu^{4+}, 4NO_3^-)_{x_2} + \frac{3x_1 + 4x_2}{2} H_2C_2O_4 \rightarrow Am_{x_1}Pu_{x_2}(C_2O_4)_{\frac{3x_1+4x_2}{2}}, nH_2O + (3x_1 + 4x_2)HNO_3 \quad \textbf{(3.21)}$$

2) Calcination under air to obtain the final compound:

$$Am_{x_1}Pu_{x_2}(C_2O_4)_{\frac{3x_1+4x_2}{2}} + O_2 \rightarrow (Am_{x_1}Pu_{x_2})O_2 + (3x_1 + 4x_2)CO_2 \quad \textbf{(3.22)}$$

The synthesis of these compounds yielded pure single-phase precursors. Analyses of the precursors (particle size, powder morphology and crystal structure) were performed by BET, SEM and XRD and the results are summarized in Table 3-1.

Table 3-1 - $Pu_{1-z}Am_zO_2$ powder characteristics [197].

	$Pu_{0.80}Am_{0.20}O_{2.00}$	**$Pu_{0.51}Am_{0.49}O_{2.00}$**	**$Pu_{0.20}Am_{0.80}O_{2.00}$**
Mean particle size (µm)	3.8 ± 0.5	3.7 ± 0.4	2.3 ± 1.2
Specific surface area ($m^2.g^{-1}$)	5.6	5.7	2.0
Crystal structure	fcc	fcc	fcc
Lattice parameter (Å)	5.394 ± 0.001	5.388 ± 0.001	5.382 ± 0.001
Referred to in this work as	PuAm80/20	PuAm50/50	PuAm20/80

The precursors powders were blended in a ball-mill during 30 minutes at 30 Hz and granulated at 150 µm. $Pu_{1-z}Am_zO_2$ pellets were shaped by uniaxial pressing at 400 MPa. A sintering step was then performed under Ar/H_2 4% at 1573 K for 30 minutes. Density of 90 % for z = 0.20, 88 % for z = 0.50 and < 80 % for z = 0.80 with respect to the theoretical density were obtained for the sintered pellets of following dimensions: 5.5 mm diameter and 6 mm high. No crack or strain was observed after sintering.

3.2.1.2 Annealing thermal treatment

As the samples were manufactured in 2007, changes in the O/M ratio and defects induced by the self-irradiation of the samples may have occurred. In order to break free from these effects and have a known starting point for some experiments, a thermal treatment was performed on some fragments of the $Pu_{0.80}Am_{0.20}O_{2-x}$ sample, with an annealing at 1273 K for 8 hours under air, with heating and cooling rates of 6 $K.min^{-1}$. These conditions were chosen based on thermodynamic calculations to ensure an O/M ratio of 2.00. In the rest of this work, these annealed samples are referred to as PuAm80/20-OM.

3.2.2. $U_{1-y-z}Pu_yAm_zO_{2\pm x}$ oxides

Five batches of uranium-plutonium mixed oxides $U_{1-y}Pu_yO_{2\pm x}$ manufactured in the nineties were used in this study. Among them, four were manufactured by powder metallurgy process and

one batch by sol-gel route. These samples were produced in the framework of the development of Sodium Fast Reactors, for which specific requirements needed to be achieved:

- An external diameter between 5.39 and 5.50 mm and a height superior to 6 mm.
- A relative density around 95.5 % TD (Theoretical density), with a value superior to 92 %.
- An O/M ratio comprised between 1.94 and 2.00.

The manufacturing techniques, as well as the specificities of the mixed oxides of interest, are described in this section.

3.2.2.1 Powder metallurgy process

A co-milling process involving UO_2 and PuO_2 raw powders in various proportions was used in order to obtain the targeted plutonium content.

Three batches of $U_{1-y}Pu_yO_{2\pm x}$ SFR pellets manufactured for the PHENIX core reactor (CEA Marcoule, France) were chosen in this study:

- A first batch of $U_{0.69}Pu_{0.31}O_{1.97}$, corresponding to annular CAPRA4 samples (Consommation Accrue de Plutonium dans les RApides), was manufactured at the LEFCA facility (CEA Cadarache, France) in 1996 [199].
- A second and third batch, $U_{0.76}Pu_{0.24}O_{2-x}$ and $U_{0.71}Pu_{0.29}O_{2-x}$ pellets, respectively named PHENIX24 and PHENIX29, was manufactured during a single campaign in 1999 at the AtPu (Atelier Plutonium) in CEA Cadarache (France) by the industrial COCA (CObroyage CAdarache) process [200].

Another batch of pellets ($U_{0.60}Pu_{0.40}O_{2-x}$), called TRABANT40 for TRAnsmutation and Burning of ActiNides in Triox, was manufactured in 1998 in the Joint Research Centre Karlsruhe (Germany) for irradiation in the HFR-Petten (The Netherlands) [201]. These pellets were produced in annular form. Among this fabrication, pellets were divided into two batches with different O/M ratios.
For the four fabrications, UO_{2+x} and PuO_2 powders were co-grinded, sieved and lubricated, pressed and sintered in reducing atmosphere. The conditions of the sintering step are gathered in Table 3-2 for each batch. The characteristics of the resulting pellets are summarized in Table 3-3.

Table 3-2 - Sintering conditions for the four batches manufactured by metallurgy process.

CAPRA4	PHENIX24/PHENIX29	TRABANT40
1943 K for 4 h under Ar/H_2 7%	1923 K for 45 min under Ar/H_2 7%	1923 K for 6 h under Ar or Ar/H_2 1%

3.2.2.2 Sol-gel route

Only one batch of $U_{1-y}Pu_yO_{2\pm x}$ (TRABANT45, with y = 0.45) was manufactured using the sol-gel route. The fabrication took place in the Joint Research Centre Karlsruhe, Germany, in 1998. Nitrate solutions of metals (uranium and plutonium) were mixed and the resulting liquid was dispersed into droplets, collected in an ammonia bath. Gelation was used to convert these

droplets into solid microspheres. The latters were dried by azeotropic distillation and thermally treated first in air at 673 K for 4h and then under Ar/H_2 5 % at 1073 K for 4h. The resulting powder was pressed into annular pellets. A sintering step of 6 h at 1923 K under Ar/H_2 1% was performed to obtain the targeted O/M ratio of 2.00.

3.2.2.3 Characterizations

The samples were characterized to ensure that the specific requirements of SFR fuels were met. Visual inspections were also performed indicating that no cracks nor chips were observed on the surface. EPMA and SEM were used to determine the U and Pu distributions within the pellets and optical imaging was performed to determine the porosity and the impurity rates. The density was calculated from the dimensions of the pellets and compared to the theoretical density.

The characteristics of the resulting pellets are summarized in Table 3-3.

In the case of the TRABANT45, the density did not lie in the targeted range, even after further thermal treatment. However, as the material was stable and the fissile material homogeneously distributed, this batch was accepted for study.

Table 3-3 - Pellets characteristics for the five $U_{1-y}Pu_yO_{2\pm x}$ batches.

	PHENIX24 [200]	**PHENIX29 [200]**	**CAPRA4 [199]**	**TRABANT40 [201]**	**TRABANT45 [201]**
Diameter (mm)	5.41 ± 0.01	5.41 ± 0.01	5.42 ± 0.01 (central hole: 1.7 ± 0.1)	5.43 ± 0.01 (central hole: 2.40 ± 0.01)	5.43 ± 0.01 (central hole: 2.32 ± 0.01)
Height (mm)	11.0 ± 0.2	11.0 ± 0.2	9.2 ± 0.3	7.7 - 8.3 ± 0.1	8.3 ± 0.1
Density (% TD)	93.7 %	93.7 %	92.0 %	93.4 - 94.2 %	86.4 %
O/M ratio (Year of measurement)	1.978 ± 0.002 (2011)	1.973 ± 0.002 (2011)	1.968 ± 0.002 (1996)	1.995 ± 0.002 (1998) 1.971 ± 0.002 (1998)	1.990 ± 0.002 (1998)

3.2.2.4 Annealing thermal treatment

In order to study the influence of the O/M ratio on the melting behaviour, pellets of PHENIX29 and TRABANT40 samples were annealed. The following thermal treatment was performed: 8 hours at 1173 K, with heating and cooling rates of 6 $K.min^{-1}$, under Ar/H_2 4% + 24 000 ppm H_2O. These conditions were chosen based on thermodynamic calculations to ensure an O/M ratio of 2.00. The latter was checked by X-Ray Diffraction (see Chapter 5 – section 5.1.2). These annealed samples are referred to as PHENIX29-OM and TRABANT40-OM in the rest of this work.

3.3. EXPERIMENTAL TECHNIQUES

3.3.1. Room temperature X-Ray Diffraction (XRD)

3.3.1.1 Experimental set-up

XRD characterizations at ambient pressure and room temperature were performed in the ATALANTE facility at CEA Marcoule, France. The experimental set-up, as well as the preparation method, was described in details by Vauchy *et al.* [202]. The diffractometer used presents the following characteristics: Bruker D8 Advance diffractometer in θ-θ Bragg-Brentano geometry, equipped with a copper source [λ(Kα_1 and Kα_2) = 1.5406 and 1.5444 Å] and a Bruker LYNXEYE linear detector, with a 3° 2θ opening angle. As described in [202] and shown in Figure 3-3, a sample stage was designed in house and nuclearized to handle radioactive materials.

The sample preparation is the following. Approximatively 50-75 mg of sample in presence of around 25 mg of a standard material (Au, Alfa Aeser, 99.96%) are manually co-milled in an agate mortar. The Au standard material is used for 2θ calibration of XRD reflexion positions. Once finely milled, polymer grease is added to the obtained mixture to avoid dispersion of the powder during the connection from the glovebox to the XRD set-up. The paste is then spread out on a low-background oriented single-crystal Silicon plate.

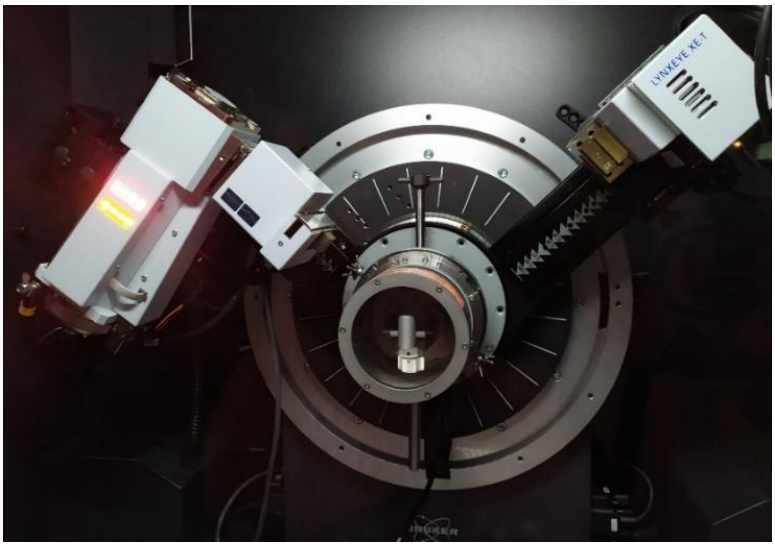

Figure 3-3: BRUKER D8-Advance with nuclearized sample stage.

3.3.1.2 Data analysis

Diffraction patterns of the actinide dioxides were obtained by scanning from 25° to 120° 2θ. A counting time of 0.5 s per step and step-intervals of 0.01° 2θ were chosen for most of the measurements. Analysis and refinement of the obtained XRD patterns were performed according to the Rietveld method [203] available in the DIFFRACplus TOPAS V4 software package [204]. The peak profiles are described by a modified Thompson-Cox-Hastings pseudo-Voigt function [205]. The background is approximated by a Chebyshev polynomial function with three terms. The zero detector and background parameters were first considered during the refinement procedure, then lattice parameter and crystallite size were assessed. The uncertainty on the lattice parameter is estimated to be 0.001 Å.

3.3.2. Scanning Electron Microscopy (SEM)

The SEM analyses were performed in the ATALANTE facility (CEA Marcoule) on fractured surfaces of the samples. A nuclearized version of the MIRA3-AMU from TESCAN was used, where the chamber of the SEM is installed inside a glovebox to allow the handling of radioactive samples [206].

3.3.3. Electron Probe Microanalyser (EPMA)

3.3.3.1 Experimental set-up

The EPMA analyses were performed in the ATALANTE facility (CEA Marcoule, France). A CAMECA SX100 device equipped with a tungsten source was used (Figure 3-4). All the measurements were performed at 20 kV for electron accelerating voltage. The U Mα, Pu Mβ and Am Mα peaks were observed using a PET crystal and the O Kα peak using a PC1 (W/Si) multilayer crystal.

Several types of analyses can be performed with the EPMA. First, WDS spectra of 2048 points were acquired in different zones of the samples, by combining L-PC1, L-PET, TAP and LiF crystals to cover a wide energy range (from 0.27 to 14 keV). The time per step was 200 ms. Then, cartographies of U, Pu, Am and O distributions were done, with horizontal and vertical resolutions of 1 µm, without background subtraction. A current of 150 nA and a time of step of 20 ms was used. The randomly positioned scanning surface is 1 mm² (1024 x 1024 pixels).

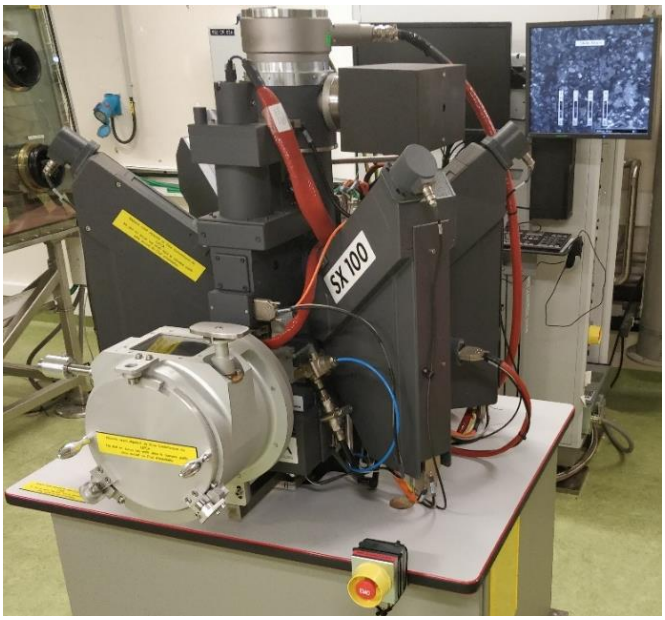

Figure 3-4: CAMECA SX100 device for EPMA at CEA Marcoule.

Prior to analysis, the sample was decontaminated and then metallised with carbon.

3.3.3.2 Data analysis

The EPMA device was calibrated for uranium, plutonium and oxygen using UO_2 and PuO_2 reference compounds. For americium, as no reference pellet was available, the calibration was performed directly using the sample. Indeed, it was evidenced that the plutonium and americium are located in the same spot, as americium is coming from α-decay of ^{241}Pu. Americium

calibrations were tested on local spots containing no uranium, resulting in the americium content expected based on the age of the sample.

For quantitative measurements, the results obtained are weight percentages of uranium, plutonium and americium. In the case of oxygen measurements, the uncertainty on the results obtained is too high to provide any usable information. Thus, oxygen, uranium, plutonium and americium mass fractions were determined by ZAF (Z – atomic number, A – Absorption and F – Fluorescence) method, taking into account the U Mγ peak interference with the Pu Mβ peak. This method allows to correct the X-Rays emitted by the samples.

Pseudo-quantitative measurements of the plutonium cartographies were also performed in this work. They were obtained by comparing the plutonium content in the quantitative measurements and the number of counts in the cartographies, allowing the determination of the function between these two variables. This method is used for assessing the plutonium content (wt.%) in each pixel of the cartography, however with a high uncertainty, as the counting time is low.

3.3.4. X-ray Absorption Spectroscopy (XAS)

The X-ray Absorption Spectroscopy is a method used to study the electronic and local structures around an atom. Its main advantage is its chemical selectivity, allowing separate contributions for each atom of the material. The analyses are sensitive to the oxidation state, the coordination chemistry of the probed element and to the distances, coordination number and species surrounding the selected element. This technique includes X-Ray Absorption Near-Edge Structure spectroscopy (XANES) and Extended X-Ray Absorption Fine-Structure spectroscopy (EXAFS).

3.3.4.1 Principle

The principle of X-ray Absorption Spectroscopy relies on the interaction between matter and X-rays, and in particular on the photoelectric effect. When the incident X-ray energy corresponds to the binding energy of a core electron of an element in the sample, a rise in the absorption, resulting from the ejection of a core electron to an empty valence level, is observed. This is called an absorption edge and can be determined for different orbitals. Thus, the K, L_1, L_2, L_3, M_1 etc edges correspond to the electrons emitted from the 1s, 2s, $2p^{1/2}$, $2p^{3/2}$, 3s orbitals.

A XAS spectrum is divided in two areas, as represented in Figure 3-5.

- The first area, located from -30 to +30 eV relative to the edge of interest, corresponds to the XANES: X-ray Absorption Near Edge Structure. Information on the electronic structure and the valence state of the atom of interest, as well as the symmetry, can be obtained.

- The second zone is located at higher energy (from 50 to 1000 eV after the edge) and corresponds to the EXAFS: Extended X-ray Absorption Fine Structure. Information on the local environment of the atom of interest can be obtained such as the distance, the nature, the disorder and the number of nearest neighbours for each coordination sphere.

In this work, only XANES was used to collect spectra at the U M_4, Pu M_4 and Am M_5 edges.

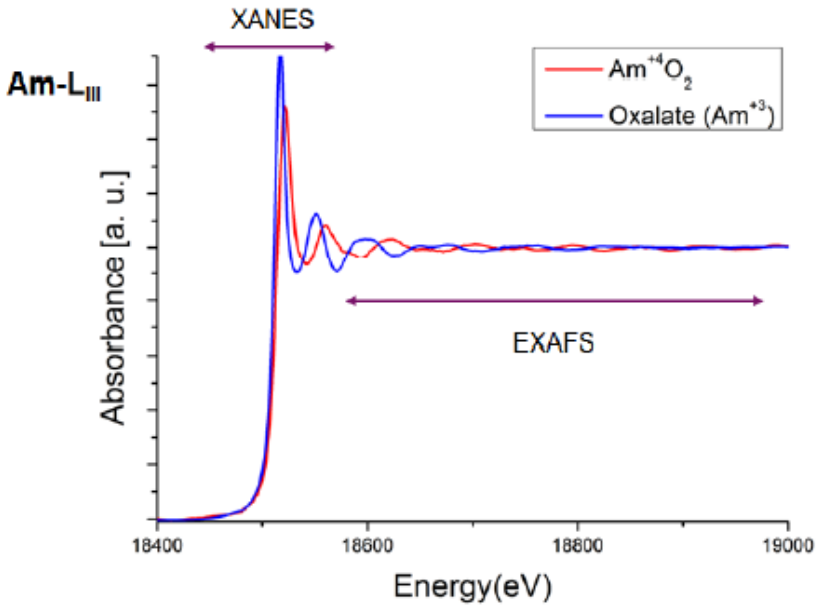

Figure 3-5: Example of a XAS spectrum of AmO_2 and $U_{0.90}Am_{0.10}O_2$ at the Am L_3 edge by Epifano *et al.* [55].

3.3.4.2 *Experimental set-up*

X-Ray Absorption Spectroscopy analyses were performed at the MARS beamline of the SOLEIL synchrotron (France) [207] and at the ACT station of the CAT-ACT beamline of the KARA synchrotron (Germany) [208]. During these experiments, High Energy Resolution Fluorescence Detection-X-ray Absorption Near the Edge Structure (HERFD-XANES) mode at low energy (3-4 keV) was used.

3.3.4.2.1 Experiments performed at the MARS beamline (SOLEIL synchrotron)

HERFD-XANES analyses of three $U_{1-y-z}Pu_yAm_zO_{2\pm x}$ samples, as well as three $Pu_{1-z}Am_zO_{2-x}$ samples, and four references were performed at the MARS beamline.

The sample preparation was performed in a glovebox of the ATALANTE facility at CEA Marcoule. Small amounts of powdered sample (1 to 5 mg) were mixed with boron nitride and pressed into pellets. In order to quantify the contribution of the various cations of the probed elements, reference pellets were manufactured using the same methodology applied for the samples. For U^{4+} and Pu^{4+}, UO_2 and PuO_2 pellets were respectively chosen as reference. For U^{5+} and U^{6+}, U_4O_9 and U_3O_8 samples were used as references. For Pu^{3+}, a $PuPO_4$ sample was prepared by a sol-gel route starting from PuO_2 and $(NH_4)_2HPO_4$ [209]. For Am^{3+}, a sample of $U_{0.90}Am_{0.10}O_{2-x}$ was used [55]. XAS spectra collected at the L_3 edge of Am at the ROBL beamline (ESFR) indicated that the americium was present only in its trivalent state [210].

The experiments were performed under dedicated operating conditions (2.5 GeV – 500 mA). The beam spot size was 300 µm x 300 µm at half-height (H x V). A double Si(111) crystal monochromator was used for the HERFD-XANES (3-5 keV). The incident energy was calibrated using the K absorption edges of potassium (3.608 keV). This calibration was performed before each change of sample and absorption edge. The HERFD-XANES spectra were obtained thanks to an emission spectrometer available on the beamline, coupled to a fluorescence detector SDD simple element KETEK. The Mβ emission lines of U (3.337 keV), Pu (3.533 keV) and Am (3.445

keV) were selected using the 220 reflection of a Si(220) crystal with a bending radius of 1 m. The samples were oriented at 45° to the incident beam. A He balloon was located between the samples, the crystal and the detector in order to reduce the absorption of the emitted and incident X-Ray. Based on the full width at half maximum of the peak of elastic diffusion located at the double energy, the global energetic resolution of the emission spectrometer was determined to be equal to 1.1 eV.

3.3.4.2.2 Experiments performed at the CAT-ACT beamline (KARA synchrotron)

Only one reference, AmO_2, was analysed by HERFD-XANES at the ACT beamline. A Si(111) double crystal monochromator was used with vertically collimating and toroidal focusing Si mirrors. The beam spot size was reduced to 500 µm x 500 µm by slits in front of the sample. The HERFD-XANES spectra were obtained using a Johann-type X-ray emission spectrometer with Rowland circle focusing geometry including four spherically bent Si(220) crystal with 1 m bending radius and a single-diode VITUS silicon drift detector. The X-ray emission spectrometer and the sample were placed inside a glovebox maintaining a constant He flow so that less than 0.1% O_2 was present in the box during the measurements. This was necessary to minimize intensity loss due to scattering and absorption of the 3-4 keV X-ray photons. The Mα_1 emission line of Am (3.445 keV) was selected. The uncertainty on the energy positions of the spectra was estimated of ± 0.05 eV.

3.3.4.3 Data analysis

The HERFD-XANES spectra at the M_4 edges were normalized at the maximum of absorption using a liner function for pre- and postedges. The position of the absorption edge was identified as the first zero crossing of the second derivative. The Athena software was used to remove the pre-edge, normalize and correct the auto-absorption [211]. The normalized spectra were refined by linear combination of the reference spectra in order to quantify the contribution of the various probed cations. Spectra at the U M_4 edges of U_4O_9 and U_3O_8 previously collected on the ID26 beamline of the ESFR (Grenoble, France), were used [212], [213] for U^{5+} and U^{6+}, while the spectra of UO_2 collected at the MARS beamline was used for U^{4+}. Spectra collected at the Pu M_4 edge of PuO_2 and $PuPO_4$ at the MARS beamline were used as reference for Pu^{4+} and Pu^{3+} respectively. For the Am M_5 edge, spectra collected at the MARS beamline for $U_{0.90}Am_{0.10}O_{2-x}$ (Am^{3+}) and at the ACT beamline for AmO_2 (Am^{4+}) were used.

3.3.5. High temperature X-Ray diffraction

High Temperature - X-Ray Diffraction measurements were performed in the ATALANTE facility (CEA Marcoule, France). The main characteristics of the experimental set-up and the analysis method are described here, further details can be found in [214]. The purpose of these experiments is to obtain phase diagram data such as phases in presence and phase boundaries, as well as lattice thermal expansion of the samples.

3.3.5.1 Experimental set-up

The diffractometer used here is a Bragg-Brentano θ-θ Bruker D8 Advance X-ray Diffractometer using copper radiation from a conventional tube source (Kα_1 + Kα_2 = 1.5406 and 1.5444 Å) operating at 40 kV and 40 mA. In order to allow the handling of radioactive materials, the device

is completely implemented in a nitrogen-filled glovebox (Figure 3-6). The device is equipped with a 1-dimensional LynX'Eye fast counting PSDdetector, with an opening angle of 3° 2θ.

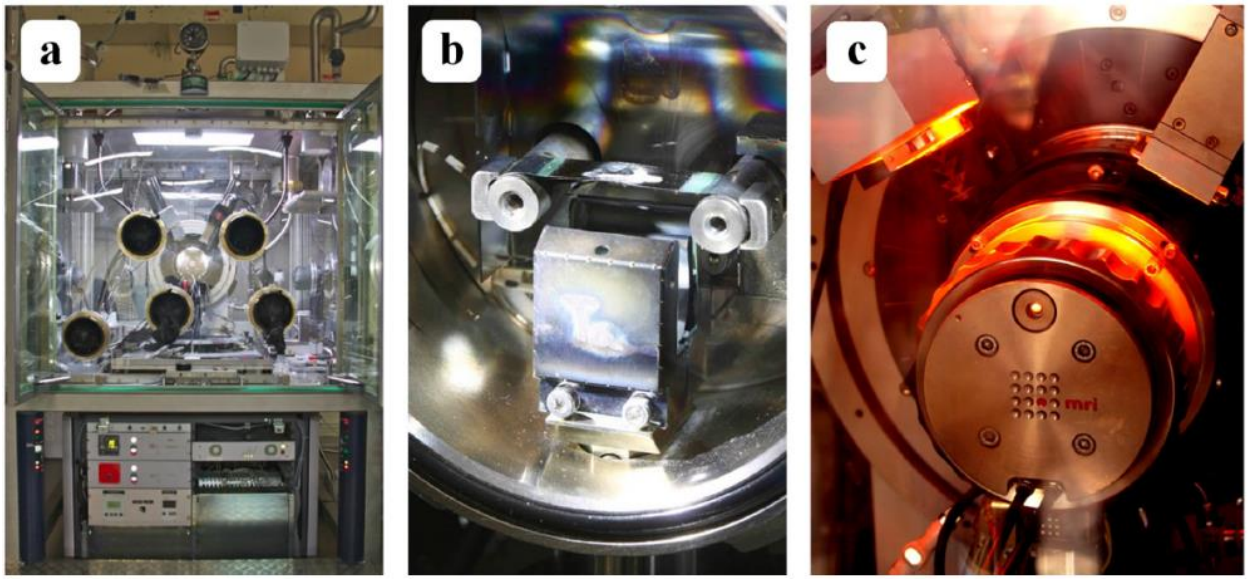

Figure 3-6: (a) BRUKER D8-Advance diffractometer in its dedicated glovebox, (b) High Temperature MRI Chamber with direct and radiant heating elements, (c) High Temperature chamber during operation [214].

A MRI-Hightemp hot stage is used to heat the powder sample up to maximum 2273 K. The furnace configuration is atmosphere-dependant:

- A Re-Pt alloy heating strip for oxygen-rich atmosphere.
- A Mo or W heating strip for inert or reducing atmosphere (used in this work).

Temperature calibrations are carried out after each setup change (strip and/or thermocouple) in steps of 100 K, from room temperature to 1873 K and back to room temperature, using a W powder as reference (lattice parameters of W as a function of temperature from [215]). A constant uncertainty of ± 15 K is estimated on the whole temperature range.

The atmosphere inside the hot stage is controlled through a constantly flowing gas. The oxygen partial pressures (pO_2) are imposed and controlled by means of a SETNAG device (Gen'air) [216]. The atmosphere used here was He/H_2 4% at a flow rate of around 10-12 $L.h^{-1}$ (P = 2 bars).

Prior to measurements, about 100 mg of sample were manually ground in an agate mortar for ten minutes to obtain fine powders. Once crushed, the powder was spread over the HT-XRD heating strip.

3.3.5.2 Data acquisition and analysis

After disposing the sample powder in the experimental chamber, prior to experiment, the string angular position and displacement were adjusted by displacement and rocking curve corrections. The scanning parameters used in this work were adapted to the purpose of the measurements and the details can be found in Appendix D.

For example, to study the lattice thermal expansion and phases of $U_{1-y-z}Pu_yAm_zO_{2\pm x}$ and $Pu_{1-z}Am_zO_{2-x}$ samples, diffraction patterns were obtained by scanning from 20 to 145° 2θ in isothermal conditions from 1873 K to room temperature every 100 K. The heating and cooling rates were 5 $K.s^{-1}$. A plateau (ranging from 20 min to 1 hour depending on the samples) was performed at each temperature stage to ensure that the thermodynamic equilibrium was reached. A counting time of 1 s, 0.5 s, or 0.3 s per step, depending on the availability of the device, and step-intervals of 0.02° were chosen.

The refinement of the phase structures was performed according to the Pawley [217] or Rietveld [203] methods, using the Bruker TOPAS 6.0 software. Instrumental contributions (geometry, tube type, slits) were included in the fitting according to the fundamental parameter approach [218]. The background was approximated by a Chebyshev polynomial function with three terms. The refinement procedure considered first the zero detector and background parameters, then lattice parameter and crystallite size. A modified Thompson-Cox-Hastings pseudo-Voigt function (PV TCHZ) was used to refine the shape of the peaks. The uncertainty of the lattice parameters is estimated to be ± 0.003 Å at any temperature based on both experimental and refinement errors.

3.3.6. Laser heating technique

3.3.6.1 Experimental set-up

The laser heating experiment was developed in the last decades at the Joint Research Centre Karlsruhe (Germany) to investigate nuclear materials at very high temperature and in particular to measure the temperature of the solid/liquid phase transitions. The experimental set-up, schematically represented in Figure 3-7, is briefly described here and further details can be found in [14], [24], [175], [176], [219].

To perform the experiment, disks or squares of the pellet of approximatively 1.5 mm thickness were first cut and then held by means of graphite screws in a graphite sample holder.

The set-up was put under a controlled atmosphere with a continuous flow of gas of 5 $L.h^{-1}$ of pressurized argon, with an overpressure of 0.3 MPa to avoid a too important vaporization. Argon was preferred to air as it tends to stabilize the O/M ratio of mixed oxides of uranium and plutonium with low Pu content, as explained in [24].

A 4.5 kW Nd:YAG continuous wave laser operating at 1064 nm was used to emit a short pulse (500 ms) of 250 W and reach temperatures exceeding 3000 K in tens of millisecond. By means of an optical fibre, the laser beam is focused on the sample surface to locally heat and melt a circular spot of approximately 3 mm diameter. The sample was then let to cool down naturally before the next pulse. The heating and cooling rates were adapted to the needs of each experiment, with in some cases pre- and post-heating steps performed at 1700 K to prevent any thermal shock of the sample and protect the sample integrity (more details in Chapter 4 – section 4.4.1 and Chapter 5 – section 5.4).

The radiance temperature T_λ at the sample's surface was measured by a fast two-channel pyrometer operating near 650 nm, with a bandwidth of 27 nm and a nominal measurement spot size of 0.5 mm in diameter. This temperature corresponds to the one measured by a pyrometer

calibrated in terms of blackbody radiance (emissivity equal to unity). Determination of the true temperature from the radiance temperature is explained in 3.3.6.2.

The pyrometer used here was calibrated before the experiments by means of two Polaron® lamps with 2 mm-wide tungsten ribbon filaments up to 2500 K and a graphite blackbody was used up to 3400 K.

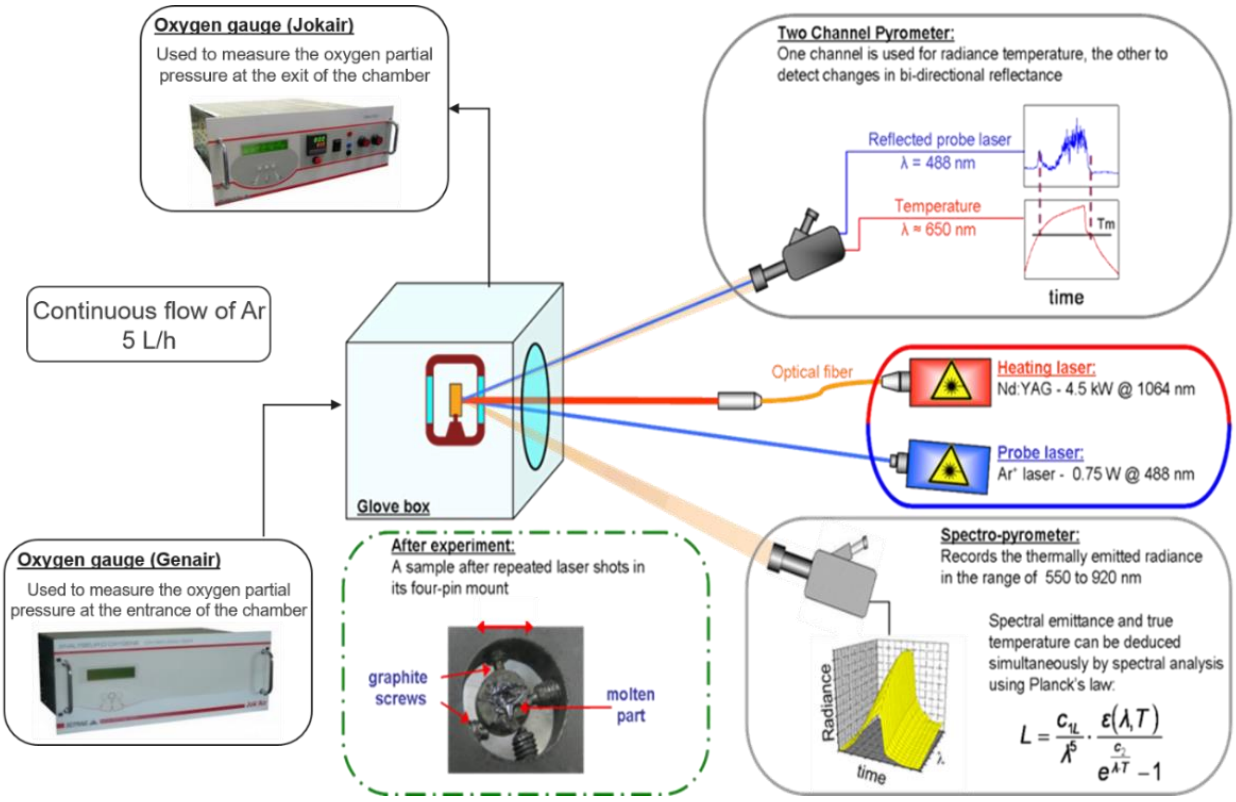

Figure 3-7: Schematic representation of the laser heating setup.

The novelty of this setup consists in the addition of two oxygen gauges, at the entrance and exit of the chamber, to monitor the oxygen partial pressure inside the autoclave during the experiments. The principle of these two SETNAG oxygen gauges [220], [221] is based on the ionic conduction of zirconia. At high temperature (T = 923 K), when a voltage is applied between the faces of a zirconia tube, an oxygen flow is created. By varying this voltage, the quantity of oxygen in the gas flowing inside the zirconia tube also varies. A residual oxygen content of few vpm ($pO_2 \approx 10^{-6}\ atm$) was measured in the gas (argon) used in this study. The oxygen partial pressure of interest here was the one at the exit of the chamber and was measured every 3 s. After each shot, the sample was allowed to cool down for the atmosphere to stabilize to its residual value.

In this work, a shift in the measurement of the pO_2 was observed compared to the moment at which the laser shot was performed. Indeed, the latter lasted 500 ms while the oxygen partial pressure was measured every 3 second at the exit of the chamber. In addition, waiting steps ranging from 30 min to 2h30 were performed for the oxygen partial pressure recorded at the exit of the experimental chamber to restabilize to its residual value. This resulted in longer recording of pO_2 compared to the shots.

3.3.6.2 Data analysis

3.3.6.2.1 Solidus/Liquidus temperatures

The true temperature T can be calculated using the following formula, valid in Wien's approximation range:

$$\frac{1}{T} - \frac{1}{T_\lambda} = \frac{\lambda}{c_2} \ln(\varepsilon_\lambda \tau_{eff}) \quad \textbf{(3.23)}$$

where T is the true temperature, T_λ the radiance temperature, λ the wavelength, c_2 (=14388 µm.K^{-1}) is the second radiation constant, ε_λ the spectral-directional emissivity and τ_{eff} corresponds to the effective total transmittance.

Here, the emissivity is referred to as the normal spectral emissivity. Because of technical issues, the emissivity of the sample could not be assessed experimentally. In this work, the emissivity of 0.83 ± 0.05 was then chosen, as it corresponds to the one experimentally determined for UO_2 and PuO_2 respectively by Manara *et al.* and De Bruycker *et al.* [14], [222]. This value is also consistent with the emissivity measured in previous works on the same type of materials by De Bruycker *et al.*, Böhler *et al.* and Strach *et al.* [24], [176], [184].

The term τ_{eff} in **(3.23)** is obtained as the product of the single transmittance factor of each optical element (the sapphire window of the autoclave and the sapphire window of the glovebox here). Their effective transmittance was measured by the pyrometer as described in [223] and equal to 0.86 for the autoclave and 0.92 for the glovebox. τ_{eff} is thus equal to 0.79 in this work.

Uncertainties on the measured temperature were expressed according to the propagation error law [219], taking into account the uncertainty associated to the calibration of the pyrometer, the emissivity and the transmittance of the optical system. With a coverage factor k = 2, the cumulative uncertainty was estimated to be ± 30 K at 3000 K for $U_{1-y-z}Pu_yAm_zO_{2\pm x}$ and ± 60 K at 3000 K for $Pu_{1-z}Am_zO_{2\pm x}$, *i.e.* ± 1 % and 2 % of the recorded temperature, respectively.

3.3.6.2.2 Oxygen concentration

The quantity of oxygen absorbed or released by the sample is calculated by integration of the variation in oxygen partial pressure. The oxygen partial pressure measured at each time step is then transposed in mass flux of dioxygen according to the following formula **(3.24)**:

$$\dot{m}_{O_2}(t) = \frac{p_{O_2}(t)\, M_{O_2}\, \dot{V}}{R\, T} \quad \textbf{(3.24)}$$

Where $\dot{m}_{O_2}(t)$ is the mass flux of dioxygen (in g.s^{-1}), $p_{O_2}(t)$ is the oxygen partial pressure measured by the setup (in atm), M_{O_2} is the molar mass of dioxygen (equals to 32 g.mol^{-1}), $\dot{V}$ is the volumetric flux (equal to 5 L.h^{-1}), R is the gas constant (taken as 0.0825 L.atm.K^{-1}.mol^{-1}) and T the temperature of the gas (300 K).

Equation **(3.24)** is integrated using the trapezoidal rule between the initial time and the time at which the atmosphere restabilizes to its initial value (Equation **(3.25)**). The result is then subtracted to the baseline in order to obtain the mass of dioxygen absorbed or released by the sample.

$$m_{O_2} = \int_{t_0}^{t_f} (\dot{m}_{O_2}(t) - \dot{m}_0)\, dt \qquad \textbf{(3.25)}$$

Where m_{O_2} is the mass of dioxygen absorbed or released by the sample (in g), t_0 is the initial time, t_f is the time at which the atmosphere reaches its initial value and $\dot{m}_0$ is the mass flux of the baseline.

The mass of dioxygen obtained is then converted into number of moles of dioxygen. This quantity is directly linked to the O/M ratio of the sample, calculated as n(O)/n(M).

In this work, the uncertainty on the resulting O/M ratio was assumed to be ± 0.005.

3.3.7. Drop calorimetry

The principle of drop calorimetry is to measure the variation in heat (enthalpy) in a sample, by dropping it from ambient temperature to a higher temperature.

3.3.7.1 Experimental set-up

The measurements were performed at the JRC Karlsruhe using a Setaram Multi Detector High Temperature (MDHTC 96 type) operating in drop mode (Figure 3-8). The experiments were performed under a constant and controlled flow (15 mL.min^{-1}) of inert He gas. Detailed information about the device can be found in [224].

To perform the measurements, sample compacted fragments of around 30 mg are introduced in a sample holder at the top of the detector at room temperature. The chamber is separated from the graphite furnace by an alumina tube. Small ingots of high purity Pt (99.9 %) are used as reference materials and dropped before and after each sample fragment.

Figure 3-8: Drop calorimeter installed in a glovebox at JRC-Karlsruhe (left box: electronics parts) [224].

The furnace is programmed to maintain a constant temperature inside the chamber, ensured by measurements with thermocouples located at different heights of the chamber surface. The heat flow signal is then stabilized at the temperature of interest during 7 hours. After this period, a sample at room temperature drops into the detector, causing a small thermal shock. A 25-min waiting step is performed between each drop to restore the temperature and the heat flow. For each temperature, 3 or 4 drops of sample were performed, depending on the size of the fragments. In this process, the enthalpy increment of the sample is proportional to the additional heat provided to the system to re-stabilize the targeted temperature.

3.3.7.2 Data analysis

The molar enthalpy increment of the sample ΔH_m from T_m to T_a can be calculated as:

$$\Delta_{T_a}^{T_m} H_m = \frac{\int \phi_S d\tau}{S} . \frac{M_S}{m_S} \quad \textbf{(3.26)}$$

Where $\int \phi_S d\tau$ is the heat provided by the furnace to bring the sample at T_m, M_S and m_S are the molar mass and the mass of the sample and S is the sensitivity of the calorimeter, computed as an average value of the two references dropped before and after the sample.

The sensitivity S of the calorimeter is determined according to the following equation:

$$S = \frac{\int \phi_r dt}{\int_{Ta}^{Tm} C_{P,R}(T) dt} . \frac{M_R}{m_R} \quad \textbf{(3.27)}$$

Where $\int \phi_r dt$ is the area of the heat flow peak integrated in time, Ta is the ambient temperature, $C_{P,R}(T)$ is the heat capacity function of the sample material and m_R and M_R are respectively its mass and molar mass.

In this work, the uncertainty on the molar enthalpy increments was determined by the standard deviation calculated for each temperature from 3 or 4 drops of the sample.

3.3.8. ThermoGravimetric Analysis (TGA)

Thermogravimetric analysis is used to determine the oxygen potential of the materials. The principle is to measure the variation in mass of a sample to follow the change in the O/M ratio when it is subjected to a temperature program in a controlled atmosphere (oxygen potential). The experiments were carried out in the ATALANTE facility at CEA Marcoule (France).

3.3.8.1 Experimental set-up

Oxygen potential measurements were performed using a SETSYS Evolution model from Setaram Solutions in TGA mode [225], installed in a glovebox. A schematic representation of the apparatus can be found in Figure 3-9.

The device is composed of a precision balance at the top (1 µg), followed by a stick to which the crucible containing the sample is attached, going down in an experiment chamber, delimited by the furnace (a graphite tube in this work). The temperature inside the experimental chamber is controlled thanks to a thermocouple stick, inserted through the bottom of the furnace.

In this work, fragments of the sample of interest (from 200 to 400 mg) are loaded into a tungsten crucible, attached to a succession of steel, quartz and tungsten hangers. Before each experiment, the balance is equilibrated to take into account the weight of sample added. The variations of mass related to the device are corrected from the one of the sample by performing the same experiment with an empty crucible and subtracting the results of the blank to the one of the sample.

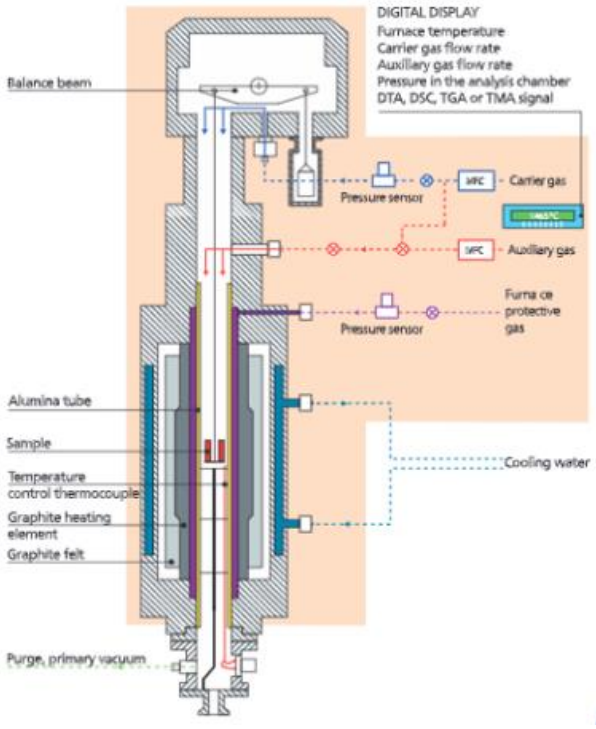

Figure 3-9: Schematic representation of a SETSYS Evolution [226].

The experiments are carried out here under a gas mixture of Ar/H_2 4% and the oxygen partial pressure, followed by oxygen gauges at the entrance and exit of the device (GENAIR and JOKAIR, see section 3.3.6.1), is varied during the experiment to adjust the H_2O/H_2 ratio.

The temperature program was as follows:

1) A first step of few hours at room temperature to stabilise the gas flow in the chamber.
2) A heating step at 10 $K.min^{-1}$ until the targeted temperature.
3) A plateau of 72 hours at the target temperature, with variations of the pO_2 in the system.
4) A cooling step at 30 $K.min^{-1}$ until room temperature.
5) A stabilisation step at room temperature.

3.3.8.2 Data analysis

Throughout the measurements, microgram order weight changes in the sample are continuously monitored as a function of the temperature and the oxygen partial pressure content.

From the weight changes, the O/M ratio of the samples is determined according to:

$$\frac{O}{M} = 2 \pm x = 2 \pm \frac{M_{sample}}{M_O} . \frac{|m_f - m_i|}{m_f} \quad \textbf{(3.28)}$$

Where x corresponds to the deviation from stoichiometry, M_{sample} is the molar mass of the sample (in g.mol^{-1}), M_O the molar mass of oxygen (equal to 16 g.mol^{-1}), m_f the mass of the sample recorded during the measurement (in g) and m_i the initial mass of the sample (in g).

In this work, the samples were annealed back to O/M = 2.00 before the measurements (see section 3.2.1.2), so m_i corresponds to the mass of the sample at the O/M = 2.000.

The oxygen potential of the sample $\Delta\overline{G_{O_2}}$ is related to the oxygen partial pressure varying along the experiments and can be calculated using the relation of Wheeler-Jones [227] **(3.29)**. This equation is commonly used for UO_{2+x} but has proven adequate for other actinide materials [46], [124], for which no correlation is proposed in the literature.

$$\Delta\overline{G_{O_2}} = -114500 + T \times \left(8.96 \times \log T - 4.42 + 9.152 \times \log\left(\frac{H_2O}{H_2}\right)\right) \quad \textbf{(3.29)}$$

Where $\Delta\overline{G_{O_2}}$ is expressed in calories and T the temperature in K.

Thus, for each step of the plateau at the targeted temperature, the variation in the oxygen potential as a function of the O/M ratio can be determined from the $\frac{H_2O}{H_2}$ ratio.

In this work, the uncertainties on the O/M ratio and oxygen potentials calculated are respectively ± 0.002 and ± 10 kJ.mol^{-1}.

3.4. CONCLUSION

In this chapter, the principles of the CALPHAD method were first presented. The thermodynamic models used for the assessment of the gas, liquid and solid phases were also briefly described, as well as the main formalisms.

In a second part, the samples of interest were presented.

In order to study the Pu-Am-O system, the manufacturing process of three $Pu_{1-z}Am_zO_{2.00}$ samples, with z = 0.22, 0.49 and 0.80, studied for the assessment of the Pu-Am-O system, was described first. The main characteristics of these pellets at the manufacturing were also detailed.

Then, for the U-Pu-Am-O system, five $U_{1-y-z}Pu_yAm_zO_{2\pm x}$ were handled. Among them, four were manufactured by powder metallurgy and the other one via a sol-gel route in the nineties. The specifications of the pellets, such as the density or the dimensions, were reported. A summary of the samples described in this section, as well as their manufacturing technique and characteristics, is given in Table 3-4.

Finally, the experimental techniques employed in this work were described. For each, the experimental procedure and the method used for data analysis were reported.

Bearing in mind the steps of the CALPHAD method, the critical review of available data being performed in Chapter 2, the next chapter will be dedicated to the acquisition of new sets of experimental data on the plutonium-americium mixed oxides.

Table 3-4 –Manufacturing technique and initial main characteristics (dimensions and density) of the samples used in this work.

Samples	Manufacturing technique	Composition at the manufacturing	Dimensions of the pellets (mm) (d = diameter, H = height)	Density at the manufacturing (% TD)
PuAm 80/20	Oxalate co-conversion (2007)	$Pu_{0.80}Am_{0.20}O_{2.00}$	d = 5.5 ± 0.1 H = 6.0 ± 0.1	90.0 %
PuAm 50/50		$Pu_{0.50}Am_{0.50}O_{2.00}$		88.0 %
PuAm 20/80		$Pu_{0.20}Am_{0.80}O_{2.00}$		< 80.0 %
PHENIX24	Co-milling (1999)	$U_{0.76}Pu_{0.24}O_{1.978}$	d = 5.41 ± 0.01 H = 11.0 ± 0.2	93.7 %
PHENIX29	Co-milling (1999)	$U_{0.71}Pu_{0.29}O_{1.973}$	d = 5.41 ± 0.01 H = 11.0 ± 0.2	93.7 %
CAPRA4	Co-milling (1996)	$U_{0.69}Pu_{0.31}O_{1.968}$	d = 5.42 ± 0.01 H = 9.2 ± 0.3 (central hole, d = 1.7 ± 0.1)	92.0 %
TRABANT40	Co-milling (1998)	$U_{0.60}Pu_{0.40}O_{1.971}$	d = 5.43 ± 0.01 H = 7.7 – 8.3 ± 0.1 (central hole, d = 2.4 ± 0.1)	93.4 – 94.2 %
TRABANT45	Sol-gel	$U_{0.55}Pu_{0.45}O_{1.990}$	d = 5.43 ± 0.01 H = 8.3 ± 0.3 (central hole, d = 2.3 ± 0.1)	86.4 %

4. EXPERIMENTAL INVESTIGATION OF THE PU-AM-O SYSTEM

This chapter presents the structural and thermodynamic investigations performed on the $Pu_{1-z}Am_zO_{2-x}$ samples (z = 0.23, 0.51, 0.80). Room temperature characterisations evidence the presence of fluorite phases for the three compositions, as well as the simultaneous presence of trivalent and tetravalent cations of U and Pu. The swelling of the lattice evidenced by XRD is attributed to a combination of the reduction of the samples and the effects of the alpha self-irradiation, the latter stabilizing the fcc structure. Complex solid phase equilibria are highlighted by HT-XRD for the three compositions from 1873 K to 303 K, as only the presence of a MO_{2-x} phase is confirmed. A phase transition is evidenced at 873 K for z = 0.80. The phase equilibria of $Pu_{0.77}Am_{0.23}O_{2-x}$ are studied at 1673 K by TGA and HT-XRD and a phase transition from a multiphasic domain MO_{2-x} + unidentified phase(s) to a monophasic MO_{2-x} domain is observed for O/M ≈ 1.75. Solid/liquid phase transitions are also determined for the first time using laser heating coupled with oxygen gauges for $Pu_{0.49}Am_{0.51}O_{2-x}$. A significant reduction of the sample is noticed during the melting, however not influencing the solidus and liquidus temperatures determined in the O/M range studied here. This chapter also higlights the complexity of the ternary Pu-Am-O system and the needs for additional experimental campaigns to overcome the remaining uncertainties.

These data will be used as input data for the modelling of the Pu-Am-O system.

4. EXPERIMENTAL INVESTIGATION OF THE PU-AM-O SYSTEM

In order to accurately describe the quaternary U-Pu-Am-O system, the investigation of its binary and ternary sub-systems is mandatory. A good knowledge of the U-O, Pu-O and U-Pu-O system was gained over the last decades. However, uncertainties remain on the americium-bearing systems. In order to overcome this lack of data, new experimental campaigns were performed to gain knowledge on the structural and thermodynamic properties on three $Pu_{1-z}Am_zO_{2-x}$ samples with z = 0.23, 0.51 and 0.80.

In section 4.1, structural properties of the materials at room temperature are presented. First, the determined chemical and isotopic compositions are given. Then, the SEM observations of the micro- and macrostructure of the samples are presented and the crystal structures determined by XRD are discussed. Finally, the cationic charge distribution and the resulting O/M ratios of the samples are given from XANES experiments. In section 4.2, the results on the solid-state phase equilibria obtained through HT-XRD experiments for the three compositions are detailed from 1873 K to room temperature. Then, in Section 4.3, the measurements of oxygen potential data on $Pu_{0.77}Am_{0.23}O_{2-x}$ at 1673 K using TGA are presented. These measurements were coupled to HT-XRD using the same experimental conditions (T, pO_2) to gain knowledge on the phase equilibria at this temperature. Finally, the solid/liquid phase transitions of $Pu_{0.49}Am_{0.51}O_{2-x}$ are discussed based on laser heating experiments in Section 4.4.

In this work, it is important to keep in mind that the samples originate from different facilities. Thus, differences in storage conditions (atmosphere, time) of the samples may induce some variations of the O/M ratio. Moreover, the materials were not always available both in CEA Marcoule (France) and JRC Karlsruhe (Germany). The samples of interest in this section and their respective availability are summarized in Table 4-1.

Table 4-1 – $Pu_{1-z}Am_zO_{2-x}$ samples and their availability at CEA Marcoule and JRC Karlsruhe.

Batches	Samples	Available at CEA Marcoule	Available at JRC Karlsruhe
z = 0.23	PuAm 80/20	**Yes**	No
z = 0.51	PuAm 50/50 - A	**Yes**	No
	PuAm 50/50 - B	No	**Yes**
z = 0.80	PuAm 20/80	**Yes**	No

4.1. CHEMICAL AND STRUCTURAL INVESTIGATION AT ROOM TEMPERATURE

Samples characterizations were performed after their manufacturing in the nineties (see Chapter 3 – section 3.2.1). However, since then, changes induced by the storage and/or the self-irradiation may have occurred. In this work, the chemical and isotopic compositions were measured by chemical analysis. Then, their macro- and microstructure were observed by SEM and their crystal structure were determined by XRD. Finally, XANES analyses was used to determine the cationic charge distribution and the O/M ratios.

Except for the synchrotron experimental campaigns, the preparation and characterizations of the samples at room temperature were performed at the ATALANTE facility, CEA Marcoule (France).

4.1.1. Chemical and isotopic compositions

Three batches of $Pu_{1-z}Am_zO_{2-x}$, with z = 0.23, 0.51 and 0.80, were studied. The initial synthesis route and manufacturing conditions, as well as the resulting characteristics of the samples (plutonium and americium contents, density, dimensions…) are detailed in Chapter 3 – section 3.2.1.

Considering the age of the samples (manufactured in 2007) and the initial plutonium isotopic compositions, variations in the initial chemical and isotopic compositions are observed. The results obtained by Thermal Ionization Mass Spectrometry are summarized in Appendix E. The plutonium and americium contents are given in Table 4-2.

Table 4-2 - Chemical and isotopic compositions of the three $Pu_{1-z}Am_zO_{2-x}$.

Samples	%Pu	%Am	Composition
PuAm 80/20	77.2 ± 0.5	22.8 ± 0.5	$Pu_{0.77}Am_{0.23}O_{2-x}$
PuAm 50/50-A	49.2 ± 0.5	50.8 ± 0.5	$Pu_{0.49}Am_{0.51}O_{2-x}$
PuAm 20/80	19.6 ± 0.5	80.4 ± 0.5	$Pu_{0.20}Am_{0.80}O_{2-x}$

4.1.2. Macro- and microstructure

SEM analyses were performed on fractured samples of PuAm 50/50-A and PuAm 20/80, as shown in Figure 4-1.

The typical microstructure of a ceramic is revealed, with well-faceted grains of around 5-10 µm size for PuAm 50/50-A and 20-50 µm for PuAm 20/80. Pores of few µm are observed in both intra- and intergranular regions of the two samples. A higher porosity was noticed in the case of the PuAm 20/80, in agreement with its lower density (< 80 % of TD) measured at the manufacturing of the samples (see Chapter 3 – section 3.2.1).

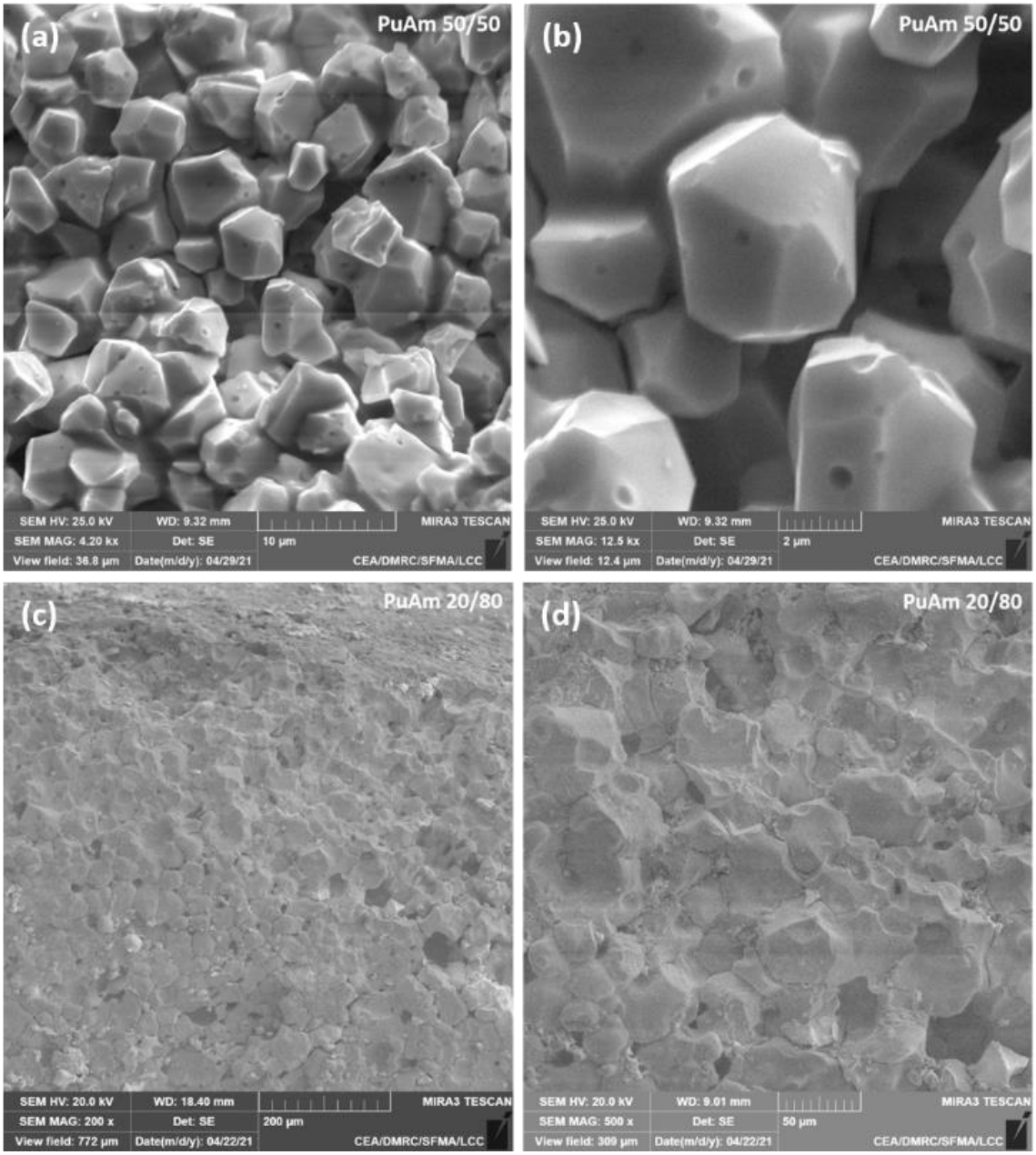

Figure 4-1: SEM images of PuAm 50/50 ((a) and (b)) and PuAm 20/80 ((c) and (d)).

4.1.3. Crystal structure

The diffraction patterns of the original samples presented in this section (see Figure 4-2) were acquired at room temperature before HT-XRD experiments.

A good resolution is obtained for the PuAm 80/20 sample, compared to the one of the PuAm 50/50-A and PuAm 20/80 diffraction patterns (see Figure 4-2). Indeed, for these two samples, less material and time for experiments were available.

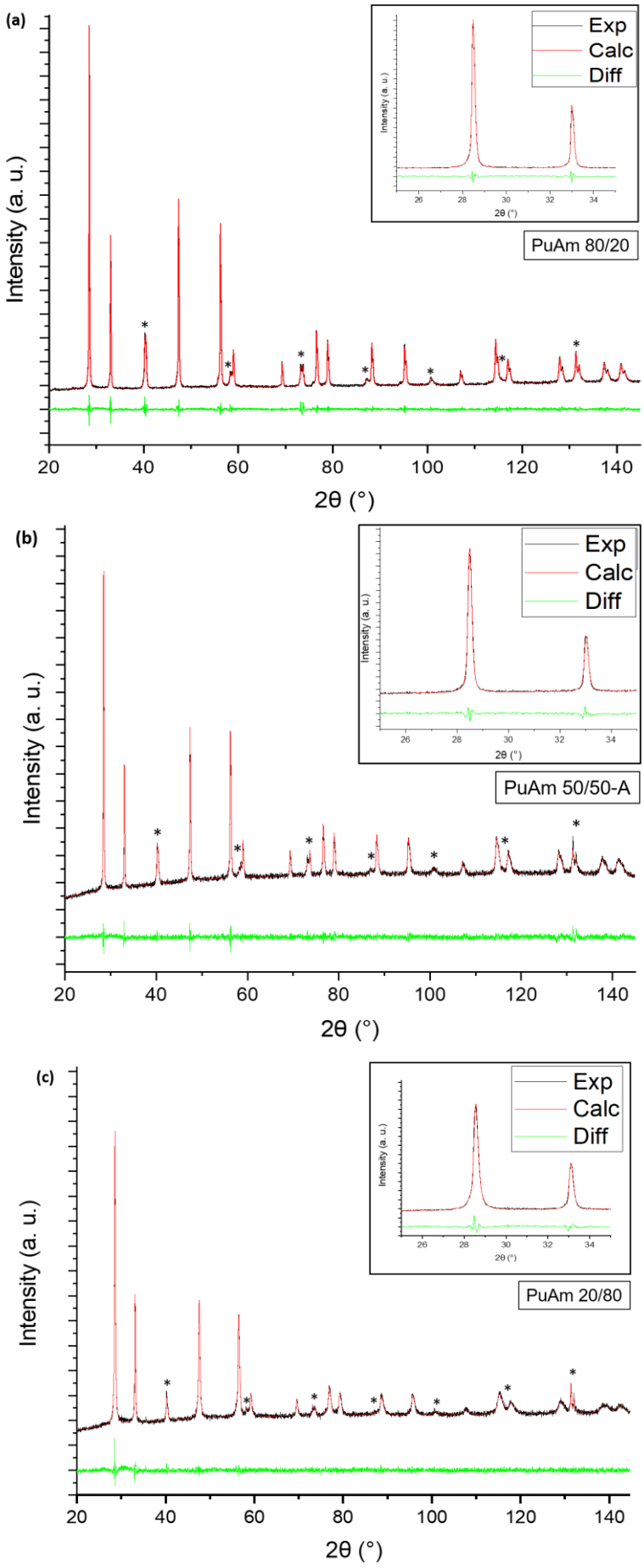

Figure 4-2: XRD pattern on powder of (a) PuAm 80/20, (b) PuAm 50/50-A and (c) PuAm 20/80 (*: XRD reflections of the Mo strip).

For the three samples, only fcc structures are observed. The phases and their proportions, as well as the lattice parameters are summarized in Table 4-3.

Table 4-3 - Refined lattice parameters obtained in this work for the $Pu_{1-z}Am_zO_{2-x}$ samples, compared to the ones at the manufacturing.

Samples	Phases and proportions	Lattice parameters obtained in this study (Å) (± 0.003)	a_0 at the manufacturing (Å) [197]	Swelling of the lattice ($\frac{a-a_0}{a_0}$) (%)
PuAm 80/20	fcc (91 %)	5.422	1 fcc phase - 5.394	0.52
	fcc (9 %)	5.414		0.37
PuAm 50/50-A	fcc (100 %)	5.415	1 fcc phase - 5.388	0.50
PuAm 20/80	fcc (86 %)	5.395	1 fcc phase - 5.382	0.24
	fcc (14 %)	5.404		0.41

As evidenced in Table 4-3, two fcc phases are observed for the PuAm 80/20 and PuAm 20/80 samples. However, based on the relatively close lattice parameters obtained for the two phases and the small proportion of the second fcc phase, the use of two fcc phases for the fit of the patterns can be questioned. Selected portions of diffraction patterns of PuAm 80/20 and PuAm 20/80 are plotted in Figure 4-3 with the results of the fits with either one or two fcc phases.

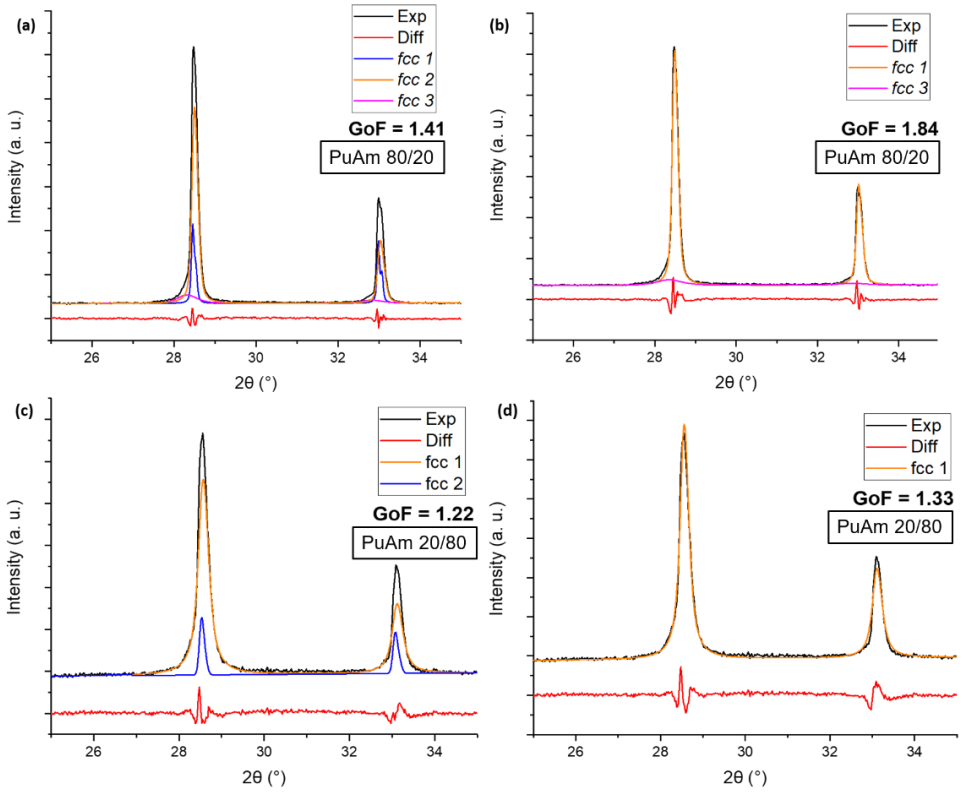

Figure 4-3: Results of the fits for the PuAm 80/20 ((a) and (b)) and PuAm 20/80 ((c) and (d)) using one fluorite phase ((a) and (c)) and two fluorite phases ((b) and (d)).

The respective "Goodness of Fit" (GoF) factors are also indicated. In the case of the PuAm 80/20 sample, a residual phase, called fcc 3, was identified on the diffraction pattern, corresponding to an impurity present on the strip, as the lattice parameter obtained corresponds to the one of the last material studied on the same strip. This phase is not taken into account in this study but is considered during the fits.

When comparing the GoF factors for the PuAm 80/20, a difference of 0.43 can be noticed between the two fits, with a better fit obtained with two fluorite phases. The two peaks, represented in blue and orange, are distinguishable, although one is broader than the other. In the case of the PuAm 20/80 sample, this difference in the GoF factors is equal to 0.11, with as well a better fit with two fcc phases. However, for this sample, broad peaks are noticed due to the bigger proportion of defects related to the high americium content. Thus, it is difficult to conclude on the existence of two phases or only one.

The lattice parameters obtained in Table 4-3 are plotted in Figure 4-4. A decrease in the lattice parameter is observed when increasing the Am content, in agreement with the smaller lattice parameter of AmO_2 (5.375 Å) compared to the one of PuO_2 (5.396 Å). The values obtained in this work are bigger than the ones obtained for the two pure poles, which indicates that the lattice parameters do not follow a Vegard's law.

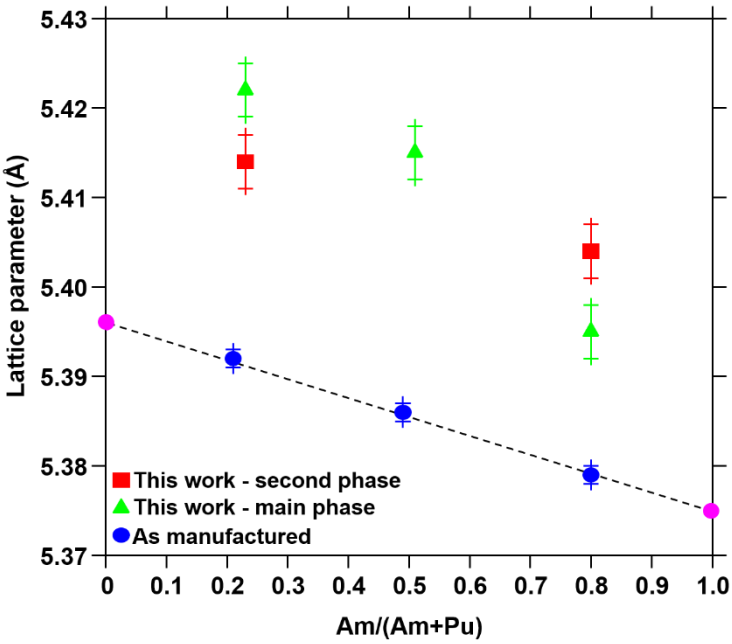

Figure 4-4: Lattice parameters obtained in this work compared to the one at the manufacturing *[197]* and the Vegard's law between the pure poles PuO_2 and AmO_2.

In this work, the fcc phases observed are assumed to be solid solutions of $Pu_{1-z}Am_zO_{2-x}$, with a complete solubility of Am in the PuO_{2-x} phase and reciprocally of Pu in AmO_{2-x}. Indeed, the lattice parameters obtained on the samples after manufacturing (in blue in Figure 4-4) follow the Vegard's law. This indicates a mixing law between PuO_2 and AmO_2 and thus confirms the hypothesis of the complete solubility.

A first explanation for the deviation from Vegard's law observed in Figure 4-4 is the deviation from stoichiometry, with a reduction of the sample. Indeed, as explained in Chapter 2 – section 2.2.2.3, the reduction of the phase leads to an increase of the lattice parameter. Unfortunately, contrarily to $U_{1-y}Pu_yO_{2\pm x}$, no relation exists between the lattice parameter and the O/M ratio for

$Pu_{1-z}Am_zO_{2-x}$ compounds. However, the slope obtained for the variation of the lattice parameters of this work as a function of the americium content is similar to the one of the Vegard's law. Based on this observation, it can be assumed that the reduction is similar for the three samples studied in this work.

Another possible explanation for the deviation from Vegard's law observed in Figure 4-4 is the natural expansion of the lattice due to the alpha self-irradiation of the samples (see Chapter 2 – section 2.2.2.4). As the samples were manufactured in 2007 and no thermal treatment was performed on them since the manufacturing, accumulation of defects due to the self-irradiation occurred in the samples. Indeed, an increase of the lattice parameters, whose value depends on the sample (ranging between 0.24 and 0.52 % depending on the phases and the samples), is noticed (see Table 4-3). The expansions calculated here are bigger than the one determined by Chikalla and Eyring for AmO_2 (0.28 %) [29] and by Noé and Fuger for PuO_2 (0.28 %) [228]. These results are also larger than the ones reported by Jankowiak *et al.* (around 0.30 %) for the same plutonium and americium contents, but for storage time up to only 400 days [81]. The lattice parameter variations also do not follow the recommendations proposed by these authors when taking into account the 15 years of storage time of this work. However, it can be noticed that the americium content does not influence the value of the saturation of the lattice expansion, as approximately 0.30 % is obtained along the whole range.

In the works of Chikalla and Eyring, Noé and Fuger and Jankowiak *et al.*, only stoichiometric compounds (O/M = 2.00) were studied. A possible decrease of the O/M ratio of the samples could also explain the increase in the lattice parameters observed here. This statement was evidenced by Belin *et al.* for $Pu_{1-z}Am_zO_{2-x}$ samples [82]. Unfortunately, contrarily to $U_{1-y}Pu_yO_{2\pm x}$, no relation between the lattice parameter and the self-irradiation exists for $Pu_{1-z}Am_zO_{2-x}$ compounds. Thus, it is most likely that the deviation from Vegard's law observed in this work is due to the combined effects of the reduction of the samples and the alpha self-irradiation.

Considering a maximum of the lattice at 0.30 %, the contribution of the reduction to the lattice can be estimated. Indeed, as the samples were manufactured over 15 years ago, the lattice expansion is expected to have reached its saturation level. For the PuAm 80/20 sample, where a swelling of 0.52 % is reported for the main phase, this would signify that the contribution of the reduction is equal to 0.22 % of the swelling. This value correspond to 0.20 % for the main phase of the PuAm 50/50-A sample. On the contrary, for the PuAm 20/80 sample, based on the low swelling of the lattice reported for the main phase (0.24 %), this would indicate that the reduction would not impact the expansion of the lattice and that the saturation of the swelling is not reached. However, considering the duration of storage, this hypothesis is not possible, as Jankowiak *et al.* observed the saturation after 200 days [81]. In addition, for this sample, the swelling of the lattice of the second phase is equal to 0.41 %, which indicates that this phase would be more reduced.

Indeed, as evidenced in Table 4-3, two fcc phases are observed for the PuAm 80/20 and PuAm 20/80 samples, in various proportions (one main phase and one secondary phase), while only one phase is observed for the PuAm 50/50 sample. When looking at the binaries systems Am-O and Pu-O (see Chapter 2 – section 2.1.1), a miscibility gap in the fcc phase is reported in the Pu-O system, for $900 < T < 1000$ K and $1.76 < O/M$ ratio < 1.94. However, at low temperature, biphasic domains [AmO_{2-x} + A-Am_2O_3] and [PuO_{2-x} + C-Pu_2O_3] are reported for $1.5 < O/M \leq 2.0$, in the Am-O and Pu-O systems respectively. Thus, no miscibility gap is expected to exist at room temperature in Pu-Am-O.

Three possibilities can be proposed for the composition of the two *fcc* phases observed in this work:

1. the two fcc phases have the same O/M ratio but different Pu and Am contents,
2. the two fcc phases have different Pu and Am contents and O/M ratios,
3. the two fcc phases exhibit the same Pu and Am contents but different O/M ratios.

In the first assumption, same O/M but different Pu and Am contents, based on the larger ionic radii of Pu compared to the one of Am, the phases with the largest lattice parameters would correspond to the phases with the highest Pu content. Thus, this would signify that for the PuAm 80/20 sample, the fcc 1 would exhibit a higher Pu content than the fcc 2. On the contrary, for the PuAm 20/80 sample, as the lattice parameter of the fcc 1 is smaller than the one of the second phase, this would signify that the Am content of the first phase would be larger than the one of the second phase. However, this assumption is not realistic based on the swellings of the lattice obtained in Table 4-3. Indeed, as previously explained, the maximum swelling (0.30 %) is independent of the Am content.

In the second assumption, a larger lattice parameter could be related to a larger Pu content or a more reduced sample. Data available on these samples are not sufficient to conclude on this hypothesis and distinguish the two contributions.

The most likely assumption is the third one, where same Pu and Am contents but different O/M ratios are considered between the two phases. For the PuAm 80/20 sample, the fcc 2 could then correspond to the "oxygen-rich" phase and the fcc 1 would be more reduced. Considering that 0.30 % of the swelling of the lattice is related to the effect of the alpha self-irradiation, this would imply that for the main phase, the contribution of the reduction would be equal to 0.22 % for the fcc 1 phase and 0.07 % for the fcc 2 phase. This confirms this hypothesis of one phase being more reduced than the other. For the PuAm 20/80 sample, the opposite behaviour is noticed. Thus, fcc 1 could be the "oxygen-rich" phase and fcc 2 the "oxygen-poor" phase.

As no relation exists between the lattice parameter, the self-irradiation and the O/M ratio for $Pu_{1-z}Am_yO_{2-x}$ samples, XANES experiments were performed to determine the O/M ratio of the three samples.

4.1.4. Cationic charge distribution

The cationic charge distribution was determined by means of X-ray Absorption Spectroscopy, in particular using HERFD-XANES. The three samples (PuAm 80/20, PuAm 50/50-A and PuAm 20/80) were prepared using few mg of powder using the procedure described in Chapter 3 – section 3.3.4.2.1 and the measurements were performed at the MARS beamline of the SOLEIL synchrotron (France). Spectra were collected at the Pu M_4 and Am M_5 edges at room temperature under atmospheric pressure.

4.1.4.1 Results

The XANES spectra collected at the Pu M_4 and Am M_5 edges for the three samples are presented in Figure 4-5. For the two edges, the spectra of the three samples are compared to the ones of the reference compounds determined in Chapter 3 – section 3.3.4.2, collected at the SOLEIL synchrotron (PuO_2 for Pu^{4+}, $PuPO_4$ for Pu^{3+} [229], $U_{0.90}Am_{0.10}O_2$ for Am^{3+} [55]) and collected at the KARA synchrotron (AmO_2 for Am^{4+}).

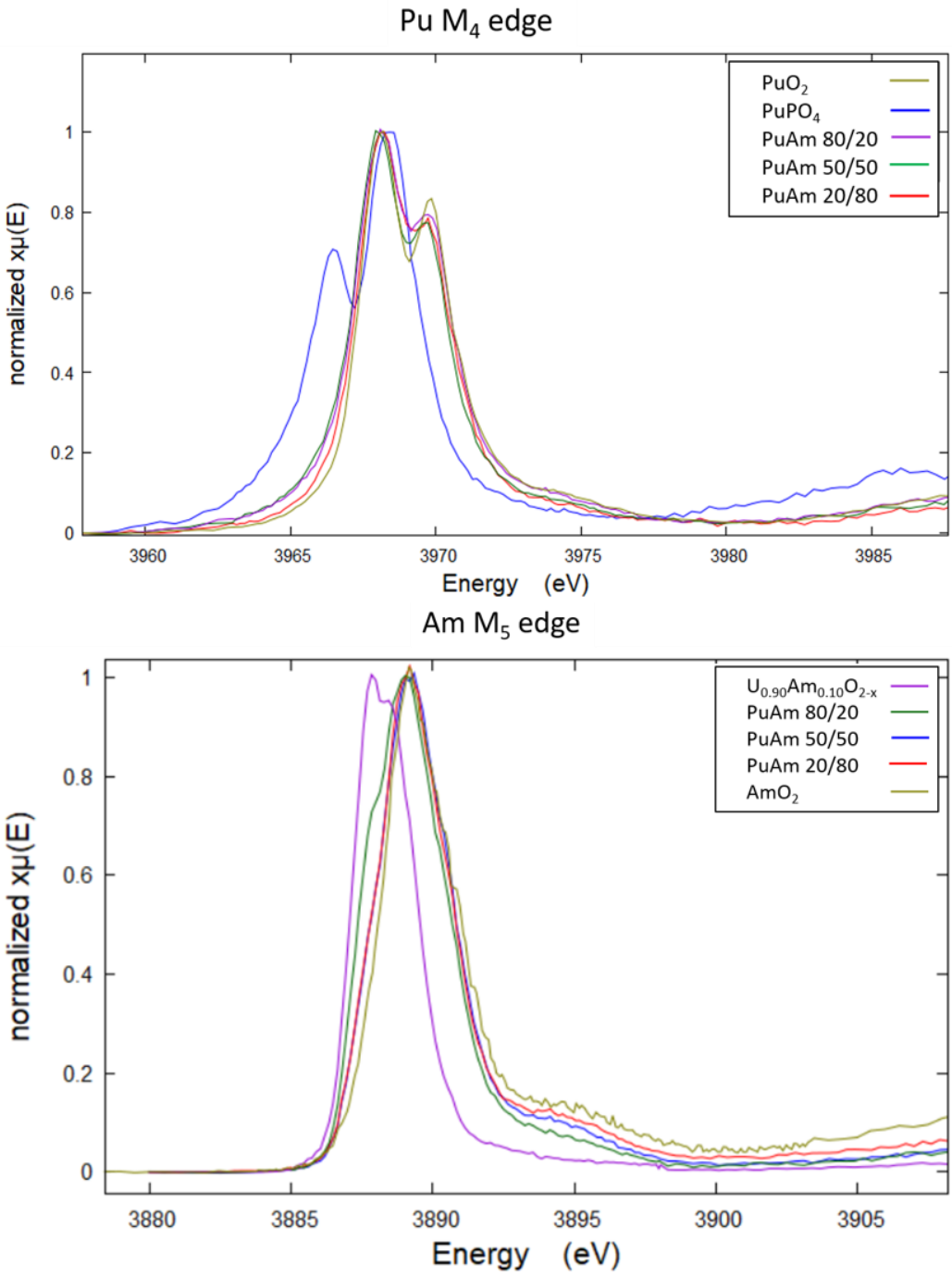

Figure 4-5: XANES spectra collected at the Pu M_4 and Am M_5 edges for the PuAm 80/20, PuAm 50/50 and PuAm 20/80 samples and their references.

When looking at the spectra collected at the Pu M_4 edge (Figure 4-5), the white line positions of the three samples, corresponding to the maxima of the spectra, are similar to the ones of PuO_2 and $PuPO_4$. It can be noticed that the spectrum of the $PuPO_4$ reference exhibits two white lines. This was also observed by Gerber *et al.* [230], who studied the Pu M_4 edge of a PuF_3 sample (pure Pu^{3+}). The authors reported that the two peaks correspond to electronic transitions associated to the trivalent oxidation state. Thus, the position of these white lines cannot be used to obtain the proportion of Pu^{3+}, as the difference between the white lines of PuO_2 and $PuPO_4$ is too small. However, the shoulder located at lower energy, around 3968 eV, indicates the presence of Pu^{3+}. Based on these observations, the proportions of Pu^{4+} and Pu^{3+} can be obtained only by linear fitting combination.

For the Am M_5 edge (Figure 4-5), the white line positions of the three samples are similar to the one of the AmO_2 reference (Am^{4+}). However, the maximum of the spectrum recorded for the PuAm 80/20 sample is shifted towards lower energy and a shoulder is observed around 3887.8 eV. This energy corresponds to the white line position of Am^{3+} (represented by $U_{0.90}Am_{0.10}O_{2\pm x}$). This observation highlights the partial reduction of the americium into its trivalent state.

The proportions of the various cations are determined by linear combination fitting of the reference spectra. The results are given in Table 4-4, as well as the O/M ratio with M = Pu or Am, obtained for the three samples.

Table 4-4 - Proportions of the cations of the probed elements and corresponding O/M ratios.

Sample	Pu M_4 edge			Am M_5 edge			O/M (±0.01)
	Pu^{3+} (%)	Pu^{4+} (%)	**O/Pu**	Am^{3+} (%)	Am^{4+} (%)	**O/Am**	
PuAm 80/20	6.80 ± 1.2	93.2	**1.97**	37.8 ± 1.5	62.2 ± 1.5	**1.82**	**1.94**
PuAm 50/50 - A	10.1 ± 1.2	89.9 ± 1.2	**1.95**	15.5 ± 1.5	84.5 ± 1.5	**1.92**	**1.94**
PuAm 20/80	2.40 ± 1.2	97.6 ± 1.2	**1.99**	17.2 ± 1.5	82.8 ± 1.5	**1.91**	**1.93**

An example of the results obtained by Linear Fitting Combination is presented in Figure 4-6 for the PuAm 80/20 sample at the Pu M_4 and Am M_5 edges.

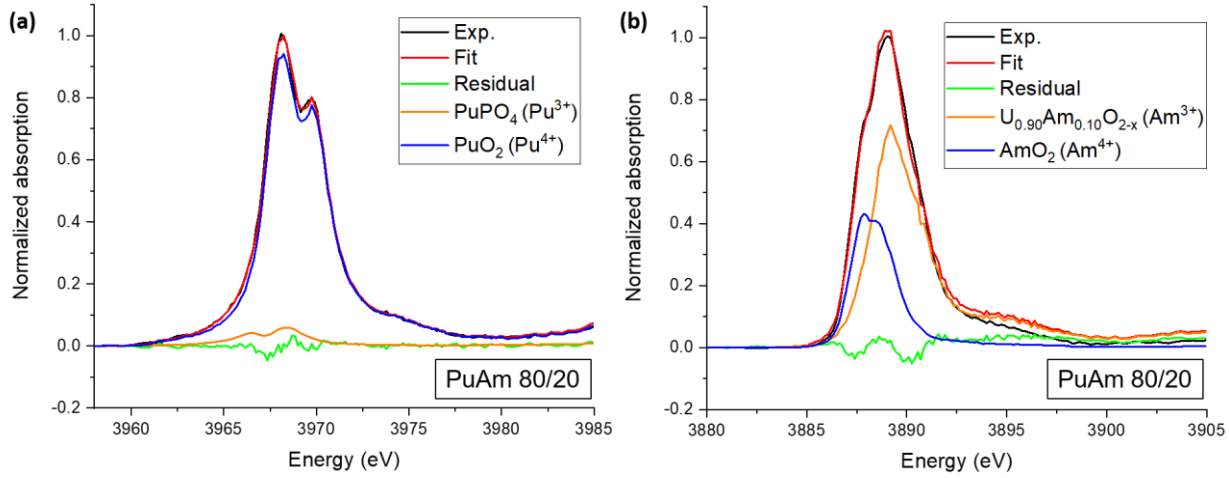

Figure 4-6: Linear Fitting Combination of PuAm 80/20 sample at (a) Pu M_4 edge and (b) Am M_5 edge.

For plutonium, the O/Pu ratios obtained are lower than 2.00. Indeed, small proportions of trivalent cations Pu^{3+} are evidenced together with tetravalent Pu^{4+}. When looking at the proportions of the americium cations, different behaviours are noticed for the three samples. For the PuAm 80/20 and PuAm 20/80, a mixture of Am^{3+} and Am^{4+} is evidenced, with the proportion of trivalent americium decreasing when increasing the Am content.

By combining the results of the O/Pu and O/Am ratios in Table 5-4 and the composition of the samples obtained by chemical analyses, the following O/M ratios are obtained: 1.94 for PuAm 80/20 and 50/50 and 1.93 for PuAm 20/80. As it can be seen, approximately the same O/M

ratio is obtained for the three samples. This observation is in agreement with the trend observed for the lattice parameter as a function of the Am content in Figure 4-4.

4.1.4.2 Discussion

4.1.4.2.1 Co-existence of Pu^{3+}/Pu^{4+} and Am^{3+}/Am^{4+}

As it can be seen in Table 4-4, trivalent and tetravalent plutonium and americium cations coexist in the samples. This observation is in contradiction with the work of Osaka *et al.* [37]. Indeed, it is expected that the reduction of plutonium starts once all the americium is reduced to Am^{3+}. For a mixed oxide of formula $Pu_{1-z}Am_zO_{2-x}$, two domains are evidenced by the model of Osaka *et al.*, summarized in Table 4-5: $\frac{O}{M} > 2 - \frac{z}{2}$ and $\frac{O}{M} < 2 - \frac{z}{2}$. In the first region, americium is supposed to become trivalent, while the plutonium is expected to remain tetravalent. On the contrary, in the second region, the reduction of the plutonium occurs while americium is already purely trivalent [43]. This model was confirmed by Belin *et al.* for z = 0.10 and 0.20 and by Prieur *et al.* [231], who determined by XANES the presence of Pu^{3+} once all the Am^{4+} was reduced in Am^{3+} [82].

In this work, based on the americium contents of the PuAm 80/20, PuAm 50/50-A and PuAm 20/80 samples (0.23, 0.51 and 0.80 respectively), the O/M ratios calculated here lie in the first region ($\frac{O}{M} > 2 - \frac{z}{2}$). Thus, the cations expected by the model of Osaka *et al.* are Pu^{4+}, Am^{4+} and Am^{3+}. However, this assumption is in disagreement with the experimental findings of this work. Indeed, trivalent plutonium is observed here, with fractions ranging between 6.50 and 10.0 %. This observation highlights that the reduction of plutonium begins before the complete reduction of americium.

As the model of Osaka *et al.* is built on hypotheses and very few experimental data, care should be taken when using it. Indeed, more data on a broader range of americium contents are needed to conclude on the reliability of this model.

Table 4-5 – Cationic charge distribution proposed by Osaka *et al.* [37] for $Pu_{1-z}Am_zO_{2-x}$.

$\boldsymbol{\frac{O}{M} > 2 - \frac{z}{2}}$	$\boldsymbol{Pu^{4+}_{1-z}Am^{4+}_{z-w}Am^{3+}_{w}O_{2-\frac{w}{2}}}$	**(4.1)**
$\boldsymbol{\frac{O}{M} < 2 - \frac{z}{2}}$	$Pu^{4+}_{1-z-v}Pu^{3+}_{v}Am^{3+}_{z}O_{2-\frac{z}{2}-\frac{v}{2}}$	**(4.2)**

4.1.4.2.2 Comparison with XRD results

In addition, the XANES results obtained here and especially the O/M ratios can be useful for the interpretation of the XRD data. Indeed, the XRD patterns obtained in section 4.1.3 indicated the presence of only fcc phases for the three materials (two for PuAm 80/20 and PuAm 20/80 and one for PuAm 50/50-A). However, as previously explained in section 4.1.3, biphasic domains [MO_{2-x} + M_2O_3] (assuming a total solubility of Pu and Am for the two phases) are expected for O/M < 2 for the three samples. A possible explanation for this observation could be the stabilization of the fcc structure due to the α self-irradiation of the samples. Indeed, in the PhD thesis of L. Medyk [54], brut and annealed samples of $U_{1-y}Pu_yO_{2\pm x}$ were studied by HERFD-XANES to determine the cationic distribution and the O/M ratios of the samples. Two thermal treatments were performed, one resulting in stoichiometric compounds and one to obtain hypo-

stoichiometric materials (around 1.93). The XANES analyses revealed the re-oxidation of all the annealed samples back to stoichiometry, while the brut samples remained hypo-stoichiometric. In this work, the three $Pu_{1-z}Am_zO_{2-x}$ samples studied were initially stoichiometric at the manufacturing (see Chapter 3 – section 2.2.2.4). Thus, these observations highlight the ability of the α self-irradiation to induce the reduction of the samples. In addition, the absence of the A- and/or C-M_2O_3 phase for these samples could be explained by a stabilization of the fcc structure by the defects induced by the self-irradiation or by the kinetics of the phase transitions. Indeed, as no sesquioxide phase was observed at the manufacturing of the samples, the formation of this phase at room temperature, without any heat brought to the system, is probably not possible. Further discussions will be provided in Chapter 6 – section 6.3.4.1.

Moreover, as explained in section 4.1.3, the swelling of the lattice, calculated in Table 4-3, originates from a combination of the effect of the α self-irradiation and the reduction of the sample, quantified in this section. The different behaviours reported in section 4.1.3 (larger swelling for the PuAm 80/20 and PuAm 50/50-A samples) could be explained by the proportions of trivalent cations Pu^{3+} and Am^{3+} reported in Table 5-4. Indeed, larger proportions of trivalent cations were determined for PuAm 80/20 and PuAm 50/50-A samples, compared to the one of the PuAm 20/80 sample. Thus, as the ionic radii of these species (1.142 Å for Pu^{3+} and 1.090 Å for Am^{3+}, both in coordination 8) are larger than the ones of Pu^{4+} (0.960 Å) and Am^{4+} (0.950 Å), the more trivalent cations, the larger the lattice. This could explain the larger swelling observed for the first two samples.

4.1.5. Conclusion

The chemical compositions and the structures of the three mixed oxides (PuAm 80/20, PuAm 50/50-A and PuAm 20/80) were determined in this section. For these samples, the plutonium and americium contents were first measured by chemical analyses. SEM imaging revealed the typical microstructure of a ceramic, with a grain size between 5 and 50 µm. The presence of inter- and intragranular pores of few µm was also evidenced. Only fcc phases were observed for the three samples (two for PuAm 80/20 and PuAm 20/80 and one for PuAm 50/50-A) when collecting XRD patterns at room temperature. The lattice parameters obtained in this work were significantly higher than the ones determined at the manufacturing of the samples. This could be explained by a combination of the swelling of the lattice induced by α self-irradiation of the samples, as they were manufactured 15 years ago, and the reduction of the samples. Finally, the cationic charge distribution determined by XANES evidenced the presence of a mixture of both Pu^{3+}/Pu^{4+} and Am^{3+}/Am^{4+} cations. This observation highlights the beginning of the reduction of plutonium before the complete reduction of americium, in disagreement with the model of Osaka *et al.*. The same O/M ratio (1.93-1.94) was calculated for the three samples. Moreover, the reduction of the samples and a possible stabilization of the fcc structure due to the effects of the α self-irradiation was evidenced in this section.

The resulting chemical compositions of the samples are summarized in Table 4-6. As previously explained, the sample PuAm 50/50-B was the only one to be available at the JRC-Karlsruhe, whose O/M ratio could not be determined experimentally. However, its composition is assumed to be the same as the PuAm 50/50-A as they originate from the same batch.

Table 4-6 - Samples compositions determined in this section.

Samples	Compositions (determined by chemical analyses and XANES)
PuAm 80/20	$Pu_{0.77}Am_{0.23}O_{1.94}$
PuAm 50/50 - A	$Pu_{0.49}Am_{0.51}O_{1.94}$
PuAm 50/50 - B	$Pu_{0.49}Am_{0.51}O_{2-x}$
PuAm 20/80	$Pu_{0.20}Am_{0.80}O_{1.93}$

Once the chemical composition and the structural properties are known at room temperature, the study of thermodynamic properties such as the solid state phase equilibria is possible, as it is described in the following section.

4.2. SOLID STATE PHASE EQUILIBRIA

4.2.1. Experimental determination

HT-XRD measurements were performed at the ATALANTE facility of CEA Marcoule (France), following the procedure described in Chapter 3 - section 3.3.5. A reducing atmosphere of He/H_2 4% + 55 ppm H_2O ($pO_2 = 10^{-28}$ atm) was used in this work and the oxygen content inside the experimental chamber was monitored by an oxygen gauge. The same thermal treatment was applied to the PuAm 80/20, PuAm 50/50-A and PuAm 20/80 samples. The scanning conditions are described in Appendix D for each sample.

4.2.2. Results and discussion

The presence of many peaks in the diffraction patterns acquired between 1873 K and room temperature highlights the complex behaviour of the mixed oxides. Difficulties in the phases determination arise as it is explained in the first part of this section.

4.2.2.1 Phase determination

For all diffraction patterns, at least two phases are observed, in various proportions. A fluorite structure, corresponding to $Pu_{1-z}Am_zO_{2-x}$, is identified over the whole temperature and for all americium contents. The variation of its lattice parameter as a function of the temperature and the Am content is discussed in the following section. Concerning the other phase(s), different behaviours are evidenced for each composition, explained in the following parts. In this work, it is important to keep in mind that the O/M ratio achieved at each temperature under the atmosphere used in this work remains unknown.

4.2.2.1.1 PuAm 80/20

The evolution of the obtained diffraction patterns between 1873 K and 303 K is represented in Figure 4-7, with a zoom on low angles.

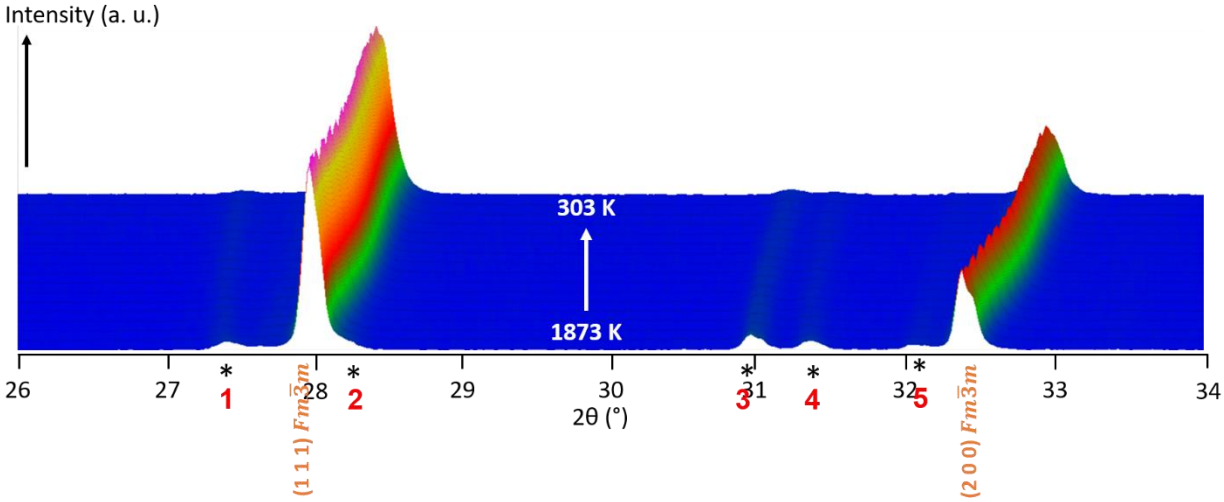

Figure 4-7: Evolution of the diffraction patterns between 26 and 34° 2θ as a function of the temperature for PuAm 80/20.

Several peaks are visible, with various intensities. The most intense peaks, located around 27.9 and 32.4° 2θ, correspond respectively to the (111) and (200) reflections of the fcc $Fm\bar{3}m$ structure. Their intensities do not vary with the temperature. A shift towards higher angles is noticed when decreasing the temperature, as observed for other actinide oxides, corresponding to a decrease of the lattice parameter (see Chapter 2 – section 2.2.3). Five other peaks, identified with * on Figure 4-7, at 27.4, 28.2, 31, 31.4 and 32.1° 2θ, are also observed, however exhibiting smaller intensities. Indeed, when comparing the intensities between the (111) reflection of the fcc phase and the one of the peak located at 31° (indicated as number 3 on Figure 4-7), an I/I_{FCC} ratio around 0.105 is calculated at 1073 K. The variation of this ratio as a function of the temperature is presented in Figure 4-8.

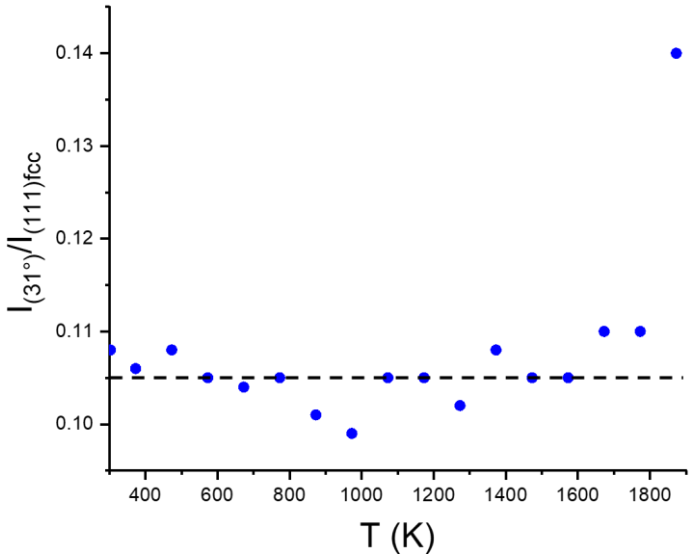

Figure 4-8: Ratio of the intensities between the peak at 31° 2θ and the (111) reflection of the fcc phase as a function of the temperature for the PuAm 80/20 sample. The dashed line represents the average value.

As it can be seen, the ratio of the intensities between the peak number 3 and the (111) reflection of the fcc phase is constant over the temperature range of this work, with an average value of 0.105. One exception is observed for T = 1873 K, however not significant, probably related to

the non-stabilisation of the sample at high temperature. The same behaviour is observed for the peaks 1, 2, 4 and 5, *i.e.* a constant ratio between their intensity and the one of the (111) reflections. These observations indicate that the proportions of the phase(s) associated to these peaks and the fcc phase remain constant throughout the whole temperature range studied here.

Different attempts were performed in order to identify the phase(s) corresponding to the five supplementary peaks. Based on the thermodynamic modelling of the Pu-Am-O system and the extrapolation of the binaries Pu-O and Am-O, several phases are identified as possible over the temperature range studied here: the hexagonal structure A-M_2O_3, the monoclinic structure B-M_2O_3 and the cubic structure C-M_2O_3. As previously described in section 4.1.3, continuous solid solutions are assumed in this work, with a total solubility of Pu and Am in the formed phases. The room temperature lattice parameters of A-Pu_2O_3, A-Am_2O_3, B-Am_2O_3, C-Pu_2O_3 and C-Am_2O_3 can be found in Chapter 2 – section 2.2.2.1 (Table 2-2). Miwa *et al.* already studied the phase equilibria in $Pu_{0.91}Am_{0.09}O_{2-x}$ (with $0 < x < 0.12$) from 300 K to 1423 K. The authors reported the existence of a phase transition from [C-M_2O_3 + MO_{2-x}] to [C'-M_2O_3 + MO_{2-x}] at 573 K (with C and C' two bcc structures and C'-M_2O_3 corresponding to the $MO_{1.61+x}$ phase) for $1.88 < O/M < 2.00$. A transition from the [C'-M_2O_3 + MO_{2-x}] domain to a biphasic [fcc + fcc] domain was also reported at 1123 K over the whole O/M ratio range. Above 1273 K, a monophasic fcc domain was indicated. Comparison with this phase determination is difficult as no indication was given on the atmosphere of the experiments. Considering the very reducing atmosphere used in this study, lower O/M ratios are expected. Moreover, in this work, higher temperatures are reached for higher americium contents. Thus, the work of Miwa *et al.* will be used for guidance only.

In a first trial, a hexagonal structure $P\bar{3}m1$, corresponding to A-M_2O_3, is considered. For this structure, three hkl reflections ((100), (002) and (10-1)) can be found between 26 and 34° 2θ. Thus, this structure could explain the three first * peaks observed in Figure 4-7. When fitting this structure, the first three * peaks are fitted and the following lattice parameters are obtained at 1873 K: a = 3.80 Å and c = 5.80 Å. These parameters are lower than the ones obtained at room temperature for the pure poles (for example, a = 3.82 Å and c = 5.98 Å for A-Am_2O_3 [46]). Moreover, the variation of the a and c lattice parameters as a function of temperature is plotted for A-Am_2O_3 [57] and A-Pu_2O_3 [17] in Figure 4-9. Assuming a mixing law between the two pure poles, the theoretical variation for PuAm 80/20 is also represented. The lattice parameters obtained at 1873 K in this work are significantly lower than the ones in Figure 4-9 (a = 3.80 Å, c = 5.80 Å experimentally vs. a = 3.88 Å, c = 6.23 Å calculated). Care should be taken when considering the lattice expansions represented in Figure 4-9. Indeed, the accuracy of using a mixing law between A-Pu_2O_3 and A-Am_2O_3 and the solubility of Pu in Am_2O_3 and Am in Pu_2O_3 could not be verified. Based on the significant difference between the theoretical and experimental lattice parameters, the existence of the A-M_2O_3 phase for PuAm 80/20 is rejected over the whole temperature range studied in this work. Moreover, even if this phase could exist for this composition, one peak, at 32.1° 2θ would remain unidentified.

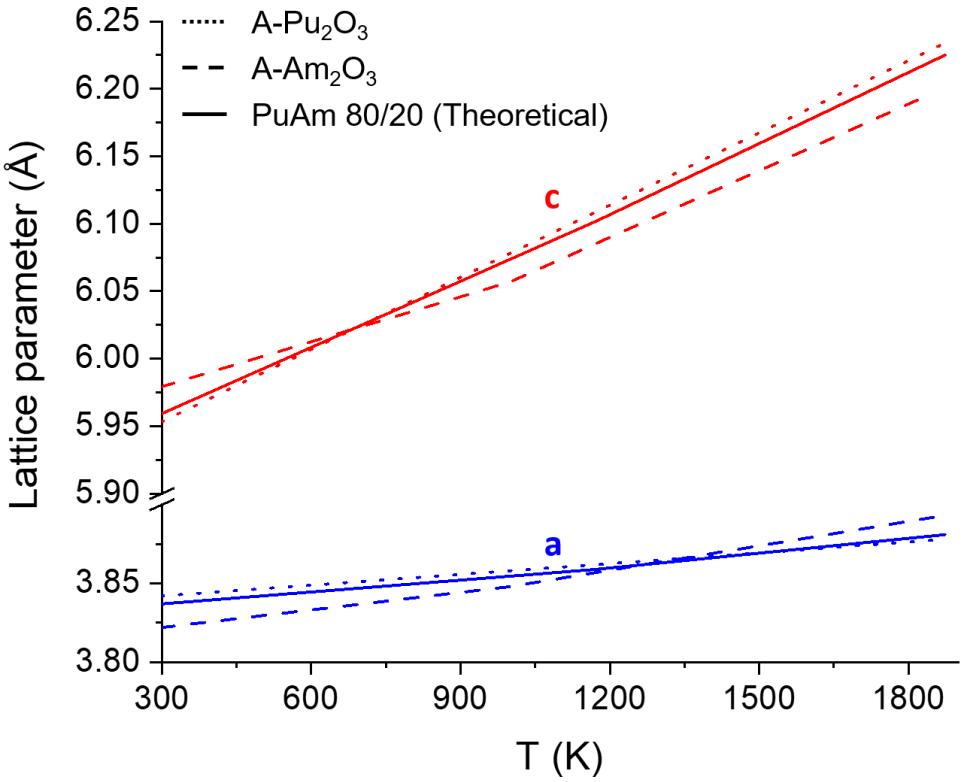

Figure 4-9: Variation of the a (in blue) and c (in red) lattice parameters as a function of temperature for A-Pu_2O_3 (dotted lines), A-Am_2O_3 (dashed lines) and PuAm 80/20 (theoretical values, full lines).

In a second trial, the cubic C-M_2O_3 phase (space group $Ia\bar{3}$) is considered. This structure is a super-structure of the fluorite phase. Three hkl reflections can also be found in the low angle range represented in Figure 4-7: (222), (321) and (400). The lattice parameters of this phase correspond to approximately twice the one of the fluorite phase. The (321) reflection, characteristics of the super-structure, should be located between the two fluorite reflections, around 30° 2θ. In the absence of this reflection, the presence of the C-M_2O_3 for PuAm 80/20 is rejected.

In addition, the existence of the B-Am_2O_3 phase is dismissed. Indeed, this phase is reported only in the Am-O system by Chikalla and Eyring [29] and Lebreton *et al.* [57] and is assumed to be metastable and observed only in the presence of A-Am_2O_3. Thus, in the absence of the latter, the B-Am_2O_3 phase is discarded.

A combination of the A-, B- and C-M_2O_3 phases is also considered but rejected as it does not lead to any conclusive results.

As the attribution of the five peaks at 27.4, 28.2, 31, 31.4 and 32.1° 2θ to A-, B- and/or C-M_2O_3 phases is unsuccessful, other research axes are proposed.

In their oxygen potential study, Otobe *et al.* [44] considered the Pu-Am-O system as an analogue of the Ce-O system. Indeed, the authors explained a change of slope at O/M = 1.77 in the oxygen potential data of $Pu_{0.50}Am_{0.50}O_{2-x}$ at 1333 K by the existence of a biphasic domain [$(Pu,Am)O_{2-x}$ + $(Pu,Am)_9O_{16}$] for O/M < 1.77. Based on this assumption, the phase diagram of the Ce-O system is plotted in Figure 4-10, with the calculated cooling path of the HT-XRD measurements in the experimental atmosphere conditions.

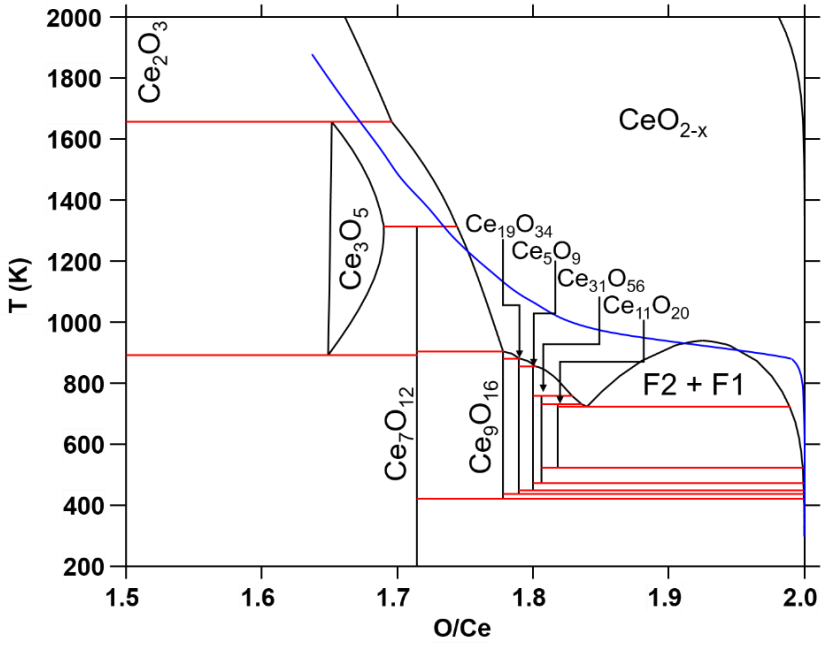

Figure 4-10: Calculated phase diagram of the Ce-O system (TAF-ID V13), with the cooling path of the HT-XRD experiment in blue for He/H_2 4% with $pO_2 = 10^{-28}$ atm.

This phase diagram is only indicative of the possible phases, as shifts of the boundaries towards higher/lower temperature and O/M ratios can be observed in the case of the Pu-Am-O system. The phases and their associated lattice parameters are described by Zinkevich *et al.* [232]. According to the diagram, at 1873 K, a biphasic domain [Ce_2O_3 + CeO_{2-x}] should be encountered. However, as the Ce_2O_3 phase is isostructural with the A-M_2O_3 phase (hexagonal structure of space group $P\bar{3}m1$), this option is discarded. Moreover, the crystal structure of the Ce_3O_5 is analogue to the one of the C-M_2O_3 phase, with space group $Ia\bar{3}$, thus it is also rejected for the fit. The $Ce_{11}O_{20}$ and Ce_7O_{12} phases are also tested in the assessment but no correspondence with unidentified phases is observed. Unfortunately, no structures are proposed in the literature for the other cerium oxides phases, thus they could not be tested. Based on this study, the Pu-Am-O system does not seem exhibit the same behaviour as the Ce-O system.

The presence of impurities due to a reaction with the Mo strip or originating from the sintering of the samples is also investigated but discarded as no damage of the strip was observed. Thus, it does not lead to any conclusive result.

The crystal structures corresponding to the five supplementary peaks (*) of Figure 4-7 remain unidentified.

4.2.2.1.2 PuAm 50/50-A

The evolution of the diffraction patterns between 26 and 33° 2θ as a function of the temperature is presented in Figure 4-11.

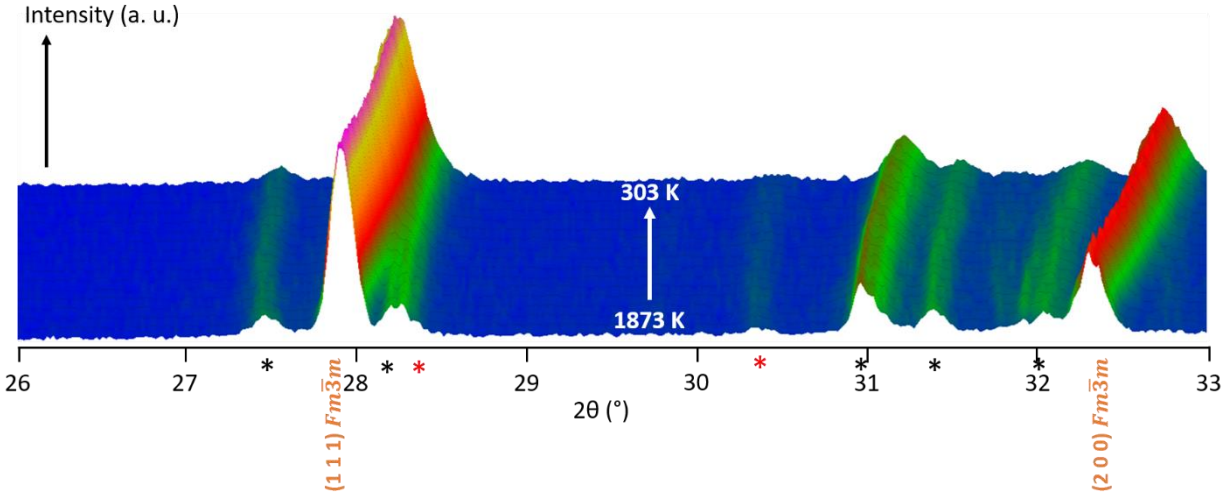

Figure 4-11: Evolution of the diffraction patterns between 26 and 33° 2θ as a function of the temperature for PuAm 50/50-A, where * corresponds to the peaks already present for PuAm 80/20 and * to the new peaks.

As for the PuAm 80/20 sample, peaks corresponding to a fluorite structure (space group $Fm\bar{3}m$, reflections (111) and (200)) are visible along the whole temperature range studied in this work. The same five unidentified * peaks (at 27.4, 31, 31.4 and 32.1° 2θ) as in the PuAm80/20 sample can be distinguished on the patterns. Two additional unknown peaks can also be observed on Figure 4-11, located at 28.4 and 30.4° 2θ at 1873 K.

For this sample, it is not possible to link the intensities of the peaks to the proportions of the phases. Indeed, as it can be seen on Figure 4-12, a significant amount of reflections are observed for the five peaks represented. Among them, doublets corresponding to the Kα_1 and Kα_2 reflections can be distinguished (peak 1 for example) but do not explain all the reflections. Thus, it is not possible to distinguish how many phases are located in one peak.

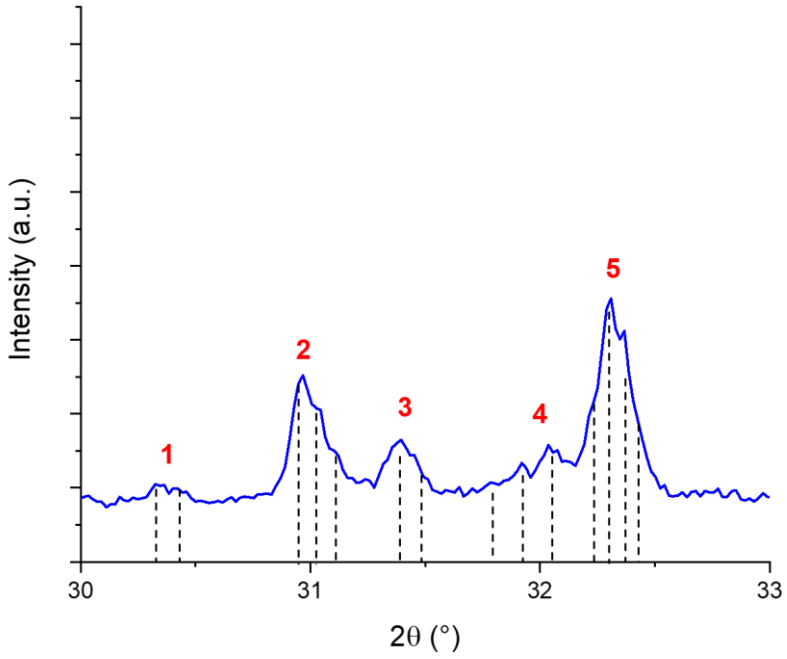

Figure 4-12: Zoom on the diffraction pattern acquired at 1873 K for PuAm 50/50-A and possible reflections.

When trying to identify the formed phases, the peaks located around 28.2° and 30.4° could indicate the presence of a C-M_2O_3 phase of cubic structure ((222) and (321) reflections of $Ia\bar{3}$). If this phase would form in the PuAm 50/50-A sample, the third (400) reflection present at low angles should also be observed after the (200) peak of the fluorite structure. Thus, the existence of the C-M_2O_3 phase for the PuAm 50/50-A sample is discarded. Moreover, the existence of a A-M_2O_3 phase is also rejected as the a and c lattice parameters obtained with the fit are similar to the ones obtained for PuAm 80/20 and thus lie below the ones of the pure poles.

Unfortunately, the eight peaks, represented by * and *, visible in Figure 4-11 remain unidentified.

4.2.2.1.3 PuAm 20/80

An even more complex behaviour is observed in the case of the PuAm 20/80 sample.

As for the PuAm 20/80 and PuAm 50/50-A samples, a fluorite structure of space group $Fm\bar{3}m$, attributed to the $Pu_{1-z}Am_zO_{2-x}$ phase is identified on the diffraction patterns along the whole temperature range studied in this work (1873 K to room temperature). However, a very low signal/noise ratio is obtained for all the diffraction patterns, as little material was available for the experiments, making the phase determination difficult.

A first problem is observed concerning the achievement of thermodynamic equilibrium between the atmosphere of the experiments (He/H_2 4%, $pO_2 = 10^{-28}$ atm) and the sample. As indicated in the scanning conditions in Appendix D, at each temperature, a waiting step of 1 hour was first performed, followed by 3 scans of 55 min each. Thus, the samples remained almost four hours at each temperature.

For the first two compositions, PuAm 80/20 and PuAm 50/50-A, the thermodynamic equilibrium was reached after the second scan at high temperature (1873 – 1673 K) and after the waiting step for the remaining temperatures. On the contrary, for the PuAm 20/80 sample, the thermodynamic equilibrium was not reached after 4 hours at 1873 K. The six successive diffraction patterns obtained at 1873 K and 1773 K are plotted in Figure 4-13.

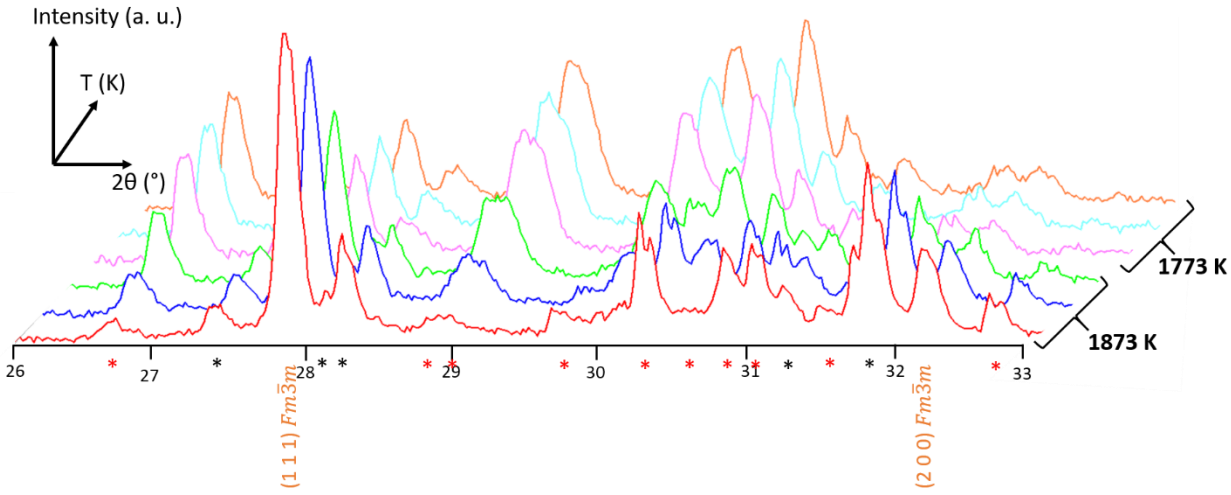

Figure 4-13: Successive diffractions patterns obtained at 1873 K (red, blue and green respectively) and 1773 K (pink, turquoise and orange respectively), from front to back, for PuAm 20/80. The * indicates the peaks already present for PuAm 20/80 and PuAm 50/50-A, while * represents the new peaks.

As it can be seen, the three patterns recorded at 1873 K do not exhibit the same positions and intensities for the various diffraction peaks. Indeed, the growth of the peaks located at 26.7, 29.0, 30.1 and 30.6° is highlighted on Figure 4-13. On the contrary, the intensity of the reflections indicative of the fluorite structure at 27.9 and 31.9° decreases along the three scans at 1873 K. Moreover, for these two peaks, a shift towards lower angles is observed along the scans. This leads to an increase of the lattice parameters, corresponding to a reduction of the oxide during the successive scans. In addition, a decrease of the intensity of the peaks located at 28.3, 31.1 and 32.3° is also observed. The achievement of the thermodynamic equilibrium can thus be questioned at the end of the plateau at 1873 K, as the intensities of the various peaks do not stabilize in the last two patterns. Moreover, these changes of intensities and positions of the peaks could be related to variations of composition of the samples occurring at 1873 K. Indeed, loss of americium can occur at such high temperature, as demonstrated by Gotcu-Freis *et al.* with an Am content increasing in the gas phase when increasing the temperature [26]. However, as no chemical analyses were performed during/after the HT-XRD experiments, it is not possible to conclude on this hypothesis. On the contrary, the same intensity and positions of the peaks are observed for the three diffractions patterns recorded at 1773 K, indicating that the thermodynamic equilibrium was reached at this temperature. Thus, the diffraction patterns collected at 1873 K are not used in the phase determination as they are assumed to not be representative of the equilibrium state.

The evolution of the diffractions patterns between 1773 K and room temperature is plotted in Figure 4-14 between 26 and 33°. Compared to the diffraction patterns of PuAm 80/20 and PuAm 50/50-A, an important number of peaks is observed, whose intensities vary with temperature.

As previously explained, two characteristics peaks of the fcc structure are visible on Figure 4-14. In addition, the unidentified peaks for PuAm 80/20 and PuAm 50/50-A (27.4, 28.2, 31, 31.4 and 32.1° 2θ) and the ones of PuAm 50/50 (28.4 and 30.4° 2θ) are also present, represented by *. Eight new peaks * are observed for the PuAm 20/80 samples, located at 26.8, 29.0, 29.1, 30.1, 30.2, 30.5, 30.8 and 31.1°, evidencing the appearance of at least one new phase.

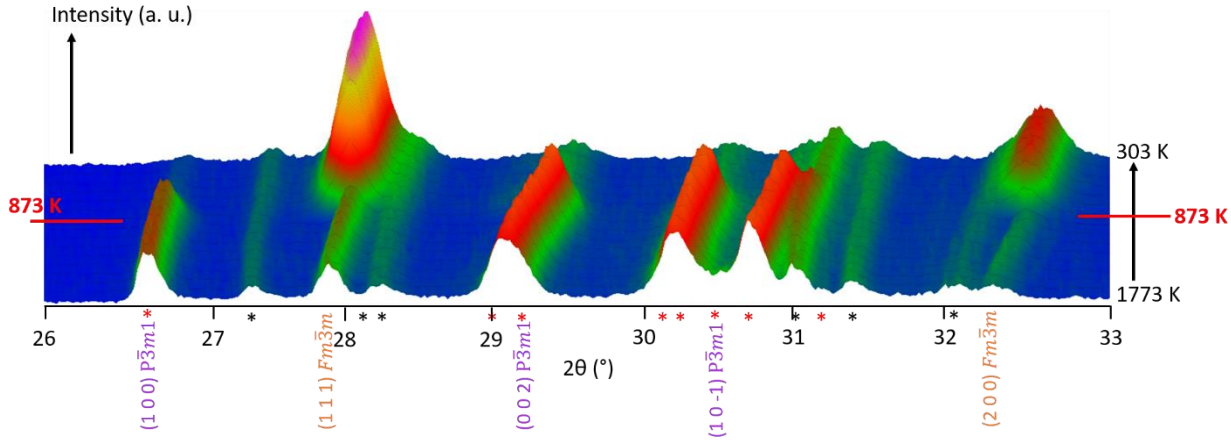

Figure 4-14: Evolution of the diffraction patterns between 26 and 33° 2θ as a function of the temperature for PuAm 20/80, where * represents the peaks already observed for PuAm 80/20 and PuAm 50/50-A and * the additional ones for PuAm 20/80.

As for the two previous compositions studied, the secondary phases expected according to the Pu-Am-O system for PuAm 20/80 are A-M_2O_3 and/or B-M_2O_3 and/or C-M_2O_3. Based on the positions and the intensities of the peaks, the existence of the A-M_2O_3 phase is proposed

(hexagonal, space group $P\bar{3}m1$). Indeed, as it can be seen in Figure 4-14, the three characteristics peaks of the structure at low angles, namely the (100), (002) and (10-1) reflections are distinguished. However, based on the low signal/noise ratio of the diffraction patterns, the a and c lattice parameters of this phase could not be determined to confirm the existence of this phase.

In the case where the A-M_2O_3 phase is present, other diffraction peaks visible on Figure 4-14 could be attributed to the B-Am_2O_3 phase (monoclinic structure, space group $C2/m$). This would be in agreement with the high americium content of the sample. However, due to the numerous amount of weak reflections attributed to a monoclinic structure, the fit of the diffraction patterns is difficult. Thus, it is not possible to attribute the reflections to the peaks visible on Figure 4-14.

The existence of the C-M_2O_3 phase (cubic, space group $Ia\bar{3}$) is also questionable. Indeed, this phase could be present and explain the peaks located at 28.2, 30.8 and 32.8°. However, as some of the peaks are located within the reflections of other phases, it is not possible to conclude on the existence of this phase.

Thus, as for the two other compositions PuAm 80/20 and PuAm 50/50-A, only the fluorite phase $Pu_{1-z}Am_zO_{2-x}$ is determined with certainty from 1773 K to room temperature for PuAm 20/80.

Moreover, as it can be seen in Figure 4-14, a change of behaviour is occurring at 873 K. Indeed, the fluorite phase, which is minor from 1773 to 873 K (see reflections (111) and (200)), becomes predominant down to room temperature. In addition, the intensities of the dominant peaks (* on Figure 4-14) present at high temperature decrease significantly between 973 and 773 K. The peak located at 26.8°, assumed to be the (100) reflection of the A-M_2O_3 phase, disappears for T < 873 K. On the contrary, it can be noticed that the intensity of the peaks already present in PuAm 50/50, indicated as * on Figure 4-14, remains constant throughout the whole temperature range. Based on these observations, a phase transition occurs at 873 K, from a multiphasic domain [MO_{2-x} + A-M_2O_3 + unidentified phases] (most likely at least B-M_2O_3) to a multiphasic domain [MO_{2-x} + unidentified phases]. However, the accurate determination of the phase boundary is not possible as the O/M ratios of the sample during the experiments remain unknown. Moreover, possible changes in the composition of the samples (mainly losses of americium) can occur at high temperature, resulting in difficulties in locating the phase boundaries.

4.2.2.1.4 Conclusion

As described in this section, the identification of the phases present from 1873 K to 303 K for the three samples is difficult, because of the poor knowledge of this system and the numerous amount of secondary phases. Table 4-7 summarizes the findings of this section in terms of phases, proportions and phase transitions.

Table 4-7 – Formed phases and associated proportions from 1873 K to 3030 K for PuAm 80/20, PuAm 50/50-A and PuAm 20/80.

Sample	Temperature range	Formed phases	Proportions
PuAm 80/20	1873 K → 303 K	MO_{2-x} + unknown phase(s)	Constant throughout the T range, MO_{2-x} phase majority
PuAm 50/50-A	1873 K → 303 K	MO_{2-x} + unknown phase(s)	Constant throughout the T range, MO_{2-x} phase majority
PuAm 20/80	1873 K → 873 K	MO_{2-x} + A-M_2O_3 + unknown phase(s) (probably B-M_2O_3)	Constant throughout the T range, A-M_2O_3 phase majority
	873 K → 303 K	MO_{2-x} + unknown phase(s)	Constant throughout the T range, MO_{2-x} phase majority

4.2.2.2 Lattice parameter of the fluorite phase as a function of temperature

The fcc structure, corresponding to the $Pu_{1-z}Am_zO_{2-x}$ phase, is identified over the whole temperature and composition ranges. Thus, the variation of the lattice parameter as a function of temperature and Am content can be studied and is plotted in Figure 4-15. The lattice parameters obtained at room temperature before thermal cycle (see section 4.1.3) are reported for comparison.

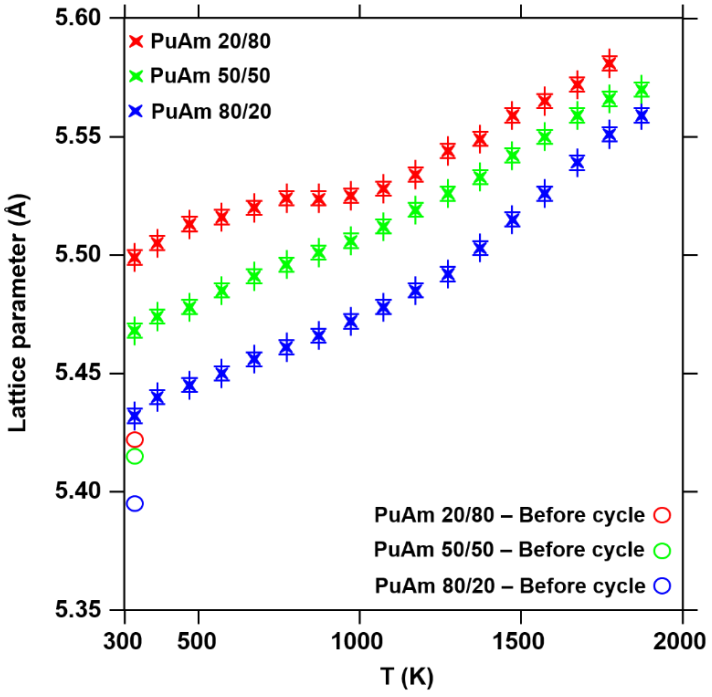

Figure 4-15: Variation of the lattice parameter of the fcc phase as a function of the temperature for PuAm 80/20 (blue), PuAm 50/50-A (green) and PuAm 20/80 (red), and lattice parameters at room temperature before thermal cycle (the uncertainties correspond to the size of the symbol).

When looking at the lattice parameters measured at room temperature after thermal treatment (5.432 ± 0.003 Å for PuAm 80/20, 5.468 ± 0.003 Å for PuAm 50/50-A and 5.499 ± 0.003 Å for PuAm 20/80), it can be noticed that they do not lie between the ones of PuO_2 (5.396 Å) and AmO_2 (5.375 Å). This is due to their initial O/M ratios determined in section 4.1.4.1 (1.94-1.93) and the reducing atmosphere used during the experiments. During the thermal cycle, a further reduction of the samples is occurring, due to the high tendency of AmO_2 to lose oxygen above 1000 K. This observation indicates a reduction behaviour of the samples amplified when increasing the Am content. Finally, the hypothesis of an expansion of the lattice due to the alpha self-irradiation is here rejected as the self-irradiation defects are annealed at high temperature.

Moreover, as explained in Chapter 2 – section 2.2.3, an increase of the lattice parameter is noticed when increasing the temperature. This observation follows the trend of other actinide oxides.

Two different behaviours can be distinguished for the three americium contents on Figure 4-15.

In the case of the PuAm 80/20 and PuAm 50/50-A samples, a continuous decrease of the lattice parameter is observed when decreasing the temperature. As described in the previous section, no phase transition is identified for these two americium contents between 1873 K and 303 K, as well as no change in composition, explaining the shape of the curve. A larger thermal expansion is observed for the PuAm 80/20 sample, equal to 2.34 % at 1873 K, compared to 1.87 % for PuAm 50/50-A. Moreover, a change of slope occurs at 1273 K for the PuAm 80/20 sample. These two observations can be linked to a more important reduction behaviour of PuAm 80/20, explained by the tendency of AmO_2 to lose oxygen above 1100 K and the higher proportion of Am^{3+} already observed in section 4.1.4.1 at room temperature.

On the contrary, a different behaviour is observed for the PuAm 20/80 sample. Indeed, a linear increase of the lattice parameter is noticed from room temperature to 773 K, where a change of slope occurs. Between 773 K and 973 K, a plateau is found, with a constant lattice parameter equal to 5.525 Å. This plateau corresponds to the phase transition [MO_{2-x} + unknown phase(s) → MO_{2-x} + A-M_2O_3 + unknown phase(s)], highlighted in section 4.2.2.1.3 and visible in Figure 4-14. Possible changes in the composition of the samples (loss of Am or Pu) can also occur during this plateau. From 973 K to 1773 K, the lattice parameter increases again linearly with the temperature. A smaller thermal expansion is observed for this sample, equal to 1.49 % at 1773 K.

The different variations of the lattice parameters with temperature and the discrepancies with the lattice parameters at room temperature highlight peculiar and complex phase equilibria in the Pu-Am-O system.

4.2.3. Conclusion

As described in this section, the determination of the phase equilibria for PuAm 80/20, PuAm 50/50 and PuAm 20/80 between 1873 K and 303 K is difficult due to numerous secondary phases, which could not be identified. The number of phases increases with the Am content. A fcc structure, corresponding to a $Pu_{1-z}Am_zO_{2-x}$ phase, was evidenced over the whole temperature and composition range. Several trials were made to identify the other phases for the three compositions, based on the existing ones in the binary Pu-O and Am-O systems and on the analogy with the Ce-O system or on possible pollution by impurities during the thermal

treatment. For the PuAm 20/80 sample, the A-M_2O_3 and B-M_2O_3 phases could be present from 1773 to 873 K but it was not possible to confirm it. Moreover, a phase transition was identified at 873 K, with the disappearance of one phase (assumed to be the A-M_2O_3 phase) and the predominance of the $Pu_{1-z}Am_zO_{2-x}$ phase down to room temperature. Changes in the Pu and Am contents of the sample were also most likely happening during this transition. Thus, the formed secondary phases in the three compositions remain unidentified apart from the existence of the fluorite $Pu_{1-z}Am_zO_{2-x}$ phase. Unfortunately, due to the lack of material available, it was not possible to repeat the experiments.

Moreover, the variation of the lattice parameter of the $Pu_{1-z}Am_zO_{2-x}$ phase was studied as a function of temperature for the three americium contents. Two different behaviours were highlighted. In the first case, for the PuAm 80/20 and PuAm 50/50-A samples, the increase of the lattice parameters was linear when increasing the temperature, indicating that no change in composition/phase proportions occurred throughout the temperature range. The differences in the shape of the curves for the two samples were assumed to originate from a more important reduction of the PuAm 80/20 sample. In the second case, an increase of the lattice parameter with temperature was also observed for the PuAm 20/80 sample up to 773 K, where a plateau was noticed between 773 K and 973 K, followed by an increase again up to 1773 K. This behaviour indicates a phase transition also observed on the evolution of the diffraction patterns.

Further experiments are needed to conclude on the phase equilibria. Indeed, the recording of the diffraction patterns during the heating cycle would have been useful to determine the temperature of formation of the secondary phases and then exclude possible residual phases during the cooling. Moreover, the determination of the O/M ratios of the sample during the experiments is of prime interest for establishing accurately the phase boundaries. To this aim, the following section presents results on the determination of the phase equilibria in the PuAm 80/20 sample at 1673 K, by combining TGA analyses and HT-XRD measurements.

4.3. PHASE EQUILIBRIA IN $Pu_{0.77}Am_{0.23}O_{2-x}$ AT 1673 K

Isothermal experiments were performed at 1673 K on the $Pu_{0.77}Am_{0.23}O_{2.00}$ sample (PuAm 80/20-O/M). Two techniques were combined in the same conditions (heat treatment and atmosphere): TGA for the determination of the oxygen potential and the variation of the O/M ratio and HT-XRD for the identification of the phases and the description of the phase transitions occurring at this temperature as a function of the O/M ratio.

In this section, the oxygen potential data are described first, followed by the results obtained by HT-XRD. Finally, a description of the phase diagram at 1673 K over the O/M ratio range studied here is proposed.

4.3.1. Oxygen potential data

4.3.1.1 Experimental procedure

Oxygen potentials of a $Pu_{0.77}Am_{0.23}O_{2-x}$ sample (PuAm 80/20-O/M) were measured using ThermoGravimetric Analysis (TGA) available at the ATALANTE facility of CEA Marcoule (France). Prior to the measurement, a fragment of this sample was annealed (see Chapter 3 – section

3.2.1.2) in order to obtain an O/M ratio equal to 2.00 and thus a known starting point. Only a brief description of the experimental procedure is given here, more details can be found in Chapter 3 - 3.3.8.

The measurements were carried out using a gas equilibrium method with an (Ar,H_2,H_2O) mixture. The lowest H_2O/H_2 ratio achievable was set as starting point for the experiment and the H_2O/H_2 ratio was then increased during the experiment to re-oxidize the sample. The resulting pO_2 was measured by an oxygen gauge at the furnace outlet (ranging in this work between $7.3x10^{-28}$ atm and $6.5x10^{-24}$ atm). A heating rate of 10 $K.min^{-1}$ was applied from room temperature to 1673 K, followed by an isothermal plateau of 72 hours at this temperature. The sample was then cooled down to room temperature at a rate of 30 $K.min^{-1}$. The variation of the mass of the sample occurring with the change of pO_2 was recorded as a function of time in isothermal conditions at 1673 K. In order to correct the mass difference measured for the sample when varying the oxygen partial pressure of the system, the same experiment was performed with an empty crucible. The oxygen potentials $\Delta\bar{G}_{O_2}$ were calculated using the relation of Wheeler-Jones [227] and the O/M ratios were assessed from the weight change of the sample.

In this work, considering the uncertainties on the temperature, the oxygen partial pressure and the mass, an uncertainty of ± 0.002 was calculated for the O/M ratio and of ± 10 $kJ.mol^{-1}$ for the oxygen potential.

4.3.1.2 Results

The variations of mass recorded for the sample (in red) and for the blank (in green) are presented as a function of time in Figure 4-16, as well as the difference of the two curves (in blue).

At the beginning of the experiment, the sample is reduced during heating (under Ar/H_2 4% and $pO_2 = 7.3x10^{-28}$ atm) until 1200 min. An O/M ratio of 1.716 is achieved (initial O/M ratio = 2.00). Afterwards, as it can be seen in Figure 4-16(b), the oxygen partial pressure was increased during eight consecutive steps, represented by the black dashed lines. A progressive increase of the mass signal is noticed during the isothermal treatment. However, it can be observed that for some pO_2 values, the mass signal was not always stable at the end of each step. Thus, the achievement of the thermodynamic equilibrium can be questioned for the steps 3, 4, 6, 7 and 8. The progressive increase in the mass signal observed during the isothermal treatment highlights the re-oxidation of the sample occurring at each change of oxygen partial pressure.

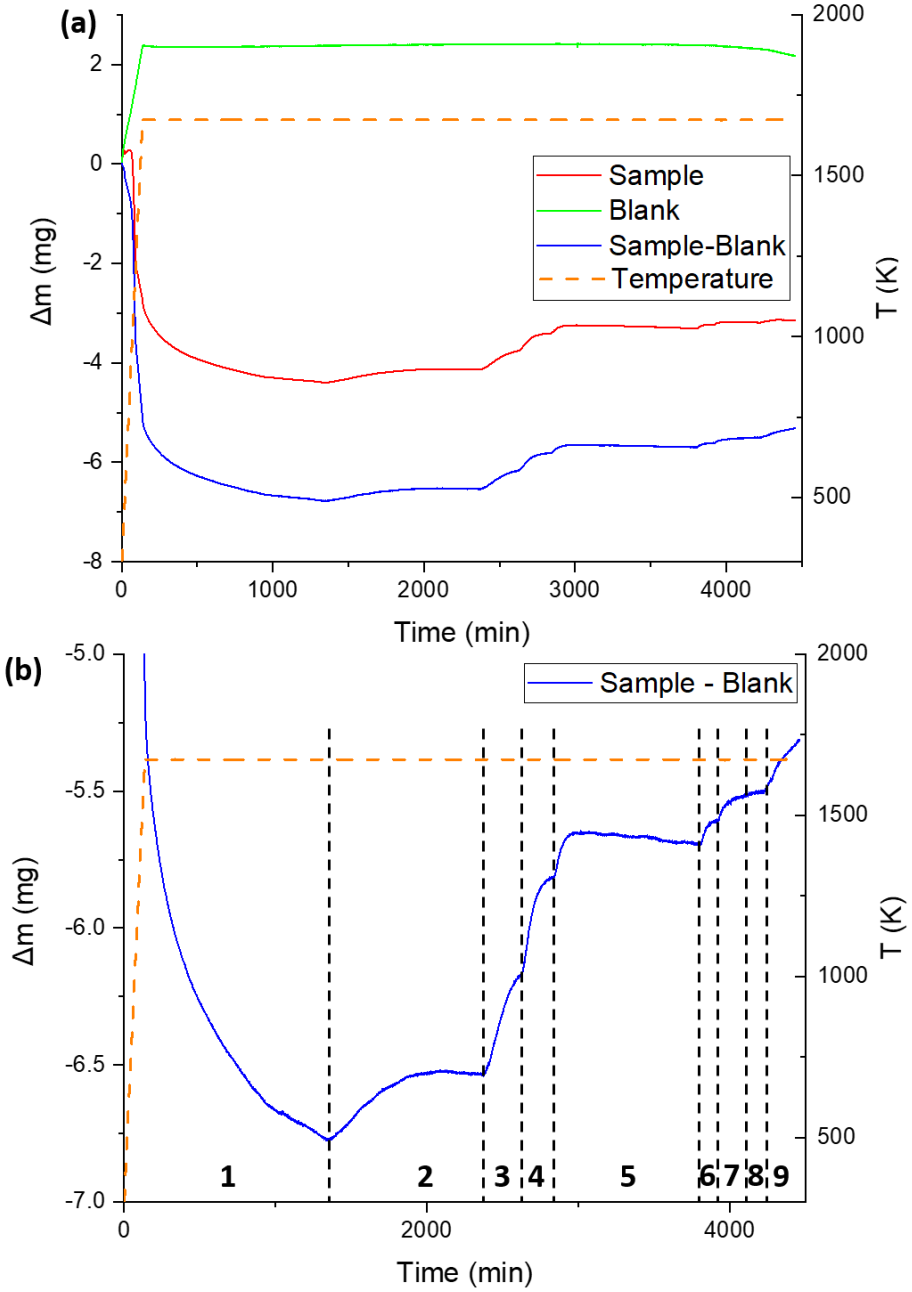

Figure 4-16: Variation of the mass signal and temperature as a function of time for PuAm 80/20. The orange dashed line corresponds to the temperature signal and the black dashed lines on (b) to the change of oxygen partial pressure.

The oxygen potential $\Delta\bar{G}_{O_2}$ and the corresponding O/M ratios determined in this work based on the variation of the mass of the sample are summarized in Table 4-8 and plotted in Figure 4-17. An increase of the O/M ratio is noticed when increasing the oxygen potential during the plateau at 1673 K, following the trend of pure and mixed oxides. A stabilization of the oxygen potential observed for O/M > 1.77 could indicate the presence of a two-phase or three-phase region in this composition range.

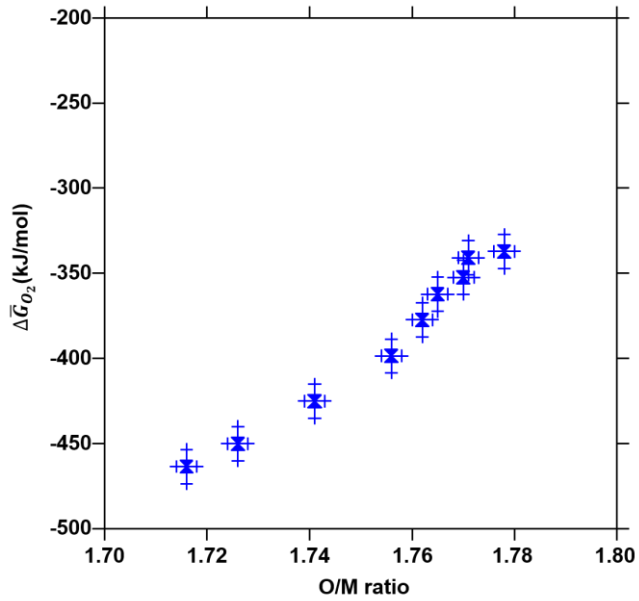

Figure 4-17: Oxygen potentials of PuAm 80/20 at 1673 K as a function of the O/M ratio.

Table 4-8 – Oxygen potential and O/M ratios determined for PuAm 80/20 at 1673 K.

Step	pO_2 (atm)	$\Delta\bar{G}_{O_2}$ (kJ/mol) (± 10)	O/M ratio (± 0.002)
1	7.3×10^{-28}	-463.62	1.716
2	1.9×10^{-27}	-450.17	1.726
3	1.2×10^{-26}	-425.15	1.741
4	7.8×10^{-26}	-398.63	1.756
5	3.6×10^{-25}	-377.42	1.762
6	1.1×10^{-24}	-362.29	1.765
7	2.2×10^{-24}	-352.44	1.770
8	5.0×10^{-24}	-340.92	1.771
9	6.5×10^{-24}	-337.14	1.778

At 1673 K, comparison of the results obtained in this work with literature data is limited to only one set of experiments from Matsumoto *et al.* [164]. In their work, the authors studied the oxygen potentials of a $Pu_{0.928}Am_{0.072}O_{2-x}$ sample at 1673 K. This work could have been used to study experimentally the influence of the Am content on the oxygen potentials. Unfortunately, the resulting O/M ratios are ranging between 1.90 and 2.00 and thus, no comparison could be made as the O/M ratios studied in this thesis are much lower. No other experimental works are available on the same americium content or at the same temperature, even for AmO_{2-x} and PuO_{2-x}. However, comparison with thermodynamic calculations and available experimental data

for other $Pu_{1-z}Am_zO_{2-x}$ samples using the CALPHAD method will be performed in Chapter 6 – section 6.3.4.2.

4.3.2. Phase equilibria

Once the O/M ratios were determined from the TGA experiments, the phases in presence in this region were studied by means of HT-XRD.

4.3.2.1 Experimental procedure

HT-XRD measurements were performed at the ATALANTE facility of CEA Marcoule (France), following the procedure described in Chapter 3 – section 3.3.5 on a PuAm 80/20-OM fragment. The experimental conditions of these measurements were adapted to reproduce as close as possible the ones of the TGA experiment. Indeed, a reducing atmosphere of He/H_2 4% + z ppm H_2O was used, with z ranging between 148 (pO_2 = 7.3x10^{-28} atm, as starting point) and 14000 (pO_2 = 6.5x10^{-24} atm, at the end of the experiment). The oxygen content inside the experimental chamber was monitored by an oxygen gauge and gradually increased during the experiment. The same thermal treatment of the TGA experiment was applied: heating from room temperature to 1673 K at 10 K.min^{-1}, isothermal plateau of 72 hours and cooling down to room temperature at 30 K.min^{-1}. Diffraction patterns were acquired between 20 and 145° 2θ, with a counting time of 0.5 s per step and with a step interval of 0.02°.

4.3.2.2 Results and discussion

As for the TGA measurements, the sample was first reduced from 2.00 down to 1.716 during the first step of the experiment. From this value, the O/M ratio was progressively increased up to 1.778, following the same oxygen potential steps as for the TGA experiments.

Diffraction patterns were collected during the whole isothermal plateau at 1673 K for the nine O/M ratios. The resulting diffraction patterns are represented in Figure 4-18, with a zoom at low angles (between 25 and 35° 2θ).

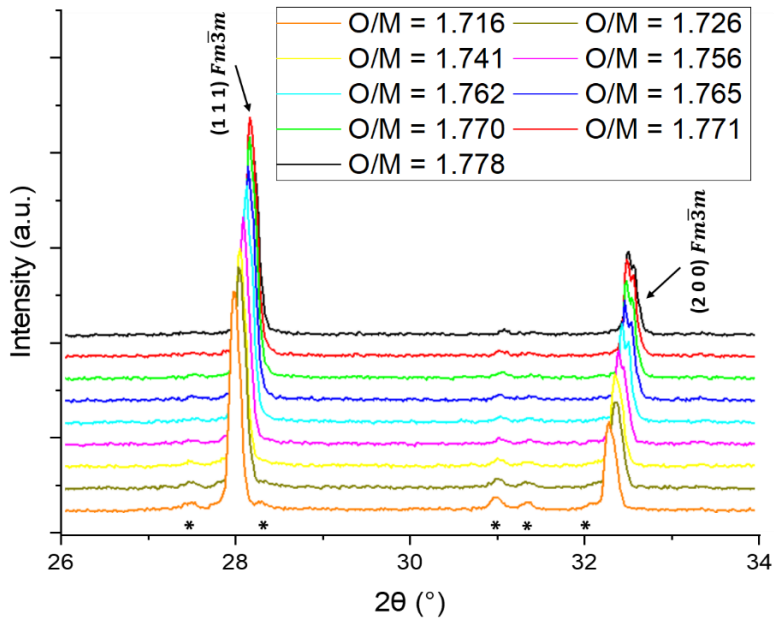

Figure 4-18: Diffraction patterns of PuAm 80/20 at 1673 K as a function of the O/M ratio.

For all patterns, several phases can be distinguished. As previously explained in section 4.2.2, the identification of the phases in presence at high temperature is difficult. Thus, as for the results obtained in section 4.2.2, the phase equilibria obtained in this section are only tentative.

Among the peaks presented in Figure 4-18, two characteristics peaks of the fcc MO_2 structure ($Fm\bar{3}m$) are observed, namely the (111) and (200) reflections. The rest of the peaks are attributed to undetermined structures, corresponding to one or several secondary phases (section 4.2.2) and identified as *.

Different behaviours can be observed throughout the O/M ratio range studied in this work:

- For an O/M ratio of 1.716, the ratio of the proportions between the fcc phase and the secondary phase(s) is equal to 95/5. This value gradually decreases until O/M = 1.741 (< 5 %). Thus, this highlights the existence of a multiphasic domain for 1.716 < O/M < 1.741.
- For O/M = 1.756, only a very small residual amount of the secondary phase(s) is noticed, which could not be quantified.
- For 1.762 < O/M < 1.778, only the fcc structure is observed.

Based on these findings, a phase transition seems to occur for 1.741 < O/M < 1.762.

The lattice parameters of the fcc structure, corresponding to MO_{2-x}, is determined for each diffraction pattern and its variation as a function of the O/M ratio is plotted in Figure 4-19. The O/M ratios determined by the TGA experiments, referring to the global O/M ratio of the sample, are used. Note that in this case, it does not correspond to the O/M ratio of the MO_{2-x} phase, as a multiphasic domain is observed at low O/M ratios. Thus, to avoid any possible confusion, the terminology "global O/M ratio" is adopted in the rest of the section.

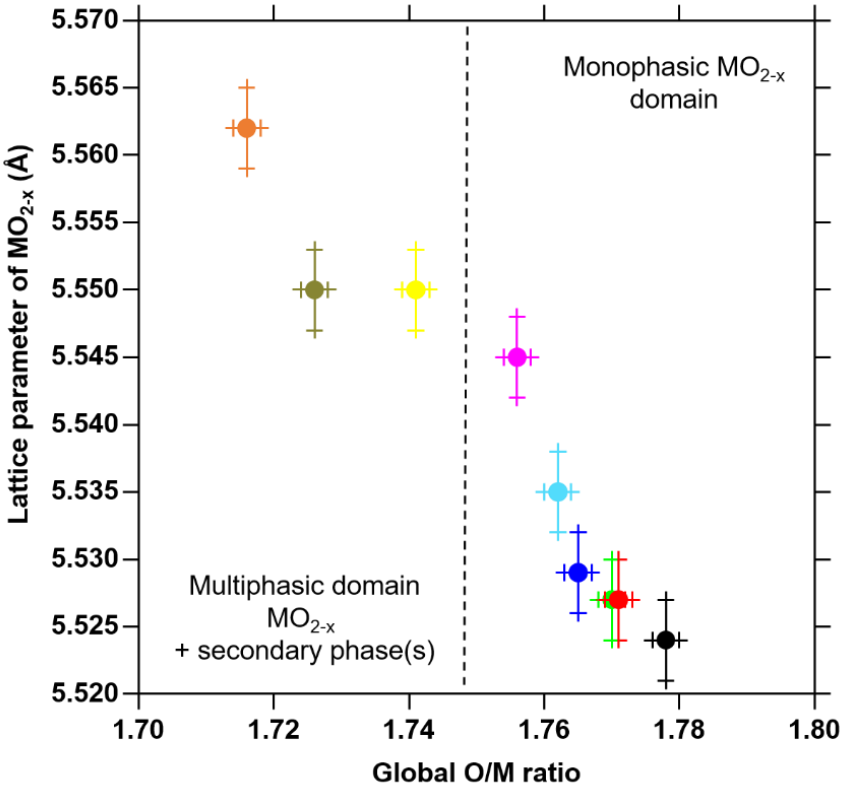

Figure 4-19: Lattice parameter of the fluorite phase as a function of the global O/M ratio for PuAm 80/20 at 1673 K.

Between O/M = 1.716 and 1.726, a decrease of the lattice parameter is noticed when increasing the O/M ratio.

For global O/M ratios equal to 1.726 and 1.741, the lattice parameter of the fluorite phase remains constant, while it decreases for higher O/M ratios. This is indicative of a phase transition, from a multiphasic domain for 1.726 < O/M < 1.741 to a monophasic region for O/M > 1.744, as it can be seen in Figure 4-18 with the slow disappearance of the unidentified secondary phase(s). In this case, the phase boundary is located for a global O/M ratio between 1.74 and 1.76. The constant lattice parameter of the MO_{2-x} phase obtained for 1.726 < O/M < 1.741 indicates that this phase does not undergo any variation of Pu and Am contents nor O/M ratio. Indeed, these variations would induce some changes in the lattice parameters as already explained in Chapter 2 – section 2.2.2.3. Thus, the variation of the global O/M ratio is related to the variation of the fraction of the secondary phases.

Based on the temperature of this experiment and the information from the binary phase diagrams, the secondary phase(s) could correspond to sesquioxide oxides M_2O_3, although the phase identification performed in the previous section did not allow concluding on it, as the lattice parameters obtained were not in agreement with the ones of the end-members. In the literature, these structures are admitted to accept only trivalent cations and thus to remain stoichiometric. Assuming the presence of stoichiometric sesquioxides and an identical MO_{2-x} phase for global O/M ratios equal to 1.726 and 1.741, the change noticed in the global O/M ratio would originate from different proportions of the phases. Indeed, higher proportions of sesquioxides would be obtained for low global O/M ratios, while these proportions would decrease when increasing the O/M ratio. However, care should be taken when considering these findings, as the determination of the formed phases at this temperature remains difficult and the existence of the sesquioxides is hypothetical. In the case where the unidentified phases would not be sesquioxides but non-stoichiometric compounds, the description of the multiphasic domain would be more complex.

From 1.756 < global O/M < 1.778, a decrease of the lattice parameter is observed again when increasing the global O/M ratio.

A peculiar behaviour is also observed for global O/M = 1.770 and 1.771 (in green and red in Figure 4-19). This observation can be explained by the similar O/M ratio of the two scans, lying in the experimental uncertainties. Moreover, for these scans, as the duration of a scan was approximately 55 min and the plateau lasted 2 hours, the achievement of the thermodynamic equilibrium can be questioned.

4.3.3. Conclusion

In this section, the phase equilibria in the $Pu_{0.77}Am_{0.23}O_{2-x}$ sample, with $0.222 \leq x \leq 0.284$, were studied at 1673 K combining TGA and HT-XRD.

In a first step, the variation of mass of the sample was measured as a function of time using TGA, under different oxygen partial pressures using $H_2/H_2O/Ar$ atmospheres. The variation of the O/M ratio was determined and linked to the oxygen potentials. An increase of the oxygen potential was reported when increasing the O/M ratio, following the trend of other oxides, although no direct comparison could be made as no data are reported in the literature at 1673 K in the same O/M range.

In a second step, HT-XRD experiments were performed following the same experimental conditions as in the TGA measurements in order to determine the formed phases at this temperature as a function of the O/M ratio. A complex behaviour was evidenced with the presence of at least two phases, one being the fluorite phase MO_{2-x}. A multiphasic domain MO_{2-x} + secondary phase(s) was observed for 1.716 to 1.741 and a monophasic MO_{2-x} domain was noticed for higher O/M ratios ($1.756 \leq O/M \leq 1.778$). The identification of the other secondary phases was not possible. The lattice parameter variation of the fluorite matrix as a function of the global O/M ratio was determined. A stabilization of the lattice parameters for global O/M ratios equal to 1.726 and 1.741 is consistent with the existence of a two-phase region [MO_{2-x}+M_2O_3] for $1.716 \leq O/M \leq 1.741$. The phase boundary from this multiphasic region to the monophasic MO_{2-x} domain is found around O/M = 1.75. Further studies are needed to identify the formed phases. However, the combination of TGA and HT-XRD was proven to be useful for assigning the overall O/M ratio of the sample to the phases identified by XRD.

4.4. SOLID/LIQUID PHASE TRANSITIONS IN $Pu_{0.49}Am_{0.51}O_{2-x}$

As reported in Chapter 2, no experimental data exist on the solid/liquid phase transitions in $Pu_{1-z}Am_zO_{2-x}$ samples. To this aim, new measurements using a laser-heating technique were performed in this work to determine the solidus and liquidus temperatures of a $Pu_{0.49}Am_{0.51}O_{2-x}$ sample (referred to as sample PuAm 50/50-B in Table 4-1). The experiments were carried out at the Joint Research Centre Karlsruhe (Germany).

First, the solidus and liquidus temperatures obtained are presented. Then, the variation of the oxygen partial pressure inside the chamber during the tests, linked to the O/M ratio of the sample, is studied. Finally, the variation of the temperatures with the O/M ratio is discussed.

4.4.1. Experimental procedure

The melting experiments were performed using the laser-heating technique, coupled with fast pyrometry, developed by Manara *et al.* [14], as described in Chapter 3 - section 3.3.6. The oxygen gauges at the entrance and exit of the autoclave allowed monitoring the oxygen partial pressure inside the vessel during the measurements.

In this work, a disk of 1.5 mm thickness and 4.7 mm diameter of $Pu_{0.49}Am_{0.51}O_{2-x}$, referred in Table 4-1 as PuAm 50/50-B, was placed in a sealed autoclave. For this sample, as only a limited amount of material was available, characterizations to determine the initial O/M ratio of the sample could not be performed and thus, the initial O/M ratio is unknown.

The experiments were carried out under argon, with a residual oxygen partial pressure of 3.4×10^{-6} atm. Five successive shots were performed on the same side of the sample. The conditions are summarized in Table 4-9. After each shot, the sample was allowed to cool down to room temperature to visually inspect the chamber and the sample, to check for possible vaporization or cracks formation. A waiting step ranging between 1h and 2h30 was performed between each shot to allow the oxygen partial pressure to restabilize to its residual value.

Table 4-9 – Conditions of the shots performed on PuAm 50/50-B.

Shot number	Conditions
1	250 W – 500 ms
2	200 W – 500 ms
3	200 W – 500 ms
4	200 W – 500 ms
5	200 W – 500 ms

Due to technical issues, the emissivity of the sample could not be measured. Unfortunately, no emissivity data are available in the literature for AmO_2. Thus, the emissivity was estimated to be equal to 0.83 ± 0.05, corresponding to the value determined for PuO_2 by De Bruycker *et al.* [24] (more details in Chapter 3 – section 3.3.6.2).

The determination of the phase transition temperatures was performed by analysis of the cooling curve of the recorded thermogram. The procedure described in Chapter 3 – section 3.3.6.2 was applied here for correcting the true temperature based on the emissivity and transmittance and for analysing the oxygen partial pressure data.

4.4.2. Results and discussion

In this part, the solidus and liquidus temperatures measured during the experiments and the assessment of the O/M ratio are described.

The Figure 4-20(a) presents the disk of the sample before the shots, with the position of the pilot laser used for alignment, and (b) shows the state of the sample after one shot. As it can be seen on Figure 4-20(a), the laser is centred on the disk and the molten pool observed on Figure 4-20(b) corresponds to the same zone. The integrity of the sample after one shot can be noticed.

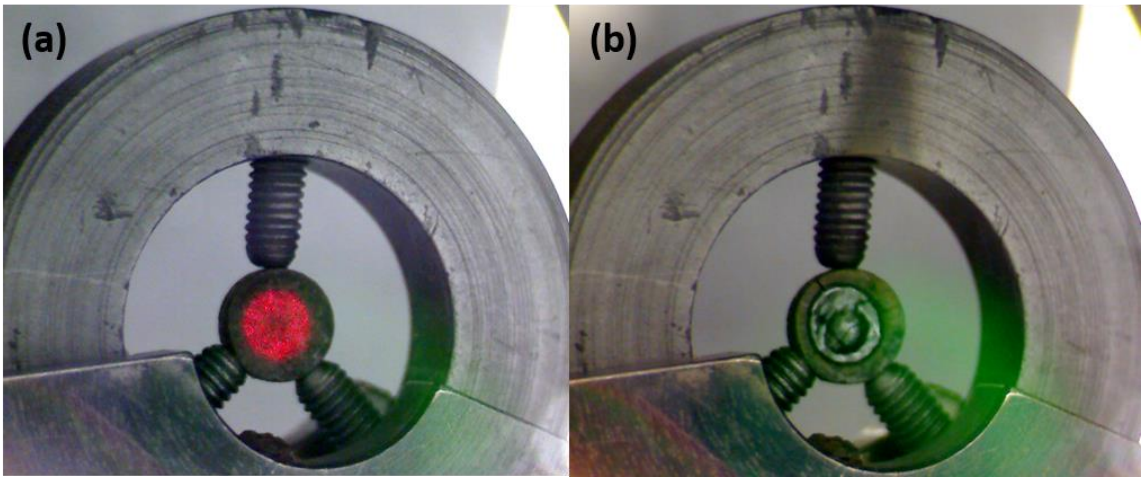

Figure 4-20: PuAm 50/50-B sample (a) before shots, with pilot laser used for the alignment and (b) after one shot.

4.4.2.1 Solidus/Liquidus temperatures

Due to the too high laser power for the first shot, no phase transition could be observed on the thermogram. Indeed, the intense laser power produced an out-of-equilibrium surface and the kinetics of cooling down to room temperature was not slow enough to distinguish any inflection point. Moreover, no solidus/liquidus temperatures could be determined on the thermogram of the shot 5 as the sample broke during the pulse. Thus, the results obtained only for the shots 2, 3 and 4 are discussed here. The corresponding thermograms (temperature as a function of time) recorded during the experiments are presented in Figure 4-21, where the laser power profile is represented in black.

The thermograms recorded here show that the melting is not congruent as no plateau is observed in the cooling curve. Two distinguishable thermal arrests are observed during cooling, corresponding to the liquidus and solidus temperatures, respectively. As illustrated in Figure 4-21(b) for the shot 4 (same observation made for the two other shots), these two thermal arrests are visible on the cooling curve, indicating that the solidus and liquidus temperatures are different enough to be distinguished with the current technique and its associated uncertainties.

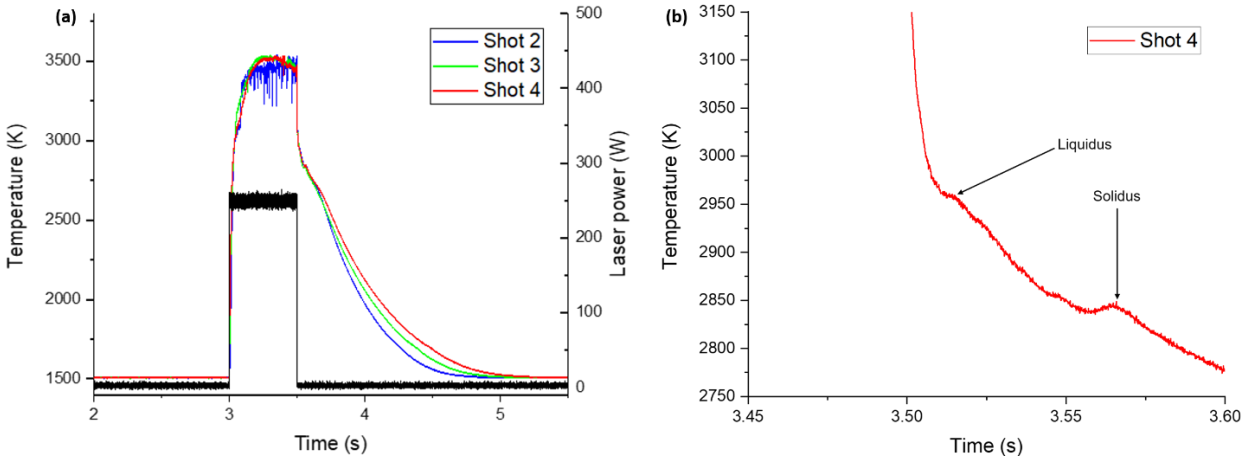

Figure 4-21: (a) Thermograms recorded for a PuAm 50/50-B sample for the shots 2, 3 and 4, with the corresponding laser power profile and (b) with a zoom on shot 4.

The temperatures of the two thermal arrests measured for the three shots are corrected to take into account the emissivity of the samples according to the procedure described in Chapter 3 – section 3.3.6.2. The resulting solidus and liquidus temperatures are reported in Table 4-10.

Table 4-10 - Solidus and liquidus temperatures measured for PuAm 50/50-B.

Shot number	$T_{solidus}$ (K)	$T_{liquidus}$ (K)
2	2834 ± 60	2960 ± 60
3	2835 ± 60	2980 ± 60
4	2845 ± 60	2956 ± 60
Average	2838 ± 60	2965 ± 60

The uncertainty on the temperature is calculated to be equal to ± 60 K (k = 2), taking into account the experimental uncertainties on the temperature determination and the uncertainty on the emissivity. Overall, a good repeatability is found for the solid/liquid transition temperatures between the three shots, highlighting the reproducibility of the measurements. The average solidus and liquidus temperatures obtained are: 2838 ± 60 K and 2965 ± 60 K, respectively.

Only one study, performed by Kato *et al.*, exists on the melting temperatures of $Pu_{1-z}Am_zO_{2-x}$ samples [174]. The authors measured the solidus and liquidus temperatures of $Pu_{0.979}Am_{0.021}O_{2.00}$ by thermal arrest using Re crucible at 2830 ± 35 K and 2937 ± 35 K, respectively. Unfortunately, they reported an interaction between the crucible and the sample and discarded the use of these results and no other experimental data exist in the literature. However, it can be noticed that the results obtained in this work here lie between the melting temperature of the two pure poles PuO_2 and AmO_2, reported by Böhler *et al.* [176] and McHenry [179] to be 3040 ± 60 K and 2383 K, respectively.

The variation of the solidus and liquidus temperatures along the shots is represented in Figure 4-22. As it can be seen, no significant variation of the solidus and liquidus temperatures is noticed throughout the shots. Thus, it appears that changes in the O/M ratio do not influence the phase transition temperatures.

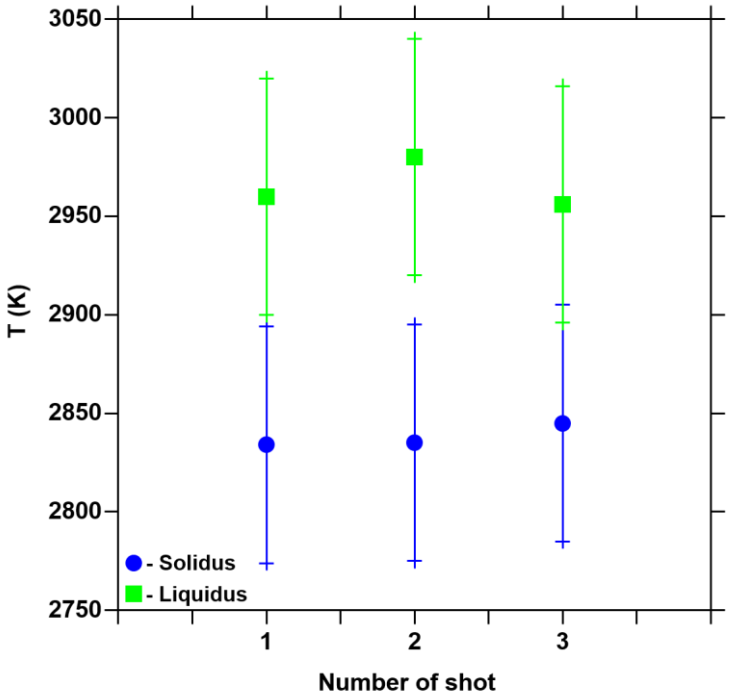

Figure 4-22: Solidus and liquidus temperatures measured for PuAm 50/50-B under Ar.

4.4.2.2 *Variation of the O/M ratio along the shots*

The oxygen partial pressure inside the experimental chamber was recorded and its variation during the experiment was measured. In this study, a residual oxygen content of 3.4 vpm (pO_2 = 3.4x10^{-6} atm) was measured in the argon. This value is plotted as baseline (dashed red line) in Figure 4-23. After each shot, the sample was left to cool down and the atmosphere to restabilize to its residual value. Note that in this study, a shift in the measurement of the pO_2 is

observed compared to the moment at which the shot is performed. Indeed, the latter lasts 500 ms while the oxygen partial pressure is measured every 3 second at the exit of the chamber.

The Figure 4-23 represents the variation in the oxygen partial pressure measured at the exit of the experimental chamber throughout the five shots performed. Even though no thermogram was recorded for the shots 1 and 5, the evolution of the pO_2 could be followed. An increase in the pO_2 occurs at each shot. In the case of the first shot, the oxygen partial pressure increases up to $1.6x10^{-4}$ atm and a waiting step of 2h30 was necessary to return at the residual value. This value decreases along the shots, with a maximum of pO_2 recorded at $1.9x10^{-5}$ atm for the fifth shot and a waiting step of one hour.

The difference between the maxima of pO_2 recorded for the shot 1 and shot 2 of approximately one decade can originate from the difference in the laser power used for these shots (250 W for shot 1 and 200 W for shot 2). Indeed, a higher power allows reaching higher temperatures, enhancing the tendency of this material to lose oxygen.

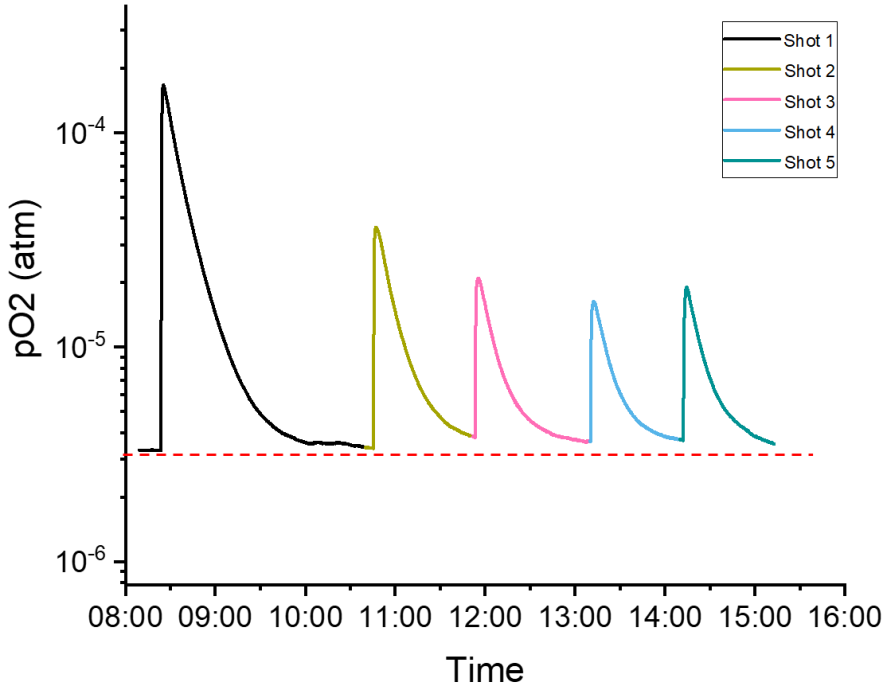

Figure 4-23: Variation of the oxygen partial pressure measured at the exit of the melting chamber throughout the five shots for PuAm 50/50-B.

The variation of the oxygen partial pressure recorded here is admitted to be related to changes in the O/M ratio of the sample. Indeed, it is assumed that only the sample can react with the oxygen present in the chamber. Thus, the increase in the oxygen partial pressure observed here corresponds to the release of oxygen by the sample during melting, so to a reduction phenomenon.

The quantity of oxygen released by the sample is calculated by integration of the variation of the oxygen partial pressure, as explained in Chapter 3 – section 3.3.6.2.2, and the resulting masses are given in Table 4-11 for the five shots. For the first shot, the mass of oxygen released by the sample is significantly higher than the ones calculated for the four other shots. As previously explained, this difference originates from the higher laser power applied in the case of the first shot, enhancing the release of oxygen. Moreover, a decrease in the oxygen mass between the second and third shot is also noticed, whereas the quantity of oxygen determined for the shots 3, 4 and 5 are similar.

As the release of oxygen by the sample is directly related to its reduction, the evolution in its O/M ratio throughout the shots is assessed. To this aim, several starting conditions and hypotheses are stated, as follows. The accuracy of these hypotheses will be discussed in Chapter 5 – section 5.4.3.3.

- The size of the laser spot (3 mm) corresponds to the diameter of the molten pool and its thickness is admitted to be of 150 µm (measured by Epifano *et al.* [48] by SEM analyses).
- The density of the PuAm 50/50-B is equal to 10.21 $g.cm^{-3}$, corresponding to 88 % of a theoretical density of 11.6 $g.cm^{-3}$ (see Chapter 3 – section 3.2.1.1).
- The oxygen is released only by the molten pool.
- The composition in Pu and Am of the sample is homogeneous and constant throughout the shots, implying that no change occurred due to the vaporization of these elements.
- The initial O/M ratio of the PuAm 50/50-B sample is considered equal to the one of the PuAm 50/50-A sample (1.94 ± 0.01), as they were both stored under the same conditions (under air for 15 years).

First, the number of moles corresponding to the molten pool is calculated and equal to $3.94x10^{-5}$ mol. Based on the initial O/M ratio admitted at 1.94, the number of mole of oxygen of the molten pool is equal to $7.66x10^{-5}$ mol. By converting the mass of oxygen released by the sample into a number of moles of oxygen, it is possible to determine the O/M ratio after each shot, given in Table 4-11.

Table 4-11 – Mass of oxygen released by the sample and difference compared to the initial O/M ratio.

Shot number	$m(O_2)$ released (µg)	Deviation from initial O/M ratio	O/M ratio obtained after each shot (± 0.01)
1	242.2	-0.096	1.84
2	50.5	-0.116	1.82
3	27.6	-0.127	1.81
4	19.8	-0.135	1.81
5	23.0	-0.144	1.80

An important reduction is determined for the first shot (-0.096 from the initial O/M ratio), whereas the amplitude of the deviation of the O/M ratio between each shot decreases throughout the four last shots. After the shot 5, a final O/M ratio of 1.797 is calculated. This value represents a significant reduction of the sample occurring throughout the shots (-0.144 compared to the initial O/M ratio).

The reduction of the PuAm 50/50-B sample evidenced here is supported by the high tendency of AmO_{2-x} to lose oxygen above 1100 K, as described in the phase diagram of the Am-O system of Epifano *et al.* [6].

4.4.2.3 Variation of the solidus/liquidus temperatures with the O/M ratio along the shots

The variation of the solidus and liquidus temperatures as a function of the O/M ratio obtained after each shot is plotted in Figure 4-24. As the solid/liquid phase transitions could not be

recorded for the shots 1 and 5, the O/M ratios calculated after these shots are represented by the dashed lines.

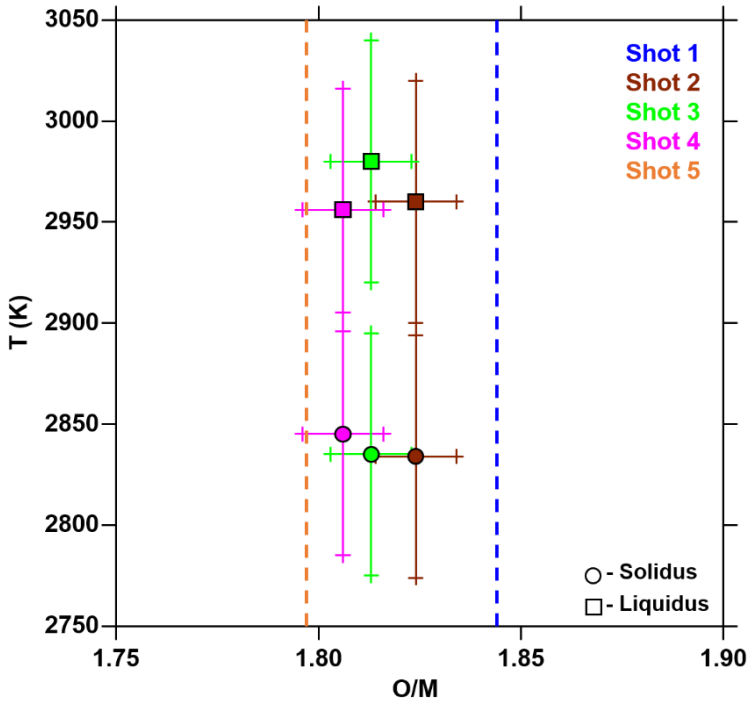

Figure 4-24: Variation of the solidus and liquidus temperatures along the shots as a function of the O/M ratio obtained after each shot.

As it can be seen, very similar solidus/liquidus temperatures are obtained for the shots 2, 3 and 4, within the experimental uncertainties. This observation indicates that the O/M ratio does not have a significant influence on these temperatures in the range of O/M ratios studied in this work. However, care should be taken when considering these data as no post-melting characterizations were performed to verify the hypotheses made to calculate the changes in the O/M ratio.

As no comparison with other $Pu_{1-z}Am_zO_{2-x}$ samples is possible, the solidus and liquidus temperatures determined in this work for $Pu_{0.49}Am_{0.51}O_{1.94}$ are compared to solidus temperatures of other mixed oxides, namely $U_{0.50}Pu_{0.50}O_{2.00}$ measured by Böhler *et al.* [176] and $U_{0.53}Am_{0.47}O_{1.97}$ measured by Epifano *et al.* [233]. The three solidus temperatures as well as the O/M ratio of the samples after melting are reported in Table 4-12.

Table 4-12 – Comparison of the solidus temperatures for various mixed oxides.

Sample	$T_{solidus}$	O/M after melting
$Pu_{0.49}Am_{0.51}O_{1.94}$ – This work	2838 ± 60 K	1.80
$U_{0.53}Am_{0.47}O_{1.97}$ – Epifano *et al.* **[233]**	2887 ± 58 K	1.93
$U_{0.50}Pu_{0.50}O_{2.00}$ – Böhler *et al.* **[176]**	2985 ± 53 K	2.00

As it can be seen, a higher solidus temperature is obtained in the case of the uranium-plutonium mixed oxides, followed by the uranium-americium and the plutonium-americium oxide. The samples follow the tendency of the pure poles, *i.e.* $T_{melt}(UO_2) > T_{melt}(PuO_2) > T_{melt}(AmO_2)$.

However, care should be taken when comparing these samples as their O/M ratio after melting significantly differs. Indeed, for $U_{1-y}Pu_yO_{2\pm x}$ and $U_{1-z}Am_zO_{2\pm x}$, it is known that a slight reduction of the samples leads to a higher melting temperature.

4.4.3. Conclusion

In this section, the melting behaviour of $Pu_{0.49}Am_{0.51}O_{2-x}$ was investigated by means of a quasi-container-less laser heating technique available at the JRC-Karlsruhe. This work constitutes the first determination of the solid/liquid phase transitions on the Pu-Am-O system.

Several shots were successively performed under argon and two thermal arrests were observed on the recorded thermograms, corresponding to the solidus and liquidus temperatures. A good repeatability of the measurements was noticed. The average temperatures of 2838 ± 60 K and 2965 ± 60 K were determined respectively for the solidus and liquidus, lying between the melting point of PuO_2 and AmO_2.

Thanks to the oxygen gauges, the variation of the oxygen partial pressure occurring during the experiments was recorded. A release of oxygen was observed during the melting, corresponding to the reduction of the sample throughout the shots. The variation of the O/M ratio along the shots was quantified, based on an initial O/M ratio equal to 1.94 before melting. A significant reduction of the sample was observed throughout the five shots, with a final O/M ratio equal to 1.80.

The variation of the solidus and liquidus temperatures as a function of the O/M ratio calculated after each shot was also studied in this work. For the two phase transition temperatures, no significant influence of the O/M ratio was noticed, as all the solidus and liquidus temperatures were similar within the experimental uncertainties.

The importance of pre- and post-melting characterizations (XRD, XAS) was evidenced in this work, with the need to confirm the various hypotheses made to calculate the changes in the O/M ratio. Moreover, further experiments are needed to gain knowledge on a broader range of americium content to conclude on its influence on the solid/liquid phase transitions.

4.5. CONCLUSION

Experimental structural and thermodynamic investigations of the Pu-Am-O system were performed in this section. The compositions of the samples of interest were first determined by chemical analyses: $Pu_{0.77}Am_{0.23}O_{2-x}$ (PuAm 80/20 sample), $Pu_{0.49}Am_{0.51}O_{2-x}$ (PuAm 50/50 samples) and $Pu_{0.20}Am_{0.80}O_{2-x}$ (PuAm 20/80 sample).

Room temperature structural properties were first investigated. XRD experiments were performed on the three samples and revealed the presence of only fcc structures. One fcc phase was observed in the PuAm 50/50 sample, whereas two fcc phases were assumed to exist in the two other samples. Based on the lattice parameters obtained in this study, an important swelling of the lattice was noticed when comparing with the ones obtained at the manufacturing of the samples. This swelling was determined to occur due to a combination of the effects of the α self-irradiation, during the storage of the samples for 15 years, and a reduction of the samples. This reduction was quantified by XANES analyses, which highlighted the simultaneous presence

of Pu^{3+}, Pu^{4+}, Am^{3+} and Am^{4+} in all the samples. From the quantification of these cations, the following O/M ratios were obtained: 1.94 for PuAm 80/20, 1.94 for PuAm 50/50-A and 1.93 for PuAm 20/80. The proportions of the cations were in disagreement with the model of Osaka *et al.*, who admitted the full reduction of Am^{4+} in Am^{3+} before the beginning of the reduction of the plutonium. A disagreement was also noticed between the phase diagram at room temperature as at these O/M ratios, a biphasic domain with a hexagonal or cubic M_2O_3 phase is expected. This observation highlighted the ability of the α self-irradiation defects to induce hypo-stoichiometry and possibly stabilize the fluorite structure.

The solid phase equilibria of the three samples were then studied by HT-XRD during cooling, from 1873 K to 303 K. Multiphasic domains were highlighted for all the samples. A fluorite structure, corresponding to the $Pu_{1-z}Am_zO_{2-x}$ phase, was evidenced over the whole temperature and composition ranges. However, the identification of the other formed secondary phases was difficult and unsuccessful for the PuAm 80/20 and PuAm 50/50 samples. The existence of the A-M_2O_3 and B-M_2O_3 phases was supposed for the PuAm 20/80 sample from 1873 K to 873 K, where a phase transition occurred, but could not be proven. In addition, changes in the composition of the sample (most likely loss of Am) were supposed. This phase transition was confirmed by the plateau observed in the variation of the lattice parameter of the fluorite phase as a function of temperature. This variation was plotted for the three compositions. An increase of the lattice parameter was noticed when increasing the temperature. For PuAm 80/20 and PuAm 50/50-A, no plateau was observed, evidencing that no phase transition occurred in the temperature and O/M ratio ranges studied. However, care should be taken as the O/M ratio remains unknown during the experiment. Further experiments are thus needed to conclude on the formed phases and the accurate location of the formed phases.

By combining TGA experiments and HT-XRD measurements, the solid phase equilibria were studied at 1673 K in $Pu_{0.77}Am_{0.23}O_{2-x}$, with $0.222 \leq x \leq 0.284$. An increase of the oxygen potential was reported when increasing the O/M ratio. The same complex behaviour as in the phase equilibria studies was evidenced, with the presence of at least two phases, one being a fluorite phase MO_{2-x}. A plateau in the lattice parameter variation as a function of the global O/M ratio highlighted the existence of a multiphasic region [MO_{2-x} + secondary phase(s)]. The phase boundary between this multiphasic domain and a monophasic MO_{2-x} domain was then identified at O/M ~ 1.75 for 1673 K. The advantage of combining TGA and XRD experiments was highlighted here to link the phase transitions to the O/M ratio.

The solid/liquid phase transitions of a $Pu_{0.49}Am_{0.51}O_{2-x}$ sample were determined for the first time by means of laser heating. Thanks to the addition of oxygen gauges in the setup, the variation of the oxygen partial pressure inside the chamber, and thus of the O/M ratio of the sample, was followed. The solidus and liquidus temperatures were measured at 2838 ± 60 K and 2965 ± 60 K respectively. A significant reduction of the sample was noticed during the melting (initial O/M ratio equal to 1.94 and final O/M ratio equal to 1.80). In addition, no significant influence of the changes of O/M ratio during the melting was noticed on the solidus/liquidus temperatures. Further studies are needed to confirm the initial and final O/M ratio, as well as other measurements on other americium contents, to have an accurate determination of the solid/liquid phase transitions of the Pu-Am-O system.

In this chapter, new structural, phase diagram and thermodynamic data were gained on the ternary Pu-Am-O system for an accurate description of the model using the CALPHAD method. To gain knowledge on the quaternary U-Pu-Am-O system, experimental investigations on $U_{1-y-z}Pu_yAm_zO_{2\pm x}$ are presented in the next chapter.

5. EXPERIMENTAL INVESTIGATION OF THE U-PU-AM-O SYSTEM

In this chapter, new structural and thermodynamic data are gained on $U_{1-y-z}Pu_yAm_zO_{2\pm x}$ samples ($0.235 \leq y \leq 0.39$ and $0.005 \leq z \leq 0.02$). EPMA and XRD analyses reveal an homogenous matrix with few U- and Pu-rich agglomerates. XANES experiments highlight the simultaneous presence of U^{5+} and Pu^{3+}/Am^{3+}, indicating a charge compensation mechanism even for stoichiometric samples. The study of the lattice thermal expansion of these samples by HT-XRD from 1873 K to 303 K shows an increase of the thermal expansion when increasing the americium content. A deviation from the literature's recommendations for T > 1373 K is noticed, due to the reduction of the samples at high temperature. No significant influence of the presence of americium is evidenced on the enthalpy increment obtained by drop calorimetry between 600 and 1800 K. On the contrary, higher heat capacities are determined in presence of americium for T > 1100 K, as Am enhances the reduction of the sample. Furthermore, an increase of the solidus temperature is noticed when increasing the Am content, however within the experimental uncertainties. Thanks to the addition of oxygen gauges in the laser heating setup used, different behaviours are noticed for the variation of the O/M ratio during the melting, based on the initial O/M ratio of the samples. Indeed, hypo-stoichiometric mixed oxides are being oxidized, while near- or hyper-stoichiometric samples are being reduced during the melting. This chapter also highlights the needs for additional experimental campaigns, with in particular post melting characterizations to conclude on the final O/M ratio of the samples.

5. EXPERIMENTAL INVESTIGATION OF THE U-PU-AM-O SYSTEM

This chapter is dedicated to the experimental investigations of $U_{1-y-z}Pu_yAm_zO_{2\pm x}$ mixed oxides. First, as the samples of interest were manufactured more than twenty years ago, the determination of their current chemical and structural properties was mandatory. To this aim, characterizations at room temperature were performed to determine the chemical composition, as well as the crystal structure, of the materials by means of EPMA and XRD (section 5.1). The cationic charge distribution was also determined by XANES. After these preliminary characterizations, the lattice thermal expansion of three samples was investigated by HT-XRD from room temperature to 1873 K (section 5.2). Then, the enthalpy increment and the derived heat capacity of $U_{0.70}Pu_{0.28}Am_{0.02}O_{2.00}$ were studied from 600 to 1800 K by drop calorimetry (section 5.3). Finally, solid/liquid phase transitions were determined using a laser heating technique as a function of the Pu and Am contents and O/M ratio (section 5.4).

It is important to keep in mind that some of the studied samples originate from different facilities. Thus, differences in their storage conditions (atmosphere, time) might have induced some variations of their O/M ratio. Moreover, the materials were not always available in both CEA Marcoule (France) and JRC Karlsruhe (Germany). The samples of interest and their respective availability are summarized in Table 5-1. In the case of the PHENIX24 and TRABANT40 samples available at the JRC-Karlsruhe, the structural properties were determined in 2020 by L. Medyk in her Ph.D. thesis, where the samples are referred to as MOX23.6-B and MOX39.4-B [234]. In the case of the TRABANT45 samples, also only available at the JRC Karlsruhe, the O/M ratio was assessed in the ESNII+ project deliverable 7.34 [235], where the corresponding sample is referred to as 14KB0040.

Table 5-1 - Samples used in this work and their availability.

Samples	Composition	Available at CEA Marcoule	Available at JRC Karlsruhe
PHENIX24	$U_{0.76}Pu_{0.235}Am_{0.005}O_{1.983}$	No	Yes
PHENIX29	$U_{0.70}Pu_{0.29}Am_{0.01}O_{1.984}$	Yes	Yes
PHENIX29-OM	$U_{0.70}Pu_{0.29}Am_{0.01}O_{1.998}$	No	Yes
CAPRA4	$U_{0.70}Pu_{0.28}Am_{0.02}O_{2.004}$	Yes	Yes
TRABANT40-A	$U_{0.60}Pu_{0.39}Am_{0.01}O_{1.995}$	Yes	No
TRABANT40-B	$U_{0.60}Pu_{0.39}Am_{0.01}O_{1.978}$	No	Yes
TRABANT40-OM	$U_{0.60}Pu_{0.39}Am_{0.01}O_{1.999}$	No	Yes
TRABANT45	$U_{0.55}Pu_{0.44}Am_{0.01}O_{2.00}$	No	Yes

5.1. CHEMICAL AND STRUCTURAL INVESTIGATIONS AT ROOM TEMPERATURE

In order to study the thermodynamic properties of $U_{1-y-z}Pu_yAm_zO_{2\pm x}$ mixed oxides, the determination of their chemical compositions and structural properties is mandatory. These characterizations were already performed after the manufacturing of the samples in the nineties (see Chapter 3 – section 3.2.2.3). However, changes induced by the storage and/or the self-irradiation may have occurred. The chemical and isotopic compositions determined by EPMA and chemical analyses are presented first. The crystal structures obtained using XRD and the O/M ratios of the samples determined using the assessed lattice parameters are presented. Finally, the cationic charge distributions obtained by XANES analyses are discussed.

5.1.1. Chemical and isotopic compositions

Five batches of $U_{1-y-z}Pu_yAm_zO_{2\pm x}$ samples, with $0.235 < y < 0.44$ and $0.005 < z < 0.02$, were studied. The manufacturing conditions (powder metallurgy or sol-gel) and samples characteristics (dimensions, plutonium content, O/M ratio…) at the date of their manufacturing are described in details in Chapter 3 – section 3.2.2.3. Considering the age of the samples (manufactured between 1996 and 1999) and the initial plutonium isotopic compositions, variations in the initial chemical and isotopic compositions are expected. Thus, prior to any measurement, the isotopic ratios, as well as the uranium, plutonium and americium contents were quantified by chemical analyses (Thermal Ionization Mass Spectrometry and Inductively Coupled Plasma-Mass Spectrometry). The results are given in Appendix E. Because of the presence of ^{241}Pu in the starting powders, a few molar percent of ^{241}Am were produced during the storage by α decay.

Following the determination of the isotopic composition, the cationic homogeneity was checked by EPMA (details in Chapter 3 – section 3.3.3), for PHENIX29, CAPRA4 and TRABANT40 samples. Examples of pseudo-quantitative cartography in Pu content are given in Figure 5-1 for the three samples.

The results obtained for the PHENIX29, CAPRA4 and TRABANT40 samples are similar, with a homogeneous Pu distribution within the matrix. Nevertheless, some uranium-rich and plutonium-rich agglomerates are observed in blue and red respectively. The U-rich zones exhibit a composition close to the one of UO_2, whereas the ones of Pu have a maximum content of 60 wt.%. The sizes of these clusters are around few tens of microns and around few microns for the U-rich and Pu-rich zones, respectively.

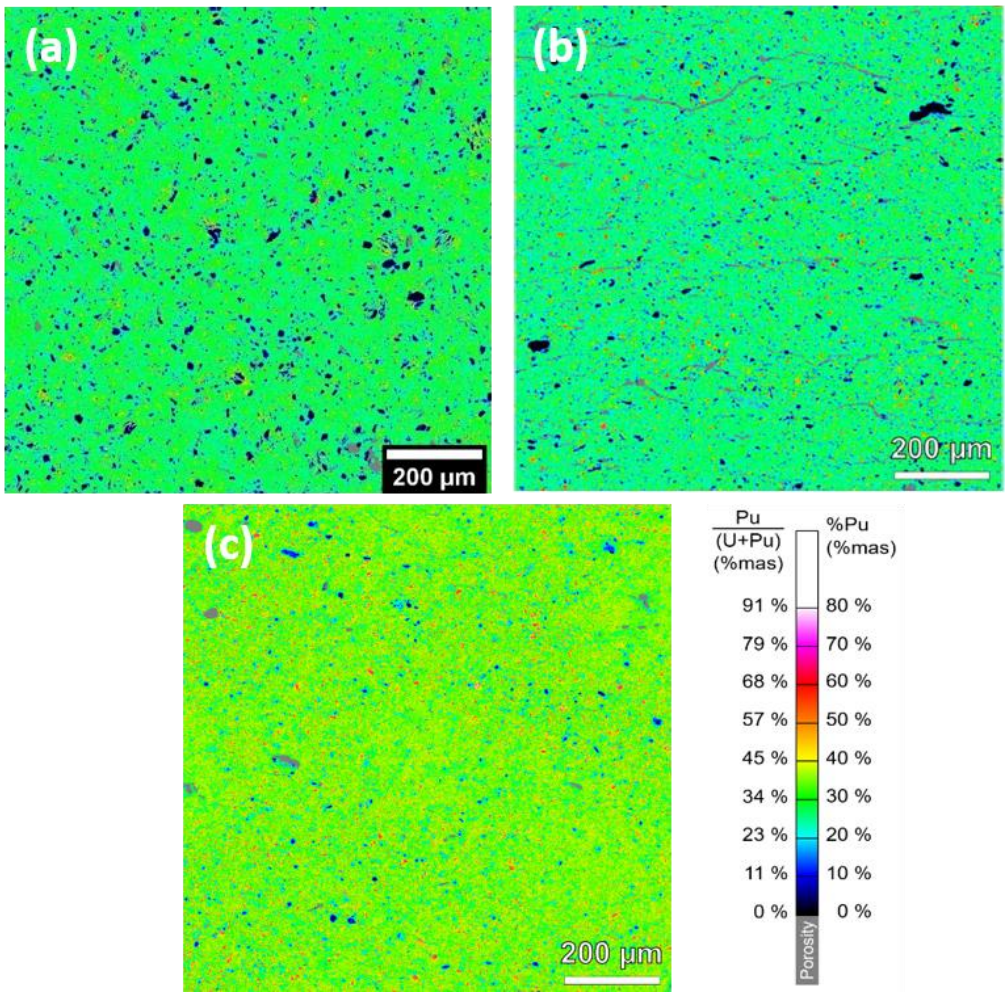

Figure 5-1: Mapping of the Pu distribution (false colours) determined by EPMA on a 1 mm² surface for (a) PHENIX29, (b) CAPRA4 and (c) TRABANT40. The grey spots correspond to porosities, obtained by differences in U and Pu maps.

From these EPMA data, the plutonium content distribution compiled over four or five cartographies (1000 x 1000 µm²) is determined. As an example, the distribution obtained for the PHENIX29 sample is plotted in Figure 5-2.

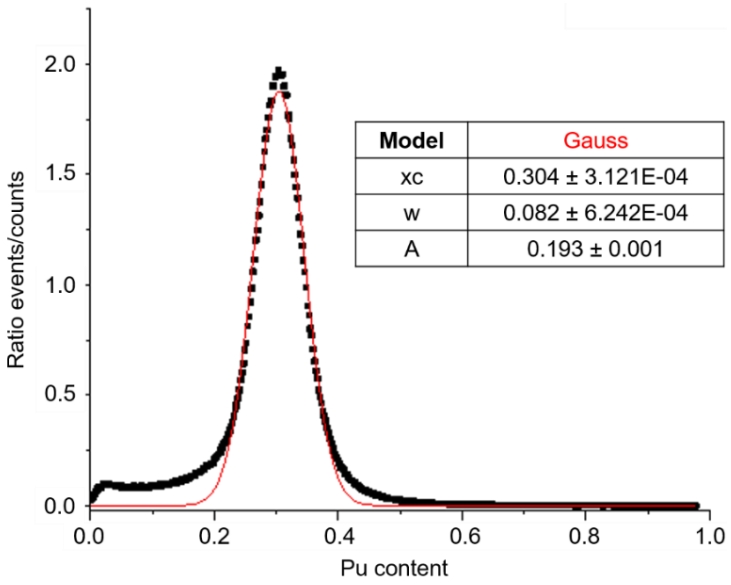

Figure 5-2: Gaussian surface distribution of the Pu content within the PHENIX29 pellet, from [54].

For the three samples, a mono-modal distribution, refined using a Gaussian function, is observed for the $U_{1-y-z}Pu_yAm_zO_{2\pm x}$ matrix composition. The position of the main mode indicates the average plutonium content of the matrix phase. A plateau is observed for $0 < y < 0.17$, representing the presence of U-rich agglomerates. By calculating the area under the curve for this range (beginning of the Gaussian curve), it is possible to quantify the surface fraction of these agglomerates. It is found that the PHENIX29 sample contains 8 % of U-rich clusters. A small proportion (around 5%) of Pu-rich agglomerates is also visible with a higher plutonium content, ranging between 40 and 50%. For the TRABANT40, fewer U-rich or Pu-rich agglomerates are evidenced, resulting in proportions of agglomerates lower than 2 %.

The average Pu contents obtained using the Gaussian distribution and the surface proportions of U- and Pu-rich agglomerates are summarized in Table 5-2 for the three batches.

Table 5-2 – Pu content of the $U_{1-y-z}Pu_yAm_zO_{2\pm x}$ matrix phase and proportions of U- and Pu-rich agglomerates obtained by EPMA for the PHENIX29, CAPRA4 and TRABANT40 samples.

Sample	Pu/(U+Pu) content of the matrix (mass.%)	U-rich agglomerates (surf.%)	Pu-rich agglomerates (surf.%)
PHENIX29	30.4 ± 0.4 %	8 %	5 %
CAPRA4	28.6 ± 0.5 %	5 %	3 %
TRABANT40	38.2 ± 0.3 %	3 %	2 %

For the three samples studied, it can be noticed that the Pu content determined by EPMA analyses differs from the one measured by chemical analyses (see Appendix E). Indeed, in the EPMA analyses, the value obtained corresponds to the composition of the matrix, whereas the value expressed in section 5.1.1 refers to the whole sample, taking also into account the U-rich and Pu-rich zones.

5.1.2. Phases and crystal structure

X-Ray Diffraction was performed on powders from PHENIX29, CAPRA4, TRABANT40, PHENIX29-OM and TRABANT40-OM samples following the procedure described in Chapter 3 – section 3.3.1. The aim was to determine the crystal structure of the phases in presence, as well as to assess the O/M ratio of the $U_{1-y-z}Pu_yAm_zO_{2\pm x}$ matrix at the date of the experiment.

Two fcc structures are systematically observed for all the samples. The diffraction pattern obtained for the PHENIX29 is presented in Figure 5-3 as an example.

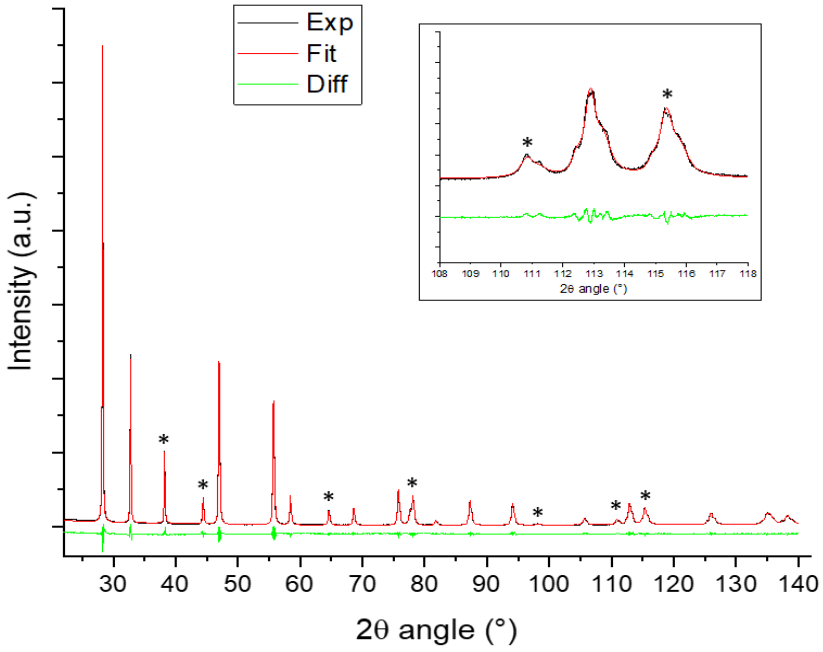

Figure 5-3: XRD pattern on powder of a PHENIX29 sample (*: reflections of the internal Au standard).

The lattice parameters and the proportions of the two phases obtained by Rietveld refinement are summarized in Table 5-3.

Table 5-3 – Refined lattice parameters and estimated O/M ratio of $U_{1-y-z}Pu_yAm_zO_{2\pm x}$ samples.

Samples	Phases	Proportion	Raw lattice parameter (± 0.001) (Å)	Corrected lattice parameter (Kato [107]) (± 0.001) (Å)	O/M ratio (± 0.005)	Global O/M ratio (± 0.005)
PHENIX29	Matrix $U_{1-y-z}Pu_yAm_zO_{2\pm x}$	92 %	5.469	5.453	1.982	1.984
	UO_2	8 %	5.482	-	2.000	
CAPRA4	Matrix $U_{1-y-z}Pu_yAm_zO_{2\pm x}$	95 %	5.463	5.447	2.005	2.004
	UO_2	5 %	5.475	-	2.000	
TRABANT40	Matrix $U_{1-y-z}Pu_yAm_zO_{2\pm x}$	97 %	5.459	5.443	1.995	1.995
	UO_2	3 %	5.482	-	2.000	
PHENIX29-OM	Matrix $U_{1-y-z}Pu_yAm_zO_{2\pm x}$	84 %	5.449		1.998	1.998
	UO_2	16 %	-	-	2.000	
TRABANT40-OM	Matrix $U_{1-y-z}Pu_yAm_zO_{2\pm x}$	100 %	5.442	-	-	1.999

Based on the EPMA results described in 5.1.1, the main phase is attributed to the $U_{1-y-z}Pu_yAm_zO_{2\pm x}$ matrix and the other phase to UO_2 for all the samples except the TRABANT40-OM. Indeed, when combining the XRD data with the results obtained by EPMA, only one matrix phase is visible for this sample. Thus, for all the other samples, the second phase is attributed to the presence of the uranium agglomerates detected (in blue in Figure 5-1). It can be noticed that the lattice parameter reported for the UO_2 phase (a = 5.482 Å) differs from the one recommended (5.470 Å). An oxidation of UO_2 into hyper-stoichiometric UO_{2+x} is excluded as it would lead to a decrease in the lattice parameter. Thus, the most probable explanation is the swelling of UO_2 lattice due to the accumulation of He, generated by Pu α decay present in the surrounding $U_{1-y-z}Pu_yAm_zO_{2\pm x}$ matrix [236].

In the case of the TRABANT40 sample, as no significant proportion of U-rich agglomerates is observed by EPMA, the attribution of this second phase to UO_2 phase can be questioned. The first reason of this choice is the small percentage of second phase determined by Rietveld analyses (< 5 %). The second is the lattice parameter, which is similar to the one of the UO_2 phases of the PHENIX29 and CAPRA4 samples. Moreover, based on the EPMA map and Pu content distribution, no broad distribution or second matrix phase is evidenced.

Because of the aging of the samples, swelling of the lattice with time induced by α decay took place in the materials. This phenomenon is taken into account to correct the obtained lattice parameters using the formula of Kato *et al.* [107], knowing the initial isotopic composition and the storage time of the samples (Table 5-3). For all samples, the swelling of the lattice reached the saturation value, corresponding to an increase of 0.29 % of the initial cell parameter. Using the corrected lattice parameter, the O/M ratio is determined using the relation of Duriez *et al.* linking the fluorite cell parameter, the plutonium content and the deviation from stoichiometry [76]. The plutonium content determined by EPMA for the matrix phase is used for the determination of the O/M ratio. The results obtained for all the phases are given in Table 5-3. By combining the proportions of the phases and the corresponding O/M ratio, the global O/M ratio of the samples is calculated (see Table 5-3).

5.1.3. Cationic charge distribution

The cationic charge distribution was determined by means of X-ray Absorption Spectroscopy, in particular using HERFD-XANES. The samples were prepared using few mg of powder using the procedure described in Chapter 3 – section 3.3.4.2.1 and the measurements were performed at the MARS beamline of the SOLEIL synchrotron (France). The three samples of interest (PHENIX29, CAPRA4 and TRABANT40) were studied during two different experimental campaigns, with spectra collected at the U M_4, Pu M_4 and Am M_5 edges. The spectra were acquired at room temperature under atmospheric pressure.

5.1.3.1 Results

As the XANES spectra of the PHENIX29 were already described in the Ph.D. work of L. Medyk for the U M_4 edge [54], only a brief summary is given here. For this sample, no spectrum could be recorded at the Am edges.

For all the edges, the spectra of the three samples are compared to the reference compounds presented in Chapter 3 – section 3.3.4.3 (UO_2 for U^{4+}, U_4O_9 for $U^{4+/5+}$ and U_3O_8 for $U^{5+/6+}$ [55], [213], PuO_2 for Pu^{4+}, $PuPO_4$ for Pu^{3+} [229], AmO_2 for Am^{4+} and $U_{0.90}Am_{0.10}O_2$ for Am^{3+} [55]).

The XANES spectra collected at the U M_4, Pu M_4 and Am M_5 edges are presented in Figure 5-4.

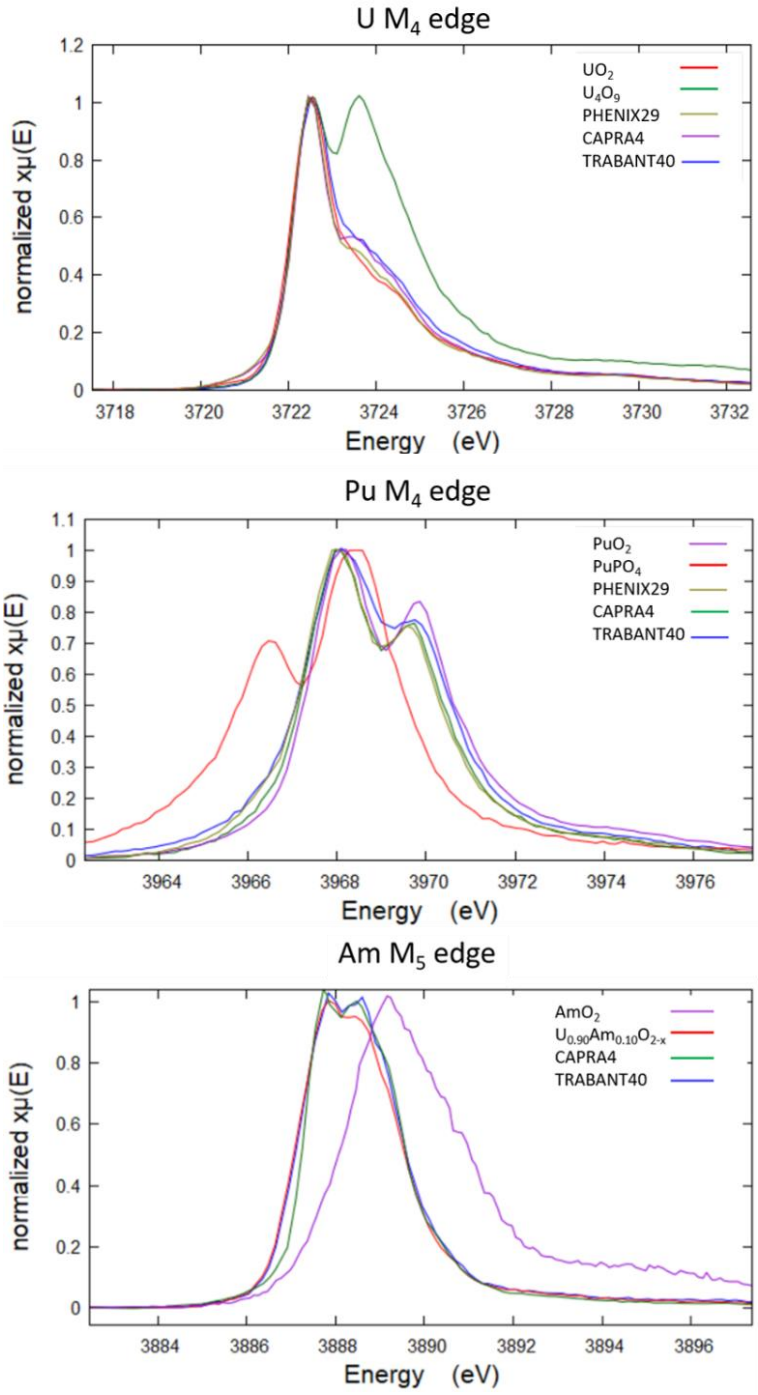

Figure 5-4: XANES spectra collected at the U M_4, Pu M_4 and Am M_5 edge for the PHENIX29, CAPRA4 and TRABANT40 samples and their references.

When looking at the U M_4 edge, the white line positions (maxima of the spectra) of the PHENIX29, CAPRA4 and TRABANT40 samples correspond to the one of UO_2. No contribution of U_3O_8 (not represented here) is noticed, thus no U^{6+} is present in the samples. Moreover, the shoulder observed around 3723.8 eV, corresponding to the second maximum of the U_4O_9, attributed to U^{5+}, evidences the presence of pentavalent uranium in the samples. Thus, a mixed valence U^{4+}/U^{5+} is systematically observed for the three samples.

For the Pu M_4 edge, a shoulder is observed around 3866.2 eV, indicating the contribution of trivalent Pu. This contribution is also highlighted by the diminution in intensity of the peak

located 3870 eV, compared to the one of PuO_2. Thus, a reduction of the plutonium, with the presence of trivalent Pu, is indicated here. A mixed valence Pu^{3+}/Pu^{4+} is systematically observed for the three samples.

Finally, for the Am M_5 edge, the white line positions of the two samples are very close or equal to the one of the Am^{3+} cation.

The proportions of the various cations are determined by linear combination fitting of the reference spectra and are given in Table 5-4, as well as the O/M ratio with M = U, Pu or Am, obtained for the three samples. For uranium, the O/U ratios obtained with the respective proportions of the cations are hyper-stoichiometric (> 2.00) for the three samples. On the contrary, for plutonium, the O/Pu ratios are lower than 2.00. When looking at the americium oxidation state, americium is present entirely under its trivalent state Am^{3+}. Thus, for the three samples studied here, the O/Am ratio is always equal to 1.50.

Table 5-4 - Proportions of the cations of the probed elements and corresponding O/M ratios, calculated using the Pu content determined by EPMA, compared to the ones determined by XRD.

Sample	U M_4 edge			Pu M_4 edge		Am M_5 edge	
	U^{4+} (%)	U^{5+} (%)	U^{6+} (%)	Pu^{4+} (%)	Pu^{3+} (%)	Am^{4+} (%)	Am^{3+} (%)
PHENIX29	94.9 ± 1.0	5.10 ± 1.0	0	74.7 ± 2.0	25.3 ± 2.0	0 ± 0.3	100 ± 0.3
CAPRA4	90.5 ± 1.2	9.50 ± 1.2	0	86.7 ± 1.8	13.3 ± 1.8	0 ± 0.3	100 ± 0.3
TRABANT40	89.7 ± 0.6	10.3 ± 0.6	0	90.1 ± 0.8	9.90 ± 0.8	0 ± 0.3	100 ± 0.3

Sample	O/U	O/Pu	O/Am	O/M ratio determined by XANES (±0.01)	O/M ratio determined by XRD (±0.005)
PHENIX29	2.03	1.87	1.50	1.98	1.984
CAPRA4	2.05	1.93	1.50	2.00	2.004
TRABANT40	2.05	1.95	1.50	2.00	1.995

By combining the results of the O/U, O/Pu and O/Am ratios in Table 5-4 and the Pu content determined by EPMA, the following O/M ratio were obtained: 1.98 for PHENIX29, 2.00 for CAPRA4 and 2.00 for TRABANT40. These data correspond to the global O/M ratio at the scale of the pellet, taking also into account the heterogeneities (uranium-rich and plutonium-rich agglomerates evidenced by EPMA). A good agreement is found with the O/M ratios determined using the lattice parameters obtained by X-Ray Diffraction, reported here in Table 5-4.

5.1.3.2 Discussions

As evidenced in Table 5-4, small proportions of U^{5+} and Pu^{3+} systemically coexist in the materials, even for stoichiometric samples such as CAPRA4 or TRABANT40. Moreover, Am^{3+} is also observed in these samples. This observation implies that an O/M ratio of 2.00 does not necessarily correspond to cations only in their tetravalent state. It appears that a charge compensation mechanism occurs here, as already discussed by Osaka *et al.* [237]. Indeed, as the oxygen potential of AmO_{2-x} is high, tetravalent americium is unstable and americium will be present only in its trivalent oxidation state [74]. Thus, Osaka *et al.* expect that once all the americium is reduced to Am^{3+}, plutonium will start to be reduced as well [37]. For a mixed oxide of formula $U_{1-y-z}Pu_yAm_zO_{2-x}$, two domains are evidenced by their model: $\frac{O}{M} < 2 - \frac{z}{2}$ and $\frac{O}{M} > 2 - \frac{z}{2}$. For the first region, americium is supposed to be trivalent, while the uranium is expected to remain tetravalent. On the contrary, for the second region, the interactions between uranium and americium are predominant, resulting in trivalent americium and pentavalent uranium to maintain the electroneutrality [237]. The regions of the model and the corresponding cations expected in this work are compared to the cations observed experimentally in Table 5-5. A disagreement between the model and the results of the PHENIX29 sample is noticed here for the uranium cations. Indeed, in this work, U^{5+} is observed in the three samples. For the plutonium cations, a disagreement is observed for the CAPRA4 and TRABANT40 samples. Indeed, a partial reduction of Am in Am^{3+} is stated by Osaka *et al.*, contrarily to the fact that in this work, all the americium present in the sample is trivalent. For these two samples, trivalent plutonium is also observed. As the model of Osaka *et al.* was built on several hypotheses and few experimental data, care should be taken when using it.

Table 5-5 – Comparison between the cations expected by the model of Osaka *et al.* [37], [237] and the ones determined experimentally.

Sample	2-z/2	Domain	Expected cations according to Osaka et al. [37], [237]	Cations observed experimentally in this work
PHENIX29 (O/M = 1.98, z = 0.01)	1.995	$O/M < 2 - \frac{z}{2}$	U^{4+} Pu^{4+} Pu^{3+} Am^{3+}	**U^{5+}** U^{4+} Pu^{4+} Pu^{3+} Am^{3+}
CAPRA4 (O/M = 2.00, z =0.02)	1.99	$O/M > 2 - \frac{z}{2}$	U^{5+} U^{4+} Pu^{4+} Am^{3+}	U^{5+} U^{4+} Pu^{4+} **Pu^{3+}** Am^{3+}
TRABANT40 (O/M = 2.00, z = 0.01)	1.995	$O/M > 2 - \frac{z}{2}$	U^{5+} U^{4+} Pu^{4+} Am^{3+}	U^{5+} U^{4+} Pu^{4+} **Pu^{3+}** Am^{3+}

In order to explain the simultaneous presence of U^{5+} and Pu^{3+}/Am^{3+}, the EPMA and XRD results can be used. The example of the TRABANT40 sample is taken here but the same explanation is valid for the CAPRA4 and PHENIX29 samples.

The proportions of U- and Pu-rich agglomerates, given in Table 5-2, are respectively 3 and 2 % of the surface. From this, the matrix phase is admitted to represent 95 % of the scanned surface

of the sample. The porosity is excluded from this analysis as it does not contribute to XANES and XRD signals.

Considering first the case of plutonium, with y = 0.382, the plutonium represents 36.3 % of the surface of the matrix phase. The same calculation is performed for the Pu-rich agglomerates, for which the Pu content is assumed to be around 0.70, resulting in 1.4 % of the surface of the agglomerates. At the scale of the scanned surface, summing the plutonium of the matrix and of the agglomerates leads to a total surface proportion of 37.7 %. Thus, the agglomerates represent 3.7 % of the whole plutonium for the TRABANT40 sample. Admitting that the plutonium in the agglomerates would be purely trivalent (the most extreme hypothesis) and knowing that the matrix phase is stoichiometric (see section 5.1.1 - Table 5-3) and does not contain any Pu^{3+} ions as stated in the model of Osaka *et al.*, the maximum amount of Pu^{3+} present in the sample would be 3.7 %. This result is not in agreement with the proportion of Pu^{3+} (9.90 ± 0.8 %) given in Table 5-4.

The same reasoning can be applied to uranium. Admitting that the uranium in the U-rich agglomerates (assumed to contain 90 % of U) would be purely pentavalent, the total amount of U^{5+} in the sample would be 4.4 %. However, according to Table 5-4, pentavalent uranium represents 10.3 % of the total uranium. The XRD results obtained in section 5.2.2 also invalidate the presence of U^{5+} in the U-rich agglomerates. Indeed, admitting that the second phase of U-rich agglomerates, is UO_{2+x}, a decrease in the lattice parameter of the UO_2 phase, linked to the oxidation, would be observed. However, this statement is not supported by the lattice parameters determined in section 5.2.2, as an increase is noticed.

In conclusion, the simultaneous existence of U^{5+} and Pu^{3+}/Am^{3+} does not originate from the U- and Pu-rich agglomerates and is thus linked to the matrix phase, highlighting a peculiar behaviour of the $U_{1-y-z}Pu_yAm_zO_{2\pm x}$ oxides.

5.1.4. Conclusion

The chemical compositions and the structures of the three samples (PHENIX29, CAPRA4 and TRABANT40) were determined in this work. For these samples, the metals distribution was found to be homogeneous by EPMA, with few uranium-rich and plutonium-rich agglomerates.

When collecting XRD patterns at room temperature, two phases were observed: one matrix $U_{1-y-z}Pu_yAm_zO_{2\pm x}$ phase and one UO_2 phase, in agreement with the agglomerates observed by EPMA. The lattice parameters determined in this work were corrected to take into account the self-irradiation of the samples and used to calculate the O/M ratio. Finally, the cationic charge distribution determined by XANES evidenced the presence of a mixture of cations, with simultaneously U^{5+} and Pu^{3+}/Am^{3+}. This observation highlighted a charge compensation mechanism for near-stoichiometric samples. The O/M ratios determined by XAS were found to be in agreement with the ones determined by XRD. The chemical compositions calculated in this work are summarized in Table 5-6 for all the samples studied in this thesis, as well as their availability depending on the facilities.

Once the chemical composition and the structural properties are known at room temperature, the study of thermodynamic properties such as the lattice thermal expansion is possible, as described in the next section.

Table 5-6 - Samples composition and availability.

Sample	Composition (ICP-MS, TIMS, DRX, XANES)
PHENIX24	$U_{0.76}Pu_{0.235}Am_{0.005}O_{1.983}$
PHENIX29	$U_{0.70}Pu_{0.29}Am_{0.01}O_{1.984}$
PHENIX29-OM	$U_{0.70}Pu_{0.29}Am_{0.01}O_{1.998}$
CAPRA4	$U_{0.70}Pu_{0.28}Am_{0.02}O_{2.004}$
TRABANT40-A	$U_{0.60}Pu_{0.39}Am_{0.01}O_{1.995}$
TRABANT40-B	$U_{0.60}Pu_{0.39}Am_{0.01}O_{1.978}$
TRABANT40-OM	$U_{0.60}Pu_{0.39}Am_{0.01}O_{1.999}$
TRABANT45	$U_{0.55}Pu_{0.44}Am_{0.01}O_{2.00}$

5.2. LATTICE THERMAL EXPANSION

In this work, three materials (PHENIX29, CAPRA4 and TRABANT40) were studied using in-situ High-Temperature X-Ray Diffraction. The evolution of their lattice parameter with temperature is described in this part.

5.2.1. Experimental determination

HT-XRD measurements were performed at the ATALANTE facility of CEA Marcoule (France), following the procedure described in Chapter 3 - section 3.3.5. A reducing atmosphere of He/H_2 4% + 55 ppm H_2O (pO_2 = $1x10^{-28}$ atm) was used. The oxygen inside the experimental chamber was monitored by an oxygen gauge, resulting in an oxygen potential ranging between -489.2 $kJ.mol^{-1}$ at 1873 K and -494.7 $kJ.mol^{-1}$ at 923 K. The thermal treatment applied to the samples and the conditions of the diffraction patterns are described in Appendix D.

5.2.2. Results

The data analysis procedure described in Chapter 3 – section 3.3.5.2 is applied here. The diffractions patterns obtained for the PHENIX29 sample before the thermal treatment at room temperature, at 1873 K and after the thermal treatment at room temperature are plotted in Figure 5-5. For the three samples, several fcc structures are observed over the whole temperature range.

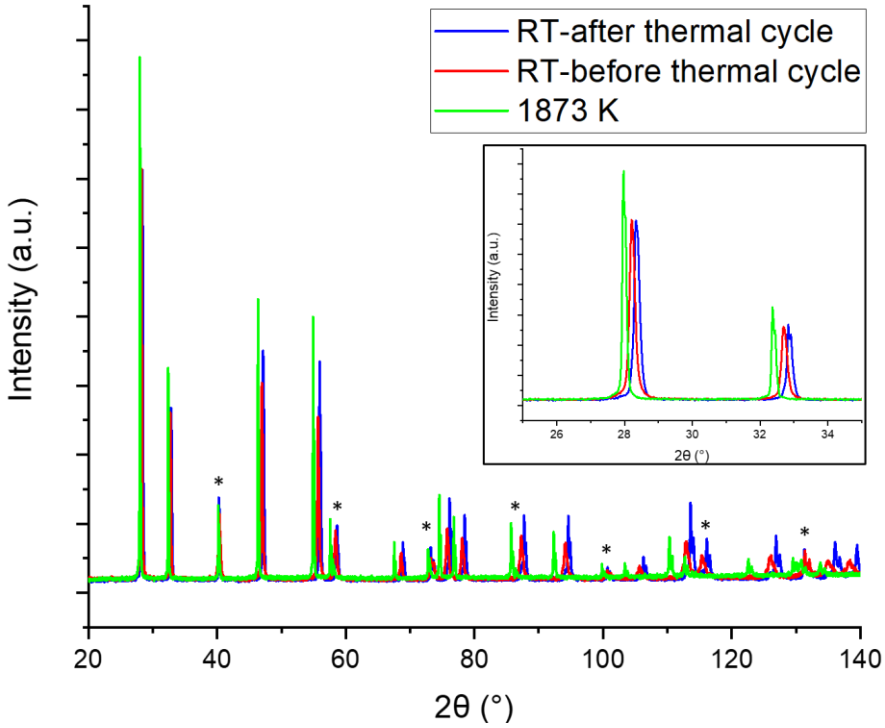

Figure 5-5: Diffraction patterns acquired at room temperature before the thermal cycle (in red), after the thermal cycle (in blue) and at 1873 K (in green) for the PHENIX29 sample (*: XRD reflections of the Mo strip).

The Figure 5-6 represents the iso-intensity map of the (111) peak of the fcc structure as a function of the temperature during cooling. A shift towards higher angles, corresponding to a decrease of the lattice parameter, is evidenced when decreasing the temperature.

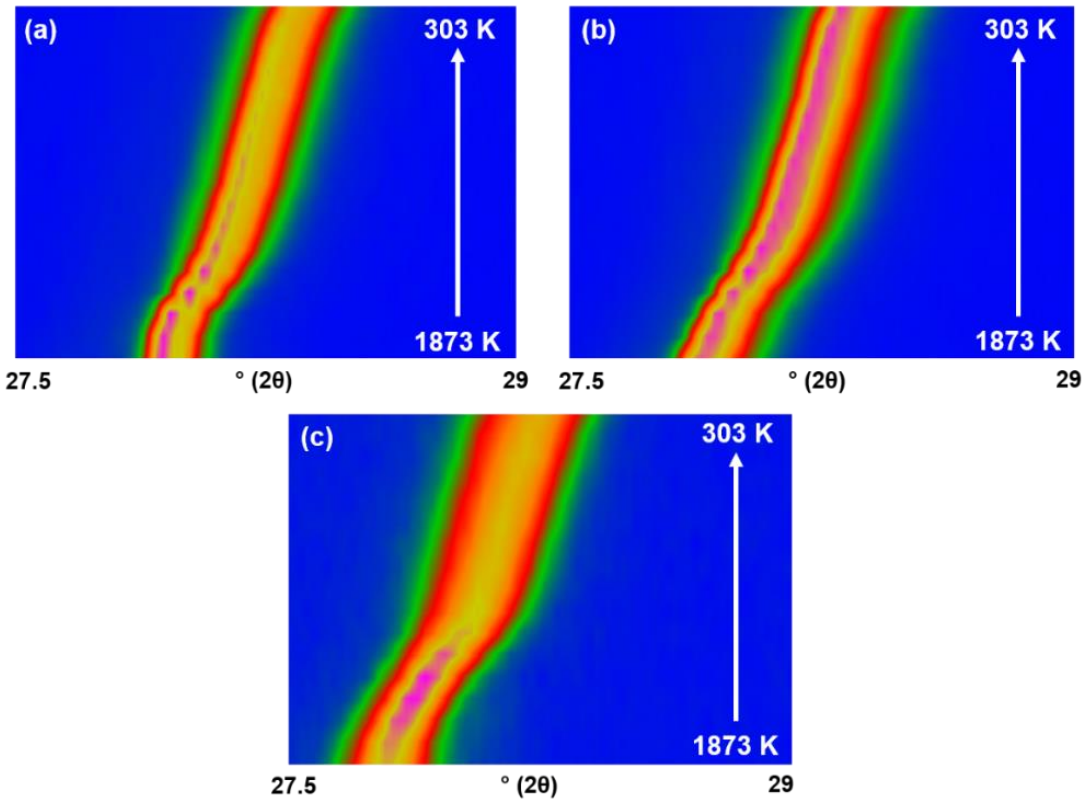

Figure 5-6: Iso-intensity map of the (111) peak of the fcc structure between 1873 and 303 K for (a) PHENIX29, (b) CAPRA4 and (c) TRABANT40 samples.

No demixtion phenomenon related to a miscibility gap in the fcc phase is observed for these three materials during cooling. Among the detected phases, one is identified as the main phase, as its proportion is 90 % for the PHENIX29 and CAPRA4 sample and 70 % for the TRABANT40. Possible explanations for the presence of residual fcc phases are discussed in the following section.

The variation of the lattice parameter of the main fcc structure with temperature is reported in Figure 5-7 for the PHENIX29, CAPRA4 and TRABANT40 samples and the corresponding lattice parameters are reported in Appendix F. For this work, the experimental uncertainties on the lattice parameter and temperature are ± 0.003 Å and ± 15 K respectively.

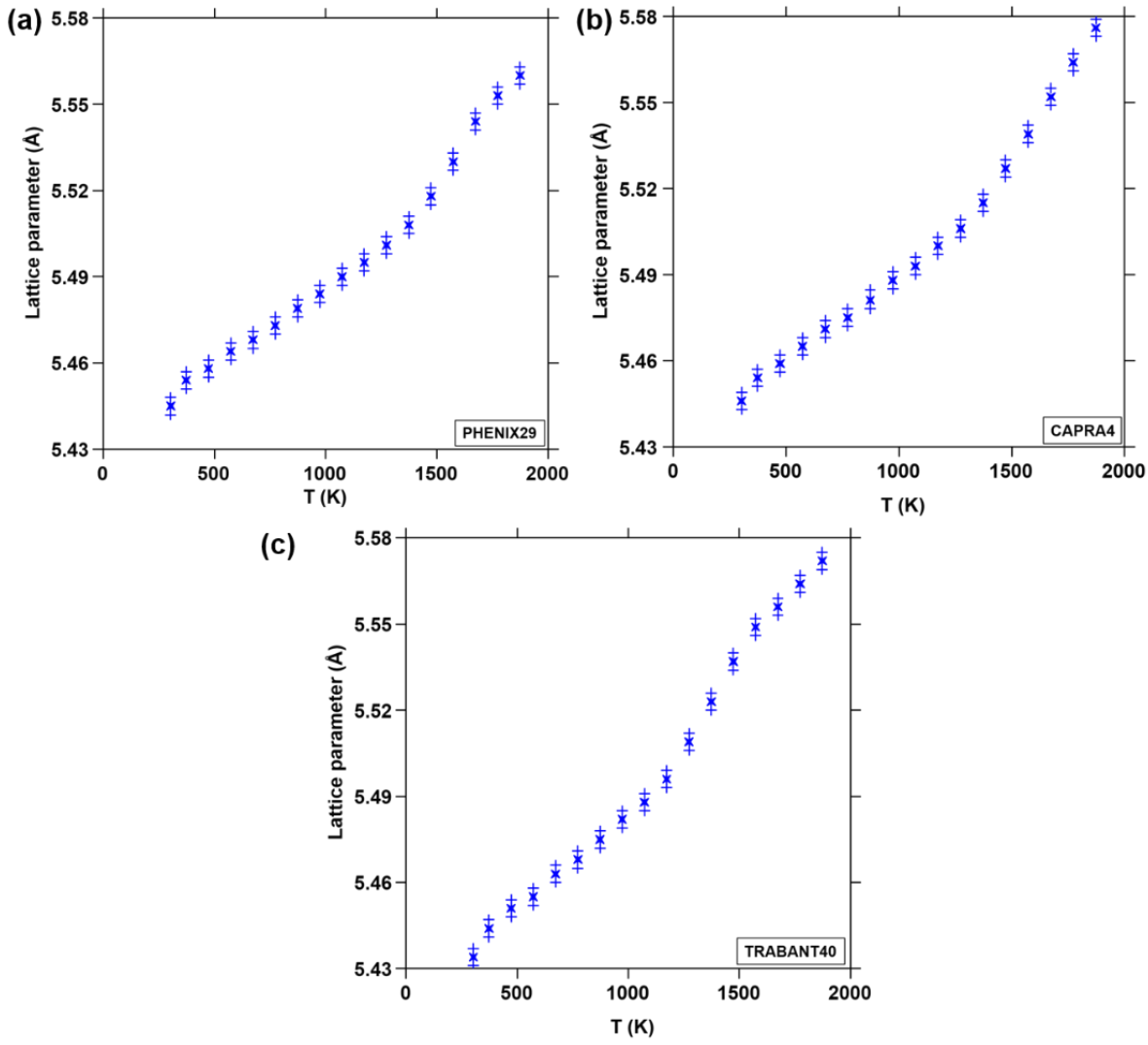

Figure 5-7: Variation of the lattice parameters as a function of temperature for (a) PHENIX29, (b) CAPRA4, (c) TRABANT40 samples. The uncertainty on T corresponds to the symbol size.

The lattice thermal expansions of the three samples derived from these lattice parameters are plotted in Figure 5-8. The results are compared to the recommendations of D.G. Martin [112] and Kato *et al.* [238]. In the case of the PHENIX29 (initial O/M ratio = 1.984), the two recommendations are used applying the proposed corrections to take into account the O/M ratio.

For the three compositions, a deviation from the recommendations of D.G. Martin and Kato *et al.* is observed: above 1500 K for the PHENIX29, above 1300 K for the CAPRA4 and on the

whole temperature range for the TRABANT40. This observation is assumed to originate from the reduction of the samples occurring at high temperature. Indeed, in the two recommendations, the O/M ratio is supposed to be constant during the whole experiment and equal to the initial O/M ratio before thermal treatment for D.G. Martin and Kato *et al.*. However, as evidenced in Chapter 2 with the oxygen potential data, a deviation from stoichiometry is occurring at high temperature. Moreover, the study of D.G. Martin does not take into account the presence of americium, which could explain the discrepancies observed. Discussions are proposed in the next section in order to determine the effect of the O/M ratio and americium content on the lattice thermal expansion.

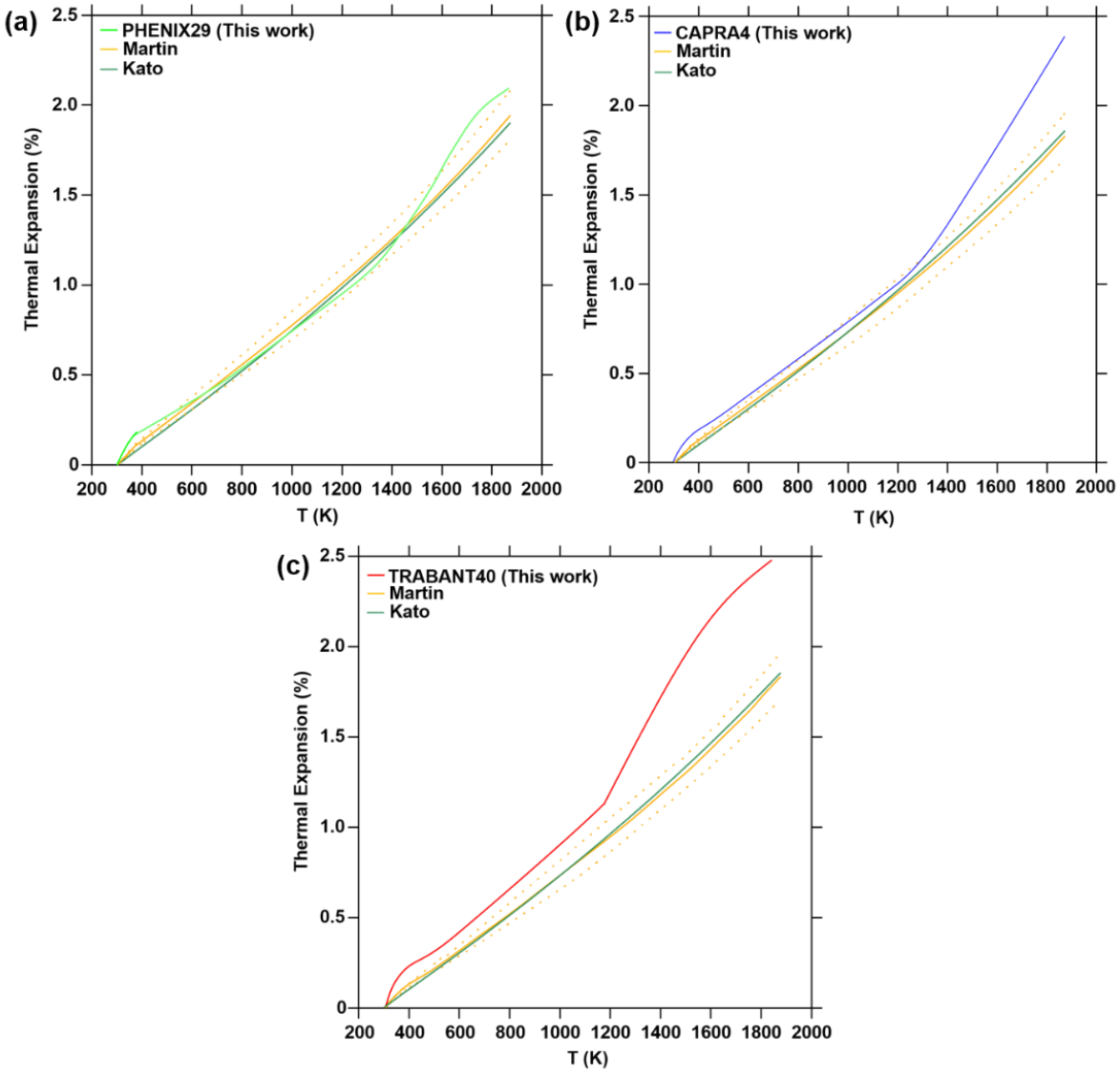

Figure 5-8: Thermal expansions of the matrix for PHENIX29, CAPRA4 and TRABANT40, from 300 to 1873 K, compared to the recommendation of D.G. Martin [10] and Kato *et al.* [238]. The dashed lines represent the uncertainties on the recommendation of D. G. Martin.

5.2.3. Discussion

For the three samples, the presence of residual fcc structures (one for PHENIX29 and TRABANT40 and two for CAPRA4) is noticed on the diffraction patterns obtained during cooling. The first residual phase is observed during cooling on the whole temperature range for all, whereas the second residual phase appears at 1373 K during cooling for the CAPRA sample.

The proportions of these phases are constant and approximately equal to 5 %.

These residual phases are probably originating from an interaction between the sample and the heating strip occurring at high temperature. This phenomenon could induce some constraints and result in two layers of material, diffracting at different angles and thus leading to two phases of different lattice parameters on the diffraction patterns.

Another explanation could be an asymmetric dilatation of the heating strip with the temperature originating from slight errors in the positioning of the heating strip. This could lead to different apparent lattice parameters observed but corresponding to two different positions of the powder and thus to two different sample displacement corrections.

Moreover, they could also originate from the inhomogeneity of the samples due to agglomerates evidenced in section 5.1.1, in particular when two phases are observed before thermal treatment.

Finally, a possible explanation for this phase is the presence of impurities originating from previous experiments on the heating strip. Indeed, the same lattice parameters were observed for the residual phase, evidencing that some material could be encrusted in the ribbon, in particular for the CAPRA4 patterns with residual impurities of TRABANT40. Considering the high temperature at which the phase is already observed here (1873 K), it is not possible to assume that the apparition of the second phase is linked to a demixtion process related to the existence of a miscibility gap in the fcc phase.

Unfortunately, due to a lack of time, it was not possible to reproduce these experiments. Based on the constant proportions of the residual phases (approximately 5 %), the presence of a residual impurity is the most likely. For all these reasons, the residual phases observed for the PHENIX29, CAPRA4 and TRABANT40 samples are not taken into account in this study as they are assumed to be an artefact of the measurements and the preparation.

In order to better understand the difference observed with Martin's recommendation for $T > 1373$ K, the deviation from the stoichiometry is determined thanks to thermodynamic calculations. For each temperature, the O/M ratio of the samples is calculated assuming the equilibrium with the gas atmosphere. The calculations were performed using the TAF-ID database V13 [195] for the U-Pu-Am-O system. For the three samples, the variation in the O/M ratio with the temperature is computed in Figure 5-9.

During cooling, from 1873 to 1273 K, the O/M ratio of the three samples is increasing, up to around 1.99. Below this temperature, a slow increase is noticed down to 873 K where it reaches 2.00. It can be noticed that during the same thermal treatment, the TRABANT40 (1.892 at 1873 K) is more reduced than the CAPRA4 (1.915 at 1873 K) and PHENIX29 (1.921 at 1873 K) samples. Among these two, the CAPRA4 sample presents lower O/M ratios than the PHENIX29.

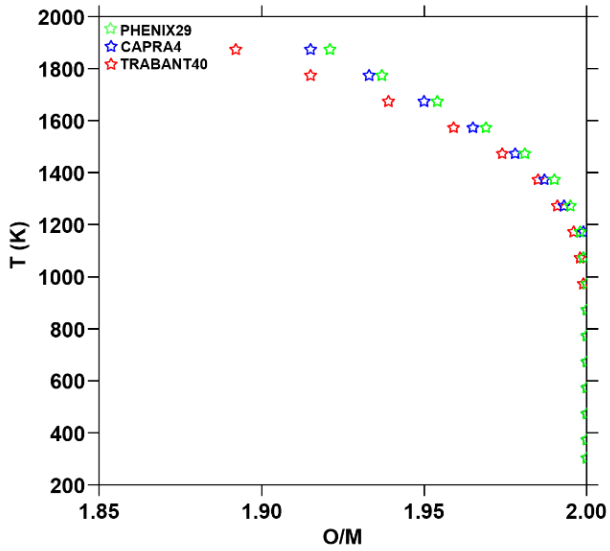

Figure 5-9: Variation in the O/M ratio of the samples with temperature (He/H_2 4% + 55 ppm H_2O).

As evidenced in Chapter 2 – section 2.2.3 and quantified with the calculations presented in Figure 5-9, a reduction of the sample is occurring at high temperature and needs to be taken into account in the lattice thermal expansion. To this aim, the recommendation of Kato *et al.* is used but in this case, the deviation from stoichiometry x is varying in the equation at each temperature according to the calculations of Figure 5-9. The resulting calculated thermal expansions are compared to the ones obtained in this work in Figure 5-10.

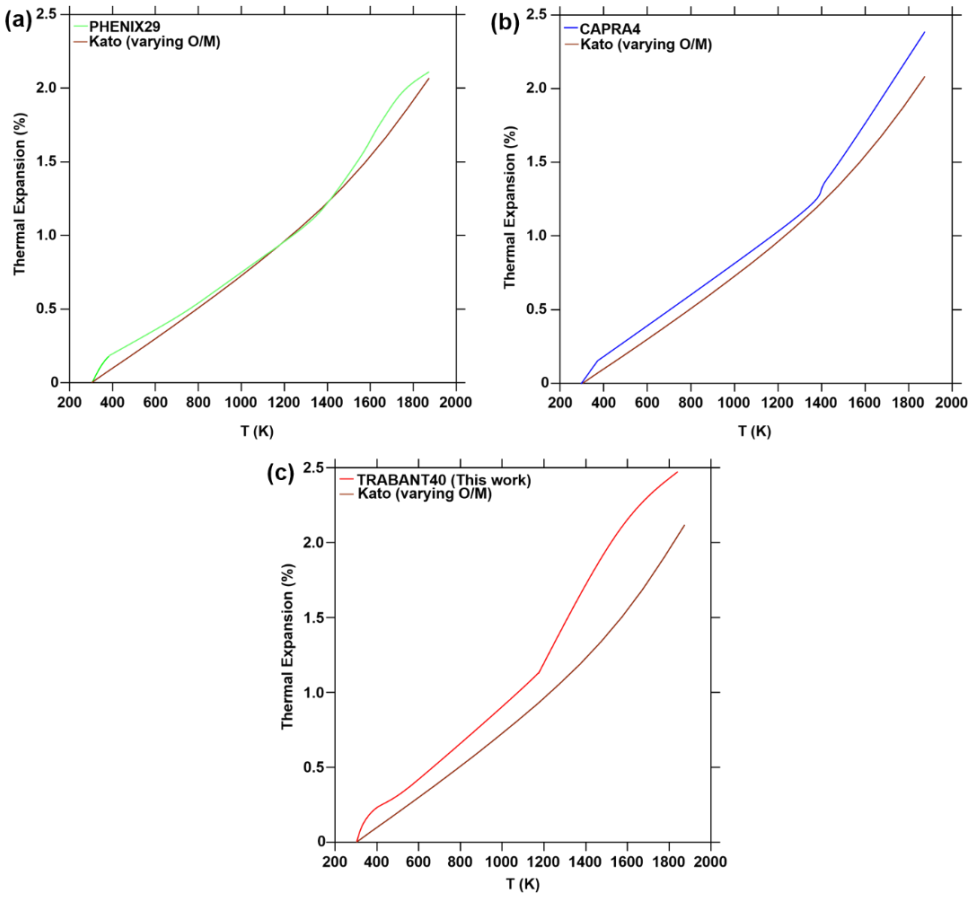

Figure 5-10: Thermal expansions of (a) PHENIX29, (b) CAPRA4 and (c) TRABANT40, compared to the recommendation of Kato *et al.* with varying O/M ratio [238].

A better agreement is noticed for the PHENIX29 on the whole temperature range and from room temperature to 1400 K for the CAPRA4 sample. On the contrary, for the TRABANT40, the thermal expansion calculated from Kato et al. still differs much from the one determined here, with too low values. Indeed, in their work, Kato et al. performed their experiments for a minimum O/M ratio of 1.97, whereas in this study the minimum value reached was 1.89. This confirms that the equation given by Kato et al. cannot be used in this study and cannot be extrapolated to lower values.

Another possible explanation for the deviation from Martin's recommendation is the presence of americium in the sample. Prieur *et al.* studied the thermal expansion of two materials, Am-MOX ($U_{0.74}Pu_{0.22}Am_{0.035}Np_{0.005}O_{2-x}$) and Np-MOX ($U_{0.74}Pu_{0.22}Am_{0.02}Np_{0.02}O_{2-x}$), from room temperature to 2023 K [124] in He/H_2 5% + 15 ppm H_2O. In their work, no deviation from the recommendation of Martin for UO_2 was reported up to 1700 K, showing that the O/M ratio remained constant up to this temperature. Above this temperature, only small differences were noticed, with a higher thermal expansion in the case of the Np-MOX sample. Based on these observations, it appears that americium has an influence on the thermal expansion only at high temperatures (T > 1700 K). However, in the study performed here, deviation from Martin's recommendation occurs at lower temperature (T > 1373 K). As previously explained, the variation of the O/M ratio has an effect on this deviation. It is thus difficult to decorrelate the influence of the americium from the effect of the O/M ratio. The variation of the lattice parameters with temperature is plotted in Figure 5-11 for the PHENIX29 and CAPRA4 samples.

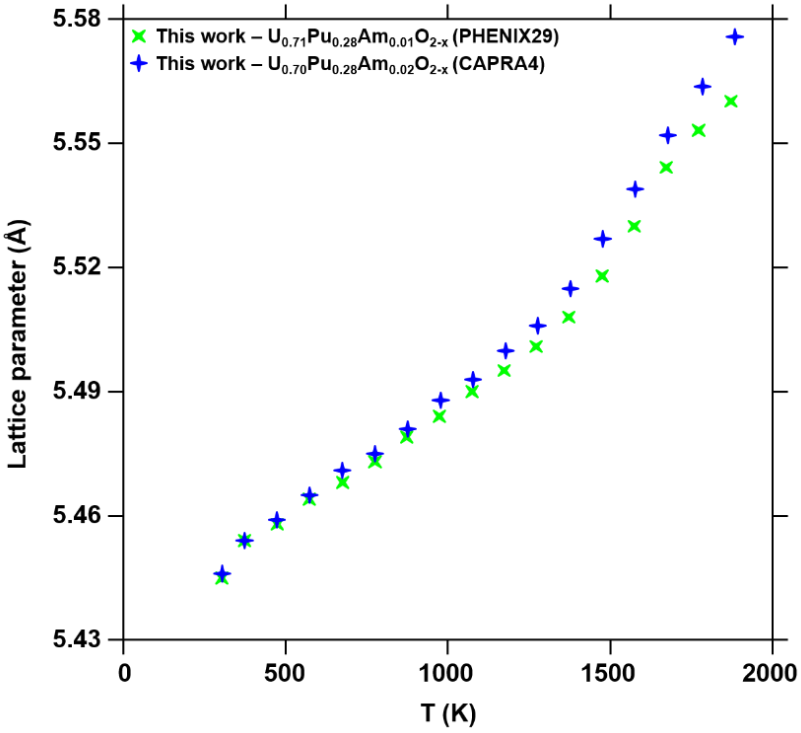

Figure 5-11: Lattice parameters of the PHENIX29 and CAPRA4 samples as a function of the temperature.

Higher lattice parameters are found in the case of the CAPRA4 sample, in agreement with lower O/M ratios compared to the ones of the PHENIX29 sample. This tendency is explained by the larger proportion of americium in the CAPRA4 (2 mol.%) than in the PHENIX29 (1 mol.%). When increasing the temperature, americium dioxide tends to become hypo-stoichiometric above 1100 K. Thus, the more americium in the sample, the lowest O/M ratio in temperature.

The presence of americium in the sample then leads to higher thermal expansions compared to $U_{1-y}Pu_yO_{2\pm x}$ samples. However, this observation is in disagreement with Truphémus [239], who determined that the americium content (< 1 mol.%) does not have any impact on the lattice parameters.

As evidenced in Figure 5-8 and Figure 5-10, the thermal expansions a measured in this work for the PHENIX29, CAPRA4 and TRABANT40 samples exhibit some discrepancies with the recommendations of D.G. Martin and Kato *et al.*. Thus, new parameters reported in Table 5-7 for the equation **(5.1)** are proposed in this work. As the thermal expansions of the PHENIX29 and CAPRA4 are similar for T < 1373 K, the same equation can be used. The fits obtained are presented in Figure 5-12.

$$a\ (\%) = b_1 + b_2 \times T - b_3 \times T^2 + b_4 \times T^3 \qquad \textbf{(5.1)}$$

Table 5-7 - Parameters of Equation (5.1) for the thermal expansion of PHENIX29, CAPRA4 and TRABANT40 samples.

		b_1	b_2	b_3	b_4
T < 1373 K	PHENIX29	-2.7x10^{-3}	10.6x10^{-6}	2.95x10^{-10}	3x10^{-13}
	CAPRA4				
	TRABANT40	-2.6x10^{-3}	11.0x10^{-6}	2.4x10^{-10}	8.5x10^{-13}
T > 1373 K	PHENIX29	-6.5x10^{-3}	14x10^{-6}	2.42x10^{-9}	1.5x10^{-12}
	CAPRA4		14x10^{-6}	2.5x10^{-9}	2x10^{-12}
	TRABANT40		18x10^{-6}	1.8x10^{-9}	8.0x10^{-13}

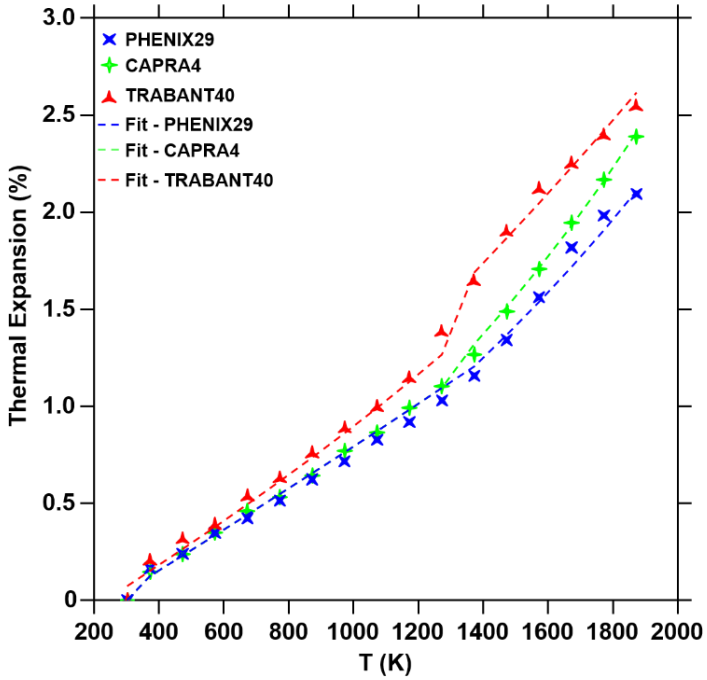

Figure 5-12: Fits of the thermal expansions of PHENIX29, CAPRA4 and TRABANT40 samples.

These equations apply to the Pu and Am contents, as well as O/M ratios, studied in this work and determined by the atmosphere used in the heat treatment. Indeed, as previously explained, variations of the atmosphere (more or less reducing) result in variations of the O/M ratio more or less important than in this work and thus could lead to changes in the thermal expansions.

5.2.4. Conclusion

The thermal expansions of the PHENIX29, CAPRA4 and TRABANT40 samples were measured by HT-XRD from 1873 K to room temperature. An increase of the lattice parameter was observed when increasing the temperature, corresponding to the dilatation of the crystal structure of the materials. The corresponding thermal expansions were compared to the recommendation of D.G. Martin commonly used in the literature [112]. A deviation was noticed for T > 1373 K. This deviation was explained by the reduction of the sample at high temperature, as evidenced with the calculated O/M ratios. The thermal expansions obtained in this work were compared to the recommendation of Kato *et al.* [238], taking into account the plutonium content and O/M ratio. A better agreement was noticed, although the thermal expansions obtained using the equation of Kato *et al.* are still underestimated. Deviations from these recommendations could be explained by the americium present in the samples studied here. Indeed, the presence of americium results in lower O/M ratios compared to $U_{1-y}Pu_yO_{2\pm x}$ samples due to Am in its trivalent state. Thus, based on the higher deviation from stoichiometry, higher thermal expansions were measured for $U_{1-y-z}Pu_yAm_zO_{2\pm x}$. In this work, new correlations for the thermal expansion were also proposed. The same parameters were used to fit the results for T < 1373 K, independent of the Pu, Am contents and O/M ratios, whereas differences were considered for higher temperatures.

Additional studies over the whole plutonium and americium contents range are necessary to confirm the validity of the recommendations proposed in this work. In addition, further TGA experiments are also needed to correlate the variation of the O/M ratio with the thermal expansion.

5.3. ENTHALPY INCREMENT AND HEAT CAPACITY

Two thermodynamic properties of interest are the enthalpy increment and the related heat capacity. To this day, no experiments were performed on $U_{1-y-z}Pu_yAm_zO_{2\pm x}$ materials. In this work, enthalpy increments of a CAPRA4 sample ($U_{0.70}Pu_{0.28}Am_{0.02}O_{2.00}$) were measured by drop calorimetry from 585 to 1790 K. The experimental results are presented in this section, as well as the heat capacity obtained by derivation of the enthalpy function.

5.3.1. Experimental procedure

Enthalpy increments $H(T) - H(298.15\,K)$, within 585 < T < 1790 K, were measured using a drop calorimetry technique, as described in Chapter 3 – section 3.3.7. Fragments of pellets ranging from 25 to 57 mg were used. The experiments were performed in a glovebox under inert atmosphere (He). After each measurement, the samples were checked to ensure their integrity. Their mass was controlled with an analytical balance of 0.1 mg sensitivity. In case of the fracture of a fragment into several pieces, the pieces weighing less than 25 mg were not selected for further investigation. Although the weights controls did not highlight any change in

mass, a variation of the O/M ratio resulting in a mass variation inferior to 0.1 mg cannot be excluded. Furthermore, as no *in-situ* mass change was recorded during the measurement, fluctuations between high temperature and room temperature could not be measured.

As explained in Chapter 3 – section 3.3.7.2, the enthalpy increment of the sample is proportional to the additional heat Q_{meas} provided to the system to heat from room temperature to the targeted temperature. However, in the case of radioactive samples containing radioactive elements such as ^{241}Am or ^{238}Pu, issues are occurring in determining these increments due to the contribution of the α self-irradiation [111]. Thus, the experiments are influenced by two phenomena as evidenced by the following formula:

$$H(T) - H(298.15\ K) = Q_{meas} + Q_{\alpha} + Q_{irr} \quad \textbf{(5.2)}$$

The first phenomenon, already evidenced in section 5.1.2, is the energy release caused by the recombination of defects accumulated in aged samples, identified as Q_{irr} in **(5.2)**. The second phenomenon is the heat generated permanently by the sample itself, namely Q_{α}. This is due to the slowdown of the α particles and the recoil nuclei produced by the α decay. In this work, the contribution of the γ-rays was neglected as it originates mainly from ^{241}Am, whose gamma rays escape from the sample and whose energy (60 keV) is too low. The heat generated by the α decay of the sample Q_{α} is given by the following formula **(5.3)**:

$$Q_{\alpha} = m_i . P_i . \Delta t \quad \textbf{(5.3)}$$

where m_i corresponds to the mass of isotope i in the sample and P_i refers to the specific heat power of the isotope *i*. For americium, only ^{241}Am is considered, as it is the only isotope in the sample and P_{Am} is equal to 0.111 mW.mg^{-1}. For plutonium, different isotopes were found in various proportions, as it can be seen in Appendix E, resulting in a total specific heat power of 0.013 mW.mg^{-1}. Δt represents the time necessary to restore the targeted temperature after the drop of the sample, considered equal to 180 s in this work.

The heat capacity was then deduced from the derivative of the enthalpy increment, as follows:

$$C_P = \left(\frac{\partial H}{\partial T}\right)_P \quad \textbf{(5.4)}$$

5.3.2. Results

The enthalpy increments of the CAPRA4 sample were determined between 585 and 1790 K. The number of measurements, the resulting mean value and the standard deviation (1 s) are reported in Table 5-8 for each temperature. For T = 686 and 889 K, only three drops could be performed due to the fragmentation of the samples.

Table 5-8 – Molar enthalpy increments (in kJ.mol^{-1}) measured for a CAPRA4 sample.

Temperature (K)	H(T) – H(298 K) (kJ.mol^{-1})	Number of measurements
585	21.34 ± 2.04	4
686	28.84 ± 0.96	3
787	40.38 ± 0.79	4
889	46.14 ± 7.11	3
990	49.43 ± 4.01	4
1092	64.99 ± 8.52	4
1194	73.85 ± 8.00	4
1296	74.05 ± 10.03	4
1397	89.34 ± 9.82	4
1500	100.06 ± 16.72	4
1603	99.12 ± 4.17	4
1703	122.86 ± 20.52	4
1790	131.46 ± 17.22	4

These results are plotted in Figure 5-13. On Figure 5-13(a), they are compared with the enthalpy increments given by Fink for the pure end-members UO_2 and PuO_2 [128], which are the major constituents of the samples studied here. On Figure 5-13(b), the enthalpy increments calculated using the Neumann-Kopp's additivity rule[3] are plotted for comparison, as well as literature values of Kandan *et al.* [135] for $U_{0.72}Pu_{0.28}O_{2.00}$ between 1000 and 1800 K. Overall, the enthalpy increments measured in this work exhibit a similar trend compared to the ones of the pure end-members and the values of Kandan *et al.*. However, three outliers, at 990, 1293 and 1603 K can be noticed. Possible reasons for these discrepancies are given in the next section.

[3]The Neumann-Kopp additivity rule is the following: "for a mixture of UO_2 and PuO_2, the properties of the solid are determined by combining the contribution from each constituent in proportion to its mole fraction" [113].

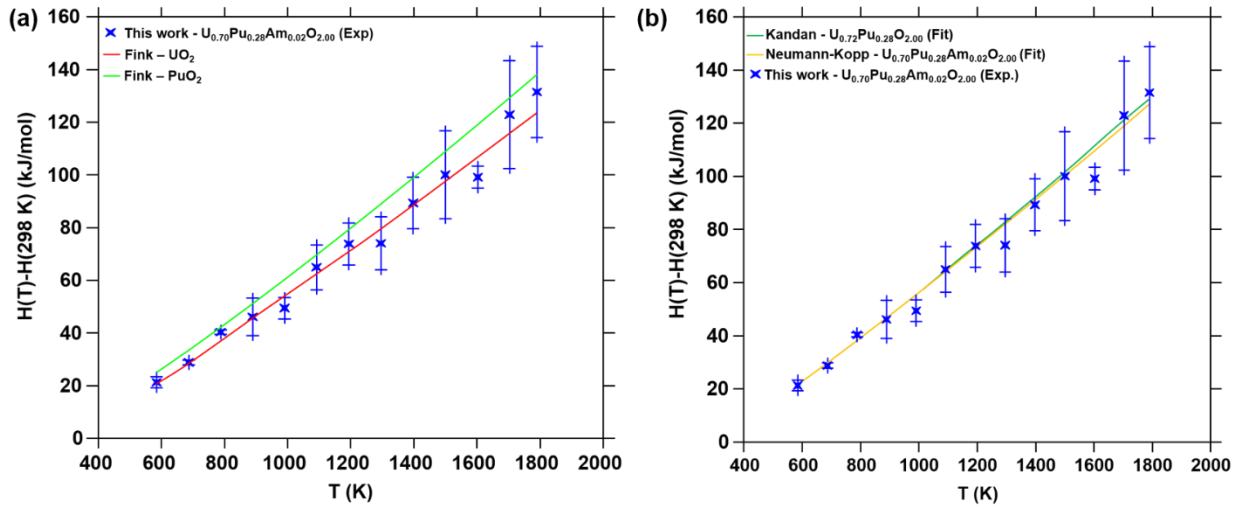

Figure 5-13: Enthalpy increments of a CAPRA4 sample measured in this work, (a) compared to the values of Fink for the pure poles UO_2 and PuO_2 [128], (b) compared to experimental literature values of Kandan *et al.* [135] and calculated data using the Neumann-Kopp's additivity rule.

The enthalpy increments $H(T) - H(298.15\,K)$ are fitted in this work using the Maier-Kelly equation commonly used in the literature, *i.e.* a 4-term polynomial function in temperature T as follows:

$$H(T) - H(298\,K) = c_0 + c_1 \times T + c_2 \times T^2 + c_3 \times T^{-1} \quad \textbf{(5.5)}$$

Two fits are performed for this work. The first one is done using all the experimental values obtained here and the second one is obtained when omitting the three outliers (990, 1293 and 1603 K). The coefficients obtained for these two fits are reported in Table 5-9, where they are compared with the ones obtained by Kandan *et al.* for $U_{0.72}Pu_{0.28}O_{2.00}$.

Similar order of magnitudes, as well as close values, are found here, resulting in a good agreement with the literature. The small discrepancies between the fits are illustrated in Figure 5-14. As it can be seen, the two fits performed in this work lie within the experimental uncertainties, except for the outlier at 1600 K. Based on the coefficient of determination R^2 given in Table 5-9, a better agreement with the experimental data is noticed for the fit omitting the three outliers (R^2 = 0.999). Thus, for the rest of this study, these coefficients are considered.

Table 5-9 - Parameters of Equation (5.5), compared with literature values of Kandan *et al.* [135].

	c_0 (J.mol^{-1})	c_1 (J.mol^{-1}.K^{-1})	c_2 (J.mol^{-1}.K^{-2})	c_3 (J.K.mol^{-1})
This work – All data (R^2 = 0.989)	-27326	74.82	7.44 x10^{-3}	14.500x10^5
This work – Without outliers (R^2=0.999)	-23655	66.24	10x10^{-3}	14.500x10^5
Kandan *et al.* ($U_{0.72}Pu_{0.28}O_{2.00}$)	-28710	77.841	5.606x10^{-3}	15.166x10^5

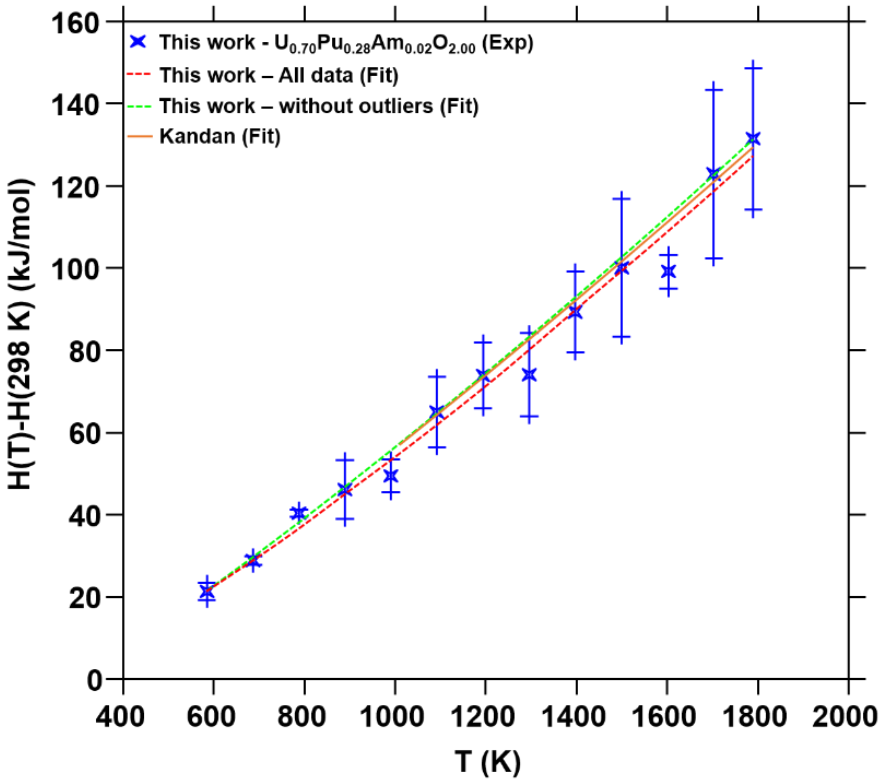

Figure 5-14: Different fits obtained in this work compared to the experimental values and the fit of Kandan *et al.* [135].

The heat capacity function of the CAPRA4 samples C_P is derived from Equation **(5.5)** from 300 to 1800 K. As generally used in the literature, a Maier-Kelley polynomial relation is used for the fit [240]:

$$C_P = b_0 + b_1 \times T - b_2 \times T^{-2} \qquad \textbf{(5.6)}$$

As no low-temperature heat capacity was measured in this work, a constraint is set on the C_P at 298.15 K, equal to the value obtained using the Neumann-Kopp additivity rule from the C_P of UO_2 [128], PuO_2 [128] and AmO_2 (see Chapter 2 – section 2.3.1.1). As no experimental data is available for AmO_2, the heat capacity derived by Konings *et al.* is considered [125]. Thus, in this work, $C_P(298\,K)$ is constrained to 64.4 $J.K^{-1}.mol^{-1}$. The following b_0, b_1, b_2 parameters of the equation **(5.6)** are obtained in this assessment:

b_0 = 70.94 $J.K^{-1}.mol^{-1}$; b_1 = 16.86x10^{-3} $J.K^{-2}.mol^{-1}$ and b_2 = 1.067x10^{6} $J.K.mol^{-1}$

The resulting heat capacity function is plotted in Figure 5-15, compared with literature data for UO_2 and PuO_2 [125], as well as with the values obtained by Kandan *et al.* [135] and by using Neumann-Kopp additivity rule as recommended by Carbajo *et al.* [113].

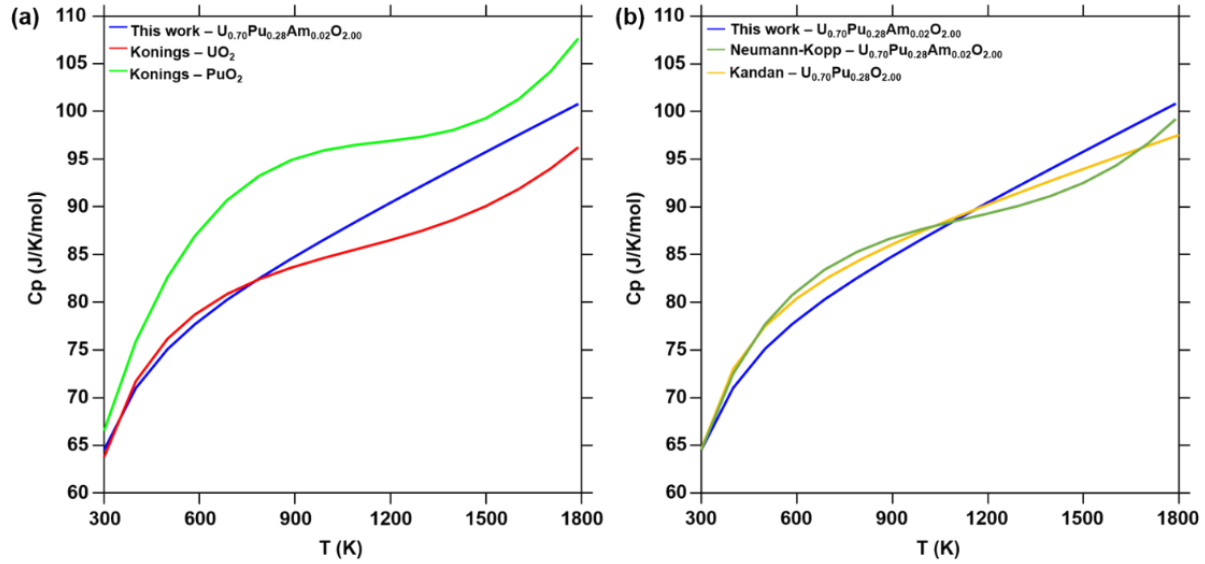

Figure 5-15: Heat capacity function obtained for the CAPRA4 sample, (a) compared to the values of Fink for the pure poles UO_2 and PuO_2, (b) compared to experimental literature values of Kandan *et al.* [135] and calculated data using the Neumann-Kopp's additivity rule.

For T < 800 K, the heat capacity curve of the CAPRA4 sample is close to the one of UO_2. Above this temperature, the data are comprised between the values of the pure poles. When comparing to literature values of Kandan *et al.* and using the Neumann-Kopp rule, different tendencies can be found for the three samples (Figure 5-15(b)). Indeed, for T < 1100 K, the data obtained in this work are lower than the ones of the literature. On the contrary, above this temperature, the heat capacity is higher than the data of recommendations of Kandan *et al.* or using the Neumann-Kopp rule. These observations are discussed in the following section.

5.3.3. Discussion

As previously explained, the heat emitted by the α decay of the sample is calculated to determine its influence on the measured enthalpies. Q_α is found to vary between 0.2 and 1.4 % of the calculated enthalpy and is thus considered as negligible in the rest of the work.

Concerning the O/M ratio of the sample, even if a variation of the O/M ratio inducing a mass change of less than 0.1 mg cannot be excluded, the drop, and thus the measurement is performed in a short time, so a constant O/M ratio is assumed during the whole experiment. In this case, based on the O/M ratio of the sample determined in section 5.1.2, the O/M ratio of this experiment is considered to be equal to 2.00.

As illustrated in Figure 5-13, three outliers (990, 1293 and 1603 K) are noticed for the enthalpy increments. Indeed, the enthalpy increments measured in this work are lower than the ones measured by Kandan *et al.* [135]. In this study, it is important to notice than the samples were not annealed before the measurements. Thus, the annealing of the defects created by the self-irradiation could contribute to an excess in the enthalpy, as described in **(5.2)**. Kato *et al.* studied the self-irradiation damages in $U_{1-y}Pu_yO_{2\pm x}$ [107] and evidenced three ranges of thermal recovery when annealing their samples. The first one, for T < 673 K, is linked to recovery of the anion Frenkel defects. The second stage, from 673 to 1073 K, corresponds to the recovery of the cation Frenkel defects and the third stage (T > 1073 K) is related to the release of helium trapped in the samples. In the work performed here, for this type of materials, the cationic

Frenkel defects have a low probability of formation [241]. Based on the results of Kato *et al.*, possible explanations for the discrepancies in the three temperatures are given here. First, the outlier at 990 K could be explained by the recovery of anion Frenkel defects, resulting in changes in the first oxygen sublattice. Indeed, a recombination of the defects present in the material causes a decrease of the apparenty enthalpy. Indeed, as the term Q_{irr} in **(5.2)** corresponds to a heat released by the sample, it lowers the calorimetric signal, which represents the energy required by the sample to reach the targeted temperature. Second, the outlier at 1293 K could be attributed to further defects recombinating resulting in the release of He (α-He trapped in vacancies and released by dissociation of the vacancies complexes), as also evidenced by Staicu *et al.* [111]. Finally, the last temperature, 1603 K, could correspond to the defect recombination of the cationic sublattice. These explanations are hypotheses and further studies are needed to confirm these statements.

When comparing the literature data of Kandan *et al.* and the enthalpy increments obtained using the Neumann-Kopp rule with the values obtained in this work, the data are close to each other within the uncertainties. On the contrary, for the heat capacity, different behaviours are noticed for the three sets of data. A change of tendency is observed around 1100 K. This phenomenon was already observed by Epifano *et al.* in the case of $U_{1-z}Am_zO_{2-x}$ materials [143] for enthalpy increments. As the enthalpy increments and heat capacity are directly linked, the same explanation can be given for the latter. The authors gave a first explanation with the possible formation of oxygen vacancies in the samples. The influence of the reduction of the samples on the heat capacity was also assumed by Smith *et al.* above 1850 K for NpO_2 [242]. For UO_2 and PuO_2 [243], [244], an increase in the C_P was reported for T > 2000 K due to oxygen Frenkel pair formation. In the case of $U_{1-z}Am_zO_{2-x}$, Epifano *et al.* reported this phenomenon to occur already above 1100 K due to the high oxygen potential of AmO_{2-x} and its instability [143]. This hypothesis is in agreement with the reduction of the sample observed already at high temperature in section 5.2.3 (Figure 5-9). Although the calculations were made here in the case of a reducing atmosphere, the tendency is observed even under pure oxygen atmosphere.

Another possible explanation given by Epifano *et al.* is the distortion of the crystal structure based on the existence of Am^{3+} in the materials. Indeed, difference in the ionic radii of the cations (see Chapter 2 – Table 2-3) can lead to changes in the lattice parameter variation and thus to an excess in lattice dilatation. This hypothesis is confirmed by the results obtained by XANES (section 5.1.3), highlighting the presence of Am^{3+} even at room temperature for the CAPRA4 sample. Moreover, this result is in agreement with the thermal expansion of the CAPRA4 sample (see section 5.2.2). Indeed, deviations from the recommendation of D.G. Martin for stoichiometric $U_{1-y}Pu_yO_{2.00}$ and of Kato *et al.* for hypo-stoichiometric samples (Figure 5-10) are observed above 1373 K due to a reduction of the sample, with an O/M ratio around 1.97-1.98, determined from thermodynamic models. Thus, as the heat capacity C_P is linked to the thermal expansion a according to the equation **(5.7)**, an excess in the lattice parameters would result in higher heat capacities. This observation was already made by Kato *et al.*, who studied the thermal expansion and heat capacity of PuO_{2-x} [117].

$$C_P = C_V + C_D = C_V \times (1 + \gamma \times a \times T) \qquad \textbf{(5.7)}$$

Where C_V is the heat capacity at constant volume V, C_D is the dilatation contribution, γ the Grüneisen constant, a the thermal expansion coefficient and T the temperature.

From the comparison of the obtained enthalpy increments with the literature data of Kandan *et al.* in which no Am is present, no clear evidence of an impact of the presence of americium can be found. However, an effect of the presence of americium is observed on the heat capacity. Indeed, as observed in section 5.1.3.1, americium is purely trivalent already at room temperature for this sample. As seen in Figure 5-9, a reduction of the sample is noticed when increasing the temperature. This reduction is due to the instability of AmO_2 at high temperature but also to the formation of hypo-stoichiometric PuO_{2-x} above 600 K. Indeed, as all the americium is already trivalent, the reduction of Pu is enhanced, leading to an increase of the proportion of Pu^{3+} in the sample. This results in a faster decrease of the O/M ratio, based on the plutonium content of the CAPRA4 sample (y = 0.28), and thus in an increase of the concentration of oxygen vacancies. These results are in agreement with the ones already observed for the thermal expansion in section 5.2.2. Therefore, the americium content would tend to increase the heat capacity of $U_{1-y-z}Pu_yAm_zO_{2\pm x}$ compared to $U_{1-y}Pu_yO_{2\pm x}$ due to these defects.

5.3.4. Conclusion

The temperature dependence of enthalpy increments of the CAPRA4 sample ($U_{0.70}Pu_{0.28}Am_{0.02}O_{2.00}$) were determined using drop calorimetry experiments from 585 to 1790 K. The experimental results were fitted and the corresponding heat capacity function was obtained by derivation.

A good agreement was obtained with the existing literature data of Kandan *et al.* [135] and the calculated values using the Neumann-Kopp's additivity rule for the enthalpy increments, except for three temperatures (approximately 990, 1293 and 1603 K). These temperatures could correspond to changes in the first oxygen sublattice, recombination of He-vacancy complexes with the release of helium and recombination in the cationic sublattice (Frenkel pairs) respectively, caused by the α self-irradiation of the samples.

For the heat capacity function, discrepancies were noticed above 1100 K, where the values obtained in this work are higher than the ones of Kandan *et al.*. This observation could be explained by the decrease of the O/M ratio and the formation of oxygen vacancies. Indeed, due to the presence of americium already stabilized in its trivalent state at room temperature, the reduction of plutonium is enhanced during the experiments. This would result in larger proportions of Pu^{3+} and thus in an increase in the concentration of defects. Moreover, the increase in the heat capacity was also linked to the steep increase in the thermal expansion evidenced earlier in this work due to the reduction of the sample (see section 5.2.2), as the two properties are linked. Thus, excess terms in the heat capacity function should be introduced for $U_{1-y-z}Pu_yAm_zO_{2-x}$ to take into account the contribution due to the formation of oxygen vacancies and associated defects in the materials.

Furthermore, no direct influence of the presence of americium on the enthalpy increments was observed. However, $U_{1-y-z}Pu_yAm_zO_{2\pm x}$ tend to have higher heat capacities than $U_{1-y}Pu_yO_{2\pm x}$ at high temperature based on its ability to enhance the reduction of Pu and the resulting oxygen vacancies formation.

5.4. SOLID/LIQUID PHASE TRANSITIONS

As reported in Chapter 2, several studies were carried out over the last decades on $U_{1-y}Pu_yO_{2\pm x}$ by means of thermal arrest and laser heating over the whole plutonium content range [24], [174], [176], [180], [181]. However, only Kato *et al.* [185] took into account the influence of americium and O/M ratio on the solidus/liquidus temperatures of $U_{1-y-z}Pu_yAm_zO_{2\pm x}$.

New measurements using a laser-heating technique were performed in this work to determine the solidus temperature of the samples described in Table 5-6. The experiments were carried out at the JRC Karlsruhe (Germany). As detailed in Chapter 3 – section 3.3.6.1, the novelty of this setup is the implementation of oxygen gauges to monitor the oxygen partial pressure (pO_2) during the measurements. The variation of the pO_2 inside the chamber during the experiments, linked to the O/M ratio of the samples, is then studied. The influence of the conditions of the shots, the plutonium and americium content and the initial O/M ratio is also evidenced in the following sections.

5.4.1. Experimental procedure

For each sample, the conditions of the shots can be found in Appendix G. In some cases, to minimize thermal shocks and ensure the thermomechanical stability of the pellet, pre- and post-heating steps at 1700 K were performed. The importance of this step to avoid cracks formation was evidenced by Welland *et al.* [245]. In addition, several successive ramps up and down were performed for some samples to improve the quality of the thermogram and allow an easier determination of the solidus temperature. From five to nine shots were performed successively on the same face of the sample. Between each shot, the sample was allowed to cool down to room temperature in order to visually inspect the sample for cracks and the chamber for possible vaporization.

As described in Chapter 3 – section 3.3.6.2, due to a failure of the spectrometer, the emissivity of the sample could not be assessed experimentally and was estimated to be equal to 0.83 ± 0.05.

The determination of the phase transition temperature was performed by analysis of the cooling curve of the recorded thermogram. The analysis procedure described in Chapter 3 – section 3.3.6.2 was applied here for correcting the true temperature based on the emissivity and transmittance and for analysing the oxygen partial pressure.

5.4.2. Results

In this part, the determination of the solidus temperatures and the assessment of the O/M ratio is presented for a PHENIX29 pellet as example. The same methodology was applied to all the samples and the results are described at the end of this section.

Images on how a molten sample looks like along the shots are presented in Figure 5-16.

Figure 5-16(a) represents the surface of the sample before the shots, while (b) is after one shot, (c) after 4 shots and (d) after 8 shots. The molten pool is clearly visible on (b), (c) and (d) and corresponds to the shiny centre of the pellet. A gradual fracturing of the sample is observed throughout the shots, with pieces detaching. In this work, the integrity of the samples was

checked between each shot and the experiments were stopped when pieces of the molten pool fell down.

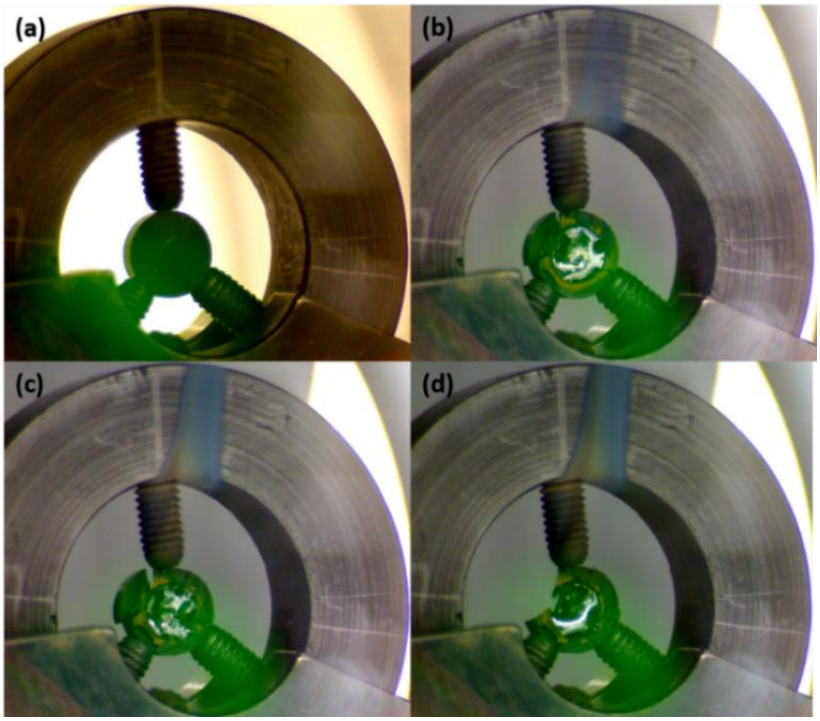

Figure 5-16: PHENIX29 sample (a) before shots, (b) after 1 shot, (c) after 4 shots and (d) after 8 shots.

5.4.2.1 *Solidus temperatures*

In the case of the PHENIX29 sample, eight successive shots were performed on a disk of the material in three different conditions (see Appendix G). A typical result of a melting experiment is presented in Figure 5-17. The red curve is the thermogram (temperature as a function of time) recorded by the pyrometer and the laser power profile of the shot is plotted in black. It is important to note that the minimum of recording of the pyrometer is 1500 K. Thus, the baseline is plotted at 1500 K on the thermogram in Figure 5-17, while the sample is actually at room temperature in reality.

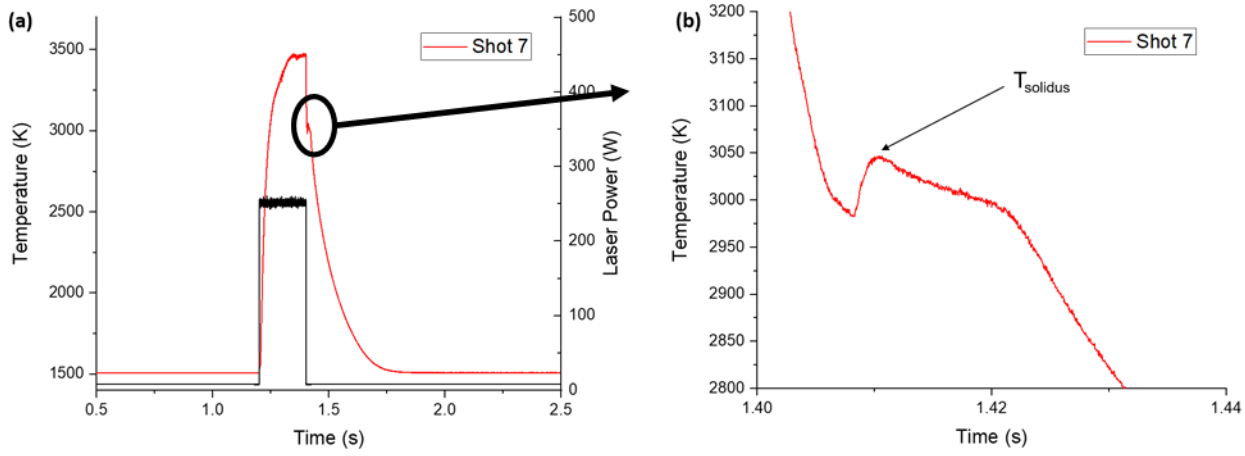

Figure 5-17: Thermogram recorded in a laser melting measurement of PHENIX29 in argon for the shot n°7, (a) with the laser power profile in black and (b) zoom on the $T_{solidus}$ range.

For mixed oxides, non-congruent melting is expected, resulting in two distinguishable thermal arrests observed during cooling, corresponding to the liquidus[4] and solidus[5] temperatures, respectively. The absence of a plateau on the cooling curve indicates that a non-congruent melting is occurring. However, in this study, only one thermal arrest was detected. In this case, as evidenced by Böhler *et al.* [176], the inflection point corresponds to the solidus temperature.

The shape of the thermogram, with a decrease of the temperature followed by an increase before the inflection point, can be explained by the super-melting of the sample. Indeed, in these temperature and time ranges (before the solidus temperature), a liquid phase remains in the molten pool. After the inflection point, the molten pool cools down naturally and only a solid phase is present.

The eight recorded thermograms are presented for comparison in Figure 5-18 under different conditions:

- For shots 1 to 2: both a pre-heating (30 s at 1700 K) and post-heating (15 s at 1700 K) steps;
- For shots 3 to 6: only a pre-heating step;
- For shots 7 and 8: no pre- or post-heating step.

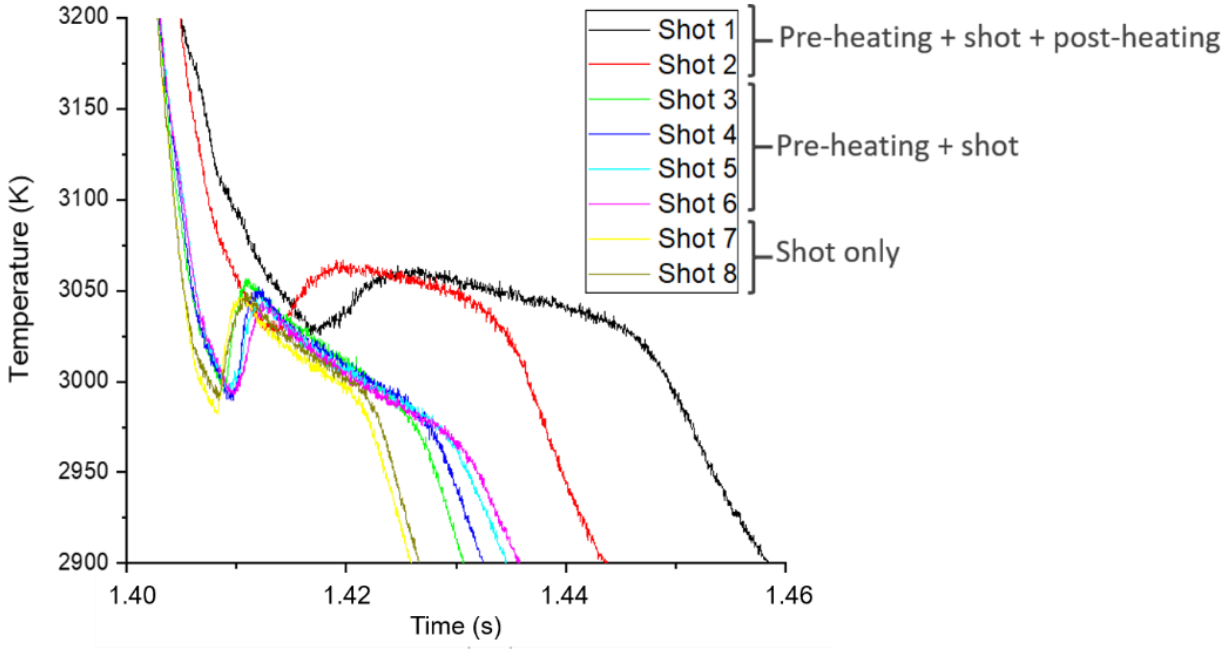

Figure 5-18: Comparison of the eight successive thermograms recorded for PHENIX29.

Overall, a good repeatability is observed for the measured temperatures between the different cycles, with similar heating/cooling curves profiles located in a close temperature range. Nevertheless, a slight offset in time and in temperature is visible for the curves of the first two shots (black and red), related to the post-heating step. On the contrary, no significant influence of the pre-heating step on the thermograms is observed. The time differences in the cooling

[4] Temperature at which the first solid germ forms during cooling.

[5] Temperature at which the last drop of cooling liquid becomes solid.

curves can originate from different kinetics of cooling or slight variations of the laser power and duration originating from the device's uncertainties. However, the slopes of the cooling curves after the solidus points remain the same for all the thermograms. The average solidus temperature obtained for the eight shots is 3046 ± 30 K. Thus, the measurements are reproducible. This temperature is in agreement with the solidus temperature determined by Kato *et al.* of 3030 K for a sample with y = 0.298 [185]. Furthermore, this temperature lies between the melting temperatures of the two end-members UO_2 and PuO_2, 3147 [14] and 3040 K [176], respectively.

The solidus temperatures obtained for the successive shots are represented in Figure 5-19.

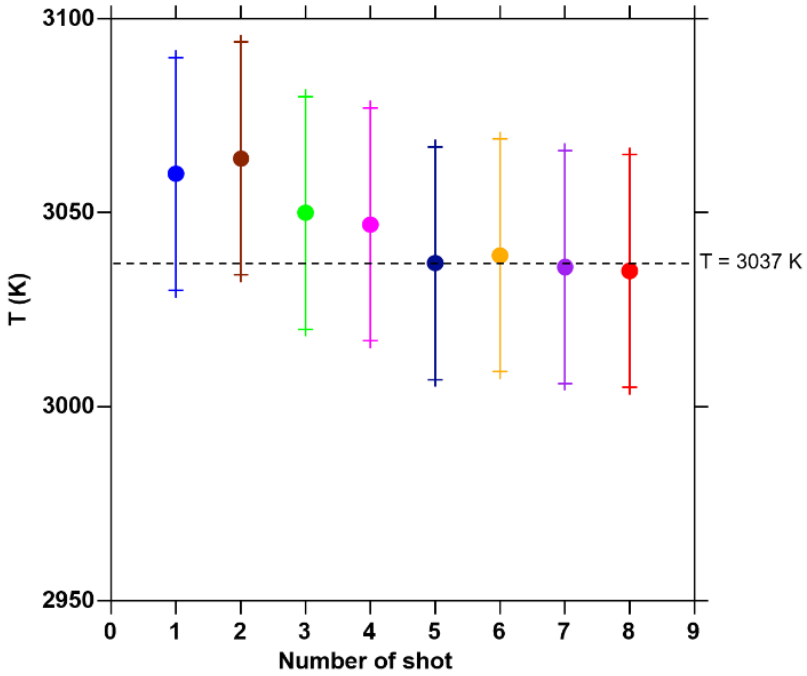

Figure 5-19: Solidus temperature of PHENIX29 recorded for each shot in Ar.

It can be observed that the temperature decreases throughout the shots, from T = 3060 K for the first shot to T = 3035 K for the last shot. Moreover, for the first two shots, performed with a post-heating step, the solidus temperatures obtained are slightly higher than the ones of the other shots (3060 and 3064 K versus 3040 K), however remaining within the experimental uncertainties. Thus, contrarily to the pre-heating step, the post-heating appears to have an influence on the solidus temperature. The dashed line illustrate the stabilization of the temperature around 3037 K at the end of the shots. However, as the uncertainty has been determined to be equal to ± 30 K, no conclusion can be drawn at this point on the decrease in temperature.

5.4.2.2 Estimation of the O/M ratio along the shots

Thanks to the oxygen partial pressure gauges, it was possible to measure the variation in the pO_2 occurring at the outlet of the chamber during the experiment. In this study, a residual oxygen content of 3.5 vpm ($pO_2 = 3.5 \times 10^{-6}\ atm$) was measured in the argon. This value is plotted as baseline (dashed red line) in Figure 5-20. After each shot, the sample was allowed to cool down and for the atmosphere to stabilize to its residual value. Note that in this study, a time shift in the measurement of the pO_2 is observed compared to the moment at which the shot is performed. Indeed, the latter lasts 500 ms while the oxygen partial pressure is measured

every 3 second at the exit of the chamber. Moreover, a waiting step ranging from 30 minutes to 1 hour was performed after each shot for the oxygen partial pressure to restabilize to its residual value.

The Figure 5-20 represents the variation in the oxygen partial pressure measured at the exit of the experimental chamber throughout the eight shots. A decrease in the pO_2 occurs after each shot. In the case of the first shot, the oxygen partial pressure decreases down to $1x10^{-17}$ atm and a value of 10^{-15} atm is reached for the shots 4 to 6. In the case of the shots 7 and 8, only a very slight depletion in oxygen was observed. In this work, it was assumed that only the sample could react with the oxygen present in the chamber. The decrease in the oxygen partial pressure observed here corresponds to the absorption of oxygen by the sample and thus to its oxidation during melting and pre/post heating steps.

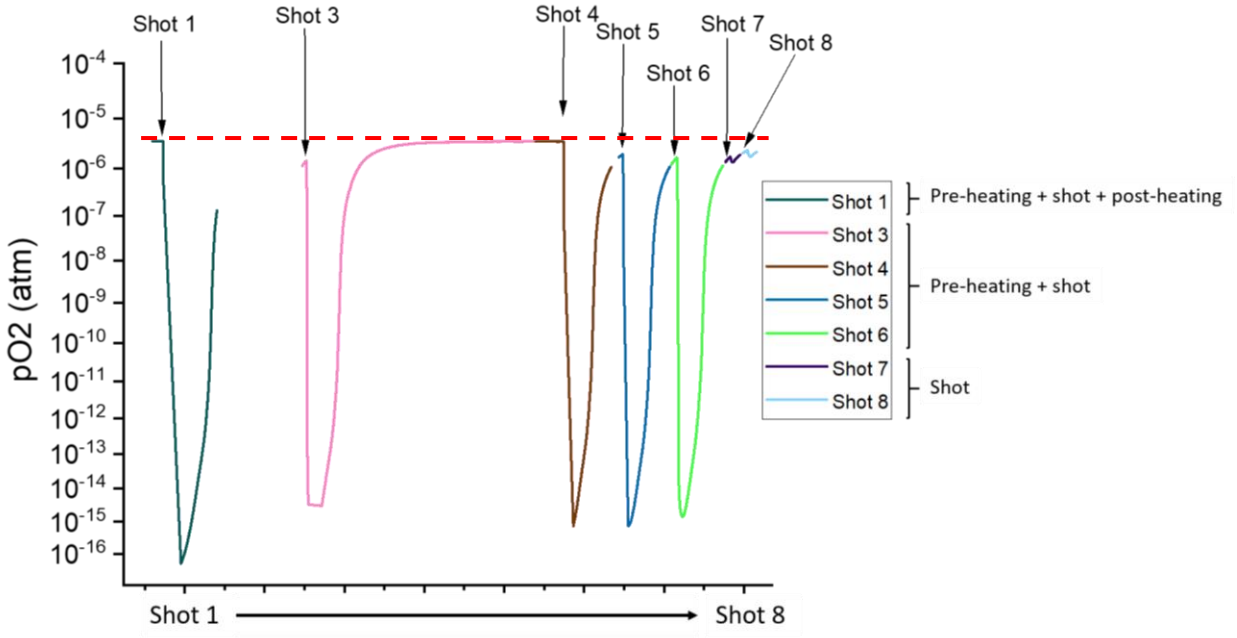

Figure 5-20: Variation of oxygen partial pressure measured at the exit of the melting chamber throughout the eight shots for PHENIX29.

The variations of the oxygen partial pressure recorded at each shot for the PHENIX24, CAPRA4, TRABANT40 and TRABANT45 samples are illustrated in Figure 5-21.

In the case of the CAPRA4 and TRABANT40-OM samples, it can be noticed that the variation of pO_2 at the first shot exhibits a different behaviour compared to the others, evidencing first an absorption of oxygen and then a release. Moreover, the pO_2 for the first shot of TRABANT40 has a different shape than the others because of a technical issue during the recording. In addition, a release of oxygen is evidenced with the pO_2 graphs of the TRABANT45 and PHENIX29-OM samples.

The different behaviours observed here are discussed in the next section.

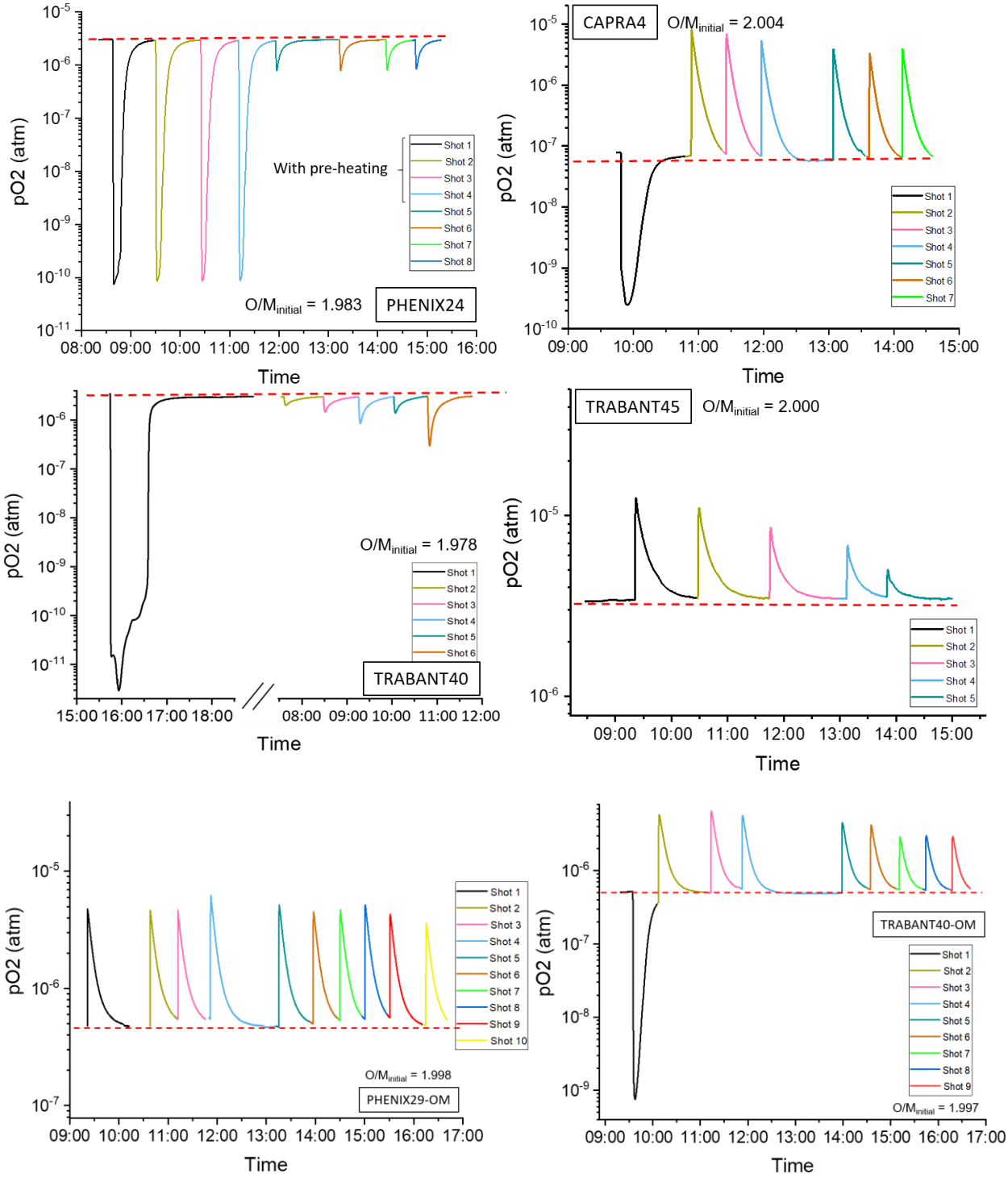

Figure 5-21: Variation of the oxygen partial pressure measured at each shot for PHENIX24, CAPRA4, TRABANT40, TRABANT45, PHENIX29-OM and TRABANT40-OM samples (dashed line: residual pO_2).

The quantity of oxygen absorbed or released by each sample is calculated by integration of the variation of the oxygen partial pressure, as explained in Chapter 3 – section 3.3.6.2.2.

In the case of the PHENIX29 sample (Figure 5-20), for the shots 1 to 6 (performed all with pre-heating), between 10 to 15 µg of oxygen are absorbed by the sample per shot, while this quantity is only around 1 µg for the last two shots (performed with no pre-heating). Further studies and explanations on the influence of the pre- and post-heating steps are proposed in the following section.

As the absorption/release of oxygen by the sample is directly related to its oxidation/reduction, the variation in its O/M ratio throughout the shots is assessed. To this aim, several starting conditions and hypotheses are made, as follows:

- The molten pool of the samples exhibits a diameter of 3 mm (corresponding to the size of the laser spot) and a thickness of 150 µm (measured by Epifano *et al.* [48] by SEM analyses). The densities of the samples are reported in Chapter 3 – Table 3-3.
- As it can be seen in 5.1.1, the sample is homogeneous with few uranium and plutonium agglomerates of 10 and 1 µm respectively. As the laser spot has a diameter of 3 mm, the composition of the samples is assumed to be homogeneous. Moreover, a constant composition in U, Pu and Am is admitted throughout the shots, implying that no change occurred due to the vaporization of these elements.
- The O/M ratios previously obtained by XRD (see section 5.1.2) are used as initial values in agreement with previous hypothesis.
- The oxygen is absorbed only by the molten pool.

The accuracy of these hypotheses is discussed in 5.4.3.3.

In a first step, the number of moles corresponding to the molten pool is calculated to be equal to 4.08×10^{-5} mol in the case of the PHENIX29 sample. Based on the initial O/M ratio of 1.984, the corresponding number of moles of oxygen present in the sample is determined to be 8.09×10^{-5} mol. This quantity is used as initial value for the calculations. Then, the mass of oxygen absorbed by the sample during the melting is calculated for each shot to determine the O/M ratio. As it can be seen in Figure 5-20, the variation in pO_2 of the shot 2 was not recorded because of a technical issue. Thus, as the shot 2 was performed in the same conditions as the shot 1 (pre-heating + shot + post-heating), the same variation in pO_2, and thus the same quantity of oxygen absorbed by the sample, is assumed for the shots 1 and 2. This hypothesis is validated when looking at the shots 3 to 6, all performed in the same conditions and all resulting in the same quantity of oxygen absorbed (around 10 µg).

The O/M ratios estimated at the end of each shot are represented in Figure 5-22 for the PHENIX29 sample.

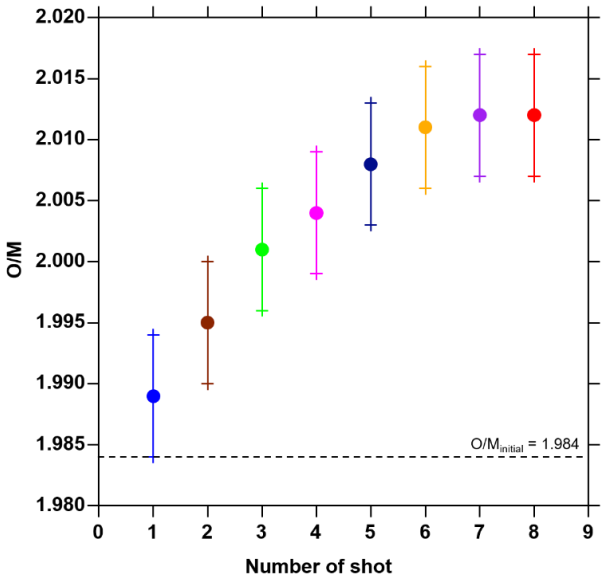

Figure 5-22: Variation of the O/M ratio of PHENIX29 obtained after each shot.

It is important to keep in mind that the O/M ratio is estimated here at room temperature after the shots and may not be representative of the actual O/M ratio at which the melting occurs (see Chapter 6 – section 6.4.3.1). The uncertainty on the O/M ratio is assumed to be ± 0.005 (see Table 5-3). For the PHENIX29 sample, a gradual increase in the O/M ratio is observed, corresponding to the oxidation of the sample. It can be noticed that for the two last shots (7 and 8), no increase is observed. A stabilisation of the O/M ratio at a final value of 2.012 is calculated. This observation is discussed in 5.4.3.5.

The variation of the solidus temperature is plotted as a function of the O/M ratio after each shot in Figure 5-23 for the PHENIX29. Here, a decrease in temperature is noticed when increasing the O/M ratio.

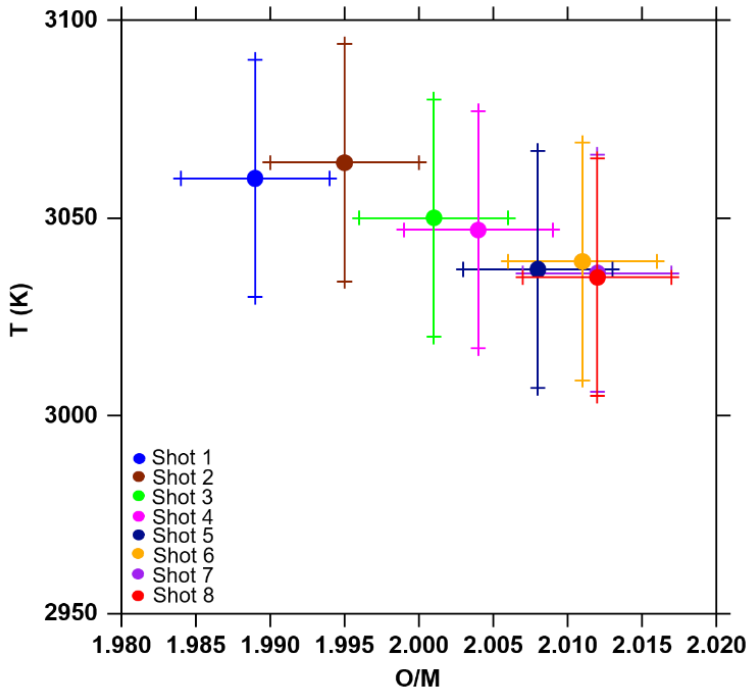

Figure 5-23: Variation of the solidus temperature of PHENIX29 as a function of the O/M ratio.

Using the same methodology previously described for the PHENIX29 sample, the variation of the solidus temperatures as a function of the O/M ratio after each shot is assessed for the other samples of interest. The results are presented in Figure 5-24 for PHENIX24, CAPRA4, TRABANT40 and TRABANT45 and in Figure 5-25 for PHENIX29-OM and TRABANT40-OM. The uncertainties are not represented for sake of clarity but remain the followings: ± 30 K for the solidus temperature and ± 0.005 for the O/M ratio. The values for the solidus temperatures and O/M ratios determined in this study for all the samples are reported in Appendix H.

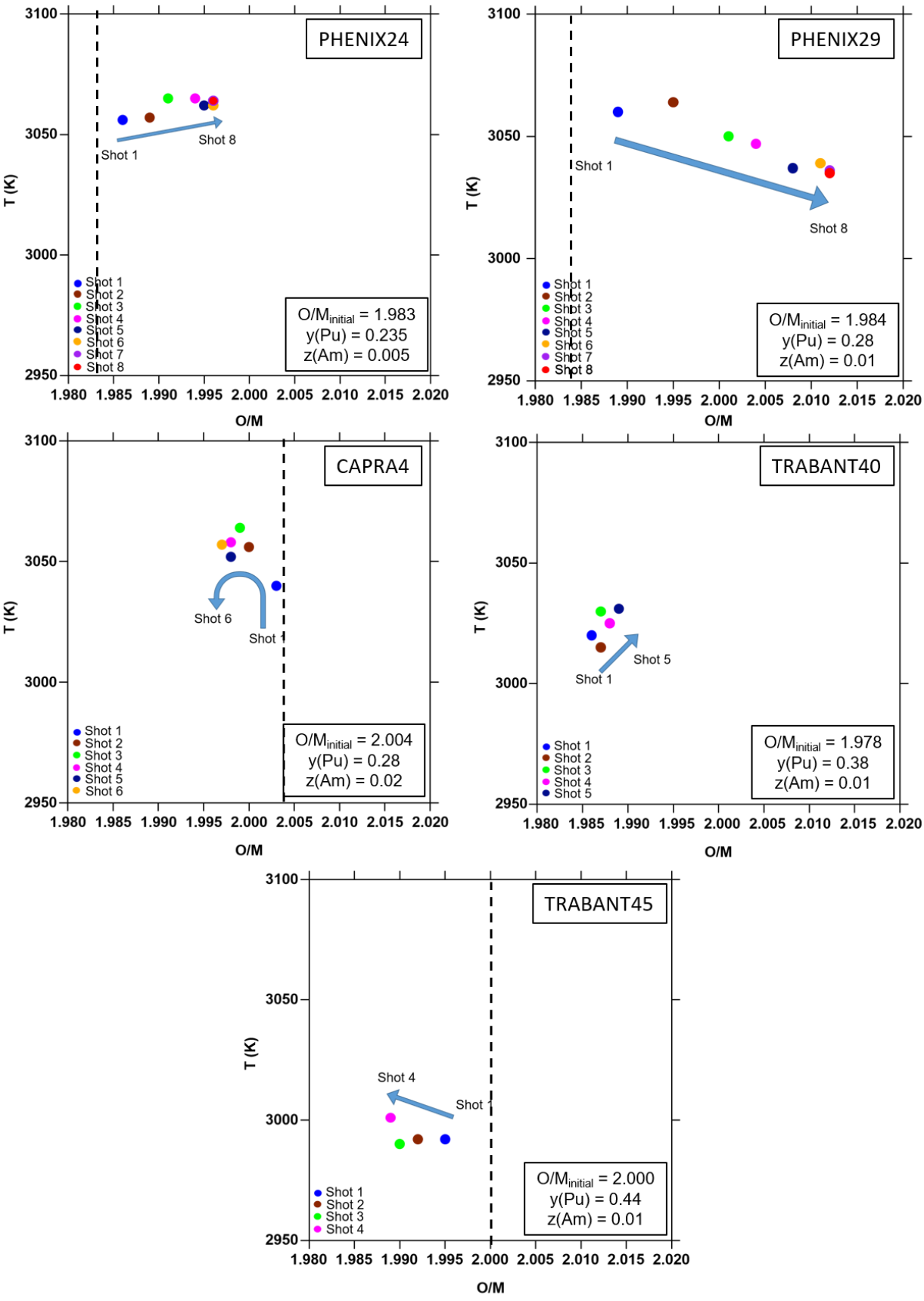

Figure 5-24: Variation of the solidus temperature as a function of the O/M ratio for the PHENIX24, PHENIX29, CAPRA4, TRABANT40 and TRABANT45 samples.

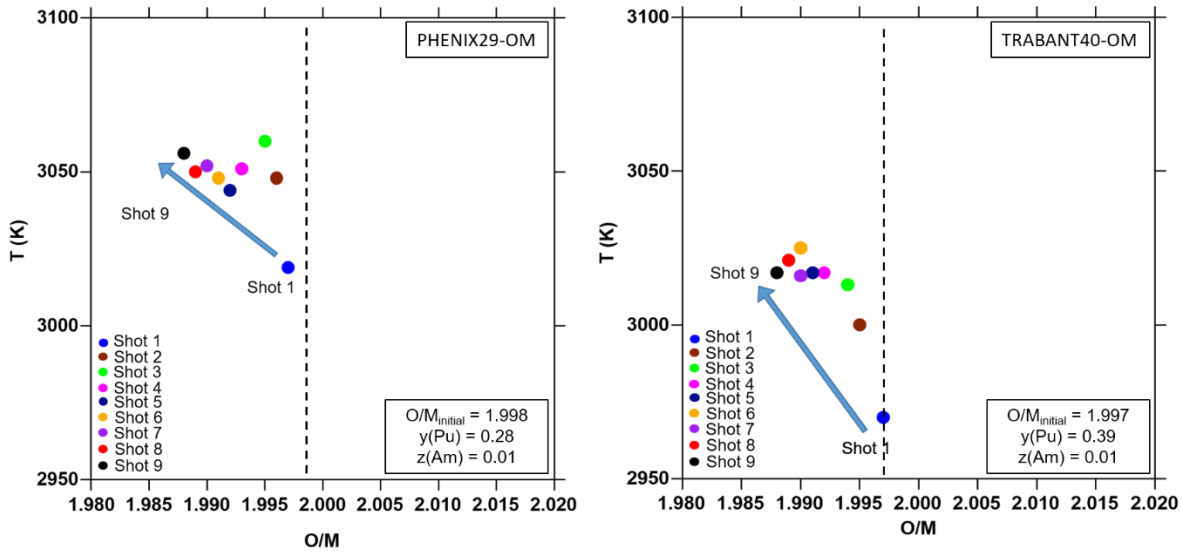

Figure 5-25: Variation of the solidus temperature as a function of the O/M ratio for the PHENIX29-OM and TRABANT40-OM samples.

As already seen in Figure 5-21, different behaviours are observed during the melting.

Indeed, for the PHENIX24, PHENIX29 and TRABANT40 samples, an oxidation is reported along the shots, linked to the uptake of O_2 from the cover gas. Among these samples, an increase of the solidus temperature when increasing the O/M ratio is observed for the PHENIX24 and TRABANT40, in contradiction with the results of the literature of Kato *et al.* [174]. However, this increase lies within the experimental uncertainties and is not significant (3056 K for the first shot and 3064 K for the last shot, for the PHENIX24 sample).

On the contrary, for the CAPRA4, TRABANT45, PHENIX29-OM and TRABANT40-OM samples, a reduction of the samples occurs during the melting, as evidenced by the increase of pO_2 in Figure 5-21. For these samples, an increase of the solidus temperature is observed when decreasing the O/M ratio, in agreement with the work of Kato *et al.*.

When looking at the samples of same composition but different initial O/M ratio, namely PHENIX29 and TRABANT40, an opposite behaviour is noticed. Indeed, the original samples are oxidized while the annealed samples are reduced during the melting. This oxidation/reduction behaviour appears to be related to the initial O/M ratio, as all the samples reduced are initially near stoichiometric and the oxidized ones are hypo-stoichiometric. The influence of the initial O/M ratio is discussed in more details in the next section and in Chapter 6 – section 6.4.3.1.

5.4.3. Discussion

5.4.3.1 Comparison with literature data

The solidus temperatures measured in this work for the seven samples are compared to existing literature on similar plutonium and americium contents, as it can be seen in Figure 5-26.

For y = 0.24, data are reported by Böhler *et al.* [176] and Strach *et al.* [184] for an O/M ratio assumed to be close to 2.00, also obtained by laser heating under argon. A significant difference of ~30 K is observed with the temperature reported by Strach *et al.*, however still within the experimental uncertainties of the data at O/M = 1.996. This work is in agreement with the study

of Böhler *et al.* for similar O/M ratios.

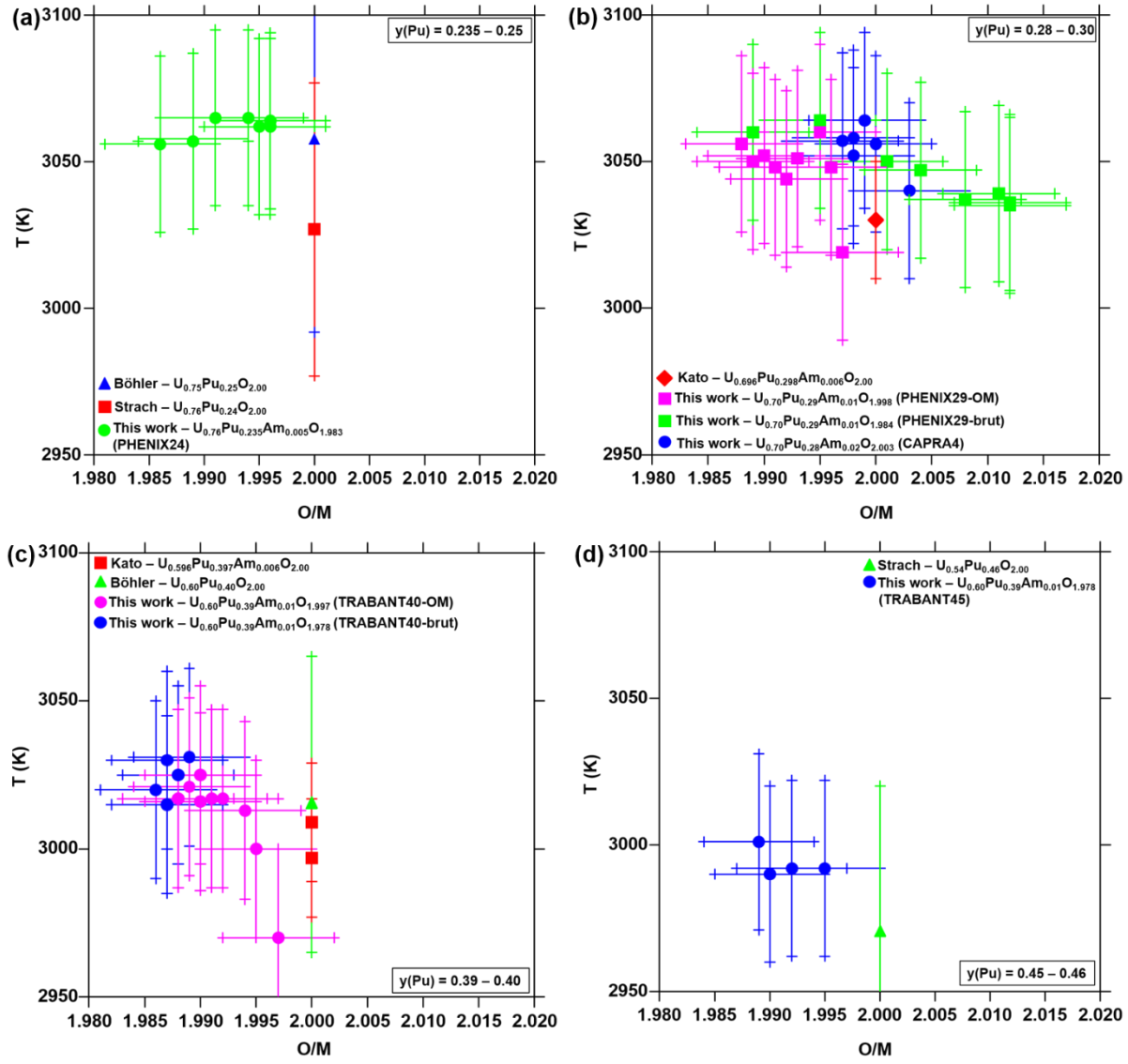

Figure 5-26: Comparison of the solidus temperatures obtained in this work with the existing literature.

For y = 0.28-0.30, only one experimental temperature is cited in the literature, obtained by Kato *et al.* by thermal arrest [174]. The temperatures obtained in this work for the PHENIX29, PHENIX29-OM and CAPRA4 samples are in good agreement with their work.

When comparing the solidus temperatures for the TRABANT40 and TRABANT40-OM samples with the literature data of Böhler *et al.* [176] and Kato *et al.* [174], a slightly lower temperature is measured in the case of the experimental value of this work at O/M=1.997, however remaining within the experimental uncertainties.

For y = 0.45, only one temperature was reported in the literature by Strach *et al.* [184], slightly lower than the results of this work.

As it can be seen in Figure 5-26 and as already stated, several parameters can influence the solidus temperature, such as pre- and post-heating steps, the plutonium and americium contents and the O/M ratio, discussed in the following section.

5.4.3.2 *Effect of the pre- and post-heating steps*

As it can be seen in Figure 5-20, no significant influence of the post-heating step is noticed in this study. Indeed, the variation of the oxygen partial pressure recorded for the shots 1 and 2 on the PHENIX29 sample is approximately the same than those of the shots 3 to 6.

On the contrary, the pre-heating step appears to influence the oxygen uptake by the sample. Indeed, a larger decrease in the oxygen partial pressure measured at the exit of the chamber for the PHENIX29 sample is recorded for the shots with a pre-heating step (30 s at 1700 K), down to $pO_2 = 10^{-18} – 10^{-17}$ atm *vs.* 10^{-7} atm without pre-heating. The same observation is made in the case of the PHENIX24 for the shots 1 to 4 (10 s at 1700 K), with a decrease up to $pO_2 = 10^{-11}$ atm vs. 10^{-7} atm without pre-heating. When looking at the quantity of oxygen absorbed by the samples, between 10 to 15 µg of oxygen is taken up by the PHENIX29 and around 7 µg for the PHENIX24 samples per shot with preheating, while this quantity is only around 1-2 µg for the shots without pre-heating. Thus, the pre-heating step enhances the oxygen absorption during the laser tests.

In order to establish the influence of the pre-heating time on the uptake of oxygen, successive pre-heating tests were performed on a fresh PHENIX29 sample with various durations, ranging from 500 ms to 10 s (conditions listed in Table 5-10). The same laser power was applied for all the tests, 40 W, resulting in a temperature of 1700 K, heating a spot of 3 mm diameter on the surface of the sample. These tests were constituted only of a pre-heating step and no shot was performed.

Table 5-10 – Conditions, oxygen uptaken and variation in the O/M ratio for each pre-heating test at 1700 K on a fresh PHENIX29 sample.

Test	Pre-heating conditions	Mass of oxygen uptaken	Δ(O/M)
1	500 ms – 40 W	+ 0.3 µg	+ 0
2	1 s – 40 W	+ 0.4 µg	+ 0
3	5 s – 40 W	+ 3.1 µg	+ 0.001
4	10 s – 40 W	+ 5.8 µg	+ 0.003

The variation of the pO_2 measured at the exit of the experimental chamber during the tests is illustrated in Figure 5-27, where the residual partial pressure ($pO_2 = 6.3x10^{-6}$ atm) is represented by the red dashed line.

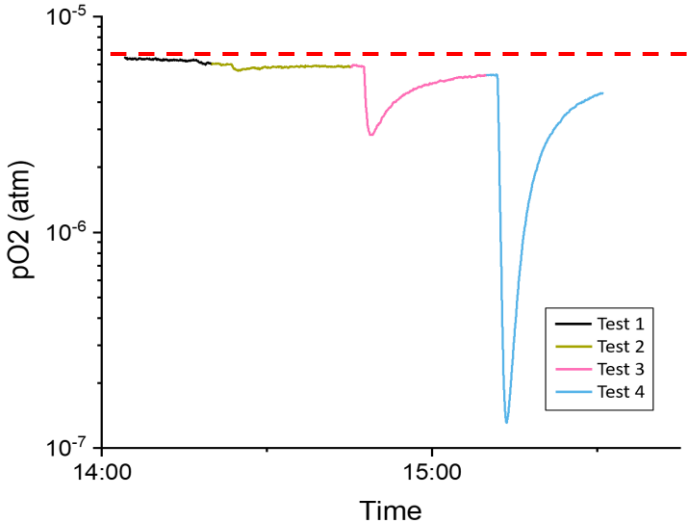

Figure 5-27: Variation of the oxygen partial pressure recorded during four successive pre-heating tests on a fresh PHENIX29 sample.

For the first two tests (500 ms and 1 s at 1700 K), no significant variation of the pO_2 is observed. When increasing the duration of the pre-heating step (5 s for the test 3 and 10 s for the test 4), a diminution of the pO_2 is noticed, and thus an increase in the oxygen absorbed by the sample, is observed. As expected, this study highlights the influence of the duration of the pre-heating step on the quantity of oxygen absorbed by the sample.

Using the same methodology applied in 5.4.2.2 for the PHENIX29 sample, the quantity of oxygen absorbed by the sample is quantified, as well as the resulting variation in the O/M ratio, reported in Table 5-10. For these calculations, as no shot was performed, there is no molten pool on the sample. However, it is assumed that only the surface at the laser spot (diameter of 3 mm) is taking up oxygen, as it is the only heated area of the sample. The same thickness as in 5.4.2.2, *i.e.* 150 µm, is used to assess the quantity of moles of the "melting zone". As it can be seen in Table 5-10, the quantity of oxygen absorbed in these tests, as well as the variation of the O/M ratio, is increasing when increasing the duration of the pre-heating step.

Because of the limited number of samples, no pre-heating tests could be performed on samples exhibiting a reduction behaviour such as the CAPRA4 and TRABANT45 samples. Further experiments are needed to study the behaviour of these types of materials during pre-heating.

Moreover, as evidenced in Figure 5-22, a stabilisation of the O/M ratio at the end of the shots observed for the PHENIX29 sample is consistent with the small absorption of oxygen (1 µg) by the sample visible in Figure 5-20. Indeed, as no step of pre- and/or post-heating was performed for the last shots, the sample was exposed to high temperature only for the short duration of the shot (0.5 s), significantly lower than for the shots 1 to 6 (between 28.5 and 43.5 s). The same stabilization phenomenon is observed for the PHENIX24 samples at an O/M ratio of 1.996.

For both samples, this stabilisation occurs after the 6th shot for this sample, corresponding to a cumulated fusion time of 3 s. However, as other samples (PHENIX29-OM and TRABANT40-OM) continue to absorb or release oxygen after 3 s of fusion (after 6 shots), the time of fusion does not seem to be correlated to the stabilisation of the O/M ratio. Thus, this stabilisation to a saturation value at high temperature for the PHENIX24 and PHENIX29 samples, both being oxidized during the shots, indicates a peculiar behaviour. Possible explanations are given in Chapter 6 – section 6.4.3. Unfortunately, no further shot could be performed as the sample

broke after 8 shots. Thus, other studies would be necessary to determine if this observation is true and repeatable.

5.4.3.3 Influence of the starting hypotheses for the estimation of the O/M ratio

The quantification of the variation of the O/M ratio during the melting observed in this study can also be questioned. In this part, the hypotheses are discussed based on the example given in 5.4.2.2 for the PHENIX29 sample.

The first hypothesis made to calculate the O/M ratio is related to the dimensions of the absorbing zone. Indeed, it is assumed that the oxygen is absorbed/released only by the molten pool of the sample. The diameter of the molten pool is admitted to correspond to the one of the laser spot (3 mm in this work). This hypothesis is validated by measuring the visible molten pool, which exhibits a bright surface as it can be seen in Figure 5-16. Concerning the thickness, it was demonstrated by Epifano *et al.* by SEM analysis that only a small part of the sample is molten during the experiments [48]. The thickness of the molten zone was determined to be 150-200 µm, however an intermediate part-molten zone was evidenced beyond with round-shaped grains starting to connect each other.

In order to verify this hypothesis, calculations of the variation of the O/M ratio are performed in three different cases for the PHENIX29 sample:

- Uptake of oxygen by the whole sample (diameter of 5 mm and thickness of 1.7 mm).
- Uptake of oxygen by the molten pool and its periphery (6% of the whole sample), corresponding to an absorbing zone of 4.7 mm diameter and 150 µm thickness or a zone with Φ = 3.6 mm and e = 250 µm.
- Uptake by only the molten pool (2% of the sample), which corresponds to the starting hypothesis.

The results of these calculations can be seen in Figure 5-28, where the measured solidus temperatures are plotted as a function of the resulting O/M ratio.

In the first case, almost no variation of the O/M ratio is observed during the melting experiments, with an initial value of 1.984 and a final value of 1.985. This case is thus assumed to not be representative of the experiments, as it is not consistent with the variation of solidus temperature observed in this work.

When looking at the second assumption, with an absorbing zone constituted of molten pool and periphery, the variation of the O/M ratio calculated is more consistent with the variation in the solidus temperatures registered, with an initial O/M ratio of 1.986 and a final value of 1.995.

Finally, in the third case scenario, the starting hypothesis assumed here, leads to a variation of the O/M ratio from 1.989 to 2.012

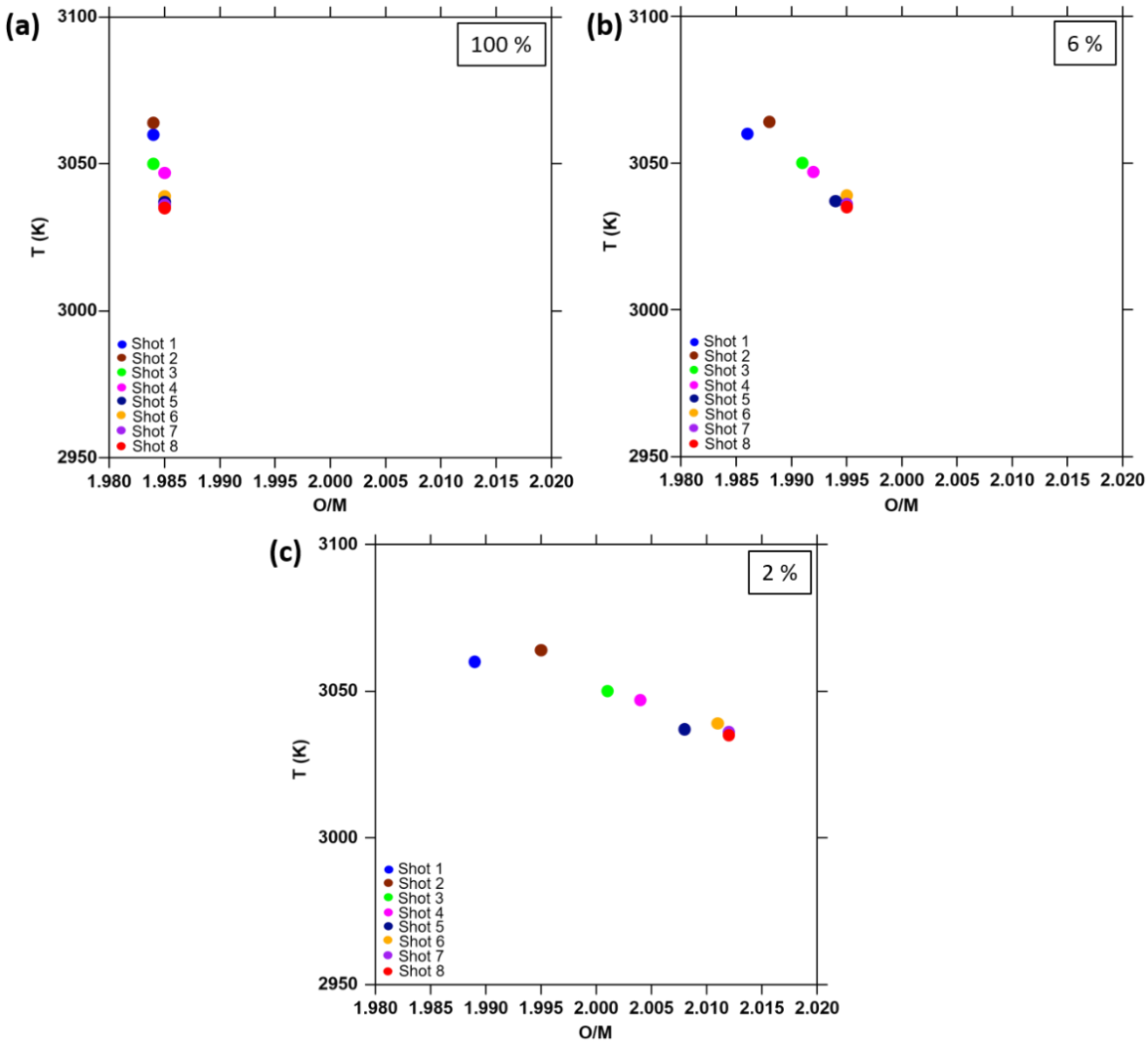

Figure 5-28: Solidus temperature of a PHENIX29 sample as a function of the O/M ratio in case where (a) 100 %, (b) 6 % and (c) 2% of the sample is taking up oxygen.

Thus, difficulties remain in the choice between the second or the third case scenario as starting conditions, based on the results exhibited in Figure 5-28. The underlying question is how much of the sample is heated up during a melting experiment. To answer this question, Welland *et al.* coupled simulations and UO_2 experiments on the laser heating technique used at the JRC-Karlsruhe to study this phenomenon [245]. The authors calculated the temperature gradient along the radius and the depth of the sample during melting, as illustrated in Figure 5-29. They demonstrated that if the centre of the laser spot is heated at around 3000 K, at a radius distance of 4 mm and at a depth of 500 µm from the centre, the temperature is only 1600 K. These gradients were calculated for a pulse of 290 ms at 810 W, power around three times higher than the one used in this work (250 W). Thus, in this study, the gradients are expected to be lower, resulting in lower temperatures in the periphery of the molten pool. It can then be expected that at the border of the sample (radial distance of 2.5 mm from the centre), the temperature will reach 1000-1500 K. In addition, the same temperature is expected at a depth of 200 µm. When considering these temperature gradients occurring during the melting within the sample, it is not possible to define the precise boundaries of the region absorbing oxygen. Thus, it is assumed that only the molten pool is reacting with the oxygen present in the atmosphere, as it is the only zone for which it is possible to define boundaries.

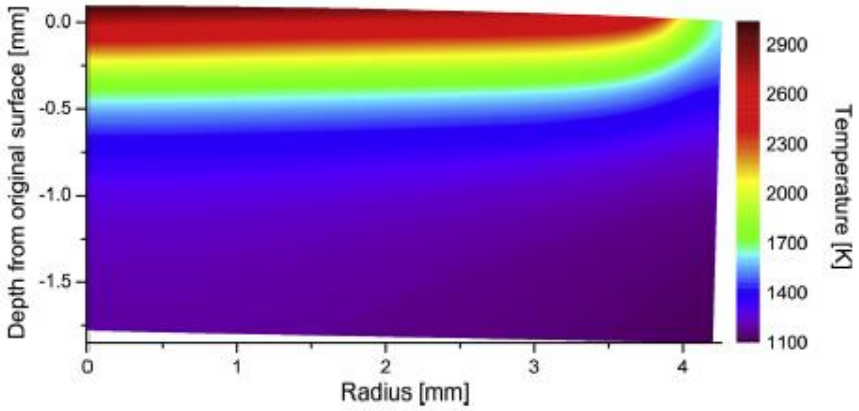

Figure 5-29: Simulated temperature gradient among the sample for a pulse of 290 ms at 810 W by Welland *et al.* [245].

Finally, the last hypothesis made to calculate the variation of the O/M ratio occurring during the melting is that the U, Pu and Am contents were homogeneous within the pellet and constant during the experiments. Three post-melting characterizations studies are available in the literature, two on $U_{1-y}Pu_yO_{2\pm x}$ by De Bruycker *et al.* and Böhler *et al.* [24], [176], and one on $U_{1-z}Am_zO_{2\pm x}$ by Epifano *et al.* [48]. For the first two, the uranium and plutonium contents were measured by SEM-EDS analyses by De Bruycker *et al.* and by XRD by Böhler *et al.*. Both studies concluded that no change in the chemical composition occurred during the melting. On the contrary, in the work of Epifano *et al.*, the uranium and americium contents after melting, determined through XAS experiments, revealed an increase in the americium content of 2-3 % after melting for z = 0.20, 0.30 and 0.50. As stated by the authors, care should be taken when considering these results as reversible segregation phenomenon occurring at high temperature cannot be excluded. Based on these observations, as no post-melting characterizations were performed in this work, it is assumed that no changes in the uranium, plutonium and americium contents are occurring during the melting experiments, based on the works of De Bruycker *et al.* and Böhler *et al.* on the same type of materials. In addition, the sapphire window of the experimental chamber was inspected between each shot to see a potential vaporization of the sample. No black powder or deposit was observed, confirming that vaporization of the sample was minimized with the current set-up.

5.4.3.4 *Effect of the Pu and Am contents*

As it can be seen in Figure 5-24, the solidus temperatures vary with the plutonium and americium contents, as well as with the O/M ratio. The influence of these first two parameters is discussed in this section.

The variation of the solidus temperature with the Pu content measured in this work is plotted in Figure 5-30. To this aim, data are selected for samples containing the same americium content (around 1 %, so PHENIX24, PHENIX29, TRABANT40 and TRABANT45) and with the same O/M ratio of about 1.990. As it can be seen, the solidus temperatures decrease linearly when increasing the plutonium content. This observation was already made by Kato *et al.* as well as by Böhler *et al.* and Strach *et al.* [174], [176], [184]. This is in agreement with the fact that the melting point of $UO_{2.00}$ (3147 ± 20 K [14]) is higher than the one of $PuO_{2.00}$ (3050 ± 60 K [176]). However, as reported in the works of De Bruycker *et al.* [24] and Böhler *et al.* [176], a minimum in the solidus temperature is expected for $0.50 < y < 0.80$. Thus, the linear decrease of the temperature with the plutonium content can only be stated up to y = 0.45.

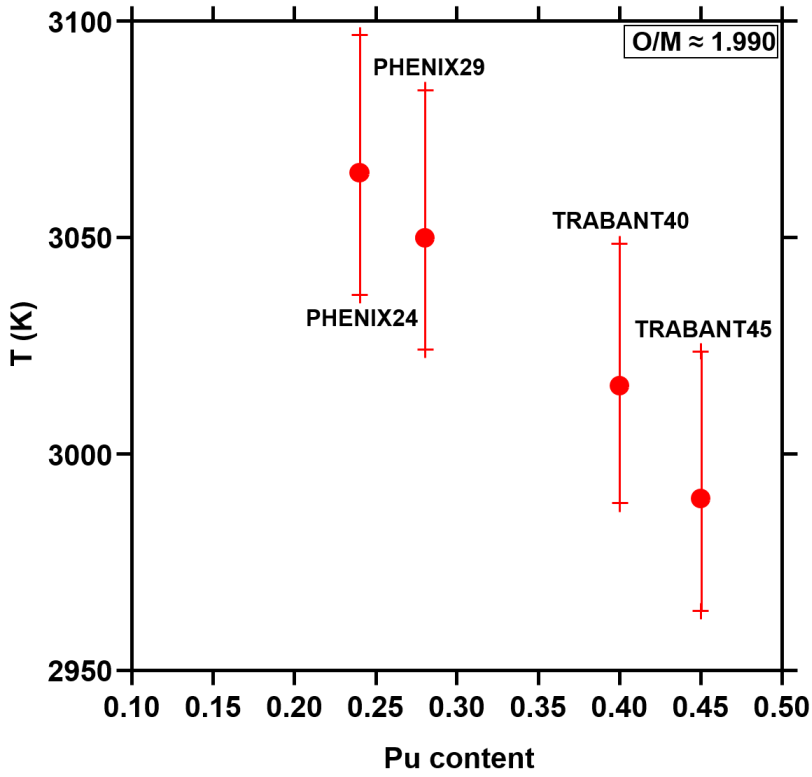

Figure 5-30: Variation of the solidus temperature as a function of the plutonium content (Am content = 0.01 and O/M = 1.990).

The influence of the americium content on the solidus temperatures is reported in Figure 5-31. Data are selected for a similar plutonium content (around 0.28-0.30) and O/M ratio (2.00). The solidus temperature of the PHENIX29 and CAPRA4 are compared to the literature value obtained by Kato *et al.* [174].

It can be observed that the temperature slightly increases when increasing the americium content, with 3030 K for z = 0.006, 3047 K for z = 0.01 and 3056 K for z = 0.02. This observation is in disagreement with the work of Kato *et al.*, who observed a decrease of 3-4 K per mol.% of AmO_2 in the sample. Moreover, Prieur *et al.* also determined the solidus temperature of Am MOX ($U_{0.74}Pu_{0.22}Am_{0.035}Np_{0.005}O_{2-x}$) and Np-MOX ($U_{0.74}Pu_{0.22}Am_{0.02}Np_{0.02}O_{2-x}$), [124] and compared their results to a $U_{1-y}Pu_yO_{2\pm x}$ of approximately the same plutonium content measured by Böhler *et al.* [176]. The authors observed a decrease in the temperature of about few tens of K for $U_{1-y-z}Pu_yAm_zO_{2\pm x}$. For these literature studies reported, the authors admitted that no change in the chemical composition and in the O/M ratio occurred during the melting. Furthermore, in the comparison between Prieur *et al.* and Böhler *et al.*, care should be taken when considering these results as they exhibit different plutonium content and O/M ratios.

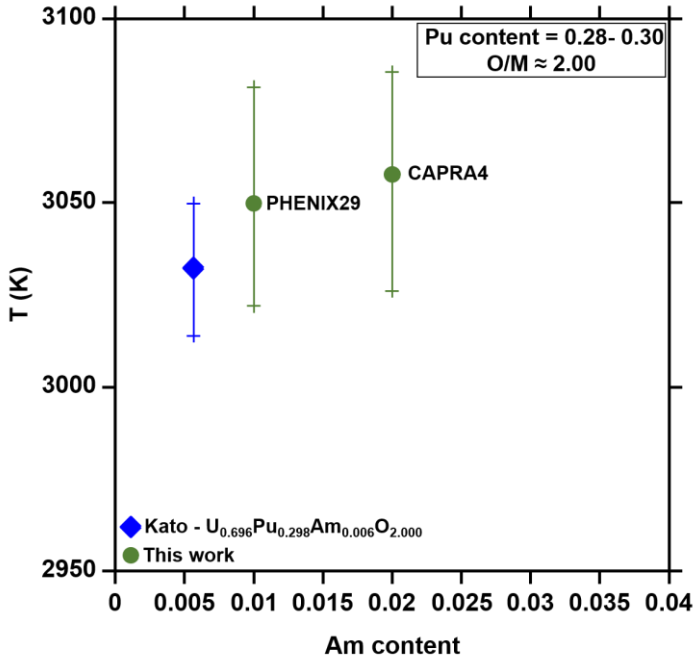

Figure 5-31: Variation of the solidus temperature as a function of the americium content (Pu content = 0.28-0.30 and O/M = 2.00).

The increase in temperature observed in this work when increasing the americium content is also in disagreement with the trend of the pure poles melting temperatures (3147 ± 20 K [14] for $UO_{2.00}$, 3050 ± 60 K [176] for $PuO_{2.00}$ and 2386 K [179] for $AmO_{2.00}$). Indeed, as the melting point of $AmO_{2.00}$ is lower than the ones of $UO_{2.00}$ and $PuO_{2.00}$, a decrease in the temperature would be expected when increasing the americium content. However, care should be taken when considering the melting point of $AmO_{2.00}$ as only one study is available and probably does not refer to stoichiometric $AmO_{2.00}$ but rather to reduced AmO_{2-x}.

In addition, one has to keep in mind the various uncertainties of the work, first on the temperatures (± 30 K in this work and ±20 K for Kato *et al.*), as well as on the O/M ratio (± 0.005) and on the Pu and Am contents (± 0.001). When considering the uncertainties on the temperature, it can be concluded that the americium content has not effect on the melting temperature for $z \leq 0.02$.

5.4.3.5 Effect of the O/M ratio

The last parameter influencing the solidus temperature studied in this work is the O/M ratio.

In this work, for the first time, the variation of the O/M ratio along the shots is observed and quantified based on hypotheses previously described. This study highlights that in the case of a gas flowing inside the experimental chamber, modification of the O/M ratio resulting in an evolution of the solidus temperatures are happening. This study gives a first insight on what is occurring during the laser shot, although the high-temperature O/M ratio of the melting remains unknown.

De Bruycker *et al.* [24] performed post-melting characterizations (XRD and SEM-EDS) on $U_{1-y}Pu_yO_{2.00}$ samples molten without pre-heating under static air, with different pulses conditions. Similar lattice parameters were obtained for the bulk and molten materials, evidencing that no significant oxygen variation occurred during the melting. The EDS analyses also indicated that

the plutonium contents did not vary during the experiments. However, as the post-melting characterizations were performed at room temperature, the authors did not exclude possible reversible segregation phenomena at high temperature. Böhler *et al.* [176] also performed XRD, XANES and Raman spectroscopy to identify possible changes in the samples compositions after the melting, performed under argon for U-rich samples and under air for Pu-rich samples. For samples molten under argon, deviations of the T_{2g} Raman peak positions were evidenced for y = 0.25 and 0.50 as well as a slight shift in the white line positions of the XANES spectra of Pu, however within the experimental uncertainties. These observations could indicate a slight reduction of the samples, however they can be considered as not significant, as XRD results showed no deviation from Vegard's law. For y = 0.40, the lattice parameter of the molten sample exhibited a small deviation from Vegard's law as well as a slight shift in the white line positions of the XANES spectra of U and Pu. These results demonstrated that an oxidation of the sample occurred with a final O/M ratio of 1.985, compared to the initial one of 1.98. Moreover, for samples molten under air, a change of O/M ratio was noticed only for y = 0.90. Indeed, when calculating the O/M ratios of the samples after melting based on the lattice parameters, an O/M ratio of approximately 1.97 (initial = 2.00) was determined. For the other samples, no quantifiable change was noticed. However, their studies were performed in a static gas configuration, with no flow in the chamber and thus no atmosphere renewal. Thus, no continuous oxygen flow was brought into the chamber during the various shots. Moreover, as no *in situ* determination of the oxygen pressure pO_2 was possible at that time, uncertainties remain on the change in O/M ratio.

However, oxidation of the samples was later observed by Strach *et al.* for $U_{1-y}Pu_yO_{2\pm x}$ melted under air [184]. This oxidation was assumed based on the decreasing recorded temperatures along the successive laser shots under air. Moreover, the authors observed dark fumes during the experiments, corresponding to a partial vaporization of the samples and possible variation in the chemical composition. Unfortunately, no post-melting characterizations were performed to quantify this oxidation and few details on the experimental procedure are given in their work.

The quantification of the O/M ratio after laser melting was made in the case of $U_{1-z}Am_zO_{2\pm x}$ by Epifano *et al.* [48]. Indeed, XAS experiments were performed on samples before and after melting under argon and air to determine possible changes in the O/M ratio. Contrary to what was expected, the oxidation of one sample molten under argon was observed for one americium content. Indeed, for z = 0.30 and an initial O/M ratio of 2.00, the final O/M value was 2.05. However, as previously explained in 5.4.3.3, the XAS analyses performed on the mixed oxides of uranium and americium also revealed a variation in the Am content of 2-3 mol.%. The work of Epifano *et al.* was performed under a static gas configuration, with no gas flowing in the chamber and thus no atmosphere renewal. Moreover, a pre-heating step at 1500 K was performed first, followed by four successive laser shots, where the sample was not allowed to cool down to room temperature. Thus, these conditions can affect the O/M ratio variation and care should be taken while comparing the results.

In the literature, quantitative results on the influence of the O/M ratio on the solidus temperature are reported in only one study performed using thermal arrest by Kato *et al.* on hypo-stoichiometric $U_{1-y-z}Pu_yAm_zO_{2\pm x}$ [174] (see Chapter 2 – section 2.3.3.2.1). Starting with O/M = 2.00, the authors noticed an increase of the solidus temperature when decreasing the O/M ratio up to 1.9. No variation of the O/M ratio was assumed to occur during the melting as closed crucibles were used. In addition, no in-situ measurements were performed.

As it can be seen in Figure 5-24 and Figure 5-25, the same observation can be made in this work, *i.e.* the solidus temperature increases when decreasing the O/M ratio. However, two exceptions can be noticed, the PHENIX24 and TRABANT40 samples. Indeed, for these materials, the solidus temperature slightly increases when increasing the O/M ratio. However, this trend lies within the experimental uncertainties and it is thus difficult to conclude properly on an increase or decrease of the temperatures.

Two different behaviours are evidenced: in some cases, the samples absorb oxygen and are oxidized (for example PHENIX24 and PHENIX29), while in other cases, the samples lose oxygen and are reduced (CAPRA4 and TRABANT45). This change of behaviour from one sample to another does not seem to be related to the plutonium or americium content. Indeed, the PHENIX24, PHENIX29 and TRABANT45 samples, exhibiting the same americium content, vary differently. Moreover, the PHENIX29 and CAPRA4 sample, of same plutonium content, also exhibit different trends. Different shot conditions can also not explain the two behaviours as the TRABANT40 and TRABANT45 were molten under the same conditions (shots of 500 ms – 250 W). The only parameter remaining to try to explain these differences is the initial O/M ratio. Indeed, when the samples are initially hypo-stoichiometric (PHENIX24 at 1.983, PHENIX29 at 1.984 and TRABANT40 at 1.978), absorption of oxygen by the sample occurs, resulting in the oxidation of the samples. On the contrary, when the samples are already stoichiometric or hyper-stoichiometric (CAPRA4 at 2.004 and TRABANT45 at 2.000), a release of oxygen is observed during the melting and thus a reduction of the samples.

In order to confirm this trend, laser heating experiments were performed on annealed samples of PHENIX29 and TRABANT40, called PHENIX29-OM and TRABANT40-OM (see Chapter 3 – section 3.2.2.4) of initial O/M ratio close to 2.00 (see Table 5-6). The solidus temperature as a function of the O/M ratio of the annealed materials (in blue) are compared with the ones of the two brut samples (in green) in Figure 5-32. The arrows on the plots indicate the oxidizing/reducing trend of the materials. It appears that the samples tend to oxidize when they are initially hypo-stoichiometric whereas they are reduced when they are stoichiometric or slightly hyper-stoichiometric. This tendency is investigated thanks to thermodynamic calculations in Chapter 6 – section 6.4.3.1.

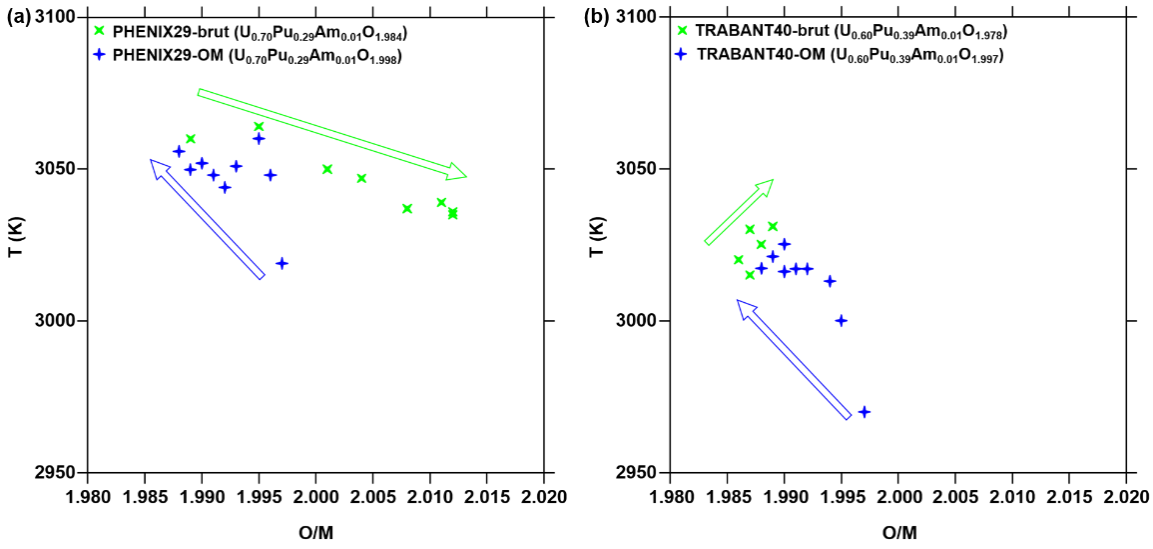

Figure 5-32: Variation of the solidus temperature as a function of the O/M ratio for (a) the PHENIX29 and PHENIX29-OM samples and (b) TRABANT40 and TRABANT40-OM samples.

In the case of the CAPRA4 and TRABANT40-OM sample, when looking at the pO_2 graphs in Figure 5-21, an absorption of oxygen can be noticed during the first shot only, followed by a release of oxygen for the rest of the shots. For these two samples, the quantity of oxygen uptaken during the first shot is not significant enough to induce any change in the initial O/M ratio, as the decrease of pO_2 or the time of absorption are not sufficient.

As evidenced by L. Medyk in her Ph.D. work [54], Raman spectroscopy coupled with EPMA revealed the inhomogeneity of the O/M ratio within the PHENIX29 sample and in particular close to the U- and Pu-rich agglomerates, as it can be seen in Figure 5-33. Thus, a redistribution of U and Pu can occur at high temperature, as well as the diffusion of oxygen in the sample. This phenomenon can explain this change in behaviour with the homogenization of possible uranium-rich or plutonium-rich agglomerates at the surface of the sample and possible absorption of the residual oxygen of the gas by americium or plutonium.

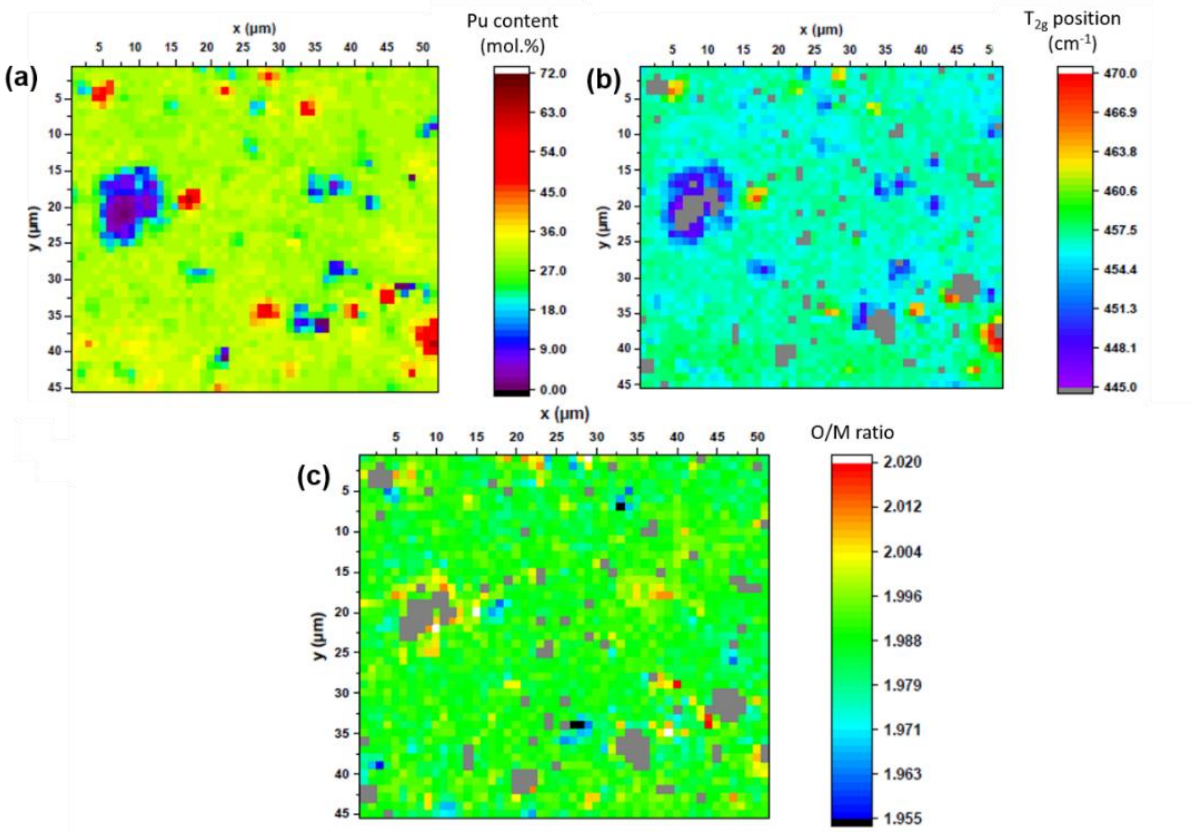

Figure 5-33: (a) Map of the Pu content by EPMA, (b) cartography of the T_{2g} position by Raman spectroscopy and (c) cartography of the O/M ratio obtained by combination of (a) and (b), for the PHENIX29 sample [54]. The grey spots correspond to points removed due to a lack of signal.

5.4.4. Conclusion

In this section, the melting behaviour of several $U_{1-y-z}Pu_yAm_zO_{2\pm x}$ materials was investigated by means of a quasi-containerless laser heating technique. The measurements were performed under argon with several experimental conditions, such as pre- and/or post-heating steps. Thanks to the recent addition of oxygen gauges at the entrance and exit of the experimental chamber, the variation of the oxygen partial pressure inside the chamber was recorded during the experiments. Uptake or release of oxygen during the melting was noticed depending on the samples and was linked to the initial O/M ratio of the samples. Based on few hypotheses, the variation of the O/M ratio occurring during the melting was quantified for the first time. The

same methodology was applied for all the samples studied in this work and the corresponding variations of the solidus temperatures as a function of the O/M ratio were determined. The influence of several parameters on these solidus temperatures was also discussed in this work.

First, it was evidenced that pre-heating steps enhance the absorption of oxygen by the sample and that the longer the step, the more oxygen is absorbed.

In a second part, the hypotheses formulated to calculate the O/M ratio were discussed. Based on the simulations performed by Welland *et al.* [245], no influence of the temperature gradients occurring in the sample during the melting was stated for the absorption of oxygen by the surroundings of the molten pool. It was thus assumed that only the molten pool was absorbing/releasing oxygen. However, further experiments are needed to conclude on the precise size of the zone of the sample reacting with the oxygen of the atmosphere. Finally, in the absence of post-melting characterizations and based on the results obtained by De Bruycker *et al.* [24], Böhler *et al.* [176] and Epifano *et al.* [48], no changes in the U, Pu and Am contents were supposed to occur during the melting.

In a third part, the influence of the plutonium content on the solidus temperature was discussed and it was noticed that an increase in the Pu content leads to a decrease in the recorded solidus temperature. This observation is in agreement with the trend already observed by Kato *et al.* and Böhler *et al.* for $y < 0.45$. The influence of the americium content was also studied. A slight increase of the temperature with an increase of the Am content was observed. This result was found to disagree with the works of Kato *et al.* [174] and Prieur *et al.* [124], who stated the opposite trend. However, based on the experimental uncertainties on the solidus temperature, as well as on the O/M ratio of the samples compared in this work, it is difficult to conclude on the impact of the Am addition on the solidus temperatures.

Finally, the effect of the O/M ratio was studied. This study reported a variation of the O/M ratio occurring during the melting with either a reduction or an oxidation of the samples. The difference in behaviour was found to be linked to the initial O/M ratio, with a tendency to absorb oxygen for initially hypo-stoichiometric samples and to lose oxygen for initially hyper- or stoichiometric samples.

In order to state on the hypotheses made to calculate the changes in the O/M ratio, further experiments are necessary to study the chemical composition and aspects of the molten pool. In particular, the combination of EPMA and Raman spectroscopy or XAS could be useful for the determination of the local Pu content and O/M ratio at the laser spot, before and after melting.

5.5. CONCLUSION

In this chapter, investigations of fundamental structural and thermodynamic properties of the $U_{1-y-z}Pu_yAm_zO_{2\pm x}$ oxides were carried out.

First, room temperature characterizations were performed to get structural insight into the materials. The chemical composition of the samples was checked by EPMA. The plutonium content of the matrix phase was determined and the presence of U-rich and Pu-rich agglomerates was revealed. XRD analyses agreed with this observation with the evidence of two phases resulted from the refinement of the patterns: one matrix phase and one UO_2 phase.

The lattice parameters obtained were used to calculate the O/M ratio of the samples. The latter was also checked by XANES analyses. These experiments also evidenced a mixture of valences of the U, Pu and Am cations, with the simultaneous presence of U^{5+} and Pu^{3+}/Am^{3+}. The co-existence of these cations was not attributed to the presence of U- and Pu-rich agglomerates but to a peculiar behaviour of the $U_{1-y-z}Pu_yAm_zO_{2\pm x}$ mixed oxides. A summary of all these characterizations was performed to define the compositions of the samples of interest and their availability.

Following the determination of the room temperature structural properties, the lattice thermal expansion of three samples (PHENIX29, CAPRA4 and TRABANT40) was studied between 1873 K and room temperature. The results were compared to the recommendations available in the literature and positive deviations from these recommendations were noticed above 1373 K for the three samples. This was explained by an important negative deviation from the stoichiometry. As the americium is already purely trivalent at room temperature, the reduction of plutonium was enhanced during the experiments at high temperature. Below 1373 K, the thermal expansion was identical for the three samples, independent of the plutonium, americium and oxygen contents.

The enthalpy increments of the $U_{0.70}Pu_{0.28}Am_{0.02}O_{2.00}$ (CAPRA4) sample were studied from 585 to 1790 K by drop calorimetry and the heat capacity was derived from the resulting function. The results obtained in this work were compared with literature data of the pure poles UO_2 and PuO_2 and with $U_{0.72}Pu_{0.28}O_{2.00}$ from Kandan *et al.*. Outlier values were observed in the enthalpy increment for 1000, 1300 and 1600 K, which could be attributed to the changes in the first oxygen sublattice, the release of He and changes in the cationic sublattice, respectively. Moreover, higher heat capacities were observed in this work above 1100 K, which could be explained as well by a possible deviation from the stoichiometry enhanced by the presence of americium.

Finally, the melting behaviour of the materials was investigated by means of a laser heating technique. For the first time, the variation of the O/M ratio occurring during the melting was assessed. The influence of several parameters on the solidus temperatures, such as pre-heating steps, the plutonium and americium contents or the O/M ratio, was discussed. The solidus temperature was found to decrease when increasing the Pu content and to increase when increasing the Am content. An increase of the solidus temperature was also reported when decreasing the O/M ratio from 2.00. The accuracy of the hypotheses made to calculate this O/M ratio was also discussed. In addition, it was found that the oxidation/reduction behaviour of the samples during melting was related to their initial O/M ratio. Indeed, the hypo-stoichiometric samples exhibited the tendency to be oxidized, while the hyper- or near-stoichiometric samples were being reduced.

The new sets of solidus temperatures and O/M ratios obtained here constitute paramount data for the representation of the phase diagram. These data will be used in the assessment of the CALPHAD model of the U-Pu-Am-O system. Experimental data on enthalpy increments will be compared to thermodynamic calculations. These thermodynamic calculations on the quaternary U-Pu-Am-O system, as well as the re-assessment of some of its various sub-systems will be presented in the next chapter.

6. THERMODYNAMIC MODELLING OF THE U-PU-AM-O SYSTEM

In this chapter, thermodynamic investigations using the CALPHAD method are performed on the U-Pu-Am-O system. The models of the liquid phases of the Pu-O and U-Pu-O systems are evaluated based on sets of laser heating data obtained after 2011. In the U-Pu-O system, a shift of the congruent melting composition towards O/M < 2.00 is observed, explained by the stabilisation of the solid solution in this range, due to a maximum of the configurational entropy of plutonium. Calculations are also performed to predict the number of moles of gas and samples interacting during the melting. A re-evaluation of the model of the Pu-Am-O system is proposed based on the new sets of experimental data obtained in this work and the available literature data, with the re-assessment of the MO_2, M_2O_3 and liquid phases. A good agreement is obtained between the model and the oxygen potential data of the literature, as well as with the phase equilibria and phase transitions obtained in this work. Significant differences are noticed with the oxygen potentials measured in this work. For the U-Pu-Am-O system, thermodynamic calculations are performed as comparison with the experimental data obtained in this work but no re-assessment is proposed. The calculated site fractions do not reproduce the peculiar behaviour evidenced experimentally as no Pu^{3+} is formed according to the model, which leads to discrepancies in the calculated heat capacities. The experimental trend is well reproduced by the model for the solid/liquid phase transitions, although uncertainties remain on the exact O/M ratio at which the melting occurs. The experimental oxidation/reduction behaviour is explained by the initial O/M ratio and the oxidizing power of the atmosphere of melting. The need for additional experiments is clearly highlighted in this chapter to overcome the uncertainties remaining on the various sub-systems of the U-Pu-Am-O system.

6. THERMODYNAMIC MODELLING OF THE U-PU-AM-O SYSTEM

Thanks to the new experimental campaigns performed in this work, new input data were obtained for the thermodynamic modelling of the U-Pu-Am-O system. As explained in Chapter 3, the U-Pu-Am-O model is based on the extrapolation of its binary and ternary sub-systems.

Thanks to the determination of a new value for the melting point of PuO_2 [176], the model of the liquid phase of the Pu-O system is reassessed in section 6.1, based on the previous model of Guéneau *et al.* [7].

The parameters of the liquid phase of the U-Pu-O system are then adjusted in section 6.2, to better reproduce recent sets of solidus/liquidus temperatures available in the literature. The melting behaviour of the $U_{1-y}Pu_yO_{2\pm x}$ oxides is then discussed as a function of the plutonium content, the O/M ratio and the atmosphere of melting.

In section 6.3, a re-assessment of the model of the Pu-Am-O system is proposed based on the experimental results detailed in Chapter 4 for the $Pu_{1-z}Am_zO_{2-x}$ samples (site fractions, phase equilibria, oxygen potential, solidus/liquidus temperature) and the data available in the literature.

Finally, in section 6.4, thermodynamic investigations of the U-Pu-Am-O system are performed using the new sets of data obtained in Chapter 5 (site fractions at room temperature, enthalpy increment, heat capacity and melting behaviour) and sets of oxygen potential data from the literature.

6.1. RE-ASSESSMENT OF THE PU-O SYSTEM

The most recent assessment of the Pu-O system was proposed by Guéneau *et al.* in 2011 [7]. In this model, the melting point measured by laser heating by De Bruycker *et al.* was taken into account. However, a more recent melting temperature was obtained in 2014 by Böhler *et al.*, highlighting the need for a reassessment of the liquid phase of the Pu-O system. The selected data are described first, followed by the assessment of the Gibbs energy of the liquid phase and the resulting phase diagram.

6.1.1. Selected data

A critical review of the available literature data on the solid/liquid phase transitions of the Pu-O system was already performed in Chapter 2 – section 2.3.3.1.2. Thus, only the selected experimental data are reported here.

In the previous assessment of the Pu-O system performed by Guéneau *et al.* [7], the melting point obtained by De Bruycker *et al.* (3017 ± 28 K) measured by laser heating was selected [222]. In this reassessment, the melting point determined by Böhler *et al.* (3050 ± 59 K) is selected for $PuO_{2.00}$ [176]. Indeed, the authors improved the experimental conditions to ensure a better mechanical stability of the sample and the repeatability of the measurements. Thus, their results are considered as more reliable compared to the temperature obtained by De Bruycker *et al.* using the same technique [222]. For Pu_2O_3, the melting point recommended by Konings *et al.* is selected (2352 ± 10 K) [125]. Because of a large scattering of the few

solidus/liquidus temperatures obtained between Pu_2O_3 and PuO_2 [20], [174], [178], these values are not used as input data but only considered for comparison.

6.1.2. Gibbs energy of the liquid phase

The model developed by Guéneau *et al.* in 2011 [7] was used as starting point for this reassessment. Based on the selected data, only the parameters of the liquid phase for the Pu-O system are modified in this work. The CALPHAD method and the Thermo-Calc software (version 2020b) were used. More details about the principles of this method and the Gibbs energy function of the liquid phase are presented in Chapter 2 – section 2.4 and Chapter 3 – section 3.1.2.

The liquid phase for the Pu-O system is described using the following two-sublattice model [192]:

$$(Pu^{3+})_P(O^{2-}, Va^{Q-}, O, PuO_2)_Q \quad \textbf{(6.1)}$$

With P and Q coefficients, equal to:

$$P = 2y_{O^{2-}} + Qy_{Va^{Q-}} \text{ and } Q = 3 \quad \textbf{(6.2)}$$

According to equation **(3.13)**, the Gibbs energy of the liquid phase G^{liq} is expressed by:

$$\begin{aligned} G^{liq} = {} & y_{O^{2-}}\,{}^0G^{liq}_{(Pu^{3+})(O^{2-})} + Qy_{Va^{Q-}}\,{}^0G^{liq}_{Pu} + Qy_{PuO_2}\,{}^0G^{liq}_{PuO_2} + Qy_O\,{}^0G^{liq}_{O} \\ & + RT\left[Q\left(y_{O^{2-}}\ln y_{O^{2-}} + y_{Va^{Q-}}\ln y_{Va^{Q-}} + y_{PuO_2}\ln y_{PuO_2} + y_O \ln y_O\right)\right] \\ & + y_{O^{2-}}y_{Va^{Q-}}\left[{}^0L_{(Pu^{3+})(O^{2-},Va^{Q-})} + \left(y_{O^{2-}} - y_{Va^{Q-}}\right){}^1L_{(Pu^{3+})(O^{2-},Va^{Q-})}\right] \\ & + y_{O^{2-}}y_{PuO_2}\,{}^0L_{(Pu^{3+})(O^{2-},PuO_2)} \end{aligned} \quad \textbf{(6.3)}$$

Here, the $L_{(Pu^{3+})(O^{2-},Va^{Q-})}$ interaction parameters describe the liquid phase in the Pu-Pu_2O_3 region whereas $L_{(Pu^{3+})(O^{2-},PuO_2)}$ is used to model the Pu_2O_3-PuO_2 composition range.

6.1.3. Results

In a first step, the melting enthalpies ΔH_{fus} of the two end-members Pu_2O_3 and PuO_2 were slightly modified to take into account the recommended values of Konings *et al.* [125]. The melting entropies ΔS_{fus} of the two end-members were then adjusted to reproduce the previously selected melting points for the two compounds [125], [176].

In a second step, the Pu_2O_3-PuO_2 solidus/liquidus curve was described by adjusting the interaction parameter between the two end-members (${}^0L_{(Pu^{3+})(O^{2-},PuO_2)}$) to reproduce the melting temperature measured by Böhler *et al.* for PuO_2 [176]. A shift of the congruent melting towards lower O/Pu ratio is observed (O/Pu = 1.95), due to the high oxygen potential of PuO_{2-x} and its ability to lose oxygen above 2000 K. The updated parameters are reported in Appendix I. The calculated phase diagram is presented in Figure 6-1(a) and a comparison with the experimental data in the Pu_2O_3-PuO_2 region is shown in Figure 6-1(b). The previous version of Guéneau *et al.* is also reported in Figure 6-1(b) for comparison. Higher solidus/liquidus temperatures are obtained in the Pu_2O_3-PuO_2 range with the re-assessed model.

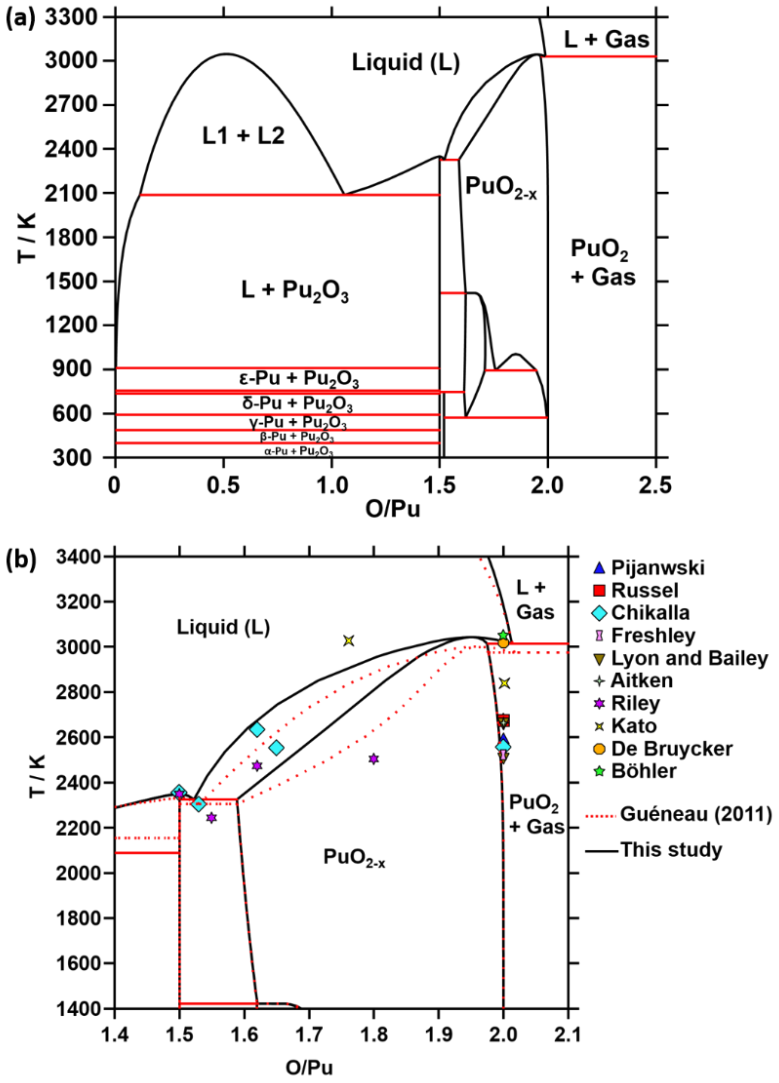

Figure 6-1: (a) Calculated phase diagram of the Pu-O system as a function of the O/Pu ratio and (b) Zoom on the 1.4 < O/Pu < 2.2 composition range.

In this re-assessment, the melting point of Pu_2O_3 is calculated at 2350 K, in agreement with the data of Chikalla (2360 ± 20 K) [20] and the recommendation of Konings *et al.* (2352 ± 10 K) [125]. The eutectic reaction (Liquid → Pu_2O_3 + PuO_{2-x}) is observed at 2325 K, in agreement with the experimental data of Chikalla (2303 K) [20]. A good agreement is also observed with the experimental data of Chikalla *et al.* [20] for O/Pu = 1.62 and 1.65. The congruent melting of PuO_2 is reported at 3042 K for O/Pu = 1.95 (compared to 3000 K for O/Pu=1.96 in [23]), in agreement with the temperature measured by Böhler *et al.* (3050 ± 59 K), although the authors reported a stoichiometric compound [176].

The invariant reaction (Liquid → PuO_{2-x} + O_2(g)) is calculated at 3015 K but no experimental data exist for comparison.

However, this model is not in agreement with the melting temperature measured by Kato for $PuO_{1.76}$. As previously explained, uncertainties remain on the exact O/M ratio of the samples and on possible changes in the composition due to non-congruent vaporization, both for Kato *et al.* [174] and Böhler *et al.* [176]. Thus, the description of the liquidus/solidus curve between Pu_2O_3 and PuO_2 is tentative and further measurements are needed to improve this model.

6.1.4. Conclusion

In this section, a critical review of the available data on solid/liquid phase transitions in the Pu-O system was performed first. The melting point of PuO_2 recently obtained by Böhler *et al.* [176], as well as the melting point of Pu_2O_3 recommended by Konings *et al.* [125], were selected for the re-assessment. The model of the liquid phase of the Pu-O system was modified and a good agreement was obtained with the selected experimental data. However, uncertainties remain in this model, as no post-melting characterizations were performed and the exact O/M ratio at the melting is unknown. The re-evaluation performed here will be used as input for the investigations of higher order systems, such as U-Pu-O, which will be described in the next section.

Moreover, these parameters constitute the reference parameters implemented in the TAF-ID V13 for the Pu-O system.

6.2. Re-assessment of the solid/liquid phase transitions in the U-Pu-O system

As for the Pu-O system, the latest assessment of the U-Pu-O system was proposed by Guéneau *et al.* in 2011 [7]. However, after 2011, other sets of solidus/liquidus temperatures on $U_{1-y}Pu_yO_{2\pm x}$ were measured by means of laser heating. Thus, a re-evaluation of the liquid phase of the U-Pu-O system is needed. First, a critical review of the available experimental data on the solid/liquid transitions in U-Pu-O is performed to select data sets for the re-assessment. The Gibbs energy function of the liquid phase of this system is then described, as well as the modified interaction parameters. Finally, the updated model is compared to the selected experimental data and discussions are proposed on the melting behaviour of $U_{1-y}Pu_yO_{2\pm x}$ as a function of the O/M ratio, the Pu content and the atmosphere of melting.

6.2.1. Selected data

A critical review of the available literature data on the solid/liquid phase transitions of the U-Pu-O system was already performed in Chapter 2 – section 2.3.3.2.1. Thus, only the selected experimental data are commented here.

For this re-assessment, the following data are selected:

- For $y < 0.50$, the solidus/liquidus temperatures obtained by Kato *et al.* [185] using Re crucibles and containing less than 1 at.% Am are used, as well as the data determined by Böhler *et al.* [176] using laser heating.
- For $y > 0.50$, only the measurements of Böhler *et al.* [176] are considered and preferred to the ones of De Bruycker *et al.* [9], based on the improvement of the experimental conditions (see Chapter 2 - section 2.3.3.2.1). The data of Strach *et al.* obtained using the same technique are omitted due to the lack of detailed information in [184].

6.2.2. Gibbs energy of the liquid phase

As for the Pu-O system, the model developed by Guéneau *et al.* [7] is used as a starting point for this reassessment. Based on the solidus/liquidus experimental data previously selected in section 6.2.1, only the parameters of the liquid phase of the U-Pu-O system are modified. For the U-Pu and U-O sub-systems, the models of Kurata [246] and Guéneau *et al.* [7] are accepted and are not described here, as no modification was performed since 2011.

The liquid phase of the ternary U-Pu-O is described using the following two-sublattice model **(6.4)**:

$$(Pu^{3+}, U^{4+})_P (O^{2-}, Va^{Q-}, O, PuO_2)_Q \qquad \textbf{(6.4)}$$

A schematic representation of the model is presented in Figure 6-2, highlighting the interactions between the different species used to describe the ternary liquid phase.

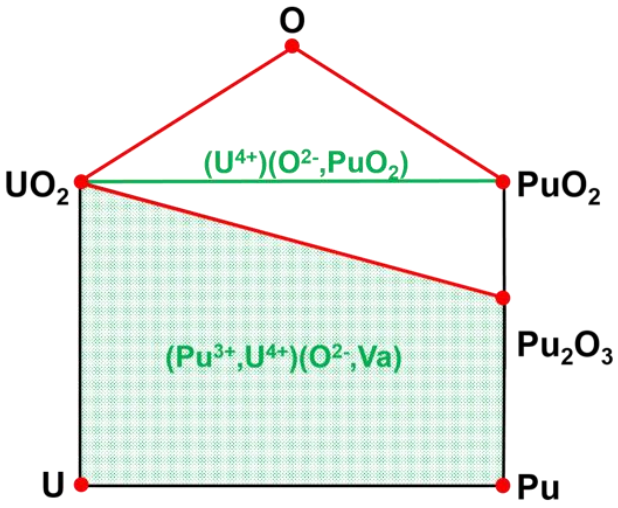

Figure 6-2: Schematic representation of the model of the liquid phase for the U-Pu-O system. In green: parameters re-assessed in this version.

The Gibbs energy function is expressed by:

$$\begin{aligned}
G^{liq} = {} & y_{O^{2-}}\,{}^0G^{liq}_{(Pu^{3+})(O^{2-})} + y_{U^{4+}}y_{O^{2-}}\,{}^0G^{liq}_{(U^{4+})(O^{2-})} + Qy_{Va^{Q-}}\,{}^0G^{liq}_{Pu} + Qy_{Va^{Q-}}\,{}^0G^{liq}_{U} \\
& + Qy_{PuO_2}\,{}^0G^{liq}_{PuO_2} + Qy_O\,{}^0G^{liq}_{O} \\
& + RT\left[P\left(y_{Pu^{3+}}\ln y_{Pu^{3+}} + y_{U^{4+}}\ln y_{U^{4+}}\right)\right. \\
& \left. + Q\left(y_{O^{2-}}\ln y_{O^{2-}} + y_{Va^{Q-}}\ln y_{Va^{Q-}} + y_{PuO_2}\ln y_{PuO_2} + y_O\ln y_O\right)\right] \\
& + \; y_{Pu^{3+}}y_{O^{2-}}y_{Va^{Q-}}\left[{}^0L_{(Pu^{3+})(O^{2-},Va^{Q-})} + \left(y_{O^{2-}} - y_{Va^{Q-}}\right){}^1L_{(Pu^{3+})(O^{2-},Va^{Q-})}\right] \\
& + \; y_{Pu^{3+}}y_{O^{2-}}y_{PuO_2}\,{}^0L_{(Pu^{3+})(O^{2-},PuO_2)} + y_{U^{4+}}y_{O^{2-}}y_{Va^{Q-}}\left[{}^0L_{(U^{4+})(O^{2-},Va^{Q-})}\right. \\
& \left. + \left(y_{O^{2-}} - y_{Va^{Q-}}\right){}^1L_{(U^{4+})(O^{2-},Va^{Q-})} + \left(y_{O^{2-}} - y_{Va^{Q-}}\right)^2\,{}^2L_{(U^{4+})(O^{2-},Va^{Q-})}\right] \\
& + \; y_{U^{4+}}y_{O^{2-}}y_O\,{}^0L_{(U^{4+})(O^{2-},O)} \\
& + y_{Pu^{3+}}y_{U^{4+}}y_{Va^{Q-}}\left[{}^0L_{(Pu^{3+},U^{4+})(Va^{Q-})} + y_{Va^{Q-}}\,{}^1L_{(Pu^{3+},U^{4+})(Va^{Q-})}\right] \\
& + y_{Pu^{3+}}y_{U^{4+}}y_{O^{2-}}y_{Va^{Q-}}\,{}^0L_{(Pu^{3+},U^{4+})(O^{2-},Va^{Q-})} \\
& + y_{U^{4+}}y_{O^{2-}}y_{PuO_2}\left[{}^0L_{(U^{4+})(O^{2-},PuO_2)} + \left(y_{O^{2-}} - y_{PuO_2}\right){}^1L_{(U^{4+})(O^{2-},PuO_2)}\right]
\end{aligned} \qquad \textbf{(6.5)}$$

In addition to the interaction parameters of the binary U-O, Pu-O [7] and U-Pu [246] sub-systems, the following ternary parameters are introduced to describe the U-Pu-O system:

- The ${}^{n}L_{(U^{4+})(O^{2-},PuO_2)}$ parameters to describe the solidus/liquidus temperatures along the UO_2-PuO_2 composition line,
- The ${}^{0}L_{(Pu^{3+},U^{4+})(O^{2-},Va^{Q-})}$ parameter to improve the description of the melting temperatures of mixed oxides in the hypo-stoichiometric range (O/M < 2.00).

6.2.3. Results

In a first step, the modified parameters of the Pu-O liquid phase obtained in section 6.1.3 are introduced in the model. In a second step, the ternary interaction parameters are reassessed to better reproduce the data selected in section 6.2.1. The thermodynamic parameters of this re-evaluation are reported in Appendix I.

The interaction parameters ${}^{0}L_{(U^{4+})(O^{2-},PuO_2)}$ and ${}^{1}L_{(U^{4+})(O^{2-},PuO_2)}$ are first modified to reproduce the selected experimental data for O/M = 2.00. The calculated isopleth section between $UO_{1.97}$ and $PuO_{1.95}$ (corresponding to the congruent melting compositions for U-O and Pu-O, more details in section 6.2.4.1) is plotted in Figure 6-3(a) and compared to the previous model of Guéneau *et al.* [7]. Lower solidus/liquidus curve are observed in this work for uranium-rich oxides whereas, on the contrary, the calculated temperatures are higher for high Pu contents. Comparison between the calculations and the selected experimental data is visible on Figure 6-3(b). A good agreement is observed with a minimum of the solidus temperature, located around y = 0.70, as already described by De Bruycker *et al.* [24] and Böhler *et al.* [176].

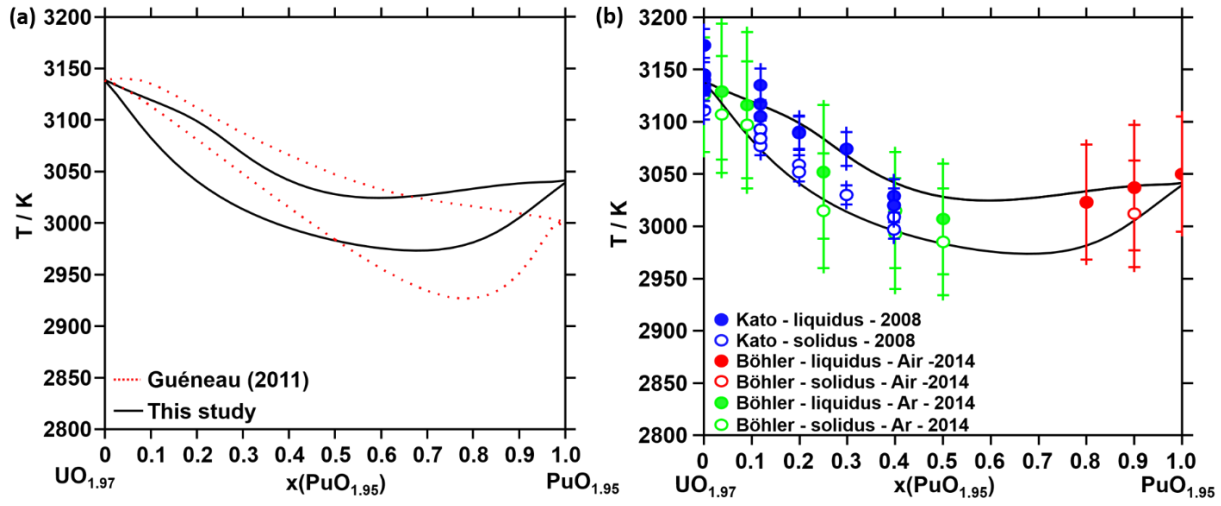

Figure 6-3: Calculated $UO_{1.98}$-$PuO_{1.96}$ phase diagram compared to (a) Guéneau *et al.* (dashed line) [7] and (b) the selected experimental data of Kato *et al.* [174] and Böhler *et al.* [176].

Finally, to describe the hypo-stoichiometric region, ${}^{0}L_{(Pu^{3+},U^{4+})(O^{2-})}$ and ${}^{0}L_{(Pu^{3+},U^{4+})(O^{2-},PuO_2)}$ were removed from the model of Guéneau *et al.* [7] and replaced by the single interaction parameter: ${}^{0}L_{(Pu^{3+},U^{4+})(O^{2-},Va^{Q-})}$. This parameter is assessed to stabilize the liquid phase towards the metallic liquid and is adjusted to describe the solidus/liquidus data of Kato measured for 1.925 < O/M < 2 for y = 0.118, 0.199 and 0.397 [185].

These experimental values of Kato *et al.* are compared to the calculated isopleth sections for y = 0.12, 0.20 and 0.40 in Figure 6-4(a), (b), (c) respectively. A general good agreement is observed, within the experimental uncertainties. Nevertheless, a systematic underestimation of the solidus temperatures is noticed in the near-stoichiometry region. However, large uncertainties still remain on these experimental data, as no detailed information nor uncertainties are given by the authors on the exact O/M ratio of the samples.

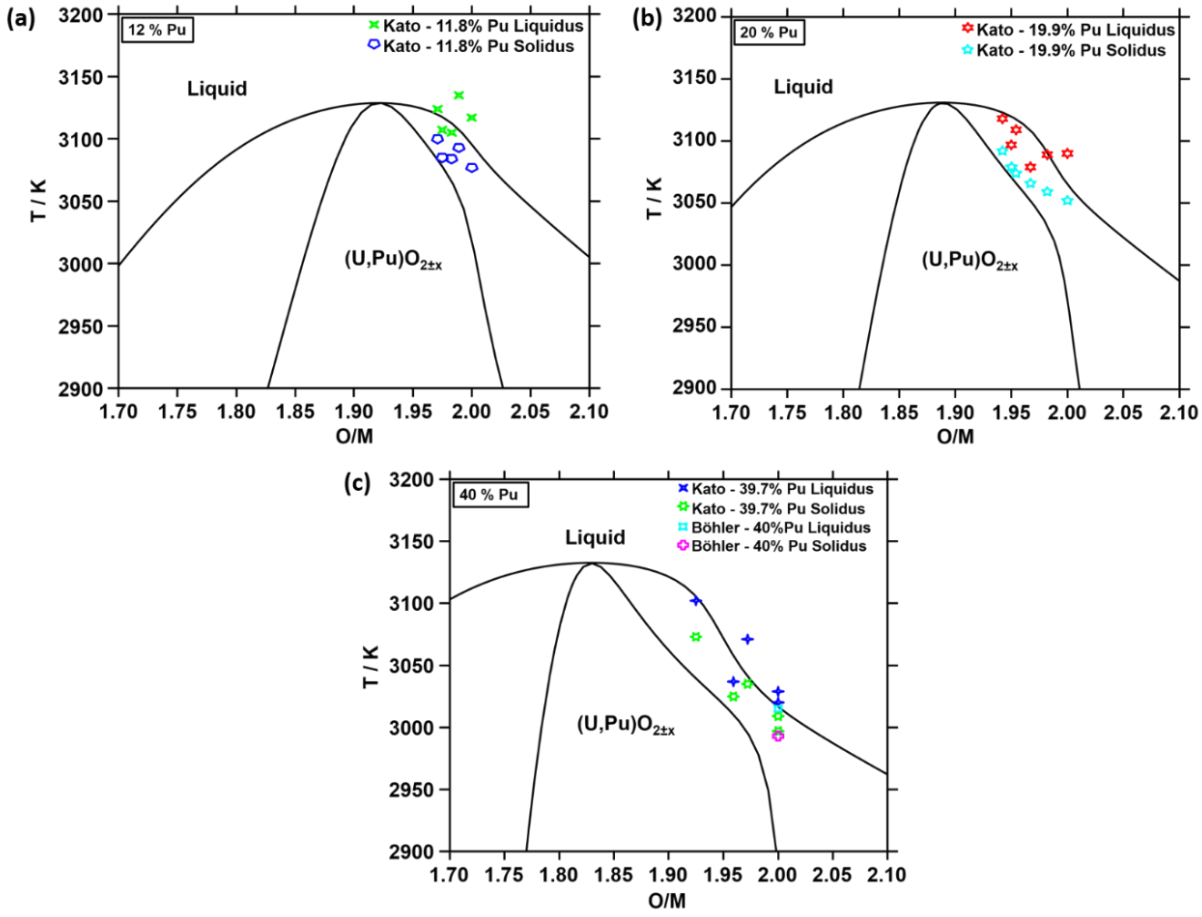

Figure 6-4: Calculated isopleths sections of the U-Pu-O diagram for y = (a) 0.12, (b) 0.20 and (c) = 0.40, compared to the selected experimental data of Kato *et al.* [185] and Böhler *et al.* [176]. The experimental uncertainties (± 35 K) are not represented here for sake of clarity.

Calculated isothermal sections of the U-Pu-O system at 1500, 2500 and 3000 K are plotted in Figure 6-5. It can be noticed that the tie lines (in green), giving the compositions of the two phases in the region [$(U,Pu)O_{2\pm x}$ + Liquid], do not lie along the UO_2-PuO_2 composition line, evidencing that the UO_2-PuO_2 system is not a pseudo-binary system. Moreover, a complex melting behaviour in the metal-oxide region is highlighted. Indeed, at 2500 and 3000 K, a miscibility gap between metallic and oxide liquid phases is observed. The miscibility gap, appearing first in Pu-O, is shifted towards high U contents when increasing the temperature. However, care should be taken when considering this composition range of the phase diagram, as no experimental data are available in this region.

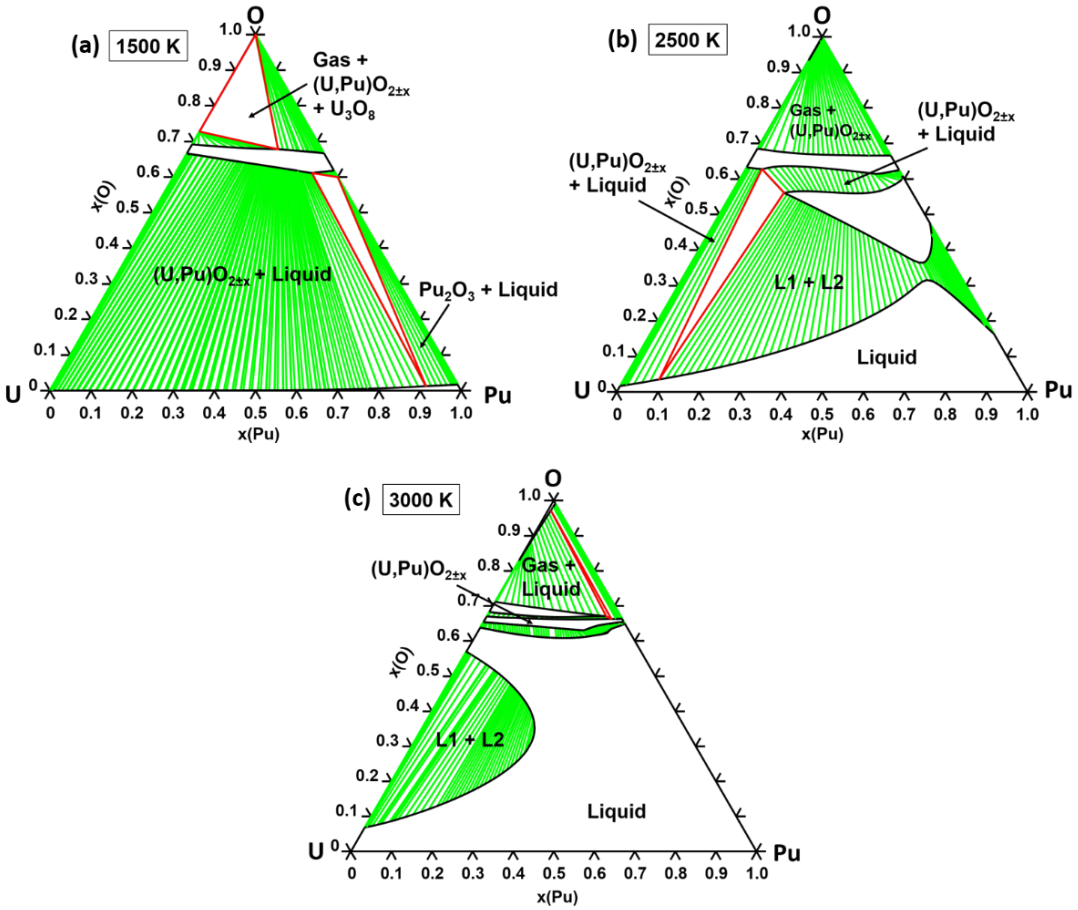

Figure 6-5: Calculated isothermal sections at (a) 1500 K (b) 2500 K and (c) 3000 K of the U-Pu-O system.

This re-assessment presents some limitations due to the lack of available experimental data. Indeed, few data are available for high Pu contents and no measurements were performed in the hyper-stoichiometric range. Further investigations are also needed for O/M < 1.90 for a better description of the maximum of the melting temperature. As no O/M ratio *in-situ* measurements were performed during the experiments used for this re-assessment, the exact O/M ratio at which the phase transitions occurred still remains unknown. Thus, uncertainties remain on broad areas of the system and the model can be considered valid for $0 < y < 0.5$ and $1.90 < O/M < 2.00$. Outside this range, this re-evaluation constitutes only a preliminary re-assessment.

Based on this model, the melting behaviour of $U_{1-y}Pu_yO_{2\pm x}$ mixed oxides and the influence of several parameters will be discussed in the next section.

6.2.4. Discussion on the solid/liquid phase transitions

The influence of several parameters on the melting behaviour of $U_{1-y}Pu_yO_{2\pm x}$ mixed oxides is discussed in this section. First, the influence of the plutonium and oxygen content is studied. Then, calculations are performed to reproduce the experimental conditions of the laser heating melting and study the influence of the atmosphere (type of gas and number of moles of gas) during the measurements.

6.2.4.1 *Influence of the Pu content and O/M ratio*

A 3D map of the solidus (in green) and liquidus (in blue) temperatures of the U-Pu-O system is calculated using a Python script and the TC-Python software (Figure 6-6(a) from the $UO_{2\pm x}$ side or (b) from PuO_{2-x}) [247].

To understand the melting behaviour of the ternary system U-Pu-O, the binary systems U-O (Figure 6-6(a)) and Pu-O (Figure 6-6 (b)) are investigated first. In the U-O system, the congruent melting point is calculated at 3139 K for O/M = 1.97 [1]. From this maximum, the solidus and liquidus temperatures decrease towards both the hypo- and hyper-stoichiometric regions (Figure 6-6(a)). For the Pu-O system, the same behaviour is noticed for O/Pu ≤ 2, with a congruent melting calculated at 3042 K for 1.95 (see Figure 6-1(b)). Thus, for the two end-members, the congruent melting is found to occur in the hypo-stoichiometric region.

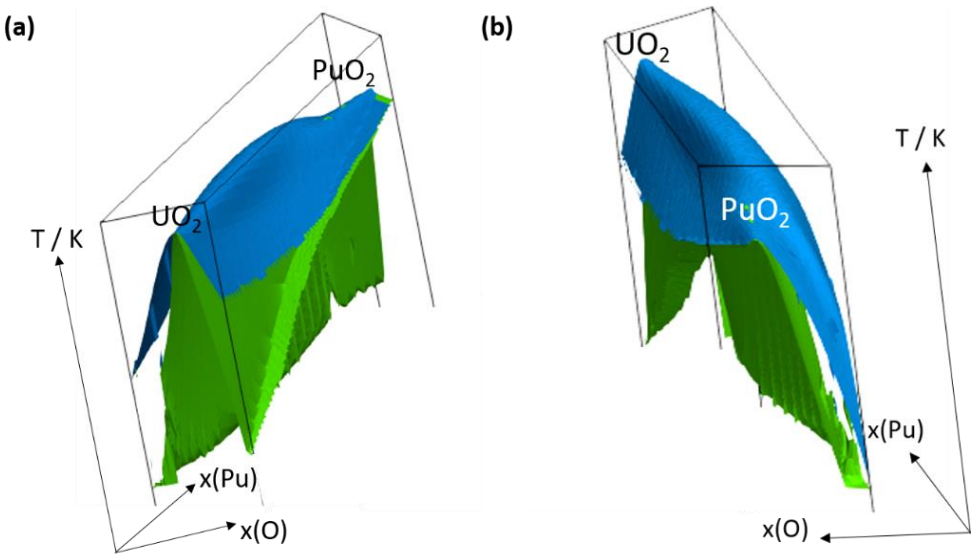

Figure 6-6: 3D map of the liquidus (in blue) and solidus (in green) temperatures in the U-Pu-O system for 0.60 < x(O) < 0.69, (a) from the $UO_{2\pm x}$ side and (b) the PuO_{2-x} side.

For the U-Pu-O system, the solidus temperature and O/M ratio calculated at the congruency are plotted in Figure 6-7(a) and (b), respectively.

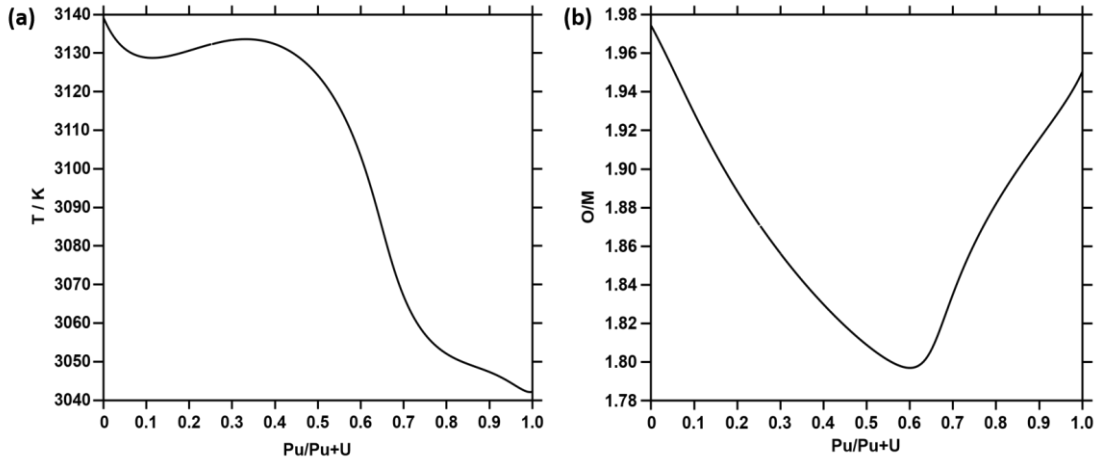

Figure 6-7: (a) Solidus temperature and (b) O/M ratio at the congruent melting as a function of the Pu content for $U_{1-y}Pu_yO_{2\pm x}$.

From $UO_{1.97}$ to $U_{0.55}Pu_{0.45}O_{1.82}$, an almost constant congruent melting temperature is observed around 3130-3140 K (Figure 6-7(a)). A decrease of the temperature is noticed down to 3042 K for $PuO_{1.95}$ when increasing the Pu content. A maximum of the melting temperature is determined at 3134 K for $U_{0.67}Pu_{0.33}O_{1.85}$. For the O/M ratio at the congruency (Figure 6-7(b)), a "V" shape is observed, with a decrease to a minimum value of 1.80 for y = 0.6, followed by an increase for higher Pu contents.

To understand the origin of this shift in the congruency towards the hypo-stoichiometric region, the stability of the mixed oxides is investigated as a function of the O/M ratio and Pu content.

Based on the model of Guéneau *et al.* [7] and as described in Chapter 3 – section 3.1.2, the Gibbs energy of $U_{1-y}Pu_yO_{2\pm x}$ is described using the following three-sublattice model:

$$(U^{3+},U^{4+},U^{5+},Pu^{3+},Pu^{4+})(O^{2-},Va)_2(O^{2-},Va)$$

Where the first sublattice corresponds to the site for uranium and plutonium cations, the second sublattice to the normal tetrahedral site for oxygen and the third sublattice to the interstitial site.

The introduction of vacancies "Va" allows to vary the occupation rates of both oxygen sites. From an O/M ratio equal to 2, the reduction of the mixed oxides leads to an increase of the oxygen vacancy concentration in the second sublattice. To compensate this oxygen loss, due to the higher oxygen potential of PuO_2 compared to the one of UO_2, the plutonium is first reduced from Pu^{4+} to Pu^{3+} according to the following reaction:

$$(U^{4+},Pu^{4+})(O^{-2})_2(Va) \rightarrow (U^{4+},Pu^{4+},Pu^{3+})(O^{2-},Va)_2(Va) + \frac{x}{2}O_{2\,(g)}$$

After complete reduction of the Pu^{4+} into Pu^{3+}, the reduction of uranium from U^{4+} to U^{3+} occurs for lower O/M ratios.

The configurational entropy S of the mixed oxide $U_{1-y}Pu_yO_{2\pm x}$ corresponds to the disorder on both metallic and oxygen sites and is expressed as a sum of the following contributions:

For plutonium:
$$S_{Pu} = -R\,(y_{Pu^{3+}} \ln y_{Pu^{3+}} + y_{Pu^{4+}} \ln y_{Pu^{4+}}) \quad \textbf{(6.6)}$$

For uranium:
$$S_U = -R\,(y_{U^{3+}} \ln y_{U^{3+}} + y_{U^{4+}} \ln y_{U^{4+}} + y_{U^{5+}} \ln y_{U^{5+}}) \quad \textbf{(6.7)}$$

For oxygen:
$$S_O = -R\begin{bmatrix} 2\,(y_{Va} \ln y_{Va} + y_{O^{-2}} \ln y_{O^{-2}})_{normal\ O\ sublattice} \\ +(y_{Va} \ln y_{Va} + y_{O^{-2}} \ln y_{O^{-2}})_{interstitial\ O\ sublattice} \end{bmatrix} \quad \textbf{(6.8)}$$

where R is the gas constant (equals to 8.314 J.mol^{-1}.K^{-1}) and y_i are the site fractions of the species occupying the different sublattices.

In the case of a reduction of the sample, the increase of the Pu^{3+} proportion, as well as of the oxygen vacancy concentration results in an increase of the total configurational entropy.

In order to illustrate this observation, the configurational entropy of the different species Pu, U, and O, as well as the sum of these contributions in the mixed oxide, are calculated in Figure 6-8 at 3000 K for y = 0.50. The dashed lines indicate the limit of stability of the phase at this temperature. A maximum of the S_{Pu} is observed for O/M = 1.84 (Figure 6-8(a)), while a

minimum of S_U is found at this O/M ratio (Figure 6-8(b)). On the contrary, a linear decrease of S_O is observed from O/M = 1.755 to 1.955 in Figure 6-8(c). The total configurational entropy, plotted in Figure 6-8(d), results from the sum of the configurational entropies of the three components. As it can be seen, the trend of the total configurational entropy is given by S_O, as O is the main species.

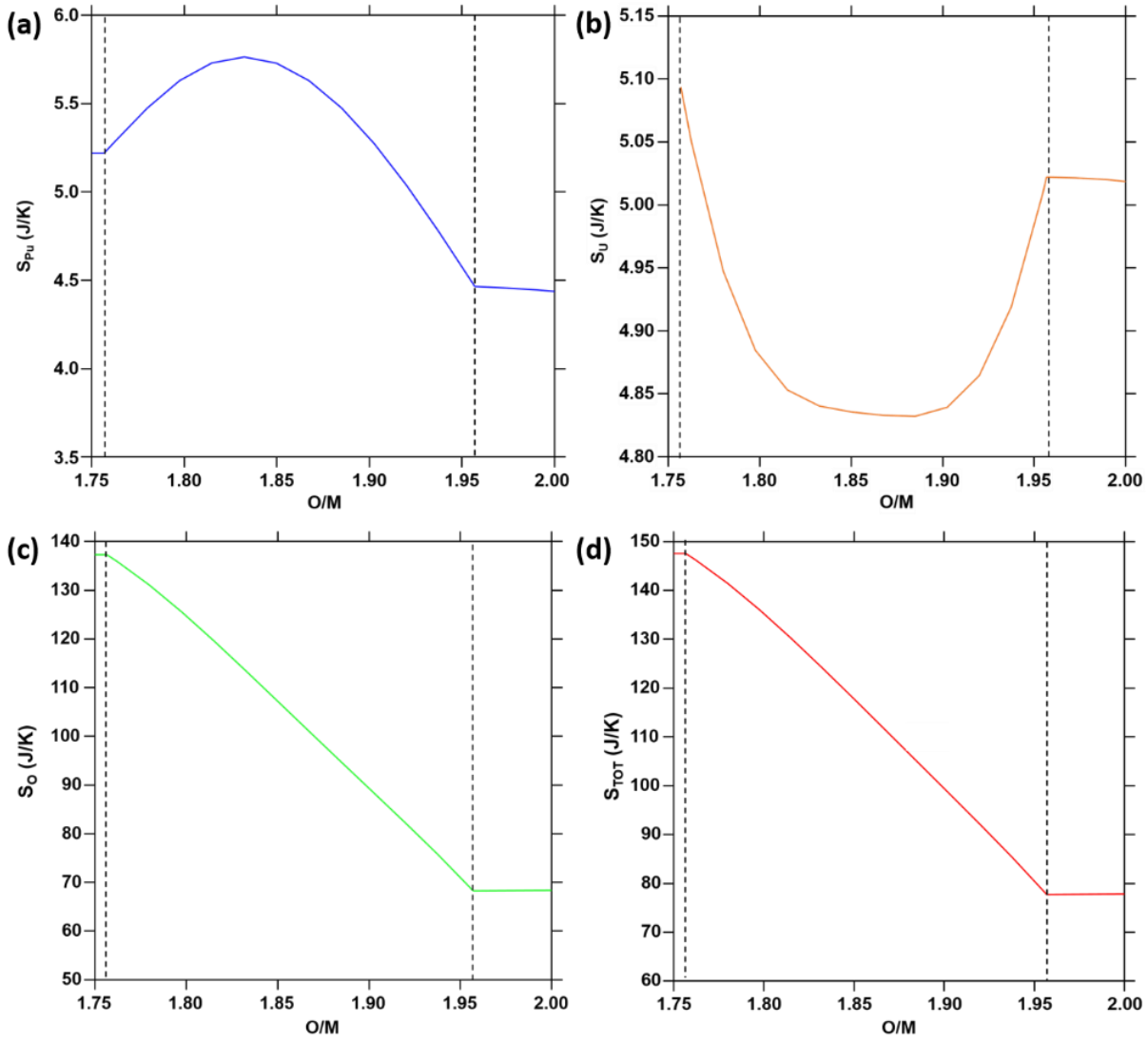

Figure 6-8: Configurational entropy of (a) Pu, (b) U, (c) O and (d) total at 3000 K as a function of the O/M ratio for y = 0.50.

For a better understanding of the trends of the configurational entropies, the site fractions of the different species are plotted for y = 0.50 and 3000 K as a function of the O/M ratio, as illustrated in Figure 6-9.

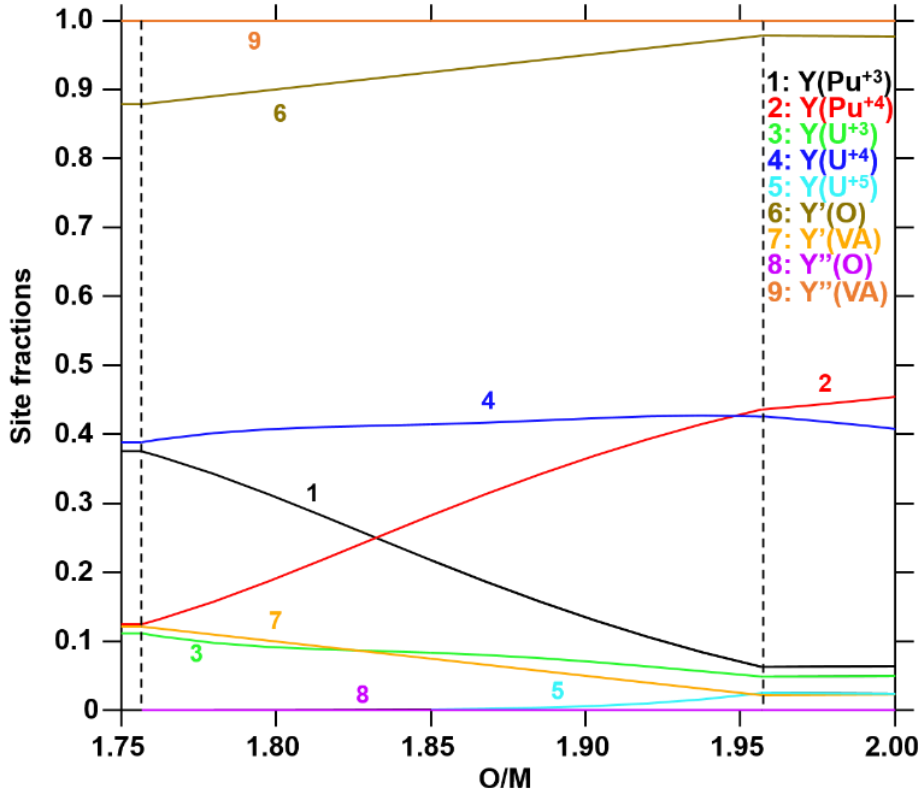

Figure 6-9: Calculated site fractions at 3000 K as a function of the O/M ratio for y = 0.50.

At O/M = 1.84, the maximum of entropy of Pu (Figure 6-8(a)), corresponds to the composition where the site fractions of Pu^{+3} and Pu^{+4} are equal, in agreement with the expression of S_{Pu} in Equation **(6.6)**. For uranium, the site fractions of U^{+4} is nearly constant over the O/M range described here. The minimum value of S_U observed at O/M = 1.84 is explained by the presence of only U^{4+} and U^{3+} for this O/M ratio. The increase of S_U observed in Figure 6-8(b) corresponds to the appearance of U^{5+} for O/M > 1.84. Thus, for O/M > 1.84, the simultaneous presence of U^{3+}, U^{5+} and Pu^{3+} is observed here at 3000 K, as it was already observed at room temperature for $U_{1-y-z}Pu_yAm_zO_{2\pm x}$ in Chapter 5 – section 5.1.3. This observation is also in agreement with the reduction of plutonium occurring before the reduction of U. For the oxygen and vacancies contributions, the trend observed in Figure 6-8(c) is related to the decreasing proportion of vacancies when increasing the O/M ratio.

As the Gibbs energy is described by $G = H - TS$, a maximum of the configuration entropy of the phase corresponds to a minimum of the Gibbs energy and thus to the most stable composition, which could explain the observed maximum melting temperature for this composition.

To illustrate this statement, a 3D map of the Gibbs energy of $U_{1-y}Pu_yO_{2\pm x}$ at 3000 K is plotted in Figure 6-10(a).

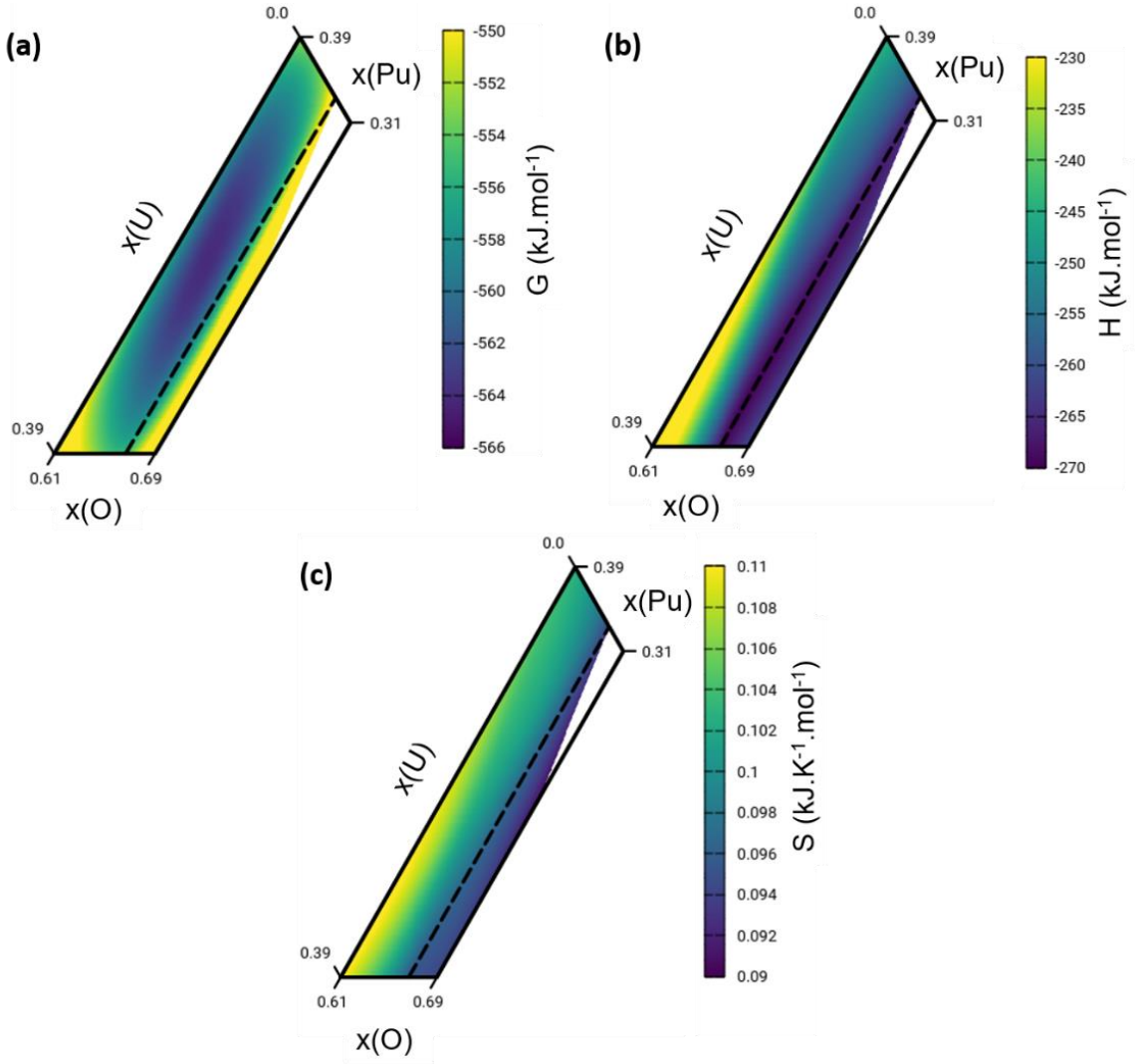

Figure 6-10: 3D map of (a) the Gibbs energy, (b) the enthalpy, (c) the entropy of $U_{1-y}Pu_yO_{2\pm x}$ as a function of the x(O) and x(Pu) at 3000 K (dashed line: UO_2-PuO_2 composition line).

A minimum of the Gibbs energy is evidenced at $U_{0.55}Pu_{0.45}O_{1.82}$. This observation explains the stabilization of the mixed oxides for O/M < 2.00, as it can be seen on the left side of the dashed lines. It is consistent with the maximum of the melting temperature located in the hypo-stoichiometric region. Higher values for the Gibbs energies are found for O/M > 2.00 and highly reduced samples.

3D maps of the enthalpy and entropy of configuration of $U_{1-y}Pu_yO_{2\pm x}$ are also calculated at 3000 K (Figure 6-10(b) and (c), respectively). The minimum of the enthalpy (leading to a stabilization of the phase) is located at O/M = 2.00 over the whole plutonium content range. The enthalpy increases with the deviation from O/M = 2, for highly reduced samples. The configurational entropy increases with the defect concentration, thus when decreasing the O/M ratio in the hypo-stoichiometric region.

The Gibbs energy of $U_{1-y}Pu_yO_{2\pm x}$ is thus a combination of both contributions of the configurational enthalpy and entropy.

From these calculations, the stabilization of $U_{1-y}Pu_yO_{2\pm x}$ in the hypo-stoichiometric range is explained. In addition, more stable compounds are also found when increasing the Pu content.

These observations described the same trend observed for the congruent melting (see Figure 6-4). These results are in agreement with the study of Aitken and Evans [181], who explained the congruent melting by the stabilization of the oxide and the formation of oxygen vacancies and Pu^{3+}/Pu^{4+} disorder.

Nevertheless, the influence of the stability of the liquid phase on the melting temperature of the mixed oxide should also be taken into account for an accurate description of the melting behaviour of $U_{1-y}Pu_yO_{2\pm x}$. However, as no thermodynamic data exist on the liquid phase, this influence could not be discussed here.

6.2.4.2 Influence of the atmosphere of melting

6.2.4.2.1 Argon or Air

As already studied by several authors, the atmosphere of melting plays a crucial role on the melting behaviour of $U_{1-y}Pu_yO_{2\pm x}$ mixed oxides.

Calculations of the solidus temperatures of $U_{1-y}Pu_yO_{2\pm x}$ and their associated O/M ratio as a function of the plutonium content are performed under air and argon at 0.3 MPa, as it can be seen in Figure 6-11(a) and (b), respectively. These calculations are performed with 5 moles of gas, one mole of metal (U+Pu) and two moles of oxygen and considering the thermodynamic equilibrium between the atmosphere and the sample.

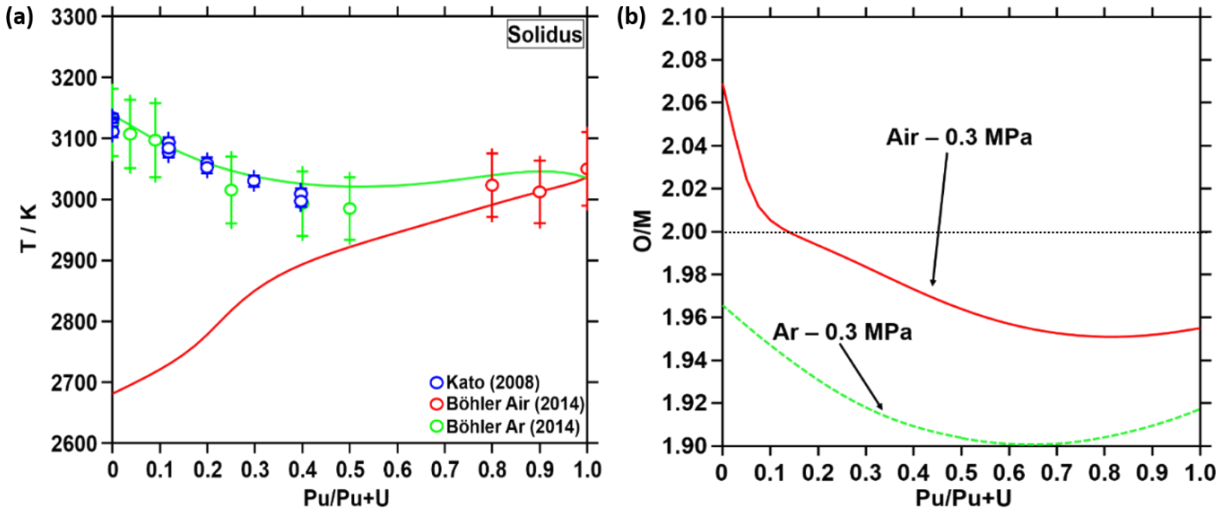

Figure 6-11: Calculated (a) solidus temperatures compared to the experimental data of Kato *et al.* [174] and Böhler *et al.* [176] and (b) O/M ratio at the solidus temperature as a function of Pu content, under air in red and argon in green. Calculations performed for 5 moles of gas and 3 moles of samples.

Under air, starting from UO_2, a significant increase of the solidus temperature is noticed when increasing the plutonium content, with T = 2683 K for UO_2 and 3037 K for PuO_2. On the contrary, under argon, a slight decrease occurs towards higher Pu contents, from 3139 K for UO_2 and 3037 K for PuO_2. A minimum is observed around y = 0.50 at 3020 K. A good agreement is obtained with the selected experimental data for the re-assessment. The liquidus temperatures, not presented here, follow the same trend.

Figure 6-11(b) presents the calculated variation of the O/M ratio at the solidus temperature as a function of the Pu content. The same trend is observed for the two atmospheres, *i.e.* a

decrease of the O/M ratio when increasing the plutonium content. Under air, the uranium-rich samples are oxidized up to y = 0.15. This hyper-stoichiometry is explained by the tendency of UO_2 to oxidize into UO_{2+x}. For 0.15 < y < 1, the samples are hypo-stoichiometric in oxygen. Under argon, the samples all present an O/M ratio below 2.00 at the solidus temperature, over the whole plutonium content range.

Thus, as already stated by Böhler *et al.* [176], argon is the most reliable atmosphere to maintain an O/M ratio as close as possible to 2 for uranium-rich samples. On the contrary, air allows to keep an O/M ratio close to stoichiometry for plutonium-rich mixed oxides (y > 0.50).

6.2.4.2.2 Number of moles of gas

In order to reproduce in the best way as possible the experimental campaigns, the quantities of gas and sample reacting with each other have to be known. Unfortunately, no direct experimental determination is possible yet. Thus, in this section, an estimation of these quantities is proposed based on thermodynamic calculations of the solidus temperature and its associated O/M ratio.

The influence of the amount of sample is not mentioned in this section as it was already discussed in Chapter 5 – section 5.4.3.3. Indeed, it was highlighted that based on the important experimental uncertainties, taking into account only the molten pool was the more appropriate choice.

Only one estimation of the number of moles of gas reacting with the molten pool of the sample is available in the literature, proposed by Quaini *et al.* in their investigation of melting temperatures in the UO_2-PuO_2-ZrO_2 system by laser heating [248]. In their work, 3 moles of samples were considered in the calculations, with one mole of gas, which was admitted to be contained in a boundary layer of laminar gas flow.

The same approach as Quaini *et al.* was already used in Chapter 4 – section 4.4.2.2 and Chapter 5 – section 5.4.2.2 to calculate the number of moles of the molten pool interacting with the oxygen (see for more details on the hypotheses). Using again the same approach and hypotheses, the following number of moles of samples and gas are calculated in the present work:

- 1.8×10^{-3} moles for a $U_{0.75}Pu_{0.25}O_2$ sample with M = 271.5 g.mol^{-1}, density = 10.5 g.cm^{-3}, diameter = 8 mm, thickness = 1 mm;
- 1.1×10^{-4} moles for the molten pool with diameter = 5 mm (size of the laser spot) and depth = 150 µm [48];
- 1.6×10^{-1} moles of gas in the whole chamber (cylinder of 20 cm long and 10 cm diameter, filled with a gas of ideal behaviour);
- 5.9×10^{-6} moles of gas in the boundary layer. A laminar flow of buffer gas is assumed in the boundary layer, represented by a cylinder of 5 mm diameter and 3 mm thickness, from the surface of the molten pool.

The solidification paths of $U_{0.75}Pu_{0.25}O_{2\pm x}$ are calculated under air and argon at 0.3 MPa in Figure 6-12. For these calculations, the number of mole of sample is assumed to be 1.1×10^{-4} moles,

corresponding to the molten pool, and the number of mole of gas is taken equal to 5.10^{-4} mol of gas, corresponding to an intermediate value between the gas contained in the boundary layer and in the whole chamber.

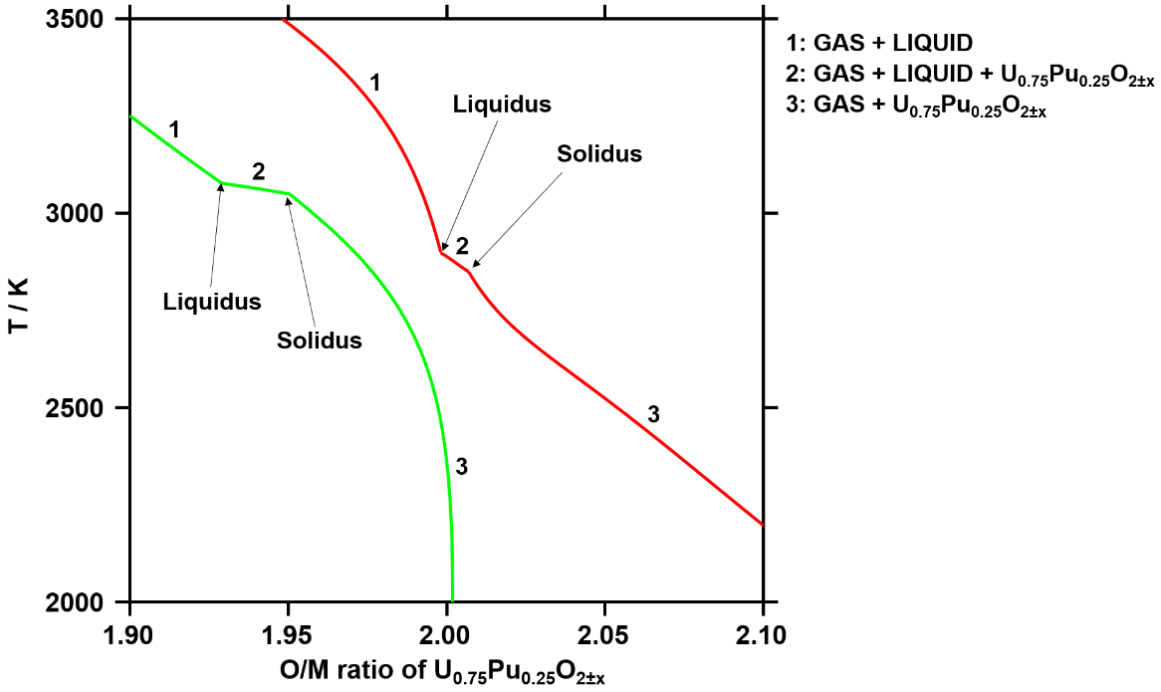

Figure 6-12: Solidification paths for $U_{0.75}Pu_{0.25}O_{2\pm x}$ as a function of the O/M ratio of the solid phase. Calculated for 5.10^{-4} moles of gas and 1.10^{-4} moles of sample under Air (in red) and Ar (in green) at 0.3 MPa.

Three domains can be observed on the solidifications paths: Gas + Liquid, Gas + Liquid + Solid and Gas + Solid. The liquidus and solidus temperatures are represented on the figure as boundaries of these domains. As expected, the liquidus temperature calculated under argon (3077 K) is higher than the one calculated under air (2898 K), in agreement with previous literature works [176], [184], [223]. The same trend is observed for the solidus temperature. In addition, as already described in Figure 6-11, the solidification path calculated under air is located at higher O/M ratio than the one calculated under Ar. Indeed, an O/M ratio of 1.93 is obtained for the liquidus temperature under Ar, while this value is equal to 2.00 under air.

To study the influence of the amount of gas reacting with the sample, the liquidus temperature and its associated O/M ratio are calculated in Figure 6-13 for $U_{0.75}Pu_{0.25}O_{2\pm x}$ and various numbers of moles of gas (air and argon). Five conditions are chosen for the amount of gas, from the gas contained only in the boundary layer to the gas contained in the whole chamber.

When looking first at the liquidus temperature (Figure 6-13(a)), two different behaviours can be noticed. Indeed, under air, a decrease of the liquidus temperature is noticed when increasing the number of moles of gas. For 5.10^{-6} mol of gas, the liquidus temperature is determined at 3039 K, against 2914 K for 10^{-3} mol of gas. These results are in agreement with the measurements of Strach *et al.*, who observed a decrease of the melting temperature throughout the successive shots under air [184]. For higher amount of gas (10^{-2} and 10^{-1} moles), no liquidus temperature is observed on the solidification paths, indicating that these conditions are not appropriate for the calculations. On the contrary, under argon, an increase of the temperature is observed when increasing the number of moles of gas. The liquidus temperature is determined

at T = 3050 K in the case of an equilibrium with the boundary layer and at T = 3130 K for 10^{-2} mol of gas.

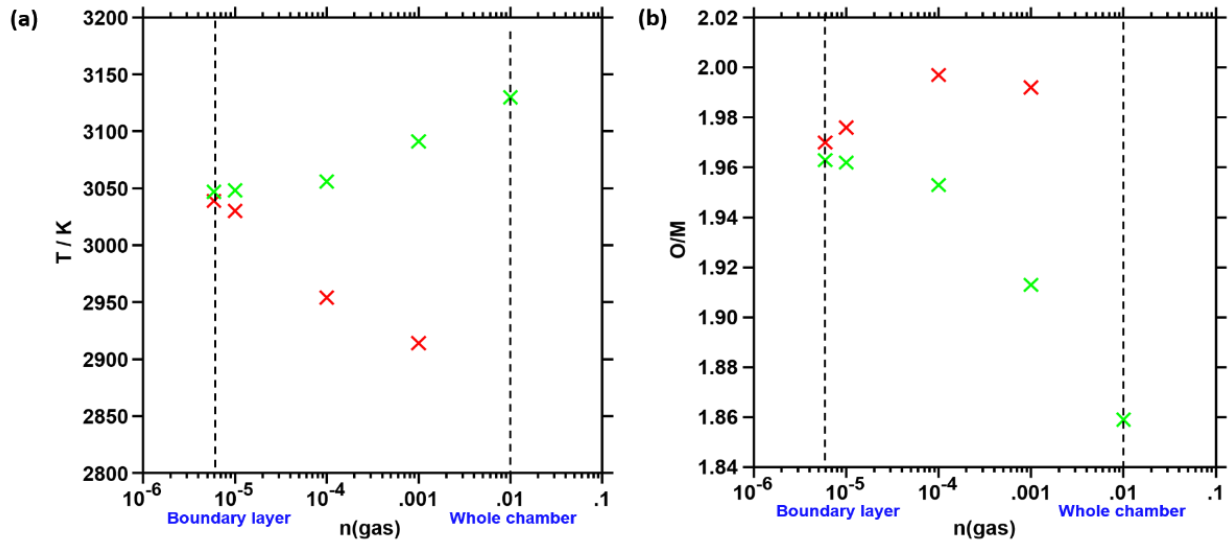

Figure 6-13: Variation of calculated (a) liquidus temperature and (b) O/M ratio for $U_{0.75}Pu_{0.25}O_{2\pm x}$ as a function of the number of moles of gas reacting with the sample (red: air - argon: green) at 0.3 MPa.

For the O/M ratio of the liquidus temperature, the opposite behaviour is observed. Indeed, under air, an increase of the O/M ratio is noticed when increasing the number of mole of gas. On the contrary, under argon, due to the reducing power of the gas, a decrease of the O/M ratio at the liquidus temperature is observed when increasing the amount of gas.

From these calculations, a first assessment of the number of moles of gas and sample reacting with each other during the melting is proposed. Indeed, as it can be seen in Figure 6-13, a stabilization of the liquidus temperature around 3040 K and of the O/M ratio around 1.95 is observed from $5.9\text{x}10^{-6}$ to 10^{-4} moles of gas under Ar and from $5.9\text{x}10^{-6}$ to 10^{-5} moles of gas under air. Thus, these ranges of amount of gas are considered as realistic and representing reasonably well the experimental conditions and will be used for the rest of the calculations performed in this work.

6.2.5. Conclusion

Based on the critical review of the experimental data on the solid/liquid phase transitions of the U-Pu-O system, highlighting important discrepancies between the various techniques used for the determination of the melting points, two sets of data were selected for the re-assessment. The parameters of the liquid phase of the U-Pu-O system were then re-evaluated using the CALPHAD method and taking into account the re-assessment previously performed for the Pu-O system. Moreover, these parameters constitute the reference parameters implemented in the TAF-ID V13 for the Pu-O and U-Pu-O systems.

Overall, a good agreement between the selected experimental data and the calculated data was obtained. The complex melting behaviour of $U_{1-y}Pu_yO_{2\pm x}$ was evidenced, with the highlight of the non pseudo-binary system UO_2-PuO_2. The congruent melting was found to be shifted towards lower O/M ratio for $U_{1-y}Pu_yO_{2-x}$ (around 1.90) compared to the end-members ($UO_{1.97}$ and $PuO_{1.95}$). This was explained by the stabilisation of the mixed oxides in the

hypo-stoichiometric region (O/M < 2), due to the increase of the configurational entropy by the formation of oxygen vacancies and Pu^{3+}/Pu^{4+} disorder occurring at high temperature. The influence of the atmosphere (argon or air) and its amount of gas reacting with the sample was discussed. It was observed that in order to reproduce the experimental conditions, the assessment of only a limited amount of gas reacting with the molten pool of the sample was proposed.

However, numerous uncertainties still remain after this re-assessment, mainly in the high Pu content range and in the hyper-stoichiometric region. Moreover, the exact O/M ratio at which the solidus/liquidus temperatures are measured remain unknown, although a tentative determination was performed in Chapter 5 – section 5.4.2 for $U_{1-y-z}Pu_yAm_zO_{2\pm x}$. An accurate determination of the amount of gas and sample reacting during the melting is also not possible. Further experimental works are thus needed to improve the model.

6.3. THERMODYNAMIC ASSESSMENT OF THE PU-AM-O SYSTEM

As described in Chapter 2, a first CALPHAD model of the Pu-Am-O system was proposed by Gotcu-Freis *et al.* [26], based on few experimental data and only at high temperature (1273 K). The extrapolation of the binary sub-systems was used, from the Am-O and Pu-Am models developed by Gotcu-Freis *et al.* [26] and the Pu-O version of Guéneau *et al.* [7]. To this day, this assessment constitutes the reference version in the TAF-ID-V12 [4]. However, an updated model of the Am-O system was proposed by Epifano *et al.* in 2017 [6]. Thus, based also on the re-assessment of the model of the Pu-O system proposed in section 6.2.3, a re-evaluation of the model of the Pu-Am-O system is needed. To this aim, a critical review to select the experimental data is performed first, followed by the re-assessment and the comparison with the structural, phase diagram and thermodynamic data obtained in Chapter 3.

6.3.1. Selected experimental data

In this section, the selection of experimental data is first presented. As the available experimental data on the Pu-Am-O were already described in details in Chapter 2, only a brief summary is given here.

Three sets of oxygen potential data are available in the literature (see Chapter 2 – section 2.3.2.2.4): Osaka *et al.* for $Pu_{0.91}Am_{0.09}O_{2-x}$ at 1123, 1273 and 1423 K [43], Otobe *et al.* for $Pu_{0.50}Am_{0.50}O_{2-x}$ between 1173 and 1333 K [44] and Matsumoto *et al.* for $Pu_{0.928}Am_{0.078}O_{2-x}$ between 1473 and 1873 K [164]. For this system, the determination of the oxygen potential variations as a function of the O/M ratio is complex, due to the existence of several phases in the Pu_2O_3-PuO_2-Am_2O_3-AmO_2 domain. In addition, in the study of Otobe *et al.*, the authors indicate the existence of a $(Pu,Am)_9O_{16}$ phase, analogue to Ce_9O_{16}, which was not reported in any other study. Moreover, in all these studies, the model of Osaka *et al.* was used [37], corresponding to a complete reduction of americium in its trivalent form before the start of the reduction of plutonium. This observation disagrees with what was evidenced in this work in Chapter 4 – section 4.1.4 with the simultaneous presence of Am^{4+} and Pu^{3+}.

Another set of available experimental data is the phase diagram data determined by Miwa *et al.*

for $Pu_{0.91}Am_{0.09}O_{2-x}$ [42]. As the oxygen potential variations in the region studied by the authors are unknown, the determination of the O/M ratios in the study is questionable. Moreover, a miscibility gap in the fluorite phase was highlighted by the authors around 1300 K. As the miscibility gap in the Pu-O system was reported for T < 1000 K, this would signify that the 9% Am in PuO_2 would increase by 300 K the boundary of the miscibility gap. In addition, the miscibility gap in the Am-O system was refuted by Epifano *et al.* [6]. Finally, in the study of Miwa *et al.*, a total reduction of the americium before the start of the reduction of the plutonium was also considered. The phase equilibria determined in the study of Miwa *et al.* are thus considered only as indicator in this re-assessment.

In addition, as discussed in Chapter 4 – section 4.2.2.1, the solid phase equilibria of PuAm 80/20, PuAm 50/50-A and PuAm 20/80 between 1873 K and room temperature remain uncertain. Indeed, several phases were observed in addition to the fluorite $(Pu,Am)O_{2-x}$ phase. However, the accurate determination of these phases was not possible and only guesses were made. Thus, these data will be used as guidelines but not as direct input data.

The solidus/liquidus temperatures and their associated O/M ratios, determined for PuAm 50/50-B in Chapter 4 – section 4.4.2 are considered for this re-assessment.

Thus, the re-evaluation of the Pu-Am-O model performed in this work is mainly based on the following experimental data:

- The oxygen potential data of Osaka *et al.* [43], measured by TGA at 1123, 1273 and 1423 K for $Pu_{0.91}Am_{0.09}O_{2-x}$ ($0 \leq x \leq 0.09$);
- The oxygen potential data of Otobe *et al.* [44], measured by EMF between 1173 and 1333 K for $Pu_{0.50}Am_{0.50}O_{2-x}$ ($0.02 \leq x \leq 0.25$);
- The oxygen potential data of Matsumoto *et al.* [164], measured by TGA at 1473, 1673, 1773 and 1873 K for $Pu_{0.928}Am_{0.072}O_{2-x}$ ($0 \leq x \leq 0.16$);
- The oxygen potential data obtained in this work by TGA and the phase equilibria obtained by HT-XRD at 1673 K for $Pu_{0.80}Am_{0.20}O_{2-x}$ ($0.22 \leq x \leq 0.29$) (see Chapter 4 – section 4.3.1);
- The solidus/liquidus temperatures and O/M ratios obtained in this work for $Pu_{0.50}Am_{0.50}O_{2-x}$ (see Chapter 4 – section 4.4.2).

6.3.2. Re-assessed parameters

Based on the selection of experimental data performed in the previous section, the model of the Pu-Am-O system is re-assessed. The model of Gotcu-Freis *et al.* [26] is used as a starting point. The interaction parameters of Epifano *et al.* [6] for the binary Am-O system, as well as the re-assessed parameters for the liquid phase of the Pu-O system (section 6.1.2) are introduced here. In this work, the gas phase from Gotcu-Freis *et al.* [26] was not modified, as no new data were obtained on the gaseous species.

The interaction parameters of three phases are modified in this work: the $(Pu,Am)_2O_3$ phase, the $(Pu,Am)O_{2-x}$ phase and the liquid phase. More details about the sublattice models used for these phases can be found in Chapter 2 – section 2.4 and Chapter 3 – section 3.1.2. A schematic representation of the solid phases of the ternary system and their associated re-assessed parameters is proposed in Figure 6-14.

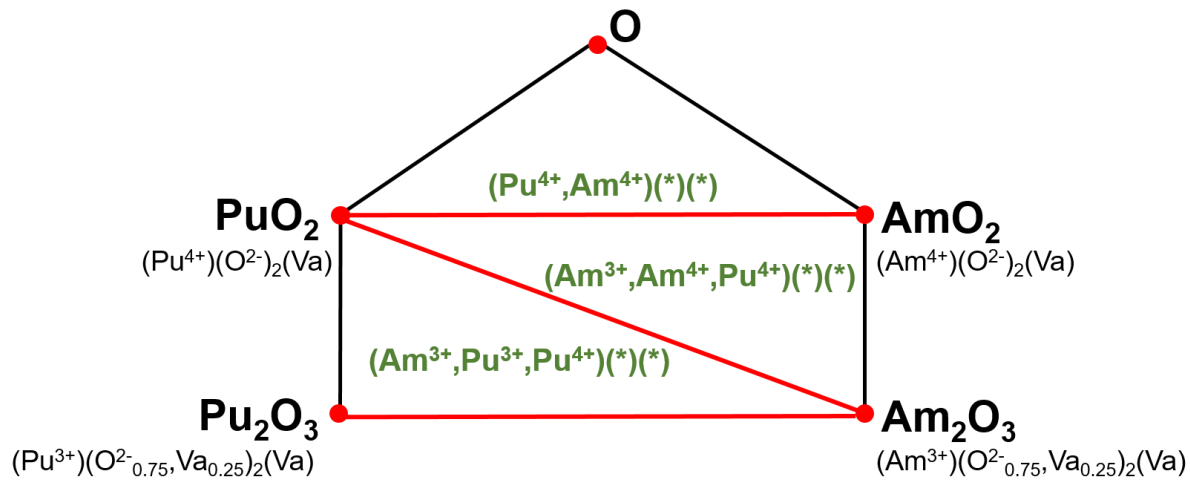

Figure 6-14: Schematic representation of the model of the MO_{2-x} phase for the Pu-Am-O system.

For the (Pu,Am)O_{2-x} phase, compared to the model of Gotcu-Freis *et al.*, the ${}^{0}L_{C1\_MO2(Am^{4+},Pu^{4+})(*)(*)}$ parameter is modified and a second order parameter ${}^{1}L_{C1\_MO2(Am^{4+},Pu^{4+})(*)(*)}$ is introduced to describe the PuO_2-AmO_2 composition line. Then, the PuO_2-Pu_2O_3-Am_2O_3 domain is described by the interaction parameter ${}^{0}L_{C1\_MO2(Am^{3+},Pu^{3+},Pu^{4+})(*)(*)}$. Finally, the PuO_2-AmO_2-Am_2O_3 region is modelled with the addition of the ${}^{0}L_{C1\_MO2(Am^{3+},Am^{4+},Pu^{4+})(*,*)}$ interaction parameter. Several parameters were removed from the model of Gotcu-Freis *et al.*, namely the interaction parameters describing the Pu_2O_3-Am_2O_3-AmO_2, the Pu_2O_3-Am_2O_3 and the Am_2O_3-PuO_2 domains.

For the (Pu,Am)$_2O_3$ phase, corresponding to the A-M_2O_3 phase (more details in Chapter 2 – section 2.4.1), the interaction parameter ${}^{0}L_{Pu2O3(Am,Pu)(O)}$ is added to the model to describe a continuous solid solution between the end members Pu_2O_3 and Am_2O_3.

For the (Pu,Am)$O_{1.61}$ phase, not modified here, an ideal mixing of both binary end-members is considered.

Finally, an interaction parameter ${}^{0}L_{Liquid(Am^{3+},Pu^{3+})(O^{2-})}$ is introduced in the model of the liquid phase to stabilize it.

The expression of the Gibbs energy functions of the three re-assessed phases is provided in Appendix I, with the optimized parameters.

6.3.3. Results

This work constitutes a preliminary re-evaluation of the Pu-Am-O system, based on the few experimental data available.

The ternary phase diagram calculated at 1273 K with this model is plotted in Figure 6-15, with a comparison with the experimental data obtained by Miwa *et al.* [42].

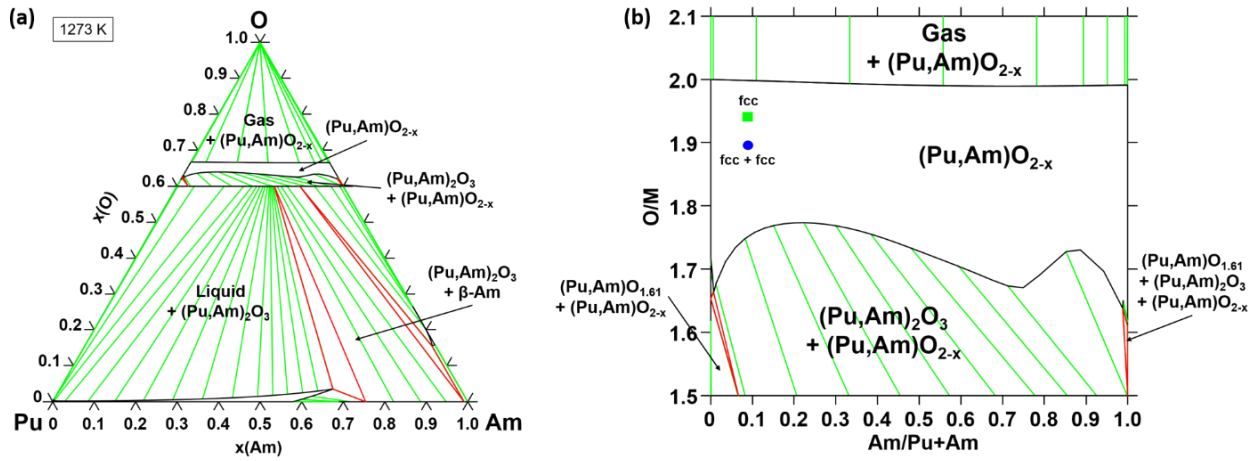

Figure 6-15: (a) Ternary Pu-Am-O phase diagram at 1273 K obtained with the re-assessment performed in this work, (b) section for 1.5 < O/M < 2.1 compared to the experimental data of Miwa *et al.* [42].

Compared to the isothermal section obtained with the model of Gotcu-Freis *et al.* [26] (see Chapter 2 – Figure 2-7), no miscibility gap is observed at 1273 K in the fcc phase with this model. A wide two-phase region [MO_{2-x}+M_2O_3] exists with both models. In addition, on Figure 6-15(b), the presence of two triphasic domains [$(Pu,Am)O_{2-x}$ + $(Pu,Am)_2O_3$ + $(Pu,Am)O_{1.61}$] at both extremities of the phase diagram indicates that a solid solution between $PuO_{1.61}$ and $AmO_{1.61}$, with the complete solubility of one compound into another, is not assessed. The presence of a continuous solid solution is possible, but no experimental data are available to describe the composition range of this phase in the ternary.

The absence of this miscibility gap in the fluorite phase at 1273 K is in disagreement with the results obtained by Miwa *et al.* [42].

The isopleth section calculated for $Pu_{0.91}Am_{0.09}O_{2-x}$ is plotted in Figure 6-16 and compared to the phase behaviour determined by Miwa *et al.*

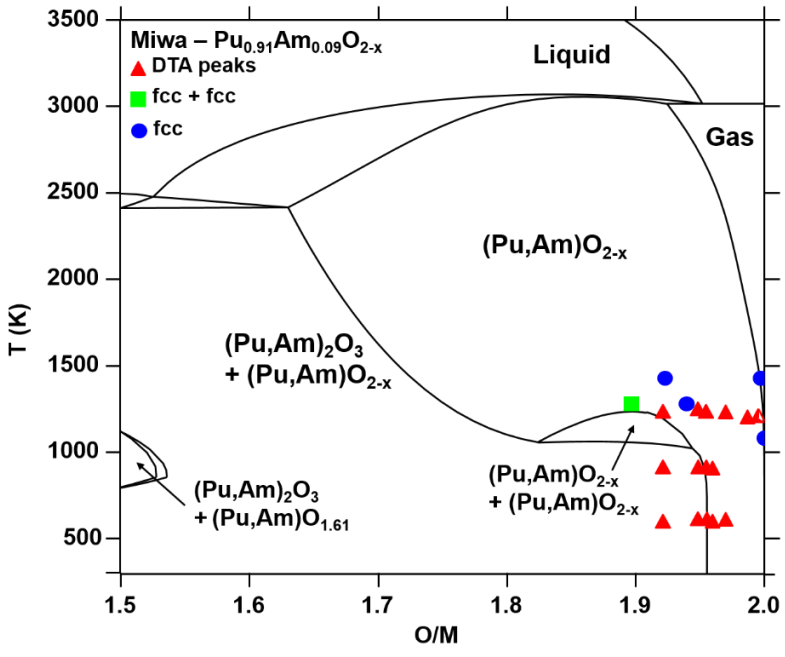

Figure 6-16: Isopleth section of $Pu_{0.91}Am_{0.09}O_{2-x}$ compared to the experiments of Miwa *et al.* [42].

On the isopleth section, it can be noticed that the limit of the miscibility gap is calculated at 1238 K, against 1278 K obtained experimentally. Thus, a reasonable agreement is admitted for the boundaries of the miscibility gap. On the contrary, the phase transition reported by Miwa *et al.* at 573 K, from [C-M_2O_3 + MO_{2-x}] to [C'-M_2O_3+MO_{2-x}] (with C and C' bcc structures), is not reproduced by this updated model. However, no experimental evidence of the existence of these C- and C'-M_2O_3 phases was shown, as the authors made the assumption of the phase transition based on the extrapolation of the binary systems. Thus, the existence of these two phases can be questioned.

Overall, a reasonable agreement is noticed between this re-assessed model and the experimental data of Miwa *et al.* [42].

The oxygen potentials data calculated for the investigated compositions of Osaka *et al.* [43], Otobe *et al.* [44] and Matsumoto *et al.* [164] are plotted and compared to the experimental values in Figure 6-17.

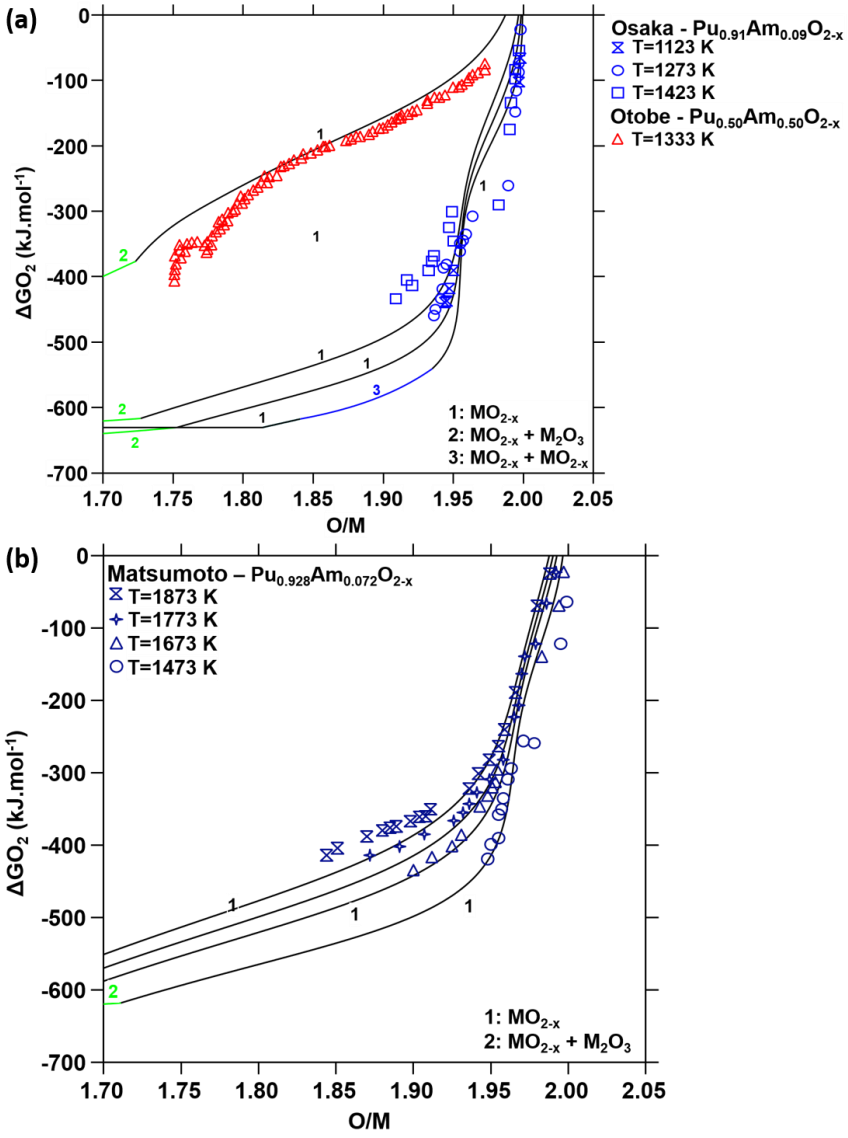

Figure 6-17: Oxygen potential data calculated using the updated model with the formed phases (domains 1, 2, 3), compared to the experimental data of (a) Osaka *et al.* [29] and Otobe *et al.* [30] and (b) Matsumoto *et al.* [31].

A good agreement is observed with the data of Otobe *et al.* for 1.77 < O/M < 2.00 [44]. However, the model does not reproduce the change of slope located at O/M = 1.77. Indeed, the authors attributed this behaviour to a phase transition towards a $(Pu,Am)_9O_{16}$ phase, which is not included in the model as no experimental determination exists. For 1.75 < O/M < 1.77, the calculated oxygen potential are overestimated compared to the experimental values.

A good agreement is observed with the data of Osaka *et al.* [43] in the near-stoichiometric region (O/M > 1.97) but discrepancies are found for lower O/M ratios, where a change of slope is noticed for an O/M equal to 1.95. Based on the model of Osaka *et al.* [37], [43], this change of slope was attributed by the authors to the complete reduction of americium (O/M = 1.95 = 2 - z/2) and the beginning of the reduction of the plutonium. The change of slope could also be attributed to a change of domain, from a monophasic to a multiphasic domain, constituted of $[MO_{2-x} + C\text{-}M_2O_3]$ phases.

The calculated oxygen potential for $Pu_{0.928}Am_{0.072}O_{2-x}$ are in good agreement with the experimental values of Matsumoto *et al.* [164], in particular for 1473 and 1673 K. For 1773 and 1873 K, lower oxygen potential are obtained with the model for O/M < 1.92.

Overall, a good agreement is obtained between the updated version of the Pu-Am-O model and the literature data selected. In the next section, the re-assessed model are compared with the experimental data obtained in Chapter 4 for the phases and site fractions measured at room temperature (section 4.1.4), the phase equilibria and solid/liquid phase transitions (sections 4.2.2 and 4.4.2) and the oxygen potential data (section 4.3.1.2).

6.3.4. Comparison with the experimental data obtained in this work

6.3.4.1 Formed phases and site fractions at room temperature

The results obtained by XRD in Chapter 4 – section 4.1.3 indicate the presence of two fcc structures, corresponding to two $(Pu,Am)O_{2-x}$ phases, for the PuAm 80/20 and PuAm 20/80 samples and only one fcc structure for the PuAm 50/50-A sample at room temperature.

At room temperature, three phases can form in the Pu-Am-O system:

- $(Pu,Am)O_{2-x}$, referred to as MO_{2-x},
- $(Pu,Am)_2O_3$, referred to as A-$(Pu,Am)_2O_3$ or A-M_2O_3,
- $(Pu,Am)O_{1.52}$, referred to as C-$(Pu,Am)_2O_3$ or C-M_2O_3.

For T > 570 K, an intermediate C'-M_2O_3 phase can be found, corresponding to $AmO_{1.62+x}$ and $PuO_{1.61+x}$, considered as the same phase in the model and also referred to as $MO_{1.61+x}$.

The compositions of the three samples studied in Chapter 4 are reported on the calculated isothermal section of the Pu-Am-O system at 300 K for comparison in Figure 6-18.

The calculated phase diagram shows the existence of a large biphasic region $[(Pu,Am)O_{2-x} + A\text{-}(Pu,Am)_2O_3]$. A narrow triphasic domain is visible on the Pu-rich side of the diagram, with the presence of the C-$(Pu,Am)_2O_3$ phase. It can be noticed that the boundary limit between the single phase $(Pu,Am)O_{2-x}$ and the two-phase region $[(Pu,Am)O_{2-x} + A\text{-}(Pu,Am)_2O_3]$ exhibits a peculiar shape, showing a stabilization of the fluorite

oxide towards low O/M ratio for americium contents ranging from 0 to approximately 0.60.

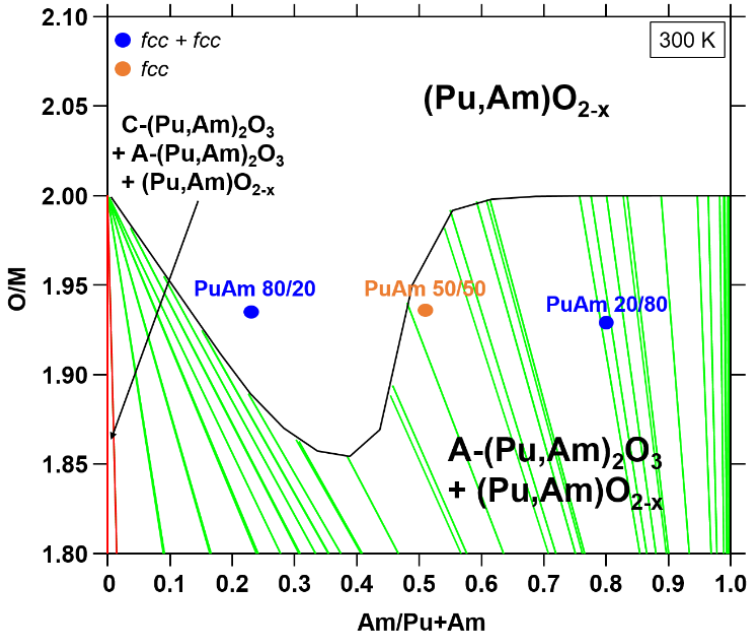

Figure 6-18: Calculated phase diagram of the Pu-Am-O system at 300 K, with the experimental points determined in Chapter 4 – section 4.1.

The calculations at 300 K are not in agreement with the phases observed in the samples. In fact, as already explained in Chapter 4 – section 4.1.3, based on the extrapolation from the binaries Am-O (Chapter 2 – Figure 2-3) and Pu-O (Chapter 2 – Figure 2-2) systems, a two-phase region [MO_{2-x} + A-M_2O_3] or [MO_{2-x} + C-M_2O_3] for Pu-rich contents is expected at room temperature, depending on the americium content. Indeed, in the Pu-O system, at room temperature, a biphasic domain [$PuO_{1.51+x}$ + PuO_{2-x}] exists, while in the Am-O system, the biphasic region corresponds to [A-Am_2O_3 + AmO_{2-x}]. Thus, the biphasic domain [MO_{2-x} + A-M_2O_3], predominant on the isothermal section, is not consistent with the observation of the two fcc phases for the PuAm 80/20 and PuAm 20/80 samples. The existence of this miscibility gap is not observed in Figure 6-18.

However, as explained in Chapter 4 – section 4.1.3, the existence of the two fcc phases for the PuAm 80/20 and PuAm 20/80 has to be further discussed. A possible explanation for the absence of the A-M_2O_3 phase could be due to the stabilisation of the fcc structure by alpha self-irradiation of the samples, as discussed in Chapter 4 – section 4.1.4 and Chapter 5 – section 5.1.3.

Moreover, the initial O/M ratio of the samples was equal to 2.00 at the manufacturing (see Chapter 3 – section 3.2.1). This means that during the 15 years of storage under air, the samples were reduced with O/M ratios determined in this work at 1.94-1.93 (see Chapter 4 – section 4.1.4). This behaviour is very different compared to $U_{1-y}Pu_yO_{2\pm x}$ mixed oxides, which either stabilize at O/M = 2.00 or are slightly oxidized during storage.

This behaviour could be explained by the self-irradiation of the samples. Indeed, $Pu_{1-z}Am_zO_{2-x}$ samples, with z = 0.23, 0.51 and 0.80, contain significant quantities of alpha emitters (^{238,239,240}Pu and ^{241}Am), with proportions increasing with the americium content, as the americium is purely ^{241}Am (see Appendix E). Based on the energy of the α particles and recoil nuclei generated, heat is generated locally during the collision cascade along the path of these

particles (20-30 nm for the recoil particle and 20 µm for the alpha particle), as explained in Chapter 2 – section 2.2.2.4. Based on the cationic and isotopic compositions of the three samples (Appendix E), their specific heat powers are calculated to be 2.9×10^{-2} W.g^{-1}, 5.9×10^{-2} W.g^{-1} and 9.0×10^{-2} W.g^{-1} for the PuAm 80/20, PuAm 50/50 and PuAm 20/80 samples respectively. These quantities are approximately ten times more important for $Pu_{1-z}Am_zO_{2-x}$ than for $U_{1-y}Pu_yO_{2\pm x}$ (5.5×10^{-3} W.g^{-1} for $U_{0.60}Pu_{0.40}O_{2.03}$ [249] and 5.7×10^{-3} W.g^{-1} for a CAPRA sample). Due to this high specific heat power of these samples, the temperature can significantly increase locally within the sample, when the decay occurs. In addition, actinide oxides such as UO_2 or $U_{1-y}Pu_yO_{2\pm x}$ present a low thermal conductivity (2-3 W.m^{-1}.K^{-1} for T > 1000 K [250]). This property is degraded during irradiation of the materials [251], increasing locally the temperature in the samples. Thus, even with this local increase of temperature, the self-irradiation defects would accumulate with time in the material and induce an athermal diffusion. The latter would enhance possible microstructural modification and phase transitions, which could explain the two fcc phases observed experimentally.

In order to discuss the variation of the O/M ratio of the samples with the self-irradiation effect, the O/M ratio of the PuAm 80/20 sample is calculated as a function of temperature considering a thermodynamic equilibrium with air (see Figure 6-19). The results highlight the tendency of the sample to be reduced for T > 1000 K, even under air. This observation is in agreement with the tendency of the pure pole AmO_2, being reduced for T > 1100 K.

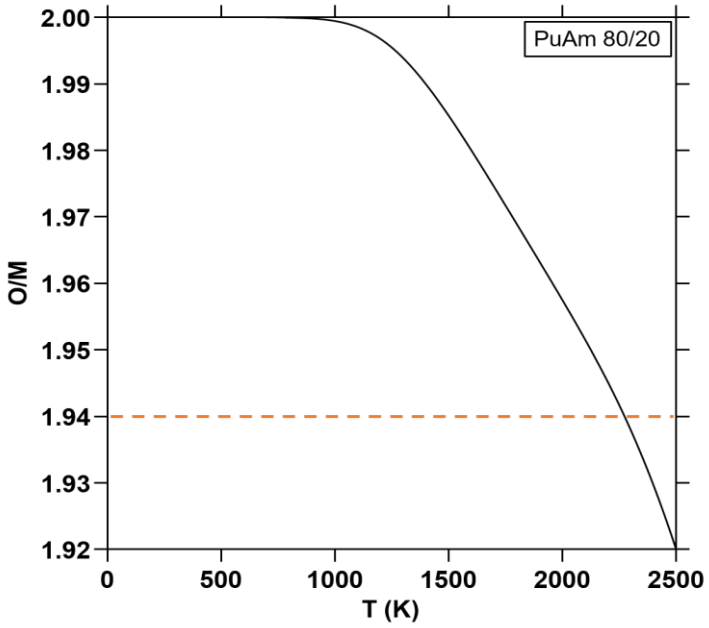

Figure 6-19: Variation of the O/M ratio as a function of temperature for the PuAm 80/20 sample in equilibrium with air. The dashed line corresponds to the O/M ratio determined experimentally in Chapter 4 – section 4.1.4.

As it can be seen, the O/M ratio determined experimentally (1.94 for the PuAm 80/20 sample) would be reached around 2250 K, while the O/M ratio calculated at 300 K is equal to 2.00. These calculations show that even if not at thermodynamic equilibrium, the samples could tend to be reduced under air during storage, due to the heat produced by the α self-irradiation. The α self-irradiation occurring in the $Pu_{1-z}Am_zO_{2-x}$ samples and their poor thermal conductivity could thus explain the reduction of the samples, because of the heat generated locally during the alpha decay.

The site fractions of the species in the samples can be calculated using the re-assessed model of the Pu-Am-O system and compared to the cationic charge distribution of the PuAm 80/20, PuAm 50/50-A and PuAm 20/80 samples determined at room temperature in Chapter 4 – section 4.1.4 by XANES experiments.

As it can be seen in Figure 6-18, a sesquioxide phase is observed additionally to the dioxide phase for the PuAm 50/50 and PuAm20/80 samples, which is not the case experimentally and thus makes the comparison with these compositions difficult. Thus, only the site fractions calculated at 300 K for $Pu_{0.77}Am_{0.23}O_{2-x}$ are compared to the cationic charge distribution obtained for the PuAm 80/20, with respect to its metallic composition, in Figure 6-20(a). As evidenced in Figure 6-19, as the O/M ratio determined for the PuAm 80/20 sample is fixed around 2250 K, the site fractions were also calculated at this temperature for comparison with the model in Figure 6-20(b).

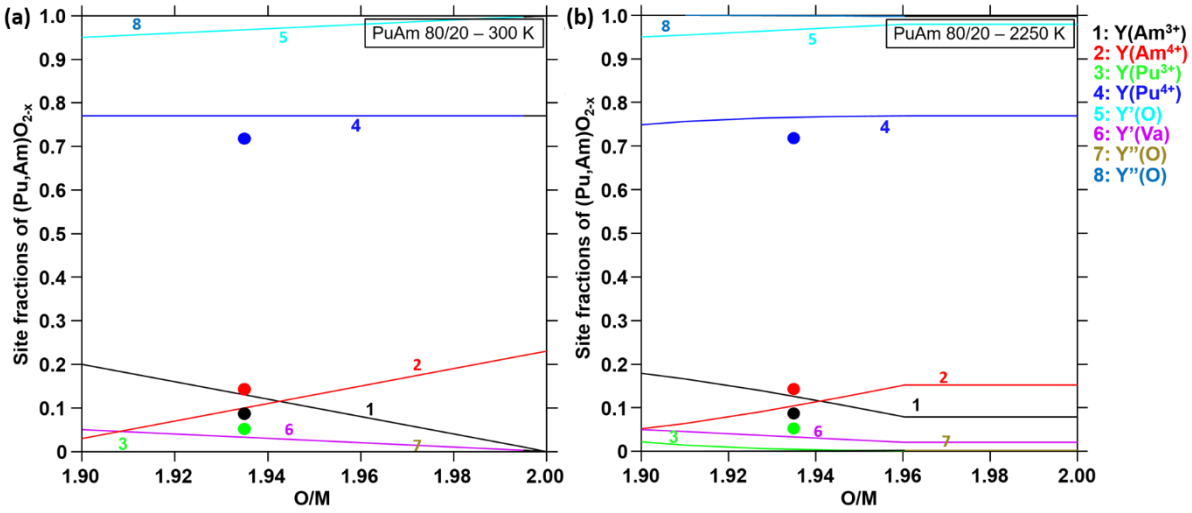

Figure 6-20: Site fractions calculated for $Pu_{0.77}Am_{0.23}O_{2-x}$ at (a) 300 K and (b) 2250 K, compared to the experimental values obtained by XANES for the PuAm 80/20 sample. The experimental uncertainties correspond to the size of the symbols (± 0.01).

A slight difference in the site fraction of Pu^{3+} is observed between 300 and 2250 K. In addition, for T = 2250 K, a stabilisation of the site fractions for O/M > 1.945 is noticed, explained by an equilibrium between the MO_{2-x} and the gas phase. At the O/M ratio of the sample (1.936), no significant difference is obtained between the two temperatures.

Experimentally, the simultaneous presence of Pu^{3+}, Pu^{4+}, Am^{3+} and Am^{4+} is evidenced, contrarily to the predictions by the model of Osaka *et al.* [43]. The calculated site fractions reveal here the presence of Pu^{4+}, Am^{3+} and Am^{4+} but no $Pu^{3+}$is predicted to form. It can also be noticed that the calculated site fractions of Pu^{4+} and Am^{3+} are overestimated compared to the experimental data, whereas the fraction of Am^{4+} is underestimated. This observation can be explained by the fact that, for the composition of the sample, this model attributes the hypo-stoichiometric behaviour to the reduction of americium in this O/M ratio range. This is consistent with the higher oxygen potential for AmO_{2-x} compared to PuO_{2-x} at a same temperature.

To conclude, a reasonable agreement is obtained between the calculated and experimental cationic site fractions. In addition, the cationic distribution determined in this work is consistent with the reduction of the samples observed towards low O/M ratios, possibly explained by alpha

self-irradiation effects.

6.3.4.2 Phase equilibria in $Pu_{0.77}Am_{0.23}O_{2-x}$ at 1673 K

Phase equilibria in $Pu_{0.77}Am_{0.23}O_{2-x}$ ($0.222 \leq x \leq 0.284$) were also determined at 1673 K by combining TGA and HT-XRD (see Chapter 4 – section 4.3).

In a first step, oxygen potentials are calculated using the re-assessed model and compared to the experimental values in Figure 6-21. The calculated oxygen potentials of the PuAm 80/20 sample obtained using the model of Gotcu-Freis *et al.* [26] are also plotted for comparison.

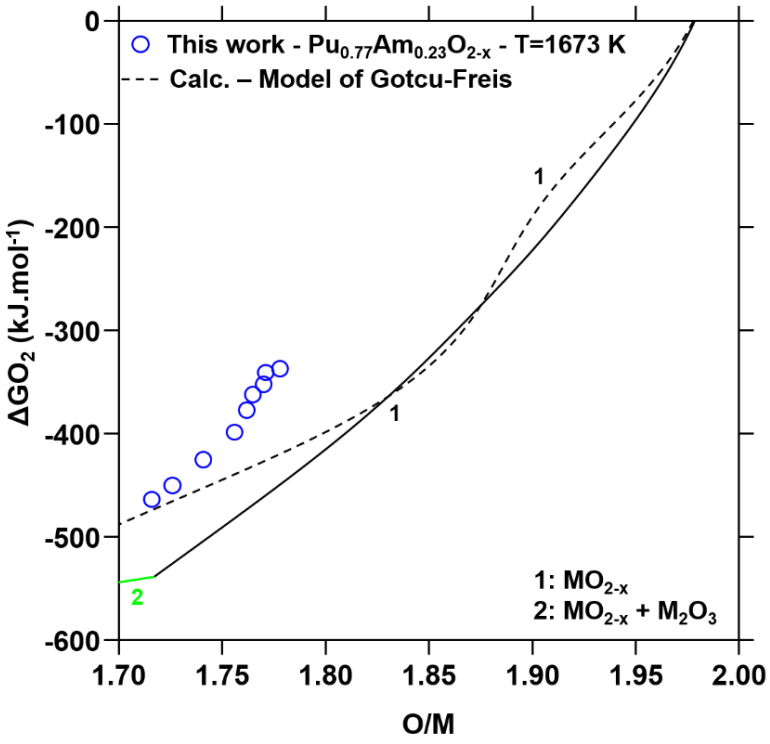

Figure 6-21: Calculated oxygen potentials for $Pu_{0.77}Am_{0.23}O_{2-x}$, compared to the experimental values and the model of Gotcu-Freis *et al.* [26]. The uncertainties are represented by the size of the symbols.

A systematic underestimation of the oxygen potential of approximately 50 kJ.mol^{-1} is noticed with the updated model whereas a better agreement is found with the model of Gotcu-Freis *et al.* for low O/M ratios [26]. However, larger deviations from the experimental data are noticed when increasing the O/M ratio. In addition, the shape of the trend obtained with the model of Gotcu-Freis *et al.* differs from the one obtained experimentally. With the updated model, this shape is better reproduced. Moreover, when looking at the formed phases along the oxygen potential curves, the calculations performed using the model of Gotcu-Freis *et al.* indicate the presence of only the MO_{2-x} phase in the O/M range studied here, while the HT-XRD experiments revealed the presence of a multiphasic domain for $1.716 \leq O/M < 1.75$.

The isopleth section for $Pu_{0.77}Am_{0.23}O_{2-x}$ is plotted in Figure 6-22 for comparison with the phase equilibria obtained by HT-XRD in Chapter 4 – section 4.3.2. A multiphasic domain was observed experimentally at 1673 K for $1.716 \leq O/M < 1.75$, while a monophasic domain was obtained for higher O/M ratio. However, the identification of the phases constituting the multiphasic domain was not possible.

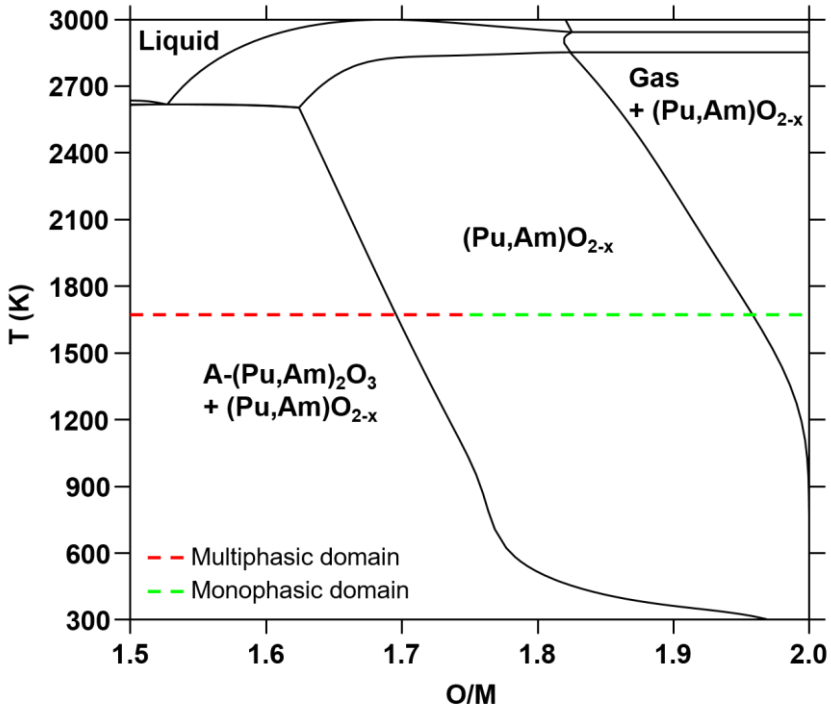

Figure 6-22: Isopleth section calculated for $Pu_{0.77}Am_{0.23}O_{2-x}$, compared to the domains evidenced by HT-XRD and ATG for the PuAm 80/20 sample.

Based on the calculations, a biphasic domain [$(Pu,Am)O_{2-x}$ + $(Pu,Am)_2O_3$] exists for $1.50 \leq O/M \leq 1.716$, where a phase transition occurs towards a monophasic $(Pu,Am)O_{2-x}$ domain when increasing the O/M ratio. Thus, a qualitative agreement is obtained between the updated model and the experimental data for the formed phases but discrepancies still remain for the position of the phase boundary.

6.3.4.3 Solid/liquid phase transitions

The solid/liquid phase transitions of a $Pu_{0.49}Am_{0.51}O_{2-x}$ (PuAm 50/50-B) sample were investigated by laser heating in Chapter 4 – section 4.4.2. Three sets of solidus and liquidus temperatures were obtained as a function of the O/M ratio. The calculated isopleth section of $Pu_{0.49}Am_{0.51}O_{2-x}$ is plotted in Figure 6-23 for comparison with these experimental values.

A good agreement is obtained between the updated model and the measured solidus/liquidus temperatures. It can be noticed that for O/M ratios higher than 1.83, an equilibrium with the gas phase is noticed, highlighting again the tendency of these mixed oxides to lose oxygen at high temperature, due to the reduction behaviour of AmO_2 and PuO_2. Moreover, the successive shots performed on the sample indicated that no significant variation of the solidus and liquidus temperatures occurred when decreasing the O/M ratio. This trend is well reproduced by the model, with a constant solidus temperature equal to 2853 K and a liquidus temperature equal to 2944 K. These temperatures are very close to the measured data (2838 ± 60 K and 2968 ± 60 K, respectively).

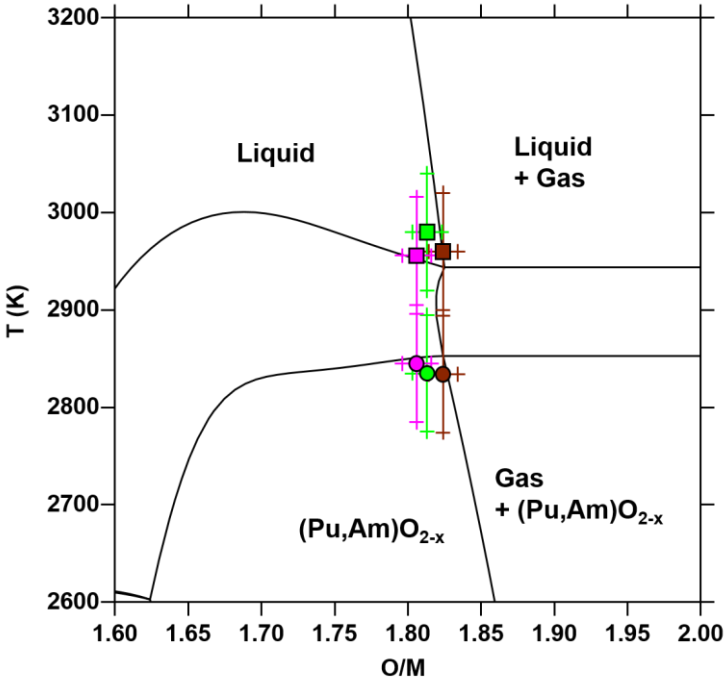

Figure 6-23: Calculated isopleth section for $Pu_{0.49}Am_{0.51}O_{2\pm x}$, compared to the solidus/liquidus temperatures and associated O/M ratios obtained in Chapter 4 – section 4.4.2.

6.3.5. Conclusion

In this section, the model of the Pu-Am-O system was re-evaluated. A critical review of the available experimental data was performed in a first step and a selection of experimental sets of data was done. The models of the $(Pu,Am)O_{2-x}$, A-$(Pu,Am)_2O_3$ and liquid phases were re-assessed to better reproduce these selected data. A good agreement was obtained with the oxygen potential data of the literature, although some discrepancies were found for low O/M ratio, where uncertainties on the phase equilibria remain. This updated model also reproduced the miscibility gap observed by Miwa *et al.* in the fluorite phase for high Pu content.

Significant differences were observed when comparing the phase equilibria obtained at room temperature in this study for the PuAm 80/20, PuAm 50/50-A and PuAm 20/80 samples. Indeed, a biphasic domain [$(Pu,Am)O_{2-x}$ + A-$(Pu,Am)_2O_3$] was predicted by the calculations, while several fcc $(Pu,Am)O_{2-x}$ phases are observed experimentally (two for PuAm 80/20 and PuAm 20/80 and one for PuAm 50/50-A). The alpha self-irradiation effects could tentatively explain the reduction of the samples, which occurred during storage.

Moreover, the site fractions calculated for the $(Pu,Am)O_{2-x}$ phase are in reasonable agreement with the ones obtained by XANES for PuAm 80/20 and no large variation is predicted when increasing the temperature, except for Pu^{3+}. In addition, the calculated oxygen potentials are systematically lower by approximately 50 $kJ.mol^{-1}$ than the experimental values for PuAm 80/20 at 1673 K. The phase transition from a multiphasic to a monophasic domain, observed experimentally between O/M = 1.74 and 1.75 at 1673 K, is qualitatively reproduced by the updated model. A very good agreement is also obtained with the solidus/liquidus temperatures measured by laser heating for the PuAm 50/50-B sample.

Thus, this work constitutes a tentative re-assessment of the model of the Pu-Am-O system. Indeed, additional experimental campaigns are needed to overcome the lack of data on this

system. In particular, the determination of the phase equilibria over the whole range of americium and oxygen contents is mandatory for an accurate description of the model.

Using the re-assessments performed here for the various binary and ternary sub-systems of the U-Pu-Am-O system, thermodynamic investigations of the quaternary system will be performed in the next section and compared to the experimental data obtained in Chapter 5.

6.4. THERMODYNAMIC INVESTIGATION OF THE U-PU-AM-O SYSTEM

No thermodynamic model is available for the quaternary system in the literature. Indeed, for decades, many authors did not take into account the influence of a small presence of americium on the U-Pu-O system. However, as reported in Chapter 2, few studies were performed by Kato *et al.* [78], [185] and Prieur *et al.* [124] for the lattice parameters, thermal expansion and melting temperature, and by Osaka *et al.* [37], Nakamichi *et al.* [169], Hirooka *et al.* [170] and Kato *et al.* [163] for the oxygen potentials. In most cases, an ideal solution was admitted between UO_2 and PuO_2. However, as described in section 6.2.3, a more complex behaviour was evidenced. It is thus needed to study the quaternary U-Pu-Am-O system based on the interactions between the different components.

This section constitutes a preliminary step for an accurate thermodynamic modelling of the quaternary system by considering the extrapolation from the following sub-systems:

- U-O from Guéneau *et al.* [7],
- Pu-O from the re-assessment performed in section 6.1.2,
- Am-O from Epifano *et al.* [6],
- U-Pu from Kurata [246], U-Am from Kurata [252] and Pu-Am from Gotcu-Freis *et al.* [26],
- U-Pu-O from the re-assessment performed in section 6.2.2,
- U-Am-O from Epifano *et al.* [28], [48],
- Pu-Am-O from the re-assessment performed in section 6.3.2.

In a first section, the phases and the site fractions at room temperature obtained in Chapter 5 – section 5.1.3 are compared to the extrapolated model. In a second part, enthalpy and heat capacity for a CAPRA4 sample are calculated and compared to the experimental values obtained in Chapter 5 – section 5.3. Then, the melting behaviour of the quaternary system is investigated and compared to the solidus temperatures and O/M ratios measured in Chapter 5 – section 5.4.2. Possible explanations for the oxidation/reduction behaviour of the samples are proposed. The available literature oxygen potential data are finally used to check the accuracy of this extrapolated model.

6.4.1. Cationic site fractions at room temperature

The cationic charge distribution determined at room temperature by XANES experiments in Chapter 5 – section 5.1.3 for the PHENIX29, CAPRA4 and TRABANT40 samples are compared to the calculated values.

As the same trend is observed for the three samples, only the example of the CAPRA4 sample is shown in Figure 6-24. The temperature of 1600 K is chosen as it corresponds to the temperature at which the initial O/M ratio at the manufacturing (1.968) is fixed, according to the Figure 5-9 in Chapter 5 – section 5.2.3. In addition, as demonstrated in section 6.3.4.1, no large variation of the site fractions is observed with the temperature.

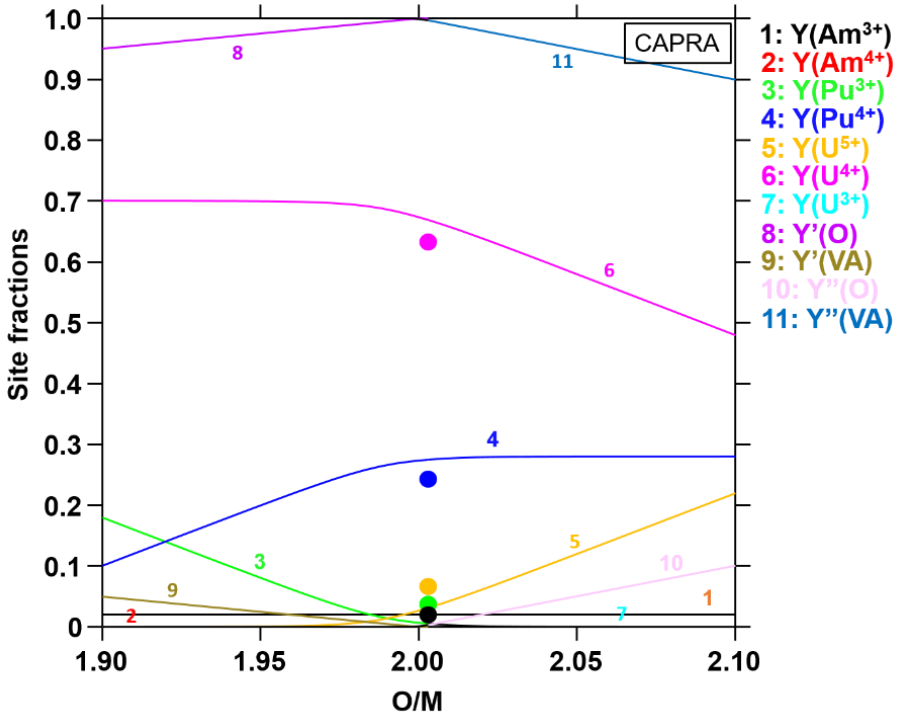

Figure 6-24: Cationic site fractions of the CAPRA4 sample calculated at 1600 K, compared to the experimental data measured by XANES in Chapter 5 – section 5.1.3. The experimental uncertainties correspond to the size of the symbol for the site fractions.

The simultaneous presence of U^{5+}, U^{4+}, Pu^{3+}, Pu^{4+} and Am^{3+} was evidenced experimentally. Based on the model of Osaka *et al.* [37], trivalent plutonium should not be observed for the CAPRA4 and TRABANT40 samples and pentavalent uranium should not be present in the PHENIX29 sample.

In these calculations, a relative good agreement is observed with the experimental proportions of U^{4+}, Pu^{4+} and Am^{3+}. On the contrary, it can be noticed that no trivalent plutonium is formed and that the calculated fraction for U^{5+} is underestimated. A better agreement is thus obtained with this model than with the model of Osaka.

6.4.2. Enthalpy and heat capacity

The experimental data obtained for the CAPRA4 are plotted in Figure 6-25 with the enthalpy increments calculated for three compositions: $U_{0.70}Pu_{0.28}Am_{0.02}O_{2.00}$, $U_{0.70}Pu_{0.30}O_{2.00}$ and $U_{0.72}Pu_{0.28}O_{2.00}$.

A good overall agreement is obtained between the experimental data and the calculated curve for the CAPRA4 sample.

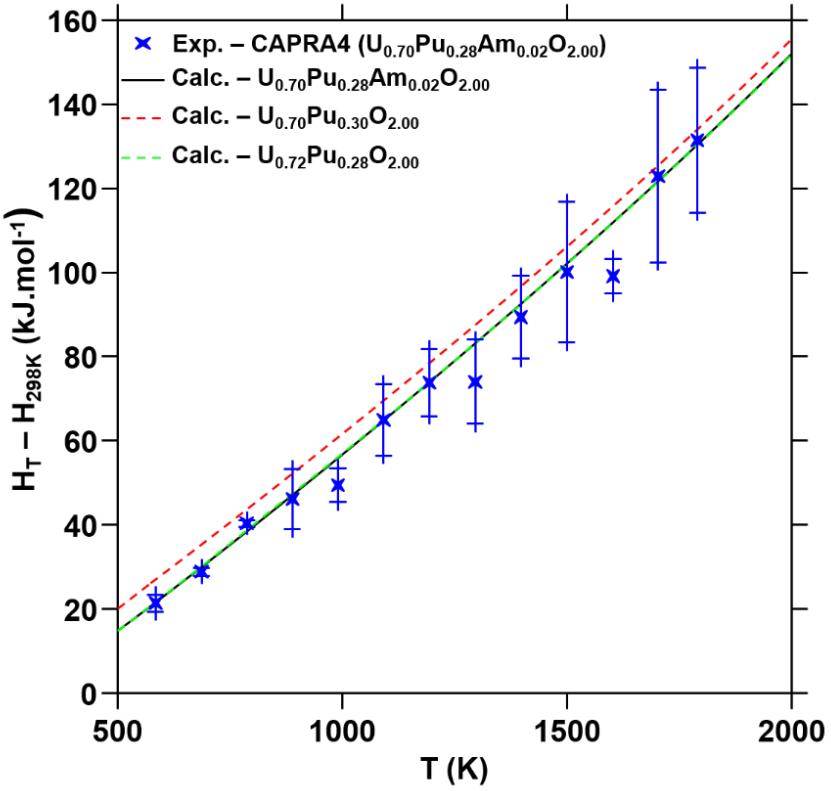

Figure 6-25: Enthalpy increments of the CAPRA4 sample compared to the calculated data for $U_{0.70}Pu_{0.28}Am_{0.02}O_{2.00}$ (black full line), $U_{0.70}Pu_{0.30}O_{2.00}$ (red dashed line) and $U_{0.72}Pu_{0.28}O_{2.00}$ (green dashed line).

Moreover, the calculated curves for the CAPRA4 sample and for $U_{0.72}Pu_{0.28}O_{2.00}$ are identical. This trend was already evidenced in Chapter 5 – section 5.3.2, where the enthalpy increments obtained in this work for the CAPRA4 sample ($U_{0.70}Pu_{0.28}Am_{0.02}O_{2.00}$) were in good agreement with the experimental data available of Kandan *et al.* for $U_{0.72}Pu_{0.28}O_{2.00}$ [135] and with the computed data using the Neumann-Kopp additivity rule for $U_{0.70}Pu_{0.28}Am_{0.02}O_{2.00}$. Moreover, as the americium originates from the natural decay of Pu, the enthalpy increment of $U_{0.70}Pu_{0.30}O_{2.00}$ was also plotted in Figure 6-25 for comparison. For this composition, higher enthalpy values are obtained. This comparison between the three compositions reveals that there is no influence of the addition of 2% Am on the enthalpy increments of $U_{1-y}Pu_yO_{2.00}$.

The heat capacity function obtained by derivation of the fit of the enthalpy increments is also compared to the calculated data for $U_{0.70}Pu_{0.28}Am_{0.02}O_{2.00}$ and $U_{0.72}Pu_{0.28}O_{2.00}$ using the thermodynamic model (see Figure 6-26). For the fit, as explained in Chapter 5 – section 5.3.2, the Cp value at 298 K was fixed at 64.4 J.K^{-1}.mol^{-1}, calculated using the Neumann-Kopp additivity rule.

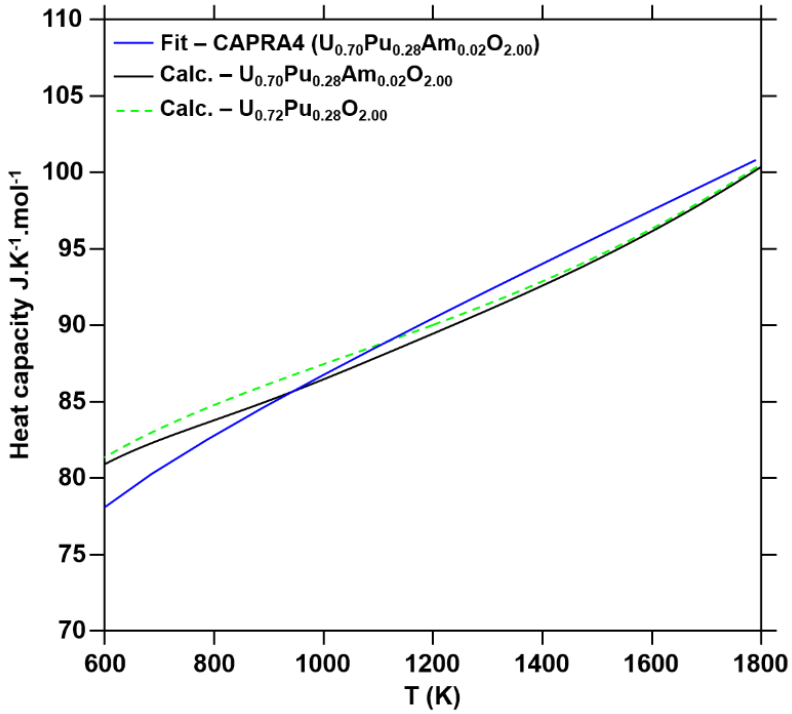

Figure 6-26: Heat capacity of the CAPRA4 sample (blue), compared to the calculated data for $U_{0.70}Pu_{0.28}Am_{0.02}O_{2.00}$ (black full line) and $U_{0.72}Pu_{0.28}O_{2.00}$ (green dashed line).

As it can be seen, a deviation from the experimental trend is observed for the thermodynamic calculations. Indeed, for $U_{0.70}Pu_{0.28}Am_{0.02}O_{2.00}$, the calculated data are overestimated up to 940 K. On the opposite, at higher temperature, the values from the fit are higher than the calculations. In addition, the calculations for $U_{0.72}Pu_{0.28}O_{2.00}$ are very close to the experimental results obtained for the CAPRA4 sample. This tendency was already observed in Chapter 5 – section 5.3.2 when comparing the fit obtained in this work with the data of Kandan *et al.* or using the Neumann-Kopp rule.

Moreover, it can be noticed that significantly lower heat capacities are obtained for the composition containing americium, between 600 and 1300 K, whereas this difference is small at higher temperatures. This observation is in disagreement with what was previously stated in Chapter 5 – section 5.3.2, *i.e.* the presence of americium tends to increase the heat capacity of $U_{1-y-z}Pu_yAm_zO_{2\pm x}$ compared to the ones of $U_{1-y}Pu_yO_{2\pm x}$ because of the oxygen vacancies formed by the reduction of Am^{4+} into Am^{3+} and Pu^{4+} into Pu^{3+}. Indeed, even if the O/M ratio of the CAPRA4 sample studied here was initially 2.00 at room temperature, a reduction was assumed to occur when increasing the temperature.

Possible explanations are proposed for these discrepancies.

The first one is related to the experimental determination of the fit. As already explained, this fit is obtained by derivation of the function of the enthalpy increments obtained in Chapter 5 – section 5.3.3. These enthalpy increments were determined from the heat flow measured during the experiments. Thus, many uncertainties and possible bias exist on the heat capacity function. Indeed, slight variation in the enthalpy increment function may induce significant changes in the heat capacity function and could explain the different behaviours observed on Figure 6-26.

The second explanation is linked to the thermodynamic model of the U-Pu-Am-O system.

Indeed, as it is based on the extrapolation of the various binary and ternary sub-systems, numerous uncertainties arise from the models of the sub-systems, in particular on americium-bearing systems. Moreover, as exhibited in section 6.4.1, differences between the model and the experiments were already observed for the site fractions determined at room temperature. Thus, discrepancies can be found at higher temperature, arising from this observation.

6.4.3. Solid/liquid phase transitions

The solid/liquid phase transitions (solidus temperatures and their associated O/M ratios) determined in Chapter 5 – section 5.4.2 for the seven samples of interest are compared here to the computed solidus and liquidus curves in Figure 6-27.

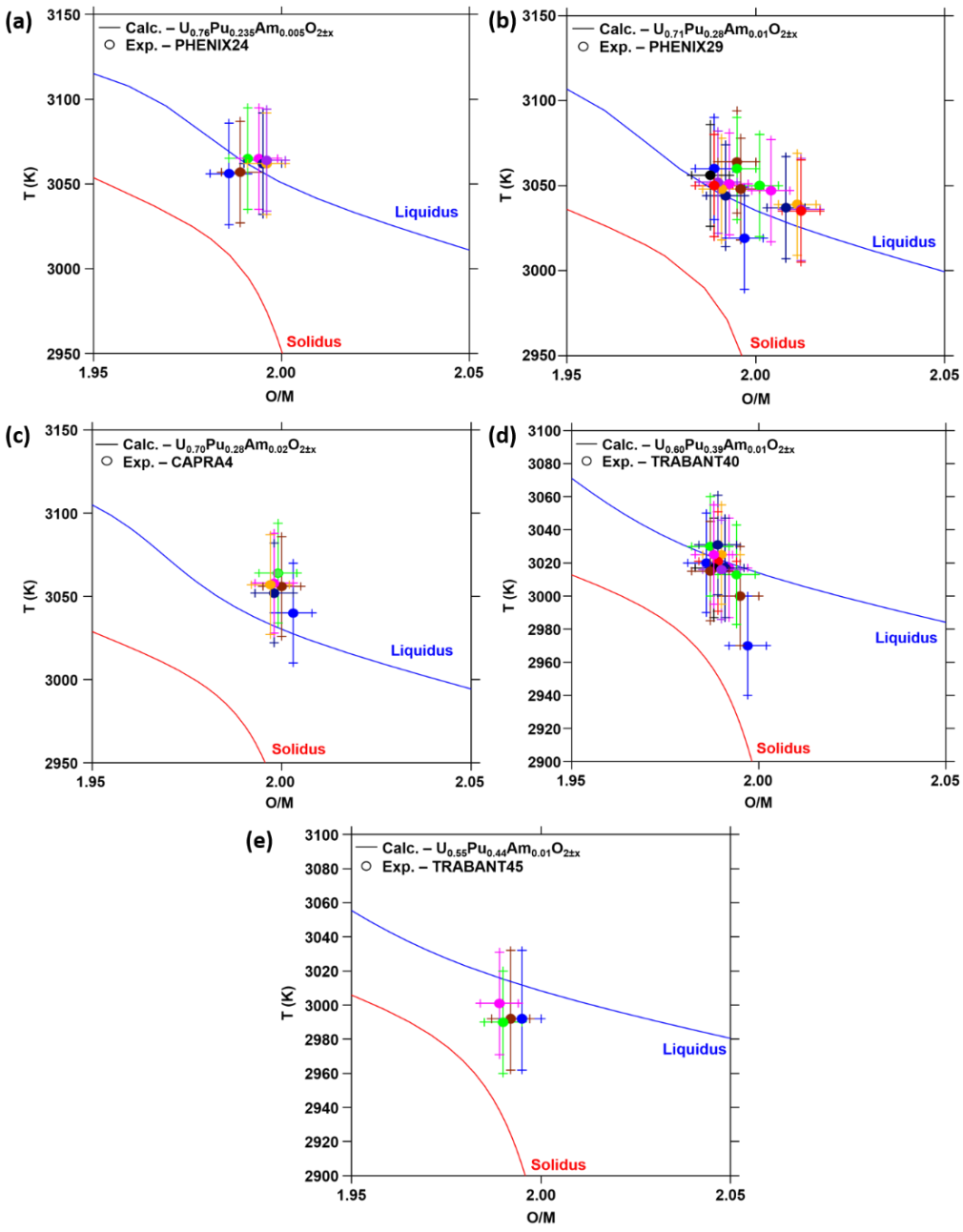

Figure 6-27: Isopleth sections of (a) PHENIX24, (b) PHENIX29, (c) CAPRA4, (d) TRABANT40 and (e) TRABANT45 samples. Comparison between the experimental points obtained in Chapter 5 and the calculated solidus and liquidus curves using the CALPHAD model.

The first observation is that the trends of the calculated curves agree with the experimental trends, *i.e.* starting from O/M = 2.00, the solidus and liquidus temperatures increase when decreasing the O/M ratio. A slight disagreement is noticed in the case of the PHENIX24 sample (Figure 6-27(a)), however within the experimental uncertainties.

The second observation is related to the positions of the calculated solidus and liquidus curves compared to the experimental solidus temperature. Indeed, when looking at the experimental points, they appear to follow the liquidus curve rather than the solidus one. For this disagreement, possible explanations are proposed:

- As only one thermal arrest was noticed on the thermograms (see Chapter 5 – Figure 5-17), the accuracy of the choice of a solidus point, determined by Böhler *et al.* [176], can be questioned.
- As discussed in section 6.2.3, uncertainties remain on the model in the hypo-stoichiometric range. Thus, it is possible that the solidus and liquidus curves are underestimated in the present model, as it was already the case for the U-Pu-O system (see Figure 6-4). Indeed, the experimental results obtained in this work (in Figure 6-28) are in relative good agreement with the experimental data of Böhler *et al.* [176], Strach *et al.* [184] and Kato *et al.* [185].
- In addition, the discrepancies can result from a wrong estimation of the O/M ratios calculated in Chapter 5 – section 5.4.2. Indeed, the O/M ratios were determined based on the integral oxygen loss or absorption by the samples, deduced from the oxygen partial pressures measured. A difference exists between the time step for the temperature measurement with the pyrometer (every 4 ms) and the one to measure the oxygen pressure (every 3 s). Knowing that it takes approximately 30 min to 1 hour for the oxygen partial pressure to restabilize to its baseline value, the O/M ratio calculated at room temperature is most likely not representative of the O/M ratio at which the melting occurs. Thus, the O/M ratio determined could correspond to an oxidation of the samples occurring during the cooling down to room temperature. Thus, the O/M ratios in Figure 6-27 could be overestimated, which would result in a shift towards lower O/M ratios of all the experimental values.

The behaviour (oxidation/reduction) of the samples during the tests is investigated in the next section.

6.4.3.1 Oxidation/reduction behaviour

As evidenced in Chapter 5 – section 5.4.3.5, the different oxides samples exhibit different behaviours depending on their initial O/M ratio. Indeed, hypo-stoichiometric samples tend to oxidize during the melting, while samples with initial O/M ≥ 2.00 tend to be reduced. In order to understand these differences, the solidification paths of PHENIX29 and PHENIX29-OM are calculated in Figure 6-28 as an example.

According to the calculations, the O/M ratio of the samples evolves during cooling. In addition, it can be seen that the solidus and liquidus temperatures are predicted at much lower O/M ratios than the ones determined experimentally after each shot from the change in the integral oxygen concentration.

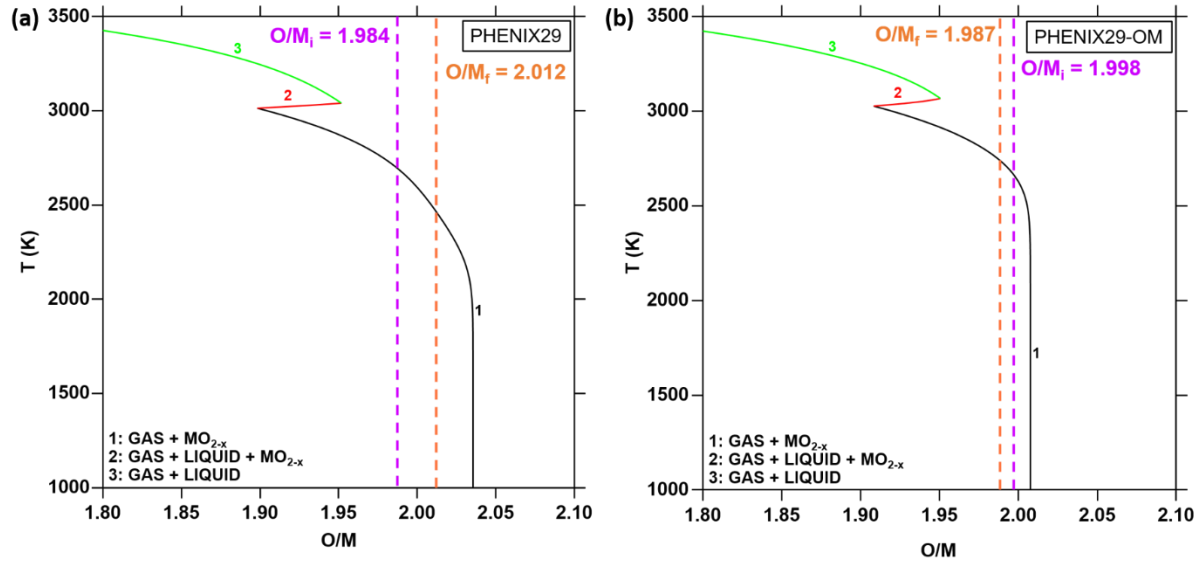

Figure 6-28 : Solidification paths of (a) PHENIX29 and (b) PHENIX29-OM samples, compared to the final O/M ratio (dashed orange line) and initial O/M ratio (dashed purple line). Calculations performed for 1.10^{-4} mol of gas (Ar + pO_2 = $3.5x10^{-6}$ atm) and $3.98x10^{-5}$ mol of molten pool.

For the PHENIX29 and PHENIX29-OM samples, the O/M ratio calculated at room temperature is higher than the experimental value. The solidification paths indicate that the final O/M ratio determined experimentally would be fixed at 2465 K for the PHENIX29 sample and at 2748 K for the PHENIX29-OM sample. In addition, as explained in Chapter 5 – section 5.4.3.5, the PHENIX29 sample is oxidized during the melting experiments, whereas the PHENIX29-OM sample is being reduced.

Moreover, when looking at the solidifications paths in Figure 6-28, the O/M ratio can be assumed to tend towards an equilibrium value and to remain constant down to low temperatures. The same calculations were performed for all the samples. According to the thermodynamic calculations, this equilibrium O/M ratio would be achieved for temperatures between 2000 and 2350 K during cooling.

To understand the oxidation/reduction behaviour of all the samples, the influence of the atmosphere is studied. The oxygen potentials of the samples are calculated for their initial O/M ratio as a function of the temperature and compared to the oxygen potential of the gas in Figure 6-29. For the latter, the calculations are performed considering an argon atmosphere with pO_2 = 3.10^{-6} atm, representative of the experimental conditions.

First, considering the volume of gas in the chamber (1.5 m^3) compared to the volume of sample (20 cm^3) and of molten pool (1 mm^3), the gas is assumed to govern the oxygen potential of the system (Sample + Gas).

The oxidation or reduction behaviour occurring during the melting is conditioned by the temperature $T_{ox/red}$ at which the oxygen potential of the gas equals the one of the sample. Above this temperature, a reduction of the sample is observed as the oxidizing power of the gas is not enough. On the contrary, below this $T_{ox/red}$ temperature, an oxidation of the sample is expected, as the oxygen potential of the gas is predominant.

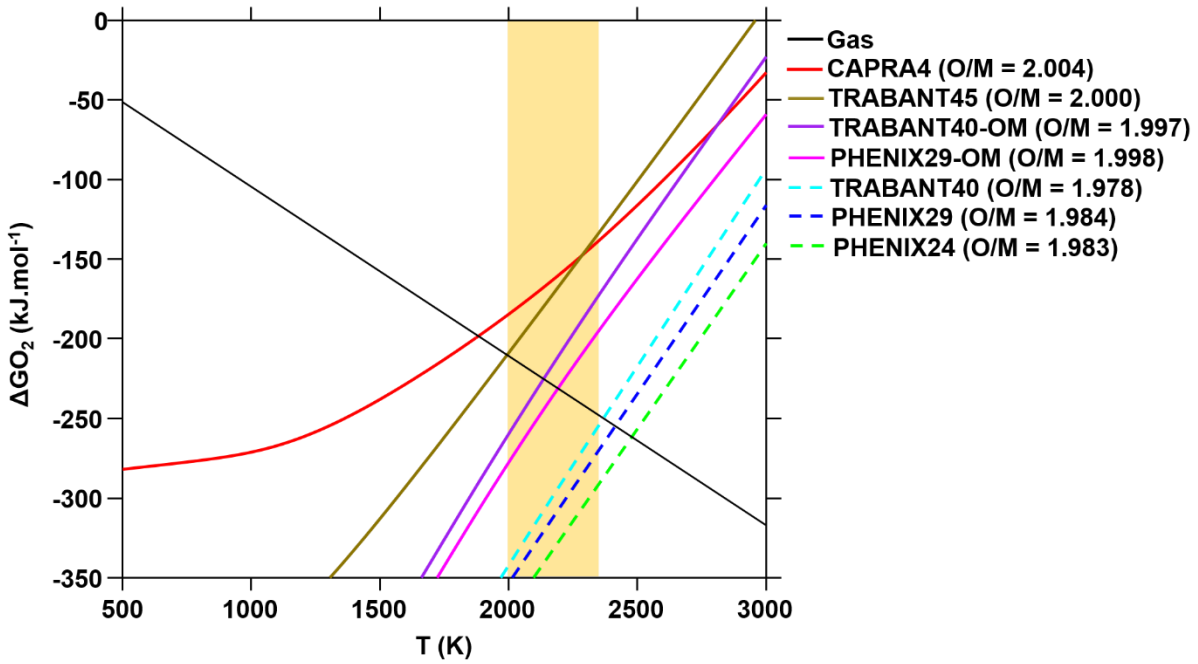

Figure 6-29: Oxygen potentials as a function of temperature for the samples studied by laser heating in Chapter 5, compared to the oxygen potential of the gas (Ar with $pO_2 = 3.10^{-6}$ atm). The yellow rectangle represents the temperature range where the equilibrium O/M ratio would be reached during cooling.

As previously explained, the equilibrium O/M ratio is assumed to be fixed for 2000 < T < 2350 K. When comparing the oxygen potentials of the gas and samples in this temperature range, two cases can be distinguished:

- For initially hypo-stoichiometric samples (PHENIX24, PHENIX29, TRABANT40), the oxygen potential of the samples is lower than the one of the gas in the temperature range of interest. Thus, the samples will be oxidized for T < 2350 K, whereas above 2350 K, a reduction of the samples can take place.

- For initially near- or hyper-stoichiometric samples:
  - For the CAPRA4 sample, the oxidation of the sample is predicted for T < 1960 K.
  - For the TRABANT45 sample, the same behaviour is observed, with an oxidation for T < 2050 K.
  - For the TRABANT40-OM and PHENIX29-OM samples, the oxidation of the samples would occur for T < 2250 K, whereas a reduction is expected above this temperature.

The temperatures Tox/red, at which $\Delta\overline{G_{O_2}(gas)} = \Delta\overline{G_{O_2}(sample)}$, are summarized in Table 6-1.

Thus, considering that the O/M ratio is fixed for 2000 < T < 2350 K, the comparison of the oxygen potentials of the samples and the melting atmosphere explains the different oxidation/reduction behaviours observed. In agreement with what was observed experimentally in Chapter 5 – section 5.4.3.5, samples with initial O/M ratio < 2.00 will be oxidized during the melting, whereas samples with initial O/M ratio ≥ 2.00 will be reduced.

Table 6-1 – Initial O/M ratio, temperature $T_{ox/red}$ at which $\Delta\overline{G_{O_2}(gas)} = \Delta\overline{G_{O_2}(sample)}$ and final experimental values (obtained after the melting of the samples in Chapter 5 – section 5.4.2.2).

Sample	Initial O/M ratio	Temperature $T_{ox/red}$, where $\Delta\overline{G_{O_2}(gas)} = \Delta\overline{G_{O_2}(sample)}$	Final experimental O/M ratio
PHENIX24	1.983	2545 K	1.996
PHENIX29	1.984	2484 K	2.012
CAPRA4	2.004	1964 K	1.997
TRABANT40	1.978	2426 K	1.990
TRABANT45	2.000	2053 K	1.988
PHENIX29-OM	1.998	2248 K	1.987
TRABANT40-OM	1.997	2185 K	1.988

Moreover, as observed in Chapter 5 – section 5.4.3.2, a stabilisation of the O/M ratio to a value of 1.996 and 2.012 after 6 shots was noticed for the PHENIX24 and PHENIX29 samples, respectively. For these two samples, the O/M ratios calculated at equilibrium at 1500 K, determined based on the solidification paths (see Figure 6-28 for PHENIX29 and Figure 6-30 for PHENIX24), are respectively 2.006 and 2.036 (Table 6-1).

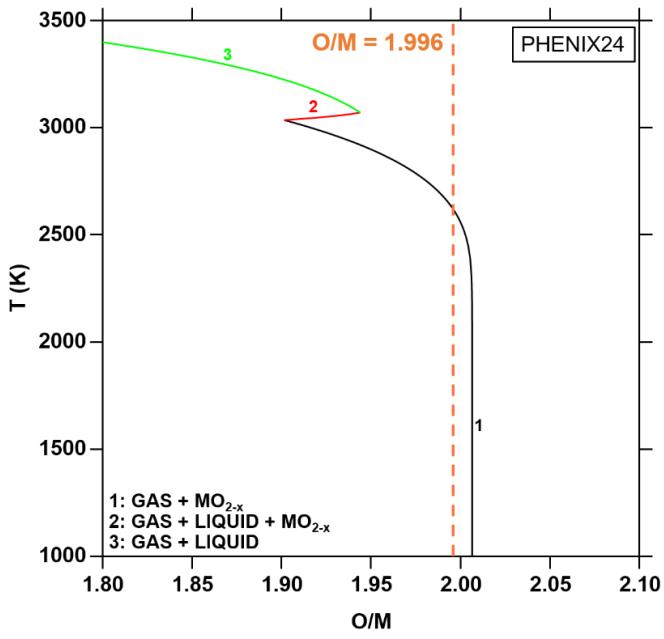

Figure 6-30: Solidification path of the PHENIX24 sample, compared to the final O/M ratio determined in Chapter 5 – section 5.4.2.2. Calculations performed for 1.10^{-4} mol Ar + pO_2 = $3.5x10^{-6}$ atm and $3.98x10^{-5}$ mol of molten pool.

Thus, in the particular case of the PHENIX sample, it can be noticed that the O/M ratio determined experimentally is close to the equilibrium value. This would explain why the samples did not absorb significant quantities of oxygen after 6 shots. The differences between the

equilibrium O/M ratio determined with the calculations and the O/M ratios determined experimentally can be explained by several reasons. The first one concerns the high uncertainties remaining on the experimental determination of the O/M ratio. Indeed, numerous hypotheses were made to calculate the O/M ratio (size of the molten pool, no change in composition…), which could not be verified experimentally. In addition, the solidification paths are calculated for 3.98×10^{-5} mol of sample, corresponding to the molten pool, and 1×10^{-4} mol of gas, corresponding to an intermediate quantity between the boundary layer and the whole chamber. Uncertainties remain on the exact amount of gas reacting with the sample, as no experimental determination is possible. Thus, a too high quantity of gas would lead to an overestimation of the equilibrium O/M ratio because of the oxidizing power of the gas ($pO_2 = 3 \times 10^{-6}$ atm).

6.4.3.2 *Influence of americium on the solid/liquid phase transitions*

In order to study the influence of americium on the solidus and liquidus temperatures of the mixed oxides, the solid/liquid transitions of $U_{1-y-z}Pu_yAm_zO_{2\pm x}$, with uranium contents (1-y-z) equal to 0.60, 0.70 and 0.80 and $0 \leq z \leq 0.05$, are plotted in Figure 6-31.

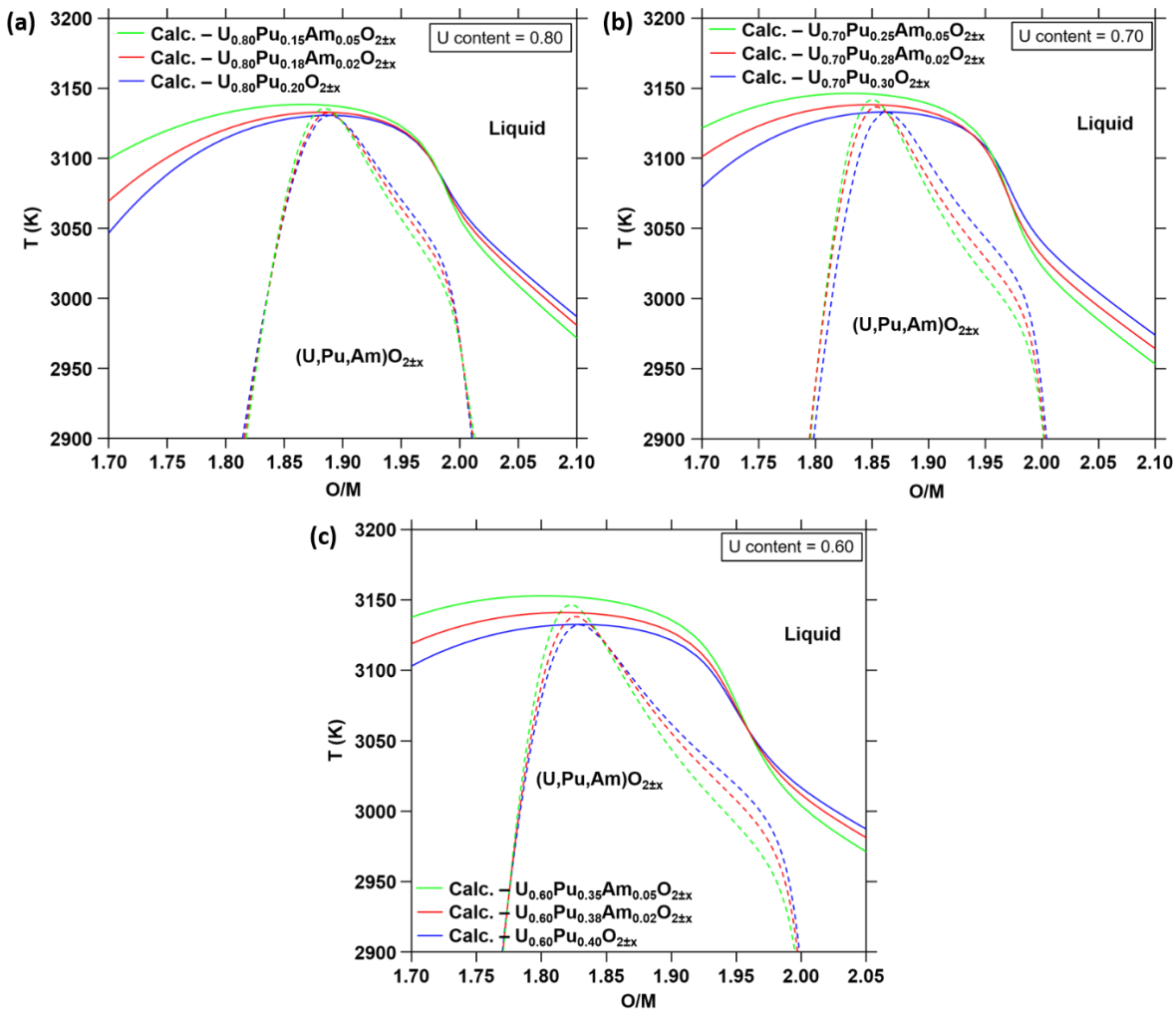

Figure 6-31: Variation of the calculated solidus and liquidus curves of $U_{1-y-z}Pu_yAm_zO_{2\pm x}$ for 1-y-z = 0.60, 0.70 and 0.80 and $0 \leq z \leq 0.05$.

As it can be seen, the maximum of the solidus and liquidus curves is shifted towards higher

temperature and lower O/M ratios when increasing the Pu and Am contents. From this maximum, three domains can be distinguished on Figure 6-31.

The first domain corresponds to O/M ratios lower than the one of the maximum of solidus/liquidus. In this region, the solidus and liquidus temperatures increase when increasing the Am content, with a more important increase in the case of the liquidus. This observation is in agreement with the results obtained in Chapter 5 – section 5.4.3.4, where an increase of the solidus temperature of 10-15 K was noticed when increasing the Am content.

The second domain corresponds to O/M ratios located between the one of the maximum of the curves and 1.95. In this region, the solidus temperature decreases when increasing the americium content, whereas the opposite behaviour is noticed for the liquidus temperature.

The third domain corresponds to O/M ratios bigger than 1.95. In this region, a decrease of both the solidus and liquidus temperatures is noticed when increasing the americium content. This trend is in agreement with the study of Kato *et al.* [174], who reported a decrease of 3 K per mol.% of Am. However, a larger decrease is predicted by the calculations (10 K per mol.% of Am).

Based on the uncertainties of the model, it is difficult to state on the influence of americium on the solid/liquid phase transitions, as it also depends on the O/M ratio and Pu content. However, it can be concluded that the effect of americium remains small up to 5 mol.%.

6.4.4. Oxygen potential data

Because of a technically issue, the oxygen potentials of the PHENIX29, CAPRA4 and TRABANT40 samples could not be measured in this work. However, three sets of literature data exist for comparison with the thermodynamic model:

- Osaka *et al.* for $U_{0.685}Pu_{0.270}Am_{0.045}O_{2-x}$ ($0 < x < 0.07$) at 1123, 1273 and 1423 K using TGA [168].
- Nakamichi *et al.* for $U_{0.665}Pu_{0.311}Am_{0.024}O_{2-x}$ ($0 < x < 0.013$) at 1473, 1573 and 1623 K using TGA [169].
- Hirooka *et al.* for $U_{0.623}Pu_{0.350}Am_{0.027}O_{2-x}$ ($0 < x < 0.04$) at 1673, 1773 and 1873 K using TGA [170].

The oxygen potential data obtained for samples containing both Am and Np are not considered in this work.

The oxygen potentials are calculated for the three compositions investigated experimentally by Osaka *et al.*, Nakamichi *et al.* and Hirooka *et al.* in Figure 6-32, and compared to the experimental values.

For all samples, a good agreement is observed for O/M ratio close to 2.00. For lower O/M ratios, a good agreement is also found with the data of Hirooka *et al.* at 1873 and 1773 K, while significant discrepancies are noticed at 1673 K. A reasonable agreement is also found with the experimental data of Nakamichi *et al.*.

However, larger deviations are observed with the data of Osaka *et al.*. The model of the quaternary system appears to underestimate systematically the oxygen potential compared to

the experimental data. The differences could be explained by the higher americium content of the sample studied by Osaka *et al.* (z = 0.042) compared to the ones of the two other studies. Indeed, a significant amount of uncertainties remains on all the americium-bearing systems.

Thus, overall, a reasonable good agreement is noticed between the experimental data and the model of the quaternary system. The comparison performed here highlights the need for additional measurements on other compositions to improve the model. In addition, as shown in Chapter 2 – section 2.3.2.2.3, only one dataset exists for the oxygen potential of $U_{1-z}Am_zO_{2-x}$, which is not enough to build a reliable model for this key ternary sub-system.

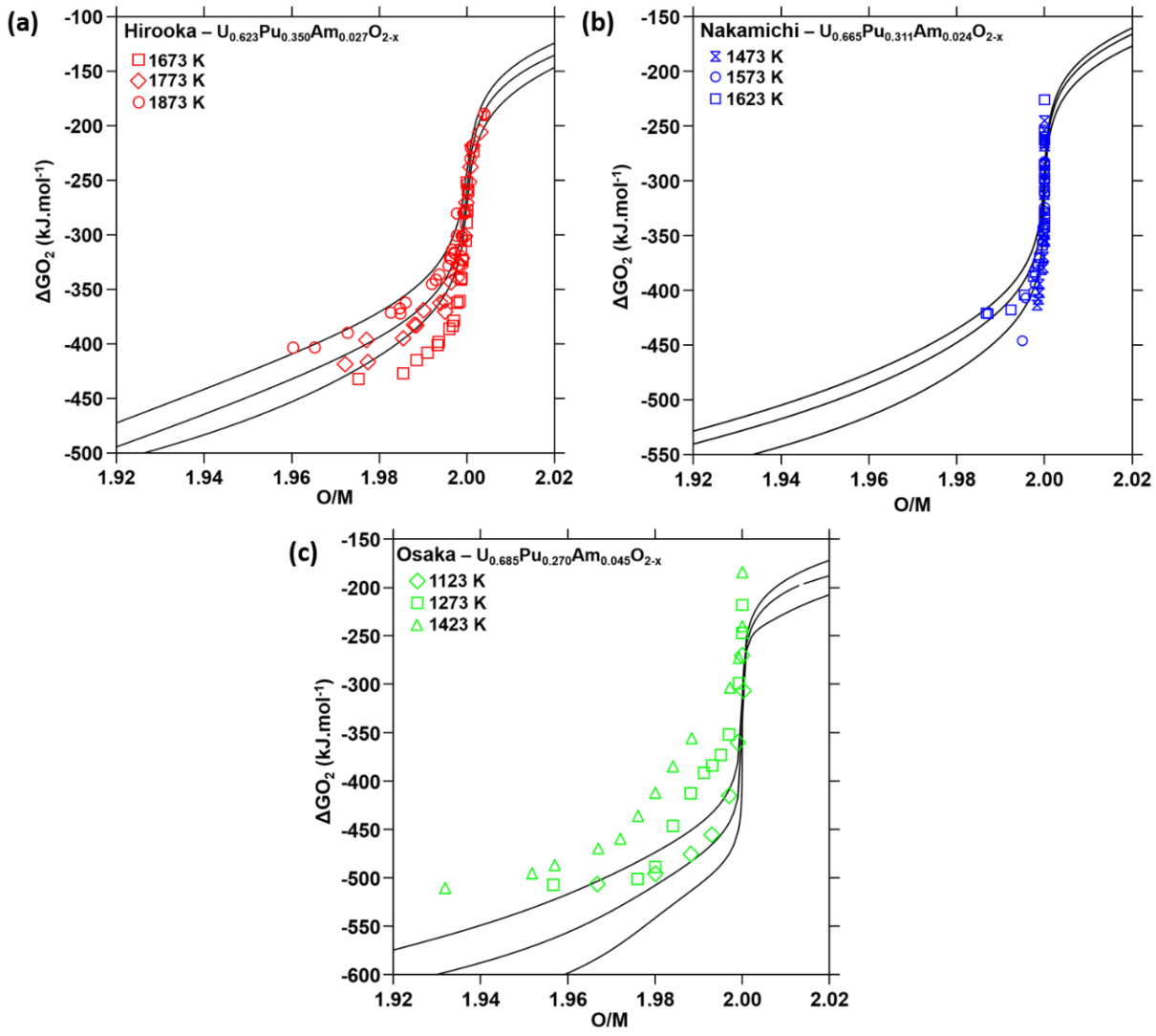

Figure 6-32: Oxygen potentials calculated for (a) $U_{0.623}Pu_{0.350}Am_{0.027}O_{2-x}$, (b) $U_{0.665}Pu_{0.311}Am_{0.024}O_{2-x}$ and (c) $U_{0.685}Pu_{0.270}Am_{0.045}O_{2-x}$, compared to the experimental data of Hirooka *et al.* [170], Nakamichi *et al.* [169] and Osaka *et al.* [168], respectively.

6.4.5. Conclusion

In this section, thermodynamic calculations were performed on the U-Pu-Am-O system by extrapolation of the binary and ternary sub-systems and the results were compared to the experimental results obtained in Chapter 5 and from the literature.

The comparison between the cationic proportions determined experimentally by XANES and the

calculated site fractions revealed the absence of the Pu^{3+} cations in the calculations, whereas a relative good agreement was observed for the proportions of U^{4+}, U^{5+}, Pu^{4+} and Am^{3+}.

The enthalpy increments of the CAPRA4 sample were well reproduced by the model, while a significant deviation was noticed for the heat capacity function, explained by a possible reduction of the samples at high temperature not represented by the calculations at O/M = 2.

The melting behaviour was also investigated and compared with the solidus temperatures and O/M ratios determined in this work. The trend of the experimental results was well reproduced by the thermodynamic calculations, *i.e.* increasing solidus and liquidus temperatures when decreasing the O/M ratio from 2.00. However, discrepancies were noticed in the positions of these temperatures and O/M ratios, attributed to a determination of the O/M ratio at room temperature, most likely not representative of the one achieved during the melting. Calculations of oxygen potentials of the samples and the atmosphere of melting (Ar with $pO_2 = 10^{-6}$ atm) allowed explaining the trend of the oxidation/reduction behaviours observed for the different samples, attributed to their initial O/M ratio. From this thermodynamic investigation, it was assumed at the O/M ratio obtained experimentally was fixed in the temperature range 2100-2350 K during the cooling down to room temperature.

No clear trend was observed for the influence of americium onto the solidus/liquidus temperatures, as it depends on both the O/M ratio range and the Pu content.

Comparison between oxygen potential values reported in the literature and calculations revealed the reliability of the extrapolated model in the near-stoichiometric range. However significant differences were found with the data of Osaka *et al.* for z = 0.045, explained by the uncertainties on the oxygen potential of Am-bearing systems.

These thermodynamic calculations on the U-Pu-Am-O system highlight the needs for additional experimental data on the ternary sub-systems U-Am-O and Pu-Am-O, as well as on $U_{1-y-z}Pu_yAm_zO_{2\pm x}$ samples with other compositions to further improve and validate this model.

6.5. CONCLUSION

In a first section, the model of the liquid phase of the Pu-O system was re-evaluated to better reproduce the melting point of PuO_2 obtained by Böhler *et al.* [176] and the solid/liquid phase transitions of the Pu_2O_3-PuO_2 domain. A good agreement was obtained, although additional experiments are needed to conclude on the exact O/M ratio of the samples achieved during the melting.

In a second section, based on the re-evaluation of the Pu-O system, the model of the liquid phase of the U-Pu-O system was also re-assessed. This work was performed to better reproduce the new sets of data of Böhler *et al.* obtained by laser heating for stoichiometric dioxides [176] and the solidus/liquidus temperatures obtained by Kato *et al.* in the hypo-stoichiometric range [174]. A good agreement was found, although, as for Pu-O, uncertainties remain on possible changes of composition during the melting. A decrease of the melting temperature was observed when increasing the Pu content up to 0.45 and increasing the O/M ratio. A shift of the congruent melting composition towards lower O/M ratios (~1.90) was also observed for $U_{1-y}Pu_yO_{2\pm x}$

compared to the end-member $UO_{1.97}$ and $PuO_{1.95}$. This observation was explained by the stabilisation of the solid solution in the hypo-stoichiometric range at high temperature, due to the increasing disorder in Pu^{3+}/Pu^{4+} and the formation of oxygen vacancies and thus a maximum in the corresponding configurational entropy. The influence of the atmosphere of melting was also investigated, with the study of the solidus/liquidus temperatures under air and argon and for different quantities of gas. Based on the calculations, a limited quantity of gas was admitted to react with the molten pool of the sample. However, further experiments are needed to conclude on the O/M ratio after the melting and the exact quantities of sample and gas interacting during the melting.

In a third section, an updated version of the model of the Pu-Am-O system was proposed, based on the few experimental data available. In this work, the models of the MO_{2-x}, A-M_2O_3 and liquid phases were re-assessed. A general good agreement was observed with the oxygen potential data of the literature, although the calculated values were systematically underestimated for low O/M ratios. A reasonable agreement was found with the experimental cationic distributions obtained experimentally in Chapter 4. Indeed, the presence of Pu^{3+} was not reproduced by the model. Significant differences were also noticed with the oxygen potential data measured in Chapter 4, whereas a good agreement was noticed with the phase equilibria. In addition, the updated model reproduced very well the solidus and liquidus temperatures determined experimentally in Chapter 4, although the initial and final O/M ratios remain unknown.

In the last section, thermodynamic calculations were performed on the U-Pu-Am-O system, based on the extrapolation of the binaries and ternaries. The cationic proportions obtained experimentally in Chapter 5 were not fully reproduced by the model, as no Pu^{3+} cations were formed in the calculations at 1600 K. Discrepancies were also observed when comparing with the heat capacity function obtained in Chapter 5, although a good agreement was noticed with the enthalpy increments. The melting behaviour of $U_{1-y-z}Pu_yAm_zO_{2\pm x}$ samples was also investigated and compared to thermodynamic calculations. The disagreement observed in the positions of the experimental points was admitted to partly originate from the experimental determination of the O/M ratio, which was performed at room temperature and was thus not representative of the O/M ratio at the melting. The oxidation/reduction behaviours observed in Chapter 5 was explained based on the thermodynamic calculations and linked to the initial O/M ratio of the sample and the oxidizing power of the gas. Finally, the oxygen potentials of the literature were reasonably well reproduced by the extrapolated model.

This study highlights the needs to perform additional experiments for a better thermodynamic description of the U-Pu-Am-O system. Indeed, uncertainties remain for high plutonium contents for O/M > 2.00 and < 1.90 in the U-Pu-O system, as well as on the compositions of the samples after melting. For the Pu-Am-O and U-Am-O systems, studies of phase equilibria and thermodynamic properties over the whole temperature and americium content ranges are needed for an accurate assessment of the model. Finally, for the U-Pu-Am-O, higher americium contents must be investigated to conclude on the influence of americium on the thermodynamic properties and phase equilibria. These studies would allow to confirm the accuracy of the extrapolation from the binaries and ternaries.

7. GENERAL CONCLUSION AND PERSPECTIVES

Uranium-plutonium mixed oxide $U_{1-y}Pu_yO_{2-x}$ is the reference fuel for Sodium Fast Reactor. In this technology, the multi-recycling of the plutonium from irradiated MOX fuel is envisaged, inducing drastic changes in the isotopic vector of the re-used plutonium. More specifically, an increase in the proportion of ^{241}Pu is expected. Based on the targeted plutonium content of SFR fuels (between 20 and 40 % Pu) and considering the half-life of ^{241}Pu ($\lambda_{1/2}$ = 14 years) and storage time between fabrication and irradiation, few mol.% of ^{241}Am (Am/(U+Pu+Am)), typically 2-3 mol.%, could accumulate in the fuels. Thus, the influence of the presence of up to 5 mol.% Am on the thermodynamic and structural properties of $U_{1-y}Pu_yO_{2-x}$ has to be investigated and predicted to foresee the fuel behaviour in reactor during normal and accidental conditions. To this aim, the CALPHAD method is used for the thermodynamic modelling of the U-Pu-Am-O system [5]. This work was articulated following the steps of the CALPHAD method.

First, the critical review of the available experimental data on the U-Pu-Am-O system and its various binary and ternary sub-systems was performed. This review highlighted the lack of data on americium-bearing system with very few data available on the Pu-Am-O and U-Pu-Am-O systems. Thus, it was concluded that new experimental campaigns on these two systems were required.

Experimental investigations on the Pu-Am-O and U-Pu-Am-O systems were then conducted. This work was performed collaboratively in two facilities: at ATALANTE in CEA Marcoule (France) and at the Joint Research Centre (JRC) Karlsruhe (Germany). The samples studied here differed between the two locations, mainly in terms of O/M ratio, due to different storage conditions (atmosphere, time). In some cases, it was not possible to perform pre-requisite characterizations to determine the compositions and O/M ratios of the samples.

Structural and thermodynamic properties of three $Pu_{1-z}Am_zO_{2-x}$ samples, with z = 0.23, 0.51 and 0.80, were then investigated experimentally. The structural characterizations were performed at the CEA Marcoule. The XRD experiments at room temperature before any thermal treatment indicated the presence of only fcc structures, corresponding to $(Pu,Am)O_{2-x}$ phases, for the three samples. No A-M_2O_3 or C-M_2O_3 phase, expected from the extrapolation of the binary Am-O and Pu-O phase diagrams, was observed experimentally. In addition, a swelling of the lattice parameter was noticed for the three samples, compared to the value obtained at the manufacturing. This phenomenon was attributed to a combination of α self-irradition defects and a reduction of the samples. The cationic distribution was investigated by XANES and revealed the co-existence of Am^{3+}, Am^{4+}, Pu^{3+} and Pu^{4+} for the three compositions. This observation highlighted the simultaneous reduction process of plutonium and americium during the 15 years of storage, contrarily to what was admitted before [43]. Based on the proportions of the cations, the O/M ratios of the samples were determined (1.94 for z = 0.23 and 0.51 and 1.93 for z = 0.80). The absence of the sesquioxide phases at room temperature for these low O/M ratios was explained by the stabilisation of the fcc structure due to the alpha self-irradiation of the materials.

The solid phase equilibria of the three samples were then investigated using HT-XRD from 1873 K to 300 K under He/H_2 4% with $pO_2 = 10^{-28}$ atm at CEA Marcoule. In this work, the O/M ratios established at each temperature step could not be determined. Complex behaviours were

evidenced for the three compositions, with the systematic presence of multiphasic domains along the whole temperature range. Furthermore, the identification of all the formed phases was unsuccessful and only a fcc $Pu_{1-z}Am_zO_{2-x}$ phase could be clearly identified experimentally for the three compositions. The existence of the A-M_2O_3 and B-M_2O_3 phases was supposed for z = 0.80 from 1873 K to 873 K, where a phase transition occurred, but could not be demonstrated.

The solid phase equilibria of $Pu_{0.77}Am_{0.23}O_{2-x}$ were then studied at 1673 K for pO_2 ranging between 10^{-28} and 10^{-24} atm by combining TGA and HT-XRD at CEA Marcoule. The mass variation measured by TGA allowed determining the O/M ratios achieved in these experiments, with 1.71 < O/M < 1.78. An increase of the oxygen potential was measured when increasing the O/M ratio, ranging between the ones of PuO_2 and AmO_2. As previously mentioned, the identification of the formed phases during the HT-XRD experiments was difficult and only the presence of a fcc MO_{2-x} phase was certified. Using the HT-XRD results, a multiphasic domain [MO_{2-x} + secondary phase(s)] was evidenced for 1.716 ≤ O/M ≤ 1.741 at 1673 K, followed by a monophasic MO_{2-x} region for O/M > 1.741.

The solid/liquid phase transitions were studied for $Pu_{0.49}Am_{0.51}O_{2-x}$ using a laser heating technique at JRC Karlsruhe. The average solidus and liquidus temperature were measured at 2838 ± 60 K and 2965 ± 60 K respectively. Thanks to the use of oxygen gauges in the setup, an increase of the oxygen partial pressure was noticed in the chamber during the melting. Based on several hypotheses on the samples composition and oxygen release, the mass of oxygen released by the samples during the melting was quantified and linked to the variation in O/M ratio along the shots. The O/M ratio of the sample after each shot was determined and a significant reduction of the sample along the shots was observed.

Additional experimental campaigns were dedicated to the investigation of various mixed oxides $U_{1-y-z}Pu_yAm_zO_{2\pm x}$, with 0.235 ≤ y ≤ 0.39 and 0.005 ≤ z ≤ 0.02. Structural investigations were performed at the CEA Marcoule, while the XANES experiments were performed at the SOLEIL synchrotron (France). EPMA analyses revealed homogeneous matrix phases with few uranium- and plutonium-rich agglomerates for all the samples. This observation is in agreement with the XRD results, where a matrix phase and UO_2 phase were highlighted. The O/M ratio of the samples was determined by XRD and by HERFD-XANES. A good agreement is obtained using these two techniques. However, XANES shows unexpected results with the systematic simultaneous presence of U^{5+} and Pu^{3+}/Am^{3+} even for samples with O/M = 2.00. These results indicate a charge compensation mechanism for the stoichiometric samples. This observation was already reported in the case of $U_{1-z}Am_zO_{2\pm x}$ oxides, where the simultaneous presence of U^{5+} and Am^{3+} was noticed [55]. It must be noted that the presence of U^{5+} and Pu^{3+} cannot be attributed to the U- and Pu-rich agglomerates but to the peculiar behaviour of the $U_{1-y-z}Pu_yAm_zO_{2\pm x}$ oxides.

The lattice thermal expansion of the matrix phase was studied from 1873 K to 300 K by HT-XRD. Deviations from the recommendations of the literature were noticed for T > 1373 K, due to the reduction of the samples. This reduction corresponds to the reduction of plutonium from Pu^{4+} to Pu^{3+}, enhanced by the presence of americium already purely trivalent at room temperature. In addition, the lattice thermal expansion was found to increase when increasing the americium content.

The enthalpy increment and heat capacity of a $U_{0.70}Pu_{0.28}Am_{0.02}O_{2.00}$ sample were studied at JRC Karlsruhe using drop calorimetry from 500 to 1800 K. A good agreement was noticed between the enthalpy increments measured in this work and the literature data for the pure poles UO_2 and PuO_2 [253] and for $U_{0.72}Pu_{0.28}O_{2.00}$ [135]. However, three outliers were observed at 1000, 1300 and 1600 K, possibly attributed to different stages of the annealing of the defects created by α self-irradiation: changes in the first oxygen sublattice, the release of He and changes in the cationic sublattice, respectively. For the heat capacities, higher values were observed for T > 1100 K compared to the pure poles and $U_{0.72}Pu_{0.28}O_{2.00}$ [135]. This behaviour was attributed to the increasing concentration of oxygen vacancies linked to the reduction of the samples observed also during the lattice thermal expansion experiments at high temperature.

The melting behaviour of the $U_{1-y-z}Pu_yAm_zO_{2\pm x}$ oxides was investigated by means of laser heating at JRC Karlsruhe. Only the solidus temperature was observed and measured for these samples. The variation of the oxygen partial pressure in the chamber was recorded during the melting and was converted into the mass of oxygen absorbed or released by the samples. Hypotheses were then made on the size, quantity and homogeneity of the molten pool interacting with the oxygen of the atmosphere. The O/M ratio of the molten pool throughout the shot was determined based on these quantities and hypotheses. A decrease of the solidus temperature was noticed when increasing the Pu content and O/M ratio, in agreement with the literature [174], [176], [184]. On the contrary, an increase of the solidus temperature was reported when increasing the Am content, in disagreement with a previous study [174], however within the experimental uncertainties. The different oxidation/reduction behaviours observed during the melting were related to the initial O/M ratios of the samples, with hypo-stoichiometric samples being oxidized and hyper-/near-stoichiometric samples being reduced.

Finally, based on the experimental results obtained in this work for the Pu-Am-O and U-Pu-Am-O systems, thermodynamic investigations of the U-Pu-Am-O system were performed. The models of the liquid phase of the Pu-O and U-Pu-O systems were re-evaluated based on new sets of melting points obtained after their last assessment in 2011 [7]. A better description of the solid/liquid phase transitions in the Pu_2O_3-PuO_2 domain was obtained. For the U-Pu-O system, the description of the UO_2-PuO_2 region as well as the hypo-stoichiometric domain was improved. A shift of the congruent melting composition towards lower O/M ratios (around 1.90) was observed and explained by the stabilization of the mixed oxide in this region, due to a maximum of the configurational entropy related to the formation of both oxygen vacancies and Pu^{3+}/Pu^{4+} mixing. Based on the thermodynamic calculations, it was evidenced that the atmosphere of melting had a significant impact on the melting behaviour of the oxides. Only a limited amount of gas interacting with the molten pool of the sample during the melting was assessed.

An updated version of the model of the Pu-Am-O system is also proposed in this work, with the re-assessment of the models of the MO_{2-x}, M_2O_3 and liquid phases. A good agreement was observed with the oxygen potential data of the literature, as well as with the phase equilibria and the solid/liquid phase transitions obtained in this work. However, some discrepancies were noticed with the formed phases at room temperature, the site fractions and the oxygen potentials measured in this work.

Finally, the thermodynamic investigation of the U-Pu-Am-O system was performed by the extrapolation of the re-assessed binary and ternary sub-systems. The comparison of the

calculated data with the experimental results obtained in this work and from the literature was performed.

A relatively good agreement was observed for the calculated site fractions compared to the cationic proportions determined experimentally by XANES. However, slight differences were observed in the values and the presence of Pu^{3+} was not reproduced by the model. The enthalpy increments calculated using the model agreed with the experimental data, whereas significant deviations were noticed for the heat capacity deduced from the enthalpy data. A qualitative agreement was obtained between the calculated solidus and liquidus curves and the melting behaviour determined experimentally, although some differences were observed for the O/M ratios calculated at the solidus. The oxidation or reduction of the samples observed experimentally was explained by thermodynamic calculations. The behaviour was found to be driven by the difference of oxygen potential between the samples and the gas phase as a function of temperature. The O/M ratio could be fixed during cooling in the temperature range 2000-2350 K. Thus, the O/M determined experimentally in this work are most likely not representative of the O/M ratio at the solidus temperature but probably result from the change in the sample composition occurring during cooling. Concerning the oxygen potential data, a reasonable good agreement was obtained with the literature data in the near-stoichiometric range. As evidenced here, this work constitutes a preliminary description of the U-Pu-Am-O system. In order to improve the description of the quaternary system, further investigations of the binary and ternary sub-systems are needed.

Although significant improvements were made in the assessment of the Am-O and U-Am-O systems [28], uncertainties remain especially on the oxygen potentials and phase equilibria in the hypo-stoichiometric range.

For the Pu-Am-O system, additional experiments on other americium contents and O/M ratios are also necessary. In particular, the study of the phase equilibria in isothermal conditions using the coupling of TGA and HT-XRD experiments used in this work would be useful to determine the phase boundaries. The identification of the formed phases in temperature over the whole americium range would be a first step in the description of the phase diagram. Moreover, the determination of the mutual solubility of Pu and Am in the MO_{2-x}, A- and C-M_2O_3 phases is required. With these additional experimental data, the thermodynamic modelling of the Pu-Am-O system could be significantly improved by adjusting the ternary interaction parameters.

Further experiments are also needed on the quaternary U-Pu-Am-O system. Indeed, in this work, a maximum americium content of 2% was investigated, while this content can range up to 5 % in SFR fuels. Thus, investigations of the thermodynamic and structural properties of samples with higher americium contents are needed for the improvement of the thermodynamic model.

In addition, post-melting characterizations on all the samples for all the chemical systems, using XAS, XRD, SEM and Raman spectroscopy are needed to conclude on the possible vaporization occurring during the melting and to verify the hypotheses made in this present work to calculate the O/M ratio after melting.

Thanks to the experimental campaigns performed in this work on $U_{1-y-z}Pu_yAm_zO_{2\pm x}$ and the few literature data available, preliminary recommendations can be proposed for the use of these oxides fuels in Sodium Fast Reactors.

One of the main concerns when designing a reactor is the margin to the fuel melting. In this work, it was highlighted that the presence of few mol.% of americium does not affect significantly the solidus and liquidus temperatures of $U_{1-y}Pu_yO_{2-x}$ oxides. Indeed, based on the calculations performed in this work, the solidus temperature will decrease by 10 K per mol.% of Am in the O/M ratio range of interest (1.94-1.99) but remains significantly higher than the temperature reached at the centre of the pellets (around 2200 K).

In addition, the heat capacity obtained in this work indicated that the higher values found in presence of americium for T > 1000 K were due to the reduction of the samples. In fact, the mixed oxides $U_{1-y-z}Pu_yAm_zO_{2\pm x}$ exhibit a high oxygen potential and thus a tendency to be reduced when increasing the temperature, with the reduction of plutonium from Pu^{4+} to Pu^{3+} enhanced by the reduction of americium into Am^{3+}. This implies that the quantity of heat to provide to the fuels for increasing its temperature increases with the americium content. Moreover, the significant reduction behaviour of the fuel is expected when increasing the temperature and americium content, leading to a slightly higher melting temperature (around 3150 K for y = 0.30 and z = 0.05 at O/M = 1.83). This implies an increase in the margin to fuel melting compared to a fuel of same plutonium content but without americium (around 3100 K at 1.86). Based on these observations, it appears that the presence of Am originating from the multi-recycling of Pu does not significantly influence and does not deteriorate the thermal behaviour of the fuel.

However, this enhanced reduction behaviour in temperature also leads to a larger thermal expansion when increasing the americium content. This observation could be a concern for the safety as it could accelerate the fuel cladding interaction phenomenon causing cracks formation in the pellets. To quantify these risks, studies of thermo-mechanical properties such as yield stress or thermal creep are needed on these fuels.

In addition, this work has also evidenced that changes in the O/M ratio of the mixed oxide were occurring during the melting, depending on the atmosphere and the initial O/M ratio of the oxide. The SFR fuels are hypo-stoichiometric in oxygen in the reactor. If the surrounding oxygen partial pressure in the atmosphere in the fuel pin is higher than the one of the fuel, the fuel could be oxidized at high temperature. This would reduce the margin to fuel melting in case of an accident. Thus, the effects of the atmosphere (oxygen partial pressure) in the fuel pin and of the O/M ratio of the fuel have to be taken into account to improve the prediction of the margin to fuel melting in Fuel Performance Codes for the safety of the reactor.

The investigation of the U-Pu-Am-O system was initiated in this work but needs to be pursued. The advantage of combining experimental research and thermodynamic modelling for an accurate description of the systems was proven in this work. In addition to these tools, kinetics of the diverse phenomena have to be studied for a complete description of the fuel's behaviour. Furthermore, investigations of the influence of the presence of other minor actinides, such as neptunium or curium, and fission products would constitute the next step of this work for a better understanding and prediction of the behaviour of irradiated nuclear fuels.

REFERENCES

[1] H. Ritchie and M. Roser, 'Energy', *Our World in Data*, Nov. 2020, Accessed: Mar. 04, 2022. [Online]. Available: https://ourworldindata.org/energy-mix

[2] 'GIF Portal - Sodium-Cooled Fast Reactor (SFR)'. https://www.gen-4.org/gif/jcms/c_42152/sodium-cooled-fast-reactor-sfr (accessed Nov. 09, 2019).

[3] R. J. M. Konings and D. Haas, 'Fuels and targets for transmutation', *Comptes Rendus Physique*, vol. 3, no. 7, pp. 1013–1022, Sep. 2002, doi: 10.1016/S1631-0705(02)01382-8.

[4] C. Guéneau *et al.*, 'TAF-ID: An international thermodynamic database for nuclear fuels applications', *Calphad*, vol. 72, p. 102212, Mar. 2021, doi: 10.1016/j.calphad.2020.102212.

[5] N. Saunders and A. P. Miodownik, 'CALPHAD (Calculation of Phase Diagrams): A Comprehensive Guide, Volume 1 - 1st Edition', 1998. https://www.elsevier.com/books/calphad-calculation-of-phase-diagrams-a-comprehensive-guide/saunders/978-0-08-042129-2 (accessed Mar. 26, 2019).

[6] E. Epifano *et al.*, 'Insight into the Am–O Phase Equilibria: A Thermodynamic Study Coupling High-Temperature XRD and CALPHAD Modeling', *Inorg. Chem.*, vol. 56, no. 13, pp. 7416–7432, Jul. 2017, doi: 10.1021/acs.inorgchem.7b00572.

[7] C. Guéneau *et al.*, 'Thermodynamic modelling of advanced oxide and carbide nuclear fuels: Description of the U–Pu–O–C systems', *Journal of Nuclear Materials*, vol. 419, no. 1–3, pp. 145–167, Dec. 2011, doi: 10.1016/j.jnucmat.2011.07.033.

[8] A. L. Smith, C. Guéneau, J.-L. Flèche, S. Chatain, O. Beneš, and R. J. M. Konings, 'Thermodynamic assessment of the Na-O and Na-U-O systems: margin to the safe operation of SFRs', *The Journal of Chemical Thermodynamics*, Apr. 2017, doi: 10.1016/j.jct.2017.04.003.

[9] D. Labroche, O. Dugne, and C. Chatillon, 'Thermodynamics of the O–U system. I – Oxygen chemical potential critical assessment in the UO2–U3O8 composition range', *Journal of Nuclear Materials*, vol. 312, no. 1, pp. 21–49, Jan. 2003, doi: 10.1016/S0022-3115(02)01322-3.

[10] D. Labroche, O. Dugne, and C. Chatillon, 'Thermodynamic properties of the O–U system. II – Critical assessment of the stability and composition range of the oxides UO2+x, U4O9−y and U3O8−z', *Journal of Nuclear Materials*, vol. 312, no. 1, pp. 50–66, Jan. 2003, doi: 10.1016/S0022-3115(02)01323-5.

[11] M. Baichi, C. Chatillon, G. Ducros, and K. Froment, 'Thermodynamics of the O–U system: III – Critical assessment of phase diagram data in the U–UO2+x composition range', *Journal of Nuclear Materials*, vol. 349, no. 1, pp. 57–82, Feb. 2006, doi: 10.1016/j.jnucmat.2005.10.001.

[12] M. Baichi, C. Chatillon, G. Ducros, and K. Froment, 'Thermodynamics of the O–U system. IV – Critical assessment of chemical potentials in the U–UO2.01 composition range', *Journal of Nuclear Materials*, vol. 349, no. 1, pp. 17–56, Feb. 2006, doi: 10.1016/j.jnucmat.2005.09.001.

[13] C. Guéneau, M. Baichi, D. Labroche, C. Chatillon, and B. Sundman, 'Thermodynamic assessment of the uranium–oxygen system', *Journal of Nuclear Materials*, vol. 304, no. 2–3, pp. 161–175, Aug. 2002, doi: 10.1016/S0022-3115(02)00878-4.

[14] D. Manara, C. Ronchi, M. Sheindlin, M. Lewis, and M. Brykin, 'Melting of stoichiometric and hyperstoichiometric uranium dioxide', *Journal of Nuclear Materials*, vol. 342, no. 1, pp. 148–163, Jun. 2005, doi: 10.1016/j.jnucmat.2005.04.002.

[15] J. D. Higgs, B. J. Lewis, W. T. Thompson, and Z. He, 'A conceptual model for the fuel oxidation of defective fuel', *Journal of Nuclear Materials*, vol. 366, no. 1, pp. 99–128, Jun. 2007, doi: 10.1016/j.jnucmat.2006.12.050.

[16] L. R. Morss, N. Edelstein, J. Fuger, and J. J. Katz, Eds., *The Chemistry of the Actinide and Transactinide Elements (3rd ed., Volumes 1-5)*, 3rd ed. Springer Netherlands, 2006. Accessed: May 10, 2019. [Online]. Available: https://www.springer.com/la/book/9781402035982

[17] E. R. Gardner, T. L. Markin, and R. S. Street, 'The plutonium-oxygen phase diagram', *Journal of Inorganic and Nuclear Chemistry*, vol. 27, no. 3, pp. 541–551, Mar. 1965, doi: 10.1016/0022-1902(65)80259-7.

[18] J.-C. Boivineau, 'Etude par rayons x du diagramme plutonium-oxygene de la temperature ambiante jusqu'a 1100°c', *Journal of Nuclear Materials*, vol. 60, no. 1, pp. 31–38, Apr. 1976, doi: 10.1016/0022-3115(76)90114-8.

[19] C. Sari, U. Benedict, and H. Blank, 'Metallographic and X-ray investigations in the Pu-O and U-Pu-O systems', *Thermodynamics of Nuclear Materials*, Dec. 1968.

[20] T. D. Chikalla, C. E. McNeilly, and R. E. Skavdahl, 'The plutonium-oxygen system', *Journal of Nuclear Materials*, vol. 12, no. 2, pp. 131–141, Jul. 1964, doi: 10.1016/0022-3115(64)90132-1.

[21] J. L. Drummond and G. A. Welch, 'The preparation and properties of some plutonium compounds. Part VI. Plutonium dioxide', *J. Chem. Soc.*, no. 0, pp. 4781–4785, Jan. 1957, doi: 10.1039/JR9570004781.

[22] J. M. Haschke, T. H. Allen, and L. A. Morales, 'Reaction of plutonium dioxide with water: formation and properties of PuO(2+x)', *Science*, vol. 287, no. 5451, pp. 285–287, Jan. 2000.
[23] C. Guéneau, C. Chatillon, and B. Sundman, 'Thermodynamic modelling of the plutonium–oxygen system', *Journal of Nuclear Materials*, vol. 378, no. 3, pp. 257–272, Sep. 2008, doi: 10.1016/j.jnucmat.2008.06.013.
[24] F. De Bruycker *et al.*, 'On the melting behaviour of uranium/plutonium mixed dioxides with high-Pu content: A laser heating study', *Journal of Nuclear Materials*, vol. 419, no. 1, pp. 186–193, Dec. 2011, doi: 10.1016/j.jnucmat.2011.08.028.
[25] C. Sari and E. Zamorani, 'An investigation in the americium oxide system', *Journal of Nuclear Materials*, vol. 37, no. 3, pp. 324–330, Dec. 1970, doi: 10.1016/0022-3115(70)90162-5.
[26] P. Gotcu-Freis, J.-Y. Colle, C. Guéneau, N. Dupin, B. Sundman, and R. J. M. Konings, 'A thermodynamic study of the Pu–Am–O system', *Journal of Nuclear Materials*, vol. 414, no. 3, pp. 408–421, Jul. 2011, doi: 10.1016/j.jnucmat.2011.05.014.
[27] R. J. Silva, G. Bidoglio, P. B. Robouch, I. Puigdomenech, H. Wanner, and M. H. Rand, 'Chemical Thermodynamics of Americium, Volume 2 - 1st Edition', 1995. https://www.elsevier.com/books/chemical-thermodynamics-of-americium/silva/978-0-444-82281-9 (accessed Mar. 27, 2019).
[28] E. Epifano, 'Study of the U-Am-O ternary phase diagram', thesis, Paris Saclay, 2017. Accessed: Feb. 26, 2019. [Online]. Available: http://www.theses.fr/2017SACLX084
[29] T. D. Chikalla and L. Eyring, 'Phase relationships in the americium-oxygen system', *Journal of Inorganic and Nuclear Chemistry*, vol. 30, no. 1, pp. 133–145, Jan. 1968, doi: 10.1016/0022-1902(68)80072-7.
[30] D. H. Templeton and C. H. Dauben, 'Crystal structures of americium compounds1', *J. Am. Chem. Soc.*, vol. 75, no. 18, pp. 4560–4562, Sep. 1953, doi: 10.1021/ja01114a051.
[31] T. L. Markin and R. S. Street, 'The uranium-plutonium-oxygen ternary phase diagram', *Journal of Inorganic and Nuclear Chemistry*, vol. 29, no. 9, pp. 2265–2280, Sep. 1967, doi: 10.1016/0022-1902(67)80281-1.
[32] C. Sari, U. Benedict, and H. Blank, 'A study of the ternary system U02-Pu02-Pu203', *Journal of Nuclear Materials*, vol. 35, no. 3, pp. 267–277, Jun. 1970, doi: 10.1016/0022-3115(70)90211-4.
[33] N. H. Brett and L. E. Russell, 'The sintering behavior and stability of (PuU)O2 solid solutions'. 1962.
[34] L. E. Russell, N. H. Brett, J. D. L. Harrison, and J. Williams, 'Observations on phase equilibria and sintering behaviour in the PuO2-UO2 system', *Journal of Nuclear Materials*, vol. 5, no. 2, pp. 216–227, Feb. 1962, doi: 10.1016/0022-3115(62)90102-2.
[35] G. Dean, J. C. Boivineau, P. Chereau, and J. P. Marcon, 'Contribution to the study of the U-Pu-O system', *Plutonium and Other Actinides*, pp. 753–761, 1970.
[36] P. R. Vasudeva Rao, S. Anthonysamy, M. V. Krishnaiah, and V. Chandramouli, 'Oxygen potential and thermal conductivity of (U, Pu) mixed oxides', *Journal of Nuclear Materials*, vol. 348, no. 3, pp. 329–334, Feb. 2006, doi: 10.1016/j.jnucmat.2005.10.004.
[37] M. Osaka, T. Namekawa, K. Kurosaki, and S. Yamanaka, 'Chemical thermodynamic representation of (U, Pu, Am)O2−x', *Journal of Nuclear Materials*, vol. 344, no. 1–3, pp. 230–234, Sep. 2005, doi: 10.1016/j.jnucmat.2005.04.047.
[38] T. M. Besmann and T. B. Lindemer, 'Thermochemical modeling of the plutonium and uranium-plutonium dioxides', Jan. 1984. [Online]. Available: http://www.osti.gov/bridge/servlets/purl/6221489-qDdMel/
[39] M. Strach, R. C. Belin, J.-C. Richaud, and J. Rogez, 'Biphasic MO2+x–M3O8–z Domain of the U–Pu–O Phase Diagram', *Inorg. Chem.*, vol. 54, no. 18, pp. 9105–9114, Sep. 2015, doi: 10.1021/acs.inorgchem.5b01544.
[40] T. Truphémus *et al.*, 'Structural studies of the phase separation in the UO2–PuO2–Pu2O3 ternary system', *Journal of Nuclear Materials*, vol. 432, no. 1–3, pp. 378–387, Jan. 2013, doi: 10.1016/j.jnucmat.2012.07.034.
[41] R. Vauchy, R. C. Belin, A.-C. Robisson, and F. Hodaj, 'High temperature X-ray diffraction study of the kinetics of phase separation in hypostoichiometric uranium–plutonium mixed oxides', *Journal of the European Ceramic Society*, vol. 34, no. 10, pp. 2543–2551, Sep. 2014, doi: 10.1016/j.jeurceramsoc.2014.02.028.
[42] S. Miwa *et al.*, 'Phase behavior of PuO2−x with addition of 9% Am', *Journal of Alloys and Compounds*, vol. 444–445, pp. 610–613, Oct. 2007, doi: 10.1016/j.jallcom.2006.10.059.
[43] M. Osaka, K. Kurosaki, and S. Yamanaka, 'Oxygen potential of (Pu0.91Am0.09)O2−x', *Journal of Nuclear Materials*, vol. 357, no. 1–3, pp. 69–76, Oct. 2006, doi: 10.1016/j.jnucmat.2006.05.044.
[44] H. Otobe, M. Akabori, and Y. Arai, 'Oxygen potential measurements of Am0.5Pu0.5O2−x by EMF method', *Journal of Nuclear Materials*, vol. 389, no. 1, pp. 68–71, May 2009, doi: 10.1016/j.jnucmat.2009.01.009.

[45] R. J. Ackermann, R. L. Faircloth, and M. H. Rand, 'A thermodynamic study of the vaporization behavior of the substoichiometric plutonium dioxide Phase1', *J. Phys. Chem.*, vol. 70, no. 11, pp. 3698–3706, Nov. 1966, doi: 10.1021/j100883a055.
[46] F. Lebreton, 'Synthèse et caractérisation d'oxydes mixtes d'uranium et d'américium', thesis, Limoges, 2014. Accessed: May 06, 2019. [Online]. Available: http://www.theses.fr/2014LIMO0009
[47] D. Prieur *et al.*, 'Melting behaviour of americium-doped uranium dioxide', *The Journal of Chemical Thermodynamics*, vol. 97, pp. 244–252, Jun. 2016, doi: 10.1016/j.jct.2016.02.003.
[48] E. Epifano *et al.*, 'Melting behaviour of uranium-americium mixed oxides under different atmospheres', *The Journal of Chemical Thermodynamics*, vol. 140, p. 105896, Jan. 2020, doi: 10.1016/j.jct.2019.105896.
[49] A. D. Murray and B. T. M. Willis, 'A neutron diffraction study of anion clusters in nonstoichiometric uranium dioxide', *Journal of Solid State Chemistry*, vol. 84, no. 1, pp. 52–57, Jan. 1990, doi: 10.1016/0022-4596(90)90183-X.
[50] B. T. M. Willis, 'Crystallographic studies of anion excess uranium oxides', *J. Chem. Soc., Faraday Trans. II; (United Kingdom)*, vol. 83:7, Jul. 1987, Accessed: Feb. 01, 2022. [Online]. Available: https://www.osti.gov/etdeweb/biblio/6141056
[51] L. Desgranges, G. Baldinozzi, G. Rousseau, J.-C. Nièpce, and G. Calvarin, 'Neutron Diffraction Study of the in Situ Oxidation of UO2', *Inorg. Chem.*, vol. 48, no. 16, pp. 7585–7592, Aug. 2009, doi: 10.1021/ic9000889.
[52] D. J. M. Bevan, I. E. Grey, and B. T. M. Willis, 'The crystal structure of β-U4O9−y', *Journal of Solid State Chemistry*, vol. 61, no. 1, pp. 1–7, Jan. 1986, doi: 10.1016/0022-4596(86)90002-2.
[53] F. Garrido, A. C. Hannon, R. M. Ibberson, L. Nowicki, and B. T. Willis, 'Neutron diffraction studies of U4O9: comparison with EXAFS results', *Inorg Chem*, vol. 45, no. 20, pp. 8408–8413, Oct. 2006, doi: 10.1021/ic060964c.
[54] L. Medyk, 'L'enjeu de la maîtrise des propriétés locales (stoechiométrie, répartition cationique…) lors de la fabrication des combustibles (U,Pu)O2-x : potentialités de la microscopie Raman', Université d'Orléans, 2021.
[55] E. Epifano *et al.*, 'Extreme multi-valence states in mixed actinide oxides', *Commun Chem*, vol. 2, no. 1, pp. 1–11, May 2019, doi: 10.1038/s42004-019-0161-0.
[56] L. R. Morss, Ed., *The chemistry of the actinide and transactinide elements*. Dordrecht: Springer, 2010.
[57] F. Lebreton, R. C. Belin, T. Delahaye, and P. Blanchart, 'In-situ X-ray diffraction study of phase transformations in the Am–O system', *Journal of Solid State Chemistry*, vol. 196, pp. 217–224, Dec. 2012, doi: 10.1016/j.jssc.2012.06.027.
[58] T. M. Besmann and T. B. Lindemer, 'Improvement to the chemical thermodynamic representation of PuO2-x and U1-zPuzOw'. 1985.
[59] H. R. Hoekstra, S. Siegel, and F. X. Gallagher, 'The uranium-oxygen system at high pressure', *Journal of Inorganic and Nuclear Chemistry*, vol. 32, no. 10, pp. 3237–3248, Oct. 1970, doi: 10.1016/0022-1902(70)80206-8.
[60] M. Caisso *et al.*, 'Evidence of Trivalent Am Substitution into U3O8', *Inorg. Chem.*, Sep. 2016, doi: 10.1021/acs.inorgchem.6b01672.
[61] B. Belbeoch, J. C. Boivineau, and P. Perio, 'Changements de structure de l'oxyde U4O9', *Journal of Physics and Chemistry of Solids*, vol. 28, no. 7, pp. 1267–1275, Jul. 1967, doi: 10.1016/0022-3697(67)90070-4.
[62] M. Strach, R. C. Belin, J.-C. Richaud, and J. Rogez, 'High Temperature X-ray Diffraction Study of the Oxidation Products and Kinetics of Uranium–Plutonium Mixed Oxides', *Inorg. Chem.*, vol. 53, no. 24, pp. 12757–12766, Dec. 2014, doi: 10.1021/ic501580x.
[63] L. Desgranges, G. Baldinozzi, D. Siméone, and H. E. Fischer, 'Refinement of the α-U4O9 Crystalline Structure: New Insight into the U4O9 → U3O8 Transformation', *Inorg. Chem.*, vol. 50, no. 13, pp. 6146–6151, Jul. 2011, doi: 10.1021/ic200316b.
[64] G. Leinders, R. Delville, J. Pakarinen, T. Cardinaels, K. Binnemans, and M. Verwerft, 'Assessment of the U3O7 Crystal Structure by X-ray and Electron Diffraction', *Inorg. Chem.*, vol. 55, no. 19, pp. 9923–9936, Oct. 2016, doi: 10.1021/acs.inorgchem.6b01941.
[65] H. R. Hoekstra, A. Santoro, and S. Siegel, 'The low temperature oxidation of UO2 and U4O9', *Journal of Inorganic and Nuclear Chemistry*, vol. 18, pp. 166–178, Mar. 1961, doi: 10.1016/0022-1902(61)80384-9.
[66] B. O. Loopstra, 'The structure of β-U3O8', *Acta Cryst B*, vol. 26, no. 5, pp. 656–657, May 1970, doi: 10.1107/S0567740870002935.
[67] B. O. Loopstra, 'Neutron diffraction investigation of U3O8', *Acta Cryst, Acta Crystallogr*, vol. 17, no. 6, pp. 651–654, Jun. 1964, doi: 10.1107/S0365110X6400158X.
[68] B. O. Loopstra, 'The phase transition in α-U3O8 at 210°C', *J Appl Cryst*, vol. 3, no. 2, pp. 94–96, Mar. 1970, doi: 10.1107/S002188987000571X.
[69] I. Grenthe, J. Drozdzynski, T. Fujino, E. C. Buck, T. E. Albrecht-Schmitt, and S. F. Wolf, *Uranium*.

[70] E. H. P. Cordfunke and P. Aling, 'System UO3+ U3O8: dissociation pressure of γ-UO3', *Trans. Faraday Soc.*, vol. 61, no. 0, pp. 50–53, Jan. 1965, doi: 10.1039/TF9656100050.
[71] H. R. Hoekstra and S. Siegel, 'The uranium-oxygen system: U3O8-UO3', *Journal of Inorganic and Nuclear Chemistry*, vol. 18, pp. 154–165, Mar. 1961, doi: 10.1016/0022-1902(61)80383-7.
[72] G. Leinders, T. Cardinaels, K. Binnemans, and M. Verwerft, 'Accurate lattice parameter measurements of stoichiometric uranium dioxide', *Journal of Nuclear Materials*, vol. 459, pp. 135–142, Apr. 2015, doi: 10.1016/j.jnucmat.2015.01.029.
[73] R. Vauchy, A. Joly, and C. Valot, 'Lattice thermal expansion of Pu1−yAmyO2−x plutonium–americium mixed oxides', *J Appl Cryst, J Appl Crystallogr*, vol. 50, no. 6, pp. 1782–1790, Dec. 2017, doi: 10.1107/S1600576717014832.
[74] S. Casalta, H. J. Matzke, and C. Prunier, 'A thermodynamic properties study of the americium-oxygen system', *Global 1995*, 1995, Accessed: Feb. 13, 2019. [Online]. Available: http://inis.iaea.org/Search/search.aspx?orig_q=RN:29055283
[75] D. Horlait, R. Caraballo, F. Lebreton, C. Jégou, P. Roussel, and T. Delahaye, 'Self-irradiation and oxidation effects on americium sesquioxide and Raman spectroscopy studies of americium oxides', *Journal of Solid State Chemistry*, vol. 217, pp. 159–168, Sep. 2014, doi: 10.1016/j.jssc.2014.05.025.
[76] C. Duriez, J.-P. Alessandri, T. Gervais, and Y. Philipponneau, 'Thermal conductivity of hypostoichiometric low Pu content (U,Pu)O2−x mixed oxide', *Journal of Nuclear Materials*, vol. 277, no. 2–3, pp. 143–158, Feb. 2000, doi: 10.1016/S0022-3115(99)00205-6.
[77] F. Grønvold, 'High-temperature X-ray study of uranium oxides in the UO2□U3O8 region', *Journal of Inorganic and Nuclear Chemistry*, vol. 1, no. 6, pp. 357–370, Dec. 1955, doi: 10.1016/0022-1902(55)80046-2.
[78] M. Kato and K. Konashi, 'Lattice parameters of (U, Pu, Am, Np)O2−x', *Journal of Nuclear Materials*, vol. 385, no. 1, pp. 117–121, Mar. 2009, doi: 10.1016/j.jnucmat.2008.09.037.
[79] R. Vauchy, A.-C. Robisson, F. Audubert, and F. Hodaj, 'Ceramic processing of uranium–plutonium mixed oxide fuels (U1−yPuy)O2 with high plutonium content', *Ceramics International*, vol. 40, no. 7, Part B, pp. 10991–10999, Aug. 2014, doi: 10.1016/j.ceramint.2014.03.104.
[80] J.-F. Vigier, P. M. Martin, L. Martel, D. Prieur, A. C. Scheinost, and J. Somers, 'Structural Investigation of (U0.7Pu0.3)O2-x Mixed Oxides', *Inorg. Chem.*, vol. 54, no. 11, pp. 5358–5365, Jun. 2015, doi: 10.1021/acs.inorgchem.5b00392.
[81] A. Jankowiak, C. Maillard, and L. Donnet, 'Structural study of Pu1−xAmxO2 (x = 0.2; 0.5; 0.8) obtained by oxalate co-conversion', *Journal of Nuclear Materials*, vol. 393, no. 1, pp. 87–91, Aug. 2009, doi: 10.1016/j.jnucmat.2009.05.009.
[82] R. C. Belin, P. M. Martin, J. Léchelle, M. Reynaud, and A. C. Scheinost, 'Role of cation interactions in the reduction process in plutonium–americium mixed oxides', *Inorg. Chem.*, vol. 52, no. 6, pp. 2966–2972, Mar. 2013, doi: 10.1021/ic3023776.
[83] M. Vespa, M. Rini, J. Spino, T. Vitova, and J. Somers, 'Fabrication and characterization of (U, Am)O2−x transmutation targets', *Journal of Nuclear Materials*, vol. 421, no. 1, pp. 80–88, Feb. 2012, doi: 10.1016/j.jnucmat.2011.11.055.
[84] K. Mayer, B. Kanellakopoulos, J. Naegele, and L. Koch, 'On the valency state of americium in (U0.5Am0.5)O2−x', *Journal of Alloys and Compounds*, vol. 213–214, pp. 456–459, Oct. 1994, doi: 10.1016/0925-8388(94)90960-1.
[85] E. Remy *et al.*, 'Fabrication of uranium–americium mixed oxide pellet from microsphere precursors: Application of CRMP process', *Journal of Nuclear Materials*, vol. 453, no. 1–3, pp. 214–219, Oct. 2014, doi: 10.1016/j.jnucmat.2014.06.048.
[86] M. Caisso, 'Etude structurale de la synthèse de microsphères d'U1-xAmxO2$\pm$δ dédiées à la fabrication de couvertures chargées en américium', PhD Thesis, Université Montpellier, 2016.
[87] T. Nishi, M. Nakada, and M. Hirata, 'Lattice parameter functions of (AmyU1−y)O2−x based on XRD and XANES measurements', *Journal of Solid State Chemistry*, vol. 256, no. Supplement C, pp. 252–255, Dec. 2017, doi: 10.1016/j.jssc.2017.09.011.
[88] D. Prieur *et al.*, 'Influence of the Microstructure on the U1-yAmyO2-x (y= 0.1; 0.15) Pellet Macroscopic Swelling', *Advances in Science and Technology*, vol. 73, Jan. 2011, doi: 10.4028/www.scientific.net/AST.73.104.
[89] D. Horlait, F. Lebreton, T. Delahaye, N. Herlet, and P. Dehaudt, 'U1-xAmxO2±δ MABB Fabrication in the Frame of the DIAMINO Irradiation Experiment', *Procedia Chemistry*, vol. 7, pp. 485–492, 2012, doi: 10.1016/j.proche.2012.10.074.
[90] F. Lebreton, D. Horlait, T. Delahaye, and P. Blanchart, 'Fabrication and characterization of U1−xAmxO2±δ compounds with high americium contents (x = 0.3, 0.4 and 0.5)', *Journal of Nuclear Materials*, vol. 439, no. 1–3, pp. 99–102, Aug. 2013, doi: 10.1016/j.jnucmat.2013.03.074.
[91] O. S. Vălu, O. Beneš, E. Colineau, J.-C. Griveau, and R. J. M. Konings, 'The low-temperature heat capacity of (U1-yAmy)O 2−x for y = 0.08 and 0.20', *Journal of Nuclear Materials*, vol. 507, pp. 126–134, Aug. 2018, doi: 10.1016/j.jnucmat.2018.04.037.

[92] D. Prieur *et al.*, 'Local Structure and Charge Distribution in Mixed Uranium–Americium Oxides: Effects of Oxygen Potential and Am Content', *Inorg. Chem.*, vol. 50, no. 24, pp. 12437–12445, Dec. 2011, doi: 10.1021/ic200910f.
[93] D. Prieur *et al.*, 'Accommodation of multivalent cations in fluorite-type solid solutions: Case of Am-bearing UO2', *Journal of Nuclear Materials*, vol. 434, no. 1–3, pp. 7–16, Mar. 2013, doi: 10.1016/j.jnucmat.2012.11.037.
[94] R. Vauchy *et al.*, 'Impact of the cation distribution homogeneity on the americium oxidation state in the U0.54Pu0.45Am0.01O2−x mixed oxide', *Journal of Nuclear Materials*, vol. 456, pp. 115–119, Jan. 2015, doi: 10.1016/j.jnucmat.2014.09.014.
[95] K. Teske, C. Nebelung, I. I. Kapshukov, L. V. Sudakov, and A. S. Bevz, 'Determination of the oxygen coefficient for hyperstoichiometric uranium-plutonium mixed oxide by a solid- electrolyte-based coulometric technique', *Journal of Nuclear Materials*, vol. 168, no. 1–2, pp. 97–100, Oct. 1989, doi: 10.1016/0022-3115(89)90569-2.
[96] J. M. Elorrieta, L. J. Bonales, N. Rodríguez-Villagra, V. G. Baonza, and J. Cobos, 'A detailed Raman and X-ray study of UO2+x oxides and related structure transitions', *Phys. Chem. Chem. Phys.*, vol. 18, no. 40, pp. 28209–28216, Oct. 2016, doi: 10.1039/C6CP03800J.
[97] N. A. Javed, 'Thermodynamic study of hypostoichiometric urania', *Journal of Nuclear Materials*, vol. 43, no. 3, pp. 219–224, Jun. 1972, doi: 10.1016/0022-3115(72)90053-0.
[98] Y. Philipponneau, 'Paramètre de maille et homogénéité des combustibles MOX'. 1993.
[99] R. Vauchy, A.-C. Robisson, R. C. Belin, P. M. Martin, A. C. Scheinost, and F. Hodaj, 'Room-temperature oxidation of hypostoichiometric uranium–plutonium mixed oxides U1−yPuyO2−x – A depth-selective approach', *Journal of Nuclear Materials*, vol. 465, pp. 349–357, Oct. 2015, doi: 10.1016/j.jnucmat.2015.05.033.
[100] B. Dacus, B. Beeler, and D. Schwen, 'Calculation of threshold displacement energies in UO2', *Journal of Nuclear Materials*, vol. 520, pp. 152–164, Jul. 2019, doi: 10.1016/j.jnucmat.2019.04.002.
[101] N. W. Ashcroft and N. D. Mermin, *Physique des solides*. Les Ulis, France: EDP Sciences, 2002.
[102] C. Hurtgen and J. Fuger, 'Self-irradiation effects in americium oxides', *Inorganic and Nuclear Chemistry Letters*, vol. 13, no. 3–4, pp. 179–188, 1977.
[103] D. Prieur *et al.*, 'Fabrication and characterization of minor actinides bearing fuels obtained by conventional powder metallurgy process', *Powder Technology*, vol. 208, no. 2, pp. 553–557, Mar. 2011, doi: 10.1016/j.powtec.2010.08.058.
[104] T. D. Chikalla and R. P. Turcotte, 'Self-radiation damage ingrowth in 238PuO2', *Radiation Effects*, vol. 19, no. 2, pp. 93–98, Jan. 1973, doi: 10.1080/00337577308232225.
[105] W. J. Weber, 'Alpha-irradiation damage in CeO2, UO2 and PuO2', *Radiation Effects*, vol. 83, no. 1–2, pp. 145–156, Jan. 1984, doi: 10.1080/00337578408215798.
[106] D. Prieur *et al.*, 'Structural investigation of self-irradiation damaged AmO2', *Journal of Solid State Chemistry*, vol. 212, pp. 7–12, Apr. 2014, doi: 10.1016/j.jssc.2013.12.016.
[107] M. Kato *et al.*, 'Self-radiation damage in plutonium and uranium mixed dioxide', *Journal of Nuclear Materials*, vol. 393, no. 1, pp. 134–140, Aug. 2009, doi: 10.1016/j.jnucmat.2009.05.020.
[108] M. Noe and J. Fuger, 'Self-radiation effects on the lattice parameter of 238PuO2', *Inorganic and Nuclear Chemistry Letters*, vol. 10, no. 1, pp. 7–19, Jan. 1974, doi: 10.1016/0020-1650(74)80211-4.
[109] D. Horlait, F. Lebreton, P. Roussel, and T. Delahaye, 'XRD Monitoring of α Self-Irradiation in Uranium–Americium Mixed Oxides', *Inorg. Chem.*, vol. 52, no. 24, pp. 14196–14204, Dec. 2013, doi: 10.1021/ic402124s.
[110] F. Lebreton *et al.*, 'α Self-irradiation Effects on Structural Properties of (U,Am)$O_{2\pm\delta}$ Materials', *EPJ Web of Conferences*, vol. 115, p. 03005, 2016, doi: 10.1051/epjconf/201611503005.
[111] D. Staicu, T. Wiss, V. V. Rondinella, J. P. Hiernaut, R. J. M. Konings, and C. Ronchi, 'Impact of auto-irradiation on the thermophysical properties of oxide nuclear reactor fuels', *Journal of Nuclear Materials*, vol. 397, no. 1, pp. 8–18, Feb. 2010, doi: 10.1016/j.jnucmat.2009.11.024.
[112] D. G. Martin, 'The thermal expansion of solid UO2 and (U, Pu) mixed oxides — a review and recommendations', *Journal of Nuclear Materials*, vol. 152, no. 2–3, pp. 94–101, May 1988, doi: 10.1016/0022-3115(88)90315-7.
[113] J. J. Carbajo, G. L. Yoder, S. G. Popov, and V. K. Ivanov, 'A review of the thermophysical properties of MOX and UO2 fuels', *Journal of Nuclear Materials*, vol. 299, no. 3, pp. 181–198, Dec. 2001, doi: 10.1016/S0022-3115(01)00692-4.
[114] J. K. Fink, 'Thermophysical properties of uranium dioxide', *Journal of Nuclear Materials*, vol. 279, no. 1, pp. 1–18, Mar. 2000, doi: 10.1016/S0022-3115(99)00273-1.
[115] T. Uchida, T. Sunaoshi, K. Konashi, and M. Kato, 'Thermal expansion of PuO2', *Journal of Nuclear Materials*, vol. 452, no. 1–3, pp. 281–284, Sep. 2014, doi: 10.1016/j.jnucmat.2014.05.039.
[116] T. Yamashita, N. Nitani, T. Tsuji, and H. Inagaki, 'Thermal expansions of NpO2 and some other actinide dioxides', *Journal of Nuclear Materials*, vol. 245, no. 1, pp. 72–78, May 1997, doi: 10.1016/S0022-3115(96)00750-7.

[117] M. Kato, T. Uchida, T. Matsumoto, T. Sunaoshi, H. Nakamura, and M. Machida, 'Thermal expansion measurement and heat capacity evaluation of hypo-stoichiometric PuO2.00', *Journal of Nuclear Materials*, vol. 451, no. 1–3, pp. 78–81, Aug. 2014, doi: 10.1016/j.jnucmat.2014.03.021.
[118] J. A. Fahey, R. P. Turcotte, and T. D. Chikalla, 'Thermal expansion of the actinide dioxides', *Inorganic and Nuclear Chemistry Letters*, vol. 10, no. 6, pp. 459–465, Jun. 1974, doi: 10.1016/0020-1650(74)80067-X.
[119] K. Minato, M. Takano, H. Otobe, T. Nishi, M. Akabori, and Y. Arai, 'Thermochemical and thermophysical properties of minor actinide compounds', *Journal of Nuclear Materials*, vol. 389, no. 1, pp. 23–28, May 2009, doi: 10.1016/j.jnucmat.2009.01.003.
[120] E. Epifano *et al.*, 'In-situ High Temperature X-ray Diffraction Study of the Am-O System', *MRS Advances*, vol. 1, no. 62, pp. 4133–4137, ed 2016, doi: 10.1557/adv.2017.200.
[121] T. Tsuji, H. Mitani, and T. Yamashita, 'Thermal expansion of uranium-plutonium dioxides', *Journal of Nuclear Science and Technology*, vol. 39, no. sup3, pp. 664–667, Nov. 2002, doi: 10.1080/00223131.2002.10875556.
[122] M. Kato, Y. Ikusawa, T. Sunaoshi, A. T. Nelson, and K. J. McClellan, 'Thermal expansion measurement of (U,Pu)O2-x in oxygen partial pressure-controlled atmosphere', *Journal of Nuclear Materials*, vol. 469, no. Supplement C, pp. 223–227, Feb. 2016, doi: 10.1016/j.jnucmat.2015.11.048.
[123] D. Prieur, G. Pagliosa, J. Spino, R. Caciuffo, J. Somers, and R. Eloirdi, 'Thermal recovery and lattice expansion of self-irradiated U0.80Am0.20O2−x, an in situ high temperature x-ray diffraction study', *Journal of Solid State Chemistry*, vol. 199, pp. 334–337, Mar. 2013, doi: 10.1016/j.jssc.2012.12.022.
[124] D. Prieur *et al.*, 'Linear thermal expansion, thermal diffusivity and melting temperature of Am-MOX and Np-MOX', *Journal of Alloys and Compounds*, vol. 637, pp. 326–331, Jul. 2015, doi: 10.1016/j.jallcom.2015.03.032.
[125] R. J. M. Konings *et al.*, 'The Thermodynamic Properties of the *f* -Elements and their Compounds. Part 2. The Lanthanide and Actinide Oxides', *Journal of Physical and Chemical Reference Data*, vol. 43, no. 1, p. 013101, Mar. 2014, doi: 10.1063/1.4825256.
[126] F. L. Oetting, 'The chemical thermodynamics of nuclear materials. VII. the high-temperature enthalpy of plutonium dioxide', *Journal of Nuclear Materials*, vol. 105, no. 2, pp. 257–261, Feb. 1982, doi: 10.1016/0022-3115(82)90382-8.
[127] D. R. Fredrickson and M. G. Chasanov, 'Enthalpy of uranium dioxide and sapphire to 1500 K by drop calorimetry', *The Journal of Chemical Thermodynamics*, vol. 2, no. 5, pp. 623–629, Sep. 1970, doi: 10.1016/0021-9614(70)90037-6.
[128] J. K. Fink, 'Enthalpy and heat capacity of the actinide oxides', *Int J Thermophys*, vol. 3, no. 2, pp. 165–200, Jun. 1982, doi: 10.1007/BF00503638.
[129] T. Nishi, A. Itoh, K. Ichise, and Y. Arai, 'Heat capacities and thermal conductivities of AmO2 and AmO1.5', *Journal of Nuclear Materials*, vol. 414, no. 2, pp. 109–113, Jul. 2011, doi: 10.1016/j.jnucmat.2011.01.019.
[130] C. Ronchi, M. Sheindlin, M. Musella, and G. J. Hyland, 'Thermal conductivity of uranium dioxide up to 2900 K from simultaneous measurement of the heat capacity and thermal diffusivity', *Journal of Applied Physics*, vol. 85, no. 2, pp. 776–789, Jan. 1999, doi: 10.1063/1.369159.
[131] C. Guéneau, A. Chartier, P. Fossati, L. Van Brutzel, and P. Martin, '7.03 - Thermodynamic and Thermophysical Properties of the Actinide Oxides☆', in *Comprehensive Nuclear Materials (Second Edition)*, R. J. M. Konings and R. E. Stoller, Eds. Oxford: Elsevier, 2020, pp. 111–154. doi: 10.1016/B978-0-12-803581-8.11786-2.
[132] M. W. D. Cooper, S. T. Murphy, M. J. D. Rushton, and R. W. Grimes, 'Thermophysical properties and oxygen transport in the (Ux,Pu1−x)O2 lattice', *Journal of Nuclear Materials*, vol. 461, pp. 206–214, Jun. 2015, doi: 10.1016/j.jnucmat.2015.03.024.
[133] J. Ralph, 'Specific heat of UO2, ThO2, PuO2 and the mixed oxides (ThxU1 –x)O2 and (Pu0.2U0.8)O1.97 by enthalpy data analysis', *J. Chem. Soc., Faraday Trans. 2*, vol. 83, no. 7, pp. 1253–1262, Jan. 1987, doi: 10.1039/F29878301253.
[134] R. Kandan, R. Babu, K. Nagarajan, and P. R. Vasudeva Rao, 'Calorimetric measurements on plutonium rich (U,Pu)O2 solid solutions', *Thermochimica Acta*, vol. 472, no. 1, pp. 46–49, Jun. 2008, doi: 10.1016/j.tca.2008.03.012.
[135] R. Kandan, R. Babu, K. Nagarajan, and P. R. Vasudeva Rao, 'Calorimetric measurements on uranium–plutonium mixed oxides', *Journal of Nuclear Materials*, vol. 324, no. 2, pp. 215–219, Jan. 2004, doi: 10.1016/j.jnucmat.2003.10.005.
[136] S. O. Vălu *et al.*, 'The high-temperature heat capacity of the (Th,U)O2 and (U,Pu)O2 solid solutions', *Journal of Nuclear Materials*, vol. 484, pp. 1–6, Feb. 2017, doi: 10.1016/j.jnucmat.2016.11.010.
[137] L. Leibowitz, D. F. Fischer, and M. G. Chasanov, 'Enthalpy of uranium-plutonium oxides: (U.8Pu.2)O1.97 from 2350 to 3000 K', *Journal of Nuclear Materials*, vol. 42, no. 1, pp. 113–116, Jan. 1972, doi: 10.1016/0022-3115(72)90016-5.

[138] R. L. Gibby, L. Leibowitz, J. F. Kerrisk, and D. G. Clifton, 'Analytical expressions for enthalpy and heat capacity for uranium-plutonium oxide', *Journal of Nuclear Materials*, vol. 50, no. 2, pp. 155–161, Mar. 1974, doi: 10.1016/0022-3115(74)90152-4.
[139] P. M. Martin, 'Catalog on MOX properties for fast reactors'. 2017.
[140] D. Bathellier, M. Lainet, M. Freyss, P. Olsson, and E. Bourasseau, 'A new heat capacity law for UO2, PuO2 and (U,Pu)O2 derived from molecular dynamics simulations and useable in fuel performance codes', *Journal of Nuclear Materials*, vol. 549, p. 152877, Jun. 2021, doi: 10.1016/j.jnucmat.2021.152877.
[141] J. P. Ottaviani *et al.*, 'Thermal property measurements of fuel A : (Pu,Am)O2', EUROTRANS, SIXTH FRAMEWORK PROGRAMME EURATOM Management of Radioactive Waste 3.4-D3.29a, 2009.
[142] O. S. Vălu, D. Staicu, O. Beneš, R. J. M. Konings, and P. Lajarge, 'Heat capacity, thermal conductivity and thermal diffusivity of uranium–americium mixed oxides', *Journal of Alloys and Compounds*, vol. 614, pp. 144–150, Nov. 2014, doi: 10.1016/j.jallcom.2014.05.083.
[143] E. Epifano *et al.*, 'High temperature heat capacity of (U, Am)O2±x', *Journal of Nuclear Materials*, vol. 494, pp. 95–102, Oct. 2017, doi: 10.1016/j.jnucmat.2017.07.009.
[144] G. C. Swanson, 'Oxygen potential of uranium--plutonium oxide as determined by controlled- atmosphere thermogravimetry', University of California, Los Alamos Scientific Laboratory, 1975. [Online]. Available: http://www.osti.gov/bridge/servlets/purl/4152409-QtASfG/
[145] T. L. Markin, A. J. Walter, and R. J. Bones, *The Determination of Oxygen/Metal Ratios for Uranium, Plutonium and (U,Pu) Oxides*. 1964. Accessed: Nov. 03, 2011. [Online]. Available: http://www.osti.gov/energycitations/servlets/purl/4060089-gyoN5X/
[146] M. Tetenbaum, *Am. Chem. Soc. Symp. Ser.*, vol. 216, pp. 109–122, 1983.
[147] T. M. Besmann, 'Phase equilibria and thermodynamics of the Pu-O system: 1400 K to 1610 K', *Journal of Nuclear Materials*, vol. 144, no. 1, pp. 141–150, Jan. 1987, doi: 10.1016/0022-3115(87)90289-3.
[148] R. E. Woodley, 'Oxygen potentials of plutonia and urania-plutonia solid solutions', *Journal of Nuclear Materials*, vol. 96, no. 1–2, pp. 5–14, Jan. 1981, doi: 10.1016/0022-3115(81)90212-9.
[149] S. Casalta, 'Etude des propriétés du système Am-O en vue de la transmutation de l'Americium 241 en réacteur à neutrons rapides', These de doctorat, Aix-Marseille 1, 1996. Accessed: Feb. 02, 2022. [Online]. Available: http://www.theses.fr/1996AIX11036
[150] H. Otobe, M. Akabori, and K. Minato, 'Oxygen potential measurement of americium oxide by electromotive force method', *Journal of the American Ceramic Society*, vol. 91, no. 6, pp. 1981–1985, Jun. 2008, doi: 10.1111/j.1551-2916.2008.02374.x.
[151] T. D. Chikalla and L. Eyring, 'Dissociation pressures and partial thermodynamic quantities for americium oxides', *Journal of Inorganic and Nuclear Chemistry*, vol. 29, no. 9, pp. 2281–2293, Sep. 1967, doi: 10.1016/0022-1902(67)80282-3.
[152] C. Thiriet and R. J. M. Konings, 'Chemical thermodynamic representation of AmO2−x', *Journal of Nuclear Materials*, vol. 320, no. 3, pp. 292–298, Aug. 2003, doi: 10.1016/S0022-3115(03)00188-0.
[153] M. Kato, K. Takeuchi, T. Uchida, T. Sunaoshi, and K. Konashi, 'Oxygen potential of (U0.88Pu0.12)O2±x and (U0.7Pu0.3)O2±x at high temperatures of 1673–1873 K', *Journal of Nuclear Materials*, vol. 414, no. 2, pp. 120–125, Jul. 2011, doi: 10.1016/j.jnucmat.2011.01.042.
[154] M. Kato, S. Nakamichi, K. Takeuchi, and T. Sunaoshi, 'Measurement of oxygen potential of at 1773 and 1873 K, and its analysis based on point defect chemistry', *Calphad*, no. 0, Nov. 2011, doi: 10.1016/j.calphad.2011.02.007.
[155] G. R. Chilton and J. Edwards, 'Oxygen potentials of U0.77Pu0.23O2+-x in the temperature range 1523-1822K', UKAEA, 1980.
[156] R. Dawar, V. Chandramouli, and S. Anthonysamy, 'Chemical potential of oxygen in (U, Pu) mixed oxide with Pu/(U+Pu) = 0.46', *Journal of Nuclear Materials*, vol. 473, pp. 131–135, May 2016, doi: 10.1016/j.jnucmat.2016.02.020.
[157] S. Hirooka, T. Matsumoto, T. Sunaoshi, and T. Hino, 'Relative oxygen potential measurements of (U,Pu)O2 with Pu = 0.45 and 0.68 and related defect formation energy', *Journal of Nuclear Materials*, vol. 558, p. 153375, Jan. 2022, doi: 10.1016/j.jnucmat.2021.153375.
[158] T. M. Besmann and T. B. Lindemer, 'Chemical thermodynamic representations of PuO2-x and U1-zPuzOw', *Journal of Nuclear Materials*, no. 130, pp. 489–504, 1985.
[159] M. Kato, M. Watanabe, T. Matsumoto, S. Hirooka, and M. Akashi, 'Oxygen potentials, oxygen diffusion coefficients and defect equilibria of nonstoichiometric (U,Pu)O2±x', *Journal of Nuclear Materials*, vol. 487, no. Supplement C, pp. 424–432, Apr. 2017, doi: 10.1016/j.jnucmat.2017.01.056.
[160] T. L. Markin and E. J. McIver, 'Thermodynamic and phase studies for plutonium and uranium-plutonium oxides with applications to compatibility calculations', in *Plutonium 1965*, 1965.

[161] C. Guéneau, A. Chartier, and L. Van Brutzel, '2.02 - Thermodynamic and Thermophysical Properties of the Actinide Oxides', in *Comprehensive Nuclear Materials*, R. J. M. Konings, Ed. Oxford: Elsevier, 2012, pp. 21–59. doi: 10.1016/B978-0-08-056033-5.00009-4.
[162] J. Edwards, R. N. Wood, and G. R. Chilton, 'Oxygen potentials of uranium-plutonium oxides in the near stoichiometric region', *Journal of Nuclear Materials*, vol. 130, no. 0, pp. 505–512, Feb. 1985, doi: 10.1016/0022-3115(85)90336-8.
[163] M. Kato, T. Tamura, and K. Konashi, 'Oxygen potentials of mixed oxide fuels for fast reactors', *Journal of Nuclear Materials*, vol. 385, no. 2, pp. 419–423, Mar. 2009, doi: 10.1016/j.jnucmat.2008.12.012.
[164] T. Matsumoto *et al.*, 'Oxygen potential measurement of (Pu0.928Am0.072)O2–x at high temperatures', *Journal of Nuclear Science and Technology*, vol. 52, no. 10, pp. 1296–1302, Oct. 2015, doi: 10.1080/00223131.2014.986243.
[165] 'EUROTRANS: EUROpean research Programme for the TRANSmutation of high level nuclear waste in an accelerator driven system', *IGD-TP | Safe Solutions for Radioactive Waste*. https://igdtp.eu/activity/eurotrans-european-research-programme-for-the-transmutation-of-high-level-nuclear-waste-in-an-accelerator-driven-system/ (accessed Mar. 29, 2022).
[166] D. Staicu, A. Zappia, and R. J. M. Konings, 'Oxygen potential measurements of fuels A, B and C', JRC, WP 3.4-D 3.36, 2010.
[167] W. Bartscher and C. Sari, 'A thermodynamic study of the uranium-americium oxide U0.5Am0.5O2 ± x', *Journal of Nuclear Materials*, vol. 118, no. 2, pp. 220–223, Sep. 1983, doi: 10.1016/0022-3115(83)90228-3.
[168] M. Osaka, I. Sato, T. Namekawa, K. Kurosaki, and S. Yamanaka, 'Oxygen potentials of (U0.685Pu0.270Am0.045)O2−x solid solution', *Journal of Alloys and Compounds*, vol. 397, no. 1–2, pp. 110–114, Jul. 2005, doi: 10.1016/j.jallcom.2005.01.024.
[169] S. Nakamichi, M. Kato, and T. Tamura, 'Influences of Am and Np on oxygen potentials of MOX fuels', *Calphad*, vol. 35, no. 4, pp. 648–651, Dec. 2011, doi: 10.1016/j.calphad.2011.06.002.
[170] S. Hirooka, T. Matsumoto, M. Kato, T. Sunaoshi, H. Uno, and T. Yamada, 'Oxygen potential measurement of (U,Pu,Am)O2±x and (U,Pu,Am,Np)O2±x', *Journal of Nuclear Materials*, vol. 542, p. 152424, Dec. 2020, doi: 10.1016/j.jnucmat.2020.152424.
[171] M. Kato, K. Morimoto, H. Sugata, K. Konashi, M. Kashimura, and T. Abe, 'Solidus and liquidus of plutonium and uranium mixed oxide', *Journal of Alloys and Compounds*, vol. 452, no. 1, pp. 48–53, Mar. 2008, doi: 10.1016/j.jallcom.2007.01.183.
[172] J. L. Bates, 'Melting Points of Hypostoichiometric Uranium Dioxide', *Journal of the American Ceramic Society*, vol. 49, no. 7, pp. 395–396, 1966, doi: 10.1111/j.1151-2916.1966.tb13293.x.
[173] R. E. Latta and R. E. Fryxell, 'Determination of solidus-liquidus temperatures in the uo2 + x system (−0.50', *Journal of Nuclear Materials*, vol. 35, no. 2, pp. 195–210, May 1970, doi: 10.1016/0022-3115(70)90100-5.
[174] M. Kato, K. Morimoto, H. Sugata, K. Konashi, M. Kashimura, and T. Abe, 'Solidus and liquidus temperatures in the UO2–PuO2 system', *Journal of Nuclear Materials*, vol. 373, no. 1, pp. 237–245, Feb. 2008, doi: 10.1016/j.jnucmat.2007.06.002.
[175] F. De Bruycker, K. Boboridis, P. Pöml, R. Eloirdi, R. J. M. Konings, and D. Manara, 'The melting behaviour of plutonium dioxide: A laser-heating study', *Journal of Nuclear Materials*, vol. 416, no. 1, pp. 166–172, Sep. 2011, doi: 10.1016/j.jnucmat.2010.11.030.
[176] R. Böhler *et al.*, 'Recent advances in the study of the UO2–PuO2 phase diagram at high temperatures', *Journal of Nuclear Materials*, vol. 448, no. 1–3, pp. 330–339, May 2014, doi: 10.1016/j.jnucmat.2014.02.029.
[177] M. Kato *et al.*, 'Effect of Oxygen-to-Metal Ratio on Melting Temperature of Uranium and Plutonium Mixed Oxide Fuel for Fast Reactor', *Transactions of the Atomic Energy Society of Japan*, vol. 7, pp. 420–428, Dec. 2008, doi: 10.3327/taesj.J08.001.
[178] B. Riley, 'HIGH TEMPERATURE OXYGEN EQUILIBRIUM IN THE PLUTONIUM--OXYGEN SYSTEM.', *Sci. Ceram. 5: 83-109 (1970).*, Jan. 1970, Accessed: Feb. 27, 2022. [Online]. Available: https://www.osti.gov/biblio/4085857
[179] R. E. McHenry, 'Melting Points of Curium and Americium Oxides', *Transactions of the American Nuclear Society*, vol. 8, no. 1, pp. 75-, 1965.
[180] W. L. Lyon and W. E. Baily, 'The solid-liquid phase diagram for the UO2-PuO2 system', *Journal of Nuclear Materials*, vol. 22, no. 3, pp. 332–339, Jun. 1967, doi: 10.1016/0022-3115(67)90051-7.
[181] E. A. Aitken and S. K. Evans, *A Thermodynamic Data Program Involving Plutonia and Urania at High Temperatures. Quarterly Report No. 4.* 1968.
[182] J. G. Reavis, Los Alamos Scientific Lab., LA-5193-PR, 1972.
[183] K. Konno and T. Hirosawa, 'Melting Temperature of Irradiated Fast Reactor Mixed Oxide Fuels', *Journal of Nuclear Science and Technology*, vol. 35, no. 7, pp. 494–501, Jul. 1998, doi: 10.1080/18811248.1998.9733897.

[184] M. Strach, D. Manara, R. C. Belin, and J. Rogez, 'Melting behavior of mixed U–Pu oxides under oxidizing conditions', *Nuclear Instruments and Methods in Physics Research Section B: Beam Interactions with Materials and Atoms*, vol. 374, pp. 125–128, May 2016, doi: 10.1016/j.nimb.2016.01.032.
[185] M. Kato, 'Melting temperatures of oxide fuel for fast reactors', *International Congress on Advances in Nuclear Power Plants 2009, ICAPP 2009*, vol. 3, pp. 1940–1947, Jan. 2009.
[186] K. KONNO and T. HIROSAWA, 'Melting Temperature of Irradiated Fast Reactor Mixed Oxide Fuels', *Journal of Nuclear Science and Technology*, vol. 35, no. 7, pp. 494–501, Jul. 1998, doi: 10.1080/18811248.1998.9733897.
[187] G. Cacciamani, 'AN INTRODUCTION TO THE CALPHAD METHOD AND THE COMPOUND ENERGY FORMALISM (CEF)', *Tecnologia em Metalurgia Materiais e Mineração*, vol. 13, no. 1, pp. 16–24, 2016, doi: 10.4322/2176-1523.1048.
[188] E. Epifano *et al.*, 'Behaviour of (U,Am)O2 in oxidizing conditions: a high-temperature XRD study', *Journal of Nuclear Materials*, vol. 531, p. 151991, Apr. 2020, doi: 10.1016/j.jnucmat.2020.151991.
[189] E. Epifano *et al.*, 'On the O-rich domain of the U-Am-O phase diagram', *Journal of Nuclear Materials*, vol. 531, p. 151986, Apr. 2020, doi: 10.1016/j.jnucmat.2020.151986.
[190] O. Redlich and A. T. Kister, 'Algebraic Representation of Thermodynamic Properties and the Classification of Solutions', *Ind. Eng. Chem.*, vol. 40, no. 2, pp. 345–348, Feb. 1948, doi: 10.1021/ie50458a036.
[191] M. Hillert, 'The compound energy formalism', *Journal of Alloys and Compounds*, vol. 320, no. 2, pp. 161–176, May 2001, doi: 10.1016/S0925-8388(00)01481-X.
[192] B. Sundman and J. Ågren, 'A regular solution model for phases with several components and sublattices, suitable for computer applications', *Journal of Physics and Chemistry of Solids*, vol. 42, no. 4, pp. 297–301, Jan. 1981, doi: 10.1016/0022-3697(81)90144-X.
[193] U. R. Kattner, 'THE CALPHAD METHOD AND ITS ROLE IN MATERIAL AND PROCESS DEVELOPMENT', *Tecnol Metal Mater Min*, vol. 13, no. 1, pp. 3–15, 2016, doi: 10.4322/2176-1523.1059.
[194] B. Sundman, B. Jansson, and J.-O. Andersson, 'The Thermo-Calc databank system', *Calphad*, vol. 9, no. 2, pp. 153–190, Apr. 1985, doi: 10.1016/0364-5916(85)90021-5.
[195] 'NEA Nuclear Science Committee - Thermodynamics of Advanced Fuels – International Database (TAF-ID)'. https://www.oecd-nea.org/science/taf-id/ (accessed Mar. 26, 2019).
[196] M. Hillert, B. Jansson, B. Sundman, and J. ågren, 'A two-sublattice model for molten solutions with different tendency for ionization', *MTA*, vol. 16, no. 1, pp. 261–266, Jan. 1985, doi: 10.1007/BF02815307.
[197] P. Coste, N. Astier, C. Maillard, C. Leorier, and A. Jankowiak, 'Fabrication of Pu1-xAmxO2 (x=0.2,0.5,0.8) pellets obtained by oxalate co-conversion', NT DTEC/SDTC/2007/07, Oct. 2007.
[198] C. Calazel *et al.*, 'Synthesis of Pu1-xAmxO2 compounds by co-conversion of Pu(IV)-Am(III) oxalate', NT DRCP/SE2A/2004/07, Jun. 2004.
[199] S. Pillon and M. Trotabas, 'BILAN DE LA PREMIERE FABRICATION INDUSTRIELLE DE COMBUSTIBLES D'OXYDE MIXTE D'URANIUM ET DE PLUTONIUM POUR LE PROJET CAPRA', p. 62, 1996.
[200] L. Aufore, 'Caractérisations dimensionnelles et microstructurales des pastilles de combustible PHENIX de la campagne de 1999 Aiguille 5- zone 2- 29%Pu', p. 39, 2017.
[201] C. Fuchs *et al.*, 'Fabrication of 3 fuel pins TRABANT2 for irradiation in HFR-Petten', Technical Note K 02 98 192, 1998.
[202] R. Vauchy *et al.*, 'New sample stage for characterizing radioactive materials by X-ray powder diffraction: application on five actinide dioxides ThO2, UO2, NpO2, PuO2 and AmO2', *J. Appl. Cryst.*, vol. 54, 2021, doi: https://doi.org/10.1107/S1600576721002235.
[203] H. M. Rietveld, 'A profile refinement method for nuclear and magnetic structures', *J Appl Cryst, J Appl Crystallogr*, vol. 2, no. 2, pp. 65–71, Jun. 1969, doi: 10.1107/S0021889869006558.
[204] TOPAS V4, 'General Profile and Structure Analysis Software for Powder Diffraction Data, User's Manual', Bruker AXS, Karlsruhe, Germany, 2008.
[205] P. Thompson, D. E. Cox, and J. B. Hastings, 'Rietveld refinement of Debye–Scherrer synchrotron X-ray data from Al2O3', *J Appl Cryst*, vol. 20, no. 2, Art. no. 2, Apr. 1987, doi: 10.1107/S0021889887087090.
[206] G. Jouan, C. Leorier, Ch. Valot, and O. Dugne, 'Implementation of an Innovative Nuclearized SEM in CEA Atalante Facility', presented at the 55th Annual Meeting on Hot Laboratories and Remote Handling, Helsinki, 2018. [Online]. Available: https://www.vtt.fi/sites/hotlab2018/.
[207] 'MARS | French national synchrotron facility'. https://www.synchrotron-soleil.fr/en/beamlines/mars (accessed Mar. 15, 2022).
[208] A. Zimina *et al.*, 'CAT-ACT—A new highly versatile x-ray spectroscopy beamline for catalysis and radionuclide science at the KIT synchrotron light facility ANKA', *Review of Scientific Instruments*, vol. 88, no. 11, p. 113113, Nov. 2017, doi: 10.1063/1.4999928.

[209] K. E. Wright, K. Popa, and P. Pöml, 'Synthesis and characterisation of PuPO 4 - a potential analytical standard for EPMA actinide quantification', *IOP Conf. Ser.: Mater. Sci. Eng.*, vol. 304, no. 1, p. 012020, 2018, doi: 10.1088/1757-899X/304/1/012020.
[210] D. Prieur *et al.*, 'Comparative XRPD and XAS study of the impact of the synthesis process on the electronic and structural environments of uranium–americium mixed oxides', *Journal of Solid State Chemistry*, vol. 230, pp. 8–13, Oct. 2015, doi: 10.1016/j.jssc.2015.03.037.
[211] B. Ravel and M. Newville, 'ATHENA, ARTEMIS, HEPHAESTUS: data analysis for X-ray absorption spectroscopy using IFEFFIT', *J Synchrotron Rad*, vol. 12, no. 4, Art. no. 4, Jul. 2005, doi: 10.1107/S0909049505012719.
[212] R. Bès *et al.*, 'New insight in the uranium valence state determination in UyNd1−yO2±x', *Journal of Nuclear Materials*, vol. 507, pp. 145–150, Aug. 2018, doi: 10.1016/j.jnucmat.2018.04.046.
[213] K. O. Kvashnina, S. M. Butorin, P. Martin, and P. Glatzel, 'Chemical State of Complex Uranium Oxides', *Phys. Rev. Lett.*, vol. 111, no. 25, p. 253002, Dec. 2013, doi: 10.1103/PhysRevLett.111.253002.
[214] R. Vauchy, R. C. Belin, J.-C. Richaud, P. J. Valenza, F. Adenot, and C. Valot, 'Studying radiotoxic materials by high temperature X-ray diffraction', *Applied Materials Today*, vol. 3, pp. 87–95, Jun. 2016, doi: 10.1016/j.apmt.2016.03.005.
[215] L. S. Dubrovinsky and S. K. Saxena, 'Thermal expansion of periclase (MgO) and tungsten (W) to melting temperatures', *Phys Chem Min*, vol. 24, no. 8, pp. 547–550, Oct. 1997, doi: 10.1007/s002690050070.
[216] 'Pompe jauge à oxygène GEN'AIR SETNAG'. https://www.setnag.com/fr/produits/gen-air-23.html (accessed May 11, 2020).
[217] G. S. Pawley, 'Unit-cell refinement from powder diffraction scans', *J. Appl. Cryst.*, vol. 14, pp. 357–361, 1981, doi: 10.1107/S0021889881009618.
[218] R. W. Cheary and A. Coelho, 'A fundamental parameters approach to X-ray line-profile fitting', *J Appl Cryst, J Appl Crystallogr*, vol. 25, no. 2, pp. 109–121, Apr. 1992, doi: 10.1107/S0021889891010804.
[219] D. Manara, M. Sheindlin, W. Heinz, and C. Ronchi, 'New techniques for high-temperature melting measurements in volatile refractory materials via laser surface heating', *Review of Scientific Instruments*, vol. 79, no. 11, p. 113901, Nov. 2008, doi: 10.1063/1.3005994.
[220] 'Oxygen pump gauge GEN'AIR SETNAG'. https://www.setnag.com/en/produits/gen-air-23.html (accessed Dec. 03, 2020).
[221] 'Measurement of partial pressure JOK'AIR-2060 SETNAG'. https://www.setnag.com/en/products/jok-air-2060-24.html (accessed Dec. 03, 2020).
[222] F. De Bruycker, K. Boboridis, D. Manara, P. Pöml, M. Rini, and R. J. M. Konings, 'Reassessing the melting temperature of PuO2', *Materials Today*, vol. 13, no. 11, pp. 52–55, Nov. 2010, doi: 10.1016/S1369-7021(10)70204-2.
[223] F. De Bruycker, 'High Temperature Phase Transitions in Nuclear Fuels for the Fourth Generation', Université d'Orléans, 2010.
[224] O. Beneš, P. Gotcu-Freis, F. Schwörer, R. J. M. Konings, and Th. Fanghänel, 'The high temperature heat capacity of NpO2', *The Journal of Chemical Thermodynamics*, vol. 43, no. 5, pp. 651–655, May 2011, doi: 10.1016/j.jct.2010.11.010.
[225] 'SETARAM | Analyse Thermique, Calorimétrie & Sorption de Gaz', *SETARAM*. https://setaramsolutions.com/fr/ (accessed Feb. 02, 2022).
[226] 'Setaram Instrumentation SETSYS Evolution DTA/DSC Brochure | PDF | LabWrench'. https://www.labwrench.com/documents/view/3949/setaram-instrumentation-setsys-evolution-dta-dsc-brochure (accessed Feb. 02, 2022).
[227] V. J. Wheeler and I. G. Jones, 'Thermodynamic and composition changes in UO2±x (x< 0.005) at 1950 K', *Journal of Nuclear Materials*, vol. 42, no. 2, pp. 117–121, Feb. 1972, doi: 10.1016/0022-3115(72)90018-9.
[228] M. Noe and J. Fuger, 'Self-radiation effects on the lattice parameter of 238PuO2', *Inorganic and Nuclear Chemistry Letters*, vol. 10, no. 1, pp. 7–19, Jan. 1974, doi: 10.1016/0020-1650(74)80211-4.
[229] K. Popa *et al.*, 'Structural investigations of PuIII phosphate by X-ray diffraction, MAS-NMR and XANES spectroscopy', *Journal of Solid State Chemistry*, vol. 230, pp. 169–174, Oct. 2015, doi: 10.1016/j.jssc.2015.07.002.
[230] E. Gerber *et al.*, 'To form or not to form: PuO2 nanoparticles at acidic pH', *Environ. Sci.: Nano*, Mar. 2022, doi: 10.1039/D1EN00666E.
[231] D. Prieur, U. Carvajal-Nunez, T. Vitova, and J. Somers, 'Local and Electronic structure of Americium-bearing PuO2', *European Journal of Inorganic Chemistry*, vol. 2013, no. 9, pp. 1518–1524, 2013.
[232] M. Zinkevich, D. Djurovic, and F. Aldinger, 'Thermodynamic modelling of the cerium–oxygen system', *Solid State Ionics*, vol. 177, no. 11, pp. 989–1001, Apr. 2006, doi: 10.1016/j.ssi.2006.02.044.

[233] E. Epifano *et al.*, 'Melting behaviour of uranium-americium mixed oxides under different atmospheres', *The Journal of Chemical Thermodynamics*, vol. 140, p. 105896, Jan. 2020, doi: 10.1016/j.jct.2019.105896.
[234] L. Medyk *et al.*, 'Determination of the plutonium content and O/M ratio of (U,Pu)O2-x using Raman spectroscopy', *Journal of Nuclear Materials*, vol. 541, p. 152439, Dec. 2020, doi: 10.1016/j.jnucmat.2020.152439.
[235] D. Staicu *et al.*, 'ESNII+ Deliverable D7-34 Characterisation measurement of properties fesh TRABANT fuel.pdf', D7.34, 2017.
[236] Z. Talip *et al.*, 'Thermal diffusion of helium in 238Pu-doped UO2', *Journal of Nuclear Materials*, vol. 445, no. 1–3, pp. 117–127, Feb. 2014, doi: 10.1016/j.jnucmat.2013.10.066.
[237] M. Osaka, K. Kurosaki, and S. Yamanaka, 'Chemical thermodynamic analysis of americium-containing UO2 and (U,Pu)O2', *Journal of Alloys and Compounds*, vol. 428, no. 1–2, pp. 355–361, Jan. 2007, doi: 10.1016/j.jallcom.2006.03.071.
[238] M. Kato, Y. Ikusawa, T. Sunaoshi, A. T. Nelson, and K. J. McClellan, 'Thermal expansion measurement of (U,Pu)O2-x in oxygen partial pressure-controlled atmosphere', *Journal of Nuclear Materials*, vol. 469, pp. 223–227, Feb. 2016, doi: 10.1016/j.jnucmat.2015.11.048.
[239] T. Truphemus, 'Etude des équilibres de phases en fonction de la température dans le système UO2-PuO2-Pu2O3 pour les céramiques nucléaires aux fortes teneurs en plutonium', thesis, Aix-Marseille, 2013. Accessed: Feb. 26, 2019. [Online]. Available: http://www.theses.fr/2013AIXM4303
[240] Chas. G. Maier and K. K. Kelley, 'AN EQUATION FOR THE REPRESENTATION OF HIGH-TEMPERATURE HEAT CONTENT DATA [1]', *J. Am. Chem. Soc.*, vol. 54, no. 8, pp. 3243–3246, Aug. 1932, doi: 10.1021/ja01347a029.
[241] H. Matzke, 'Atomic transport properties in UO2 and mixed oxides (U, Pu)O2', *J. Chem. Soc., Faraday Trans. 2*, vol. 83, no. 7, pp. 1121–1142, 1987, doi: 10.1039/F29878301121.
[242] A. L. Smith, J.-Y. Colle, O. Beneš, R. J. M. Konings, B. Sundman, and C. Guéneau, 'Thermodynamic assessment of the neptunium–oxygen system: Mass spectrometric studies and thermodynamic modelling', *The Journal of Chemical Thermodynamics*, vol. 103, pp. 257–275, Dec. 2016, doi: 10.1016/j.jct.2016.07.040.
[243] R. J. M. Konings and O. Beneš, 'The heat capacity of NpO2 at high temperatures: The effect of oxygen Frenkel pair formation', *Journal of Physics and Chemistry of Solids*, vol. 74, no. 5, pp. 653–655, May 2013, doi: 10.1016/j.jpcs.2012.12.018.
[244] R. Szwarc, 'The defect contribution to the excess enthalpy of uranium dioxide-calculation of the frenkel energy', *Journal of Physics and Chemistry of Solids*, vol. 30, no. 3, pp. 705–711, Mar. 1969, doi: 10.1016/0022-3697(69)90024-9.
[245] M. J. Welland, R. Böhler, L. Vlahovic, K. Boboridis, and D. Manara, 'Co-development of experimental and simulation methods for the laser flash heating and melting technique: The thermoelastic effects of UO2', *International Journal of Thermal Sciences*, vol. 132, pp. 174–185, Oct. 2018, doi: 10.1016/j.ijthermalsci.2018.05.035.
[246] M. Kurata, 'Thermodynamic assessment of the Pu-U, Pu-Zr, and Pu-U-Zr systems', *Calphad*, vol. 23, no. 3, pp. 305–337, Sep. 1999, doi: 10.1016/S0364-5916(00)00004-3.
[247] 'TC-Python', *Thermo-Calc Software*. https://thermocalc.com/products/software-development-kits/tc-python/ (accessed Apr. 06, 2022).
[248] A. Quaini *et al.*, 'High temperature investigation of the solid/liquid transition in the PuO2–UO2–ZrO2 system', *Journal of Nuclear Materials*, vol. 467, pp. 660–676, Dec. 2015, doi: 10.1016/j.jnucmat.2015.10.007.
[249] K. Takeuchi, M. Kato, T. Sunaoshi, S. Aono, and M. Kashimura, 'Effective thermal conductivity of MOX raw powder', *Journal of Nuclear Materials*, vol. 385, no. 1, pp. 103–107, Mar. 2009, doi: 10.1016/j.jnucmat.2008.09.033.
[250] Y. Philipponneau, 'Thermal conductivity of (U, Pu)O2−x mixed oxide fuel', *Journal of Nuclear Materials*, vol. 188, no. 0, pp. 194–197, Jun. 1992, doi: 10.1016/0022-3115(92)90470-6.
[251] D. Staicu, '2.06 - Thermal Properties of Irradiated UO2 and MOX☆', in *Comprehensive Nuclear Materials (Second Edition)*, R. J. M. Konings and R. E. Stoller, Eds. Oxford: Elsevier, 2020, pp. 149–172. doi: 10.1016/B978-0-12-803581-8.11726-6.
[252] M. Kurata, 'Thermodynamic database on U-Pu-Zr-Np-Am-Fe alloy system II — Evaluation of Np, Am, and Fe containing systems-', *IOP Conf. Ser.: Mater. Sci. Eng.*, vol. 9, p. 012023, Mar. 2010, doi: 10.1088/1757-899X/9/1/012023.
[253] R. J. M. Konings, O. Beneš, and J.-C. Griveau, '2.01 - The Actinides Elements: Properties and Characteristics', in *Comprehensive Nuclear Materials*, R. J. M. Konings, Ed. Oxford: Elsevier, 2012, pp. 1–20. doi: 10.1016/B978-0-08-056033-5.00008-2.
[254] T. Ogawa, 'Alloying behaviour among U, Np, Pu and Am predicted with the Brewer valence bond model', *Journal of Alloys and Compounds*, vol. 194, no. 1, pp. 1–7, Apr. 1993, doi: 10.1016/0925-8388(93)90636-2.

[255] F. H. Ellinger, K. A. Johnson, and V. O. Struebing, 'The plutonium-americium system', *Journal of Nuclear Materials*, vol. 20, no. 1, pp. 83–86, Jul. 1966, doi: 10.1016/0022-3115(66)90024-9.
[256] P. E. A. Turchi, A. I. Landa, and P. A. Söderlind, 'Thermodynamic assessment of the Am–Pu system with input from ab initio', *Journal of Nuclear Materials*, vol. 418, no. 1, pp. 165–173, Nov. 2011, doi: 10.1016/j.jnucmat.2011.06.034.
[257] R. Belin, P. Martin, E. Gavilan, M. Reynaud, and A. Scheinost, 'On the Role of Americium in the Reduction Process in Plutonium-Americium Oxides'. 2011.
[258] S. Miwa, Y. Ishi, and M. Osaka, 'Effect of oxygen potential on the sintering behavior of MgO-based heterogeneous fuels containing (Pu, Am)O2−x', *Journal of Nuclear Materials*, vol. 389, no. 3, pp. 402–406, Jun. 2009, doi: 10.1016/j.jnucmat.2009.02.016.
[259] R. Vauchy *et al.*, 'Actinide Oxidation State and O/M Ratio in Hypostoichiometric Uranium–Plutonium–Americium U0.750Pu0.246Am0.004O2–x Mixed Oxides', *Inorg. Chem.*, vol. 55, no. 5, pp. 2123–2132, Mar. 2016, doi: 10.1021/acs.inorgchem.5b02533.
[260] I. May, N. D. Bryan, and R. Alvares, *Recent Advances In Actinide Science*. Royal Society of Chemistry, 2007.

APPENDIXES

APPENDIX A – Intermetallic phase diagrams

1- Uranium-Americium

Results of solubility tests are the only experimental data available on the U-Am system [252]. A first version of the phase diagram was proposed by Kurata [252]. Another phase diagram representation was obtained by computational methods by Ogawa [254], based on the estimation of the interaction between metal atoms. To this day, the U-Am phase diagram proposed by Kurata [252] is used as reference and is shown in Figure 1. At room temperature, two phases can be distinguished: the double hexagonal close-packed α-Am phase and the fcc alpha-U phase. This system is characterized by the immiscibility of both elements at all temperatures.

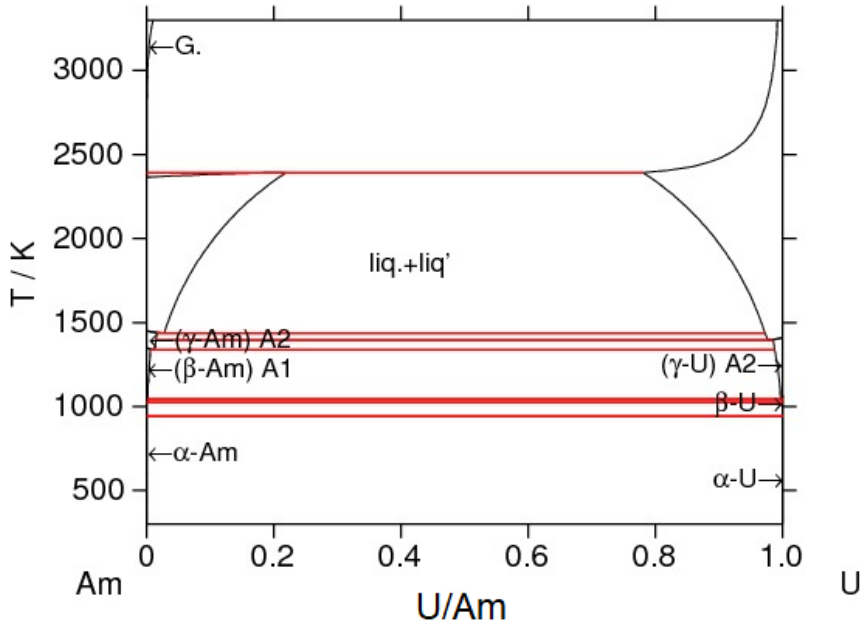

Figure 1 : Calculated U-Am phase diagram [252].

2- Plutonium-Americium

The phase diagram of the plutonium-americium system was first determined by Ellinger *et al.* [255] for the complete composition range for temperatures below 1073 K. Kurata [252], as well as Turchi *et al.* [256], also presented two different phase diagrams, both based on calculations. The latest update of the Pu-Am phase diagram was performed by Gotcu *et al.* [26], by means of the CALPHAD method. The current description of this system (see Figure 2) is tentative due to the experimental uncertainties.

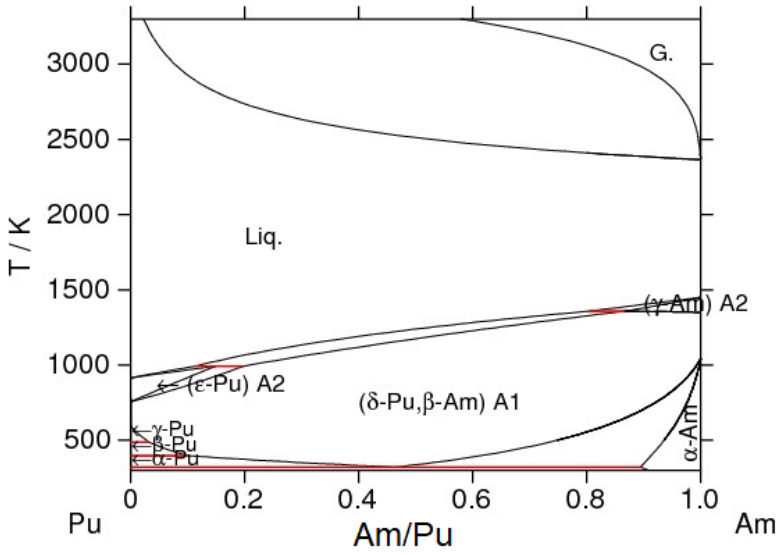

Figure 2 : Calculated Pu-Am phase diagram [21].

3- Uranium-Plutonium

As compared to U-Am and Pu-Am systems, more experimental data are available in the literature concerning the U-Pu phase diagram [246]. The description by Kurata [246] (Figure 3) is chosen as the most accurate, regarding the available experimental data. As experimental information on the phase boundary between the η and β-U phases are limited, its representation bellow it is only based on calculations. A more complex behaviour at room temperature, compared to the two previously described metallic systems, can be noticed. Indeed, intermediate phases ζ and η are observed with no crystal structure information available.

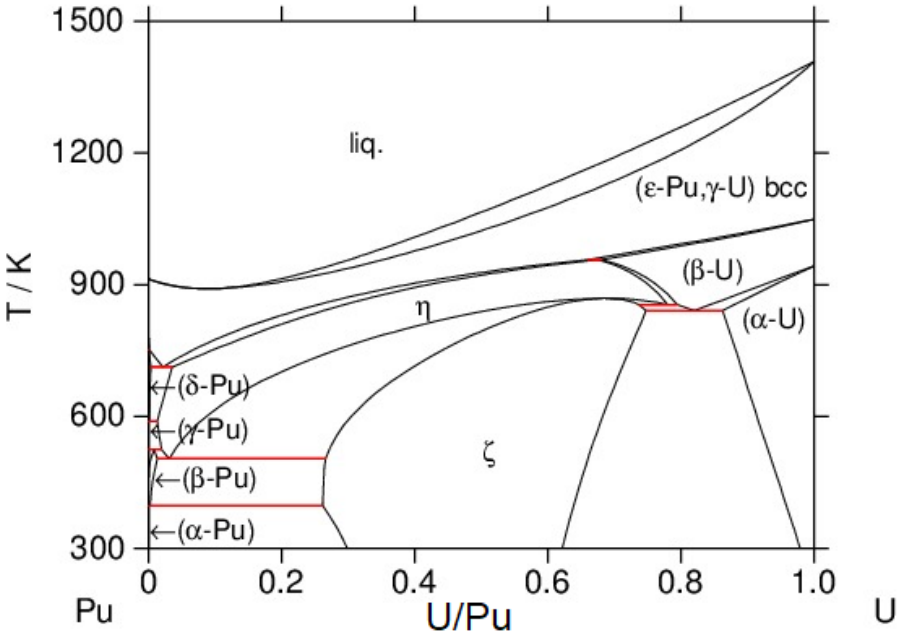

Figure 0-1 : Calculated U-Pu phase diagram [29].

Appendix B – Crystallographic data at room temperature of $Pu_{1-z}Am_zO_{2-x}$ (Chapter 2 – section 2.2.2.2.2)

		Lattice parameters		
	Space group	a (Å)	O/M (* = estimated value)	Ref.
$Pu_{0.992}Am_{0.008}O_{2-x}$	$Fm\bar{3}m$	5.400	1.92*	[257]
$Pu_{0.982}Am_{0.018}O_{2-x}$	$Fm\bar{3}m$	5.3954	2.00	[73]
$Pu_{0.979}Am_{0.021}O_{2-x}$	$Fm\bar{3}m$	5.3960	2.00	[78]
$Pu_{0.936}Am_{0.064}O_{2-x}$	$Fm\bar{3}m$	5.3944	2.00	[78]
$Pu_{0.928}Am_{0.072}O_{2-x}$	$Fm\bar{3}m$	5.3975	2.00	[78]
$Pu_{0.923}Am_{0.077}O_{2-x}$	$Fm\bar{3}m$	5.3948	2.00	[73]
$Pu_{0.91}Am_{0.09}O_{2-x}$	$Fm\bar{3}m$	5.397	2.00	[42]
		5.411	1.94	[42]
		5.413	1.92	[42]
		5.418	1.93	[258]
		5.405	1.97	[258]
$Pu_{0.90}Am_{0.10}O_{2-x}$	$Fm\bar{3}m$	5.409	1.96*	[257]
$Pu_{0.80}Am_{0.20}O_{2-x}$	$Fm\bar{3}m$	5.411	1.94*	[257]
$Pu_{0.79}Am_{0.21}O_{2-x}$	$Fm\bar{3}m$	5.3916	2.00	[73]
		5.392		[81]
$Pu_{0.51}Am_{0.49}O_{2-x}$	$Fm\bar{3}m$	5.3859	2.00	[73]
		5.386		[81]
$Pu_{0.50}Am_{0.50}O_{2-x}$	$Fm\bar{3}m$	5.383		[44]
$Pu_{0.20}Am_{0.80}O_{2-x}$	$Fm\bar{3}m$	5.38	2.00	[73]
		5.379		[81]

Appendix C – Crystallographic data at room temperature of $U_{1-y-z}Pu_yAm_zO_{2\pm x}$ (Chapter 2 – section 2.2.2.2.4)

		Lattice parameters			
	Phase	a_1 (Å)	a_2 (Å)	O/M	Ref.
$U_{0.879}Pu_{0.118}Am_{0.003}O_{2-x}$	fcc	5.4622		2.000	[174]
	fcc	5.4632		1.989	[174]
	fcc	5.4652		1.983	[174]
	fcc	5.4693		1.975	[174]
	fcc	5.4699		1.974	[174]
	fcc	5.4696		1.971	[174]
$U_{0.797}Pu_{0.199}Am_{0.004}O_{2-x}$	fcc	5.4558		2.000	[174]
	fcc	5.4595		1.982	[174]
	fcc	5.4626		1.967	[174]
	fcc	5.4699		1.950	[174]
	fcc	5.4734		1.942	[174]
$U_{0.75}Pu_{0.246}Am_{0.004}O_{2-x}$	fcc	5.456		1.987	[259]
	fcc	5.457		1.984	[259]
	fcc	5.458		1.977	[259]
$U_{0.695}Pu_{0.30}Am_{0.005}O_{2-x}$	fcc	5.4475		2.000	[260]
	fcc	5.4480		1.999	[260]
	fcc	5.4514		1.987	[260]
	fcc	5.4518		1.981	[260]
	fcc + fcc	-	-	1.965	[260]
	fcc + fcc	-	-	1.935	[260]
	fcc + fcc	-	-	1.929	[260]
	fcc + fcc	-	-	1.924	[260]
$U_{0.696}Pu_{0.298}Am_{0.006}O_{2-x}$	fcc	5.4466		2.000	[78]
$U_{0.703}Pu_{0.29}Am_{0.007}O_{2-x}$	fcc	5.449		2.000	[260]

	fcc	5.4482		2.000	[260]
	fcc	5.4485		2.000	[260]
	fcc	5.4490		2.000	[260]
	fcc	5.4479		2.000	[260]
	fcc	5.4484		1.997	[260]
	fcc	5.4492		1.993	[260]
	fcc	5.4496		1.986	[260]
	fcc	5.4503		1.980	[260]
	fcc + fcc	5.4478	5.4569	1.959	[260]
	fcc + fcc	5.4507	5.4727	1.942	[260]
	fcc + fcc	5.4522	5.4677	1.932	[260]
	fcc + fcc	5.4503	5.4718	1.924	[260]
	fcc + fcc	5.4495	5.4784	1.909	[260]
$U_{0.596}Pu_{0.397}Am_{0.007}O_{2-x}$	fcc	5.4404		2.000	[78]
	fcc	5.4449		1.972	[78]
	fcc + fcc	5.4421	-	1.959	[78]
	fcc + fcc	5.4435	-	1.949	[78]
	fcc + fcc	5.4458	-	1.925	[78]
	fcc + fcc	5.4439	-	1.916	[78]
$U_{0.54}Pu_{0.45}Am_{0.01}O_{2-x}$	fcc	5.437		2.00	[94]
	fcc	5.439	5.496	< 2.000	[94]
$U_{0.787}Pu_{0.198}Am_{0.015}O_{2-x}$	fcc	5.4538		2.000	[78]
	fcc	5.4540		2.000	[78]
	fcc	5.4554		1.996	[78]
	fcc	5.4559		1.993	[78]
	fcc	5.4561		1.988	[78]
	fcc	5.4593		1.981	[78]
	fcc	5.4637		1.967	[78]
	fcc	5.4609		1.961	[78]

	fcc	5.4661		1.953	[78]
	fcc	5.4707		1.947	[78]
$U_{0.585}Pu_{0.396}Am_{0.019}O_{2-x}$	fcc	5.4381		2.000	[78]
	fcc + fcc	5.4473	-	1.961	[78]
$U_{0.377}Pu_{0.60}Am_{0.023}O_{2-x}$	fcc + fcc	5.4247	-	2.000	[78]
$U_{0.676}Pu_{0.30}Am_{0.024}O_{2-x}$	fcc	5.4469		2.000	[260]
	fcc + fcc	5.4480	5.4598	1.951	[260]
$U_{0.514}Pu_{0.463}Am_{0.024}O_{2-x}$	fcc	5.4332		2.000	[78]
	fcc	5.4339		2.000	[78]
	fcc	5.4397		1.976	[78]
	fcc + fcc	5.4398	-	1.957	[78]
	fcc + fcc	5.438	-	1.934	[78]
	fcc	5.5067		1.718	[78]
	fcc	5.5032		1.733	[78]
$U_{0.584}Pu_{0.383}Am_{0.033}O_{2-x}$	fcc	5.4384		2.000	[78]
$U_{0.537}Pu_{0.428}Am_{0.035}O_{2-x}$	fcc	5.4358		2.000	[78]

Appendix D – Scan parameters of the HT-XRD experiments (Chapter 3 – section 3.3.5.2)

Sample	Scanning angles	Time step	Step interval	Heating/cooling rate	Number of scans per T	Waiting time per T
PuAm 80/20	20-145° 2θ	1 s	0.02°	5 $K.s^{-1}$	3	3600 s
PuAm 50/50		0.5 s			2	- 1000 s from 1873 to 1673 K - 3600 s from 1573 K to RT
PuAm 20/80					3	3600 s
PuAm 80/20-OM				0.17/0.5 $K.s^{-1}$	/	/
PHENIX29	20-140° 2θ	0.3 s		5 $K.s^{-1}$	- 2 at 1873 K - 1 from 1773 K to RT	2000 s
CAPRA4	20-145° 2θ	0.5 s			4	3600 s
TRABANT40					2	2000 s

Appendix E – Isotopic compositions of the samples used in this work

Sample	U		Pu		Am	
	% U	Isotopic composition	% Pu	Isotopic composition	% Am	Isotopic composition
PuAm 80/20	/		77.2	^{238}Pu = 0.004 ^{239}Pu = 0.766 ^{240}Pu = 0.213 ^{241}Pu = 0.010 ^{242}Pu = 0.007	22.8	^{241}Am = 1
PuAm 50/50	/		49.2	^{238}Pu = 0.004 ^{239}Pu = 0.766 ^{240}Pu = 0.213 ^{241}Pu = 0.010 ^{242}Pu = 0.007	50.8	^{241}Am = 1
PuAm 20/80	/		19.6	^{238}Pu = 0.004 ^{239}Pu = 0.766 ^{240}Pu = 0.212 ^{241}Pu = 0.010 ^{242}Pu = 0.007	80.4	^{241}Am = 1
PHENIX29	70.3	^{235}U = 0.003 ^{238}U = 0.997	29.0	^{238}Pu = 0.002 ^{239}Pu = 0.703 ^{240}Pu = 0.277 ^{241}Pu = 0.008 ^{242}Pu = 0.010	0.7	^{241}Am = 1
CAPRA4	69.1	^{235}U = 0.002 ^{238}U = 0.998	28.5	^{238}Pu = 0.017 ^{239}Pu = 0.601 ^{240}Pu = 0.275 ^{241}Pu = 0.036 ^{242}Pu = 0.071	2.4	^{241}Am = 1
TRABANT40	60.1	^{235}U = 0.003 ^{238}U = 0.997	38.6	^{238}Pu = 0.002 ^{239}Pu = 0.709 ^{240}Pu = 0.272 ^{241}Pu = 0.007 ^{242}Pu = 0.010	1.3	^{241}Am = 1

Appendix F – Lattice parameters of the fcc phase in temperature for the PHENIX29, CAPRA4 and TRABANT40 samples (Chapter 5 – section 5.2.2)

	PHENIX29	CAPRA4	TRABANT40
1873 K	5.560	5.576	5.572
1773 K	5.553	5.564	5.564
1673 K	5.544	5.552	5.556
1573 K	5.530	5.539	5.549
1473 K	5.518	5.527	5.537
1373 K	5.508	5.515	5.523
1273 K	5.501	5.506	5.509
1173 K	5.495	5.500	5.496
1073 K	5.490	5.493	5.488
973 K	5.484	5.488	5.482
873 K	5.479	5.481	5.475
773 K	5.473	5.475	5.468
673 K	5.468	5.471	5.463
573 K	5.464	5.465	5.455
473 K	5.458	5.459	5.451
373 K	5.454	5.454	5.445
303 K	5.445	5.446	5.434

Appendix G – Conditions of the melting experiments for U-Pu-Am-O (Chapter 5 – section 5.4.1)

Sample	Shots n°	Pre-heating	Shot	Post-heating
PHENIX24	1 to 4	10 s / 40 W	500 ms / 250 W	/
	5 to 8	/	500 ms / 250 W	/
PHENIX29	1 & 2	30 s / 40 W	500 ms / 250 W	15 s / 40 W
	3 to 6	30 s / 40 W	500 ms / 250 W	/
	7 & 8	/	500 ms / 250 W	/
CAPRA4	1 & 2	Ramp up : 0 → 60 W in 1 s	500 ms / 250 W	/
	3 to 6	Ramp up : 0 → 60 W in 500 ms	500 ms / 250 W	/
TRABANT40	1 to 6	/	500 ms / 250 W	/
TRABANT45	1 to 5	/	500 ms / 250 W	/
PHENIX29-OM	1 to 7	/	500 ms / 250 W	/
	8	/	500 ms / 250 W	Ramp down: 250 W → 40 W in 100 ms
	9	/	500 ms / 250 W	Ramp down: 200 W → 40 W in 100 ms
TRABANT40-OM	1	/	500 ms / 250 W	
	2	/	500 ms / 250 W	Ramp down: 250 W → 40 W in 100 ms
	3	/	500 ms / 250 W	Ramp down: 250 W → 40 W in 150 ms
	4 to 6	/	500 ms / 250 W	Ramp down: 250 W → 40 W in 200 ms
	7	/	500 ms / 250 W	/
	8	/	500 ms / 250 W	Ramp down: 250 W → 100 W in 100 ms
	9	/	500 ms / 250 W	/

Appendix H – Solidus temperature and O/M ratio obtained in this work for $U_{1-y-z}Pu_yAm_zO_{2\pm x}$ (Chapter 5 – section 5.4.2)

	Shot n°	Solidus temperature (K) ± 30 K	O/M ratio after shot (± 0.005)
PHENIX24 y(Pu) = 0.235 z(Am) = 0.005 O/M(initial) = 1.986	1	3056	1.986
	2	3057	1.989
	3	3065	1.991
	4	3065	1.994
	5	3062	1.995
	6	3062	1.996
	7	3064	1.996
	8	3064	1.996
PHENIX29 y(Pu) = 0.28 z(Am) = 0.01 O/M(initial) = 1.984	1	3060	1.989
	2	3064	1.995
	3	3050	2.001
	4	3047	2.004
	5	3037	2.008
	6	3039	2.011
	7	3036	2.012
	8	3035	2.012
CAPRA4 y(Pu) = 0.28 z(Am) = 0.02 O/M(initial) = 2.004	1	3040	2.004
	2	3056	2.001
	3	3064	2.000
	4	3058	1.999
	5	3052	1.998
	6	3057	1.998

TRABANT40 y(Pu) = 0.39 z(Am) = 0.01 O/M(initial) = 1.978	1	3020	1.986
	2	3015	1.987
	3	3030	1.987
	4	3025	1.988
	5	3031	1.989
TRABANT45 y(Pu) = 0.44 z(Am) = 0.01 O/M(initial) = 2.00	1	2992	1.995
	2	2992	1.992
	3	2990	1.990
	4	3001	1.989
PHENIX29-OM y(Pu) = 0.28 z(Am) = 0.01 O/M(initial) = 1.998	1	3019	1.997
	2	3048	1.996
	3	3060	1.995
	4	3051	1.993
	5	3044	1.992
	6	3048	1.991
	7	3052	1.990
	8	3050	1.989
	9	3056	1.988
TRABANT40-OM y(Pu) = 0.39 z(Am) = 0.01 O/M(initial) = 1.997	1	2970	1.997
	2	3000	1.995
	3	3013	1.994
	4	3017	1.992
	5	3017	1.991
	6	3025	1.990
	7	3016	1.990
	8	3021	1.989
	9	3017	1.988

Appendix I – Re-assessed parameters of the Pu-O, U-Pu-O and Pu-Am-O models (Chapter 6).

Pu-O

Parameters	Previous version (2011)	This work
G(Liq,Pu^{3+}:O^{2-};0) - 3.H^{298}(O)-2.H^{298}(Pu)	+GPU2O3 + 113000 - 47.92*T	+GPU2O3 +72000 - 30.19*T
G(Liq,PuO_2;0) - 2.H^{298}(O)-H^{298}(Pu)	+GPUO2 + 67000 - 22.2*T	+GPUO2 + 68320 - 22.3*T
L(Liq,Pu^{3+}:O^{2-},Va;0)	77451.8 + 23.48*T - 20231.6*(y_{O2-} - y_{Va})	77451.8 + 23.48*T
L(Liq,Pu^{3+}:O^{2-},Va;1)	-	-20231.60
L(Liq,Pu^{3-}:O^{2-},PuO_2;0)	+60 000 – 20 000 (y_{O2-} - y_{PuO2})	+60 000

U-Pu-O

Parameters	Previous version (2011)	This work
L(Liq,Pu^{3+},U^{+4}:O^{2-};0)	-20000	-
L(Liq,Pu^{3+},U^{+4}:O^{2-};Va ;0)	-	480000 – 670*T
L(Liq,U^{4+}:O^{2-},PuO_2;0)	-10000	1075600 – 360*T
L(Liq,U^{4+}:O^{2-},PuO_2;1)	-	-55000
L(Liq,Pu^{3+},U^{+4}:O^{2-},PuO_2;0)	+80000	-

Pu-Am-O

Parameters	Previous version (2011)	This work
L(Liq,Am^{3+},Pu^{3+}:O^{2-};0)	-	-50000
L(C1,Am^{4+},Pu^{4+}:*;*;0)	-10550	-40000
L(C1,Am^{4+},Pu^{4+}:*;*;1)	-	-20000
L(C1,Am^{3+},Am^{4+},Pu^{4+}:*;*;0)	-	-80000
L(C1,Am^{3+},Pu^{3+},Pu^{4+}:*;*;0)	-120000	-280000
L(C1,Am^{3+},Pu^{3+}:*;*;0)	-76000	-
L(C1,Am^{3+},Pu^{4+}:*;*;0)	+69555 – 35*T	-
L(C1,Am^{3+},Am^{4+},Pu^{3+}:*;*;0)	-300000	-
L(PU2O3,Am,Pu:O;0)	-140000	-298681 + 82.9*T

ETUDE DE L'INFLUENCE DE LA PRESENCE D'AMERICIUM SUR LES PROPRIETES THERMODYNAMIQUES ET STRUCTURALES DES OXYDES MIXTES $(U,Pu)O_{2\pm x}$

Ces travaux de thèse s'inscrivent dans le développement de l'oxyde mixte d'uranium et de plutonium $U_{1-y}Pu_yO_{2-x}$ combustible de référence pour la future génération (génération IV) de Réacteurs à Neutrons Rapides (RNR). Dans ce cadre, le (multi-)recyclage du plutonium extrait des combustibles $U_{1-y}Pu_yO_{2-x}$ irradiés est envisagé. La teneur en plutonium y envisagée dans ces combustibles est comprise entre 0,20 et 0,40 et leur stœchiométrie en oxygène, ou rapport Oxygène/Métal (M = U+Pu+Am), doit être comprise entre 1,94 et 1,99. Ce plutonium issu du multi-recyclage induit des changements dans sa composition isotopique initiale avec une diminution de la teneur en ^{239}Pu et une augmentation de celles en ^{238}Pu et ^{241}Pu. Avec une période de 14 ans, la désintégration beta du ^{241}Pu entraine la formation de jusqu'à 5 mol% de ^{241}Am dans l'oxyde en cas de stockage prolongé du combustible entre sa fabrication et son utilisation en RNR. L'influence de l'américium sur les propriétés thermodynamiques et structurales des oxydes mixtes $U_{1-y}Pu_yO_{2-x}$ doit donc être étudiée afin de prédire le comportement du combustible en réacteur aussi bien en conditions d'irradiation nominales qu'accidentelles.

L'objectif principal de ce travail a donc été de travailler sur le développement de la modélisation thermodynamique du système U-Pu-Am-O par la méthode CALPHAD (CALculation of PHAse Diagram). Cette méthode semi-empirique permet de calculer les diagrammes de phases et les données thermodynamiques de systèmes multi-éléments par extrapolation des modèles des sous-systèmes binaires et ternaires inclus. Les éléments d'entrée pour cette approche sont des données expérimentales structurales (cristallographie, phases à l'équilibre, degrés d'oxydation des éléments…) et thermodynamiques (enthalpies, capacités calorifiques, températures de transition de phase, potentiels d'oxygène…).

Ces travaux de thèse s'inscrivent dans le cadre du projet européen INSPYRE (Investigations Supporting MOX Fuel Licensing for ESNII Prototype Reactors) et les échantillons $U_{1-y-z}Pu_yAm_zO_{2\pm x}$ ont été fournis par le projet européen ESFR-SMART (European Sodium Fast Reactor Safety Measures Assessment and Research Tools). Les mesures de propriétés thermodynamiques et structurales ont été réalisées conjointement à ATALANTE, CEA Marcoule (France) et au Joint Research Centre Karlsruhe (Allemagne).

Ces travaux de thèse ont été articulés selon les étapes suivantes :

- Dans une première étape, l'étude bibliographique sur les données structurales et thermodynamiques pour le quaternaire U-Pu-Am-O et ses sous-systèmes binaires et ternaires a montré que les systèmes U-O, Pu-O et U-Pu-O sont bien connus et disposent de modèles thermodynamiques fiables. En revanche, le manque de données sur les systèmes contenant de l'américium a été mis en évidence, en particulier pour les systèmes Pu-Am-O et U-Pu-Am-O. Pour palier à cette limitation, des campagnes expérimentales devaient être menées afin d'acquérir de nouvelles données structurales et thermodynamiques sur ces deux systèmes.

- Dans une deuxième étape, le système Pu-Am-O a été étudié expérimentalement. Pour cela, trois échantillons de $Pu_{1-z}Am_zO_{2-x}$ (z = 0,23, 0,51 et 0,80) fabriqués en 2007 ont été utilisés. Les caractérisations structurales ont été réalisées au CEA Marcoule. Les résultats obtenus par Diffraction des Rayons X (DRX) à température ambiante ont révélé la présence de phases fluorines MO_{2-x} (M=Pu+Am) dans les trois échantillons. De plus, un gonflement de la maille par rapport aux données de fabrication a été mis en évidence et attribué à une combinaison des effets de l'auto-irradiation alpha et de la réduction des oxydes mixtes. Cette dernière a été quantifiée à l'aide d'analyses par Spectroscopie d'Absorption X (HERFD-XANES). Des rapports

O/M de 1.94-1.93 ont été déterminés. Ces analyses ont également pu révéler la présence simultanée des cations Pu^{3+}, Pu^{4+}, Am^{3+} et Am^{4+}. La coexistence de ces cations indique donc une réduction simultanée du plutonium et de l'américium ce qui est en désaccord avec les résultats existant dans la littérature. La réduction des échantillons est induite par l'auto-irradiation alpha et il a été supposé que les défauts associés à cette dernière stabilise la structure fluorine.

Des campagnes de mesures par Diffraction des Rayons X Haute Température (DRX-HT) ont été réalisées au CEA Marcoule sous He/H_2 4 % ($pO_2 = 10^{-28}$ atm) afin de déterminer les phases en présence pour les trois compositions entre 1873 K et 303 K. L'identification exhaustive des nombreuses phases ainsi révélées a été impossible de par la complexité du système. Ainsi, seule une phase fluorine MO_{2-x} a pu être identifiée avec certitude dans les gammes de teneur en américium et de température étudiées. Une transition de phase a été observée à 873 K pour le composé $Pu_{0,20}Am_{0,80}O_{2-x}$, attribuée probablement à la disparition de la phase A-M_2O_3 à plus basse température. L'étude de la variation du paramètre de maille de la phase fluorine avec la teneur en américium et la température a montré une dilatation typique des oxydes d'actinides et les résultats sont cohérents avec la transition de phase observée pour z = 0,80.

De plus, des mesures d'Analyses Thermogravimétrique (ATG) et de DRX-HT ont été réalisées au CEA Marcoule dans des conditions identiques afin de déterminer les équilibres de phase à 1673 K pour $Pu_{0,77}Am_{0,23}O_{2-x}$. La gamme de pression partielle d'oxygène étudiée dans ces mesures était 10^{-28}-10^{-24} atm (Ar/H_2 4 %). Dans cette gamme, des rapports O/M compris entre 1,716 et 1,778 ont été déterminés grâce au suivi de la variation de masse de l'échantillon. Il a été observé que le potentiel d'oxygène de l'oxyde mixte mesuré pour $1,716 \leq O/M \leq 1,778$ augmente avec le rapport O/M. Comme expliqué précédemment, seule une phase MO2-x a pu être identifiée avec certitude sur les diffractogrammes. Les mesures de DRX-HT ont révélé l'existence d'un domaine multiphasique [MO_{2-x} + une ou plusieurs phases non identifiées] pour $1,716 \leq O/M < 1,75$, suivi d'un domaine monophasé MO_{2-x} pour $O/M > 1,75$.

Enfin, des mesures de températures de solidus et liquidus ont été réalisées au JRC Karlsruhe pour la première fois par chauffage laser sur l'échantillon $Pu_{0,49}Am_{0,51}O_{2-x}$. Grâce à l'utilisation de sondes à oxygène en entrée et sortie du dispositif expérimental, la variation de pression partielle d'oxygène (pO_2) dans la chambre de mesures durant la fusion a pu être enregistrée. Sur la base de quelques hypothèses sur la taille de la zone fondue et sa composition chimique et de la variation de pO_2, une réduction importante de l'échantillon lors des expériences de fusion a pu être mise en évidence. Les résultats obtenus ont permis de montrer que dans la gamme de rapports O/M mise en évidence, la stœchiométrie en oxygène n'influait pas sur les températures de solidus et liquidus mesurées.

La troisième étape a été dédiée à l'étude expérimentale du système quaternaire U-Pu-Am-O réalisée en utilisant des échantillons $U_{1-y-z}Pu_yAm_zO_{2\pm x}$, avec $0,235 \leq y \leq 0,39$ et $0,005 \leq z \leq 0,02$, fabriqués dans les années 1990. Les caractérisations structurales ont été réalisées au CEA Marcoule ainsi qu'au synchrotron SOLEIL. Les analyses par microsonde électronique et par DRX ont révélé la présence d'une matrice $U_{1-y-z}Pu_yAm_zO_{2\pm x}$ homogène de structure fluorine avec néanmoins la présence de quelques amas micrométriques enrichis en U ou Pu à température ambiante. Le rapport O/M de chaque échantillon a été déterminé via leur paramètre de mailles après correction du gonflement dû à l'auto-irradiation.

Ces résultats ont été confirmés par XANES. De plus, ces analyses XANES ont permis de révéler la présence simultanée et systématique de U^{4+}/U^{5+} et Pu^{3+}/Pu^{4+} et Am^{3+} même pour des échantillons stœchiométriques. Ceci démontre qu'un mécanisme de compensation de charges $U^{5+}/Pu^{3+}+Am^{3+}$ existe dans ces oxydes mixtes. Il a été démontré que cette distribution cationique ne provient pas de la présence des amas U et Pu et est donc bien spécifique à ces oxydes mixtes.

Des campagnes de mesures par DRX-HT ont ensuite été menées entre 1873 K et 303 K afin de mesurer la dilatation thermique de la phase fluorine pour trois échantillons d'oxyde $U_{1-y-z}Pu_yAm_zO_{2\pm x}$. Des écarts par rapport aux recommandations de la littérature ont été mis en évidence, probablement liés à une réduction importante des échantillons à haute température. Un gonflement de la maille plus important a été observé lorsque la teneur en américium augmente dans les échantillons.

L'incréments enthalpique et la capacité calorifique de l'oxyde $U_{0,70}Pu_{0,28}Am_{0,02}O_{2,00}$ ont été calculés à l'aide de mesures réalisées par calorimétrie à chute entre 600 et 1800 K. Aucune influence de la présence d'américium n'a été observée pour les données d'incrément enthalpique par rapport à l'oxyde $U_{1-y}Pu_yO_2$. En revanche, une augmentation de la capacité calorifique pour T > 1100 K a été mise en évidence pour l'échantillon contenant de l'américium. Comme pour la dilatation thermique, cette observation pourrait être liée une importante réduction de l'échantillon et donc du plutonium comme l'américium est déjà purement trivalent à température ambiante.

Enfin, les températures de solidus ont été mesurées pour sept échantillons d'oxyde $U_{1-y--z}Pu_yAm_zO_{2\pm x}$ par chauffage laser. La variation du rapport O/M des échantillons après chaque tir a été déterminée grâce à la mesure de la pression partielle d'oxygène dans le dispositif expérimental. Une augmentation de la température de solidus a été observée avec l'augmentation de la teneur en américium alors que cette température diminue avec la teneur en plutonium. Différents comportements ont été mis en évidence concernant la variation du rapport O/M des échantillons pendant la fusion. En effet, les échantillons initialement sous-stœchiométriques (O/M < 2) ont tendance à s'oxyder pendant la fusion, tandis que les échantillons stœchiométriques ou légèrement sous-stœchiométriques se réduisent.

- Dans une dernière étape, la modélisation thermodynamique du système U-Pu-Am-O a été effectuée. Pour cela, les modèles de la phase liquide des systèmes Pu-O et U-Pu-O ont d'abord été réévalués sur la base de la sélection des données de températures de fusion les plus récentes. Pour le système U-Pu-O, un décalage de la composition congruente à la fusion a été observé vers le domaine sous-stœchiométrique (O/M~1.90). Ce phénomène a été expliqué par la stabilisation de la solution solide dans cette région, liée au désordre (lacunes d'oxygène et Pu^{3+}/Pu^{4+}) et à l'augmentation de l'entropie de configuration à haute température pour l'oxyde mixte par rapport aux pôles purs UO_2 et PuO_2. Grâce aux nouvelles données mesurées pour le système Pu-Am-O et les données disponibles dans la littérature, une réévaluation des modèles des phases MO_{2-x}, M_2O_3 et liquide a été proposée. Un bon accord a été obtenu entre le modèle et les données expérimentales pour les potentiels d'oxygène de la littérature ainsi que pour les équilibres de phase. En revanche, un écart significatif (~50 $kJ.mol^{-1}$) subsiste avec les potentiels d'oxygène mesurés dans ce travail.

Finalement, les données thermodynamiques et structurales mesurées pour le système U-Pu-Am-O ont été comparées au modèle thermodynamique du quaternaire, basé sur l'extrapolation de ses sous-systèmes binaires et ternaires. Un accord raisonnable est obtenu entre le modèle et les données expérimentales. L'influence de la présence d'américium reste très faible jusqu'à 5 mol.%. Cependant, des écart subsistent avec des données expérimentales, indiquant que de nouvelles mesures, en particulier sur les ternaires U-Am-O et Pu-Am-O sont nécessaires pour améliorer le modèle thermodynamique du système U-Pu-Am-O.

université PARIS-SACLAY

ÉCOLE DOCTORALE
Sciences Chimiques : Molécules, Matériaux, Instrumentation et Biosystèmes (2MIB)

Titre : Etude de l'influence de la présence d'américium sur les propriétés thermodynamiques et structurales des oxydes mixtes $(U,Pu)O_{2\pm x}$

Mots clés : Combustible nucléaire, americium, thermodynamique, structure

Résumé : L'oxyde mixte d'uranium et de plutonium $U_{1-y}Pu_yO_{2-x}$ est le combustible de référence pour la future génération de réacteurs à neutrons rapides à caloporteur sodium (Génération IV). La teneur en plutonium de ce combustible sera comprise entre 0,20 et 0,40 et leur stœchiométrie en oxygène ou rapport Oxygène/Métal (M = U+Pu+Am) devra être entre 1.94 et 2.00. De plus, pour ce combustible, le multi-recyclage du plutonium est envisagé. Cette étape induit des changements dans la composition isotopique initiale du plutonium, avec une diminution de la teneur en ^{239}Pu et une augmentation de celles en ^{238}Pu et ^{241}Pu. Avec une demi-vie de 14 ans, la désintégration bêta du ^{241}Pu entraine la formation de ^{241}Am dans le combustible avec une teneur Am/M pouvant aller jusqu'à 5 mol%. L'influence de l'américium sur les propriétés thermodynamiques et structurales de l'oxyde mixte doit donc être étudiée et prédite. L'objectif de cette thèse est la modélisation thermodynamique du système U-Pu-Am-O par la méthode CALPHAD, qui repose sur l'extrapolation des modèles des sous-systèmes binaires et ternaires. La première étape a consisté en l'analyse critique des données expérimentales disponibles dans la littérature sur les différents systèmes, qui a mis en évidence le manque de données sur les systèmes contenant de l'américium. Dans le système Pu-Am-O, des nouvelles données expérimentales ont été obtenues sur les équilibres de phases, les potentiels d'oxygène et les températures de transition solide/liquide pour des oxydes mixtes $Pu_{1-z}Am_zO_{2-x}$ avec z=0,23, 0,51 et 0,80. Les propriétés structurales (phases en présence, distribution cationique, expansion thermique) et thermodynamiques (incrément enthalpique, température de solidus) de différents oxydes mixtes $U_{1-y-z}Pu_yAm_zO_{2\pm x}$ (avec $0,235 < y < 0,39$ et $0,005 < z < 0,02$) ont ensuite été étudiées. Lors des mesures de températures de solidus par chauffage laser, grâce à l'utilisation de sondes à oxygène, la variation du rapport O/M des échantillons a pu être quantifiée pour la première fois. Sur la base de ces mesures, les modèles des systèmes Pu-O, U-Pu-O et Pu-Am-O ont été réévalués par la méthode CALPHAD pour mieux reproduire les données expérimentales. Le comportement à la fusion du système U-Pu-O a été étudié et a révélé un décalage de la température de fusion congruente des oxydes mixtes dans le domaine sous-stœchiométrique en oxygène. Les calculs thermodynamiques ont permis d'expliquer ce phénomène par la stabilisation de la solution solide dans ce domaine liée à la formation de défauts à haute température. La modélisation thermodynamique du système U-Pu-Am-O a également été comparée aux données expérimentales. L'oxydation ou la réduction des échantillons observées expérimentalement lors du chauffage laser a pu être expliquée par les calculs montrant une oxydation favorisée dans le cas d'échantillons initialement sous-stœchiométriques et une réduction favorisée pour des échantillons initialement sur- ou stœchiométriques. Sur la base des calculs d'applications et des résultats expérimentaux obtenus sur le système U-Pu-Am-O, une faible influence de la présence d'américium sur les propriétés thermodynamiques et structurales des oxydes $U_{1-y-z}Pu_yAm_zO_{2\pm x}$, pour des teneurs en Am jusqu'à z = 0,02, a été établie.

université PARIS-SACLAY

ÉCOLE DOCTORALE
Sciences Chimiques : Molécules, Matériaux, Instrumentation et Biosystèmes (2MIB)

Title : Study of the influence of americium on thermodynamic and structural properties of $(U,Pu)O_{2\pm x}$ mixed oxides

Keywords : Nuclear fuel, americium, thermodynamics, structure

Abstract : Uranium-plutonium mixed oxide $U_{1-y}Pu_yO_{2-x}$ is the reference fuel for future sodium fast reactors (Generation IV). The plutonium content considered for this fuel ranges between 0.20 and 0.40 and its oxygen stoichiometry or Oxygen/Metal ratio (M = U+Pu+Am) must be between 1.94 and 2.00. Furthermore, a multi-recycling of the plutonium is envisaged, which will induce a change in the initial isotopic composition with a decrease in the ^{239}Pu content and an increase in the proportions of ^{238}Pu and ^{241}Pu. Due to the half-life of ^{241}Pu ($\lambda_{1/2}$ = 14 years) and the elapsed time between fabrication and irradiation, up to 5 mol.% of ^{241}Am could be present in the fuel due to the β-decay of ^{241}Pu. The influence of the presence of Am on the thermodynamic and structural properties of $U_{1-y}Pu_yO_{2-x}$ has to be determined and predicted. The objective of this work is the thermodynamic modelling of the U-Pu-Am-O using the CALPHAD method, which is based on the extrapolation of the binary and ternary sub-systems. The first step consisted in performing a critical review of the experimental available data on the different sub-systems, highlighting the lack of data on americium-bearing systems. For the Pu-Am-O system, experimental data were obtained on phase equilibria, oxygen potential and solid/liquid phase transitions for $Pu_{1-z}Am_zO_{2-x}$ mixed oxides with z = 0.20, 0.50 and 0.80. Structural (phases, cationic distribution, lattice expansion) and thermodynamic (enthalpy increment, heat capacity, melting behaviour) properties of various $U_{1-y-z}Pu_yAm_zO_{2\pm x}$ ($0.235 < y < 0.39$ and $0.005 < z < 0.02$) were also investigated. During the laser heating experiments, the variation of the O/M ratio of the samples was quantified thanks to oxygen gauges. Based on these new sets of data, the models of the Pu-O, U-Pu-O and Pu-Am-O systems were re-assessed using the CALPHAD method to better reproduce the experimental data. The melting behaviour of the U-Pu-O system was investigated and highlighted a shift of the congruent melting composition towards the hypo-stoichiometric range. Thermodynamic calculations explained this observation by the stabilisation of the solid solution in this domain due to the formation of defects at high temperature. The thermodynamic modelling of the quaternary U-Pu-Am-O was also compared to the experimental data. The oxidation or reduction behaviour of the samples evidenced in the experiments was explained by thermodynamic calculations evidencing an oxidation favoured in the case of initially hypo-stoichiometric samples and a reduction enhanced for initially hyper- or near-stoichiometric oxides. Based on the thermodynamic calculations and the experimental results obtained for the U-Pu-Am-O system, a small influence of the presence of up to 2 % americium on the structural and thermodynamic properties of $U_{1-y-z}Pu_yAm_zO_{2\pm x}$ was highlighted.